

OFDM AIR-INTERFACE DESIGN FOR MULTIMEDIA COMMUNICATIONS

OFDM AIR-INTERFACE DESIGN FOR MULTIMEDIA COMMUNICATIONS

Proefschrift

ter verkrijging van de graad van doctor
aan de Technische Universiteit Delft,
op gezag van de Rector Magnificus Prof. dr. ir. J. T. Fokkema
voorzitter van het College van Promoties,
in het openbaar te verdedigen op dinsdag 2 april 2002 om 10.30 uur

door

Klaus WITRISAL

Diplomingenieur der Elektrotechnik,
Technische Universität Graz,
geboren te Graz, Oostenrijk.

Dit proefschrift is goedgekeurd door de promotoren:

Prof. dr. ir. L. P. Ligthart

Prof. dr. R. Prasad

Toegevoegd promotor:

Dr. ir. G. J. M. Janssen

Samenstelling promotiecommissie:

Rector Magnificus	voorzitter
Prof. dr. ir. L. P. Ligthart	Technische Universiteit Delft, promotor
Prof. dr. R. Prasad	Aalborg University, Denmark, promotor
Dr. ir. G. J. M. Janssen	Technische Universiteit Delft, toegevoegd promotor
Prof. ir. W. Dik	Technische Universiteit Delft
Prof. dr. H. Rohling	Technische Universität Hamburg-Harburg, Duitsland
Prof. dr. ir. W. C. van Etten	Universiteit Twente
Prof. dr. ir. J. W. M. Bergmans	Technische Universiteit Eindhoven

ISBN: 90-76928-03-7

Copyright © 2002 Klaus Witrissal

All rights reserved. No part of the material protected by this copyright notice may be reproduced or utilized in any form or by any means, electronic or mechanical, including photocopying, recording or by any information storage and retrieval system, without permission from the author Klaus Witrissal.

Cover Design by Arnold Zwanenburg (<http://www.polypo.com>)

Printed in Austria

To Silke
and my parents

Summary

The aim of this dissertation is the investigation of the key issues encountered in the development of wideband radio air-interfaces. Orthogonal frequency-division multiplexing (OFDM) is considered as the enabling technology for transmitting data at extremely high rates over time-dispersive radio channels. OFDM is a transmission scheme, which splits up the data stream, sending the data symbols simultaneously at a drastically reduced symbol rate over a set of parallel sub-carriers.

The first part of this thesis deals with the modeling of the time-dispersive and frequency-selective radio channel, utilizing second order Gaussian stochastic processes. A novel channel measurement technique is developed, in which the RMS delay spread of the channel is estimated from the level-crossing rate of the frequency-selective channel transfer function. This method enables the empirical channel characterization utilizing simplified non-coherent measurements of the received power versus frequency.

Air-interface and multiple access scheme of an OFDM-based communications system are proposed and investigated in part two of this work. Cumulative data rates up to 155 Mbit/s are reached under optimum channel conditions, in indoor and short range outdoor scenarios at low mobility (pedestrian speed). Wireless LANs (local area networks) are a typical application for the system.

Synchronization and channel estimation algorithms are developed and evaluated, utilizing a known training symbol, which is periodically transmitted in the beginning of the fixed frame structure. It has been concluded that robust and efficient synchronization and channel estimation schemes – critical tasks for an OFDM receiver – are enabled by this training symbol, at the cost of a very small overhead.

Detailed topics in synchronization include the analysis of a fine timing-offset estimation algorithm over multipath channels, and the analysis of the impact of DC-offsets and carrier feed-through on a popular frequency-synchronization scheme. A remedy is found for the latter issue.

For the up-link, pre-equalization is suggested in a time-division duplexing (TDD)

scheme to pre-compensate for the frequency-selectivity of the radio channel and thereby to simplify the data detection at the base station. Synchronization is mostly done by the mobiles, which implies a distribution of the high complexity involved. Concepts are presented for keeping the power of the up-link signal “constant” and for estimating the remaining synchronization-offsets.

The main signal processing algorithms for the OFDM transceivers have been implemented and validated on a DSP-based experimental platform, which operates in real-time, however, at drastically downscaled data rate.

Forward error correction coding is an essential part of OFDM schemes, because frequency-diversity is exploited by spreading the coded data symbols over the “large” signal bandwidth. The performance of coded OFDM systems is evaluated, indicating that increased system bandwidth and channel delay spread (the latter under certain constraints) lead to enhanced performance. A novel antenna diversity technique is proposed, which can improve the performance at low computational complexity, if the system bandwidth and/or the channel’s delay spread are small.

Generally, it has been concluded that the OFDM scheme is an efficient and robust method for transmitting data at very high rates. However, some critical hardware issues, as for instance the linearity of amplifiers and the phase noise of local oscillators, have to be solved.

Table of Contents

Summary	i
Table of Contents	iii
Chapter 1 – General Introduction.....	1
1.1 Towards Fourth Generation Mobile Systems	1
1.2 Wideband Air-interface Design using OFDM.....	3
1.3 Framework and Goal of this Ph.D. Project.....	6
1.4 Organization of this Thesis	6
1.4.1 Part I: Channel Characterization	7
1.4.2 Part II: OFDM System Proposal and Evaluation.....	7
1.5 Problems Addressed in this Dissertation.....	9
1.6 References.....	11
Part I: Channel Characterization	15
Chapter 2 – Modeling of the Frequency-Selective Radio Channel	17
2.1 Introduction.....	17
2.2 Characterization of the Mobile Radio Channel	18
2.2.1 Components of a Multipath Channel Model	19
2.2.2 Definitions	20
2.2.3 Variation of Channel Parameters Due to Bandwidth Limitation	24
2.3 Frequency-Domain Channel Modeling.....	26
2.3.1 The WSSUS Channel Model.....	26
2.3.2 Channel Description.....	29

2.3.3	Relation to (Physical) Channel Parameters	30
2.4	Frequency-Domain Channel Simulation	33
2.4.1	Model Description.....	33
2.4.2	Implementation of the Simulation Scheme	34
2.4.3	FD-Simulation Results	35
2.4.4	Differences to Time-Domain Simulation Schemes	39
2.5	Application to mm-Wave Radio Channels.....	39
2.5.1	Discussion of Measurement Results	40
2.5.2	Discussion of Channel Parameters.....	42
2.5.3	Overview of Channel Models.....	45
2.5.4	Applicability of the FD-model.....	47
2.6	Conclusions.....	48
2.7	References.....	50
Chapter 3 – Channel Measurement Technique based on the FD-Level Crossing Rate.....		55
3.1	Introduction.....	55
3.2	Frequency-Domain Level Crossing Rate	57
3.2.1	Derivation of the LCR_f from the Continuous FD-Channel Model.....	57
3.2.2	LCR_f for a Deterministic Two-Ray Channel.....	64
3.2.3	Derivation of the LCR_f for the Sampled Case.....	65
3.2.4	Discussion and Summary	72
3.3	Application to Channel Measurements	73
3.3.1	Channel Measurement Procedure	73
3.3.2	Validation of the Method using Measurement Results.....	74
3.3.3	Validation by Time-domain Channel Simulations	76
3.3.4	Discussion of the Measurement Method.....	79
3.4	Analysis of the Influence of Noise.....	79
3.4.1	Mathematical Modeling	81
3.4.2	Derivation of LCR_f from the Continuous FD-Channel Model.....	82
3.4.3	Discrete-Frequency Analysis for Rayleigh Channels.....	86
3.4.4	Evaluation and Application of the Analytical Results.....	87
3.4.5	A Robust Measurement Procedure	92
3.4.6	Extended Measurement Procedure	96
3.5	Conclusions and Recommendations	96
3.6	References.....	97

Part II: OFDM System Proposal and Evaluation.....	101
Chapter 4 – OFDM Introduction and System Modeling.....	103
4.1 Introduction.....	103
4.2 OFDM Introduction and System Model.....	104
4.2.1 OFDM Introduction and Block Diagram	104
4.2.2 Design of the OFDM Signal	106
4.2.3 OFDM System Model	109
4.2.4 Synchronization Errors.....	114
4.3 Performance of an Uncoded OFDM System.....	119
4.3.1 Mathematical Modeling	120
4.3.2 Analytical Evaluation of the BER.....	121
4.3.3 Performance Results.....	127
4.4 Conclusions and Recommendations	131
4.5 References.....	133
Chapter 5 – OFDM System Proposal and Emulation System.....	135
5.1 Introduction.....	135
5.2 OFDM Based System Proposal	136
5.2.1 Air Interface Physical Layer.....	137
5.2.2 Up- and Down-link Multiple Access Scheme	145
5.2.3 Architecture of the Transceivers.....	147
5.2.4 Forward Error Correction Coding.....	148
5.2.5 Link Budget	151
5.3 The Emulation System	152
5.3.1 Description of the Emulation System	154
5.3.2 Hardware Characteristics.....	158
5.3.3 Implementation of the Channel Simulator	160
5.4 Summary and Conclusions	163
5.5 References.....	165
Chapter 6 – DSP Algorithm Development for the Down-Link.....	167
6.1 Introduction.....	167
6.2 Overview of Synchronization Steps.....	169
6.2.1 Classification of Synchronization Techniques	169
6.2.2 Design of the Training Symbol.....	170
6.2.3 Frame Timing Synchronization	171
6.2.4 Fractional Frequency-Offset Synchronization	175

6.2.5	Application of the FFT	177
6.2.6	Integer Frequency-Synchronization	178
6.2.7	Remaining Timing-Offset Synchronization	181
6.2.8	Sampling Frequency-Offsets	185
6.2.9	Carrier Phase-Offset	187
6.2.10	Summary and Conclusions	189
6.3	Impact of DC-Offsets and Carrier Feed-Through on Fractional Frequency-Synchronization.....	189
6.3.1	Mathematical Modeling and Definitions.....	191
6.3.2	Analysis of the Synchronization Algorithm	191
6.3.3	Extension of the Algorithm	196
6.3.4	Analytical and Simulation Results.....	197
6.3.5	Conclusions and Recommendations	201
6.4	Channel Estimation	202
6.4.1	Wiener Filtering for Noise Reduction.....	203
6.4.2	Computational Results	206
6.4.3	Concluding Remarks	212
6.5	Experimental Results.....	213
6.5.1	Performance Results for the Full-Rate Receiver	214
6.5.2	Performance Results for the Quarter-Rate Receiver.....	218
6.5.3	Discussion of the Channel's Time-Variability	220
6.5.4	Conclusions and Recommendations	222
6.6	References.....	223
Chapter 7 – DSP Algorithm Development for the Up-Link.....		227
7.1	Introduction.....	227
7.2	Pre-Equalization in OFDM.....	228
7.2.1	OFDM System Model	228
7.2.2	Impact of Synchronization Errors	228
7.2.3	Channel Reciprocity and Pre-Equalization	229
7.2.4	Is the Channel Reciprocal?.....	229
7.3	Power Limiting Strategies for Pre-equalization	230
7.3.1	Phase Pre-Equalization for Phase-Modulation Schemes	230
7.3.2	Phase and Magnitude Pre-Equalization with Power Limiting	231
7.4	Performance Results.....	234
7.4.1	Application of Phase Pre-Equalization for QPSK.....	235
7.4.2	Application of Pre-Equalization with Power Limiting	235
7.5	Synchronization Parameter Estimation on the Up-link.....	237

7.5.1	Magnitude of the Constellation Values.....	238
7.5.2	Estimation of the Up-link Timing-Offset.....	239
7.6	Experimental Results.....	244
7.6.1	Performance over Different Radio Channels	244
7.6.2	Impact of the I/Q-Modulator and -Demodulator	245
7.7	Conclusions.....	246
7.8	References.....	248
Chapter 8 – Performance Evaluation and Enhancement of COFDM.....		249
8.1	Introduction.....	249
8.2	Performance of a Coded OFDM System.....	250
8.2.1	Review of the Concept of Effective E_b/N_0	251
8.2.2	Assessment of the Concept of Effective E_b/N_0	256
8.2.3	PDF of the Effective E_b/N_0	258
8.2.4	Performance Results and Discussion	262
8.2.5	Summary.....	268
8.3	Performance Enhancement using Antenna Diversity	270
8.3.1	Antenna Diversity for OFDM Using Cyclic Delays.....	271
8.3.2	Even/odd Sub-carrier Transmitter Diversity	275
8.3.3	Performance	277
8.3.4	Discussion of the Diversity Schemes.....	280
8.4	Conclusions and Recommendations	282
8.5	References.....	283
Chapter 9 – Conclusions and Recommendations		285
9.1	Part I: Channel Characterization.....	285
9.1.1	Modeling of the Frequency-Selective Radio Channel.....	285
9.1.2	Channel Measurement Technique using the FD-Level Crossing Rate.....	286
9.2	Part II: OFDM System Proposal and Evaluation.....	287
9.2.1	OFDM System Modeling	287
9.2.2	OFDM Air-Interface and Multiple Access Scheme Proposal	288
9.2.3	Issues in utilizing the 60 GHz Frequency-Band.....	289
9.2.4	Synchronization and Channel Estimation on the Down-Link.....	289
9.2.5	Pre-Equalization for the Up-Link	291
9.2.6	Emulation System and OFDM Implementation	292
9.2.7	Performance Evaluation and Enhancement of COFDM.....	293
Appendix A – Correlation Coefficient for the Discrete Impulse Response		295

A-1 Definitions	295
A-2 Calculation of the Correlation Coefficient	296
A-3 References	297
Appendix B – FD-Level Crossing Rate in the Presence of Noise	299
B-1 Derivation of the FD-Level Crossing Rate	299
B-2 Approximation 1	300
B-3 Approximation 2	301
B-4 References	302
Appendix C – Analysis of Fine Timing-Offset Estimation	303
C-1 Review of Estimation Technique and System Model	303
C-2 Estimation Bias over Dispersive Channels	305
C-3 Estimation Variance on the AWGN Channel	306
C-4 Estimation Variance on Rayleigh Fading Channels	308
C-5 References	310
Appendix D – PDF of Wide-band Average Received Power	311
D-1 PDF of Average Received Power for Rayleigh Fading Channels	311
D-1.1 Approximations	313
D-1.2 Analytical and Simulation Results	315
D-2 PDF of Average Power for Ricean Fading Channels	318
D-2.1 Approximations	319
D-2.2 Analytical and simulation results	320
D-3 References	324
List of Acronyms	325
Publications by the Author	329
Journal Papers	329
Conference Papers	329
Reports	331
Relation to this Thesis	331
Samenvatting	333
Acknowledgements	335
Curriculum Vitae	337

Chapter 1 – General Introduction

1.1 Towards Fourth Generation Mobile Systems

The expected convergence of the internet and mobile telephony fuels major research and development efforts in the telecommunications industries. “Third generation” (3G) cellular systems, called IMT-2000 (International Mobile Telecommunications in the year 2000) or UMTS (Universal Mobile Telecommunications System), are currently deployed to meet this demand, supporting data rates up to 2 Mbit/s for local coverage and at least 144 kbit/s for wide-area coverage [1]–[3].

But will those systems become as successful as their ancestors, particularly the (digital) second-generation systems like GSM (Global System for Mobile Communications), which for many years largely exceeded the expected growth rates, reaching penetration factors of well above 50 % in most western European countries? Are the new services offered sufficient motivation to buy new, in the beginning certainly rather expensive, mobile phones? Will the enormous cost of rolling-out such systems including license fees ever be amortized?

In my opinion, mobile “telephones” are *the* prerequisite to achieve large penetration rates with internet services. Many disadvantages of current internet access methods are eliminated: there is no need to buy or possess a computer, to cable a modem, to subscribe with an internet service provider, to go through lengthy start-up and log-in procedures, etc. Moreover, niche-time can be used to browse the Web; for instance the time spent on public transport, commuting to ones work. Advanced services can make effective use of the mobility aspect: Location-based services can provide the user with information related to his whereabouts (restaurant guide, cultural program, etc.), which is most useful in an unknown city but can be interesting in ones home-town as well.

For the mass-market, main ingredients for a successful deployment of 3G systems are:

- cheap, easy-to-use terminals,

- large color displays, and
- attractive billing schemes (flat rates).

The huge success of the Japanese i-mode system, which implements the above-mentioned features (however, providing low data rates compared to UMTS), proves the interest of the consumer in mobile internet services [4]. On the other hand, voice telephony (possibly augmented by still images and video) will remain an important application in future systems, where enhanced capacity and spectral efficiency need to be achieved.

While the roll-out of 3G systems is under progress, research activities on the fourth generation (4G) have already started [5]–[9]. At the time being, however, there is no clear vision which ingredients will define this future system generation. Certainly, transmission rates will be further increased – bit rates in the order of 100 Mbit/s are considered –, but many doubt that it will ever be feasible (affordable) to provide such data rates with nation-wide coverage. For local coverage, on the other hand, current wireless local area networks (W-LAN) standards can already provide data rates up to 54 Mbit/s. (Those W-LAN standards are: IEEE 802.11a in the USA, HIPERLAN/2 in Europe, and MMAC in Japan [10], [11]).

Therefore, a popular vision suggests to combine W-LAN systems for high peak data rates with cellular systems (GSM, UMTS) for wide area-coverage, and to allow inter-system handovers [12]. Technical aspects of air-interface standards for multi-standard terminals supporting W-LAN and cellular technologies are discussed in [13]. However, the more important factor for the user may be the simple fact that a W-LAN can be installed and operated by the user, free of cost for subscription and call-charges. That is, the user may own a part of the system infrastructure, and eventually – provided the required billing mechanisms are in place – even charge “foreign” terminals for accessing the system at his premises. This factor may become a key-ingredient of 4G systems. Other challenges to be solved in order to realize multi-standard systems include hardware issues for terminals supporting multiple air-interface standards, the above mentioned inter-system handovers, billing aspects, and security/privacy.

But is such an integration of systems enough reason to speak of a new system generation, particularly if only current air-interface standards are considered?

The scenarios weakly supported by current technology point out some limitations. Ad-hoc networking for instance, where a number of terminals form a small wireless network passing on information from node-to-node without the aid of an access point or a base station, is a concept that will become increasingly important [14]. “Bluetooth,” intended as a cable-replacement [15], supports this idea at somewhat limited bit-rates up to about 800 kbit/s and at very limited ranges of a few meters. At higher rates, the IEEE 802.11 W-LAN standard is considered by many as an enabling technology for ad-hoc networks [16]. Serious problems are encountered, however, when its current multiple access control (MAC) protocol is applied in such systems [16].

A wireless digital recording or television studio requires the support of multiple constant-rate data streams at specified bit-error-rates and low delay – a scenario that is very different to the previous one. A centralized, scheduled MAC could be most efficient for such applications, which may also be supported by 4G systems.

Last but not least, a “real” 4G air-interface to be developed may support data rates in the order of 100 Mbit/s at full mobility, i.e., at velocities up to 200–300 km/h [5]–[9], [12]. The term Mobile Broadband Systems (MBS) refers to this type of technology, in a number of references [5]–[7].

In this thesis, radio air-interface technology for future wide-band communications systems is studied, starting with the mathematical modeling of the fading radio channel.

This work has been motivated on the one hand by the huge potential market of wide-band communications systems, particularly of wireless LANs, and on the other hand – and more importantly –, by the technological challenge of developing air-interfaces for transmitting such large data rates over the hostile mobile radio channels. The following section elaborates on the technology aspect.

1.2 Wideband Air-interface Design using OFDM

Multipath propagation is the primary issue in the air-interface design for wideband (high data-rate) communications systems: multiple replicas of the transmitted signal arrive at the receiver with various propagation delays, due to reflections on all kinds of objects and obstacles in the environment. Therefore, if a high-rate data stream is transmitted on such a channel, multiple data symbols interfere with each other, making the data recovery difficult. At 155 Mbit/s, for instance, the symbol period is about 13 ns using QPSK (quadrature phase shift keying) and neglecting error correction coding.

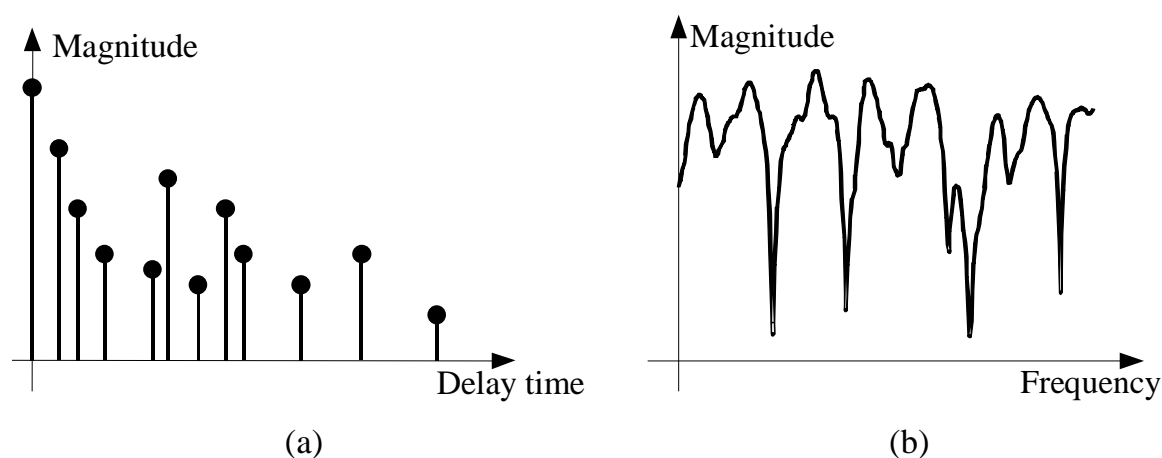


Figure 1-1: (a): Impulse response of a multipath radio channel. (b): Frequency-selective channel transfer function. The Fourier transform relates the impulse response and the transfer function.

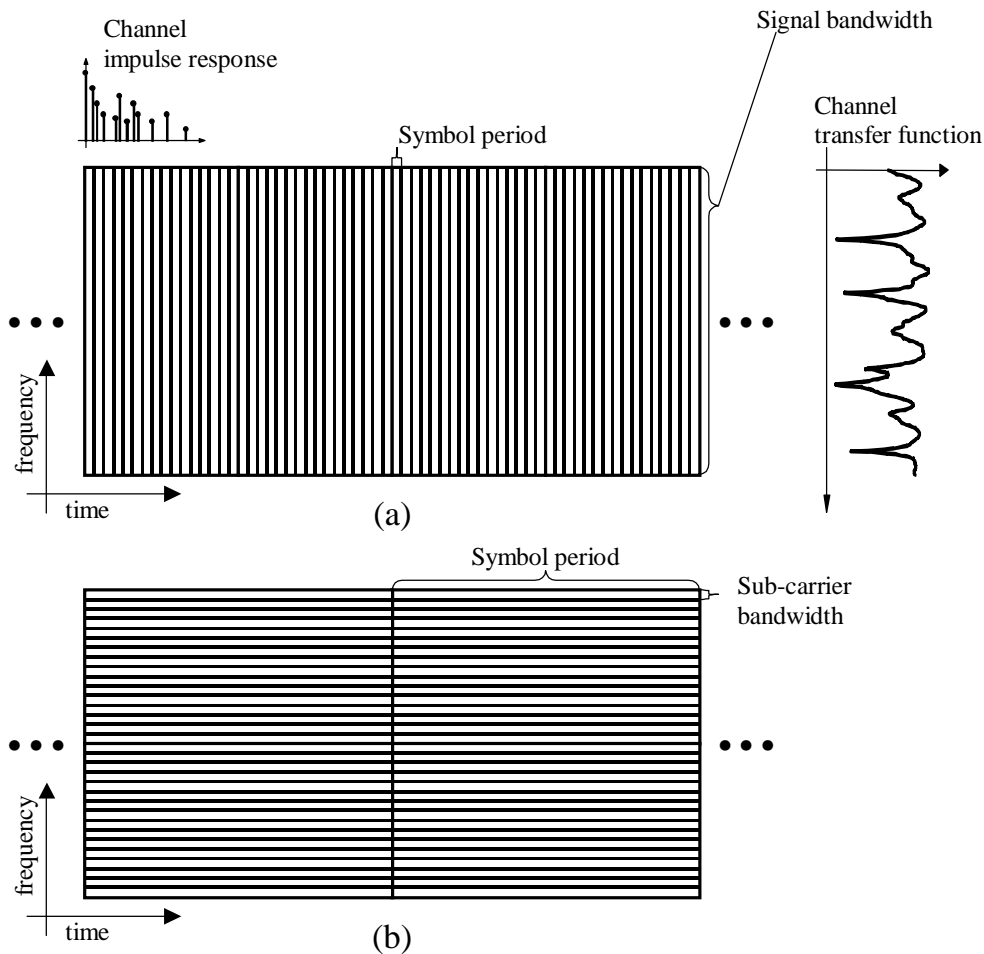


Figure 1-2: Symbol period and signal bandwidth in comparison with the channel impulse response and channel transfer function. (a): Single carrier system (serial transmission); (b): Multi-carrier system (OFDM) with parallel sub-channels.

This value can be compared with the (relative) delay of a reflected path with, say, 30 m path length difference, being 100 ns, which demonstrates that the combination of multiple data symbols is observed at the receiver at any given time instant. This phenomenon is called “inter-symbol-interference” (ISI). Receivers have to eliminate the ISI. Mathematically, the influence of the channel can be described as a convolution of the transmitted signal by the channel impulse response depicted in Figure 1-1a. Figure 1-2a illustrates the relation of the symbol period and the time-extent of the channel impulse response for a serial wideband transmission system.

Another characteristic property of a multipath radio channel is the frequency-selectivity of its transfer function (TF), as shown in Figure 1-1a. (The TF is the response of the channel to a narrow-band signal as a function of the frequency.) It is noted that the TF is the Fourier transform of the channel impulse response. The comparison of the signal bandwidth of the serial data stream and the channel transfer function demonstrates that a wide-band signal gets distorted when it is transmitted over such a channel (see Figure 1-2a).

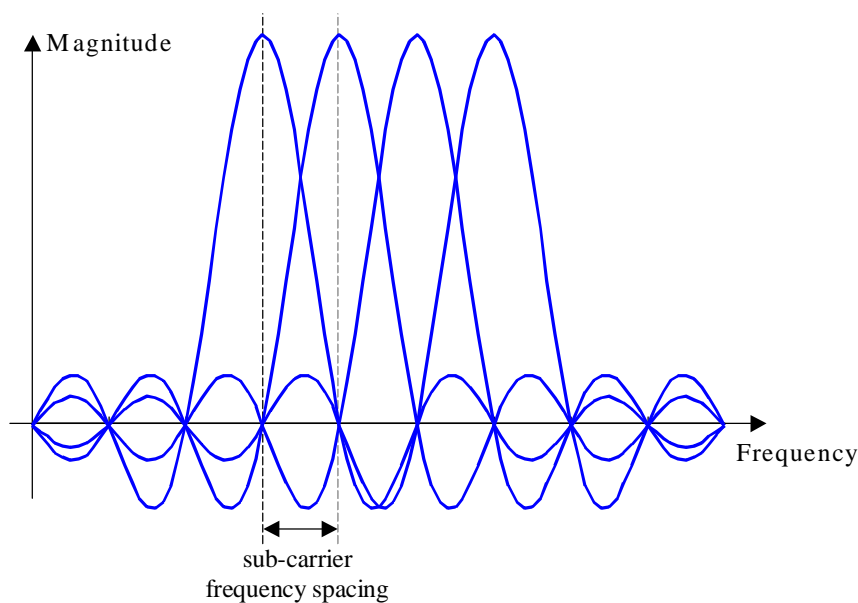


Figure 1-3: The overlapping spectra (sinc-functions) of four adjacent OFDM sub-carriers. At one sub-carriers center frequency, all other spectra are zero, demonstrating the sub-carrier orthogonality.

Equalization is the standard method to combat inter-symbol-interference in a single-carrier system [17]. Equalizers consist of linear filters whose purpose is to combine the signal components arriving at various delay times. The main challenge is to adapt the filter coefficients to the time-variant channel conditions. The methods for achieving this adaptation are computationally extremely demanding, particularly if long filters are required as in our case, where the channel impulse response typically spans many data symbols.

Orthogonal frequency division multiplexing (OFDM) can drastically simplify the equalization problem [11], [18]–[23]. In OFDM, the high-rate serial data stream is split up into a number (several dozens up to a few thousand) of parallel data streams at a much lower (common) symbol rate, which are modulated on a set of sub-carriers (frequency division multiplexing). Figure 1-2b illustrates the parallel transmission principle. High spectral efficiency is achieved by selecting a specific (orthogonal) set of sub-carrier frequencies. Inter-carrier-interference is avoided due to the orthogonality, although the spectra of the sub-carriers actually overlap (see Figure 1-3). The idea is to make the symbol period long with respect to the channel impulse response in order to reduce ISI. This implies that the bandwidth of the sub-carriers gets small (with respect to the channel’s coherence bandwidth [17]), thus the impact of the channel is reduced to an attenuation and phase distortion of the sub-carrier symbols (“flat fading”), which can be compensated by efficient one-tap equalization.

Digital signal processing is used to generate a complex-valued baseband signal contain-

ning all OFDM sub-carrier signals. (The block diagram of an OFDM transmission chain is shown in Chapter 4.) Next to the correct estimation of the channel transfer function, which is required for equalization, the following problems require particular attention in the implementation of OFDM modems:

- Linear power amplifiers are needed at the transmitter (and pre-amplifiers at the receiver) to avoid any distortion of the OFDM signal. Distortion would lead to inter-carrier-interference (ICI), implying performance degradation.
- At the receiver, synchronization issues are of prime importance. The start of the OFDM symbols and the exact location of the sub-carrier frequencies have to be found to be able to recover the data symbols (time- and frequency-synchronization).
- Phase noise of any mixer oscillators also yields ICI and thus has to be avoided/minimized.

1.3 Framework and Goal of this Ph.D. Project

The main topic of this dissertation is the design of the air-interface of an OFDM-based, wide-band mobile communications system for indoor and low-range, low-mobility outdoor scenarios. Wireless computer networks (W-LAN) are the intended application of such systems, enabling wireless multimedia communications. This work was conducted under the framework of a cooperative research program between Delft University of Technology (Delft, The Netherlands) and Korea Telecom (Seoul, South Korea). Funding was provided by Korea Telecom.

The emphasis of this study lay on the physical radio link. Wireless transmission of ATM (asynchronous transfer mode) cells should be supported at peak data rates of 155 Mbit/s, according to the target specifications of the air-interface multiple access scheme under development. The 60 GHz mm-wave frequency band was considered, mainly because the required bandwidth in the order of several hundreds of MHz is only available at these frequencies [24]. The mathematical modeling of the radio channel was the first goal of this project. Another important aspect was the implementation and validation of the proposed system on a hardware platform to be developed.

A number of students have contributed to the project and to this Ph.D. thesis, working on their graduation projects or on internships [25]–[35].

1.4 Organization of this Thesis

This Ph.D. thesis is divided in two parts. In Part I, the wide-band radio channel is modeled and investigated, while the OFDM system design is presented in Part II.

1.4.1 Part I: Channel Characterization

The radio channel model is probably the most important tool for the design of a communications system. It has to appropriately describe the relevant properties of the physical channel, and it should be suitable for computer simulations and analytical studies of the system under development. As in OFDM information is transmitted over a set of parallel sub-carriers, the main aspect of interest is the frequency-selectivity of the channel transfer function caused by multipath propagation.

The “frequency-domain channel model” proposed and studied in Chapter 2 of this dissertation directly describes this property by characterizing the variations of the transfer function via second-order stochastic properties. The model’s behavior is compared to physical propagation mechanisms and its parameters are related to parameters of the radio channel. Throughout this thesis, the model is applied for the design and evaluation of the OFDM system.

In Chapter 3, the *frequency-domain* level crossing rate (LCR_f) of the channel transfer function is analyzed. The LCR_f specifies the number of up-going level crossings over a given threshold per unit of bandwidth. Originally, the motivation for this study was to derive parameters equivalent to the (time-domain) level crossing rate and average fade duration [36], which are considered to be useful in the development and evaluation of mobile communications systems [37].

The most relevant application, however, was found in a slightly different field. It was discovered in this Ph.D. research that the LCR_f can be used for estimating the RMS delay spread of the channel, which is the most significant single parameter for characterizing the channel’s time-dispersion (and frequency-selectivity). This relationship enables channel measurements using a rather simple measurement setup, because it is sufficient to scan the *power* transfer function of the channel versus frequency to determine the LCR_f . The novel measurement technique is extensively studied in Chapter 3.

1.4.2 Part II: OFDM System Proposal and Evaluation

Chapter 4 gives a brief introduction to the OFDM transmission technique. System models are derived for the analysis of various aspects of OFDM. In Chapter 4, for instance, they are used to evaluate the bit-error-rate (BER) performance of an uncoded OFDM system, considering various modulation- and detection schemes, and different channel conditions. The results will serve as benchmarks for the evaluation of the OFDM receivers investigated in this thesis.

The air-interface and multiple access scheme of a novel OFDM-based wide-band communications system are described in Chapter 5. The system supports the transmission of single asynchronous transfer mode (ATM) cells at bit-rates up to 155 Mbit/s. To efficiently transmit such short data packets (one ATM cells consists of just 53 bytes) at

defined quality of service requirements, a fixed (but potentially asymmetric) frame structure is employed with time-division duplexing (TDD). Training symbols periodically transmitted on the down-link are used by the mobile for synchronization and channel estimation, while pre-equalization is considered for the up-link to enable coherent detection at the base station without introducing additional training symbols.

Chapter 5 also describes a digital signal processor (DSP) based experimental platform, the so-called “emulation system”, which has been developed for demonstrating the OFDM air-interface. All parameters have been largely downscaled to decrease the required processing speed (and to thereby simplify the software and hardware development), enabling the implementation of the transmitter and the receiver on single (but separate) DSP chips. A third DSP is used to simulate the multipath radio channel. Analog hardware performs in-phase/quadrature (I/Q) -modulation (to an intermediate frequency) and -demodulation, introducing frequency-offsets. Thus, real-time frequency-synchronization algorithms can be demonstrated. All system components are interconnected by analog, complex-valued baseband signals (I/Q-signals).

In Chapter 6, the signal processing steps for the down-link are investigated and evaluated. The estimation of synchronization parameters and of the channel transfer function are thoroughly described, utilizing the periodically transmitted training symbol. Novel contributions in this chapter concern the analysis of a highly accurate timing-synchronization scheme, and the investigation of the impact of DC-offsets and carrier feed-through on a popular class of frequency-synchronization techniques. The latter study leads to an extension of the technique with improved robustness against these impairments.

To save transmission power, to enhance the spectral efficiency, and to simplify the symbol detection, pre-equalization has been proposed for the up-link of the OFDM system. That is, the up-link symbols are pre-distorted using channel knowledge from the down-link, in order to compensate for the phase rotations and attenuations of the data symbols, introduced by the multipath radio channel. Channel reciprocity and slow time-variability are assumed. In Chapter 7, a number of basic issues of this principle are investigated, as for instance synchronization steps and techniques for limiting the transmitted power on the up-link. Moreover, it is discussed whether the channel reciprocity can be exploited for pre-equalization as proposed.

Forward error correction coding is a crucial component of most OFDM systems. Errors caused by the frequency-selective channel on severely attenuated sub-carriers can be corrected using the reliable data of strong(er) sub-carriers. That is, the frequency-diversity of the wide-band radio channel is exploited.

In Chapter 8, the performance of coded OFDM systems is evaluated using the “concept of effective E_b/N_0 ” [38]. In this method, the fading pattern of the radio channel is converted to a scalar value, the effective E_b/N_0 , which quantifies the signal-to-noise

ratio on an AWGN channel resulting in equivalent error rates. Channel simulations have to be performed to generate realistic fading patterns that can then be transformed to error rate results in this way. A novel extension to this concept is presented in this thesis. The probability density function of the effective E_b/N_0 is related to channel parameters, allowing for the analytical computation of average error rates and outage probabilities.

Novel antenna diversity schemes are proposed in the second part of Chapter 8 to enhance the performance in cases where the frequency-diversity of the channel is small (“flat” fading channels).

General conclusions and recommendations are summarized in Chapter 9.

1.5 Problems Addressed in this Dissertation

The following problems are analyzed in this Ph.D. thesis:

- ◆ Modeling of the frequency-selective radio channel
 - Characterization of frequency-selective, Ricean fading radio channels
 - Modeling of the frequency-selective channel using second order statistics of complex Gaussian random processes
 - Simulation of the frequency-selective channel transfer function in the frequency-domain
 - Application of the channel model to mm-wave radio channels
 - Selection of typical parameters for 60 GHz indoor and outdoor channels
- ◆ Measurement of channel parameters based on the frequency-domain level crossing rate (LCR_f) of the channel transfer function
 - Derivation of the LCR_f of a frequency-selective Ricean channel from its second order stochastic model
 - Impact of channel parameters on the LCR_f
 - Impact of the frequency-domain sampling interval (for Rayleigh channels)
 - Estimation of the RMS delay spread (a measure for the length of the channel impulse response) from the LCR_f
 - Independence of the LCR_f from the channel impulse response for Rayleigh channels with given RMS delay spread
 - Analysis of the influence of noise on the RMS delay spread estimation technique
- ◆ OFDM basics
 - Consideration of hardware aspects in the design of the OFDM system

- Modeling of an idealized OFDM system and the impact of (small) synchronization errors
- Bit-error-rate performance evaluation of an uncoded OFDM system over Ricean channels using several modulation schemes and coherent/differential detection
- ◆ Proposal of an OFDM-based air-interface and multiple access scheme for the transmission of ATM cells at data rates up to 155 Mbit/s
 - Discussion of the link budget of the system at 60 GHz
- ◆ Development of a DSP-based emulation system for the demonstration of the air-interface
 - Analysis of important hardware characteristics
 - Development of a channel simulator
- ◆ Development and analysis of synchronization algorithms for OFDM receivers
 - Design of a training symbol
 - Development and analysis of synchronization steps for time, carrier-frequency, sampling-frequency, and carrier-phase synchronization
 - Implementation of the synchronization algorithms on the emulation system
 - Performance analysis of a timing-offset estimation scheme in Ricean channels
 - Analysis of the impact of DC-offsets and carrier feed-through on a frequency synchronization scheme
 - Proposal of an enhanced frequency-synchronization scheme that is robust against DC-offsets and carrier feed-through
- ◆ Development and analysis of a computationally efficient channel estimation scheme using the training symbol
 - Reduction of the computational complexity of a Wiener filter used for minimizing the estimation error
 - Optimization of a fixed filter for various channel conditions
 - Performance evaluation in time-variant channels using the emulation system
 - Simulation of a channel prediction scheme for performance enhancement in time-variant channels
- ◆ Proposal and analysis of a pre-equalization technique for the up-link of a time-division-duplex OFDM system
 - Proposal and evaluation of transmit power limitation strategies required at the mobile
 - Development and evaluation of synchronization algorithms for the up-link
 - Implementation of the pre-equalization scheme and the synchronization algo-

gorithms on the emulation system

- ◆ Performance evaluation of convolutionally coded OFDM systems (with bit-level interleaving) using the concept of “effective E_b/N_0 ” [38]
 - Assessment of the concept of effective E_b/N_0
 - Application to OFDM systems
 - Modeling the probability density function of the effective E_b/N_0 for given channel- and OFDM system parameters
- ◆ Proposal and evaluation of antenna diversity techniques for the OFDM transmitter and/or receiver

1.6 References

- [1] *IEEE Personal Communications*, Special Issue on IMT-2000: Standards Efforts of the ITU, vol. 4, no. 4, Aug. 1997.
- [2] T. Ojanperä and R. Prasad, “An Overview of Air Interface Multiple Access for IMT-2000/UMTS,” *IEEE Communications Magazine*, vol. 36, no. 9, pp. 82–95, Sept. 1998.
- [3] M. W. Oliphant, “The Mobile Phone Meets the Internet,” *IEEE Spectrum*, vol. 36, no. 8, pp. 20–28, Aug. 1999.
- [4] K. Enoki, “i-mode: the mobile Internet service of the 21st century,” in Proc. *ISSCC 2001 (Solid-State Circuits Conference)*, 2001, pp. 12–15.
- [5] L. M. Correia and R. Prasad, “An Overview of Wireless Broadband Communications,” *IEEE Communications Magazine*, vol. 35, no. 1, pp. 28–33, Jan. 1997.
- [6] M. Dinis and J. Fernandes, “Provision of Sufficient Transmission Capacity for Broadband Mobile Multimedia: A Step Toward 4G,” *IEEE Communications Magazine*, vol. 39, no. 8, pp. 46–54, Aug. 2001.
- [7] M. Prögler, C. Evcı, and M. Umehira, “Air Interface Access Schemes for Broadband Mobile Systems,” *IEEE Communications Magazine*, vol. 37, no. 9, pp. 106–115, Sept. 1999.
- [8] H. Rohling, R. Grünheid, and D. Galda, “OFDM Air Interface for the 4th Generation of Mobile Communication Systems,” in Proc. *6th international OFDM-Workshop (InOWo’01)*, Hamburg, Sept. 2001, pp. 0-1-0-28.
- [9] NTT DoCoMo, “The Path to 4G Mobile,” *IEEE Communications Magazine*, vol. 39, no. 3, pp. 38–41, March 2001 (Advertisement).
- [10] R. van Nee, G. Awater, M. Morikura, H. Takeshi, M. Webster, and K. W. Halford, “New High-Rate Wireless LAN Standards,” *IEEE Communications Magazine*, vol. 37, no. 12, pp. 82–88, Dec. 1999.

- [11] R. van Nee and R. Prasad, *OFDM for Wireless Multimedia Communications*. Boston: Artech House, 2000.
- [12] L. M. Pereira, “Fourth Generation: Now, it is personal!,” in Proc. *PIMRC 2000 (11th International Symposium on Personal Indoor Mobile Radio Communications)*, London, Sept. 2000, pp. 1009–1016.
- [13] J. Kalliokulju, P. Meche, M. J. Rinne, J. Vallström, P. Varshney, and S.-G. Häggman, “Radio Access Selection for Multistandard Terminals,” *IEEE Communications Magazine*, vol. 39, no. 10, pp. 116–124, Oct. 2001.
- [14] S. Giordano and W. W. Lu, “Challenges in Mobile Ad Hoc Networking,” *IEEE Communications Magazine*, vol. 39, no. 6, p. 129, June 2001 (Guest Editorial).
- [15] R. Schneiderman, “Bluetooth’s Slow Dawn,” *IEEE Spectrum*, vol. 37, no. 11, pp. 61–65, Nov. 2000.
- [16] S. Xu and T. Saadawi, “Does the IEEE 802.11 MAC Protocol Work Well in Multihop Wireless Ad Hoc Networks?” *IEEE Communications Magazine*, vol. 39, no. 6, pp. 130–137, June 2001.
- [17] J. G. Proakis, *Digital Communications*, 3rd ed. New York: McGraw Hill, 1995.
- [18] R. Prasad, *Universal Personal Communications*. Boston: Artech house, 1998, ch. 10.
- [19] O. Edfors, M. Sandell, J. J. van de Beek, D. Landström, F. Sjöberg, “An Introduction to Orthogonal Frequency-Division Multiplexing,” *Research Report TULEA 1996:16*, Division of Signal Processing, Luleå University of Technology, <http://www.sm.luth.se/csee/sp/publications.html>.
- [20] M. Speth, S. A. Fechtel, G. Fock, and H. Meyr, “Optimum Receiver Design for Wireless Broad-Band Systems Using OFDM–Part I,” *IEEE Trans. Commun.*, vol. 47, no. 11, pp. 1668–1677, Nov. 1999.
- [21] S. B. Weinstein and P. M. Ebert, “Data Transmission by Frequency-Division Multiplexing Using the Discrete Fourier Transform,” *IEEE Trans. Commun. Techn.*, vol. COM-19, no. 5, pp. 628–634, Oct. 1971.
- [22] J. A. C. Bingham, “Multicarrier Modulation for Data Transmission: An Idea Whose Time has Come,” *IEEE Communications Magazine*, pp. 5–14, May 1990.
- [23] L. J. Cimini, “Analysis and Simulation of a Digital Mobile Channel using Orthogonal Frequency Division Multiplexing,” *IEEE Trans. Commun.*, vol. COM-33, no. 7, pp. 665–675, July 1985.
- [24] P. F. M. Smulders, *Broadband Wireless LANs: A Feasibility Study*. PhD Thesis, Eindhoven University of Technology, Eindhoven, The Netherlands, 1995.

-
- [25] V. Tutucu, "Channel Estimation for OFDM System in Multipath Fading Environments for Wireless Broadband Communications," *M.Sc. Thesis*, IRCTR S-028-98, Delft University of Technology, Sept. 1998.
- [26] J. Purwaha, "Wide-band Channel Measurements at 60 GHz in Indoor Environments," *M.Sc. Thesis*, Delft University of Technology (IRCTR), Aug. 1998.
- [27] R. el Hattachi, "Measurements and Modeling of the 18 GHz Radio Channel," *M.Sc. Thesis*, IRCTR S-029-98, Delft University of Technology, Aug. 1998.
- [28] P. Teneva, "Pseudo Real-time Simulation of an OFDM System for Wireless Broadband Communications: OFDM Transmitter," *Research Report*, IRCTR, Delft University of Technology, Jan. 1999.
- [29] K. Büke, "DSP Manual," *Research Report*, IRCTR S-025-99, Delft University of Technology, July, 1999.
- [30] K. Büke, "Assessment of OFDM Based Air-interface Techniques Using an Emulation Platform: Investigation and Implementation of OFDM Synchronization Algorithms," *M.Sc. Thesis*, IRCTR S-001-00, Delft University of Technology, Jan. 2000.
- [31] I. Gultekin, "DSP Software Implementation for a Broadband Air-interface Emulation Platform: Onderzoek naar de seriële interace tussen de PC an de DSP board en het maken van een GUI voor de DSP applicaties," *Graduation Thesis*, Haagse Hogeschool, June 2000 (in Dutch).
- [32] K. S. Lidsheim, "A survey of peak-to-average power reduction methods for the OFDM transmission schemes," *Research Report KWATT*, IRCTR S-024-00, Delft University of Technology, Sept. 2000.
- [33] A. Snijders, "Emulator: De testopstelling voor OFDM," *Graduation Thesis*, IRCTR S-030-00, Technische Hogeschool Rijswijk, Nov. 2000 (in Dutch).
- [34] D. Murargi, "Channel Estimation Enhancement in OFDM Systems for Wireless Multimedia Communications," *M.Sc. Thesis*, IRCTR S-028-98, Delft University of Technology and Technical University of Lisbon, July 2001.
- [35] G. Landman, "Frequency Domain Study of the Wide-Band Mobile Propagation Channel," *M.Sc. Thesis*, Delft University of Technology (IRCTR), Aug. 2001.
- [36] W. C. Jakes Jr., *Microwave Mobile Communications*. New York: Wiley-Interscience, 1974.
- [37] J. D. Parsons, *The mobile radio propagation channel*. New York: Wiley-Interscience, 2000.
- [38] S. Nanda and K. M. Rege, "Frame error rates for convolutional codes on fading channels and the concept of effective E_b/N_0 ," *IEEE Trans. Veh. Technol.*, vol. 47, no. 4, pp. 1245–1250, Nov. 1998.

Part I: Channel Characterization

Chapter 2 – Modeling of the Frequency-Selective Radio Channel

2.1 Introduction

“The channel model is the bread and butter for the telecommunications engineer” – this is how Ramjee Prasad, former Professor for Mobile Communications at Delft University of Technology, used to emphasize in his lectures the importance of the channel model for designing radio interfaces for wireless communications systems. And this was not just a phrase to keep the students’ attention. – The channel models really are the foundation, mobile communications systems are built on.

As the main topic of this thesis is the design of OFDM air-interfaces, the goal of this chapter is the description and discussion of an appropriate channel model for such systems. This model must allow for

- analytical treatment of OFDM related problems and for
- efficient computer simulation schemes,

to address two general requirements. According to the system’s key specifications, it should fit to physical radio channels in the mm-wave frequency band, for indoor (in-room) and short-range outdoor environments.

Radio propagation in a mobile radio channel is determined mainly by its multipath nature. Multiple reflections, and sometimes a line-of-sight (LOS) component of the transmitted signal arrive at the receiver via different propagation paths and therefore with different amplitudes and delay times. As an effect of this, the narrowband-received power fluctuates dramatically when observed as a function of location (or time) and frequency. In the early days of mobile systems, the communications

engineer was mainly interested in the time-variability of narrowband channels, which were thus studied extensively (see e.g. [1]). By that time, transmission bandwidths were small, thus flat-fading was a reasonable assumption. As the systems evolved, demand for higher transmission rates has been increasing, making the channel's time dispersion (which is equivalent to its frequency-selectivity) a major issue.

In OFDM, the channel's variability in the frequency-domain (FD) has a similar role as the time-variance in a (flat-fading) narrowband system. Usually, the channel can be assumed to be static during the transmission of at least one OFDM symbols. In indoor wireless local area networks (WLAN), the channel is even considered quasi stationary during up to a whole data packet or frame period.

The following section reviews the propagation mechanisms that have to be characterized by the channel model. The main properties of interest for the OFDM system design are emphasized and important channel parameters are defined.

The so-called frequency-domain channel model (FD-model) is proposed and analyzed in Section 2.3. The model describes the frequency-selective fading by the delay power spectrum (DPS) of the channel, the Fourier transform of the spaced-frequency correlation function [2]. This approach is dual to defining the time-variability by the Doppler power spectrum [3], which is often referred to as Jakes' fading model [1], [4]. Expressions are given, relating the DPS (being specified by just two to four parameters) to the most important physical channel parameters. Rayleigh and Ricean fading channels are considered.

A direct implementation of the FD-channel model in a computer simulation scheme is proposed in Section 2.4. The outputs of this simulator are (complex-valued) frequency-selective channel transfer functions. The differences are emphasized between this approach and (conventional) time-domain simulators, which generate channel impulse responses.

Section 2.5 summarizes the basic results of a number of measurement campaigns. Some of them were performed at Delft University of Technology, others were found in the literature. We elaborate on the suitability of the proposed channel model for describing the radio channels investigated.

Conclusions and recommendations are given in Section 2.6.

2.2 Characterization of the Mobile Radio Channel

This section starts with a qualitative description of the main propagation mechanisms resulting from multipath wave interference. Section 2.2.2 reviews mathematical definitions that are useful for the characterization of wide-band, frequency-selective, mobile radio channels. Important channel parameters are introduced and their physical interpretation is developed.

2.2.1 Components of a Multipath Channel Model

For the mathematical description of a multipath radio channel, it is convenient to distinguish three mechanisms; namely:

- path loss,
- shadowing, and
- multipath interference.

The former two are described by *large-scale* channel models, which essentially provide information about the average received power at a certain location. Path loss strictly describes the dependency of this average power on the distance between transmitter and receiver, while shadowing accounts for the fluctuations observed at a fixed distance, due to geometric features of the propagation environment. These fluctuations occur for instance because of the blocking of relevant propagation paths, e.g., the line-of-sight component, as the mobile moves around.

Highly sophisticated large-scale models that typically employ geographical information system (GIS) databases in order to account for topographical features are incorporated in the cell-planning tools used by mobile system operators. In indoor environments, ray-tracing models are often used to predict the received signal strength at a given location.

Such models are not relevant, however, for the design of new transmission techniques. For this application, the description of the effects of multipath interference is required, since the air-interface has to cope with them. These effects are often referred to as *small-scale* fading.

Small-scale models are valid within (small) local areas, where the signal fluctuations due to shadowing and path loss can be neglected. The dimension of such a local area is therefore limited to approximately $5 \dots 40\lambda$, where λ is the wavelength of the radio frequency (RF) carrier. (Due to the small wavelengths below one centimeter, this range may be even larger in the mm-wave band.)

The channel model investigated in this chapter is limited to the description of small-scale effects. A set of *average* parameters specifies the channel's behavior within a local area. These parameters are the normalized received power¹, P_0 , the Ricean K-factor, K , and the RMS delay spread (RDS), τ_{rms} . Note, however, that each realization obtained from the model has varying instantaneous parameters denoted $\{\hat{P}_0, \hat{K}, \hat{\tau}_{rms}\}$, since the model is a stochastic one. (To be specific, it is a Gaussian wide-sense stationary uncorrelated scattering (WSSUS) model, as shown in Section 2.3, and [5], [6]). The amount of variation of these parameters from the local-area parameters depends in

¹ The (dimensionless) normalized received power is defined as the ratio of the received power P_{rx} and the transmitted power P_{tx} . Equivalently, the absolute received power P_{rx} [W] could be used for channel description.

particular on the observed bandwidth. When the bandwidth is much greater than the coherence bandwidth, then the multipath is completely resolved and the channel parameters vary little, since the individual multipath amplitudes do not change rapidly within a local area. However, if the system is narrowband, then multipath is not resolved, and the path amplitudes at each resolvable (delay) time-bin (being spaced by the reciprocal of the bandwidth) vary due to multipath interference. This leads to the fluctuation of the instantaneous channel parameters within the local area (*cf.* [6], [7]).

The mathematical definitions of the channel parameters are given in the following section. Thereby, the behavior indicated above will be revisited based on the equations presented.

The selection of these parameters is an attempt to specify the main characteristics of the frequency-selective channel with a minimum number of variables. A very strong indication for the significance and suitability of the parameters chosen will follow from the analysis of the FD-level crossing rate in Chapter 3.

2.2.2 Definitions

2.2.2.1 Channel Impulse Response

It is most illustrative to start with the definition of the channel impulse response (IR), which is the straightforward formulation of the sum of discrete multipath components impinging at the receiver. In complex lowpass equivalent notation, the IR is written as

$$h(\tau) = \sum_i \beta_i e^{-j\theta_i} \delta(\tau - \tau_i), \quad (2-1)$$

where $\{\beta_i\}$, $\{\theta_i\}$, and $\{\tau_i\}$ are the propagation paths' amplitudes, phases, and delays, respectively, and τ is the delay-time variable. Normally, the delay of the first (shortest) ray is defined as $\tau_0 = 0$, because the absolute delay-times are not important, only the time-dispersion is. Therefore τ is called the excess delay-time, and it follows that $\tau_i > 0$ for $i > 0$, i.e., the channel impulse response is causal.

Note that in a real environment, the parameters $\{\beta_i\}$, $\{\theta_i\}$, and $\{\tau_i\}$ are time-variant. For the sake of simplicity, this time dependency was omitted in (2-1). Within a local area, i.e., for displacements in the order of a few wavelengths λ , the ray amplitudes $\{\beta_i\}$ and the delays $\{\tau_i\}$ can be considered relatively static – corresponding to the assumption of a negligible change of the shadowing. The ray phases $\{\theta_i\}$, however, change unpredictably within the interval $[0, 2\pi)$, because they are related to the absolute path-lengths².

² It is an open issue whether the assumption of discrete paths is viable. Generally, each reflection will show some time-dispersion, and therefore a frequency-dependent magnitude. However, for a given observation bandwidth, such physical paths can normally be approximated by (a number of) discrete Dirac-impulses.

2.2.2.2 Channel Parameters

All channel parameters introduced here are defined from the (static) power delay profile (PDP), which is a function derived from the channel IR (2-1). The PDP specifies the ray-power versus delay-time structure of the IR, being

$$p(\tau) = \sum_i \beta_i^2 \delta(\tau - \tau_i). \quad (2-2)$$

As the ray phases are dropped in this equation, the channel parameters must be (largely) constant within the local area, provided that the propagation paths are fully resolvable.

The first parameter is the (normalized) received power, being the sum of the ray powers

$$P_0 = \sum_i \beta_i^2. \quad (2-3)$$

The Ricean K-factor is the ratio of the dominant path's power to the power in the scattered paths, defined as

$$K = \frac{\beta_{i,\max}^2}{P_0 - \beta_{i,\max}^2}, \text{ where } \beta_{i,\max} = \max_i \{\beta_i\}. \quad (2-4)$$

It will be seen that the K-factor specifies the depth of the fades within a local area, as the Ricean probability density function (PDF) will be used to characterize the amplitude distribution of the channel response. Larger K-factors relate to shallower fades.

Note that in the presence of a line-of-sight, the first ray is the dominant one, implying that $\beta_{i,\max} = \beta_0$ at $\tau_0 = 0$.

Finally, the RMS delay spread is introduced, which is the second central moment of the (power normalized) PDP, written as

$$\tau_{rms} = \sqrt{\overline{\tau^2} - \bar{\tau}^2}, \text{ where } \bar{\tau}^m = \sum_i \tau_i^m \beta_i^2 / P_0, m = \{1, 2\}. \quad (2-5)$$

τ_{rms} is considered to be the most important single parameter for specifying the time-extent of the dispersive channel. It also characterizes the frequency-selectivity, since τ_{rms} is related to the average number of fades per bandwidth, and to the average bandwidth of the fades (see Section 3.2).

Smulders states, based on channel measurements over bandwidths of 2 GHz in the 60 GHz band, that mm-waves have sufficiently small wavelengths to be modeled as rays following discrete paths (see [8], p. 432 f.).

2.2.2.3 Channel Transfer Function

An equivalent description of the time-dispersive channel is obtained by applying the Fourier transform to the IR, yielding the channel transfer function (TF). This step will demonstrate that a time-dispersive channel is also frequency-selective.

Firstly, the time variability is re-introduced to the IR (2-1),

$$h(\tau, t) = \sum_i \beta_i(t) e^{-j\theta_i(t)} \delta(\tau - \tau_i(t)), \quad (2-6)$$

leading to the time-variant TF,

$$H(f, t) = \int_{-\infty}^{\infty} h(\tau, t) e^{-j2\pi f\tau} d\tau = \sum_i \beta_i(t) e^{-j[2\pi f\tau_i(t) + \theta_i(t)]}. \quad (2-7)$$

The magnitude of this function shows rapid variations with respect to both, the time- and frequency variables. $H(f, t)$ can be seen as the vector sum of the ray amplitudes $\{\beta_i(t)\}$, with vector-angles $[2\pi f\tau_i(t) + \theta_i(t)]$. As the ray phases $\{\theta_i(t)\}$ change rapidly for small displacements, the vector sum changes, causing the location and time-variability. The frequency-dependency is due to the different delay times $\{\tau_i(t)\}$, which, at different frequencies, also lead to drastic changes in the vector sum. The phases at two specific frequencies differ more with larger excess delay times $\{\tau_i(t)\}$. This suggests a dependency of the time-extent of the impulse response (which is characterized by the RMS delay spread), and the number of fades per unit of bandwidth. In Chapter 3, Section 3.2, this relation is extensively studied.

2.2.2.4 Magnitude Distribution

Due to the quasi-random phases of the terms of (2-7), $H(f, t)$ can be seen as the sum of a (large) number of random variables (RV) with amplitudes $\{\beta_i(t)\}$, and uniformly distributed phases over $[0, 2\pi)$. Assuming that a considerable number of rays has similar magnitudes (except for possibly one dominant ray), the central limit theorem leads to the conclusion that $H(f, t)$ has a complex Gaussian distribution. Without the dominant ray it is zero-mean, otherwise it is non-zero mean. The magnitude $R = |H(f, t)|$ of the complex Gaussian process is described by the Ricean PDF

$$p_R(r) = \frac{r}{\psi_0} e^{-\frac{(r^2 + \rho^2)}{2\psi_0}} I_0\left(\frac{r\rho}{\psi_0}\right), \quad (2-8)$$

where ψ_0 is the common variance of the real and imaginary components of the complex Gaussian process, ρ is the amplitude of the mean of $H(f, t)$, $\rho = |E\{H(f, t)\}|$, and $I_0(\bullet)$ is the zero-th order modified Bessel function of the first kind. For the zero-mean case ($\rho = 0$), the Ricean PDF reduces to the Rayleigh PDF³.

³ If the dominant component $\tau_{i,\max}$ occurs at a delay time different to $\tau_0 = 0$ (or at a non-zero

The parameters of (2-8) are related to the channel parameters P_0 and K as

$$\rho^2 = \beta_{i,\max}^2 = P_0 \frac{K}{K+1} \quad \text{and} \quad 2\psi_0 = P_0 - \beta_{i,\max}^2 = P_0 \frac{1}{K+1}. \quad (2-9)$$

Note that ρ^2 is the power of the dominant component, while $2\psi_0$ is the power of the scattered components. If the central limit theorem (plus dominant path) is not perfectly valid, then the parameters given in eq. (2-9) may still express a best fit of the Ricean distribution to the given channel. However, in this case, the magnitude of the dominant path $\beta_{i,\max}$ may be rather seen as an “equivalent” dominant path gain, which does not strictly relate to one physical propagation path.

2.2.2.5 Band-Limiting the Transfer Function and Sampling the Impulse Response

For computer simulation schemes, a sampled version of the channel IR is required, which implies the band-limitation of the respective TF. Let us first introduce the latter. A sampling interval T_s in the time-domain limits the bandwidth to $\pm \frac{BW}{2} = \pm \frac{1}{2T_s}$. Multiplication of the TF (2-7) by a rectangular window $W_{BW}(f)$ applies such band-limitation,

$$H_{BW}(f, t) = H(f, t) \cdot W_{BW}(f), \quad \text{where} \quad W_{BW}(f) = \begin{cases} 1 & \text{if } |f| \leq \frac{BW}{2} \\ 0 & \text{if } |f| > \frac{BW}{2} \end{cases}. \quad (2-10)$$

This step is equivalent to a convolution of the IR by a sinc-function,

$$h_{BW}(\tau, t) = h(\tau, t) * \text{sinc}(\tau/T_s) = \sum_i \beta_i(t) e^{-j\theta_i(t)} \text{sinc} \frac{\tau - \tau_i(t)}{T_s}, \quad (2-11)$$

where $\text{sinc } x = \begin{cases} \frac{\sin \pi x}{\pi x} & \text{if } x \neq 0 \\ 1 & \text{if } x = 0 \end{cases}$. Clearly, rays stop being resolvable, if the delay-time

separation between adjacent rays is in the range of T_s or below.

Sampling in the time-domain can be seen as a multiplication by a train of Dirac-impulses with period T_s . It therefore has the effect of convoluting the frequency-domain representation by a pulse train with period $1/T_s = BW$ [11]. The prior band-limitation keeps the thereby duplicated spectra from overlapping (i.e., aliasing is avoided), which essentially means that no information is lost through the sampling. The sampled IR becomes

$$h_{BW, n_\tau}(t) = \sum_i \beta_i(t) e^{-j\theta_i(t)} \text{sinc} \frac{n_\tau T_s - \tau_i(t)}{T_s}, \quad (2-12)$$

Doppler frequency), then the mean will become zero as well, as a (deterministic) complex harmonic component results. However, the amplitude distribution is still appropriately described by the Ricean distribution. (This case is described by Rice as the “Distribution of Noise plus Sine Wave” [9], [10]).

with $n_\tau = \{\dots, -1, 0, 1, 2, \dots\}$ being the discrete delay time index. From this equation, one can observe that the IR has contributions of all propagation paths at any time-bin n_τ . (Except if a ray has an excess delay of $\tau_i = kT_s$, where k is an integer – to be exact). Even at negative delay times, some “leakage” of the (causal) IR is evident. From (2-12) it also becomes clear that, for limited time-resolution or bandwidth, the sampled IR (at any time-bin n_τ) is rapidly time-variant, due to the time-dependency of the superimposed rays’ phases $\{\theta_i(t)\}$. Calculating channel parameters from this sampled IR results in instantaneous parameters $\{\hat{P}_0, \hat{K}, \hat{\tau}_{rms}\}$, which are time-variant, even within a local area, as discussed in Section 2.2.1. The variability of these parameters is shown in Section 2.2.3, based on simulation results.

The application of the central limit theorem again leads to the conclusion that complex Gaussian processes appropriately model the coefficients $\{h_{BW,n_\tau}(t)\}$ (cf. [6], [12]). Their variances follow the so-called average power delay profile, which usually decays with increased delay-time. In various channel models, the IR is described in this way (see e.g., [24]–[16]). The complex Gaussian distribution also applies to the ray gains of IRs derived from the FD-channel model, which is proposed in Section 2.3.

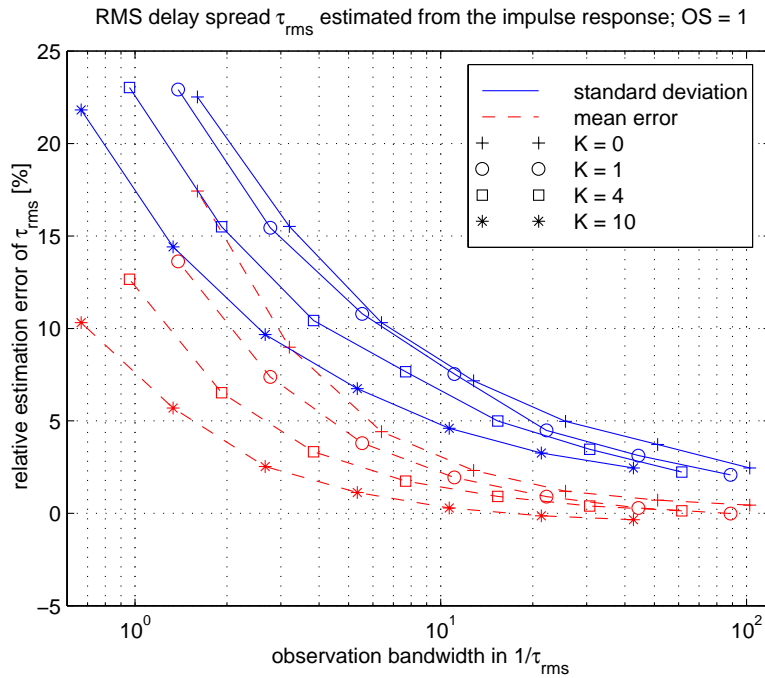
The above analysis is an attempt to describe theoretically the behavior of the time-variant, frequency-selective radio channel. It focuses on the aspects that are important for a deeper understanding of the FD-channel model. Therefore, particularly the frequency-selectivity of a band-limited, quasi-static channel has been discussed.

2.2.3 Variation of Channel Parameters Due to Bandwidth Limitation

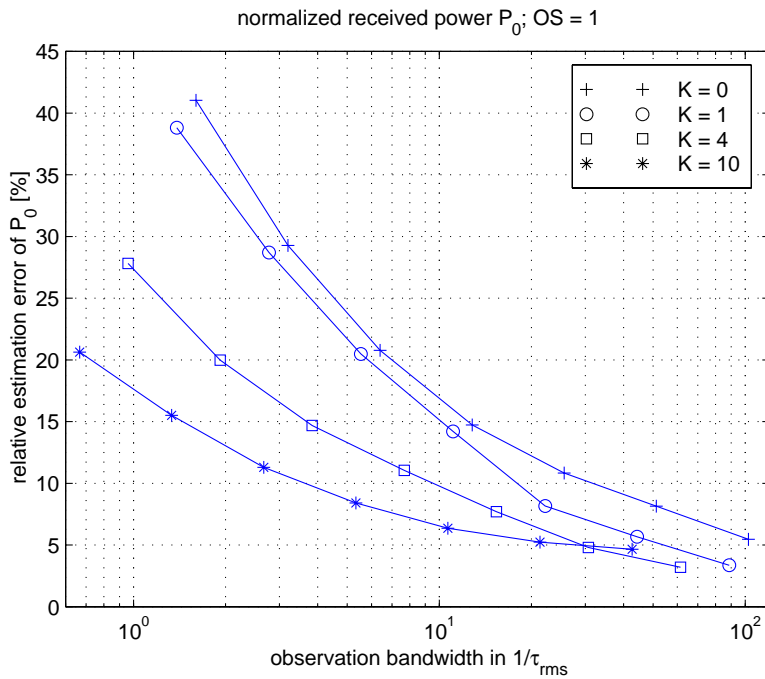
Simulation results are presented in this section, of the variability of instantaneous channel parameters within a local area.

Channel realizations were generated with a time-domain (TD) simulation scheme, which produces channel impulse responses. The simulation model assumes a line-of-sight ray at $\tau = 0$, a Poisson process of ray-arrivals (of approx. 60 rays), an exponentially decaying average power delay profile, and complex Gaussian ray amplitudes (compare [16] for one cluster; see Section 2.5.3). In a second step, the impulse responses were normalized to get the required K-factor K , $\tau_{rms} = 1$ and $P_0 = 1$ [15], allowing for simple evaluation of the estimation error. Applying the Fourier transform to the generated IRs, (complex-valued, discrete-frequency) TFs were obtained, with arbitrary bandwidth.

The variability of $\hat{\tau}_{rms}$ and \hat{P}_0 within a local area is depicted in Figure 2-1a and Figure 2-1b, respectively. For analyzing $\hat{\tau}_{rms}$, the simulated TFs were transformed back to the delay time-domain using the inverse discrete Fourier transform (DFT) without windowing. Consecutively, $\hat{\tau}_{rms}$ was determined from the positive- τ part of the obtained, sampled channel IR, using eq. (2-5). \hat{P}_0 is simply the average power of the band-



(a)



(b)

Figure 2-1: (a): Bias and standard deviation of the instantaneous RMS delay spread $\hat{\tau}_{rms}$ within a local area due to band-limitation. (The bias is caused by leakage effects). (b): Standard deviation of the instantaneous normalized received power \hat{P}_0 within a local area.

limited TFs.

The standard deviations of these parameters decrease with increasing bandwidth, because individual “propagation” paths become gradually more resolvable. The estimation bias in $\hat{\tau}_{rms}$ (see Figure 2-1a) is due to leakage effects.

Reduced variance and bias for higher K -factor are intuitively explained by the fact that the (deterministic) dominant path largely determines Ricean channels. Note that K has most influence on the instantaneous values of the average power P_0 . This behavior can be anticipated, since K directly relates to the depth of the fades. I.e., a channel with a high K -factor (which has shallow fades) shows less variation in this parameter, than for instance a Rayleigh fading channel (which has quite deep fades).

2.3 Frequency-Domain Channel Modeling

The channel model proposed in this section describes the correlation properties of the channel transfer function in the frequency-domain. Starting from the definition of the channel correlation functions (and power spectra), this so-called frequency-domain channel model is derived. Mathematical expressions are given, relating the model’s parameters to (physical) channel parameters.

2.3.1 The WSSUS Channel Model

The channel correlation functions and power spectra are a set of functions defining the small-scale characteristics of multipath fading channels in more detail than the channel parameters given above. Introducing some assumptions will lead to the channel model used throughout this work. In particular, we concentrate in this work on the correlation properties of the time-variant transfer function $H(f,t)$ (see (2-7)), because this function determines the channel’s impact on an OFDM system modeled as a set of parallel Gaussian channels (see Section 4.2, [17]). Considering the mobile radio channel as a linear time-variant system, it is seen that the TF $H(f,t)$ is only one possible channel representation (from the family of Bello’s system functions [5], [6]). Another one is, for instance, the time-variant impulse response given by (2-6).

Let us first define the channel correlation functions assuming that those functions are wide-sense stationary. This means that the autocorrelation function

$$\phi_H(f_1, f_2, t_1, t_2) = E\{H^*(f_1, t_1)H(f_2, t_2)\} \quad (2-13)$$

depends only on the frequency-separation $\Delta f = f_1 - f_2$ and on the time-separation $\Delta t = t_1 - t_2$, but not on the absolute observation frequencies $\{f_1, f_2\}$ and times $\{t_1, t_2\}$. In other words, the time-variant transfer function $H(f,t)$ is wide-sense stationary (WSS) with respect to both variables f and t . The channel is thus characterized for all times and all frequencies by the so-called spaced-frequency, spaced-time correlation function

$$\phi_H(\Delta f, \Delta t) = E\{H^*(f, t)H(f + \Delta f, t + \Delta t)\}. \quad (2-14)$$

It can be shown that this assumption is equivalent to the introduction of the wide-sense stationary and uncorrelated scattering (WSSUS) channel (see e.g., [5], [6], [2]). In the WSSUS channel, the WSS-property applies to the time variability of the IR $h(\tau, t)$. The uncorrelated scattering (US) property is based on the assumption that the attenuation and phase of a propagation path at delay time τ_i is uncorrelated to the attenuation and phase at delay time τ_k , for $i \neq k$.

In order to apply the concept of the WSSUS channel to real radio channels, the quasi-WSSUS channel (QWSSUS) was introduced by Bello [5]. A QWSSUS channel has the properties of a WSSUS channel within a local area, and for a limited bandwidth and time.

Furthermore, it should be noted that for Gaussian processes, the WSS property implies stationarity in the strict sense. If the distribution of the TF $H(f, t)$ is complex Gaussian, with zero- or non-zero mean, then the amplitude distribution is Rayleigh or Ricean, respectively. As this agrees to the channel properties derived in Section 2.2.2, and as Gaussian processes generally simplify any stochastic mathematical analysis, the complex Gaussian case will be assumed.

In Figure 2-2, an overview is given of the most commonly used correlation functions and power spectra defining the stochastic properties of the time-variant channel IR, and TF. These system functions are found in the center of the figure, surrounded by their second order moments, which are interrelated by Fourier transforms. As mentioned above, our focus lies on the spaced-frequency, spaced-time correlation function depicted just above the center of this figure.

2.3.1.1 Special Cases

Most of the analysis presented in this thesis concentrates on the case of the time-invariant frequency-selective channel. The channel is then described by the TF $H(f)$, which is a WSS complex Gaussian stochastic process in f , according to the above assumptions. The second order statistical functions characterizing $H(f)$ are the spaced-frequency correlation function $\phi_H(\Delta f) = \phi_H(\Delta f, 0)$ and its Fourier transform (FT), the delay power spectrum (DPS) $\phi_h(\tau)$ (see Figure 2-2). A mathematical description of the DPS will be the basis of the so-called frequency-domain (FD) channel model.

More familiar is the dual approach of modeling the time variability of a narrowband channel as a WSS complex Gaussian stochastic process $H(t)$. An example for this method is widely known in the literature as Jakes' fading model [1]. Compared to the FD model, the frequency variable is exchanged with the time variable, and the second order statistics are the spaced-time correlation function $\phi_H(\Delta t) = \phi_H(0, \Delta t)$ and the Doppler power spectrum $S_H(\nu)$ for Doppler frequency ν , which are a Fourier pair as well (see Figure 2-2).

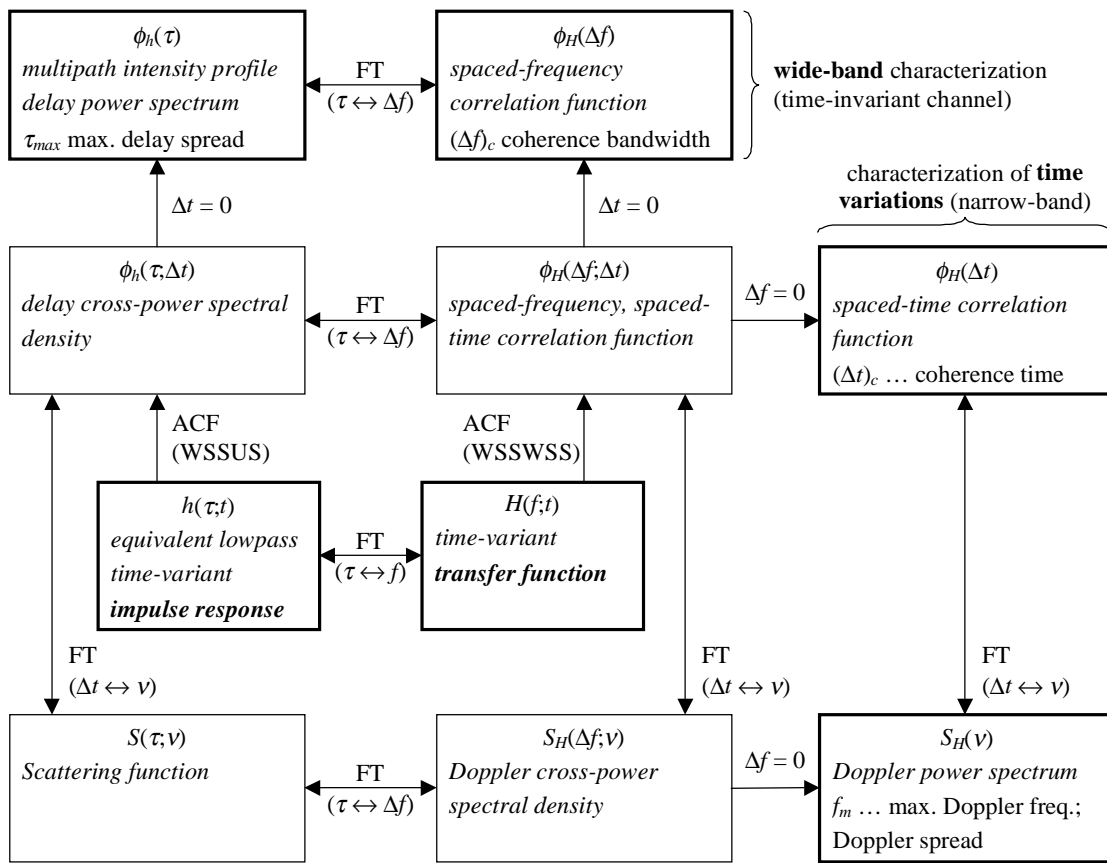


Figure 2-2: Overview of the two time-variant system functions described – the channel impulse response and the channel transfer function – and a set of correlation functions (second order moments) describing their stochastic properties.

2.3.1.2 Additional Channel Parameters

Figure 2-2 also introduces some additional channel parameters, which are derived from the correlation functions and power spectra.

Coherence-time and -bandwidth indicate the ranges (in time and frequency) over which the TF $H(f, t)$ shows significant correlation. They are defined as the time- or frequency-separations Δt and Δf , where the spaced-time or -frequency correlation functions, respectively, drop below 0.9. (Sometimes 0.5 is used for this threshold.)

Related to the power spectra, the maximum delay spread and the Doppler spread are defined, corresponding to the maximum delay-time and frequency-components in these spectra.

Often, mathematical relations are given in-between these parameters, i.e., between the coherence-bandwidth and the (reciprocal of the) maximum delay spread or the RMS delay spread, and between the coherence-time and the (reciprocal of the) Doppler spread. However, these relations loose significance in the Ricean case, since the dominant component (leading to the non-zero mean of the Gaussian distribution)

causes a constant additive term in the channel correlation functions [15]. Therefore, these relationships should be used with care.

2.3.2 Channel Description

The delay power spectrum (DPS) characterizes the frequency-selectivity in the FD-channel model. In agreement with measurements reported in [24], the shape of the DPS is defined as shown in Figure 2-3. It is specified by four parameters: ρ^2 – the normalized power of the direct ray; Π [1/s] – the normalized power density of the constant-level part; τ_1 [s] – the duration of the constant level part; and γ [1/s] – the decay exponent of the exponentially decaying part. Mathematically, the DPS can be written as

$$\phi_h(\tau) = \begin{cases} 0 & \tau < 0 \\ \rho^2 \delta(\tau) & \tau = 0 \\ \Pi & 0 < \tau \leq \tau_1 \\ \Pi e^{-\gamma(\tau-\tau_1)} & \tau > \tau_1 \end{cases} \quad (2-15)$$

In many cases, the number of (free) parameters can be further decreased. The exponentially decaying DPS is a good approximation for most practical channels, which is implemented by letting $\tau_1 = 0$. The existence of a line-of-sight (LOS) ray at $\tau = 0$ implies that the channel TF has non-zero mean, thus the fading envelope distribution is Ricean. Rayleigh fading channels have $\rho = 0$.

For the analysis it is appropriate to define $u = \tau_1 \gamma$, being a single parameter to account for the shape of the DPS. u can take values $u \in [0, \infty]$, where the two extreme cases $u = 0$ and $u = \infty$ describe an exponentially decaying and a rectangular DPS, respectively. Note that in the latter case (rectangular DPS), the maximum excess delay will be much smaller than for $u = 0$, thus u can be used to adjust this parameter (see below).

Relations between the model parameters defined above and the channel parameters are presented in Section 2.3.3.

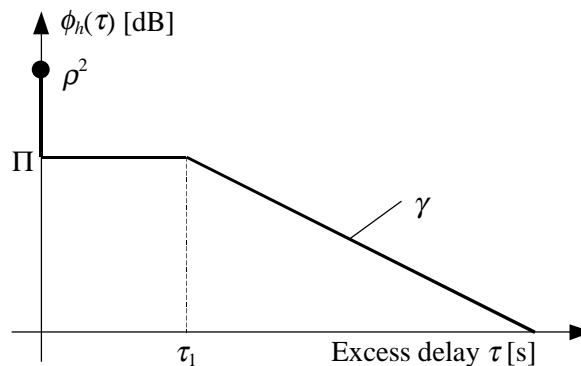


Figure 2-3: Model of the delay power spectrum (DPS).

2.3.3 Relation to (Physical) Channel Parameters

For the application of the FD-channel model, it is most important to relate its parameters $\{\rho^2, \Pi, \gamma, \tau_1\}$ to the channel parameters defined in Section 2.2.2: the normalized received power P_0 , the Ricean K-factor K , and the RMS delay spread τ_{rms} .

The channel parameters derived from the channel model are the local-area means, as discussed in Section 2.2. Finite bandwidth realizations or measurements within a local area have ‘instantaneous’ channel parameters $\{\hat{P}_0, \hat{K}, \hat{\tau}_{rms}\}$ spread around those means.

Table 2-1 gives an overview of expressions relating the model parameters $\{\rho^2, \Pi, \gamma, \tau_1\}$ to the channel parameters $\{P_0, K, \tau_{rms}\}$ and vice versa. The derivation of these equations is outlined below. For notational convenience we introduce $u_1 = u + 1$, $u_2 = u^2/2 + u + 1$, and $u_3 = u^3/3 + u^2 + 2u + 2$, with $u = \tau_1 \gamma$. An important special case is given by $u = 0$, the exponentially decaying DPS, which is an appropriate description for many practical channels. Table 2-1 also lists the simplified expressions for this case.

2.3.3.1 Derivation of Channel Parameters

From the continuous DPS $\phi_h(\tau)$ defined by (2-15), the analytical expressions given in

Table 2-1: Relation between model and channel parameters. (The symbols are defined in the text).

model \rightarrow channel	
$u = \tau_1 \gamma \in [0, \infty]$	$u = 0$
$P_0 = \rho^2 + \frac{\Pi}{\gamma} u_1$	$P_0 = \rho^2 + \frac{\Pi}{\gamma}$
$K = \frac{\rho^2 \gamma}{\Pi u_1}$	$K = \frac{\rho^2 \gamma}{\Pi}$
$\tau_{rms} = \frac{1}{\gamma} \sqrt{\frac{1}{K+1} \frac{u_3}{u_1} - \frac{1}{(K+1)^2} \frac{u_2^2}{u_1^2}}$	$\tau_{rms} = \frac{1}{\gamma} \frac{\sqrt{2K+1}}{K+1}$
channel \rightarrow model	
$u = \tau_1 \gamma$ (must be known)	$u = 0$
$\rho^2 = P_0 \frac{K}{K+1}$	$\rho^2 = P_0 \frac{K}{K+1}$
$\gamma = \frac{1}{\tau_{rms}} \sqrt{\frac{1}{K+1} \frac{u_3}{u_1} - \frac{1}{(K+1)^2} \frac{u_2^2}{u_1^2}}$	$\gamma = \frac{1}{\tau_{rms}} \frac{\sqrt{2K+1}}{K+1}$
$\Pi = \frac{P_0}{K+1} \cdot \frac{\gamma}{u_1}$	$\Pi = \frac{P_0}{K+1} \gamma$

Table 2-1 can be derived for the expected values of normalized received power P_0 , Ricean K-factor K , and RMS delay spread τ_{rms} . P_0 relates to the DPS as

$$P_0 = \int_0^{\infty} \phi_h(\tau) d\tau = \rho^2 + \Pi \cdot \left[\tau_1 + \frac{1}{\gamma} \right]. \quad (2-16)$$

The K-factor is used to characterize the amplitude distribution of Ricean channels, relating the power of the direct path to the power of the scattered paths.

$$K = \frac{\rho^2}{P_0 - \rho^2} = \frac{\rho^2}{\Pi \cdot (\tau_1 + 1/\gamma)} \quad (2-17)$$

The RMS delay spread τ_{rms} is the single most important parameter characterizing the frequency-selectivity. It can be interpreted as the centralized second moment of the normalized DPS

$$\tau_{rms} = \sqrt{\overline{\tau^2} - (\bar{\tau})^2}, \quad (2-18)$$

where

$$\bar{\tau} = \int_0^{\infty} \tau \frac{\phi_h(\tau)}{P_0} d\tau = \Pi \cdot \left[\frac{\tau_1^2}{2} + \frac{\tau_1}{\gamma} + \frac{1}{\gamma^2} \right], \text{ and} \quad (2-19)$$

$$\overline{\tau^2} = \int_0^{\infty} \tau^2 \frac{\phi_h(\tau)}{P_0} d\tau = \Pi \cdot \left[\frac{\tau_1^3}{3} + \frac{\tau_1^2}{\gamma} + \frac{2\tau_1}{\gamma^2} + \frac{2}{\gamma^3} \right]. \quad (2-20)$$

2.3.3.2 Spaced-Frequency Correlation Function

The spaced-frequency correlation function is used repeatedly throughout this thesis to implement the channel-behavior in the mathematical analysis of the radio channel and in the analysis of OFDM system aspects. It is derived from the DPS (2-15) via the Fourier transform:

$$\begin{aligned} \phi_H(\Delta f) &= E\{H^*(f)H(f + \Delta f)\} = F\{\phi_h(\tau)\} = \\ &\rho^2 + \Pi \cdot \tau_1 \text{sinc}(\tau_1 \Delta f) e^{-j\pi \tau_1 \Delta f} + \Pi \cdot \frac{1}{\gamma + j2\pi \Delta f} e^{-j2\pi \tau_1 \Delta f} \end{aligned} \quad (2-21)$$

For $\tau_1 = 0$, i.e., for the special case of an exponentially decaying DPS, the spaced-frequency correlation function can be written as

$$\phi_H(\Delta f) = \frac{P_0}{K+1} \left(K + \frac{1}{1 + j2\pi \Delta f \tau_{rms} K_1} \right), \quad (2-22)$$

where, $K_1 = (K+1)/\sqrt{2K+1}$.

2.3.3.3 Maximum Excess Delay

The shape factor u introduces another degree of freedom in the channel model, which allows the variation of the maximum excess delay τ_{max} by a certain factor, for a given RMS delay spread τ_{rms} . Strictly speaking, the maximum delay spread is infinite due to the exponentially decaying part of the DPS, which never becomes zero. In practice, however, multipath components can be neglected that are attenuated very significantly. We therefore define the maximum excess delay as the delay time, where the exponentially decaying part has decreased by about 43 dB. Such attenuation is reached, if the duration of the exponentially decaying part is exactly $\tau_{exp} = 10/\gamma$, leading to the maximum delay spread $\tau_{max} = \tau_1 + \tau_{exp} = \tau_1 + 10/\gamma$. Expressed in terms of channel parameters this is

$$\tau_{max} = \tau_{rms} (u + 10) \frac{u_1(K + 1)}{\sqrt{u_1 u_3 (K + 1) - u_2^2}}, \quad (2-23)$$

which simplifies for $u = 0$ (i.e., $\tau_1 = 0$) to

$$\tau_{max} = \tau_{rms} 10 \frac{K + 1}{\sqrt{2K + 1}} = 10 \tau_{rms} K_1. \quad (2-24)$$

It is seen that τ_{max} and τ_{rms} are related by a factor, which is a function of K and u . Figure 2-4 illustrates this factor. According to this definition, τ_{max} is exactly ten times larger than τ_{rms} at $K = 0$, and $u = 0$. Larger K -factors generally increase this factor,

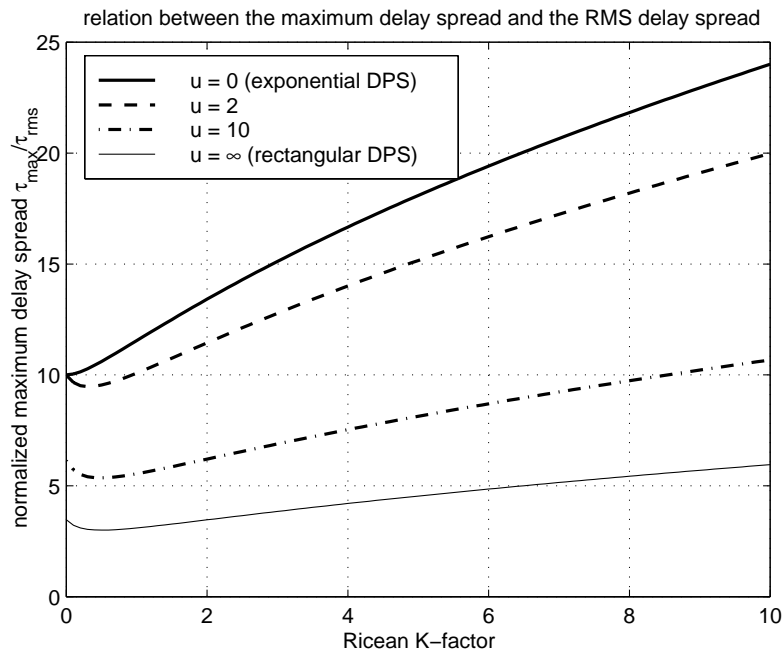


Figure 2-4: Factor between the maximum delay spread τ_{max} and the RMS delay spread τ_{rms} , as a function of the Ricean factor K and with the shape factor u as a parameter.

larger parameters u decrease it. For instance, τ_{max} is only about three times τ_{rms} for the rectangular DPS, at low K -factors.

As the maximum delay spread τ_{max} defines the maximum “frequency” component of the DPS, it is this parameter which defines the Nyquist frequency when a sampled version of the channel transfer function is needed in measurements or computer simulations. That is, the sampling interval in the frequency-domain must be smaller than $1/(2\tau_{max})$.

2.4 Frequency-Domain Channel Simulation

The discussion of simulation schemes in this section is restricted to the case of static (time-invariant) frequency-selective channels. Such simulations are – for instance – appropriate for the study of OFDM systems, with a system model that reduces the channel including the IFFT at the OFDM transmitter and the FFT at the receiver to a set of parallel Gaussian (sub-) channels (see Chapter 4, [17]). These sub-channels have complex attenuation factors given by the channel’s TF $H(f)$ at the frequency instants of the OFDM sub-carriers $f = nF$, where F [Hz] is the sampling interval in the frequency-domain and $n = \{0, 1, 2, \dots, N - 1\}$. The simulation scheme presented in this section directly generates $H(f)$ for well defined channel parameters.

In some cases, for instance for evaluating channel estimation schemes, the time-variability of the TF is also of great importance. The extension of the static simulation scheme to a time-variant one is discussed. A discussion of the channel-variability in an OFDM-based wireless LAN system is given in Section 5.2.1.2. The induced performance degradation is studied in Section 6.5.3.

2.4.1 Model Description

The simulation system for time-invariant channels is shown in Figure 2-5. Real-valued white (or wide-band) Gaussian random processes $W(f)$ in the frequency-domain are generated by a noise source. The appropriate spaced-frequency correlation is obtained by FD-filtering of $W(f)$ with a (low-pass) filter $g(f)$. The output of this filter is the real-valued, colored noise process ${}_rH'(f) = W(f) * g(f)$, where $*$ denotes convolution. The inverse FT of ${}_rH'(f)$ (in delay-time-domain representation) is complex-valued and hermitian, i.e., symmetric with respect to the $\tau = 0$ axis. It is not causal, in contrast to the impulse response (IR) of a real channel. The required causality in the time-domain is obtained by applying the Hilbert transform to ${}_rH'(f)$ and adding the result ${}_iH'(f)$ as $H'(f) = {}_rH'(f) - j \cdot {}_iH'(f)$. Doing this, the negative part of the IR is canceled.

The amplitude of the TF $|H'(f)|$ is Rayleigh distributed since $H'(f)$ is a complex Gaussian noise process. A Ricean fading channel may be simulated by adding a complex constant $\rho \cdot e^{j\theta_\rho}$ to $H'(f)$, representing the LOS path at $\tau = 0$.

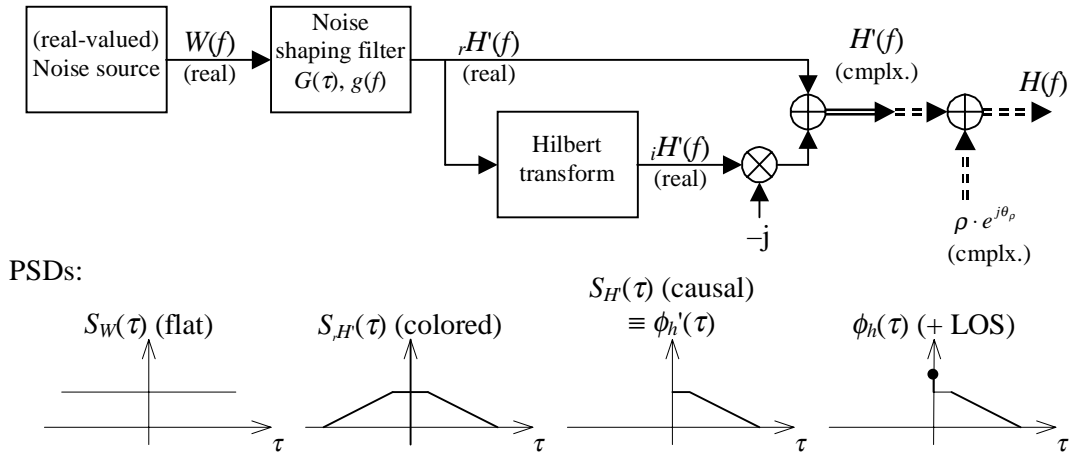


Figure 2-5: Frequency-domain simulation of the frequency-selective radio channel.

2.4.2 Implementation of the Simulation Scheme

To obtain a computer simulation program producing TFs with the desired DPS, two elements of the above simulation scheme must be appropriately designed; the noise-shaping filter $g(f)$ and the variance of the noise source σ_w^2 . The simulator produces a sampled version of the TF, $H(nF)$, where F [Hz] is the sampling interval in the frequency-domain and $n = \{0, 1, 2, \dots, N-1\}$. F must be selected according to the sampling theorem, i.e., $F < 1/(2\tau_{max})$.

The power spectral density (PSD) of the output of the simulation scheme (which is in τ -domain) has to match the continuous DPS defined by (2-15). This is achieved by designing the filter $g(nF)$ to have a TF $G(\tau)$ proportional to the DPS (for $\tau > 0$; i.e. skipping the LOS component). Any classic filter design method can be used in this process [11]. By definition we let $|G(\tau)| = 1$ during the constant-level part (or at $\tau = 0^+$ – if there is no constant-level part), which leads to the variance $\sigma_w^2 = \Pi/(4F)$, as derived below.

2.4.2.1 Derivation of the Variance of the Noise Source

The noise source produces independent, real-valued noise samples with variance σ_w^2 . The sequence $W(nF)$ thus has a (periodic) spectrum with constant PSD

$$S_w(\tau) = \sigma_w^2 F. \quad (2-25)$$

Applying these samples to the noise shaping filter with amplitude TF

$$|G(\tau)| = \begin{cases} 1 & |\tau| \leq \tau_1 \\ e^{-\gamma(|\tau| - \tau_1)} & |\tau| > \tau_1 \end{cases}, \quad (2-26)$$

leads to the PSD of $\text{Re}\{H(nF)\}$ written as

$$S_{,H'}(\tau) = \sigma_w^2 F |G(\tau)|. \quad (2-27)$$

The next step in the simulation scheme is the addition of the Hilbert transformed (HT) sequence, which increases the PSD for $\tau > 0$ by a factor of four. (The HT cancels the negative- τ part of the Fourier spectrum, while doubling the positive- τ part, resulting in four-fold power for $\tau > 0$). This yields the PSD to be compared with the model (the DPS) as

$$S_{H'}(\tau) = 4\sigma_w^2 F |G(\tau)| \equiv \phi_h(\tau), \quad \text{for } \tau > 0, \quad (2-28)$$

which yields $\sigma_w^2 = \Pi/(4F)$.

2.4.2.2 Extension to a Time-Variant Channel Simulator

In order to extend this static simulation scheme to a time-variant one, the TF $H(f_1, t)$ must have the required Doppler spectrum when the time-variations are investigated at any given frequency $f = f_1$. This may be achieved by generating a number of independent TFs $H(f, t = k \cdot T_s)$, $k = \{1, 2, 3, \dots\}$ and filtering them in time-direction at each frequency sample, according to a specific Doppler spectrum. (Separability of the joint time-frequency correlation function $\phi_H(\Delta f, \Delta t)$ is thereby assumed⁴). A set of N filters is required for applying time-variability to the transfer functions in this way.

It should be noted that this simulation scheme gets rather complex. It might thus be preferable to use a conventional fading simulator – one that generates a (time-variant) IR – and transform the IR to the frequency-domain, if required. Usually, the IR is defined by much less than N coefficients, therefore the complexity is reduced.

2.4.3 FD-Simulation Results

In Figure 2-6, a simulated TF is shown (Figure 2-6a) and compared to a measured one (Figure 2-6b). The two channels' IRs are given in Figure 2-7a and b, both derived from the respective TFs using the inverse discrete FT (IDFT) without windowing. The measurement was performed with a network analyzer, observing a bandwidth of 1 GHz around a center frequency of 11.5 GHz⁵. The channel parameters $P_0 = -62.1$ dB, $K = -1.9$ dB, and $\tau_{rms} = 9.0$ ns were extracted from the measured TF (Figure 2-6b), and (with $\tau_1 = 0$) used to generate the simulated TF (see Figure 2-6a). (The method proposed in Section 3.3 of this thesis was employed to estimate the channel parame-

⁴ Separability of the two-dimensional spaced-frequency, spaced-time correlation function $\phi_H(\Delta f, \Delta t)$ means that it can be written as a product $\phi_H(\Delta f, \Delta t) = \phi_H(\Delta f) \cdot \phi_H(\Delta t)$. This assumption is valid if $\tau_{max} f_m \ll 1$ [18], which is given for practical propagation channels (τ_{max} denotes the maximum excess delay; f_m is the Doppler spread).

⁵ The author would like to thank Dr. G. J. M. Janssen for providing measurement results for the validation of the proposed methods [14]. The measurements were conducted at the TNO Physics and Electronics Laboratory in The Hague, The Netherlands, in the period of August – December 1991.

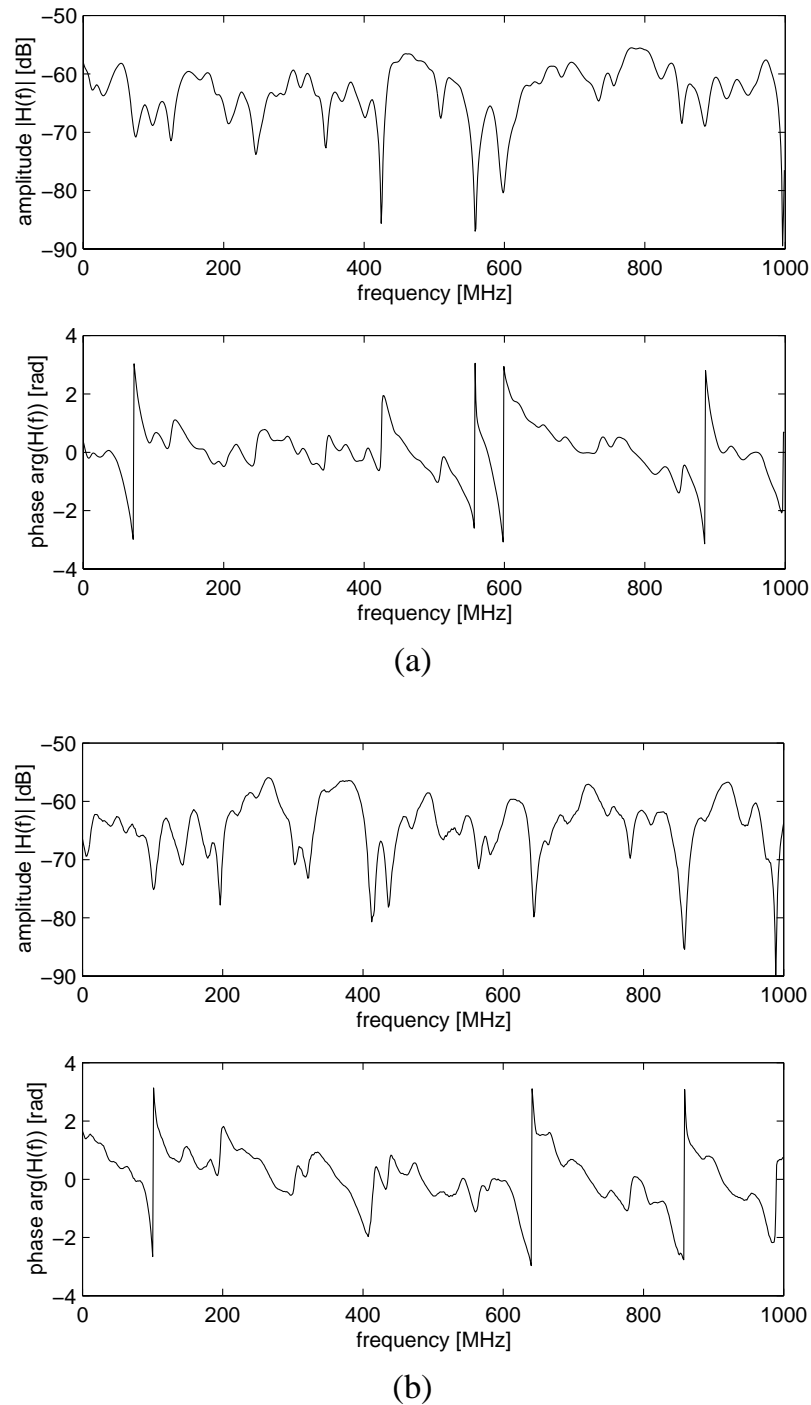


Figure 2-6: (a): Simulated transfer function (TF); (b): TF measured with a network analyzer (corrected for linear phase shift);

ters.) Both TFs have a length of 801 samples. A 15-tap FIR filter was used for the noise shaping filter $g(nF)$ in the simulation scheme.

The TF is obtained from a stochastic simulation model. Therefore we do not expect it to be identical to the measured TF. However, it is clearly seen that the characteristic of the fading is well reproduced. Originally, a linearly increasing phase shift was evident in the measured TF corresponding to the propagation delay of the shortest path. In the

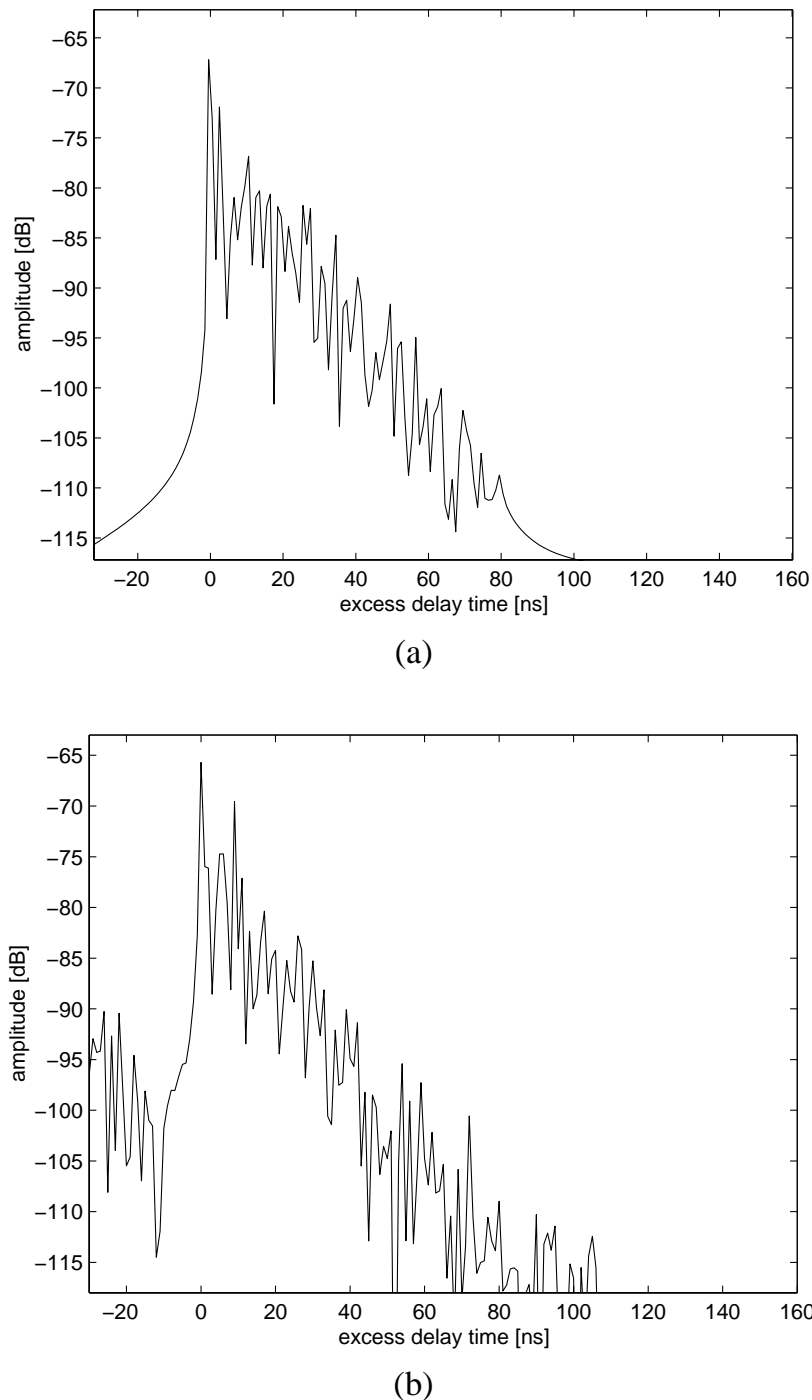


Figure 2-7: (a) Impulse response (IR) derived by IDFT from the simulated TF shown in Figure 2-6a. (b): Impulse responses derived from the measured TF (see Figure 2-6b).

illustration this was compensated, to have the first component arrive at (excess) delay $\tau = 0$, in agreement with the simulation model.

The probability density function (PDF) and the cumulative distribution function (CDF) of the simulated amplitude TF are shown in Figure 2-8 and compared to the Rayleigh distribution. Because of the low K-factor ($K = -1.9$ dB), good agreement is evident.

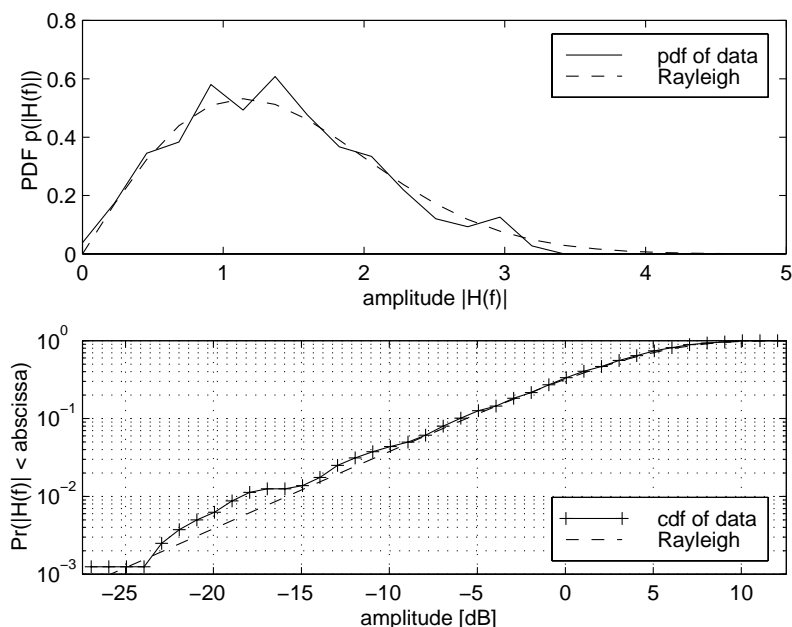


Figure 2-8: PDF and CDF of the amplitude of the simulated transfer function.

Second order statistical properties estimated from simulated TFs are shown in Figure 2-9. The power spectrum obtained by averaging over periodograms of 100 simulated TFs agrees well with the used DPS model (upper plot). The lower plot shows (spaced-frequency) correlation properties and compares them to the theoretical function given by (2-21). Coherence bandwidths are determined by solving numerically for the fre-

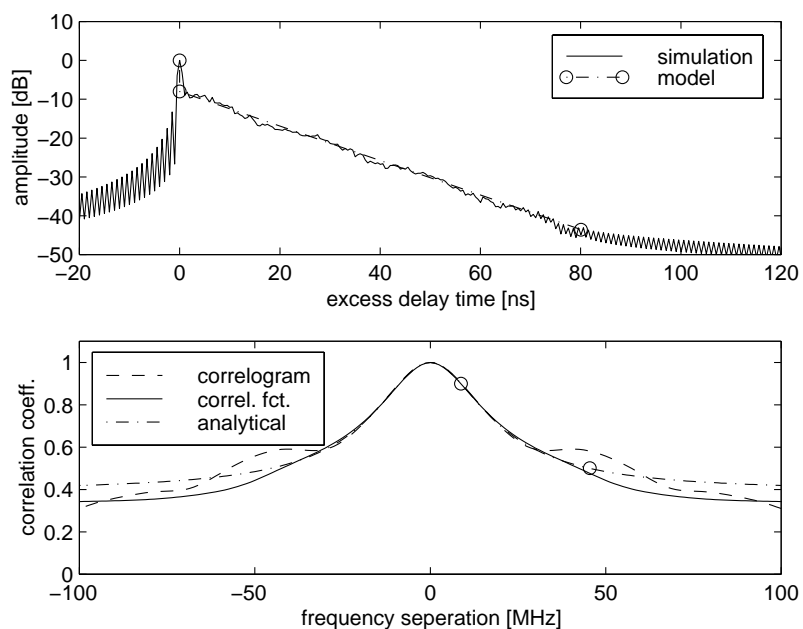


Figure 2-9: Delay power spectrum (DPS) and spaced-frequency correlation function for the FD-simulation model. Upper plot: DPS and estimated power spectrum. Lower plot: Correlogram; estimated and analytical correlation functions; markers ‘o’: Coherence bandwidths 0.5 and 0.9.

quency-separations, where the correlation function's magnitude drops to 0.9 (or 0.5 – according to the definition).

2.4.4 Differences to Time-Domain Simulation Schemes

The equally spaced tap-gains of the sampled (and band-limited) impulse response are *not* uncorrelated, according to the analysis shown in Section 2.2.2 (see eq. (2-12)). That is, there exists a certain autocorrelation between different delay-bins of the IR. This correlation results from the band-limitation needed for the time-quantization, which implies a convolution of the discrete, non-sampled impulse response with a sinc-function. Another effect of this convolution is visible in spectral components at negative delay-values, due to leakage effects. The FD-simulation scheme shows these properties (see Figure 2-7a and Figure 2-9).

Many time-domain simulators, however, implement the channel impulse response by simply generating *independent*, complex-valued path gains at the (sample-spaced) delay bins. Leakage effects, i.e., components at negative delays, are not considered either (see e.g. [6], Figure 1.12; [19]). (One sampled simulation model, which does consider those effects is described in [18].)

In particular, these simplifications are used, when the channel models are applied for the design of digital radio interfaces. Normally, the resulting differences are negligible, but there are cases, where the impact gets important. An example is discrete Fourier transform (DFT) based channel estimation schemes for OFDM. Such channel estimators determine firstly a coarse estimate of the channel TF, for instance from a training sequence. In order to reduce the mean-square-error (MSE) of the estimate, the next step is a transform of the transfer function to the delay time domain, yielding a noisy channel impulse response. In this form, likely noise components – at negative or very large delay values – can be identified and set to zero, followed by a back transformation to the frequency-domain. The result is an estimate of the channel TF with enhanced signal-to-noise ratio (SNR) and hopefully reduced MSE. The simulation of such a scheme suggests excellent performance, if a so-called ‘sample-spaced’ channel simulator is used, because then the channel IR is indeed zero at the sample-bins set to zero. On a real channel, however, important information is lost, as channel taps are set to zero which correspond to leakage-components. This leads to irreducible error floors in terms of bit-error-rate and MSE [20]–[22]. In this respect, the proposed FD-simulation model has an inherent advantage over conventional, sampled TD-models, because the correlation among channel taps and leakage effects are considered, in closer agreement to reality.

2.5 Application to mm-Wave Radio Channels

This section has two main purposes. Firstly, the suitability of the proposed FD-channel model and simulation scheme is verified, and secondly, parameters are found for the

model. These goals are approached through a discussion of measurement campaigns reported in the literature.

In particular, our focus lies on mm-wave radio channels, which is the considered frequency-band for the communications system described in Part II of this thesis. Within the mm-wave frequencies, the 60 GHz band has received most attention in the literature, for the following main reasons: Large amounts of bandwidth are unallocated in this band; bandwidths that are required for communications systems at the intended data rates of 100 Mbit/s and above. Another advantage of 60 GHz is due to a physical property of the propagation channel at this specific frequency. Oxygen absorption leads to attenuation above 11 dB/km, between 57 and 63 GHz. This attenuation (additional to the path loss) is believed to enable shorter reuse distances in cellular systems because it counteracts co-channel interference. Over short distances, the additional attenuation can be neglected.

It is a general property of mm-wave propagation that the behavior of propagation rays is well characterized by geometric optics. That is, waves do not penetrate through walls or other obstacles, and wave reflection is the main mechanism leading to multipath. Scattering, diffraction, and wave guiding are considered far less important [23].

This section starts with a discussion of measurement results (Section 2.5.1). In Section 2.5.2, typical channel parameter values are given. The influence of features of the propagation environment on those parameters is discussed. Channel models suggested in the literature are treated separately, in Section 2.5.3. Section 2.5.4 deals with the applicability of the newly proposed FD-channel model to (mm-wave) radio channels – the validation of the FD-model.

2.5.1 Discussion of Measurement Results

A major activity in the field of mm-wave propagation has been conducted in the framework of the European RACE (Research into Advanced Communications systems in Europe) project 2067, Mobile Broadband Systems (MBS) [23], [24]. The measurement campaigns described include material characterization, and indoor and outdoor propagation studies. Ray-tracing models have been developed for predicting propagation parameters and for investigating the impact of environment features, antenna characteristics, etc.. An extensive list of literature on mm-wave propagation is found in the “Final report on propagation aspects” of the RACE-MBS project [23].

Partly related is the activity carried out within the COST 231 (European Co-Operation in the field of Scientific and Technical research) program [8]. This study also covers indoor and outdoor channels. A major contribution on indoor propagation originates from the research of Smulders, conducted at Eindhoven University of Technology [24].

Other work on indoor channel is found in [12], [14], [15], and [25]–[35], outdoor studies are presented in [36]–[38]. Note that most of the work has been done on indoor

channels and their modeling, probably also because of the range limitation of mm-wave propagation.

The main parameters of interest for applying the FD-model to mm-wave channels are the normalized received power (NRP), P_0 , the Ricean K -factor, K , and the RMS delay spread, τ_{rms} . For the air interface design, the latter two parameters, $\{K, \tau_{rms}\}$ are generally sufficient. The NRP is required for link budget considerations (see Chapter 5).

While most studies present results of τ_{rms} and the NRP, the K -factor is unfortunately commonly not investigated.

Generally, it is difficult to compare measurements conducted by various research groups, because of

- differences in the measurement equipment and method used,
- different antenna characteristics and configurations,
- different parameters measured and presented, and
- different environments investigated.

We try to organize this comparison and overview by discussing the parameters of interest and elaborating on the impact of some of the above listed factors. Only wide-band measurements are considered, because of the importance of characterizing the time-dispersive and frequency-selective nature of the channel. The modeling of these channel properties is essential for the air-interface design, the intended application of the channel model under development.

2.5.1.1 Measurement Set-Ups and Techniques

Most indoor measurement campaigns use vector network analyzers to scan the channel transfer function (phase and magnitude) versus frequency (see e.g., [8], [12]–[15], [31], and [33]–[35]). The conditions to use such equipment are short distances, because a phase reference must be provided between the transmitting and the receiving sides, and a (quasi) static channel, because of the time it takes to acquire the frequency transfer function. These conditions are feasible in indoor scenarios. The main advantages of this approach are the high time-resolution achieved by scanning over a large bandwidth, and the good SNR, because a narrowband (continuous wave) signal is transmitted in which the whole transmit power is concentrated. The delay-time resolution investigated is normally around 1 ns, corresponding to a scanning bandwidth of 1–2 GHz. In [38], a network analyzer was used for outdoor measurements.

Correlation type channel sounders were developed for the extensive measurement campaigns performed in the RACE-MBS project [23], [24]. For outdoor channels, a wide-band test signal (chirp) was generated by rapidly sweeping a carrier over a bandwidth of up to 200 MHz [36], [39]. A separate indoor channel sounder is based on

the transmission of a pseudo random binary sequence and a sliding-correlator on the receiver's side (see [40]). Similar equipment was employed in [32] for indoor measurements, and in [37] for outdoor measurements.

Within this Ph.D. research, a novel, non-coherent channel measurement technique was developed that can estimate the NRP, K -factor, and of τ_{rms} from swept-frequency *power* measurements. No phase measurement is required, which simplifies the equipment needed. The measurement technique is described in detail in Chapter 3 of this thesis. Measurement campaigns conducted with this method at TU-Delft are described in [25]–[28]. Indoor and outdoor channels were studied, at 17 and 60 GHz.

2.5.2 Discussion of Channel Parameters

The RMS delay spread (RDS) τ_{rms} and the Ricean K -factor are the two most important parameters for specifying the channel's frequency-selective nature, in the context of air-interface design. It will be seen from the study of the frequency-domain level crossing rate that the RDS determines the number of fades per bandwidth, while the K -factor specifies the depth of the fades (see Chapter 3). The normalized received power (NRP) just determines the average signal-to-noise ratio (SNR). Since the SNR is usually considered as a variable in any kind of system studies, absolute values of NRP are not of major importance for the air-interface design.

2.5.2.1 RMS Delay Spread

The following main features of the propagation environment influence the RDS. Note that the mentioned properties are applicable for indoor channels only. Similar features, however, will also have an impact on the RDS in outdoor scenarios.

Room size

Generally, the RDS increases with the room size. Such behavior was for instance reported in the work by Smulders [24], who measured typical values of RDS between 15 and 45 ns in small rooms with dimensions $\leq 24 \times 11 \times 4.5$ m³, and values between 30 and 70 ns in larger rooms.

These values are rather large, compared to the results from many other indoor measurement campaigns found in the literature. Main reason for the large values is – next to the large rooms investigated, – the antenna design implemented. The biconical horn antennas, having an omnidirectional radiation pattern in the azimuth plane, a 3-dB beam-width of 9° in the elevation plane, and a directivity of 9 dBi, were designed such that the NRP hardly depends on the position within a room. Therefore, they radiate quite a large fraction of the transmitted power towards the walls, leading to strong first reflections and long delay spreads. Although the delay spreads are quite large, this design might be of advantage, because self-shadowing effects become less harmful. That is, signal loss due to the obstruction of the LOS-path by the user (see

[41]) is assumed to be less significant for such antenna set-ups.

Antenna directivity

Directive antennas attenuate parts of the impinging reflected waves. Therefore, the RDS usually decreases, as more directive antennas (in the azimuth plane) are employed.

Such behavior is clearly seen from measurements and ray-tracing simulations performed by T. Manabe *et al.* [31]. In a room with dimensions of $13.5 \times 8 \times 2.6$ m, they measured typical RDS-values of 18, 14, 5, and 1 ns, for, respectively, an omnidirectional antenna ($\lambda/2$ -dipol), and antennas with 3 dB beam-widths of $\sim 60^\circ$, $\sim 10^\circ$, and $\sim 5^\circ$.

A similar study based on a ray-tracing tool is presented in the final report of the RACE-MBS project [23]. In the investigated room of approximate dimensions $11 \times 7 \times 3$ m³, different antenna configurations were evaluated, leading to RDS-values of 20 – 25 ns for the less directional antennas, and values (significantly) lower than 5 ns for the most directional ones.

In order to investigate this anticipated dependency between the RDS and the antenna characteristics, Smulders has conducted some additional measurements using a 15 dBi circular-horn antenna (in stead of the 9 dBi omnidirectional biconical horn antenna) on one side of the measured link [24]. His results confirm the expected behavior if median values of RDS are considered (RDS decreases from ~ 40 ns to ~ 25 ns). However, the max. RDS values observed were even larger than for the standard antenna configuration (increase from ~ 48 ns to ~ 60 ns). A similar behavior was reported by Bultitude *et al.* [33], who performed a measurement campaign at 40 GHz, in a large open office environment. It is a possible explanation that the more directive antenna, which also has the higher gain, may emphasize some reflected paths with a rather large delay time. Such paths contribute strongly to the RDS.

Building material

The reflectivity of building material is expected to be another important factor influencing the RDS. This behavior was e.g. reported by Smulders [24], who measured higher RDS values in a small room with metal walls (room dimensions $\sim 10 \times 9 \times 3$ m³; $\tau_{rms} \cong 45$ ns), than in a much larger auditorium room with walls covered by wood and acoustically soft material (room dimensions $\sim 30 \times 21 \times 6$ m³; $\tau_{rms} \cong 35$ ns). In a small room ($\sim 13 \times 9 \times 4$ m³) with wood-covered walls, RDS-values of ~ 20 ns were measured.

Outdoor measurements

Measurements in seven different streets downtown Oslo were reported in [23], [24], [36] (MBS-RACE project). The RDS is typically lower than 20 ns, except for one measurement where a major reflection source (tourist bus) was located on the street. In the latter case the RDS was < 50 ns. The maximum delay spread (the sliding delay window, i.e., the shortest period of the IR containing 90 % of the received energy) is

less than 45 ns for 90 % of the measurement points. However, maximum values up to 270 ns were observed. Results from measurements at city squares show higher values of RDS and maximum delay spread.

Outdoor measurement results reported in [25], [26] (for 17 GHz), [38] (for 60 GHz), [37] (for 40, 60 GHz) also show RMS delay spread values starting below 20 ns and occasionally going up to about 100 ns and above [38]. Little work has been done on outdoor propagation in mm-wave bands.

2.5.2.2 Ricean K -factor

Parameter pairs of RMS delay spread, τ_{rms} and the Ricean K -factor are required for modeling multipath radio channels using the FD-channel model introduced in Section 2.3. While statistics of the RDS are found in most propagation studies, the Ricean K -factor is often not (explicitly) investigated. Many studies assume Rayleigh fading amplitude distributions, i.e., K -factors of zero. In situations where the line-of-sight (LOS) between transmitter and receiver is obstructed, this assumption may be reasonable. However, as a LOS path is often required for reliable transmission at mm-wave frequencies [41], the K -factor becomes an important channel parameter. Typical values of K are given below. The influence of a LOS path and the influence of the antenna characteristics are investigated.

Influence of a line-of-sight path

Two measurement campaigns that consider the K -factor were conducted by Janssen [14], [15] and by Bohdanowicz [25], [26]. Although those measurements were performed at lower frequency-bands (at 2.4, 4.75, and 11 GHz, and at 17 GHz, respectively), the results are interesting for modeling the 60 GHz channel. One important reason is that most of the measurement situations were similar to the expected scenarios for 60 GHz systems, where both, the transmitter and the receiver are typically located within the same room. Moreover, results for all these frequency-bands are quite similar, suggesting that a shift to the 60 GHz band would not have a large impact, either. The comparative study of a 1.7 GHz and a 60 GHz channel presented in [32] confirms the latter.

Characteristic channel parameters reported by Janssen ([14], [15]) are $\tau_{rms} \cong 10$ ns, $K \cong 2.5$ dB in LOS situations, and $\tau_{rms} \cong 15$ ns, $K \cong -3$ dB without LOS. All measurements were performed in relatively small rooms.

The 17 GHz channel study by Bohdanowicz ([25], [26]) gives typical K -factors between 0.3 and 2.5 dB for LOS indoor scenarios ($\tau_{rms} \cong 5 \dots 17$ ns), and values around -1 dB for indoor non-LOS situations ($\tau_{rms} \cong 9$ ns). Larger K -factors of 3 ... 5 dB were determined from outdoor LOS measurements, where $\tau_{rms} \cong 20 \dots 30$ ns.

Clearly, increased K -factors are observed in the presence of a (dominant) LOS path, corresponding to amplitude distributions with shallower fades. While K -factors below -3 dB can be well represented by the Rayleigh distribution, higher values should be

modeled by the Ricean distribution. In particular if $K \geq 0$ dB, i.e., the dominant path carries greater or equal power than all the reflected paths, the Ricean model must be used.

Antenna directivity

It is expected that more directive antennas yield higher K-factors, because – if the antennas are pointed towards one another, – the dominant path is amplified while the reflected ones are attenuated. Inspection of the impulse responses shown by Manabe *et al.* in [31] confirm such behavior. Unfortunately, no values of K-factors are given there.

The channel model parameters given by Smulders [24] and by Kunisch *et al.* [12] can be used to estimate the Ricean K-factor and investigate the impact of the antennas' directivity. Those model parameters were obtained from 60 GHz channel measurements.

Smulders' model parameters [24] imply that even for the 15 dBi directive antenna, and in the presence of a LOS path, the K-factor would be less or equal to -6 dB, and therefore well described by the Rayleigh model. Note that in this study the directive (receive) antenna was not pointed towards the transmitter. This may be a partial explanation for this unexpected result.

Kunisch's model parameters [12] correspond to Ricean K-factors between 7.3 dB and 25 dB (and τ_{rms} between 5.7 and 1 ns, respectively). Kunisch's measurement set-up used an 8 dBi antenna at the transmitter and two receiver antennas pointed towards the transmitter, with respective gains of 20 and 22 dBi. It appears that such an antenna configuration can effectively reduce the multipath fading. Adaptive antennas (beam-forming) can avoid the need of pointing the antenna manually.

Larger K-factors reduce τ_{rms} , when the decay exponents of the average power delay profile remain constant. This is also seen from the equations given in Table 2-1, where γ should be considered constant. The model parameters given by Kunisch [12] confirm that such a dependency may exist, at least within one room.

2.5.3 Overview of Channel Models

Most of the (stochastic) channel models proposed in the literature for mm-wave channels are based on the indoor propagation model presented by Saleh and Valenzuela [16]. This section first reviews their model. Secondly, a number of modifications are discussed for its application to mm-wave channels. The suitability of the FD-channel model for this frequency band is studied in Section 2.5.4.

2.5.3.1 Review of the Saleh and Valenzuela Model

The Saleh and Valenzuela model is a method to generate time-discrete channel impulse responses as defined by eq. (2-1). Stochastic processes are specified to model the

ray arrival times $\{\tau_i\}$, the ray amplitudes $\{\beta_i\}$, and the ray phases $\{\theta_i\}$.

The ray phases are considered to be independent random variables that are uniformly distributed over $[0, 2\pi)$, because the phases vary over that range when the path-lengths change by just one wavelength.

Two Poisson processes implement the ray-arrival process. Reflections are assumed to arrive in clusters, where the first Poisson process models the arrival times of the clusters with some fixed rate Λ [1/s]⁶. Subsequent ray-arrivals within the clusters are realized by the second Poisson process with rate $\lambda_\tau \gg \Lambda$. Per definition, the first ray and the first cluster arrive at $\tau = 0$. A Poisson process of (ray) arrivals implies exponentially distributed inter-arrival times, written as

$$p(\Delta\tau) = \lambda_\tau \exp[-\lambda_\tau(\Delta\tau)], \quad (2-29)$$

where $\Delta\tau$ is the delay time difference between consecutive paths of the same cluster.

The probability distribution of the path gains $\{\beta_i\}$ is a Rayleigh distribution. (Therefore, the path gains including the uniformly distributed path phases $\{\beta_i e^{j\theta_i}\}$ follow a complex Gaussian distribution.) Introducing the variables l and k for indexing the cluster and ray-within-cluster, respectively, the mean square values of the magnitudes $\{\overline{\beta_{kl}^2}\}$ are written

$$\overline{\beta_{kl}^2} = \overline{\beta_{00}^2} e^{-T_l/\Gamma} e^{-\tau_{kl}/\gamma_{sv}}, \quad (2-30)$$

where $\{T_l\}$ and $\{\tau_{kl}\}$ are the cluster and ray-within-cluster arrival times, respectively, and Γ and γ_{sv} are the corresponding power decay time-constants. This function is called the average power delay profile (PDP), because it characterizes the average ray power of the impulse response as a function of the excess delay-time. It is composed of a set of exponentially decaying parts, one for each cluster of rays.

For more details on the Saleh and Valenzuela model, the reader is referred to [16].

2.5.3.2 Modifications to the Model

Several authors have applied a number of modifications to the above-described model in order to match it to mm-wave channels.

Most of the implementations found in the literature reduce the number of clusters to one (see e.g. [12]–[15]). This simplification is made, since in a typical indoor mm-wave channel, the reflections originate all from within one room, leading to a single,

⁶ According to [16], the formation of clusters is related to the building superstructure, i.e., clusters of rays typically originate from (steel-reinforced) exterior or interior walls or large metal doors or objects. The rays within the clusters are due to reflections in the vicinity of the transmitter or receiver. Clustering of rays is therefore a property of indoor channels at longer ranges and at lower carrier frequencies, where propagation through walls is possible. Clustering of rays also occurs in outdoor channels [42]–[44].

dense cluster of ray arrivals. Remember that mm-wave frequencies hardly penetrate through building material. An exception is the work of Park [35], who gives a set of parameters for the original, multi-cluster version of Saleh and Valenzuela's model. Park investigated indoor channels at 60 GHz.

In several cases, the model has been augmented by a separately specified path at $\tau_0 = 0$ ([12]–[15]) in order to extend the model to Ricean channels by introducing a (dominant) LOS path.

Smulders [24] proposes a composite average PDP, where the exponentially decaying part of the single cluster is preceded by a constant-level part. The reason for introducing this part is to better describe first-order reflections arriving at similar strength due to the antenna design chosen. Such a constant-level part is also implemented in the frequency-domain channel model proposed in this Thesis (see Section 2.3.2).

Janssen shows in [15] how to adjust the generated discrete-time impulse responses in order to exactly realize a given set of channel parameters $\{P_0, K, \tau_{rms}\}$. (Note that those are local-area mean parameters; see Section 2.2.2). He also suggests a method to incorporate small-scale fading effects resulting from movements within a local area. That mechanism is based upon ray-arrival directions relative to the assumed transceiver movement.

2.5.4 Applicability of the FD-model

The proposed frequency-domain (FD) channel model characterizes the mobile radio channel by its delay power spectrum (DPS), the Fourier transform of the spaced-frequency correlation function. This model agrees well with the modified (single-cluster) versions of the Saleh and Valenzuela model introduced above, because the DPS of the FD-model is described in an almost equivalent way to the average power delay profile of the (single-cluster) Saleh and Valenzuela model. In the FD-model, Ricean channels may be implemented using the discrete, direct path at $\tau_0 = 0$. Moreover, a constant-level part is incorporated as in [13], which allows for a better match to certain channel impulse responses, and which also enables varying the maximum excess delay in some range, as investigated in Section 2.3.3.

According to the overview of channel models presented above, a single cluster of rays is an appropriate description of mm-wave indoor channels, where the transmitter and receiver are typically located within the same room. The suitability of the proposed channel model for such scenarios was also confirmed by the comparison of measurement results to computer simulations (see Section 2.4.3).

Clustering of rays can be implemented in the proposed model by modifying the DPS accordingly, i.e., by defining a DPS consisting of multiple exponentially decaying parts. Similarly, arbitrary outdoor channels could be realized. However, using the model for the design of OFDM systems, I am confident that the simple model

introduced in Section 2.3.2 is applicable to a much wider range of actual environments. For such systems, the most important channel properties are the correlation among (adjacent) sub-carriers and the distribution of their amplitudes (or powers). These properties are well preserved by the model as long as the channel parameters are matched to the environment under investigation. And these parameters can be freely (and easily) chosen in the proposed model. It can be even proven that, for Rayleigh fading channels and for small frequency-separations, the correlation coefficient in frequency-domain is independent of the channel model (see Appendix A). (The correlation coefficient is the normalized auto-correlation function of the squared magnitudes of the TF.) This finding strongly supports the claim that such a simple stochastic model is sufficient for many air-interface design problems.

2.6 Conclusions

The main novelties discussed in this Chapter concern the so-called frequency-domain (FD) channel model and its implementation on a computer simulation scheme. The FD-model is the frequency-domain dual of Jakes' Doppler-spectrum model [1], [3], [4]. Just as in Jakes' model the (narrowband) channel's time-variability is described by the spaced-time correlation function and by the Doppler spectrum, in the FD-model the (time-invariant) channel's frequency-selectivity is described by the spaced-frequency correlation function and by the delay power spectrum. (The power spectra and correlation functions are inter-related by Fourier transforms.) The simulation scheme introduced directly generates realizations of channel transfer functions with well-defined channel parameters. Note that a frequency selective channel is equivalent to a time-dispersive (multipath) channel. The major advantages of the proposed models are:

- Good agreement with physical propagation channels, in particular in mm-wave frequency bands and in indoor environments (see Section 2.5).
- Availability of analytical expressions relating model parameters to physical channel parameters and vice versa, allowing to straightforwardly match the model to any given environment (see Section 2.3.3).
- Suitability for OFDM system design, the goal of this research (see Part II).
- The simplicity of the model allows for the mathematical analysis of many aspects of transmission schemes, like the performance evaluation and optimization of bit-error-rates, synchronization, and channel estimation schemes (see Part II).
- Availability of an efficient simulation model (see Section 2.4).

However, the extension of the simulation model from the static version presented, to a time-variant version is rather complex. This may be a disadvantage of the FD-model.

The (physical) channel parameters specifying the FD-model are elaborately discussed.

The channel at a local area of dimensions of a few wavelengths (approx. $5 \dots 40 \lambda$) is defined by a set of fixed parameters: the normalized (or average) received power P_0 , the Ricean K-factor K , and the RMS delay spread τ_{rms} . At a limited observation bandwidth, however, these parameters appear to be time- (or location) variant within a local area, because individual propagation paths are not resolvable and multipath interference between them leads to rapid (small-scale) variations of the resulting channel impulse response. Reduced-bandwidth simulations performed with the FD-model also show a variability of these instantaneous parameters among realizations.

It was suggested that the RMS delay spread τ_{rms} and the Ricean K-factor are equally important for the characterization of frequency selective multipath radio channels. In the next chapter, it will be shown that τ_{rms} effectively specifies the number of fades per bandwidth and their average bandwidth, while the K-factor describes the depth of fades. Most experimental studies, however, investigate τ_{rms} only. The K-factor is analyzed in rather few cases, although line-of-sight conditions and directional antennas are commonly considered –, two factors that are anticipated to increase the K-factor. Rayleigh fading channels have a K-factor of zero.

Channel parameters depend on a number of features of the propagation environment and of the antenna set-up. Larger rooms and more reflective building materials gener-

Table 2-2: Typical channel parameters of frequency-selective, mm-wave radio channels.

<i>Title</i>	<i>Comments and Reference</i>	<i>Antenna configuration</i>	<i>RMS delay spread</i>	<i>Ricean K-factor</i>
Small / medium room, LOS	measur. at 2.4, 4.75, and 11 GHz [14], [15]	~2.5 dBi bi-conical antennas (~100° beam-width)	10 ns	2.5 dB
Small / medium rooms, non-LOS			15 ns	-3 dB (Rayleigh)
Outdoor			30 ns	3 dB
Medium room, directional ant.	High-gain antenna pointed at BS; 60 GHz [12]	BS: 8 dBi PS: ~20 dBi	5 ns	10 dB
Computer room (~10×9×3 m ³)	60 GHz [13]	9 dBi bi-conical antennas (~9° beam-width)	45 ns	0 (Rayleigh)
Large Hall (~43×41×7 m ³)			60 ns	0 (Rayleigh)
Corridor (~45×2.5×3 m ³)			75 ns	0 (Rayleigh)
Lecture room (~13×9×4 m ³)			20 ns	0 (Rayleigh)

BS: Base Station; PS: Portable station

ally increase the RMS delay spread τ_{rms} . Higher antenna directivity decreases τ_{rms} and increases the K -factor. The presence of a line-of-sight between the transmit- and receive-antennas leads to larger K and sometimes to lower τ_{rms} . Within the same environments and with similar antenna set-ups, the frequency band has surprisingly little influence on those parameters. A list of typical parameter-values with short descriptions of the main features of the corresponding environments is given in Table 2-2. Mm-wave channels (e.g. 60 GHz) are considered for the multimedia communications system studied in Part II of this thesis. Most investigations of these channels conclude that a line-of-sight between the transmitter and the receiver is required for reliable communications. However, the results from [13], where a special antenna design was used, suggest that the reflections can be sufficient as well.

Since the channel parameters are influenced by many factors and in ways that are hard to predict, a method is desirable to measure them in a cheap and simple way. The next chapter presents a method that can be used to accurately estimate these parameters $\{P_0, K, \tau_{rms}\}$ from scans of the channel's power response versus frequency. Standard laboratory equipment can be used to apply that scheme.

2.7 References

- [1] W. C. Jakes Jr., *Microwave Mobile Communications*. New York: Wiley-Interscience, 1974.
- [2] J. G. Proakis, *Digital Communications*, 3rd edition. New York: McGraw Hill, 1995.
- [3] M. J. Gans, "A Power-Spectral Theory of Propagation in the Mobile-Radio Environment," *IEEE Trans. Veh. Technol.*, vol. VT-21, no. 1, pp. 27–38, Feb. 1972
- [4] R. H. Clarke, "A Statistical Theory of Mobile-Radio Reception," *Bell Syst. Tech. J.*, vol. 47, pp. 957–1000, July–Aug. 1968.
- [5] P. A. Bello, "Characterization of randomly time-variant linear channels," *IEEE Trans. on Commun. Systems*, vol. CS-11, pp. 360-393, Dec. 1963.
- [6] R. Steele, *Mobile Radio Communications*. New York: John Wiley and Sons, 1992.
- [7] T. S. Rappaport, *Wireless Communications: Principles and Practice*, Upper Saddle River: Prentice-Hall, 1996.
- [8] European Commission, Cost Action 231, *Digital mobile radio towards future generation systems*, Final Report, EUR 18957, Luxembourg, ISBN 92-828-5416-7, 1999.

-
- [9] S. O. Rice, "Mathematical Analysis of Random Noise," *Bell Syst. Tech. J.*, vol. 23, pp. 282–332, July 1944; vol. 24, pp. 46–156, Jan. 1945.
- [10] S. O. Rice, "Statistical Properties of a Sine Wave Plus Random Noise," *Bell Syst. Tech. J.*, vol. 27, pp. 109–157, 1948.
- [11] A. V. Oppenheim and R. W. Schaffer, *Discrete-time Signal Processing*, 2nd edition. New Jersey: Prentice-Hall, 1999.
- [12] J. Kunisch, E. Zollinger, J. Pamp, and A. Winkelmann, "MEDIAN 60 GHz Wideband Indoor Radio Channel Measurements and Model," in *Proc. IEEE Vehic. Techn. Conf. (VTC'99-fall)*, Amsterdam, The Netherlands, Sept. 1999, pp. 2393–2397.
- [13] P. F. M. Smulders, *Broadband Wireless LANs: A Feasibility Study*. PhD Thesis, Eindhoven University of Technology, Eindhoven, The Netherlands, 1995.
- [14] G. J. M. Janssen, P. A. Stigter, and R. Prasad, "Wideband indoor channel measurements and BER analysis of frequency selective multipath channels at 2.4, 4.75 and 11.5 GHz," *IEEE Trans. on Commun.*, vol. 44, no. 10, pp. 1272–1288, Oct. 1996.
- [15] G. J. M. Janssen, *Robust receiver techniques for interference-limited radio channels*, Ph.D. Thesis, Delft Univ. of Techn., Delft, The Netherlands, June 1998.
- [16] A. A. M. Saleh and R. A. Valenzuela, "A statistical model for indoor multipath propagation," *IEEE J. Select. Areas Commun.*, vol. 5, no. 2, pp. 128–137, Feb. 1987.
- [17] O. Edfors, M. Sandell, J. J. van de Beek, D. Landström, and F. Sjöberg, "An introduction to orthogonal frequency-division multiplexing," Division of Signal Processing, Luleå University of Technology, Research Report TULEA 1996:16 (<http://www.sm.luth.se/csee/sp/publications.html>).
- [18] Weimin Zhang, "Simulation and modelling of multipath mobile channels," in *Proc. VTC'94 (IEEE Vehicular Technology Conference)*, Stockholm, Sweden, 1994, pp. 160–164.
- [19] K. Pahlavan and A. H. Levesque, *Wireless Information Networks*. New York: John Wiley and Sons, 1995.
- [20] A. Chini, M. S. Tanany, and S. A. Mahmoud, "Transmission of high rate ATM packets over indoor radio channels," *IEEE J. Select. Areas Commun.*, vol. 14, no. 3, pp. 469–476, Apr. 1996.
- [21] O. Edfors, *Low-complexity algorithms in digital receivers*. PhD Thesis, Luleå University of Technology, Luleå, Sweden, Sept. 1996.

- [22] J.-J. van de Beek, O. Edfors, M. Sandell, S. K. Wilson, and P. O. Börjesson, “On channel estimation in OFDM systems,” in *Proc. IEEE Vehic. Technol. Conf.*, Chicago, IL, July 1995, pp. 815–819.
- [23] L. M. Correia, *et al.*, “Final Report on Propagation Aspects”, RACE 2067, Deliverable *R2067/IST/2.2.5/DS/P/070.b1*, RACE Central Office, European Commission, Brussels, Dec. 1995.
- [24] S. A. Mohamed, G. Løvnes, E. Antonsen, R. Rækken, B. Nigeon and J. J. Reis: “Report on Propagation Measurements”, RACE 2067, Deliverable *R2067/BTL/2.2.2/DS/P/ 035.b1*, RACE Central Office, European Commission, Brussels, Dec. 1994.
- [25] A. Bohdanowicz, G. J. M. Janssen, S. Pietrzyk, “Wideband indoor and outdoor multipath channel measurements at 17 GHz,” in *Proc. VTC’99-fall (IEEE Vehicular Technology Conference)*, Amsterdam, The Netherlands, Sept. 1999, pp. 1998–2003.
- [26] A. Bohdanowicz, “Wideband indoor and outdoor radio channel measurements at 17 GHz,” Delft Univ. of Technol., UbiCom-Technical Report/2000/2, Jan. 2000 (<http://www.ubicom.tudelft.nl/docs/>).
- [27] R. El Hattachi, J. M. M. de Nijs, K. Witrisal, and R. Prasad, “Characterization and simulation of the 18 GHz radio channel,” in *Proc. IEEE Benelux 6th Symposium on Vehicular Technology and Communications*, Brussels, Belgium, Oct. 1998.
- [28] J. Purwaha, A. Mank, D. Matic, K. Witrisal, and R. Prasad, “Wide-band channel measurements at 60 GHz in indoor environments,” in *Proc. IEEE Benelux 6th Symposium on Vehicular Technology and Communications*, Brussels, Belgium, Oct. 1998.
- [29] J. J. G. Fernandes, J. C. Neves, and P. F. M. Smulders, “MM-Wave Indoor Radio Channel Modelling vs. Measurements,” *Wireless Personal Comm.*, vol. 1, no. 3, pp. 211–219, Kluwer, 1995.
- [30] A. Kato, T. Manabe, *et al.*, “Measurements of Millimeter Wave Indoor Propagation and High-Speed Digital Transmission Characteristics at 60 GHz,” in *Proc. PIMRC’97 (IEEE 8th Intern. Symp. on Personal Indoor Mobile Radio Commun.)*, pp. 149 – 154, Helsinki, Sept. 1997.
- [31] T. Manabe, Y. Miura, and T. Ihara, “Effects of Antenna Directivity on Indoor Multipath Propagation Characteristics at 60 GHz,” in *Proc. PIMRC’95 (IEEE 6th Intern. Symp. on Personal Indoor Mobile Radio Commun.)*, pp. 1035–1039, Sept. 1995.

- [32] R. Davies, M. Bensebti, M. A. Beach, and J. P. McGeehan, "Wireless Propagation Measurements in Indoor Multipath Environments at 1.7GHz and 60GHz for Small Cell Systems," in *Proc. 41st IEEE Veh. Techn. Conf.*, pp. 589-593, St. Louis, USA, May 1991.
- [33] R. J. C. Bultitude, R. F. Hahn, and R. J. Davies, "Propagation Considerations for the Design of an Indoor Broad-Band Communications System at EHF," *IEEE Trans. Veh. Technol.*, vol. 47, no. 1, pp. 235-245, Feb. 1998.
- [34] J. Hübner, S. Zeisberg, K. Koora, and A. Finger, "Simple channel model for 60 GHz indoor wireless LAN design based on complex wideband measurements," in *Proc. IEEE Vehic. Techn. Conf. (VTC'97)*, 1997, pp. 1004–1008.
- [35] J.-H. Park, Y. Kim, Y.-S. Hur, K. Lim, and K.-H. Kim, "Analysis of 60 GHz Band Indoor Wireless Channels with Channel Configurations," in *Proc. PIMRC'98 (IEEE 9th Intern. Symp. on Personal Indoor Mobile Radio Commun.)*, Taiwan, Sept. 1998, pp. 617–620.
- [36] G. Løvnes, J. J. Reis, and R. H. Rækken, "Channel Sounding Measurements at 59 GHz in City Streets," in *Proc. PIMRC'94 (IEEE 5th International Symposium on Personal Indoor Mobile Radio Communications)*, The Hague, The Netherlands, Sept. 1994, pp. 496–500.
- [37] S. W. Wales and D. C. Rickard, "Wideband propagation measurements of short range millimetric radio channels," *Electronics and Commun. Eng. Journal*, pp. 249–254, Aug. 1993.
- [38] N. Daniele, D. Chagnot, and C. Fort, "Outdoor millimetre-wave propagation measurements with line of sight obstructed by natural elements," *IEE Electronics Letters*, vol. 30, no. 18, pp. 1533–1534, Sept. 1994.
- [39] G. Løvnes, S. E. Paulsen, and R.H. Rækken, "A versatile channel sounder for millimetre wave measurements," in *Proc. PIMRC'93 (IEEE 4th International Symposium on Personal Indoor Mobile Radio Communications)*, Yokohama, Japan, Sept. 1993.
- [40] D. C. Cox, "Delay Doppler Characteristics of Multipath Propagation at 910 MHz in a Suburban Mobile Radio Environment," *IEEE Trans. Ant. and Prop.*, vol. 20, no. 5, pp. 625–635, Sept. 1972.
- [41] M. Flament, *On 60 GHz Wireless Communication Systems*. PhD Thesis, Chalmers Univ. of Techn., Göteborg, Sweden, 2000.
- [42] G. L. Turin, F. D. Clapp, T. L. Johnston, S. B. Fine, and D. Lavry, "A statistical model of urban multipath propagation," *IEEE Trans. Veh. Technol.*, vol. VT-21, pp. 1–9, Feb. 1972.
- [43] H. Suzuki, "A statistical model for urban radio propagation," *IEEE Trans. Commun.*, vol. COM-25, pp. 673–680, July 1977.

- [44] H. Hashemi, “Simulation of the urban radio propagation channel,” *IEEE Trans. Veh. Technol.*, vol. VT-28, pp. 213–224, Aug. 1979.

Chapter 3 – Channel Measurement Technique based on the FD-Level Crossing Rate

3.1 Introduction

Channel measurements are required to obtain parameters for the channel model proposed in the previous chapter. A novel technique for conducting such measurements is introduced here, which is based on the frequency-domain level crossing rate (LCR_f) of the fading radio channel.

Usually, the level crossing rate (LCR) is defined and investigated for time-dependent stochastic processes, where it specifies the number of up-going level crossings through a given threshold. In this chapter, the LCR_f of the transfer function (TF) of a frequency-selective channel is studied, specifying the average number of fades per bandwidth.

From the analysis of the LCR_f , which is one of the main topics of this chapter, it was recognized that the LCR_f is proportional to the RMS delay spread (RDS) τ_{rms} of the multipath-fading channel. That is, the average number of fades per bandwidth (and also the average bandwidth of the fades) is related to τ_{rms} by a given factor. This factor was studied on the basis of the frequency-domain (FD) channel model introduced in the previous chapter. It has been noticed that the factor does depend on the K -factor of the Ricean fading channel, but the actual form of the channel model has little or no impact.

This property can be used for estimating the RDS from the LCR_f , which can be determined from non-coherent channel measurements (power-vs.-frequency sweeps of the channel TF). Since the normalized received power P_0 and the Ricean K -factor can be derived from such data as well [1], full sets of channel parameters $\{P_0, K, \tau_{rms}\}$ can be

obtained from pure power measurements. Hence, standard laboratory equipment may be used to conduct channel measurements, as e.g. a swept-frequency continuous-wave (CW) signal generator and a power meter or spectrum analyzer. Its simplicity makes the method particularly useful at extremely high frequencies (> 30 GHz; millimeter wave band), where for instance network analyzers become very cumbersome and expensive. Moreover, large distances can be allowed between the transmitter and the receiver, because no reference connection is required.

Since the proposed measurement method is based on a statistical model, a sufficiently large bandwidth must be observed to obtain high accuracy, just like a large frequency-band must be scanned with a network-analyzer in order to obtain a certain time-resolution. An advantage of our method is that – because of ergodicity – the observation bandwidth can be increased by analyzing the combined data of a number of ‘narrow-band’ measurements performed in a ‘local area’. The size of this local area must be selected sufficiently small for the channel parameters not to vary due to shadowing. Well de-correlated spectra can be obtained when the receiver’s location is changed in the order of one or a few wavelengths λ . Especially at the millimeter wave band with wavelengths below 1 cm, many spectrum samples can thus be taken within small areas.

Note that due to the lack of phase information, the Fourier transform cannot be used for transforming a magnitude TF to the delay time-domain, which would allow determining delay spread parameters as the RDS directly. However, the causality of the impulse response implies that the Hilbert transform describes the relationship between the real and imaginary components of the complex valued TF. Donaldson *et al.* have applied this property for analyzing magnitude TFs [2], yielding estimates of the channels’ impulse responses. Their method can be an alternative way of determining delay spread parameters using this type of measurements.

This chapter begins with the analysis of the LCR_f based on the FD-channel model introduced in the previous chapter (see Section 3.2). For the Rayleigh fading case it is proven that the channel impulse response has no influence on the factor relating τ_{rms} and the LCR_f . Some impact of the FD sampling interval will be seen, because level crossings may be overlooked if it is selected too large.

A measurement procedure derived from the relation of τ_{rms} and the LCR_f is described in Section 3.3, and its performance is investigated. We find that an observation bandwidth of $10/\tau_{rms}$ leads to estimation errors with standard deviations in the order of 10 ... 15 %.

The method’s sensitivity to additive noise is of major concern for its practical application, since additional level crossings caused by the noise lead to a systematic overestimation of the RDS. Such noise may be due to measurement inaccuracies, when scan-

ning the channel TF. This problem is extensively studied in Section 3.4.

The Chapter is concluded in Section 3.5, where also recommendations for further work are given.

3.2 Frequency-Domain Level Crossing Rate

The level crossing rate (LCR) is usually defined for time-domain fading (or other time-dependent stochastic processes) as the average number of crossings per second at which the envelope of a signal $\xi(t)$ crosses a specified level r in an up-going direction. Its dimension is $[s^{-1}]$.

Considering the TF in the frequency-domain, the LCR_f gives the average number of crossings per Hertz bandwidth at which the amplitude $R(f) = |H(f)|$ of the TF crosses a level r in an up-going direction. This LCR_f will be denoted by $N_R(r)$, its dimension being $[s]$.

The derivation of the LCR_f is firstly conducted on the basis of the FD-channel model, which describes the frequency-selectivity as a continuous stochastic process (see Chapter 2, Section 2.3). A solution is found for Ricean and Rayleigh fading channels. We apply this result for analyzing the impact of channel parameters (τ_{rms} and Ricean K-factor) and model parameters (the shape of the delay power spectrum (DPS)) on the LCR_f . A proportional relationship between the LCR_f and τ_{rms} is found. In Section 3.2.2, the significance of this relation is assessed by analyzing a deterministic two-ray channel.

As mentioned above, the LCR_f can be used to estimate the RDS of time-dispersive radio channels. In order to employ this relationship for channel investigations, the power response of the channel has to be scanned versus frequency, which is usually done at discrete frequency points. Selecting thereby the sampling interval in the frequency-domain too large, some level crossings may be overlooked, leading to a bias in the estimated τ_{rms} . In order to analyze the impact of sampling, the LCR_f is also derived for the sampled case (see Section 3.2.3). This study is limited to Rayleigh channels, however, because for the Ricean case, the mathematical expressions involved require numerical solutions.

Moreover, it will be shown that for Rayleigh channels the proportionality relationship between τ_{rms} and LCR_f is independent of the channel impulse response.

3.2.1 Derivation of the LCR_f from the Continuous FD-Channel Model

The following derivation is based on the FD-channel model introduced in Chapter 2, Section 2.3, which characterizes the frequency-selectivity (time-dispersive nature) of the multipath radio channel based on its delay power spectrum (DPS):

$$\phi_h(\tau) = \begin{cases} 0 & \tau < 0 \\ \rho^2 \delta(\tau) & \tau = 0 \\ \Pi & 0 < \tau \leq \tau_1 \\ \Pi e^{-\gamma(\tau-\tau_1)} & \tau > \tau_1 \end{cases} \quad (3-1)$$

For notational convenience we introduce $u = \tau_1 \gamma$, expressing the ‘shape’ of the DPS, and $u_1 = u + 1$, $u_2 = u^2/2 + u + 1$, and $u_3 = u^3/3 + u^2 + 2u + 2$.

3.2.1.1 Proof of the Proportionality of the LCR_f and the RMS Delay Spread

An analytical expression for the LCR of Ricean processes with cross-correlated real- and imaginary parts of the underlying complex Gaussian process $H'(f) = {}_r H'(f) + j {}_i H'(f)$ is given as (cf. [3], and [4], [5])

$$N_R(r) = \frac{r\sqrt{2\beta}}{\pi^{3/2}\psi_0} e^{-\frac{r^2+\rho^2}{2\psi_0}} \int_0^{\pi/2} \cosh\left(\frac{r\rho}{\psi_0} \cos\theta\right) \left\{ e^{-(\alpha\rho \sin\theta)^2} + \sqrt{\pi}\alpha\rho \sin(\theta) \operatorname{erf}(\alpha\rho \sin\theta) \right\} d\theta, \quad (3-2)$$

where $\psi_0 = \frac{1}{2}\phi_H(0) = \frac{1}{2}\Pi u_1 / \gamma$ is the variance of the real or imaginary component of $H'(f)$ (i.e. half of the power of the scattered rays), and $\alpha = -\frac{\dot{\phi}_0}{\psi_0 \sqrt{2\beta}}$ and $\beta = -\ddot{\psi}_0 - \frac{\dot{\phi}_0^2}{\psi_0}$ account for the second order statistics of $H'(f)$. ($\dot{\phi}_0$ and $\ddot{\psi}_0$ are given in (3-4).) $H'(f)$ is defined by the DPS (3-1) after subtraction of the LOS-component $\rho^2 \delta(\tau)$, or equivalently by its auto-correlation function (ACF):

$$\phi_{H'}(\Delta f) = F\{\phi_h(\tau)\} = \Pi \left[\tau_1 \operatorname{sinc}(\tau_1 \Delta f) e^{-j\pi\tau_1 \Delta f} + \frac{1}{\gamma + j2\pi\Delta f} e^{-j2\pi\tau_1 \Delta f} \right] \quad (3-3)$$

Note that the real and imaginary parts of this ACF denote respectively the ACF of the real *or* imaginary component of $H'(f)$, and the cross-correlation function (CCF) *between* its real- and imaginary components, written as $\phi_{H'}(\Delta f) = 2[\phi_{{}_r H'}(\Delta f) + j\phi_{{}_r H' {}_i H'}(\Delta f)]$. To calculate α and β , the curvature of the ACF $\phi_{{}_r H'}(\Delta f)$ and the gradient of the CCF $\phi_{{}_r H' {}_i H'}(\Delta f)$ have to be evaluated at $\Delta f = 0$, yielding

$$\ddot{\psi}_0 = \frac{d^2}{d\Delta f^2} \phi_{{}_r H'}(\Delta f) \Big|_{\Delta f=0} = -2\pi^2 \frac{\Pi}{\gamma^3} u_3 \quad \text{and} \quad (3-4a)$$

$$\dot{\phi}_0 = \frac{d}{d\Delta f} \phi_{{}_r H' {}_i H'}(\Delta f) \Big|_{\Delta f=0} = -\pi \frac{\Pi}{\gamma^2} u_2. \quad (3-4b)$$

Next, it will be shown that the LCR_f for the FD-model can be expressed in the form

$$N_R(r') = \tau_{rms} \cdot f(K, u, r'), \quad (3-5)$$

where $f(K, u, r')$ is the proportionality factor between τ_{rms} and the LCR_f . Note that this factor is constant at a given K-factor, normalized threshold level r' , and DPS shape defined by u . It will be seen below that the impact of the channel model (written by u) is usually negligible.

With (3-4) we get

$$\alpha = \sqrt{\frac{\gamma}{\Pi}} \frac{u_2}{\sqrt{u_3 u_1^2 - u_2^2 u_1}} \quad \text{and} \quad (3-6)$$

$$\beta = 2\pi^2 \frac{\Pi}{\gamma^3} \left[u_3 - \frac{u_2^2}{u_1} \right].$$

The threshold level r is related to the square root of the normalized received power P_0 (the RMS amplitude of the TF), to eliminate the influence of P_0 from the LCR_f :

$$r' = r / \sqrt{P_0} = r / \sqrt{\rho^2 + \frac{\Pi}{\gamma} u_1}. \quad (3-7)$$

Using (3-6), (3-7), $\psi_0 = \frac{1}{2}\Pi u_1 / \gamma$, and the expression for $\tau_{rms}(K, \gamma, u)$ from Table 2-1 (Section 2.3.3, page 30) yields with (3-2)

$$N_R(r') = \tau_{rms} \cdot a \cdot e^{-b} \int_0^{\pi/2} \cosh(c \cdot \cos \theta) \left\{ e^{-(d \cdot \sin \theta)^2} + \sqrt{\pi} d \cdot \sin \theta \cdot \text{erf}(d \cdot \sin \theta) \right\} d\theta, \quad (3-8)$$

where

$$a = \frac{4}{\sqrt{\pi}} r' (K+1)^{3/2} \sqrt{\frac{u_3 u_1 - u_2^2}{u_3 u_1 (K+1) - u_2^2}}$$

$$b = r'^2 (K+1) + K$$

$$c = 2r' \sqrt{K(K+1)}$$

$$d = \sqrt{K} \frac{u_2}{\sqrt{u_1 u_3 - u_2^2}} \quad (3-9)$$

It is observed from (3-9) that $\{a, b, c, d\}$ are expressed as functions of $\{K, u, r'\}$, i.e., they are independent of τ_{rms} , which proves (3-5).

This result can be used for estimating τ_{rms} from the LCR_f , which can be obtained from non-coherent wide-band measurements (i.e. from wide-band power measurements) [6]. It enables the wide-band characterization of the radio channel using a very simple measurement principle, as explained in the introduction. Section 3.3 discusses this method in detail.

3.2.1.2 Average Bandwidth of Fades

The average bandwidth of fades (ABF), $B_R(r)$, is the mean value for the bandwidth over which the amplitude $R(f)$ of the TF is below a specified level r . Equivalently to the respective time-domain parameter (the average duration of fades [7]), the ABF is written as

$$B_R(r) = \frac{F_R(r)}{N_R(r)}, \quad (3-10)$$

where $F_R(r)$ denotes the (Ricean) CDF of the signal envelope, i.e., the probability that $R(f)$ is below the level r .

$$F_R(r) = \Pr\{R(f) \leq r\} = \frac{1}{\psi_0} e^{-\frac{\rho^2}{2\psi_0} r} \int_0^r x e^{-\frac{x^2}{2\psi_0}} I_0\left(\frac{x\rho}{\psi_0}\right) dx \quad (3-11)$$

In this equation, $I_0(\bullet)$ designates the zeroth-order modified Bessel function of the first kind.

Computational results of the normalized level crossing rate and the average bandwidth of fades are shown in Figure 3-1a and b, respectively. They are compared to computer simulations generated with the FD-simulation scheme introduced in Chapter 2, Section 2.4. The comparison clearly demonstrates that the analytical expressions describe the statistical properties of the simulated channel appropriately.

3.2.1.3 Influence of Channel and Model Parameters

Using the analytical expressions, the influence of the channel parameters $\{P_0, K, \tau_{rms}\}$ and the influence of the shape of the DPS (expressed by $u = \tau_1 \gamma$) on the LCR_f and on the ABF is studied.

One of the main results is that the LCR_f is proportional to τ_{rms} , as seen from the mathematical analysis above. For this reason it is appropriate to show LCR_f and ABF normalized to τ_{rms} . Furthermore, the result is independent of the NRP P_0 , if the threshold variable r is normalized to $\sqrt{P_0}$. Therefore, the shape of the LCR_f is characteristic for particular K-factors (and parameters u) as seen from the factor $f(K, u, r')$ in (3-5). Normalized LCR_f and ABF are depicted in Figure 3-2a and b, respectively, as a function of r' and for various K-factors and parameters u .

It is observed from these figures that even in the extreme cases $u = 0$ (exponentially decaying DPS) and $u = \infty$ (rectangular DPS), the LCR_f and ABF remain similar, provided τ_{rms} and K are kept constant. The dependency on u disappears completely for $K = 0$, i.e., for Rayleigh fading channels. For any K , the LCR_f at $r' = 1$ ($r = \sqrt{P_0}$) shows little variation, which is also evident from Figure 3-3a, illustrating the factor $f(K, u, r' = 1)$ as a function of K with parameter u . Figure 3-3b depicts the systematic

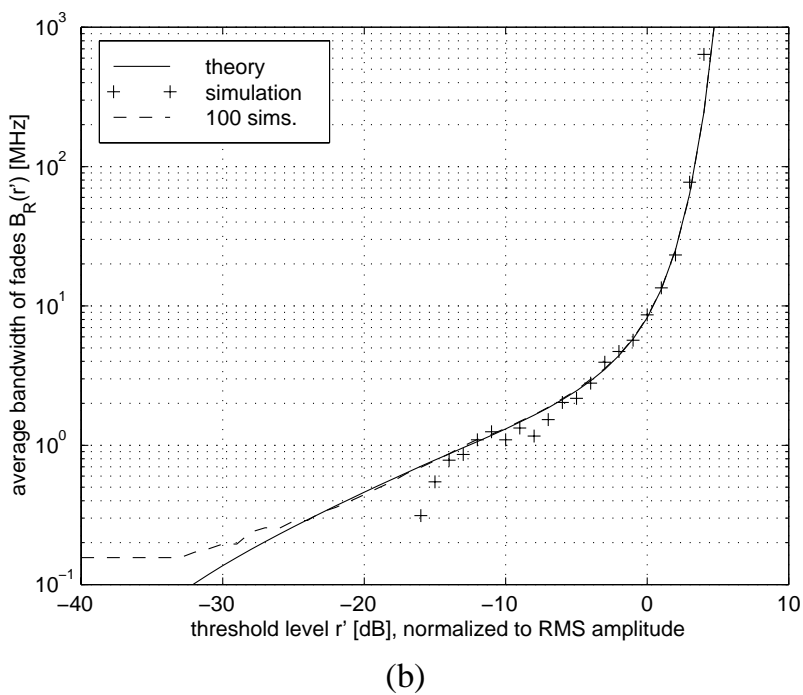
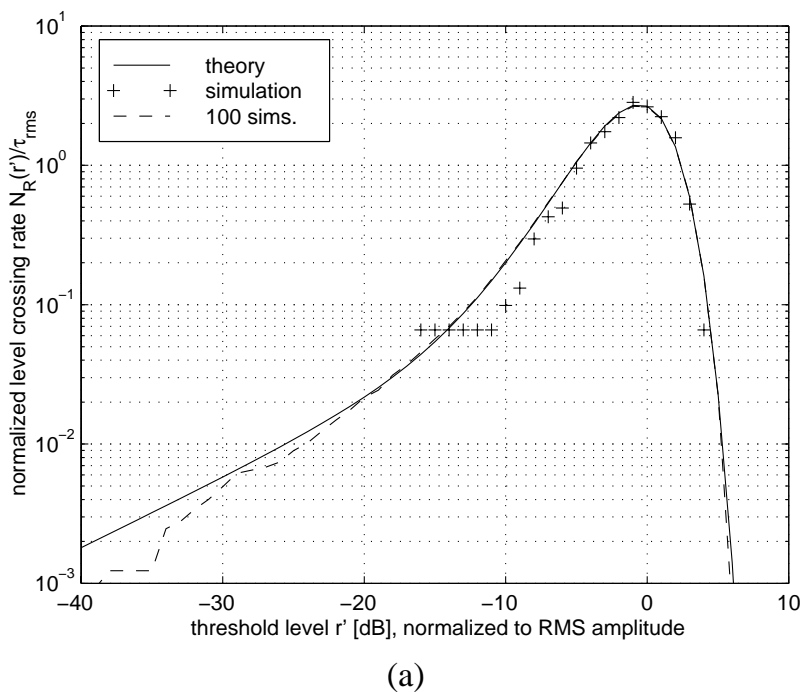
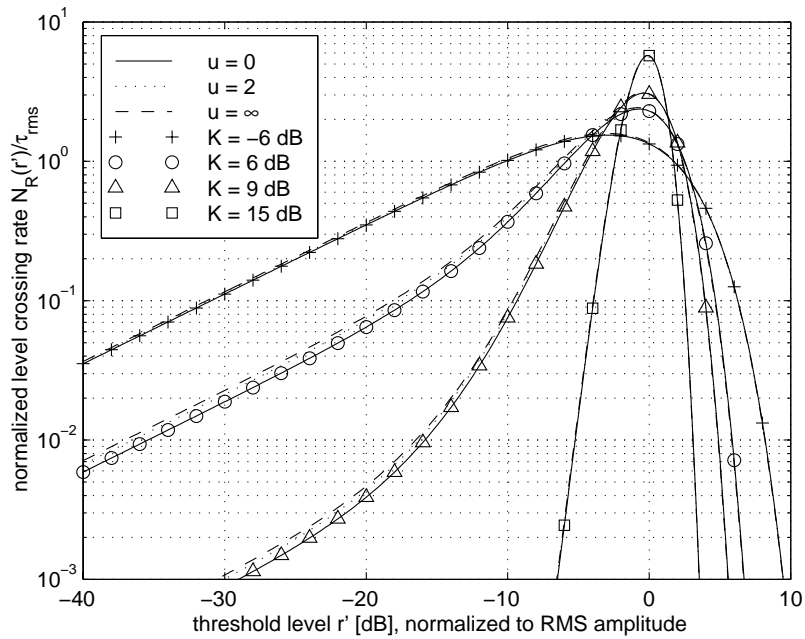
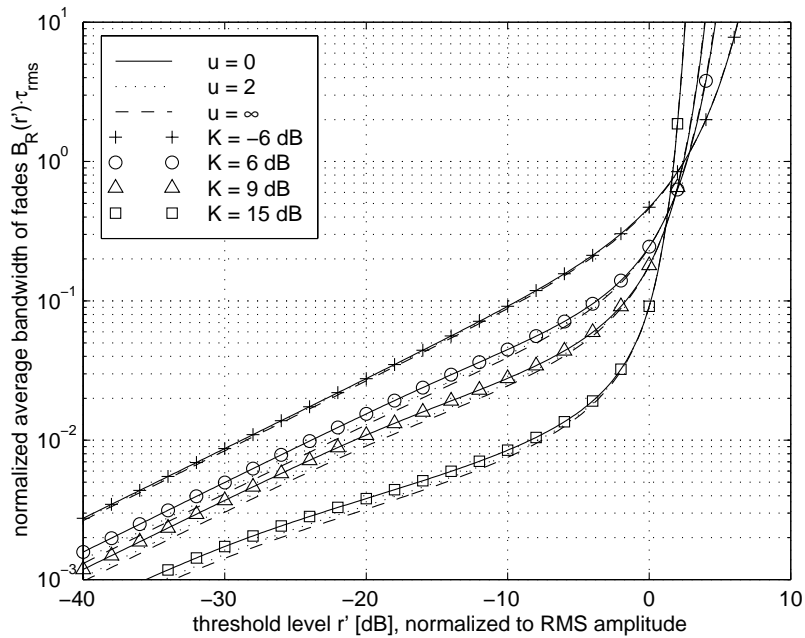


Figure 3-1: (a): Normalized level crossing rate for Ricean K -factor $K = 7.5$ dB. Analytical results compared with results from one single simulation and averaged results from 100 simulations (simulated bandwidth 1.28 GHz; $\tau_{rms} = 25.3$ ns); (b): Average bandwidth of fades for the same simulations.

estimation error that would yield from using (3-5) with $u = 0$ for estimating τ_{rms} of channels with $u = \{2, \infty\}$. It is seen that the difference of $f(K, u, r' = 1)$ for a rectangular DPS and an exponentially decaying one is less than 4% at any given K -factor. The other curves in Figure 3-3 are described in Section 3.2.2.



(a)



(b)

Figure 3-2: (a): LCR_f for various K -factors and parameters u ; (b): ABF for the same parameters. Both figures are normalized to τ_{rms} and $\sqrt{P_0}$. The small influence of the shape of the delay power spectrum (expressed by the parameter u) is observed.

From the behavior of the LCR_f -curves, conclusions can be drawn on the significance of the channel parameters $\{P_0, K, \tau_{rms}\}$ used in this study. Each of them has a very distinct impact on the LCR_f , thus one might expect them to have different impact on performance results as well.

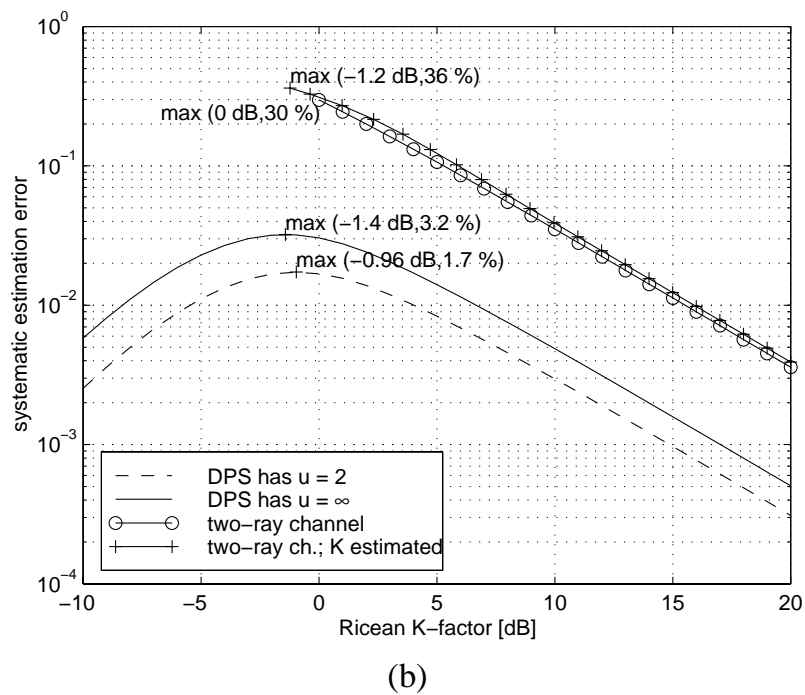
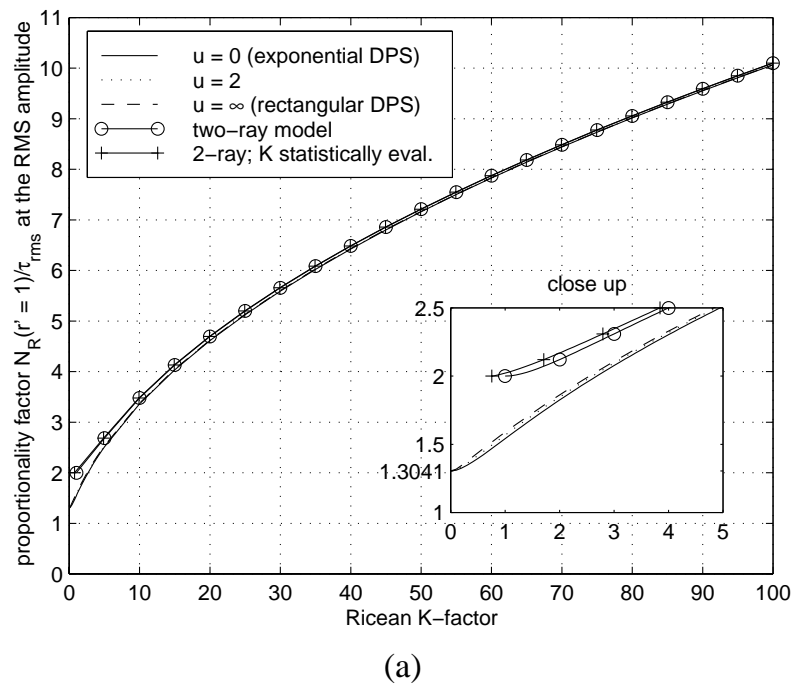


Figure 3-3: (a): The factor $f(K, u, r' = 1) = N_R(r' = 1)/\tau_{rms}$ as a function of the Ricean K-factor for various channel models. (b): Estimation error of τ_{rms} , when $f(K, u = 0, r' = 1)$ is used, but the channels are characterized by other models.

The Ricean K-factor characterizes the depth of the fades about the mean power given by P_0 . Therefore, the distribution of the signal-to-noise ratio is related to P_0 and K , which generally determines the bit error rate (BER) achievable, at a given noise and interference power level.

The RMS delay spread specifies the number of fades per bandwidth and the average bandwidth of the fades. Considering multi-carrier transmission systems (e.g. coded OFDM), one would expect a dependency of the BER on the number of fades within the transmission bandwidth. From the LCR_f , this parameter is seen to be strictly related to τ_{rms} . Performance evaluations of OFDM systems have confirmed these observations (see Sections 4.3 and 8.2).

For (non-equalized) single-carrier modulation schemes, the relationship between τ_{rms} and the BER is even more obvious, since the delay spread determines the amount of inter-symbol-interference, which itself impacts on irreducible error floors. Numerous studies are available for various modulation and detection schemes, reporting on qualitative and quantitative relations between τ_{rms} and the BER. Although no general result is known, τ_{rms} is probably the most important single parameter for characterizing the time-dispersion or frequency-selectivity of the wide-band radio channel.

3.2.2 LCR_f for a Deterministic Two-Ray Channel

In this section, a brief analysis is presented in order to assess the validity of the proportionality factor $f(K, u, r')$ (which relates the LCR_f to τ_{rms}) for different channel models. A deterministic two-ray model is investigated for this purpose. The IR of such a channel is defined as

$$h(\tau) = \beta_0 e^{j\theta_0} \delta(\tau) + \beta_1 e^{j\theta_1} \delta(\tau - \tau_\delta), \quad (3-12)$$

where $\beta_0 \geq \beta_1$ are the ray amplitudes, $\{\theta_0, \theta_1\}$ are the ray phases, and $\tau_\delta > 0$ is the relative delay among the two paths. Applying the FT leads to the amplitude TF

$$R(f) = |H(f)| = \sqrt{\beta_0^2 + \beta_1^2 + 2\beta_0\beta_1 \cos(2\pi\tau_\delta f + \theta_1 - \theta_0)}. \quad (3-13)$$

From (3-13), the LCR_f is seen to be constant:

$$N_R(r) = \begin{cases} \tau_\delta & \beta_0 - \beta_1 \leq r \leq \beta_0 + \beta_1 \\ 0 & \text{otherwise} \end{cases} \quad (3-14)$$

τ_{rms} must be calculated for this model to obtain the normalized LCR_f , which is the proportionality factor required. Analyzing the IR yields

$$\tau_{rms} = \tau_\delta \frac{\beta_0\beta_1}{\beta_0^2 + \beta_1^2} = \tau_\delta \frac{\sqrt{\kappa}}{\kappa + 1}, \quad (3-15)$$

where $\kappa = \beta_0^2 / \beta_1^2$ is the power ratio of the two rays. Taking κ as K -parameter, (3-14) and (3-15) can be used to derive the proportionality factor as a function of K (see Figure 3-3a, ‘○—○’).

In fact, the Ricean distribution is not describing the amplitude distribution of (3-13), thus comparing κ to the Ricean K -factor in (3-5) might be inappropriate. One method

of deriving K from a set of amplitude values R is to calculate $E\{R\}$ and $E\{R^2\}$. The ratio $E\{R\}^2/E\{R^2\}$ can then be related to K as elaborated in [1]. Using this definition of K , the proportionality factor is found as indicated by ‘+—+’ in Figure 3-3a.

The similarity of all the results shown in this graph confirms the significance of the relationship found between τ_{rms} and the LCR_f . It suggests that the proposed measurement method can be applied quite generally, i.e., even if the investigated propagation channel does not match to the model defined by eq. (3-1). This statement is further evaluated below.

In Figure 3-3b, the error of τ_{rms} is depicted, resulting from strictly using $f(K, u = 0, r' = 1)$ when estimating τ_{rms} for channels described by the two-ray model (and by the FD-model for $u = \{2, \infty\}$). If a two-ray channel is evaluated with this method, the maximum error is 36 % when both rays have equal powers, and it drops below 10 % when κ is above 6 dB.

3.2.3 Derivation of the LCR_f for the Sampled Case

The derivation of the LCR_f for the sampled channel TF is the goal of this section. Purpose of this analysis is to evaluate the impact of the sampling interval, which – if selected too large – may lead to systematic errors in the τ_{rms} estimation, because level crossings in-between sampling instants may be overlooked. Note that the following derivations are limited to Rayleigh channels, because for the Ricean case the mathematical expressions do not yield analytical solutions.

The probability of a level crossing between adjacent samples is the probability that the current sample’s magnitude R_n is larger than a specified threshold value, $R_n \geq r$, while the preceding sample R_{n-1} was smaller, $R_{n-1} < r$. The LCR_f is thus written as

$$N_R(r) = \Pr(R_n \geq r, R_{n-1} < r) / F, \quad (3-16)$$

where F [Hz] is the sampling *interval* in the frequency-domain, and R_n and R_{n-1} denote correlated random variables. Knowledge of the bivariate cumulative distribution function (CDF) of $\{R_n, R_{n-1}\}$, $F_{R_n, R_{n-1}}(r_1, r_2)$, is required to obtain the LCR_f from

$$\Pr(R_n \geq r, R_{n-1} < r) = \Pr(R_{n-1} < r) - \Pr(R_n < r, R_{n-1} < r) = F_{R_{n-1}}(r) - F_{R_n, R_{n-1}}(r, r), \quad (3-17)$$

where $F_{R_{n-1}}(r) = F_{R_n, R_{n-1}}(\infty, r)$ is the CDF of any one sample, e.g. R_{n-1} . Using an expression of the bivariate Rayleigh CDF given in [8] (eq. (10-10-3)), the probability (3-17) becomes

$$\Pr(R_n \geq r, R_{n-1} < r) = e^{-r^2} \left[Q_1 \left(\sqrt{\frac{2}{1-\rho_c}} r', \sqrt{\frac{2\rho_c}{1-\rho_c}} r' \right) - Q_1 \left(\sqrt{\frac{2\rho_c}{1-\rho_c}} r', \sqrt{\frac{2}{1-\rho_c}} r' \right) \right], \quad (3-18)$$

where $Q_1(a, b)$ is the Marcum’s Q -function (see [9], (2-1-123)), r' is the normalized

threshold level $r' = r/\sqrt{2\psi_0} = r/\sqrt{P_0}$, and ρ_c is the correlation coefficient of the squared magnitudes defined as $\rho_c = \text{cov}(R_n^2, R_{n-1}^2) / \sqrt{\text{var}(R_n^2) \text{var}(R_{n-1}^2)}$, $0 \leq \rho_c < 1$. ρ_c is related to the auto-correlation of the underlying complex Gaussian process Z_n ($|Z_n| = R_n$) by $\rho_c = |\psi_1|^2 / \psi_0^2$, where $\psi_m = \frac{1}{2} E\{Z_n Z_{n+m}^*\}$. An alternative expression for (3-18) is given as (cf. [10])

$$\Pr(R_n \geq r, R_{n-1} < r) = e^{-r'^2} - \frac{1}{2\pi} \int_{-\pi}^{\pi} e^{-2r'^2 \frac{1+\sqrt{\rho_c} \sin \theta}{1-\rho_c}} \frac{1-\rho_c}{1+\rho_c+2\sqrt{\rho_c} \sin \theta} d\theta. \quad (3-19)$$

It is seen that the crossing probability (3-18), (3-19) is solely determined by the correlation coefficient ρ_c and by r' . Calculating ρ_c based on the stochastic or deterministic model of a Rayleigh distributed process (e.g. for the FD-channel model defined by (3-1)) thus leads to the level crossing rate.

This section continues with the derivation of an approximation for (3-18) (and (3-19)) for the case that $\rho_c \rightarrow 1$, which is for instance given when the sampling interval approaches zero, $F \rightarrow 0$. Note that in this limit, the sampled case approaches the continuous case analyzed above (Section 3.2.1).

Secondly, the correlation coefficient is derived from the FD-channel model and – in Appendix A – from the discrete impulse response defined by eq. (2-1), Section 2.2.2. It will become evident that a common expression relates ρ_c to τ_{rms} in the limit $F \rightarrow 0$. Therefore, there is no influence of the channel impulse response on the proportionality factor between τ_{rms} and the LCR_f for the continuous case and for Rayleigh fading channels.

Based on the analytical results, the impact of sampling on the LCR_f is evaluated.

3.2.3.1 Approximation of the Crossing Probability for the Sampled Case

Both expressions for the sampled version of the LCR_f , eqs. (3-18) and (3-19), are difficult to evaluate if ρ_c is close to one. The goal of this derivation is to find an approximation for this case.

In order to find an asymptotic expression for (3-18) in the limit $\rho_c \rightarrow 1$, we use the relation of the Marcum's Q -function to the CDF of a Ricean random variable (see [9], (2-1-142))

$$1 - Q_1(a, b) = \int_0^b v e^{-(v^2+a^2)/2} I_0(av) dv. \quad (3-20)$$

When av becomes large, $I_0(av)$ may be replaced by its asymptotic expression, as suggested in [4], eq. (3.10-19). This yields the following approximation for the Ricean CDF, being valid for $ab \gg 1$ and $a \gg |b - a|$ (see [4]), which is fulfilled for $\rho_c \rightarrow 1$.

$$1 - Q_1(a, b) \cong \frac{1}{2} + \frac{1}{2} \operatorname{erf} \frac{b-a}{\sqrt{2}} - \frac{1}{\sqrt{8\pi a}} e^{-(b-a)^2/2} \left[1 - \frac{b-a}{4a} + \frac{1+(b-a)^2}{8a^2} \right] \quad (3-21)$$

Replacing the error function by the first terms of its power series expansion, the most important terms of (3-21) can be identified,

$$\operatorname{erf} \frac{b-a}{\sqrt{2}} = \frac{2}{\sqrt{\pi}} \left[\frac{b-a}{\sqrt{2}} - \frac{(b-a)^3}{6\sqrt{2}} + \dots \right]. \quad (3-22)$$

For the two Q -functions in (3-18), $b-a$ and a are

$$(b-a)_{I,II} = \mp (1 - \sqrt{\rho_c}) \sqrt{\frac{2\rho_c}{1-\rho_c}} r' \cong \mp \sqrt{\frac{1-\rho_c}{2}} r' \ll 1$$

$$a_{I,II} = \begin{cases} \frac{1}{\sqrt{\rho_c}} \sqrt{\frac{2}{1-\rho_c}} r' \cong \sqrt{\frac{2}{1-\rho_c}} r' \gg 1 \\ \sqrt{\frac{2}{1-\rho_c}} r' \cong \sqrt{\frac{2}{1-\rho_c}} r' \gg 1 \end{cases}, \quad (3-23)$$

respectively, where the approximations and the inequities hold for $\rho_c \rightarrow 1$. Keeping the most significant terms yields

$$Q_1(a, b)_{I,II} \cong \frac{1}{2} - \frac{1}{\sqrt{2\pi}} (b-a)_{I,II} + \frac{1}{\sqrt{8\pi a_{I,II}}} \cong \frac{1}{2} \pm \frac{1}{2} \sqrt{\frac{1-\rho_c}{\pi}} r' + \sqrt{\frac{1-\rho_c}{\pi}} \frac{1}{4r'}. \quad (3-24)$$

Substituting these expressions for the Q -functions in (3-18), the approximation

$$\Pr(R_n \geq r, R_{n-1} < r) \cong \frac{r' e^{-r'^2}}{\sqrt{\pi}} \sqrt{1-\rho_c}, \quad (3-25)$$

is obtained, which becomes exact in the limit $\rho_c \rightarrow 1$. This condition is fulfilled strictly for $F \rightarrow 0$, i.e., for an infinitely small sampling interval, and approximately, if the sampling theorem holds. The systematic error is less than $\sim 1\%$ and $\sim 5\%$, for $\rho_c \geq 0.9$ and $\rho_c \geq 0.65$, respectively, and for thresholds r' between -6 dB and 6 dB (see Figure 3-4). Larger negative errors are evident for smaller r' , since the sampling interval gets more impact as the fades get deeper and narrower.

3.2.3.2 Calculation of the Correlation Coefficient ρ_c

The correlation coefficient is obtained from $\rho_c = |\psi_1|^2 / \psi_0^2$, where $\psi_m = \frac{1}{2} E\{Z_n Z_{n+m}^*\}$ is the auto-correlation function of the discrete complex Gaussian process, which is underlying the sampled Rayleigh process. Therefore, ψ_m has to be determined from the channel model in order to calculate the LCR_f for the sampled case. This calculation is given here for the FD-channel model, and in Appendix A, for a generic discrete channel impulse response.

The spaced-frequency correlation function for the Rayleigh case (see eq. (3-3)), leads

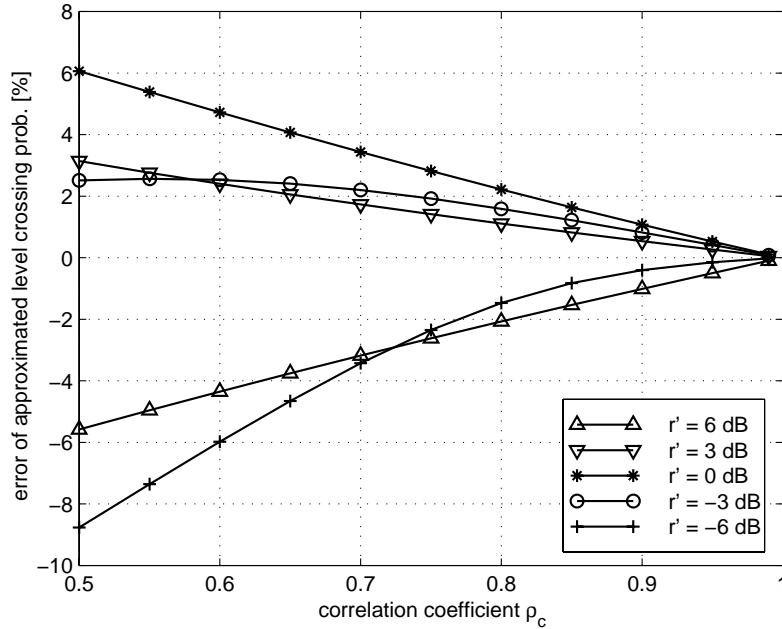


Figure 3-4: Error of the approximated level crossing probability for the sampled case. Relative error [%] as a function of the correlation coefficient ρ_c , with r' as a parameter.

to ρ_c for the FD-channel model, with $\psi_m = \frac{1}{2}\phi_H(mF)$. For the two important special cases of an exponentially decaying DPS ($u = 0$) and a rectangular DPS ($u = \infty$), ρ_c becomes

$$\rho_c = \begin{cases} \frac{1}{1 + (2\pi\tau_{rms}F)^2} & \text{for } u = 0 \\ \text{sinc}^2(2\sqrt{3}\tau_{rms}F) & \text{for } u = \infty \end{cases} \quad (3-26)$$

Introducing the series expansions of the functions involved in the above expressions, the common approximation

$$\rho_c \cong 1 - (2\pi\tau_{rms}F)^2 \quad (3-27)$$

is obtained, in the limit $F \rightarrow 0$.

It is shown in Appendix A that the same approximation (3-27) holds for any arbitrary channel IR. Therefore, there is no dependency of the level crossing probability on any of the channel model parameters, provided the channel is a Rayleigh channel. The validity of the approximations introduced is discussed below.

3.2.3.3 Approximated LCR_f

Inspection of eqs. (3-26) and (3-27) suggests that the LCR_f is proportional to τ_{rms} , for the following reasons. Provided that the sampling theorem is not violated (i.e., strictly speaking, for $F \rightarrow 0$), the LCR_f must be independent of the sampling interval F . Therefore, the probability (3-18) must be proportional to F , to yield a constant LCR_f

with (3-16). This implies that (3-18) is also proportional to τ_{rms} , because it is seen from (3-27) that F and τ_{rms} have the same influence on ρ_c . Thus the LCR_f is proportional to τ_{rms} .

Based on the approximation (3-25), this observation can be confirmed mathematically. With (3-27) and (3-16), the LCR_f for Rayleigh fading channels becomes

$$N_R(r') \cong 2\sqrt{\pi} r' e^{-r'^2} \tau_{rms}, \quad (3-28)$$

which clearly shows the proportionality.

Note, moreover, that (3-28) is identical to the result of the continuous-frequency analysis presented in Section 3.2.1 [cf. eq. (3-2), for $K = 0$ (i.e., $\rho = 0$)]. Therefore, the difference of the approximation (3-28) to the exact LCR_f for the sampled case (which can be calculated from (3-16) and (3-18) or (3-19), with (3-26)) quantifies the impact of a finite sampling-interval. This impact is analyzed below.

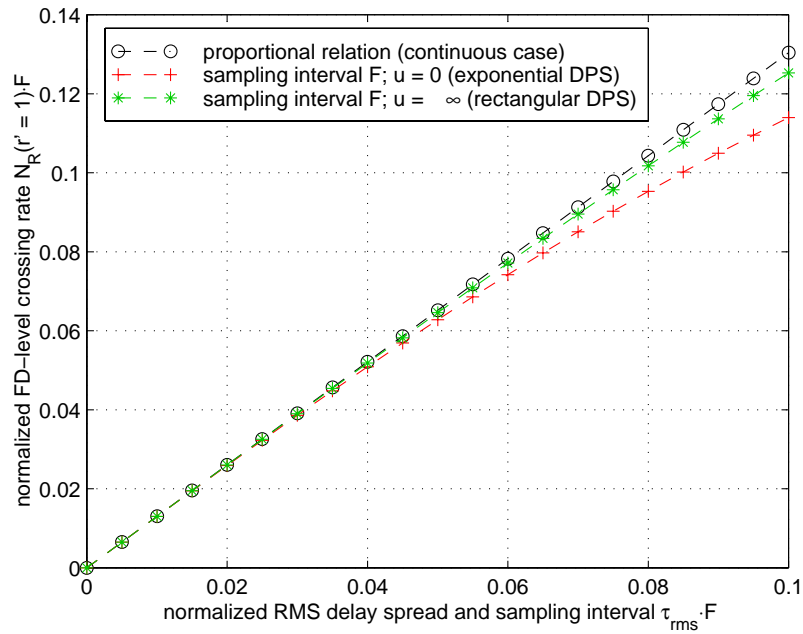
3.2.3.4 Discussion of the Impact of Sampling

Results of LCR_f vs. τ_{rms} are depicted in Figure 3-5a. Due to sampling effects, there is a deviation between the exact LCR_f for the sampled case ('+--+' for $u = 0$ and '*--*' for $u = \infty$) and the linear relation obtained from the continuous model and the approximations ('o--o'). An increasing number of level crossings is missed, when the sampling interval is selected too large with respect to the channel's τ_{rms} .

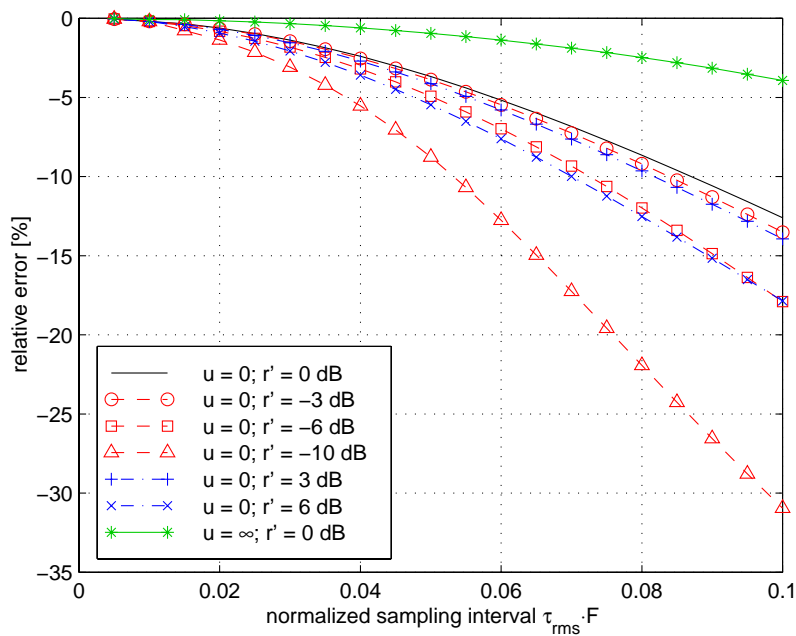
Figure 3-5b illustrates the systematic estimation error resulting from the application of the linear relation (3-5) for estimating τ_{rms} from the power-frequency-scan of a channel with a certain sampling interval F . To analyze this error, the exact LCR_f is calculated from (3-16) and (3-18), with (3-26) for a specific $\tau_{rms} \cdot F$. (As seen from (3-26), the product $\tau_{rms} \cdot F$ determines ρ_c , therefore, τ_{rms} can be normalized in this way). The proportional relation (3-5) (and (3-28)) is applied to calculate the erroneous estimate $\hat{\tau}_{rms}$ for this observed LCR_f , leading to the relative estimation error

$$\varepsilon_\tau = \frac{\hat{\tau}_{rms}}{\tau_{rms}} - 1 = \frac{LCR_{f, \text{sampled case}}}{LCR_{f, \text{continuous case}}} - 1. \quad (3-29)$$

Considering the Nyquist theorem, the sampling interval should be $F \leq 1/(2\tau_{max})$, which means at $K = 0$ (and $u = 0$) that $\tau_{rms} \cdot F \leq 1/20$, following eq. (2-24), Section 2.3.3. In this range of $\tau_{rms} \cdot F$, the maximum bias is below 4 %, at $r' = 1$. The errors increase for smaller thresholds r' , where the fades get deeper and narrower, and also for larger ones (see Figure 3-5b; curves '---' and '- · - ·'). Investigating the channel model with the rectangular DPS, i.e., $u = \infty$, the errors decrease, since channels having shorter impulse responses imply higher oversampling (see Figure 3-5b; curve '*---*', for $r' = 1$).



(a)



(b)

Figure 3-5: Influence of sampling on the proportionality of τ_{rms} and the LCR_f . Parameters: Rayleigh fading; $F = 1$ Hz. (a): LCR_f vs. τ_{rms} at $r' = 1$, $u = \{0, \infty\}$. Continuous and sampled cases. (b): Relative error of the proportional relationship (continuous case). All results for $u = 0$ except for ‘*—*’, where $u = \infty$.

3.2.3.5 Independence from the Channel Impulse Response

A number of simulation results are depicted in Figure 3-6 in order to support the claimed independence of the relation between the LCR_f and τ_{rms} from the channel IR.

Sets of 500 impulse responses were generated for this purpose, where each IR consisted of $L = 15$ rays with unit variance, Rayleigh distributed magnitudes, and arrival times being uniformly distributed within a unit time interval. The IRs were then normalized with respect to power and τ_{rms} . Next, the exact LCR_f was calculated for each IR (for $r' = 1$), using equations (3-16) and (3-18) (or (3-19)), with the correlation coefficient obtained from (A-6) (see Appendix A).

Figure 3-6 illustrates the error compared with the proportionality relationship as a function of the (normalized) sampling interval $\tau_{rms} \cdot F$. The errors' mean, minimum and maximum values are indicated as well as their standard deviation.

A systematic error is evident from this figure, which is zero at $F = 0$ and which increases with F . Remarkable are also the errors' small standard deviations, meaning that ρ_c is largely independent of the structure of the IR. Minimum and maximum values are evidence for an asymmetric distribution of errors about the mean. Thereby, above average values of ρ_c lead to larger negative errors of the LCR_f . A simulation for a smaller number of rays would show similar mean errors, but increased standard deviations.

To obey to the sampling theorem, $F < 1/(2\tau_{max}) \cong 1/(20\tau_{rms})$ should be given. In this range of F , the mean error is less than $\sim 2\%$. The mean error as a function of F is com-

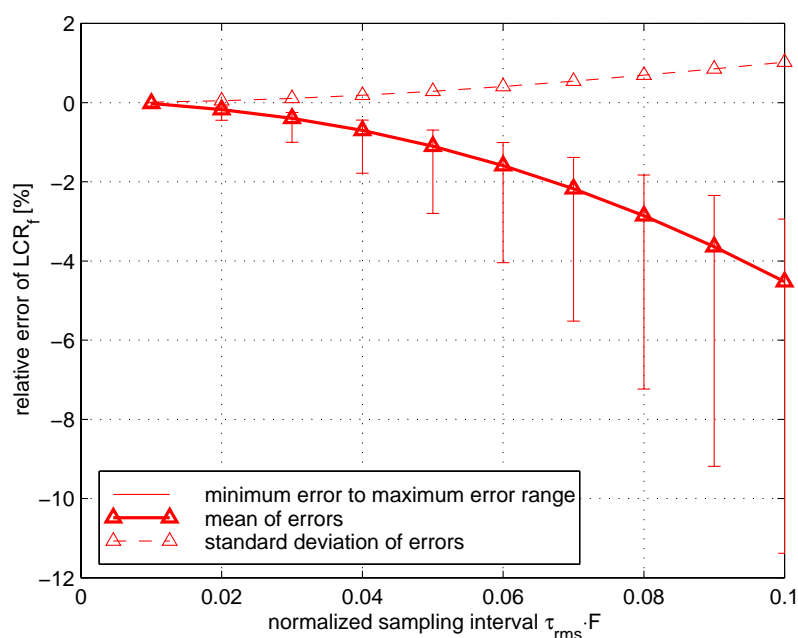


Figure 3-6: Relative error of the LCR_f compared with the proportional relation (at $r' = 1$). These results are for simulated random impulse responses with $L = 15$ rays.

parable to the curve shown in Figure 3-5 for the case of the rectangular DPS. Indeed, the ensemble of simulated IRs agrees with this model of a rectangular average power delay profile.

3.2.4 Discussion and Summary

In Section 3.2.1, it was shown that a strict proportional relationship exists between the level crossing rate of a frequency-selective radio channel in the frequency domain (LCR_f , $N_R(r')$), and the channel's RMS delay spread τ_{rms} . This relation is written as $N_R(r') = \tau_{rms} f(r', K, u)$ (3-5), where the proportionality factor $f(r', K, u)$ is a function of the threshold level at which the LCR_f is observed (r'), the Ricean K-factor of the channel (K), and channel parameters (expressed by u). It was suggested to use this relation for estimating the channel's τ_{rms} using simple swept-frequency power measurements, from which the LCR_f can be determined. The measurement principle is further discussed in Section 3.3.

The Ricean K-factor can be determined prior to applying (3-5). However, the impact of the current channel on $f(r', K, u)$ (expressed by u) remains an uncertainty, and might thus be a source of systematic estimation errors.

In Appendix A it is shown for Rayleigh fading channels that the *channel model does not influence the proportionality factor* between the LCR_f and τ_{rms} . This finding strongly supports the claim that the LCR_f is a valuable means for estimating τ_{rms} in a simple way.

Analytical results from eq. (3-5) have shown that the proportionality factor does depend on the channel model in the general Ricean case. The factor has been compared for widely varying channel models, suggesting that the impact is very small and can thus be neglected in many cases. So is the difference of $f(r', K, u)$ for a rectangular delay power profile and an exponentially decaying one less than 4 % at any K-factor, and at $r' = 1$.

A deterministic two-path channel model was analyzed in Section 3.2.2 to assess the relationship between the LCR_f and τ_{rms} . Although this model is very different to the Rayleigh and Ricean stochastic models on which eq. (3-5) was based, similar proportionality factors were found.

The proportionality relationship (3-5) was derived from the FD-channel model (see Section 2.3), which describes the frequency-selective transfer function of the multipath channel as a *continuous*, WSS stochastic process. In Section 3.2.3, the LCR_f was derived for the sampled case, i.e., for transfer functions given at discrete frequency-instants. When the sampling interval is selected too large, then some level-crossings in-between sampling instants may be overlooked, and the LCR_f deviates from the value suggested by (3-5). The systematic errors introduced have been analyzed.

3.3 Application to Channel Measurements

In this Section, we discuss the application of the relationship between the LCR_f and the RMS delay spread τ_{rms} for estimating τ_{rms} . A measurement procedure is introduced and validated using experimental data. Finally, the estimation accuracy is evaluated based on computer simulations.

3.3.1 Channel Measurement Procedure

A practical channel measurement procedure based on the power response in the frequency domain is outlined in this section. Although the procedure operates only on power measurements, where no information about the phase of the received signal is available, all the important channel parameters (i.e. the average received power P_0 , Ricean K -factor, RMS delay spread τ_{rms}) and their statistics can be obtain.

The measurement setup comprises of a transmitter and a receiver. The transmitter is made up of a sine wave generator, an up-converter, an amplifier, and a transmit antenna. The receiver consist of an antenna, a preamplifier, a down-converter and a power meter (e.g. a spectrum analyzer) [11]–[14].

Calibration measurements are necessary in order to evaluate the amount of noise and inaccuracy caused by the system itself. This stage gives calibration data, which can then compensate for the frequency response of the measurement system. It also quantifies the noise caused by the system, which is necessary to evaluate the influence of noise on the τ_{rms} estimation (see Section 3.4).

Once the calibration data has been gathered, the channel measurements can be performed. For each point within the frequency range to be measured (e.g. $10/\tau_{rms}$ bandwidth) the transmitter sends a sine signal, the power of which is measured by the power meter tuned to the frequency of the transmitted wave. At the end of the procedure a sampled magnitude transfer function in the measured frequency range is composed $R_n = |H(nF)|$, $n = \{1, 2, \dots, N\}$. From the data, the channel parameters are obtained in the following steps:

1. Compensation for the measurement system's characteristics is performed by subtracting the calibration data [dB] from the measurement data.
2. The average received power $\hat{P}_0 = \frac{1}{N} \sum_{n=1}^N R_n^2$ is estimated.
3. The Ricean K -factor is determined, e.g. by the method given in [1], based on the average power \hat{P}_0 and the average amplitude $\hat{R} = \frac{1}{N} \sum_{n=1}^N R_n$.
4. The RMS delay spread $\hat{\tau}_{rms}$ is estimated from the LCR_f at threshold level $r = \sqrt{\hat{P}_0}$ (i.e., at $r' = 1$)⁷, using (3-5) and (3-30).

⁷ Other threshold levels could be selected as well, but $r' = 1$ is most simple to determine, it is close

The above procedure describes the steps to be followed to obtain the channel parameters from one measured TF. Several measurements performed at one particular location can be combined, leading to improved estimation results, as elaborated below.

3.3.1.1 Approximation of the Proportionality Factor

For measurements, the following approximation of $f(K,u,r')$ at $u = 0$ and $r' = 1$ can be used, which results in errors below 1 % for all values of K , compared to the exact $f(K,u = 0,r' = 1)$:

$$\tilde{f}(K,u = 0,r' = 1) = \begin{cases} \frac{1}{4}K^{3/2} + 1.3041 & K \leq 1 \\ \sqrt{K} \frac{K+1}{K+0.31} & K > 1 \end{cases} \quad (3-30)$$

3.3.1.2 Increasing the Effective Measurement Bandwidth

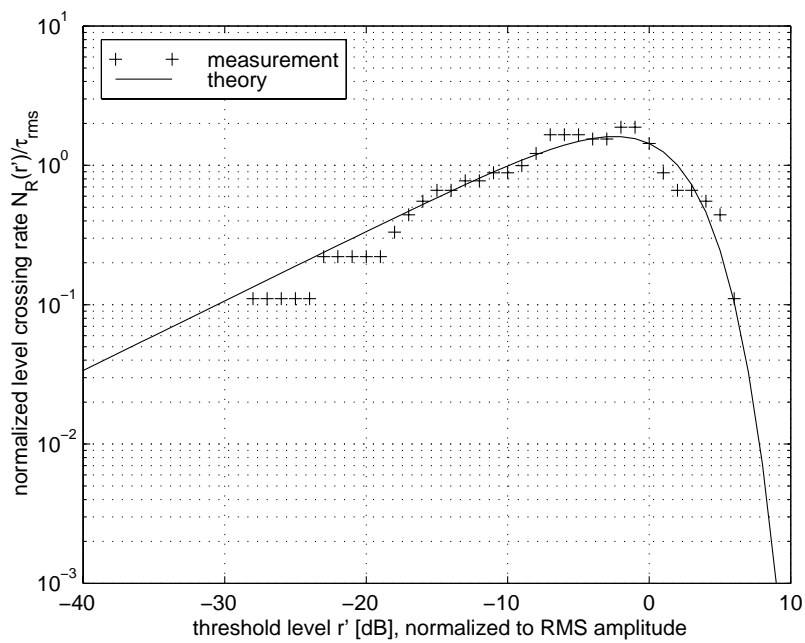
The accuracy obtained depends heavily on the observation bandwidth, since the measurement method is based on a statistical model. By increasing the bandwidth, the number of detected level crossings is increased, and thus the accuracy of the estimated RDS is enhanced. A valuable advantage of the proposed method is found in the fact that – because of ergodicity – the observation bandwidth can be extended not only by increasing the bandwidth of the measurement, but also by combining data from several measurements that are performed within a local area. This local area must be sufficiently small (maximum size $\cong 5 \dots 40\lambda$) so that we can assume the channel parameters (and thus the statistical properties of the channel) to be constant. In other words, the shadowing must be constant (see Section 2.2). Data collected for such a cluster of measurements is analyzed as follows. The NRP and the K-factor are determined by simply combining all measured amplitudes and calculating \hat{R} and \hat{P}_0 for the resulting data set. Level crossing rates must be calculated for each measurement separately, but at a common threshold r' . Consecutively, they are averaged to obtain the LCR_f for the combined data set.

The proposed method is evaluated below, using channel measurements performed with a network analyzer, and using time-domain channel simulations.

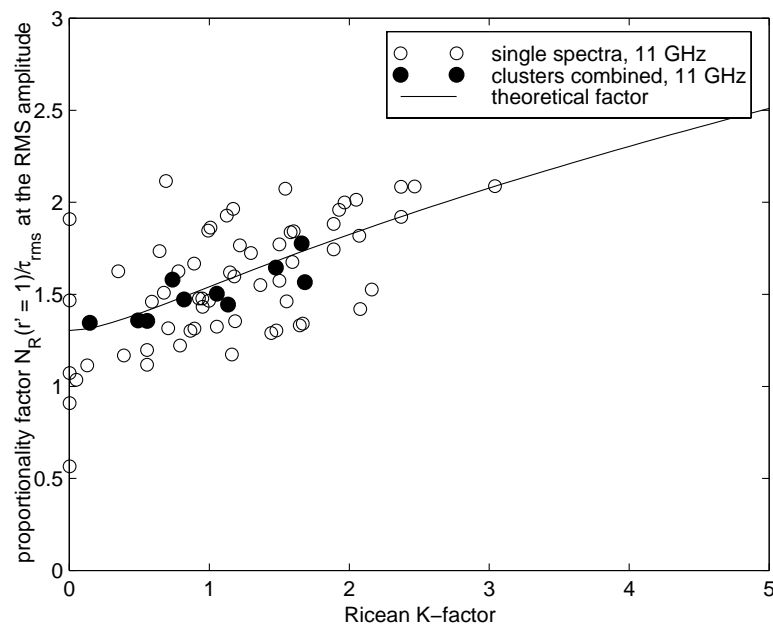
3.3.2 Validation of the Method using Measurement Results

Coherent measurements conducted with a network analyzer allow the calculation of the channel's IR, from which a reference-value of τ_{rms} can be derived. Clusters of six

to the maximum of the $N_R(r')$ curves thus yielding nearly optimum accuracy, and the dependency of $f(K,r',u)$ on u is very small at this r' (cf. Figure 3-2a). One could also estimate τ_{rms} at a set of threshold levels and consecutively combine the estimates to enhance the accuracy. In [15], performance results are depicted for such a scheme, indicating some improvement.



(a)



(b)

Figure 3-7: (a): Comparison of measured and theoretical level crossing rates for matched channel parameters. (b): Indicated points: Empirical proportionality factor between the estimated LCR_r obtained from the amplitude TF and the reference τ_{rms} obtained from the IR. Curve ('—'): Theoretical factor $f(K, u = 0, r' = 1)$. The mismatch indicates the estimation error.

measurements were investigated within the local areas (of diameter = 2λ). Each TF scanned had 1 GHz bandwidth around a center frequency of 11.5 GHz [16] (see footnote 5 on page 35).

Figure 3-7a shows the empirical LCR_f of one measured TF as a function of r' and the analytical curve for the estimated parameters \hat{K} and $\hat{\tau}_{rms}$ (assuming $u = 0$). The good agreement demonstrates the suitability of the FD-model for characterizing the frequency-selective channel.

To assess the accuracy of the estimated RDS, the proportionality factor $\hat{N}_R(r'=1)/\tau_{rms}$ is depicted in Figure 3-7b as a function of the Ricean K-factor. The estimated LCR_f $\hat{N}_R(r'=1)$ and K-factor \hat{K} were derived from the amplitude TF $R_n = |H(nF)|$ using the proposed method to be evaluated and (the reference) τ_{rms} was calculated from the channel IR using a conventional method [17], [18].

The RDS was estimated for every single measured TF and also for the combined data sets of each cluster of six measurements. The theoretical factor $N_R(r' = 1)/\tau_{rms} = f(K,0,1)$ is shown in the same figure for comparison. The distance between this curve and the data points indicates the estimation error. It is observed from this figure that the estimation error is decreased significantly by investigating the combined data of the measurement clusters.

3.3.3 Validation by Time-domain Channel Simulations

Channels obtained from a time-domain (TD) channel simulator were analyzed for evaluating estimation errors. This approach was taken because τ_{rms} is defined from the channel's IR – the output of the TD simulator.

3.3.3.1 Computer Simulation Scheme

The TD simulation model assumes a line-of-sight ray at $\tau = 0$, a Poisson process of ray-arrivals (of approx. 60 rays), an exponentially decaying average power delay profile, Rayleigh distributed ray amplitudes, and uniformly distributed ray phases (compare [17] for one cluster; and Section 2.5.3). In a second step, the generated impulse responses were normalized to get the required K-factor K , $\tau_{rms} = 1$ and $P_0 = 1$ [19], allowing for simple evaluation of the estimation error. Applying the Fourier transform to the generated IRs, (complex-valued, discrete-frequency) TFs were obtained.

The FD-sampling interval of these TFs, F , is related to the maximum delay spread τ_{max} of the channel impulse responses, which can be written as a function of the Ricean K-factor and τ_{rms} (see eq. (2-24) on page 32). Using this expression of τ_{max} , the oversampling factor OS is defined as

$$OS = \frac{1}{2\tau_{max} F} = \frac{1}{20\tau_{rms} F} \frac{\sqrt{2K+1}}{K+1}. \quad (3-31)$$

In the simulations of this section, $OS = 1$ was used.

3.3.3.2 Accuracy of the Estimation Technique

After generating TFs for well-defined channel parameters, the RMS delay spreads were estimated using the proposed procedure, yielding $\hat{\tau}_{rms}$. The estimation error is defined as

$$\varepsilon_{\tau} = \frac{\hat{\tau}_{rms} - \tau_{rms}}{\tau_{rms}}. \quad (3-32)$$

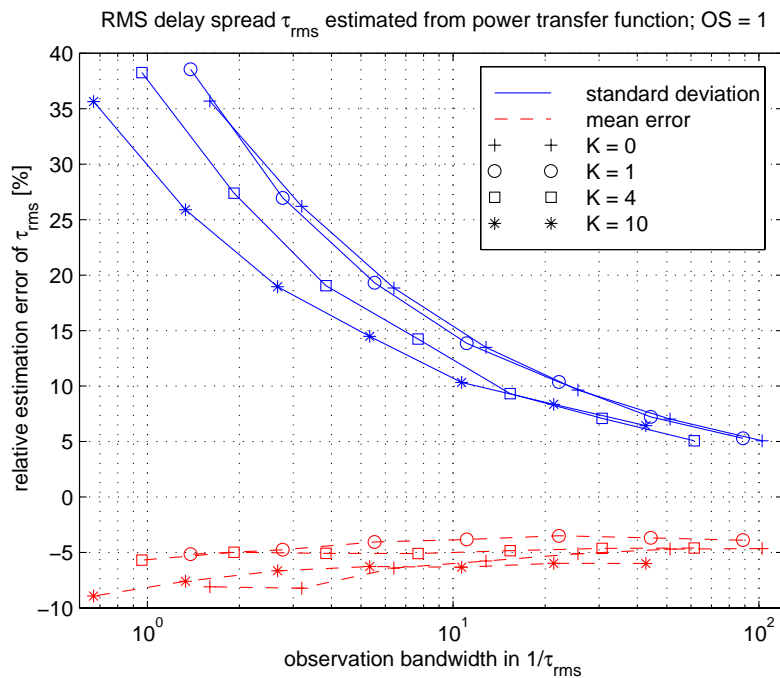
Performing simulations for different values of K and different observation bandwidths, the mean and standard deviation of the error ε_{τ} are investigated. Results are depicted in Figure 3-8a, as a function of the normalized observation bandwidth. (The PDF of the estimation error ε_{τ} was observed to be appropriately described by a Gaussian distribution.)

For the estimation method described above, a small systematic estimation error ($\sim -5\%$) and decreasing standard deviation with increased bandwidth can be seen from the results. The systematic error agrees fairly with the bias introduced by the sampling of the TF, which was analyzed in Section 3.2.3 for $K = 0$. (Note that in the simulation here $\tau_{rms}F = 0.05$ at $K = 0$.) The results given in Figure 3-5b can thus be used for canceling this systematic error.

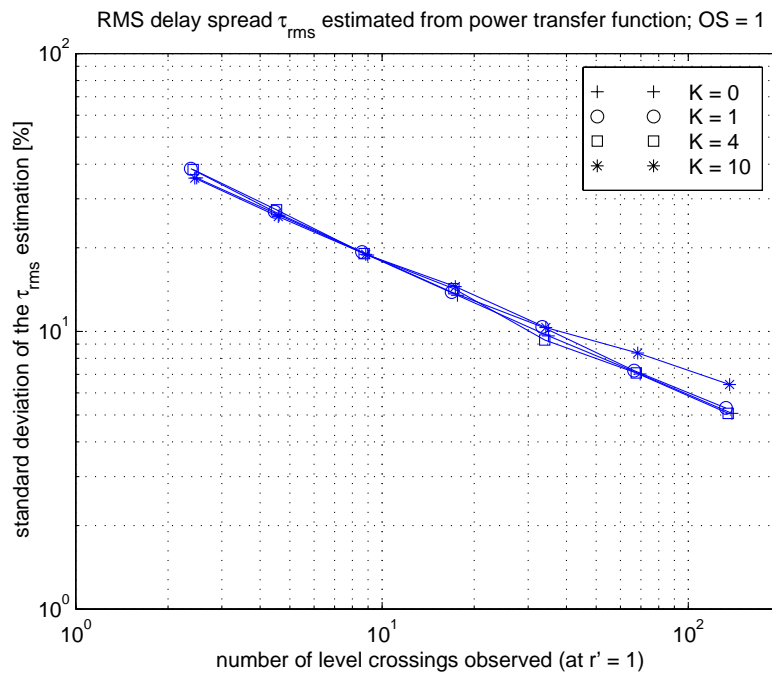
However, the bias is also partly caused by a bias in the estimated K -factors, because the K -factor estimation is performed prior to the τ_{rms} estimation. An evaluation of the accuracy of this estimation step is a recommended topic for further work. It can result in a compensation table that indicates the required corrections as a function of the normalized sampling interval and K -factor.

In Figure 3-8b, the standard deviation of the error is shown as a function of the number of level crossings. This diagram clearly reveals that the number of observed level crossings determines the estimation accuracy. Note that the variance appears to be proportional to the reciprocal of the level crossing rate, i.e., the standard deviation $\sigma_{\varepsilon_{\tau}} \propto 1/\sqrt{N_R(r')}$.

The results given in Figure 3-8 specify the estimation error of τ_{rms} compared to the local area mean parameters, i.e., compared to the constant parameters of the WSSUS channel model. Considering a limited bandwidth, however, there is a certain variation of the instantaneous channel parameters within a local area anyway, because the structure of the impulse response is not resolved completely (see Section 2.2). This variation of the instantaneous channel parameters was investigated in Section 2.2.3 (see Figure 2-1). The results given there should be compared to the accuracy of the novel estimation technique for τ_{rms} (Figure 3-8), because the estimation error of the novel method includes the variation of the channel parameters due to the limited observation bandwidth.



(a)



(b)

Figure 3-8: Relative estimation error of τ_{rms} , derived from sets of hundred TD simulations. (a): Mean and standard deviation of the estimation error ε_τ as a function of the normalized bandwidth. (b): Standard deviation of the estimation error ε_τ as a function of the number of level crossings.

It is seen that the standard deviations of these parameters are in the same order of magnitude as the estimation errors of the proposed τ_{rms} estimation technique. The stan-

standard deviation of τ_{rms} due to bandwidth limitation is by a factor of about two below the standard deviation of the estimation error, at a given bandwidth. The error between the estimated τ_{rms} and the instantaneous τ_{rms} was also evaluated in order to analyze the correlation between the two values. A small decrease of standard deviation compared with the result shown in Figure 3-8 (about -10%) indicates that the deviations from the local-area-mean parameters are partly correlated. A correlation coefficient of about 0.45 was obtained from the computer simulations.

3.3.4 Discussion of the Measurement Method

It is seen that the RDS can be estimated with reasonable accuracy when the observation bandwidth is larger than $10/\tau_{rms}$, or when more than ten level crossings are present. While the required bandwidth might be higher than the bandwidth needed for other measurement techniques, it can be increased easily by combining multiple measurements performed within a small local area. Another advantage lies in the simplicity of the hardware that can be used. It makes the method particularly interesting at extremely high frequencies (millimeter wave band), where e.g. network analyzers become very expensive and cumbersome due to the phase reference required, which is very difficult to provide over large distances. A clear advantage compared to other channel sounding techniques is that no specific equipment must be designed. A continuous wave frequency generator and a power meter or spectrum analyzer may be used to collect measurement data.

Preliminary measurement campaigns performed at Delft University of Technology ([11]–[14]) have shown the practical suitability of the described methods. But they have also led to the discovery of an interesting problem. Even a small measurement noise level may increase the number of level crossings detected. Improved measurement methods have been proposed in these references to reduce this effect. The following section gives the theoretical analysis of the impact of measurement noise. These investigations show that the frequency-domain sampling interval of the measurements should be selected as large as possible to minimize the influence of noise.

3.4 Analysis of the Influence of Noise

A major practical problem of the novel technique for estimating τ_{rms} is its sensitivity to additive noise in the measured power TF. This noise may introduce additional level crossings and thus lead to systematic overestimation of τ_{rms} , as illustrated in Figure 3-9. In this section, the influence of noise on the LCR_f is analyzed mathematically. Introducing the noise to the frequency-domain (FD) channel model, which is modeled as a continuous stochastic process, quantifies the impact of noise for the general case of Ricean fading channels. However, this analysis is not sufficient, because a measurement is typically performed on discrete-frequency instants, spaced by the sampling

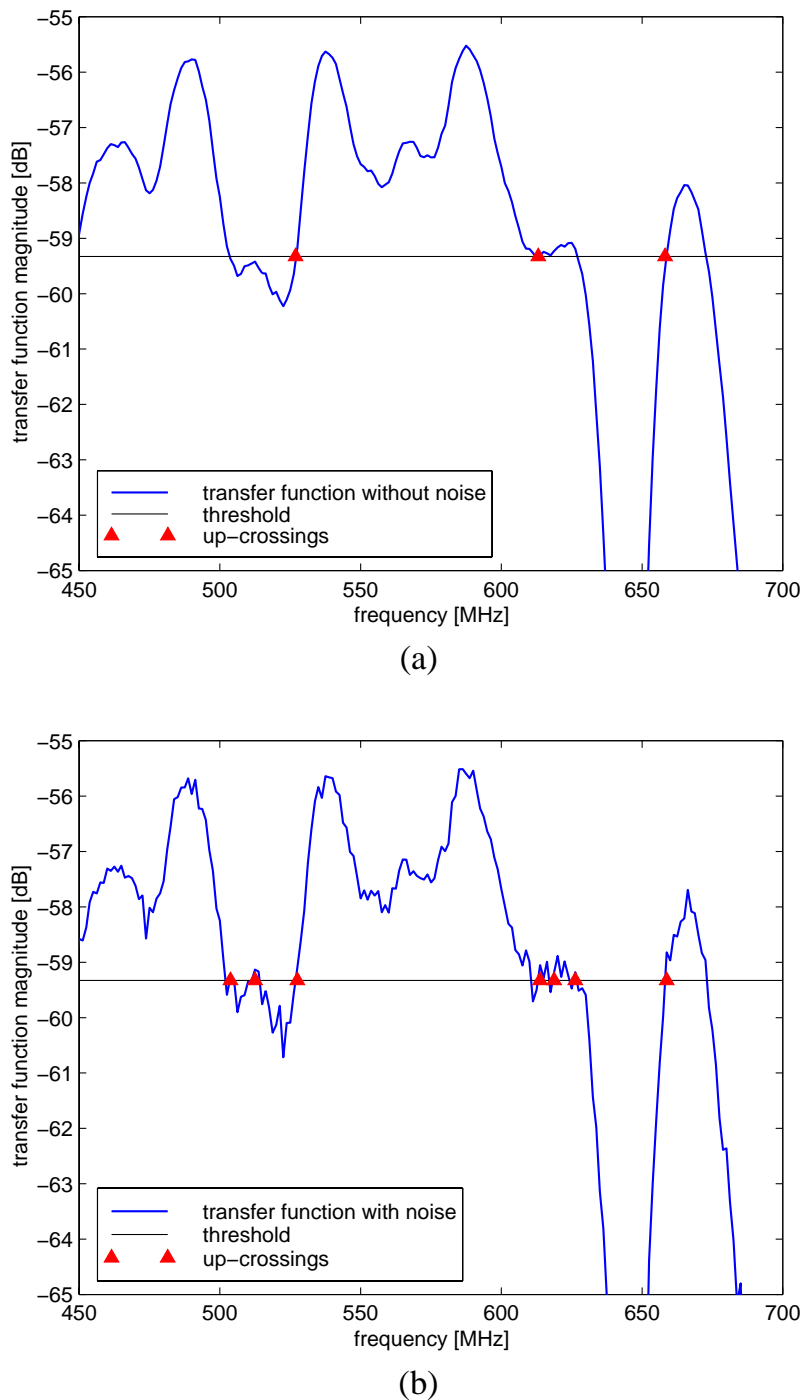


Figure 3-9: Influence of noise on the level crossing rate. (a): Channel transfer function without additive noise. (b): Channel transfer function with additive noise.

interval F . The result from the analysis of the continuous-time model predicts a large impact of the sampling interval on the noise's influence, but it fails to describe that impact accurately, due to the inappropriate mathematical model. To elaborate on this effect, we also investigate the LCR_f for the sampled case. This analysis is again limited to Rayleigh channels, however.

The analytical results presented can be used for evaluating the systematic estimation

error due to a given noise level. Unfortunately, the result is less suitable for correcting this systematic error. Computer simulations have indicated that applying the analytical result can indeed reduce the systematic estimation error; the error's variance, however, is boosted at the same time.

More successfully, a method was applied that reduces the influence of noise on the counted LCR_f by introducing a second threshold [12]. Thereby, level crossings are ignored, which are likely due to noise and not due to fades. For a good performance, the threshold separation must be adapted to the noise and channel parameters. This method is presented in Section 3.4.5 and basic performance results are given.

3.4.1 Mathematical Modeling

The measurement noise is introduced to the FD-channel model (see eq. (3-1), Section 3.2.1 and Section 2.3) as an additive band-limited Gaussian noise component. To model the independence of the additive noise samples, band-limitation to $\pm 1/(2F)$ is assumed, where F [Hz] is the sampling *interval* in the frequency-domain. Note that the sampling interval has been introduced although the mathematical model is a continuous one. The magnitude of the noise process is defined by the power density Π_N [1/s], yielding the noise power $P_N = \Pi_N/F = E\{|n_n|^2\}$. The $\{n_n\}$ denote independent complex Gaussian noise samples that are added to the complex-valued TF $H(nF)$. The FD-channel model and the model for the noise process are depicted in Figure 3-10.

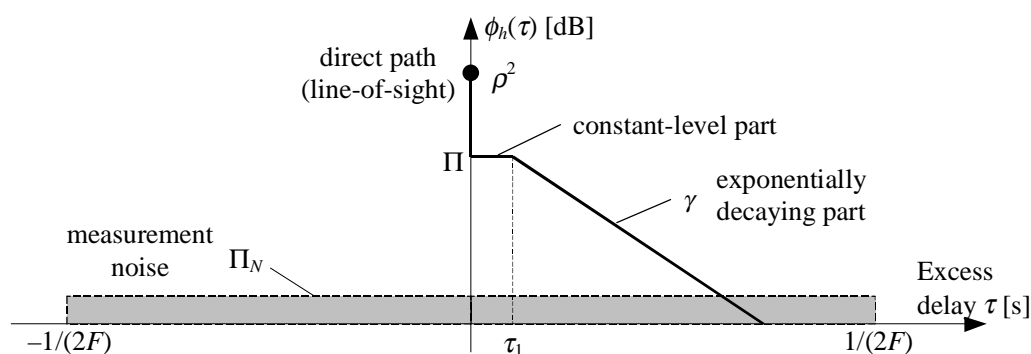


Figure 3-10: Model of the delay power spectrum (DPS) with additive measurement noise.

3.4.1.1 Definitions

The noise power is related to the variance of the (zero-mean) complex Gaussian noise process underlying the Ricean fading process. This is written $N' = P_N/(2\psi_0)$, where $\psi_0 = \frac{1}{2}\phi_H(0) = \frac{1}{2}\Pi u_1/\gamma$. $\phi_H(\Delta f)$ is the auto-covariance of the channel transfer function (see eq. (3-3)). (Note that the line-of-sight component is excluded from the normalization term.)

The additive noise component increases the average power of the observed TF and it decreases the K-factor as

$$\begin{aligned}\tilde{P}_0 &= P_0 + P_N = \rho^2 + 2\psi_0(1 + N') = P_0 \left(1 + \frac{N'}{K + 1}\right), \\ \tilde{K} &= K/(1 + N')\end{aligned}\quad (3-33)$$

Independence of the noise processes is assumed. The tilde indicates parameters influenced by the additive noise. Since usually $N' \ll 1$, this influence is small and can be neglected in the mathematical derivations and in channel parameter estimation. That is, $\tilde{K} \cong K$, $\tilde{P}_0 \cong P_0$, and furthermore $\tilde{r}' \cong r'$.

The above definitions specify the first order statistics, i.e., (the change of) the amplitude distribution. Second order statistics, as the LCR_f can be derived from the spaced-frequency correlation function, which for our model is given by

$$\begin{aligned}\tilde{\phi}_H(\Delta f) &= \phi_H(\Delta f) + P_N \text{sinc}(\Delta f / F); \\ \phi_H(\Delta f) &= \rho^2 + \Pi \left[\tau_1 \text{sinc}(\tau_1 \Delta f) e^{-j\pi\tau_1 \Delta f} + \frac{e^{-j2\pi\tau_1 \Delta f}}{\gamma + j2\pi\Delta f} \right].\end{aligned}\quad (3-34)$$

It will be seen below that the influence of noise depends strongly on the sampling *interval* F . Therefore, this parameter must be appropriately defined. According to Nyquist's sampling theorem, $F \leq 1/(2\tau_{max})$ must be given, where τ_{max} is the maximum excess delay of the channel. The oversampling factor OS , as defined by eq. (3-31) will be used to specify F in relation to τ_{rms} and K .

Calculating the level crossing rate for the continuous model described above (using the equations given in Section 3.2.1) yields a compact expression quantifying the impact of noise for Ricean channels. These derivations are outlined in Section 3.4.2 and in Appendix B. In practice, however, the LCR_f is determined from measurements taken at discrete frequency instants. The LCR_f is quite sensitive to this sampling; therefore we also analyze the LCR_f for the sampled case, called the discrete-frequency LCR_f (see Section 3.4.3). This analysis is limited to the Rayleigh fading case, however. For the Ricean case, a constant correction factor is introduced to the result from the continuous-frequency analysis, which can partly correct for sampling effects (Section 3.4.2.1).

3.4.2 Derivation of LCR_f from the Continuous FD-Channel Model

It is shown in Section 3.2.1 that without additive noise, the LCR_f , $N_R(r')$, and the RMS delay spread τ_{rms} are proportional as $N_R(r') = \tau_{rms} f(r', K, u)$ (3-5). The proportionality factor $f(r', K, u)$ – the normalized LCR_f (of a channel having $\tau_{rms} = 1$) – is a function of the Ricean K -factor K , the normalized threshold level $r' = r/\sqrt{P_0}$ (normalized to the average power), and the channel model parameter u . The latter has little impact on $f(r', K, u)$ and can thus be let $u = 0$ in practice (see Figure 3-2 and Figure 3-3).

The straight, dashed lines in Figure 3-11 show this proportionality relationship. In or-

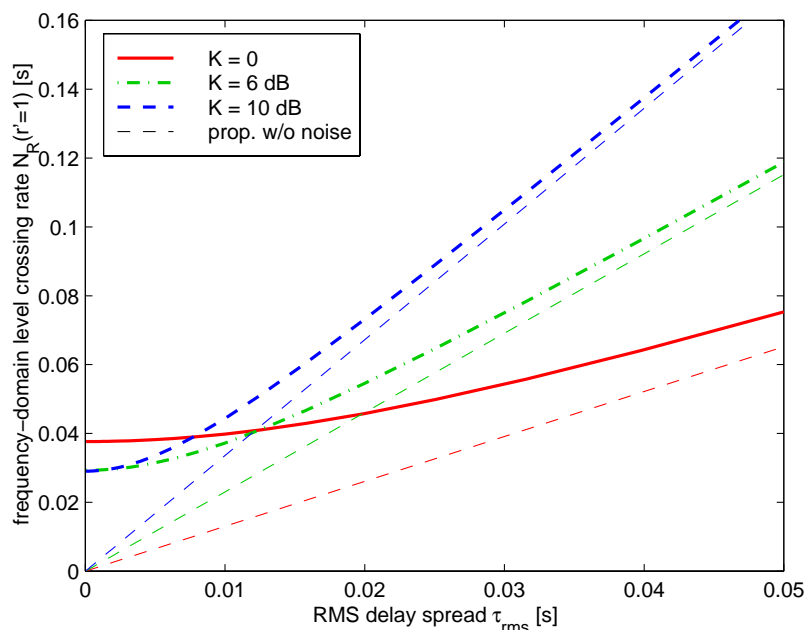


Figure 3-11: Relation between τ_{rms} and the LCR_f with and without noise. The asymptotic behavior is seen. Relative noise power $N' = 0.01$; sampling interval $F = 1$ Hz. LCR_f for $r' = 1$ and $c_s = 1$.

der to apply it for estimating τ_{rms} , the factor $f(r', K, u)$ must be known. It can be calculated from eq. (3-8) with (3-9), or from the approximation (3-30).

Measurement noise may raise the level crossing rate for a given channel. The idea of this analysis is to quantify the impact of noise on the LCR_f , and to use the resulting equation for correcting for it.

With the mathematical model and the definitions introduced in Section 3.4.1, and with two approximations (see Appendix B), a rather simple relation (3-35) between the LCR_f influenced by noise, $\tilde{N}_R(r')$, and τ_{rms} is found.

$$\sqrt{\left(\tilde{N}_R(r')\right)^2 - \frac{N'}{F^2} c_s^2 h^2(r', K)} = \tau_{rms} f(r', K, u) \quad (3-35)$$

Figure 3-11 illustrates its behavior for various K -factors. It is seen that noise determines the level crossing rate at low τ_{rms} , where the number of level crossings due to the multipath channel is low.

Just as the factor $f(r', K, u)$ is the normalized LCR_f for the multipath radio channel, so is $h(r', K)$ the LCR_f for the additive, uncorrelated measurement noise, scaled by $\sqrt{N'}/F$ (⁸). Note that this result was obtained from the continuous FD-channel model, considering noise with a flat, band-limited spectrum. The constant c_s is used to correct for

⁸ This statement becomes clear when the special case of a flat fading channel is considered (i.e., $\tau_{rms} = 0$), where level crossings are due to noise only.

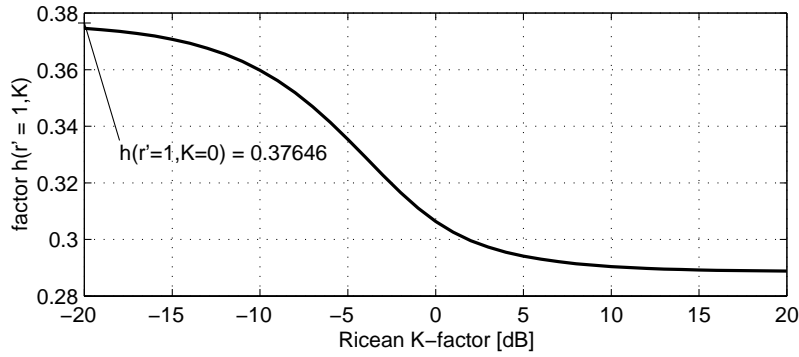


Figure 3-12: Evaluation of $h(r', K)$ at $r' = 1$.

sampling effects that are overlooked by this approach. A thorough explanation of this issue and the value of c_s are given in Section 3.4.2.1.

Note that the right-hand-side of (3-35) is the LCR_f for the noiseless case (compare eq. (3-5)), therefore, the left-hand-side quantifies the influence of noise on the LCR_f . To evaluate the expression, the factor $h(r', K)$ is needed, which is shown in Figure 3-12 as a function of K , at $r' = 1$. It is obtained from (see Appendix B)

$$h(r', K) = \sqrt{\frac{\pi}{3}} r' \sqrt{K+1} \cdot e^{-r'^2(K+1)-K} I_0(2r' \sqrt{K(K+1)}), \quad (3-36)$$

where I_0 is the zero-th order modified Bessel function of the first kind.

The components of the LCR_f due to the fading channel and due to measurement noise, and the total LCR_f can be seen as the sides of a right-angled triangle. Its hypotenuse stands for the LCR_f of the noisy measurement, while the adjacent sides are the component LCR_s , as illustrated in Figure 3-13. It appears that the two uncorrelated noise processes correspond to LCR -components in orthogonal directions of a plane, while their vector sum's length corresponds to the total LCR . Note that this observation was made from (3-35). It was not tried to prove mathematically if this is a general property of the LCR of sums of (independent) stochastic processes.

The nature of the square root in (3-35) indicates that the estimation of τ_{rms} becomes more difficult when the measured LCR_f , $\tilde{N}_R(r')$, gets in the range of the subtracted

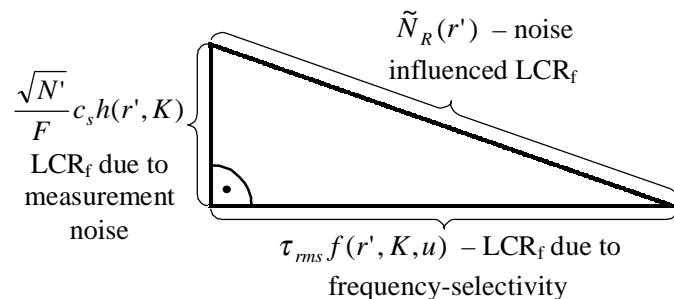


Figure 3-13: Interrelation of level crossing rates in the noise-influenced case.

term $(\sqrt{N'}/F)c_s h(r', K)$. No meaningful result can be obtained when it is smaller than this value. This difficulty is also seen from Figure 3-11 and Figure 3-13. It corresponds to the case where the observed LCR_f is less than the (expected) LCR_f -component due to the (specified) measurement noise. In Figure 3-11, this value is seen as the LCR_f at $\tau_{rms} = 0$. In Figure 3-13 it would mean that the hypotenuse becomes shorter than the side representing the noise component, which is impossible.

A main conclusion drawn from (3-35) is that the sampling interval F has a major impact on the influence of noise. Doubling the sampling interval has the same effect as reducing the noise power by a factor of four. While the sampling interval can be easily increased – as long as the sampling theorem is not violated –, it is usually very difficult to reduce the noise. Thus the sampling interval should always be selected as large as possible. An over-sampled measurement should be down-sampled appropriately prior to the estimation of τ_{rms} .

3.4.2.1 Correcting for Sampling Effects

The solution given by eq. (3-35) was obtained through the introduction of the measurement noise to the continuous time (and -frequency) model shown in Section 3.4.1. The measurement is done on discrete frequency instants however, which leads to a systematic underestimation of the LCR_f compared to the theory, because the continuous model also considers level crossings in-between sampling points. Such crossings occur mostly due to the interpolation implied by the flat, band-limited model for the measurement noise (see also [20]).

Computer simulations have been performed in order to quantify this error and to in-

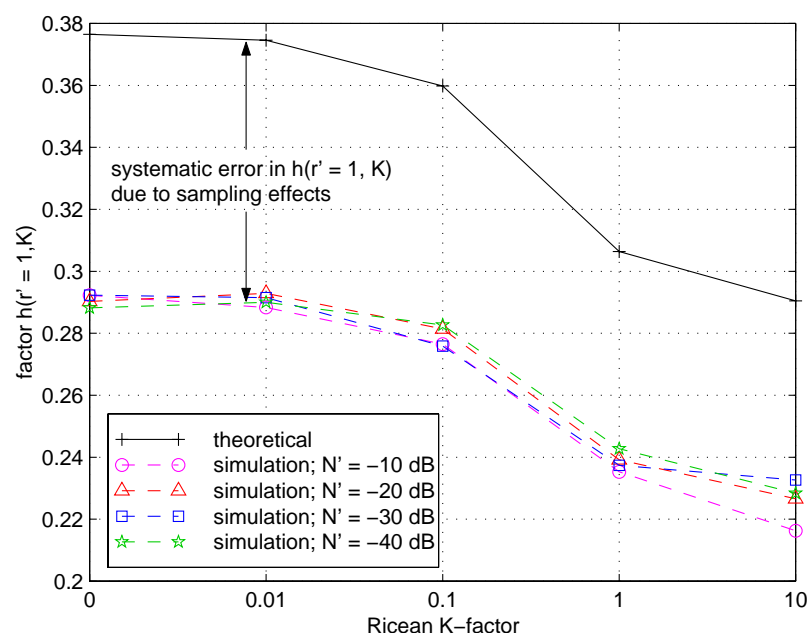


Figure 3-14: Simulated factor $h(r', K)$ compared to the theoretical one. A constant offset of approx. -22% is observed.

investigate the possibility of incorporating it in the constant $h(r',K)$. Results are depicted in Figure 3-14, where the simulated $h(r',K)$ as a function of K is compared to the theoretical one, at $r' = 1$. The simulation was performed for different values of N' . Ensembles of flat-fading channels ($\tau_{rms} = 0$) with Ricean amplitude distribution according to K were generated. It is observed that the simulated $h(r',K)$ is below the theoretical one, by approximately 22 %.

Multiplication of $h(r',K)$ in eq. (3-35) by $c_s = 0.78$ can account for this modeling error. The suitability of this correction factor will be seen from numerical evaluations and computer simulations presented below.

3.4.3 Discrete-Frequency Analysis for Rayleigh Channels

The correction factor c_s can account for the modeling deficiencies of the additive noise process. However, as the sampling interval is increased, also level crossings may be overlooked, which are due to fades. For Rayleigh channels, all effects related to the sampling of the noisy magnitude TF can be extracted from the discrete-frequency analysis presented in Section 3.2.3.

The LCR_f for a discrete Rayleigh process has been shown to be a function of the threshold level r' , and the correlation coefficient between the squared magnitudes of adjacent samples, ρ_c . In order to evaluate the impact of noise, this correlation coefficient has to be determined for the frequency-selective channel plus additive noise.

ρ_c is related to the auto-correlation coefficients of the underlying complex Gaussian process Z_n as $\rho_c = |\psi_1|^2 / \psi_0^2$, where $\psi_i = \frac{1}{2} E\{Z_n Z_{n+i}^*\}$. Eq. (3-26) gives the correlation coefficient for the noiseless case, for an exponentially decaying and a rectangular delay spectrum. In the limit $F \rightarrow 0$, ρ_c can be approximated as given in eq. (3-27), regardless of the channel model or channel impulse response.

For the LCR_f with noise, we find

$$\tilde{\rho}_c = \frac{\rho_c}{(1 + N')^2}. \quad (3-37)$$

The exact expressions for $\tilde{\rho}_c$ (i.e., (3-37) with (3-26)), together with (3-18) (or (3-19)), is used in Section 3.4.4 to evaluate the influence of the sampling interval on the LCR_f . Approximation (3-27) is used below to verify the equation for the noise influenced LCR_f obtained from the continuous model, (3-35), and to evaluate c_s analytically.

3.4.3.1 Validation of the Result Obtained from the Continuous Model

In the limit $\rho_c \rightarrow 1$, the level crossing probability for the sampled case can be approximated by eq. (3-25) (see Section 3.2.3.1). This condition is fulfilled for $F \rightarrow 0$ (meaning that the continuous case is approached) and for $N' \ll 1$. Under these assumptions, and using (3-37) and approximation (3-27), the LCR_f for noise influenced Rayleigh

fading channels becomes

$$\tilde{N}_R(r') \cong 2\sqrt{\pi} r' e^{-r'^2} \sqrt{\frac{N'}{F^2} \frac{1}{2\pi^2} + \tau_{rms}^2} . \quad (3-38)$$

After some manipulations it is seen that this equation is equivalent to (3-35), for $K = 0$. Based on this result we can also verify the value of c_s for Rayleigh channels. Letting $\tau_{rms} = 0$ leads to the special case of the flat channel, where level crossings are caused by the additive noise only. Comparing (3-38) and (3-35) then gives

$$c_s \cdot h(r', K = 0) = \sqrt{2/\pi} r' e^{-r'^2} . \quad (3-39)$$

From this expression and (3-36) (for $K = 0$) follows $c_s = \sqrt{6}/\pi \cong 0.78$. The simulation results shown in Figure 3-14 suggest that this correction factor is also appropriate for any other K-factor.

3.4.4 Evaluation and Application of the Analytical Results

3.4.4.1 Discussion of the Analytical Results for Rayleigh Channels

In this sub-section, we study the applicability and the limitations of the analytical expressions as derived above, for Rayleigh channels. The relation between τ_{rms} and the LCR_f is depicted in Figure 3-15a for the noiseless and the noise-corrupted cases. The results from the continuous analysis (eqs. (3-5) and (3-35)) – for the noise-corrupted case with and without the correction factor c_s , i.e., for $c_s = \{1, 0.78\}$ – and the exact results from the discrete analysis ((3-16) and (3-18), with (3-37) and (3-26), for $u = 0$) are compared. Figure 3-15b shows the relative systematic error of the simpler and more general results from the continuous model compared with the exact results from the discrete analysis.

For all curves, the RMS amplitude was taken as the threshold level for calculating LCR_f , i.e., $r' = 1$. A fixed sampling interval $F = 1$ Hz and a fixed, relative noise strength $N' = 0.01$ were selected.

A thorough analysis of the noiseless case was given in Section 3.2.3.4. The relative estimation error ε_τ is also defined there, in eq. (3-29).

The presence of measurement noise causes an increase of the LCR_f . The relative increase is largest in the region of low τ_{rms} , where the level crossings due to noise get dominant. The error of (3-35) (continuous case) without correction (i.e., for $c_s = 1$) is seen to raise towards 22 % as $\tau_{rms} \rightarrow 0$ (curves ‘●—●’ in Figure 3-15a and b). This illustrates the sampling effects for the additive noise that were discussed in Section 3.4.2.1. When the correction factor $c_s = 0.78$ is introduced, the curves for the discrete and the continuous analysis agree well, if $\tau_{rms} \leq 1/(20F)$ (Figure 3-15a, ‘+—+’ and ‘○—○’). For larger τ_{rms} , the influence of the sampling is leading to deviations, as in

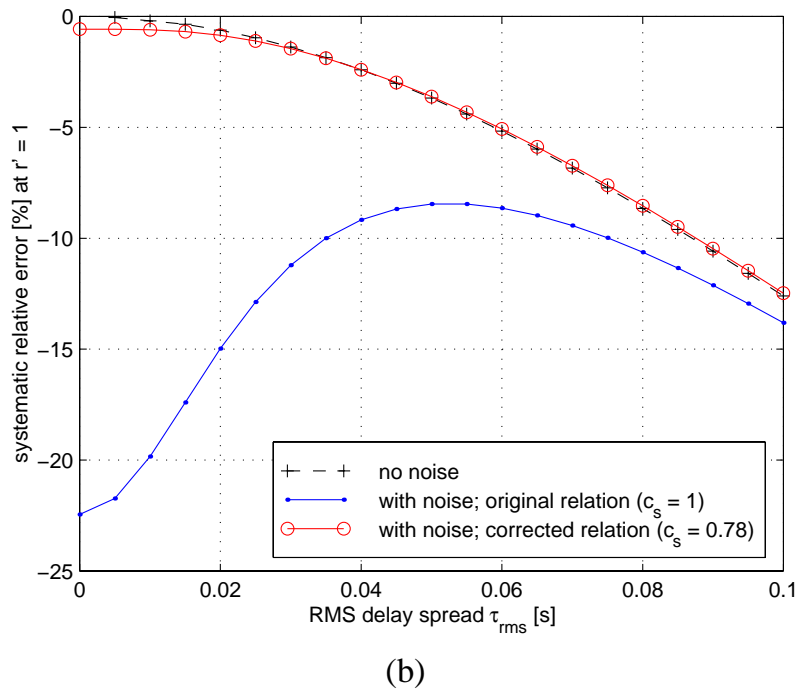
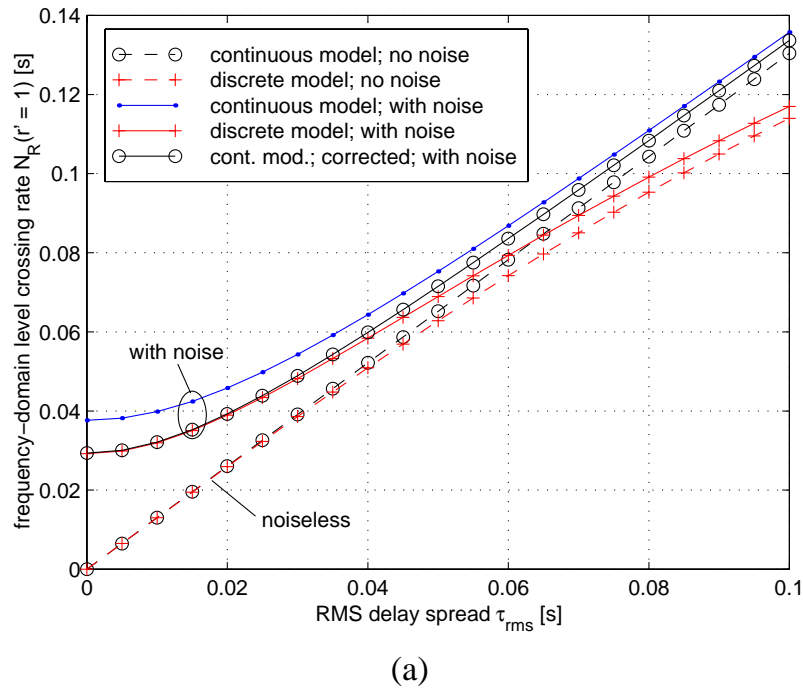


Figure 3-15: Influence of noise and sampling on the relation of τ_{rms} and the LCR_f . Rayleigh fading; noise power $N' = 0.01$; sampling interval $f_s = 1$ Hz; $u = 0$, $r' = 1$. (a): LCR_f vs. τ_{rms} . (b): Relative error of the relation obtained from the continuous model vs. τ_{rms} .

the noiseless case. Thereby, the relative error is very similar to the one for the noiseless case (compare ‘ \circ — \circ ’ and ‘ $+ - - +$ ’ in Figure 3-15b). Close inspection reveals a small residual error $< 1\%$ at $\tau_{rms} = 0$, which is due to the approximation $1 + N' \cong 1$, used in (3-35). This error reduces for smaller N' .

3.4.4.2 Influence of Noise on Estimating τ_{rms}

In this sub-section we investigate the systematic error resulting from the application of the conventional, linear relationship for estimating τ_{rms} from noise-afflicted measurements of the LCR_f . That is, (3-5) is used to derive $\hat{\tau}_{rms}$ from a noise-influenced LCR_f , which is either obtained from the equations presented above (see Figure 3-16a), or from simulated channel transfer functions (see Figure 3-16b).

The relative errors shown are derived equivalently to (3-29), but this time the errors due to noise were to be evaluated, i.e.

$$\varepsilon_\tau = \frac{\hat{\tau}_{rms}}{\tau_{rms}} - 1 = \frac{LCR_{f, \text{noise influenced}}}{LCR_{f, \text{noiseless}}} - 1. \quad (3-40)$$

All results are shown as a function of the noise power N' , at $r' = 1$. Parameters are the Ricean K -factor, and the sampling interval expressed by the oversampling factor OS (3-31).

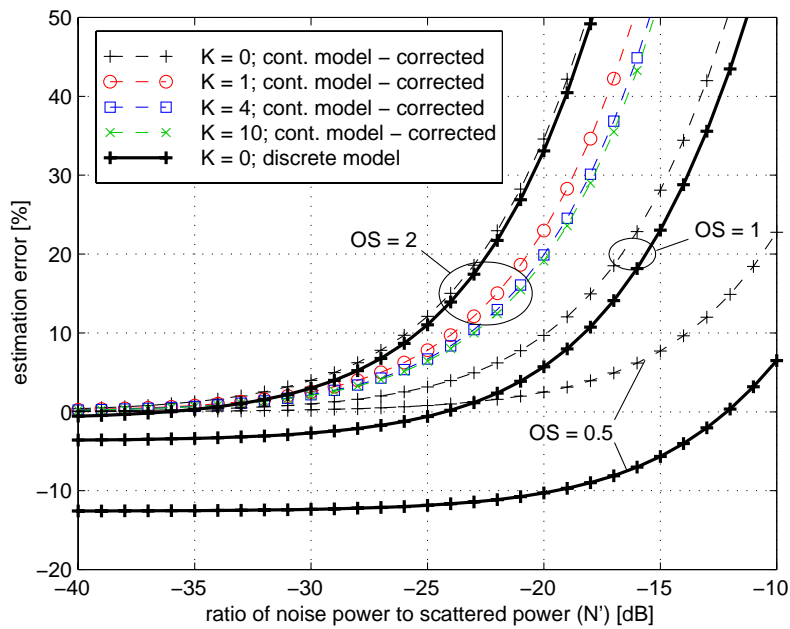
We first discuss the analytical results depicted in Figure 3-16a. As expected, the additive measurement noise increases the LCR_f if it exceeds a certain value. The important role of the sampling interval F is noticed. Doubling F has the same effect as reducing the noise power by a factor of four (-6 dB), according to the above equations. At $OS = 1$, the systematic error stays below $\sim 10\%$, if the noise power expressed by N' is below ~ -18 dB. Due to the definition of OS as a function of F and K (3-31), the Ricean K -factor seems to have little influence on the results.

For the Rayleigh fading case, the noise-influenced LCR_f was calculated from the equations for the discrete analysis and from the equations for the continuous model. The difference among them corresponds to the impact of the sampling interval F if it is selected too large. (That is, when level crossings due to fades are missed, because the sampling theorem is violated). As seen from Figure 3-16a, and from Figure 3-15, the continuous analysis fails to describe these effects. It only describes the impact of additive noise.

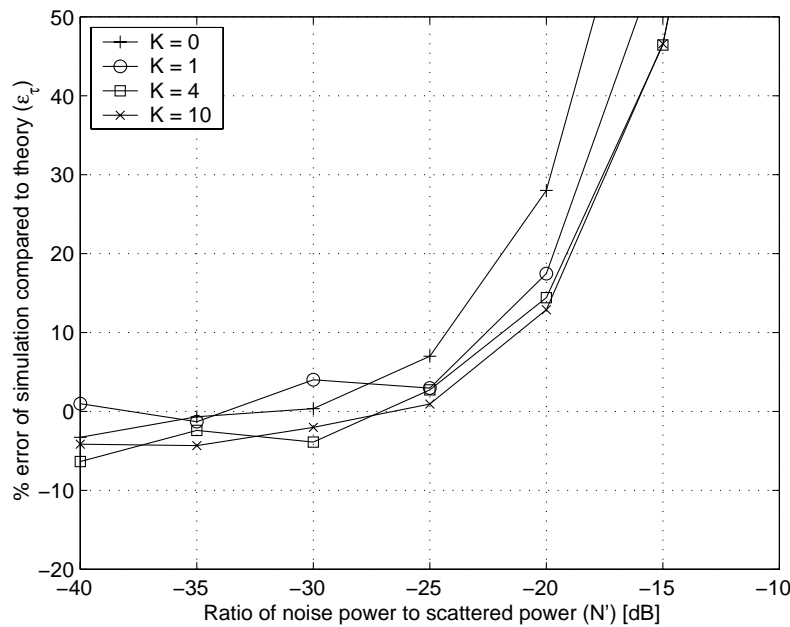
An oversampling factor of 0.5 leads to systematic underestimation of τ_{rms} by $\sim 12\%$ (in the absence of noise). Since noise tends to increase the LCR_f , those adverse effects partly cancel, therefore, about 15 dB more noise can be tolerated for $OS = 0.5$, compared to $OS = 2$.

The analytical results have been validated by computer simulations, using the simulation scheme introduced in Section 3.3.3.1⁹. Complex noise samples were added to the generated transfer functions (TF) to introduce the measurement noise. Consecutively, the measurement procedures were applied to the TFs' amplitudes. The mean values and standard deviations of relative estimation errors were derived from ensembles of

⁹ The computer simulations in this section have been performed by Giovanni Landman. More simulation results can be found in [21].



(a)



(b)

Figure 3-16: Bias of the standard estimation method as a function of measurement noise power. Parameters are the Ricean K-factor, and the sampling interval expressed by the oversampling factor OS. The LCR_t is evaluated at r' = 1. (a): Analytical results; (b): Simulation results; OS = 2

simulated channels.

In Figure 3-16b, simulation results (mean-errors) are depicted for OS = 2. A good match with the theoretical results is evident. The errors' standard deviations are discussed below.

3.4.4.3 Standard Deviations of Estimation Errors

It was seen from the comparison of the analytical results and computer simulation results that the analytical expressions provide a reliable prediction of the noise-induced bias of the τ_{rms} -estimates. In this section, simulation results are used to evaluate the standard deviations of the estimates. The standard estimation method employing eq. (3-5) is analyzed here.

The errors' standard deviations depend on the observation bandwidth. Larger bandwidth implies that more level crossings can be observed, therefore, the performance of the statistical method for estimating τ_{rms} improves. Simulation results as a function of the bandwidth were shown in Section 3.3.3.2. It is seen that the standard deviation is approx. 10 ... 15 % for an observed bandwidth of $10/\tau_{rms}$. This bandwidth was used in all further simulations. τ_{rms} was estimated from the LCR_f at $r' = 1$.

In the presence of noise, a deterioration is seen as N' is increased, because the additive noise reduces the accuracy of the LCR_f determined from the TF (see Figure 3-17; lines marked by '+'). The simulation shown is for $K = 1$ and for two-fold oversampling.

The other lines in this figure are discussed in Sections 3.4.4.4 and 3.4.5.2.

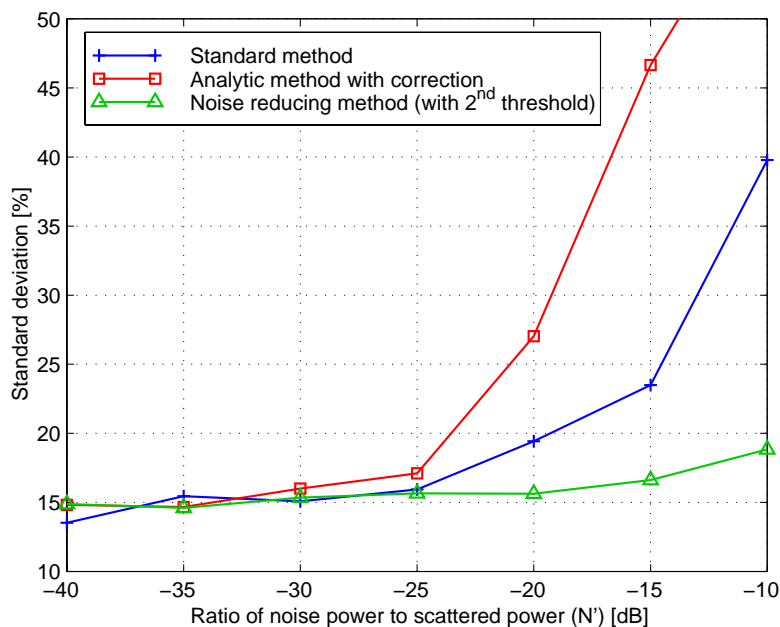


Figure 3-17: Standard deviations of the τ_{rms} estimation errors as a function of the power of the additive noise. τ_{rms} is estimated from the LCR_f at $r' = 1$, using different estimation methods. $K = 1$, $OS = 2$.

3.4.4.4 Noise Cancellation by Applying the Analytical Results

In Figure 3-18, the performance of the RMS delay spread estimation method is depicted, this time when noise is accounted for by using (3-35) – the analytical result allowing to separate the noise's component from the LCR_f – with $c_s = 0.78$. All results are for an oversampling factor of two ($OS = 2$) and τ_{rms} estimated from the LCR_f at $r' = 1$.

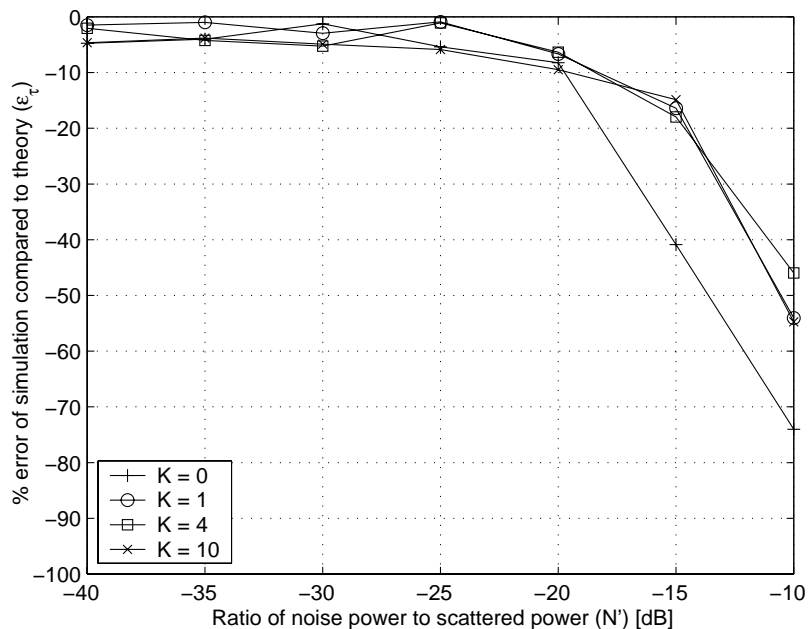


Figure 3-18: Systematic estimation error of τ_{rms} using the analytical relationship for correcting for noise. $OS = 2$; $c_s = 0.78$; LCR_f determined at $r' = 1$.

Some improvement can be seen for this extended method (compare Figure 3-18 and Figure 3-16), however, τ_{rms} is underestimated at high N' . The underestimation is due to the application of the non-linear (hyperbolic) relation (3-35) for estimating τ_{rms} from the noise-corrupted LCR_f (see Figure 3-11). Considering that the measured LCR_f -values have a certain standard deviation (depending on the observation bandwidth), the non-linear translation curve introduces some bias to the estimates. In particular, when the measured LCR_f is lower than the subtracted noise term, then the square root in (3-35) gets a negative argument. In these cases, the τ_{rms} value was taken as zero, which adds to this bias.

Also the estimates' variance is increased when using eq. (3-35), because the transformation functions (see Figure 3-11) get flatter as the influence of noise increases. This is confirmed by the standard deviation results shown in Figure 3-17b (curve marked by '□'). While the systematic errors suggest that approx. 5 dB more noise can be tolerated when noise is corrected for by using (3-35) with $c_s = 0.78$, the errors' standard deviations show that the estimates are thereby getting far less accurate.

We conclude that the original measurement procedure utilizing eq. (3-5) can be used in the area where the systematic error due to noise is sufficiently small. Eq. (3-35) (with $c_s = 0.78$) can be used to identify this area. Robust measurement methods – as the one described below – should be applied if noise cannot be neglected.

3.4.5 A Robust Measurement Procedure

A robust measurement procedure is briefly discussed in this section, which was suggested by Chris van den Bos and studied by the author in cooperation with Adrian

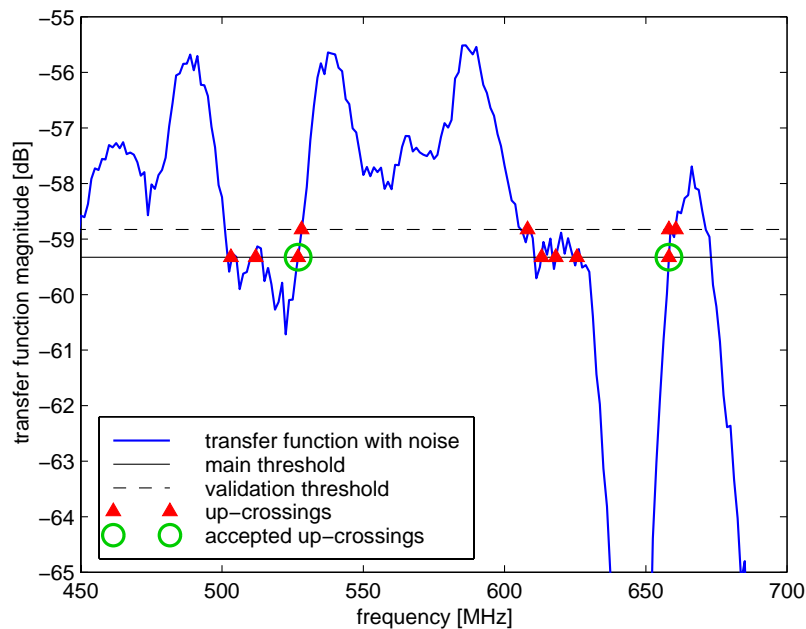


Figure 3-19: Illustration of the robust measurement method using a validation threshold.

Bohdanowicz¹⁰. The idea of this method is to neglect during the counting process level crossings that are likely due to noise and not due to the fading.

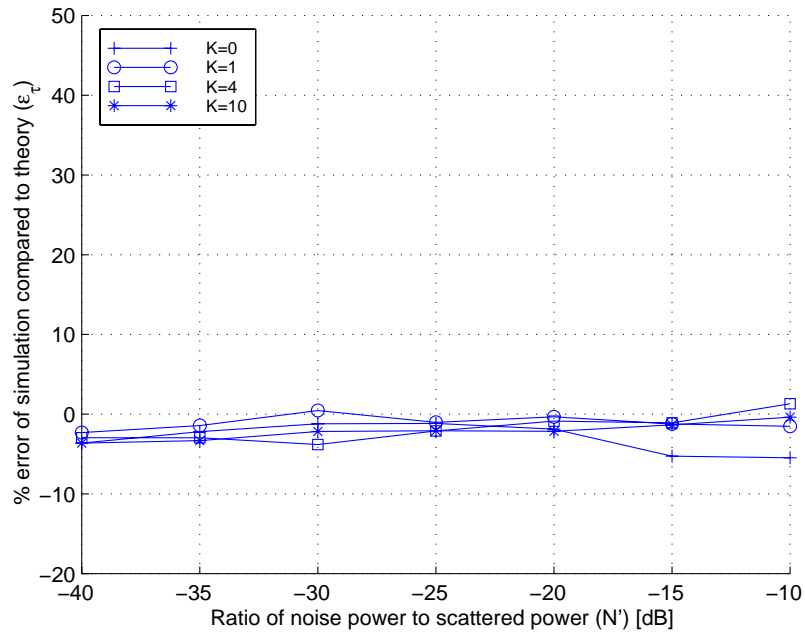
3.4.5.1 Introduction of an Additional Threshold

The proposed algorithm augments the standard procedure for determining the FD-level crossing rate by introducing an additional threshold, which is then used to validate the level crossings through the standard threshold (see Figure 3-19). The modified algorithm works as follows.

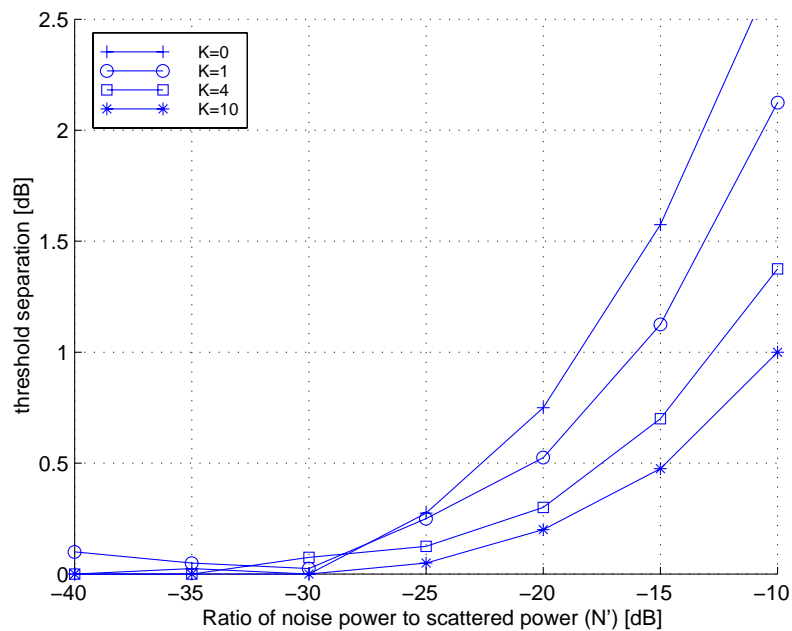
Firstly, the crossings through the standard threshold are identified in the measured data. Then, for each crossing, the data between two crossings (the one, which is investigated and the next one) is analyzed. If there is a crossing through the additional threshold (placed above the standard one) within the analyzed interval, the crossing is accepted. If, however, the data does not exceed the additional threshold within the interval, the crossing is rejected. As a result, only the crossings likely caused by the channel variability are counted.

The method was used by A. Bohdanowicz in his measurement campaign as presented in [12]. Although the promising potential of reducing the influence of noise from the calculation of the LCR was presented there, no detailed investigation of the method's performance was given. In the following section, we investigate this method with a relation to the parameters of the underlying channel model, based on computer simulations. No attempt was made to describe the performance or the required parameters

¹⁰ C. v. d. Bos and A. Bohdanowicz are with the Ubiquitous Communications Program, Delft University of Technology, Department of Electrical Engineering.



(a)



(b)

Figure 3-20. (a): Systematic estimation error of τ_{rms} for the two-threshold method; $OS = 2$; LCR_f determined at $r' = 1$. (b): Optimal threshold separations for $OS = 2$.

analytically.

3.4.5.2 Performance of the Method

A large set of channel impulse responses is generated as described in Section 3.3.3.1. For each noise level N' and Ricean K -factor, the optimal threshold separation is then calculated by means of minimizing the error of the estimated τ_{rms} . The simulation re-

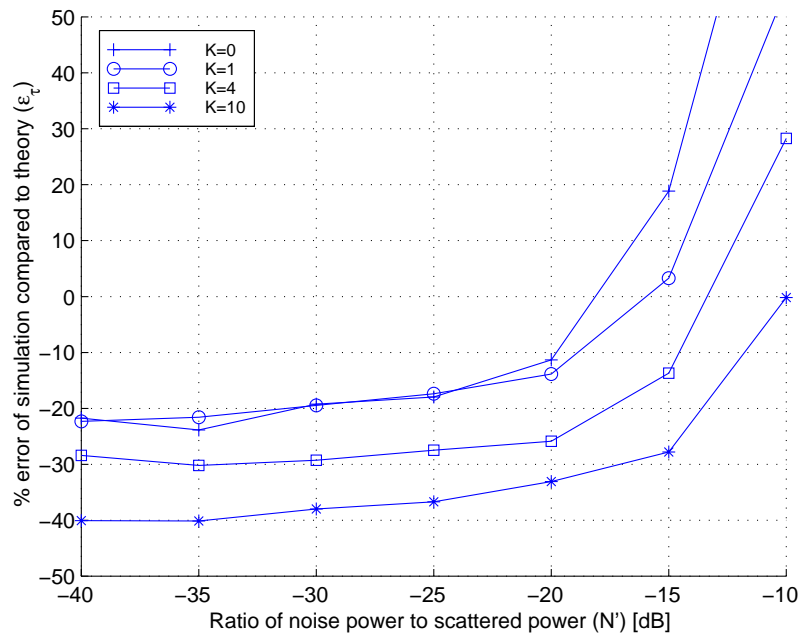


Figure 3-21. Systematic estimation error of τ_{rms} with a global threshold separation of 1 dB. $OS = 2$; LCR_r determined at $r' = 1$.

sults of the proposed method are depicted in Figure 3-20a, whereas the optimal settings of the proposed filtering method (the optimal threshold separations) are shown in Figure 3-20b (for $OS = 2$).

By comparing the results from Figure 3-20a with those presented in Figure 3-16b, one can conclude that, indeed, the method can be used to reduce the influence of noise on the RDS estimation. The comparison shows that for higher values of N' the estimation error is drastically reduced, while for low values, effectively no ‘filtering’ is required and the method performs as well as the one based on the standard LCR calculation.

The method can be used to increase the accuracy of the τ_{rms} estimation at the presence of a significant noise level, but the threshold separation must be set appropriately (see Figure 3-20b). It is seen from Figure 3-17 that the impact of noise on the standard deviation of the estimates has also improved significantly (curve marked by ‘ Δ ’), compared to the other methods.

The results presented in Figure 3-20b show that the optimal threshold separation is a function of two parameters, N' and K . Although we do not provide the explicit formula for this relation, the curves from Figure 3-20b can be followed in practical applications to set the correct threshold separation for each measurement. A different oversampling factor (approximately) shifts the curves for $OS = 2$ to the left or right by $20 \cdot \log(OS/2)$ dB.

The importance of the threshold separation is presented in Figure 3-21, where a common value was used for all the measurements. Better performance at higher values of N' (when compared to Figure 3-16b) is paid by an increased underestimation of RDS in the range of low N' values.

3.4.6 Extended Measurement Procedure

The measurement procedure introduced in Section 3.3.1 may be extended if measurement noise is an issue that cannot be neglected. Again the procedure starts with the acquisition of calibration data, from which also the noise power is derived. Consecutively, sampled magnitude transfer functions of the channel $R_n = |H(nF)|$, $n = \{1, 2, \dots, N\}$ are measured. From the data, the channel parameters are obtained in the following steps, which include testing for the necessity of noise-suppression:

1. Compensation for the measurement system's characteristics is performed by subtracting the calibration data [dB] from the measured transfer function.
2. The average received power $\hat{P}_0 = \frac{1}{N} \sum_{n=1}^N R_n^2$ is estimated.
3. The Ricean K-factor is determined, e.g. by the method given in [1], based on the average power \hat{P}_0 and the average amplitude $\hat{R} = \frac{1}{N} \sum_{n=1}^N R_n$. Note that noise has negligible influence on this and on the previous step, if $N \leq \sim 0.01$ (compare (3-33)).
4. Based on the noise power, sampling interval, and Ricean K-factor, the increase of the LCR_f due to noise is evaluated, employing eq. (3-35).
5. The RMS delay spread $\hat{\tau}_{rms}$ is estimated from the LCR_f at threshold level $r = \sqrt{\hat{P}_0}$ (i.e., at $r' = 1$), using (3-5) and (3-30). If according to the previous step, noise cannot be neglected, then the LCR_f is determined by the robust method described in Section 3.4.5.

3.5 Conclusions and Recommendations

In this chapter, an elaborate study of the frequency-domain level crossing rate (LCR_f) of a frequency-selective radio channel is presented. The LCR_f is the average number of up-going level crossings of the channel transfer function (with respect to a specified threshold) per unit of bandwidth. It has been derived analytically from second order statistical properties of the FD-channel model, which was proposed in Chapter 2, Section 2.3.

Using these analytical results, the influence of channel parameters has been investigated. It was observed that the RMS delay spread τ_{rms} is proportional to the absolute value of the LCR_f , while the Ricean K -factor determines the shape of the LCR_f -function vs. the threshold level. That is, τ_{rms} specifies the number of fades per bandwidth and K indicates the depth of the fades. By defining the threshold level relative to the normalized received power P_0 of the channel, any dependency of the LCR_f on P_0 is eliminated. Since these three parameters $\{\tau_{rms}, K, P_0\}$ have such distinct and different effects on the LCR_f , it was concluded that they comprise a most significant set of parameters to specify frequency-selective radio channels.

It was observed that other parameters describing the channel model have little impact on the LCR_f , as for instance the shape of the delay power spectrum or the actual structure of the channel impulse response. For Rayleigh fading channels, it has been shown that any dependency on the channel impulse response disappears, provided that the sampling interval is sufficiently small.

Because of the proportionality between the LCR_f and τ_{rms} , rather simple swept-frequency power measurements can be used to estimate the three most relevant channel parameters $\{\tau_{rms}, K, P_0\}$. Standard procedures allow determining P_0 and K , while the newly discovered relation leads to estimates of τ_{rms} . The estimation accuracy of this technique depends on the observation bandwidth. It can be enhanced by combining multiple measurements performed within a small local area.

Unfortunately, the method to determine τ_{rms} is quite sensitive to measurement noise. The influence of noise on the proportionality relation has been analyzed, yielding a compact expression that allows the separation of the channel's and the noise's contributions to the level-crossing rate.

The analytical result shows that increasing the frequency-domain sampling-interval by a particular factor has the same effect as reducing the noise power by the square of this factor, which is thus a valuable means of noise reduction. Thereby it is important not to violate against the sampling theorem. Moreover, the analytical results can be used for partial compensation of the influence of noise. Unfortunately, this technique increases the standard deviation of the estimated τ_{rms} .

To enhance the robustness against noise, another method is presented, which uses two thresholds when counting the level-crossing rate. This allows for identification and removal of level crossings that are likely caused by noise and not by fades. The drawback of this technique is that the threshold separation must be adapted according to noise and channel parameters to get the optimum result. Selecting the threshold appropriately, both the mean and standard deviation of the estimation errors remain close to the noiseless case. A fixed threshold separation leads to sub-optimum results. Finding analytic expressions for the optimum threshold separation is subject for further work, as well as the appropriate estimation of the noise power.

3.6 References

- [1] F. van der Wijk, A. Kegel, and R. Prasad, "Assessment of a pico-cellular system using propagation measurements at 1.9 GHz for indoor wireless communications," *IEEE Trans. Veh. Technol.*, vol. 44, no. 1, pp. 155–162, Feb. 1995.

- [2] B. P. Donaldson, M. Fattouche, and R. W. Donaldson, “Characterization of in-building UHF wireless radio communication channels using spectral energy measurements,” *IEEE Trans. on Antennas and Prop.*, vol. 44, no. 1, pp. 80–86, Jan. 1996.
- [3] M. Pätzold, U. Killat, F. Laue and Y. Li, “On the Statistical Properties of Deterministic Simulation Models for Mobile Fading Channels,” *IEEE Trans. Veh. Technol.*, Vol. 47, No. 1, pp. 254–269, Feb. 1998.
- [4] S. O. Rice, “Mathematical Analysis of Random Noise,” *Bell Syst. Tech. J.*, vol. 23, pp. 282–332, July 1944; vol. 24, pp. 46–156, Jan. 1945.
- [5] S. O. Rice, “Statistical Properties of a Sine Wave Plus Random Noise,” *Bell Syst. Tech. J.*, vol. 27, pp. 109–157, 1948.
- [6] K. Witrisal, Y.-H. Kim, and R. Prasad, “RMS delay spread estimation technique using non-coherent channel measurements,” *IEE Electronics Letters*, vol. 34, no. 20, pp. 1918–1919, Oct. 1998.
- [7] W. C. Jakes Jr., *Microwave Mobile Communications*. New York: Wiley-Interscience, 1974.
- [8] M. Schwartz, W. R. Bennett, and S. Stein, *Communication Systems and Techniques*. New York: McGraw-Hill, 1966.
- [9] J. G. Proakis, *Digital Communications*, 3rd Edition. New York: McGraw Hill, 1995.
- [10] M. K. Simon and M.-S. Alouini, “A Simple Single Integral Representation of the Bivariate Rayleigh Distribution,” *IEEE Commun. Letters*, vol. 2, no. 5, pp. 128–130, May 1998.
- [11] A. Bohdanowicz, G. J. M. Janssen, S. Pietrzyk, “Wideband indoor and outdoor multipath channel measurements at 17 GHz,” in *Proc. VTC’99-fall (IEEE Vehicular Technology Conference)*, Amsterdam, The Netherlands, Sept. 1999, pp. 1998–2003.
- [12] A. Bohdanowicz, “Wideband indoor and outdoor radio channel measurements at 17 GHz,” Delft Univ. of Technol., UbiCom-Technical Report/2000/2, Jan. 2000 (<http://www.ubicom.tudelft.nl/docs/>).
- [13] R. El Hattachi, J. M. M. de Nijs, K. Witrisal, and R. Prasad, “Characterization and simulation of the 18 GHz radio channel,” in *Proc. IEEE Benelux 6th Symposium on Vehicular Technology and Communications*, Brussels, Belgium, Oct. 1998.

-
- [14] J. Purwaha, A. Mank, D. Matic, K. Witrisal, and R. Prasad, "Wide-band channel measurements at 60 GHz in indoor environments," in *Proc. IEEE Benelux 6th Symposium on Vehicular Technology and Communications*, Brussels, Belgium, Oct. 1998.
- [15] K. Witrisal, Y.-H. Kim, and R. Prasad, "A New Method to Measure Parameters of Frequency-Selective Radio Channels using Power Measurements," *IEEE Trans. on Commun.*, vol. 49, no. 10, pp. 1788–1800, Oct 2001.
- [16] G. J. M. Janssen, P. A. Stigter, and R. Prasad, "Wideband indoor channel measurements and BER analysis of frequency selective multipath channels at 2.4, 4.75 and 11.5 GHz," *IEEE Trans. on Commun.*, vol. 44, no. 10, pp. 1272–1288, Oct. 1996.
- [17] A. A. M. Saleh and R. A. Valenzuela, "A statistical model for indoor multipath propagation," *IEEE J. Select. Areas Commun.*, vol. 5, no. 2, pp. 128–137, Feb. 1987.
- [18] S. J. Howard and K. Pahlavan, "Autoregressive modeling of wide-band indoor radio propagation," *IEEE Trans. Commun.*, vol. 40, no. 9, pp. 1540–1552, Sep. 1992.
- [19] G. J. M. Janssen, *Robust receiver techniques for interference-limited radio channels*. Ph.D. Thesis, Delft University of Technology, Delft, The Netherlands, 1998.
- [20] K. Witrisal and A. Bohdanowicz, "Influence of Noise on a Novel RMS Delay Spread Estimation Method," in *Proc. PIMRC 2000 (11th International Symposium on Personal Indoor Mobile Radio Communications)*, London, Sept. 2000, pp. 560–566.
- [21] G. Landman, "Frequency Domain Study of the Wide-Band Mobile Propagation Channel," *M.Sc. Thesis*, Delft University of Technology (IRCTR), Aug. 2001.

Part II: OFDM System Proposal and Evaluation

Chapter 4 – OFDM Introduction and System Modeling

4.1 Introduction

The aim of this chapter is to provide some theoretical background on the OFDM transmission technique, which is the general topic of the rest of this thesis. A brief introduction to OFDM is given in Section 4.2. We review the block diagram of a “classic” OFDM system, which employs a guard interval to mitigate the impairments of the multipath radio channel. We also discuss several design considerations related to hardware properties and derive the mathematical model for an idealized system, leading to the conclusion that data symbols can be transmitted independently of each other (i.e., without inter-symbol-interference (ISI) and inter-carrier-interference (ICI).) Moreover, the effects of synchronization imperfections are analyzed, like carrier frequency and phase offsets, and timing errors.

Section 4.3 introduces a method of calculating uncoded BERs for this idealized OFDM system model. This method is largely based on work presented in [1]. Differential and coherent detection schemes can be evaluated for Rayleigh and Ricean fading channels. The results obtained are used in later chapters as a benchmark, in order to evaluate the loss of implemented algorithms for the OFDM modems. We also show that, for the system proposal under investigation, differential detection in time-direction is much preferable to differential detection in frequency direction. Imperfect synchronization and channel estimation may be assessed by extending the system model used and by incorporating the SNR degradations due to ICI and ISI. Basic aspects are discussed in this chapter. Issues for a further refinement of the methods are addressed.

The rest of this chapter is organized as follows. The introduction to OFDM and the

derivation of the simplified system models are presented in Section 4.2. In Section 4.3, the performance evaluation of the uncoded OFDM system is outlined, followed by conclusions and recommendations in Section 4.4.

4.2 OFDM Introduction and System Model

Orthogonal frequency division multiplexing (OFDM) is a parallel transmission scheme, where a high-rate serial data stream is split up into a set of low-rate sub-streams, each of which is modulated on a separate sub-carrier (SC) (frequency division multiplexing). Thereby, the bandwidth of the sub-carriers becomes small compared with the coherence bandwidth of the channel, i.e., the individual sub-carriers experience flat fading, which allows for simple equalization. This implies that the symbol period of the sub-streams is made long compared to the delay spread of the time-dispersive radio channel.

Selecting a special set of (orthogonal) carrier frequencies, high spectral efficiency is obtained, because the spectra of the sub-carriers overlap, while mutual influence among the sub-carriers can be avoided (see Figure 1-3 in Chapter 1). The derivation of the system model shows that, by introducing a cyclic prefix (the so-called guard interval (GI)), the orthogonality can be maintained over a dispersive channel (see Section 4.2.3).

This section starts with a brief introduction to the OFDM transmission technique, based on the description of the system's block diagram. We then discuss some hardware-related design considerations (Section 4.2.2) that become relevant if an OFDM system is implemented in hardware. For instance the DC-subcarrier and sub-carriers near the Nyquist-frequency must be avoided. Next, we derive the system model for a perfectly synchronized system (Section 4.2.3), and we investigate the impact of the most relevant synchronization errors (Section 4.2.4).

For a more elaborate introduction to OFDM, the reader may refer to the respective chapters of [2], [3], and to [4]–[6]. An excellent overview over the effects of many non-ideal transmission conditions is given in [7], wherein numerous further references are found.

4.2.1 OFDM Introduction and Block Diagram

Figure 4-1 shows the block diagram of a simplex point-to-point transmission system using OFDM and forward error correction coding. The three main principles incorporated are:

- The *inverse discrete Fourier transform* (IDFT) and the *discrete Fourier transform* (DFT) are used for, respectively, modulating and demodulating the data constellations on the orthogonal sub-carriers [8]. These signal processing algorithms replace the banks of I/Q-modulators and -demodulators that would otherwise be required.

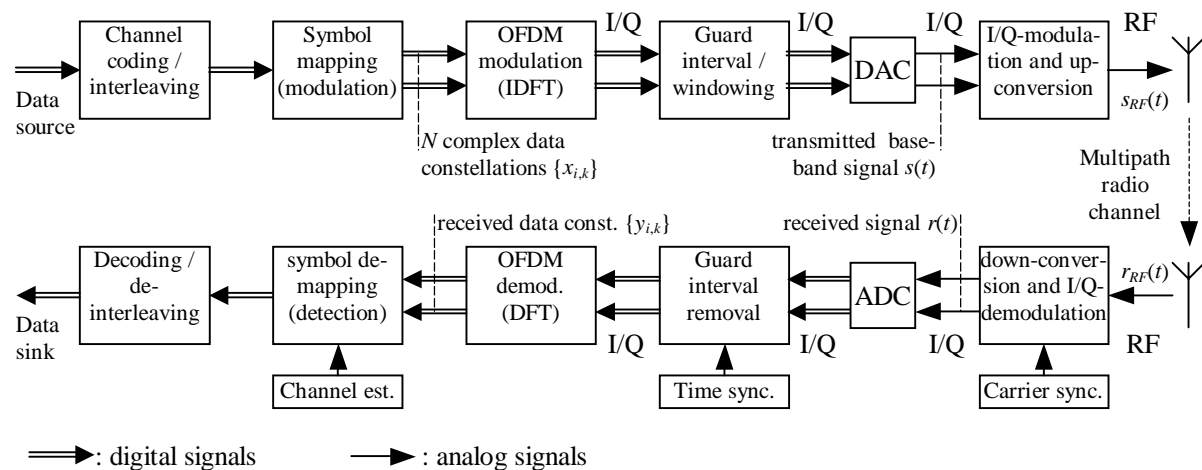


Figure 4-1: Simplex, point-to-point transmission using OFDM.

The analysis of Section 4.2.3 will show this equivalence.

Note that at the input of the IDFT, N data constellation points $\{x_{i,k}\}$ are present, where N is the number of DFT points. (i is an index on the sub-carrier; k is an index on the OFDM symbol). These constellations can be taken according to any phase-shift-keying (PSK) or quadrature-amplitude-modulation (QAM) signaling set (*symbol mapping*). The N output samples of the IDFT – being in time-domain – form the base-band signal carrying the data symbols on a set of N orthogonal sub-carriers. In a real system, however, not all of these N possible sub-carriers can be used for data, as elaborated in Section 4.2.2.3.

Usually, N is taken as an integer power of two, enabling the application of the highly efficient (inverse) fast Fourier transform (IFFT; FFT) algorithms for modulation and demodulation.

- The second key principle is the introduction of a *cyclic prefix* as a *guard interval* (GI), whose length should exceed the maximum excess delay of the multipath propagation channel [9]. Due to the cyclic prefix, the transmitted signal becomes “periodic”, and the effect of the time-dispersive multipath channel becomes equivalent to a cyclic convolution, discarding the guard interval at the receiver. Due to the properties of the cyclic convolution, the effect of the multipath channel is limited to a point-wise multiplication of the transmitted data constellations by the channel transfer function, the Fourier transform of the channel impulse response, i.e., the sub-carriers remain orthogonal (see [4]–[7]). This conclusion will also follow from the derivation of the system model in Section 4.2.3. The only drawback of this principle is a slight loss of effective transmit power, as the redundant GI must be transmitted. Usually, the GI is selected to have a length of one tenth to a quarter of the symbol period, leading to an SNR loss of 0.5–1 dB. (See also Figure 4-2).

The equalization (*symbol de-mapping*) required for detecting the data constella-

tions is an element-wise multiplication of the DFT-output by the inverse of the estimated channel transfer function (*channel estimation*). For phase modulation schemes, multiplication by the complex conjugate of the channel estimate can do the equalization. Differential detection can be applied as well, where the symbol constellations of adjacent sub-carriers or subsequent OFDM symbols are compared to recover the data.

- *Forward error correction* (FEC) coding and (frequency-domain) *interleaving* are the third crucial idea applied. The frequency-selective radio channel may severely attenuate the data symbols transmitted on one or several sub-carriers, leading to bit-errors. Spreading the coded bits over the band-width of the transmitted system, an efficient coding scheme can correct for the erroneous bits and thereby exploit the wide-band channel's frequency-diversity. OFDM systems utilizing error correction coding are often referred as coded OFDM (COFDM) systems. In Chapter 8, the performance of coded OFDM systems is evaluated. The bit-error-rate (BER) of the uncoded system is analyzed in Section 4.3.

The complex equivalent base-band signals generated by digital signal processing are in-phase/quadrature (*I/Q*)-modulated and *up-converted* to be transmitted via an RF-carrier. The reverse steps are performed by the receiver.

Synchronization is a key issue in the design of a robust OFDM receiver. *Time-* and *frequency-synchronization* are paramount to respectively identify the start of the OFDM symbol and to align the modulators' and the demodulators' local oscillator frequencies. If any of these synchronization tasks is not performed with sufficient accuracy, then the orthogonality of the sub-carriers is (partly) lost. That is, inter-symbol-interference (ISI) and inter-carrier-interference (ICI) are introduced. The effect of small synchronization errors is analyzed in Section 4.2.4. Synchronization algorithms are discussed in Chapter 6.

4.2.2 Design of the OFDM Signal

The proposal of a realistic OFDM-based communications system was one of the goals of this research project. Therefore, we elaborate here on some hardware related design considerations, which are often neglected in theoretical studies. Elements of the transmission chain that have impact on the design of the transmitted OFDM signal are:

- The time-dispersive nature of the mobile channel, which the transmission scheme must be able to cope with.
- The bandwidth limitation of the channel. The signal should occupy as little bandwidth as possible and introduce a minimum amount of interference to systems on adjacent channels.
- The transfer function of the transmitter/receiver hardware. This transfer function reduces the useable bandwidth compared to the theoretical one given by the sam-

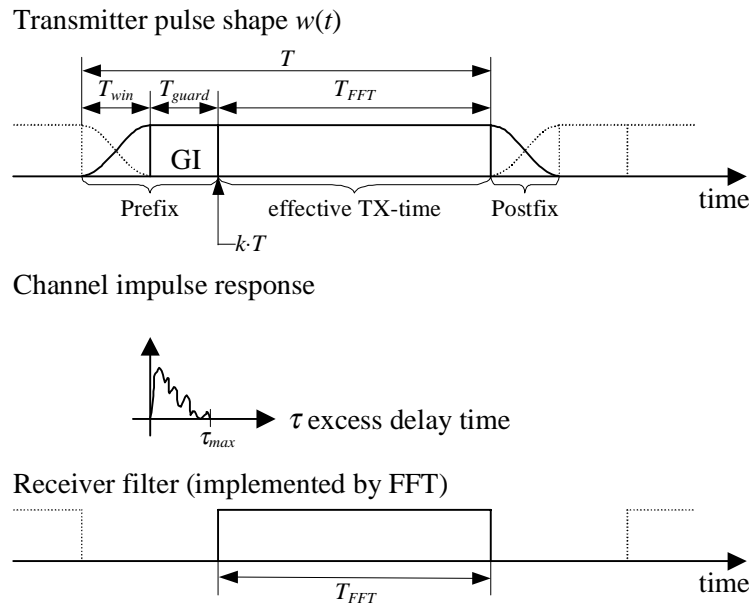


Figure 4-2: Cyclic extension and windowing of the OFDM symbol.

pling theorem. I.e., some oversampling is required.

- Phase-jitter and frequency offsets of the up- and down-converters, and Doppler spreading of the channel.

4.2.2.1 Guard Interval

As mentioned above, a guard interval (GI) is introduced to preserve the orthogonality of the sub-carriers and the independence of subsequent OFDM symbols, when the OFDM signal is transmitted over a multipath radio channel. The guard interval, a cyclic prefix, is a copy of the last part of the OFDM symbol, which is transmitted before the so-called “effective” part of the symbol (*cf.* Figure 4-2). Its duration T_{guard} is simply selected larger than the maximum excess delay of the (worst-case) radio channel. Therefore, the effective part of the received signal can be seen as the cyclic convolution of the transmitted OFDM symbol by the channel impulse response.

4.2.2.2 Windowing

A rectangular pulse has a very large bandwidth due to the side-lobes of its Fourier transform being a sinc-function. Windowing is a well-known technique to reduce the level of these side-lobes and thereby reduce the signal power transmitted out of band. In an OFDM system, the applied window must not influence the signal during its effective period. Therefore, cyclically extended parts of the symbol are pulse-shaped as depicted in Figure 4-2 [3].

Note that this additional cyclic prefix extends the GI to some extent. I.e., the delay-spread robustness is slightly enhanced. On the other hand, the efficiency is further reduced, as the window part is also discarded by the receiver. The orthogonality of the

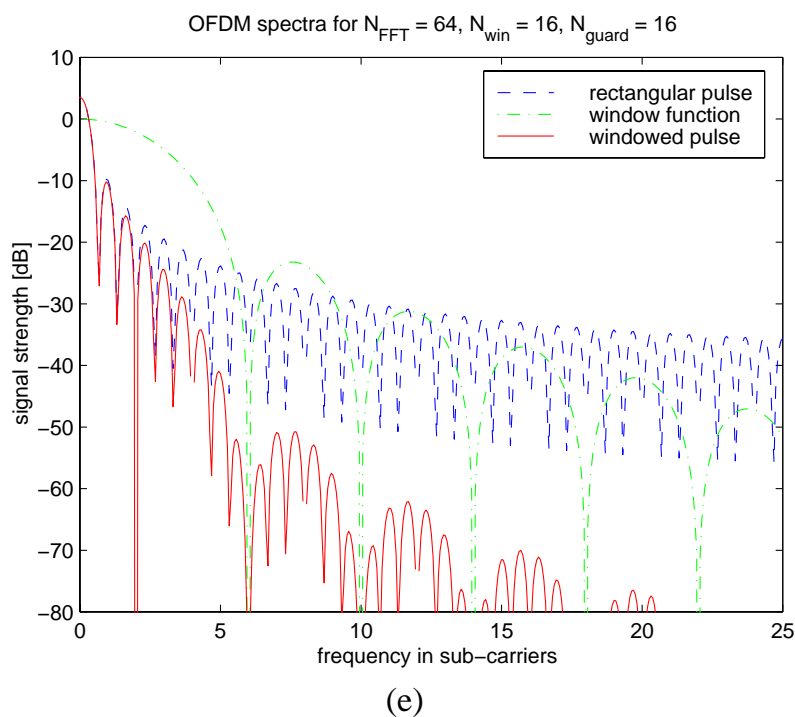
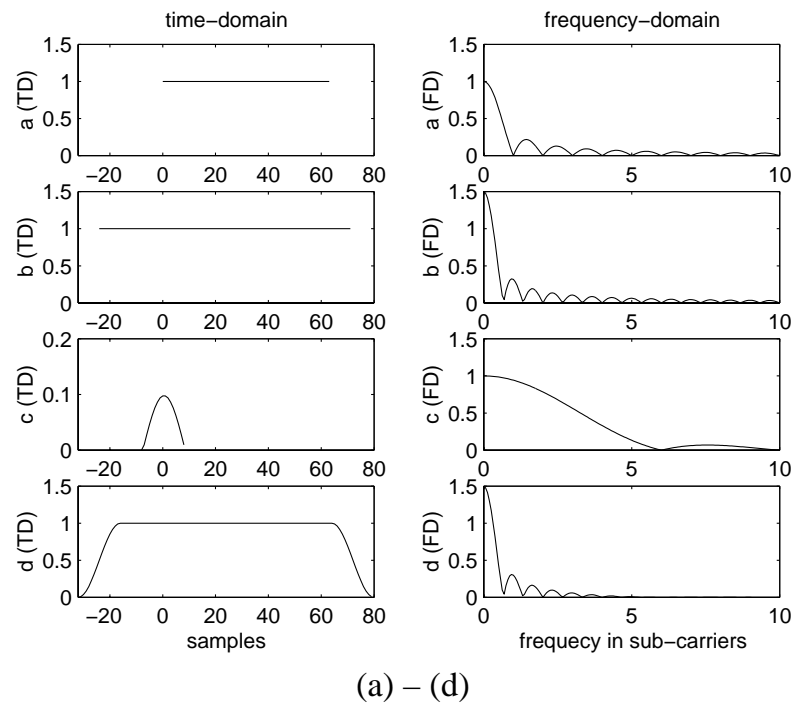


Figure 4-3: (a): Shape and spectrum of the OFDM receive filter (realized by FFT); (b): rectangular pulse of duration T and its spectrum; (c): sine-half-wave used for pulse-shaping and its spectrum; (d): transmitter pulse prototype $w(t)$ and its spectrum. (e): Spectra of (b)–(d) in logarithmic scale.

sub-carriers of the OFDM signal is restored by the rectangular receiver filter implemented by the DFT (Figure 4-2), requiring the correct estimation of the DFT start time $k \cdot T$, where T is the OFDM symbol period.

The symbol periods in Figure 4-2 are given as times. Since the implementation is usually done on digital hardware, those periods are also often defined in terms of samples. N , N_{guard} , and N_{win} then define the number of samples in the effective part, guard-, and windowing-interval, respectively. The effective part is also referred to as the “FFT-part”, because this part of the OFDM symbol is applied to the FFT to recover the data at the receiver.

Spectrum of the transmitter pulse shape

Windowing of the transmitter pulse using a raised-cosine function can be seen as a convolution of the extended rectangular pulse of duration T with a sine-half-wave, as shown in Figure 4-3. In the frequency-domain, this convolution means a multiplication of the sinc-spectrum of the rectangular pulse with the spectrum of the sine-half-wave. It is seen that this multiplication reduces the side-lobes of the transmitter pulse shape.

In Figure 4-3 (a), the zeros of the spectrum occur at positions $i \cdot F = i/T_{FFT}$, $i = \{\pm 1, \pm 2, \dots\}$, i.e., at those positions, where the adjacent sub-carriers are located. The extension of the rectangular pulse to length $T = T_{FFT} + T_{guard} + T_{win}$ reduces the distance between zeros to $1/T$ (Figure 4-3 (b)). The windowing function (Figure 4-3 (c)) has zeros at positions $\pm 1/T_{win} \cdot \{3/2, 5/2, 7/2, \dots\}$.

4.2.2.3 System Transfer Function (ADCs, DACs, IF-Filters, RF Front-end, etc.)

Because of the low-pass filters required for the analog-to-digital and digital-to-analog conversion (ADC and DAC) of the transmitted and received (baseband) signals, not all N sub-carriers can be used, if an N -point IFFT is applied for modulation. The sub-carriers close to the Nyquist frequency $f_s/2$ will be attenuated by these filters and thus cannot be used for data transmission (see Figure 4-4). ($f_s = 1/T_s$ is the sampling frequency.) Also the DC-sub-carrier might be heavily distorted by DC offsets of the ADCs and DACs, by carrier feed-through, etc., and should thus be avoided for data.

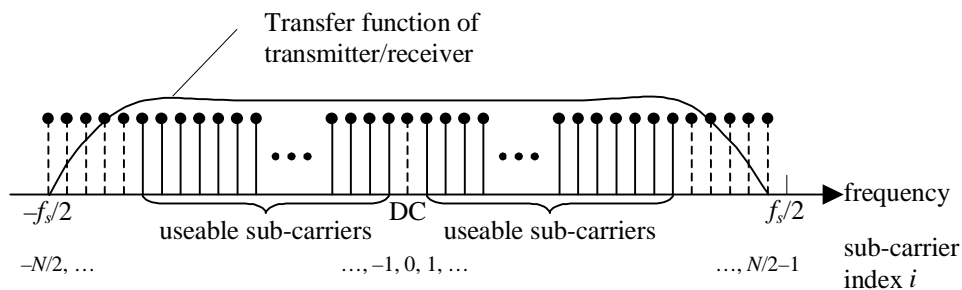


Figure 4-4: Transfer function of the transmitter/receiver hardware and its impact on the design of an OFDM system.

4.2.3 OFDM System Model

The above-introduced features of the OFDM signal are defined mathematically in this section. This will lead to the conclusion that, using the OFDM principle, data symbols

can be transmitted over multipath radio channels without influencing each other.

4.2.3.1 Signal Model and Definitions

Mathematically, the OFDM signal is expressed as a sum of the prototype pulses shifted in the time- and frequency directions and multiplied by the data symbols. In continuous-time notation, the k -th OFDM symbol is written

$$s_{RF,k}(t-kT) = \begin{cases} \operatorname{Re} \left\{ w(t-kT) \sum_{i=-N/2}^{N/2-1} x_{i,k} e^{j2\pi \left(f_c + \frac{i}{T_{FFT}} \right) (t-kT)} \right\} & kT - T_{win} - T_{guard} \leq t \leq kT + T_{FFT} + T_{win} \\ 0 & \text{otherwise} \end{cases} \quad (4-1)$$

Most of the mathematical symbols have been defined in the previous figures already. A complete list of symbols is given below:

T	Symbol length; time between two consecutive OFDM symbols
T_{FFT}	FFT-time; effective part of the OFDM symbol
T_{guard}	Guard-interval; duration of the cyclic prefix
T_{win}	Window-interval; duration of windowed prefix/postfix for spectral shaping
f_c	Center frequency of the occupied frequency spectrum
$F = 1/T_{FFT}$	frequency spacing between adjacent sub-carriers
N	FFT-length; number of FFT points
k	index on transmitted symbol
i	index on sub-carrier; $i \in \{-N/2, -N/2+1, \dots, -1, 0, 1, \dots, N/2-1\}$
$x_{i,k}$	signal constellation point; complex {data, pilot, null} symbol modulated on the i -th subcarrier of the k -th OFDM symbol

$w(t)$ denotes the transmitter pulse shape defined as

$$w(t) = \begin{cases} \frac{1}{2} \left[1 - \cos \pi (t + T_{win} + T_{guard}) / T_{win} \right] & -T_{win} - T_{guard} \leq t < -T_{guard} \\ 1 & -T_{guard} \leq t \leq T_{FFT} \\ \frac{1}{2} \left[1 + \cos \pi (t - T_{FFT}) / T_{win} \right] & T_{FFT} < t \leq T_{FFT} + T_{win} \end{cases} \quad (4-2)$$

Finally, a continuous sequence of transmitted OFDM symbols is expressed as

$$s_{RF}(t) = \sum_{k=-\infty}^{\infty} s_{RF,k}(t-kT) \quad (4-3)$$

The simulated spectrum of such an OFDM signal is depicted in Figure 4-5 for different

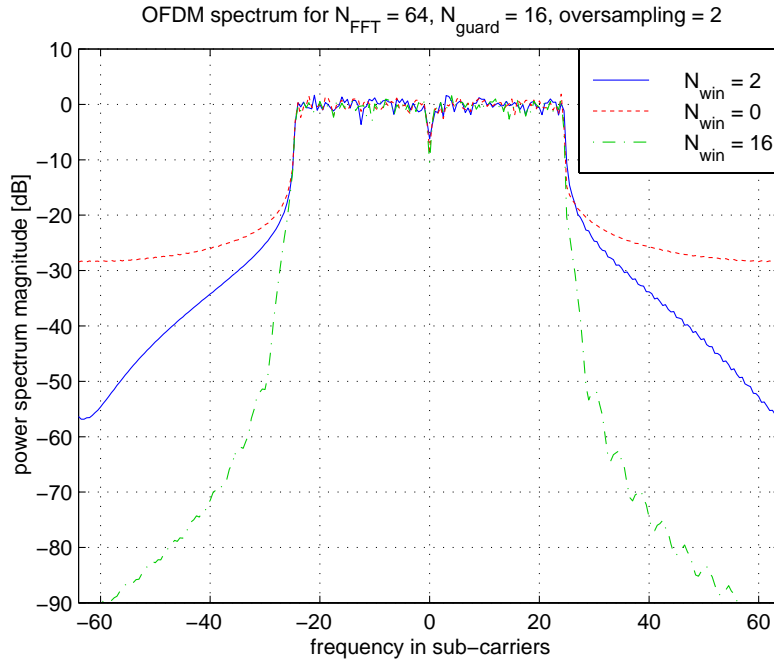


Figure 4-5: Spectrum of an OFDM signal with 64 sub-carriers and different window lengths. Two-fold oversampling has been applied in the time-domain; 48 sub-carriers are used for data.

window lengths.

4.2.3.2 Lowpass Equivalent Transmitted Signal

From eqs. (4-1)–(4-3), the complex equivalent lowpass signal transmitted can be directly given. The complex envelope of the OFDM signal is written

$$s(t) = \sum_{k=-\infty}^{\infty} s_k(t - kT), \quad (4-4)$$

with

$$s_k(t - kT) = \begin{cases} w(t - kT) \sum_{i=-N/2}^{N/2-1} x_{i,k} e^{j2\pi\left(\frac{i}{T_{FFT}}\right)(t - kT)} & kT - T_{win} - T_{guard} \leq t \leq kT + T_{FFT} + T_{win} \\ 0 & \text{otherwise} \end{cases} \quad (4-5)$$

Note the similarities of this expression to the equation of a Fourier series

$$v(t) = \sum_{n=-\infty}^{\infty} c(nf_0) e^{j2\pi n f_0 t}, \quad (4-6)$$

where the complex-valued Fourier coefficients $c(nf_0)$ represent the complex-valued signal constellation points $x_{i,k}$, and the frequencies nf_0 correspond to the sub-carrier

frequencies i/T_{FFT} .

In a digital system, this modulated waveform can be generated by an inverse discrete Fourier transform (IDFT) or by its computationally efficient implementation, the IFFT. The data constellations $x_{i,k}$ are the input to this IFFT; the time-domain OFDM symbol is its output.

4.2.3.3 Time-Dispersive Channel

The influence of the time-variant, multipath fading radio channel is expressed by its (lowpass equivalent) impulse response $h(\tau, t)$ plus AWGN $n(t)$:

$$r(t) = h(\tau, t) * s(t) + n(t) = \int_0^{\tau_{max}} h(\tau, t) s(t - \tau) d\tau + n(t) \quad (4-7)$$

The range of integration in this convolutional integral (* denotes convolution) has been limited to $[0, \tau_{max}]$, because the channel impulse response is zero elsewhere. Excess delay $\tau = 0$ of the channel is defined as the delay time at which the first wave arrives at the receiver. Thus, transmit and receive time instants are mathematically defined equal (compare Figure 4-2). τ_{max} is the maximum excess delay of the channel.

Two assumptions are made to simplify the derivation of the received signal. The channel is considered quasi-static during the transmission of the k -th OFDM symbol, thus $h(\tau, t)$ simplifies to $h_k(\tau)$. Furthermore, we define the maximum excess delay $\tau_{max} < T_{guard}$. Therefore, there is no interference of one OFDM symbol on the effective period of the consecutive one (*cf.* Figure 4-2). I.e., inter-symbol-interference (ISI) is suppressed in case of sufficiently accurate time synchronization.

4.2.3.4 OFDM Demodulation

The demodulation of the OFDM signal should be performed by a bank of filters, which are “matched” to the effective part $[kT, kT + T_{FFT}]$ of the OFDM symbol (see Figure 4-2). The reverse operation to eq. (4-6), i.e., the extraction of the Fourier coefficients $c(nf_0)$ ($= x_{i,k}$) from the time-domain signal $v(t)$ ($= r(t)$), exactly formulates such a bank of matched filters. It is written

$$c(nf_0) = \frac{1}{T_0} \int_{T_0} v(t) e^{-j2\pi n f_0 t} dt, \quad (4-8)$$

where T_0 is the integration period being equivalent to T_{FFT} . In a digital implementation, a DFT or (preferably) a FFT is used to realize these filters.

Assuming knowledge of the exact time-instants kT at which the OFDM symbols start, we try to extract the transmitted signal constellations $x_{i,k}$ from the received signal $r(t)$. The received signal constellations are denoted $y_{i,k}$.

$$y_{i,k} = \frac{1}{T_{FFT}} \int_{t=kT}^{kT+T_{FFT}} r(t) e^{-j2\pi i(t-kT)/T_{FFT}} dt = \frac{1}{T_{FFT}} \int_{t=kT}^{kT+T_{FFT}} \left[\int_{\tau=0}^{\tau_{max}} h_k(\tau) s(t-\tau) d\tau + n(t) \right] e^{-j2\pi i(t-kT)/T_{FFT}} dt \quad (4-9)$$

Because of the integration ranges in eq. (4-9) and $\tau_{max} < T_{guard}$, there is no influence of the adjacent OFDM symbols transmitted, and $s(t)$ can be replaced by $s_k(t)$, eq. (4-5).

$$y_{i,k} = \frac{1}{T_{FFT}} \int_{t=kT}^{kT+T_{FFT}} \left[\int_{\tau=0}^{\tau_{max}} h_k(\tau) \sum_{i'=-N/2}^{N/2-1} x_{i',k} e^{j2\pi \left(\frac{i'}{T_{FFT}}\right)(t-kT-\tau)} d\tau \right] e^{-j2\pi i(t-kT)/T_{FFT}} dt + \frac{1}{T_{FFT}} \int_{t=kT}^{kT+T_{FFT}} n(t) e^{-j2\pi i(t-kT)/T_{FFT}} dt \quad (4-10)$$

Note that $w(t-kT) = 1$ in the range of integration. The window is thus omitted in this equation. The second integral in eq. (4-10) leads to independent additive noise samples $n_{i,k}$ since the complex exponential terms represent orthogonal functions. Substituting $u = t - kT$, for the ease of notation, and changing the order of integration and summation yields

$$y_{i,k} = \sum_{i'=-N/2}^{N/2-1} x_{i',k} \frac{1}{T_{FFT}} \int_{u=0}^{T_{FFT}} \left[\int_{\tau=0}^{\tau_{max}} h_k(\tau) e^{j2\pi i'(u-\tau)/T_{FFT}} d\tau \right] e^{-j2\pi iu/T_{FFT}} du + n_{i,k} = \sum_{i'=-N/2}^{N/2-1} x_{i',k} \frac{1}{T_{FFT}} \int_{u=0}^{T_{FFT}} \left[\int_{\tau=0}^{\tau_{max}} h_k(\tau) e^{-j2\pi i'\tau/T_{FFT}} d\tau \right] e^{-j2\pi(i-i')u/T_{FFT}} du + n_{i,k} \quad (4-11)$$

The inner integral of the second expression represents the Fourier transform of $h_k(\tau)$ at the frequency instants $i'/T_{FFT} = i'F$, which is the sampled channel transfer function at time kT . It is expressed by the channel coefficients

$$h_{i',k} = FT\{h_k(\tau)\} = \int_{\tau=0}^{\tau_{max}} h_k(\tau) e^{-j2\pi i'\tau/T_{FFT}} d\tau = H(i'F, kT). \quad (4-12)$$

Using this notation, the output of the receiver filter bank simplifies to

$$y_{i,k} = \sum_{i'=-N/2}^{N/2-1} x_{i',k} h_{i',k} \frac{1}{T_{FFT}} \int_{u=0}^{T_{FFT}} e^{-j2\pi(i-i')u/T_{FFT}} du + n_{i,k} \quad (4-13)$$

The integral in this equation has the value 1, only if $i = i'$. For $i \neq i'$, i and i' being integer values, the integral is zero. Thus we finally obtain

$$y_{i,k} = x_{i,k} h_{i,k} + n_{i,k}. \quad (4-14)$$

From this form it is seen that a perfectly synchronized OFDM system can be viewed as a set of parallel Gaussian channels as depicted in Figure 4-6 [4]–[6]. The multipath

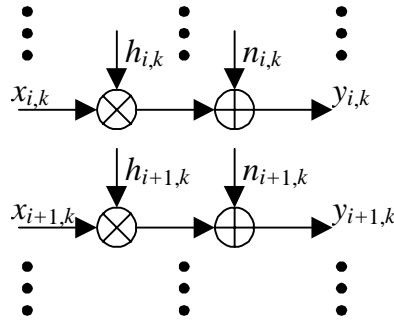


Figure 4-6: Idealized OFDM system model. The sub-channels of the OFDM system can be considered as parallel Gaussian channels under the assumptions of perfect time- and carrier synchronization and perfect suppression of multipath by the guard interval.

channel introduces an attenuation/amplification and phase rotation according to the (complex-valued) channel coefficients $\{h_{i,k}\}$.

Channel estimation is required in order to retrieve the data contained in these signal constellations, because the receiver must have a phase (and amplitude) reference to correctly detect the transmitted symbol. Differential detection can be used alternatively, in which case the decision is made by comparing the phases (and amplitudes) of symbols transmitted over adjacent sub-carriers or subsequent OFDM symbols.

Due to the attenuation/amplification, each sub-carrier typically has an individual signal-to-noise ratio (SNR). The SNR per sub-carrier (after the DFT) is defined as

$$(E_c / N_0)_{i,k} = E\{|x_{i,k}|^2\} |h_{i,k}|^2 / \sigma_N^2, \quad (4-15)$$

where $\sigma_N^2 = E\{|n_{i,k}|^2\}$ is the noise variance. With the normalized received power being written $P_0 = E\{|h_{i,k}|^2\}$, the average SNR becomes $\overline{E_c / N_0} = E\{|x_{i,k}|^2\} P_0 / \sigma_N^2$. Usually, the signal energy is normalized to unity, i.e., $E\{|x_{i,k}|^2\} = 1$.

4.2.4 Synchronization Errors

As an introduction to the work on synchronization algorithms, the relevant effects of synchronization errors are reviewed in this section. Original work on this topic is found in numerous publications (see e.g. [10], [11]). A comprehensive overview is given in [7].

4.2.4.1 FFT Time Synchronization Error

The impact of an FFT-timing offset at the receiver can be analyzed mathematically by shifting the integration interval of the matched filter bank, eq. (4-9). For a timing error of δt , the ideal interval $t \in [kT, kT + T_{FFT}]$ becomes $t \in [kT + \delta t, kT + T_{FFT} + \delta t]$ and (4-9) is written

$$y_{i,k} = \frac{1}{T_{FFT}} \int_{t=kT+\delta t}^{kT+T_{FFT}+\delta t} r(t) e^{-j2\pi i(t-kT-\delta t)/T_{FFT}} dt \quad (4-16)$$

δt is assumed to be sufficiently small (typically $\delta t < T_{guard}$) that no ISI arises due to the timing error. In other words, the error is small enough for the channel impulse response to remain within the guard interval. Therefore, the receiver window still does not overlap with the preceding or consecutive OFDM symbol, i.e., no energy is collected from these adjacent OFDM symbols, and the demodulated signal can be expressed from the transmitted symbol $s_k(t)$ again (compare eq. (4-10)). Following the same steps as in Section 4.2.3 (eqs. (4-9)–(4-14)), we obtain for the second part of eq. (4-11) (with $u = t - kT - \delta t$),

$$y_{i,k} = \sum_{i'=-N/2}^{N/2-1} x_{i',k} \frac{1}{T_{FFT}} \int_{u=0}^{T_{FFT}} \left[\int_{\tau=0}^{\tau_{max}} h(\tau) e^{-j2\pi i' \tau / T_{FFT}} d\tau \right] e^{-j2\pi [(i-i')u + i'\delta t] / T_{FFT}} du + n_{i,k} \quad (4-17)$$

Moving the term $e^{-j2\pi i' \delta t / T_{FFT}}$ out of the integral yields the expression for the demodulated signal constellations in case of a timing error,

$$y_{i,k} = x_{i,k} h_{i,k} e^{-j2\pi i \delta t / T_{FFT}} + n_{i,k} = x_{i,k} h_{i,k} e^{-j2\pi i \delta t' / N} + n_{i,k}, \quad (4-18)$$

where $\delta t'$ is the timing offset in samples. It is evident that a timing offset gives rise to a progressive phase rotation of the signal constellations. The phase rotation is zero at the center frequency and it linearly increases towards the edges of the frequency band. It is easily verified from eq. (4-18) that a timing-offset of one sample introduces a phase shift of $\pm\pi$ to the outermost sub-carriers (having $i \cong \pm N/2$), regardless of the FFT-length. In Figure 4-7, this effect is visualized for a 64-carrier OFDM system with zero carriers at f_c and at the edges of the frequency band.

If coherent detection is utilized, the induced progressive phase rotation is detected implicitly by the channel estimation algorithm. The subsequent equalization (sub-carrier-wise multiplication of the received symbols by the inverse of the estimated channel coefficients) will thus automatically correct for small timing-offsets. No performance degradation is thereby caused. However, if the timing offset is too large, ISI and ICI are introduced because energy is also collected from one of the adjacent OFDM symbols, leading to a partial loss of orthogonality [7].

Differential detection is also robust to small timing-offsets. If the differential detection is applied in the frequency-direction, the progressive phase rotation may reduce the distance between the compared constellation points, however, which can lead to a performance degradation. Such performance results are given in Section 4.3.3.

A (small) *sampling* frequency offset leads to a (slowly) increasing timing offset, and therefore to a progressive phase rotation at an increasing slope. Larger errors yield ICI, because the SC-spacing at the receiver can no longer be assumed equal to the SC-spacing at the transmitter. (The SC-spacing is defined as $F = 1/(NT_s)$, where T_s is the

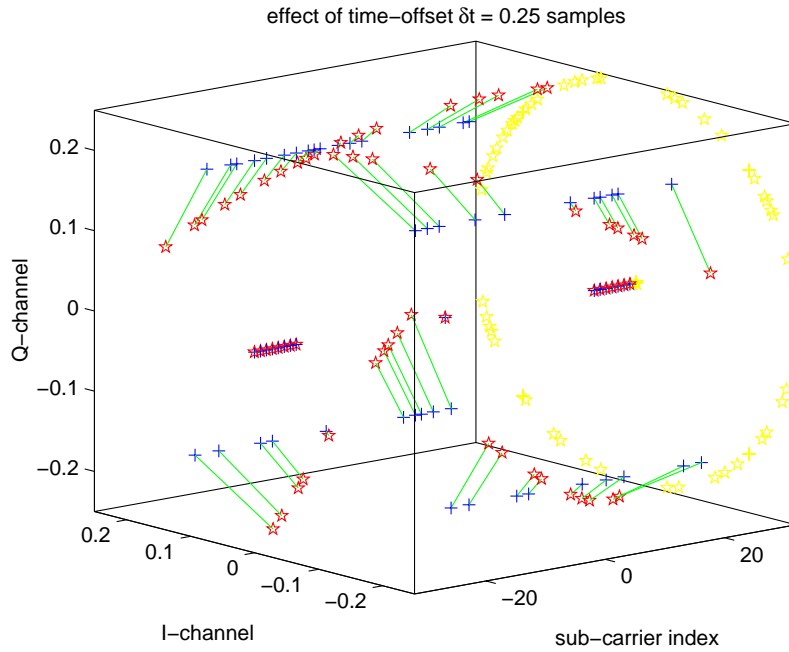


Figure 4-7: Visualization of the influence of an FFT timing offset on the demodulated signal constellations. A linearly increasing phase rotation is observed with increased frequency distance to the center frequency. ‘+’ indicate QPSK constellations without the influence of a timing-offset; ‘☆’ depict the rotated data symbols.

sampling period.)

4.2.4.2 Carrier Synchronization Error

Frequency offsets are typically introduced by a (small) frequency mismatch in the local oscillators of the transmitter and the receiver. Doppler shifts can be neglected in indoor environments.

The impact of a frequency error can be seen as an error in the frequency instants, where the received signal is sampled during demodulation by the FFT. Figure 4-8 depicts this two-fold effect. The amplitude of the desired sub-carrier is reduced (‘+’) and inter-carrier-interference ICI arises from the adjacent sub-carriers (‘o’).

Mathematically, a carrier offset can be accounted for by a frequency shift δf and a phase offset θ in the lowpass equivalent received signal

$$r'(t) = r(t)e^{j(2\pi\delta f t + \theta)}. \quad (4-19)$$

With eq. (4-9) we obtain

$$y_{i,k} = \frac{1}{T_{FFT}} \int_{t=kT}^{kT+T_{FFT}} r(t) e^{j(2\pi\delta f t + \theta)} e^{-j2\pi i(t-kT)/T_{FFT}} dt = e^{j2\pi\theta} \frac{1}{T_{FFT}} \int_{t=kT}^{kT+T_{FFT}} \left[\int_{\tau=0}^{\tau_{\max}} h(\tau) s(t-\tau) d\tau + n(t) \right] e^{j2\pi\delta f t} e^{-j2\pi i(t-kT)/T_{FFT}} dt \quad (4-20)$$

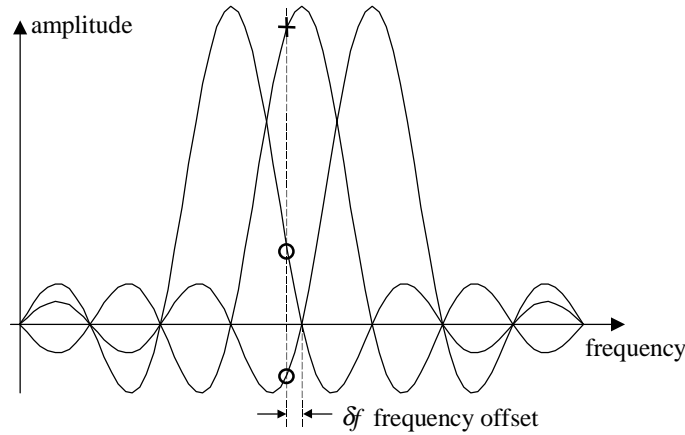


Figure 4-8: Inter-carrier-interference (ICI) arises in case of a carrier synchronization error. The figure illustrates the spectra of three individual sub-carriers. These spectra are superimposed in the OFDM signal spectrum.

Repeating the derivation leading to eq. (4-13), the received constellation points become

$$y_{i,k} = e^{j(\theta+2\pi\delta f k T)} \sum_{i'=-N/2}^{N/2-1} x_{i',k} h_{i',k} \frac{1}{T_{FFT}} \int_{u=0}^{T_{FFT}} e^{-j2\pi(\frac{i-i'}{T_{FFT}}-\delta f)u} du + n_{i,k}. \quad (4-21)$$

Due to the frequency error, the integral is not equal zero for $i \neq i'$, neither it is one for $i = i'$, as in the idealized case above. I.e., the orthogonality between sub-carriers has been partly lost. The evaluation of this expression yields two terms. The first term (for $i = i'$) accounts for equal phase rotation and attenuation of all sub-carriers, the second one (for $i \neq i'$) describes the ICI.

$$y_{i,k} = e^{j(\theta+2\pi\delta f k T)} x_{i,k} h_{i,k} \frac{1}{T_{FFT}} \int_{u=0}^{T_{FFT}} e^{j2\pi\delta f u} du + e^{j(\theta+2\pi\delta f k T)} \sum_{\substack{i'=-N/2 \\ i' \neq i}}^{N/2-1} x_{i',k} h_{i',k} \frac{1}{T_{FFT}} \int_{u=0}^{T_{FFT}} e^{-j2\pi(\frac{i-i'}{T_{FFT}}-\delta f)u} du + n_{i,k} \quad (4-22)$$

These expressions are valid for a frequency-offset $\delta f < 0.5$ SC. For larger offsets, the transmitted data symbols $x_{i,k}$ would get shifted by one or more positions in the frequency-direction. I.e., the data symbol of the i -th transmitted SC would appear at the $(i + \delta f_i)$ -th SC at the receiver, where $\delta f_i = \text{round}(\delta f / F)$ is the integer part of the frequency-error in sub-carriers.

The ICI term can be seen as an additional noise term and can thus be represented as a degradation of SNR. The amount of degradation has been evaluated by Pollet *et al.* [10] for AWGN channels and by Moose [11] for dispersive fading channels (see also [7]). Frequency-offsets up to 2 % of the sub-carrier spacing F are negligible, according to their results. Even 5–10 % can be tolerated in many situations.

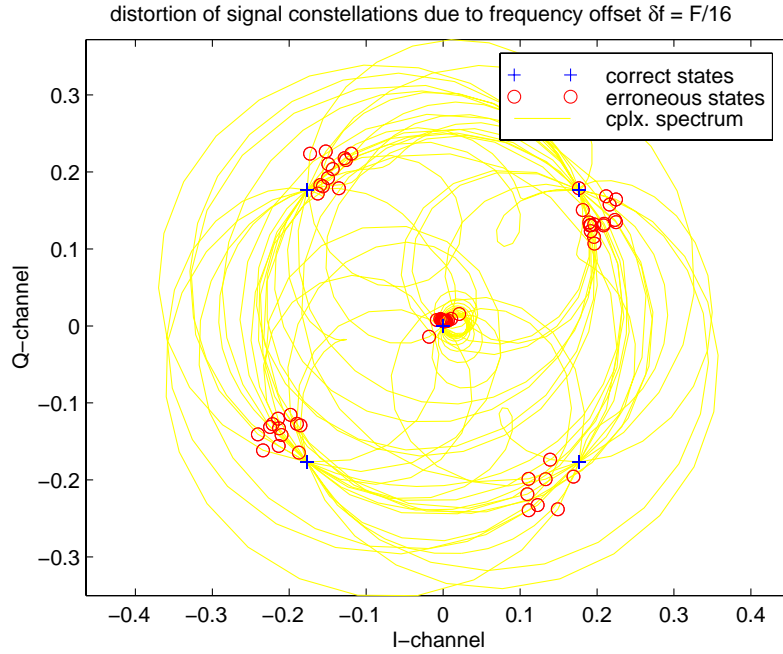


Figure 4-9: Phase rotation due to carrier offset of 1/16 of the sub-carrier spacing. The received signal constellations distorted by ICI are shown.

Evaluation of the phase rotation and attenuation due to a frequency error yields

$$y_{i,k} = x_{i,k} h_{i,k} \text{sinc}(\delta f T_{FFT}) \exp\{j[\theta + 2\pi\delta f(kT + T_{FFT}/2)]\} + n'_{i,k}, \quad (4-23)$$

using

$$\frac{1}{T_{FFT}} \int_0^{T_{FFT}} e^{j2\pi\delta f t} dt = \frac{1}{j2\pi\delta f T_{FFT}} [e^{j2\pi\delta f T_{FFT}} - 1] = e^{j\pi\delta f T_{FFT}} \frac{\sin \pi\delta f T_{FFT}}{\pi\delta f T_{FFT}} = e^{j\pi\delta f T_{FFT}} \text{sinc} \delta f T_{FFT}. \quad (4-24)$$

The noise term $n'_{i,k}$ includes the additional noise due to ICI.

Figure 4-9 depicts the rotation and distortion of the received signal constellation points for a carrier offset of $\delta f = F/16$, $\theta = 0$, and for QPSK modulation ('o'). The scattering of the resulting complex valued signal constellations is caused by ICI. The figure also shows the projection of the continuous Fourier spectrum of one OFDM symbol on the complex plane, i.e., the spectrum in-between the sub-carrier frequencies. This line results from the superposition of the continuous sinc-spectra of individual sub-carriers of one OFDM symbol. If a frequency-offset is present, the DFT samples this spectrum at the wrong frequency-instants – leading to ICI –, which is indicated in the figure by 'o'. Without frequency-offset, the QPSK constellations are recovered perfectly, as seen from the points marked by '+'.

4.2.4.3 Common Carrier and Timing Offset

Evaluating the above expressions for simultaneous timing (δt), frequency (δf ; $\delta f_i = \text{round}(\delta f/F)$) and phase (θ) offsets, the system model for the generalized case is

obtained. It is written as

$$y_{i+\delta f_i, k} = x_{i, k} h_{i, k} \text{sinc}[(\delta f - \delta f_i F) T_{FFT}] e^{j\Psi_{i, k}} + n'_{i, k}, \quad (4-25)$$

where the phase distortion due to the synchronization errors is expressed by

$$\Psi_{i, k} = \theta + 2\pi\delta f \left(kT + \frac{T_{FFT}}{2} + \delta t \right) + 2\pi\delta t \frac{i}{T_{FFT}}. \quad (4-26)$$

Note again that the noise variable $n'_{i, k}$ in (4-25) includes the noise caused by ICI and/or ISI.

Often, the timing offset is expressed in samples, i.e., $\delta t' = \delta t/T_s$, and the frequency-offset is normalized to the sub-carrier spacing $\delta f' = \delta f/F$. Using these symbols, the phase distortions are expressed by

$$\Psi_{i, k} = \theta + 2\pi\delta f' \left(\frac{1}{2} + k \frac{N + N_{guard} + N_{win}}{N} + \frac{\delta t'}{N} \right) + 2\pi\delta t' \frac{i}{N}. \quad (4-27)$$

4.3 Performance of an Uncoded OFDM System

In this section, analytical expressions are derived for the bit-error probabilities of uncoded OFDM systems over Rayleigh and Ricean fading channels. The analysis is based on the work by Proakis (Appendix B of [1]). The obtained expressions are very general, allowing the evaluation of various modulation schemes, demodulation and channel estimation techniques. The application of the formulas is shown for BPSK, QPSK, 8-PSK, and 16-QAM modulation, with coherent detection (perfect channel estimation) and differential detection.

The idealized system model derived in Section 4.2.3 is employed in this study. By incorporating in the system model the SNR degradation due to synchronization errors, Doppler spread, or phase noise (which cause ICI and/or ISI), or by incorporating the mean-square-error of channel estimation techniques, the effect of these impairments on the BER can be analyzed. The systematic phase rotations induced by synchronization errors must be considered as well. While we leave the evaluation of the SNR degradations for future work, we briefly investigate the effects of phase rotations in presence of (small) synchronization offsets.

The results presented in this section will serve as benchmarks in the performance evaluation of various signal-processing aspects of the OFDM air-interfaces, which are treated in Chapter 6 and 7. In OFDM, differential detection can be employed in the time- and frequency-directions. From the BER of differential detection it is evident that the time-direction is preferable for the OFDM system parameters under investigation, since the channel variations versus frequency are larger.

Section 4.3.1 reviews the OFDM system model and channel model. The derivation of

the average BER is explained in Section 4.3.2. Performance results are given in Section 4.3.3.

4.3.1 Mathematical Modeling

The OFDM system models derived in Section 4.2 are used in this analysis. For the sake of simplicity we slightly change the indexing, however, as we only investigate the time- or frequency direction at a time. The system model of eq. (4-14) becomes

$$y_k = x_k h_k + n_k, \quad (4-28)$$

where $\{x_k\}$ and $\{y_k\}$ are the transmitted and received signal constellation points (modulated data symbols), respectively, the $\{h_k\}$ account for the correlated, complex-valued attenuation factors introduced by the time- and/or frequency-selective radio channel, and the $\{n_k\}$ denote samples of an AWGN process with $E\{|n_k|^2\} = \sigma_N^2$. The index k can be used as a time- or as a frequency-index, depending on the system aspect under investigation. The attenuation factors thereby constitute the time- or frequency-transfer function of the channel, respectively:

$$h_k = \begin{cases} H(f, kT) & \text{at given } f \\ H(kF, t) & \text{at given } t \end{cases}, \quad (4-29)$$

where T is the duration of an OFDM symbol including the guard and windowing intervals, and F denotes the frequency spacing between adjacent OFDM sub-carriers.

The channel model is introduced in the analysis by considering respectively the spaced-time and spaced-frequency correlation functions of the (wide-sense stationary uncorrelated scattering – WSSUS; see Chapter 2 and [1], [12], [13]) channel.

For describing the frequency-variability, the frequency-domain channel model is used (see Section 2.3). Thereby, we confine ourselves to the case of the exponentially decaying delay power spectrum, where a direct relation can be given between the channel parameters $\{P_0$ – average power, K – Ricean factor, and τ_{rms} – RMS delay spread} and the channel correlation function

$$\phi_H(\Delta f) = E\{H^*(f)H(f + \Delta f)\} = \frac{P_0}{K+1} \left(K + \frac{1}{1 + j2\pi\Delta f\tau_{rms}K_1} \right). \quad (4-30)$$

In this equation, $K_1 = (K+1)/\sqrt{2K+1}$, Δf is the frequency-lag, and $*$ denotes the complex conjugate. The normalized received power (average power) is defined as $P_0 = E\{|h_k|^2\}$.

To model the time-variability, the so-called Jakes Doppler spectrum can be used [14], augmented by a line-of-sight (LOS) component $\rho e^{j(2\pi f_\rho t + \theta_\rho)}$ at a given Doppler frequency f_ρ . Such a Doppler spectrum corresponds to a spaced-time correlation function

$$\phi_H(\Delta t) = E\{H^*(t)H(t+\Delta t)\} = \frac{P_0}{K+1} \left(K e^{j2\pi f_m \Delta t} + J_0(2\pi f_m \Delta t) \right), \quad (4-31)$$

where $J_0(\bullet)$ denotes the zero-th order Bessel function of the first kind, Δt is the time-lag, and f_m is the maximum Doppler frequency. ($f_m = v_m/\lambda = v_m f_c/c$, where v_m is the mobile's velocity, λ is the wavelength, f_c is the carrier frequency, and c is the speed-of-light.)

4.3.2 Analytical Evaluation of the BER

Analytical expressions for the BER are derived in this section. Following [1], we start our analysis with defining the symbol transmitted as $x_{k,i}$, which is an element of the symbol set $\{x_{k,m}\}$, $m = \{1, 2, \dots, M\}$. (M is the order of the modulation scheme.) At the receiver's site, an optimum detector will choose the symbol $x_{k,n} \in \{x_{k,m}\}$, which minimizes the distance metric

$$M_d(x_{k,n}) = |y_k - \hat{h}_k x_{k,n}|^2. \quad (4-32)$$

This symbol is assumed to be most likely the transmitted symbol. The term $\hat{h}_k x_{k,n}$ in this equation accounts for the channel estimation. An error occurs when the metric calculated for a symbol $x_{k,n} \neq x_{k,i}$ is smaller than the metric for the transmitted symbol $x_{k,i}$. The probability for this event is written as

$$P_e = \Pr\{M_d(x_{k,n}) < M_d(x_{k,i})\} = \Pr\{D < 0\}, \quad (4-33)$$

where $D = M_d(x_{k,n}) - M_d(x_{k,i})$ is called the decision variable. Using (4-32), D becomes

$$D = y_k \hat{h}_k^* (x_{k,i}^* - x_{k,n}^*) + y_k^* \hat{h}_k (x_{k,i} - x_{k,n}) + |\hat{h}_k|^2 (|x_{k,n}|^2 - |x_{k,i}|^2). \quad (4-34)$$

From the channel and system models, y_k is known to be a complex Gaussian random variable. The same holds for \hat{h}_k , which is an estimate of the transfer function $H(f,t)$. Thus, the decision variable D is a special case of the generic quadratic form (see Appendix B in [1])

$$D = \sum_{l=1}^L (A |X_l|^2 + B |Y_l|^2 + C X_l Y_l^* + C^* X_l^* Y_l), \quad (4-35)$$

where X_l and Y_l are complex-valued Gaussian random variables, and A , B , and C are constants. In our case $L = 1$, considering one transmitted symbol over one (sub-) channel¹¹.

The error probability is the probability that $D < 0$, which is evaluated in Appendix B of [1]. This probability is denoted as the integral over the pdf of D

¹¹ The equation for $L > 1$ allows for the evaluation of diversity schemes [1], [15]–[17].

$$P_e = \Pr\{D < 0\} = \int_{-\infty}^0 p(D) dD. \quad (4-36)$$

For $L = 1$, the solution to this integral is written [1]

$$P_e = Q_1(a, b) - \frac{v_2/v_1}{1+v_2/v_1} I_0(ab) e^{-\frac{1}{2}(a^2+b^2)}, \quad (4-37)$$

where $I_n(x)$ is the n -th order modified Bessel function of the first kind and $Q_1(a, b)$ is the Marcum's Q function, which can be expressed in terms of Bessel functions as

$$Q_1(a, b) = e^{-\frac{1}{2}(a^2+b^2)} \sum_{n=0}^{\infty} (a/b)^n I_n(ab), \quad b > a > 0. \quad (4-38)$$

The parameters a , b , v_1 , and v_2 must be related to the moments of X_l and Y_l , and to the constants A , B , and C . As given in [1], these are obtained from

$$\begin{aligned} a &= \left[\frac{2v_1^2 v_2 (\alpha_1 v_2 - \alpha_2)}{(v_1 + v_2)^2} \right]^{1/2} \\ b &= \left[\frac{2v_1 v_2^2 (\alpha_1 v_1 + \alpha_2)}{(v_1 + v_2)^2} \right]^{1/2} \\ v_{1,2} &= \sqrt{w^2 + \frac{1}{4(\psi_{xx}\psi_{yy} - |\psi_{xy}|^2)(|C|^2 - AB)}} \mp w \\ w &= \frac{A\psi_{xx} + B\psi_{yy} + C\psi_{xy}^* + C^*\psi_{xy}}{4(\psi_{xx}\psi_{yy} - |\psi_{xy}|^2)(|C|^2 - AB)} \\ \alpha_1 &= 2(|C|^2 - AB)(|\bar{X}_1|^2 \psi_{yy} + |\bar{Y}_1|^2 \psi_{xx} - \bar{X}_1^* \bar{Y}_1 \psi_{xy} - \bar{X}_1 \bar{Y}_1^* \psi_{xy}^*) \\ \alpha_2 &= A|\bar{X}_1|^2 + B|\bar{Y}_1|^2 + C\bar{X}_1^* \bar{Y}_1 + C^* \bar{X}_1 \bar{Y}_1^* \end{aligned} \quad (4-39)$$

These equations are applied to our problem by comparing eqs. (4-34) and (4-35). Letting $Y_1 = y_k$ and $X_1 = \hat{h}_k$ in (4-34), the constants $A = |x_{k,n}|^2 - |x_{k,i}|^2$, $B = 0$, and $C = x_{k,n} - x_{k,i}$ are found, representing the properties of the modulation scheme. The behaviors of the channel and of the channel estimation technique will be expressed by the first and second moments of the random variables X_1 and Y_1 . These are

$$\begin{aligned} \bar{X}_1 &= E\{\hat{h}_k\} \\ \bar{Y}_1 &= E\{y_k\} \\ \psi_{xx} &= \frac{1}{2}[E\{|\hat{h}_k|^2\} - |\bar{X}_1|^2] \\ \psi_{yy} &= \frac{1}{2}[E\{|y_k|^2\} - |\bar{Y}_1|^2] \\ \psi_{xy} &= \frac{1}{2}[E\{\hat{h}_k y_k^*\} - \bar{X}_1 \bar{Y}_1^*] \end{aligned} \quad (4-40)$$

The derivation of these parameters from the channel and system definitions is given in

the following sub-section. Coherent and differential detection are investigated.

4.3.2.1 Application of the Mathematical Models

Coherent detection with perfect channel estimation

The k -th symbol received is defined in eq. (4-28) as $y_k = x_k h_k + n_k$. Perfect channel estimation means that the receiver has exact knowledge about the attenuation factor h_k , denoted by $\hat{h}_k = h_k$. Considering the transmitted symbol $x_{k,i}$ as a constant yields

$$\begin{aligned}\bar{X}_1 &= E\{h_k\} = \rho \cdot e^{j\theta_\rho}, \\ \bar{Y}_1 &= E\{x_{k,i} h_k + n_k\} = x_{k,i} E\{h_k\} + E\{n_k\} = x_{k,i} \rho \cdot e^{j\theta_\rho}, \\ \psi_{xx} &= \frac{1}{2}[E\{|h_k|^2\} - |\bar{X}_1|^2] = \frac{1}{2}[P_0 - \rho^2], \\ \psi_{yy} &= \frac{1}{2}[E\{|x_{k,i} h_k + n_k|^2\} - |\bar{Y}_1|^2] = \frac{1}{2}[|x_{k,i}|^2 (P_0 - \rho^2) + \sigma_N^2], \\ \psi_{xy} &= \frac{1}{2}[E\{h_k (x_{k,i} h_k + n_k)^*\} - \bar{X}_1 \bar{Y}_1^*] = \frac{1}{2} x_{k,i}^* [P_0 - \rho^2],\end{aligned}\tag{4-41}$$

where $\rho e^{j\theta_\rho}$ is the LOS-component, with arbitrary phase θ_ρ and with an amplitude defined by $\rho^2 = P_0 K/(K+1)$.

Differential detection

With differential detection, the decision for the received symbol y_k is made based on the adjacent symbol $y_{k-1} = x_{k-1} h_{k-1} + n_{k-1}$. For phase modulation schemes, this can be seen as a detection based on the channel estimate $\hat{h}_k = y_{k-1}/x_{k-1} = h_{k-1} + n_{k-1}/x_{k-1} = h_{k-1} + n'_k$, where $E\{|n'_k|^2\} = \sigma_{N'}^2$. Note that $\sigma_{N'}^2 = \sigma_N^2$, if the magnitude of x_{k-1} is one. The parameters \bar{Y}_1 and ψ_{yy} are then equal as in eqs. (4-41). The additional noise term n'_k , the correlation between h_k and h_{k-1} , and the Doppler shift of the LOS-component are expressed in

$$\begin{aligned}\bar{X}_1 &= E\{h_{k-1} + n'_k\} = \rho \cdot e^{j(\theta_\rho - 2\pi f_\rho T)}, \\ \psi_{xx} &= \frac{1}{2}[NR P + \sigma_{N'}^2 - \rho^2], \text{ and} \\ \psi_{xy} &= \frac{1}{2} x_{k,i}^* [E\{h_{k-1} h_k^*\} - \rho^2 e^{j2\pi f_\rho T}].\end{aligned}\tag{4-42}$$

For evaluating differential detection in the frequency-direction, let $T = 0$. Using the channel correlation functions given in Section 4.3.1, the correlation ψ_{xy} between the attenuation factors at two adjacent symbols becomes

$$\psi_{xy} = \frac{1}{2} x_{k,i}^* \frac{P_0}{K+1} \begin{cases} \frac{1}{1 - j2\pi F \tau_{rms} K_1} & \text{in frequency} \\ J_0(2\pi f_m T) & \text{in time} \end{cases}.\tag{4-43}$$

Note that the influence of the channel-variability is expressed by this correlation-value only, which is defined by the parameter-products $\tau_{rms} F$ and $f_m T$, for the two cases un-

der consideration.

Performance results are given in Section 4.3.3. It will be shown that differential detection in the time-direction is more robust than the frequency-domain variant, for the OFDM system under consideration, i.e., for a wide-band indoor wireless LAN.

4.3.2.2 Application to Different Modulation Schemes

Assigning different constellation values to the variable $x_{k,n} \neq x_{k,i}$, the probability can be calculated that an erroneous symbol $x_{k,n}$ has been detected while the symbol $x_{k,i}$ was transmitted. This allows for many modulation schemes an exact calculation of the BER and for others the evaluation of close approximations.

In the following analysis we assume that all possible transmitted symbols $x_{k,i} \in \{x_{k,m}\}$ occur with equal probability.

BPSK and QPSK

Exact results can be obtained for BPSK and QPSK modulation. The signal constellations for these techniques are depicted in Figure 4-10. For both schemes it is sufficient to consider (any) one transmitted symbol, due to symmetries. This symbol will be the +1, taken from the set $\{x_{k,m}\} = \{1, -1\}$ for BPSK, and from $\{x_{k,m}\} = \{1, j, -1, -j\}$ for QPSK. Note that $|x_{k,m}|^2 = 1$ for both modulation types.

BPSK is analyzed by evaluating the parameters A and C for $x_{k,i} = 1$ and $x_{k,n} = -1$. The bit error probability is equal to the symbol error probability P_e (see eq. (4-37)).

Gray-coded QPSK transmits two bits per symbol on orthogonal carriers (I- and Q-components). Thus, the error probabilities can be analyzed independently and the BER equals their average. Suitable parameters for A and C are found by (e.g.) assigning $x_{k,i} = 1$ and $x_{k,n} = \{j, -j\}$.

Calculating the probability that $x_{k,n}$ has been detected, provided $x_{k,i}$ was transmitted, the I/Q-plane is divided in two parts. An error occurs when the received symbol falls within the half plane being closer to $x_{k,n}$ than to $x_{k,i}$. No error occurs otherwise (see Figure 4-10). Note that for the case of QPSK it is not necessary to evaluate the two-error-event explicitly. The overlapping one-error-events account for one error *each* in

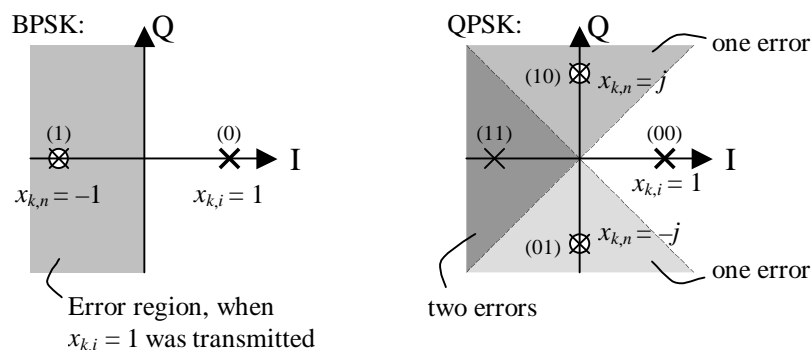


Figure 4-10: Selection of $x_{k,i}$ and $x_{k,n}$ for the performance evaluation of BPSK and QPSK.

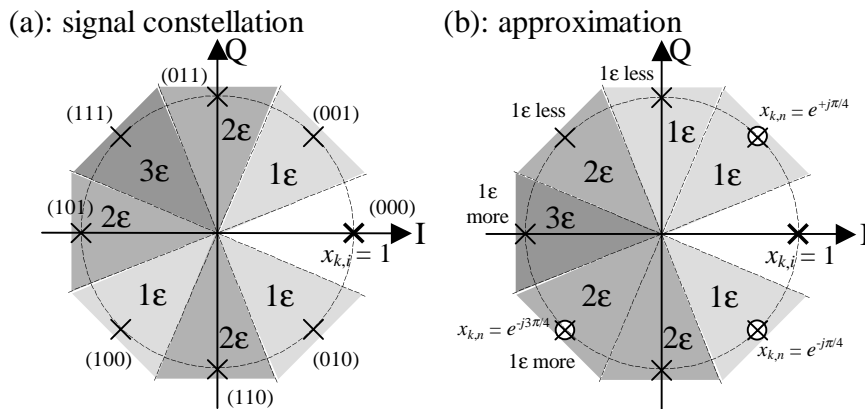


Figure 4-11: Error regions for 8-PSK, when $x_{k,i} = 1$ was transmitted. (a) Signal constellations and correct number of errors for each decision range. (b) Approximation by evaluating error probabilities from the three error-states $x_{k,n}$ shown. In some error regions, one extra error is considered, in other regions, one error is missed (indicated as 1ε more and 1ε less).

this region, thus the two-error-event is included automatically. This may seem as an advantage because computational complexity reduces, however, when evaluating higher order modulation schemes, many of those half-planes will overlap and it is sometimes not possible to obtain the exact number of errors for all decision regions. This will be seen in the following case.

8-PSK

Upper and lower bounds on the BER can be calculated for 8-PSK. An exact calculation is not possible, because the eight signal states are not separable in the two orthogonal dimensions of the I/Q-plane.

Due to symmetries it is again sufficient to consider one transmitted symbol, $x_{k,i} = 1$. Figure 4-11 illustrates how errors occur in estimating error probabilities. The signal constellations are shown in Figure 4-11a together with the exact numbers of errors for each decision region. (Errors are denoted by 'ε'.) Figure 4-11b shows the actual numbers of errors for each of these regions, when three different error states $x_{k,n}$ are evaluated and averaged. Clearly, too few errors are considered in some of the decision regions, while too many are considered in others. Thus the computational results are a (close) approximation. The most likely errors, however, are appropriately treated.

16-Quadrature Amplitude Modulation (QAM)

16-QAM can be evaluated without any error. Four different transmitted symbols occurring with equal probabilities and 24 error events must be considered. Some of them must be subtracted in order to account for overlapping decision regions. A possible set of symbols $x_{k,i}$ and $x_{k,n}$ to be used are listed in Table 4-1. The complex signal constellations x_k are denoted $(\text{Re}\{x_k\}, \text{Im}\{x_k\})$. Error events whose probability must be subtracted in the final result are written $(\text{Re}\{x_k\}, \text{Im}\{x_k\})^{-1}$. All values must be divided by $\sqrt{10}$ to have an average power of one. Figure 4-12 illustrates the signal constellations

and error events for the symbol $x_{k,i} = (-3,3)$, which carries the data symbol (0000).

Table 4-1: Transmitted symbols and error events for the evaluation of 16-QAM modulation.

<i>Transmitted symbol</i> $x_{k,i}$	<i>Error symbols</i> $x_{k,n}$
$(-3,3)$	$(-1,3), (3,3), (7,3)^{-1},$ $(-3,1), (-3,-3), (-3,-7)^{-1}$
$(-1,3)$	$(-3,3), (1,3), (5,3),$ $(-1,1), (-1,-3), (-1,-7)^{-1}$
$(-3,1)$	$(-1,1), (3,1), (7,1)^{-1},$ $(-3,3), (-3,-1), (-3,-5)$
$(-1,1)$	$(-3,1), (1,1), (5,1),$ $(-1,3), (-1,-1), (-1,-5)$

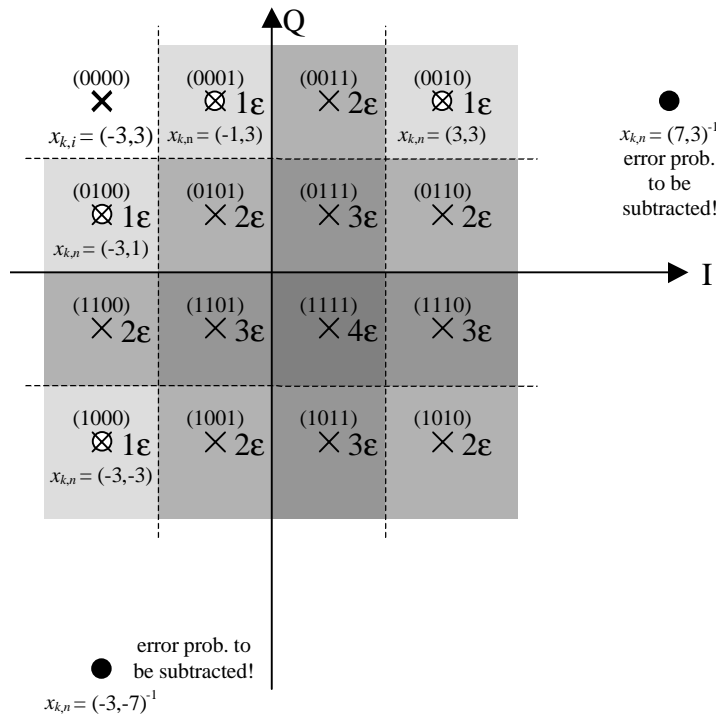


Figure 4-12: Illustration of the error events in 16-QAM, when the symbol $x_{k,i} = (-3,3)$ was transmitted.

16 Star-QAM

16 Star-QAM can be treated as a combination of 8-PSK and a binary amplitude modulation. The binary AM is evaluated by transforming the I- and Q-variables to an $r^2 = I^2 + Q^2$ variable, resulting in similar expressions to the above defined ones. This is described in [16] and [17].

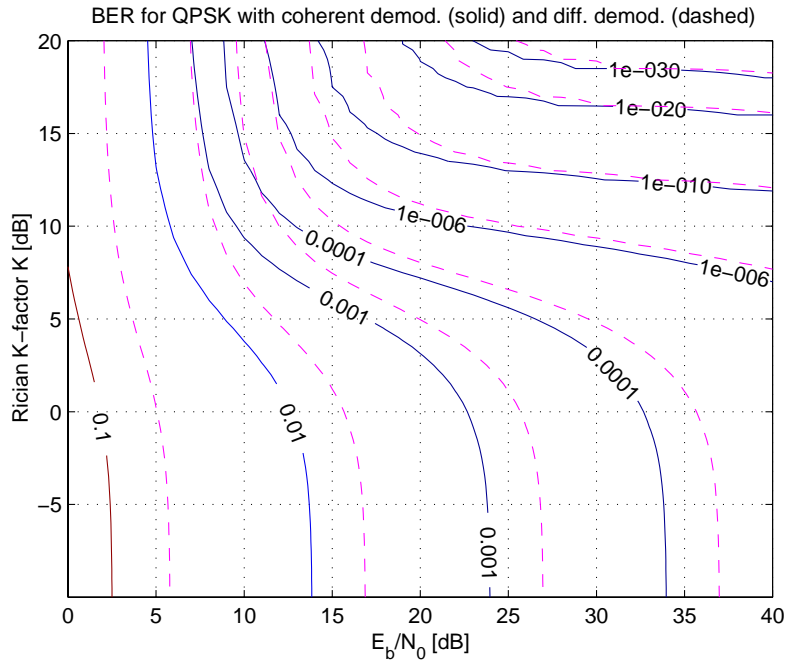


Figure 4-13: Performance of QPSK for coherent detection (perfect channel estimation) (‘—’) and for differential detection with $F = 0$, i.e., with perfect correlation between adjacent sub-carriers (flat fading) (‘---’).

4.3.3 Performance Results

Some observations can be made from the mathematical expressions derived above (eqs. (4-41)–(4-43)):

- (i) For coherent detection, the statistical parameters – and thus the performance results – only depend on P_0 , ρ , and σ_N^2 . In other words, the performance depends on the average signal-to-noise ratio (SNR) $SNR \propto P_0 / \sigma_N^2$ and on the Rician K-factor $K = \rho^2 / (P_0 - \rho^2)$.
- (ii) The same holds in the limits $F \rightarrow 0$ or $T \rightarrow 0$ (i.e., for flat fading) for differential detection.
- (iii) The performance of differential detection degrades for $F > 0$ (or $T > 0$), because of a systematic estimation error in $\hat{h}_k = h_{k-1} + n'_k$, since $h_{k-1} \neq h_k$. The parameter products $\tau_{rms}F$ and f_mT define the degradation, according to eq. (4-43).

Performance results (average BER) for (i) and (ii) and QPSK modulation are shown in Figure 4-13, as a function of the average SNR per bit (denoted E_b/N_0)¹² and as a func-

¹² Several signal-to-noise ratio (SNR) parameters are used in this thesis: The SNR denoted E_b/N_0 is the average SNR per data bit. It thus depends on the order M of the modulation scheme. The average SNR of the subcarrier symbols, being independent of the modulation scheme, is written as SNR_{SC} (see Section 6.2.7.2). In Section 6.2.3, the SNR of the time-domain OFDM signal is defined, written as

tion of K , where

$$\frac{E_b}{N_0} = \frac{E\{|x_{k,m}|^2\}}{\log_2(M)} \frac{P_0}{\sigma_N^2}. \quad (4-44)$$

It is observed from the figure that the SNR required to achieve a certain BER-performance is dramatically increased for small K -factors (for Rayleigh channels). A 3-dB disadvantage of SNR is evident for the differential detection method, since two noise processes with equal variance are present –, the noise of the channel estimate and the noise of the data symbol to be detected.

A performance comparison of different modulation schemes is presented in Figure 4-14. Note that the result for 16-QAM (differential) is a theoretical one, because differential demodulation for this scheme is hard to accomplish. Again the advantage of a high K -factor is seen. With coherent detection, equivalent performance is obtained for BPSK and QPSK. This is not the case for differential detection on AWGN or Ricean channels, where BPSK has an additional advantage of 1–2 dB over QPSK (see also [1]). It is important to note that twice the symbol energy is used with QPSK, because two bits are transmitted per symbol. The higher order modulation schemes (8-PSK and 16-QAM) require approximately 3–4 dB more signal power than QPSK.

Taking into account the channel variability, irreducible error floors arise (see Figure 4-15). Both versions of differential detection have been evaluated for Rayleigh fading channels, QPSK modulation, and for the following parameters. For detection in the frequency-direction, the channel's RMS delay spread τ_{rms} was assumed to be three samples, which corresponds to a maximum delay spread of about thirty samples, assuming an exponentially decaying channel delay profile (see Section 2.3.3.3). For 128 FFT-points, this value corresponds to about one quarter of the FFT-time, which is also about the time duration that would be selected for the guard interval. It is seen that the irreducible error floor associated with such – quite realistic – parameters ($\tau_{rms}F = 3/128$) lies around 10^{-2} (curve ‘○—○’).

The time-variability for differential detection in time-direction corresponds to a mobile moving at 20 m/s, to a carrier frequency of 60 GHz, and to a symbol length of 1.3 μ s. According to the system model, inter-carrier-interference (ICI) due to the Doppler spreading has been neglected¹³. While the symbol duration assumed is rather short, the mobility considered is by an order of magnitude higher than the expected mobility

SNR. This value is different to the previous ones, because not all FFT-points are used for data sub-carriers. In Chapter 8, the coding scheme is incorporated in some other SNR parameters.

¹³ That ICI truly is negligible for the system parameters selected is suggested from the comparison of the maximum Doppler frequency and the OFDM sub-carrier spacing. The former, being 4 kHz is just 0.4 % of the latter, which is 1 MHz. An approximate equation for the SNR-degradation due to mobility can be found for instance in [7]. Its evaluation leads to the same conclusion (see Section 6.5.3.1).

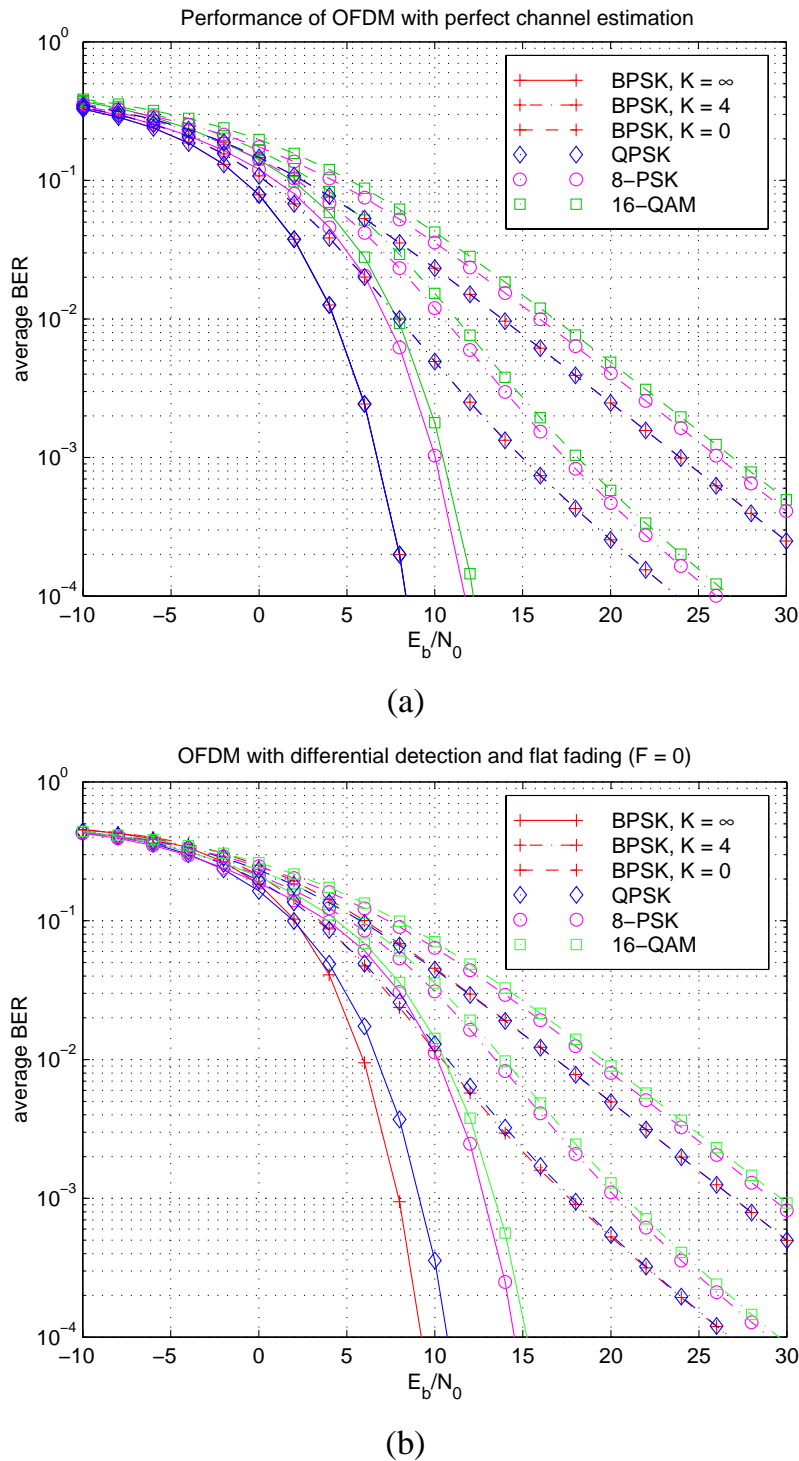


Figure 4-14: Performance of different modulation schemes. (a): Coherent detection with perfect channel estimation. (b): Differential detection with $F = 0$, i.e., perfect correlation between adjacent sub-carriers (flat fading).

in an indoor wireless-LAN system. Despite this, the error-floor is much lower for this method of differential detection (curve '* - - *').

The other results depicted analyze the influence of synchronization errors. In the frequency-domain results, ICI and ISI have been neglected, which is exact as long as the

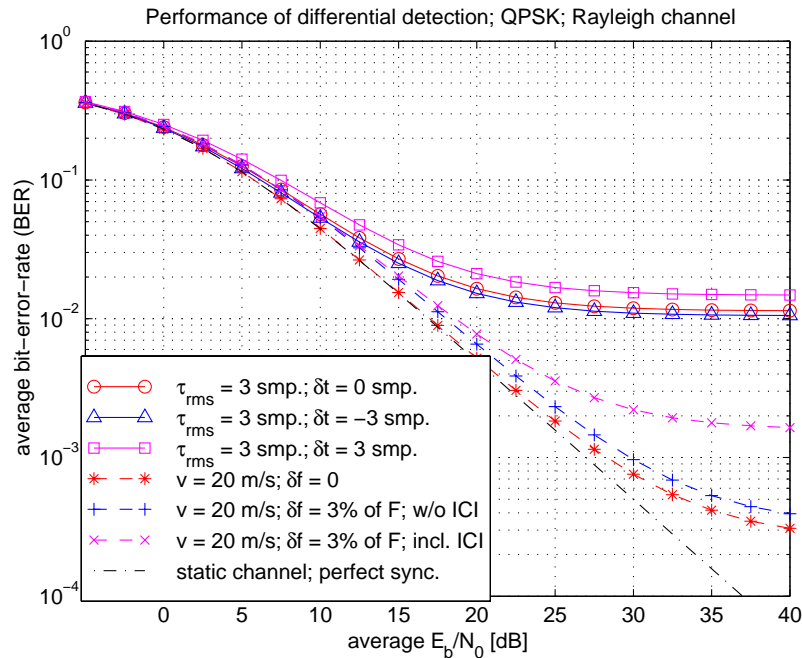


Figure 4-15: The channel variability is leading to irreducible error floors for the differential modulation schemes. Differential QPSK is evaluated over Rayleigh fading channels.

channel impulse response remains within the guard interval. In other words, the performance impact results from the systematic phase rotations only that are – as seen from the extended system model (Section 4.2.4) – due to the time-synchronization error. Such phase rotations mean for the differential detection techniques that the signal constellation points compared typically move closer together, which implies a performance degradation.

Note however, that a negative timing offset equal to the channel's τ_{rms} slightly *improves* the performance. This is because the channel as well induces some systematic phase rotation, which is – in the case discussed – cancelled by the phase rotation due to timing-offset¹⁴. The impact on the performance is small, however, for the offsets evaluated.

In the curves depicting the performance for the detection scheme in time-direction, the impact of ICI due to a frequency-offset is shown as well. ICI has been included using the approximation from [7]. It is seen that the impact of the phase distortion is evident at all SNR-values, while ICI determines the error floor at high SNR.

In Figure 4-16, the performance of differential QPSK (in frequency-direction) is

¹⁴ The progressive phase rotation due to a timing-offset can be utilized for timing synchronization (see Section 6.2.7). Thereby, the systematic phase rotation due to the channel leads to a bias in the estimate. If this biased estimate is used for timing-synchronization, optimum performance is achieved, because the systematic phase rotations due to the channel and due to the bias compensate each other.

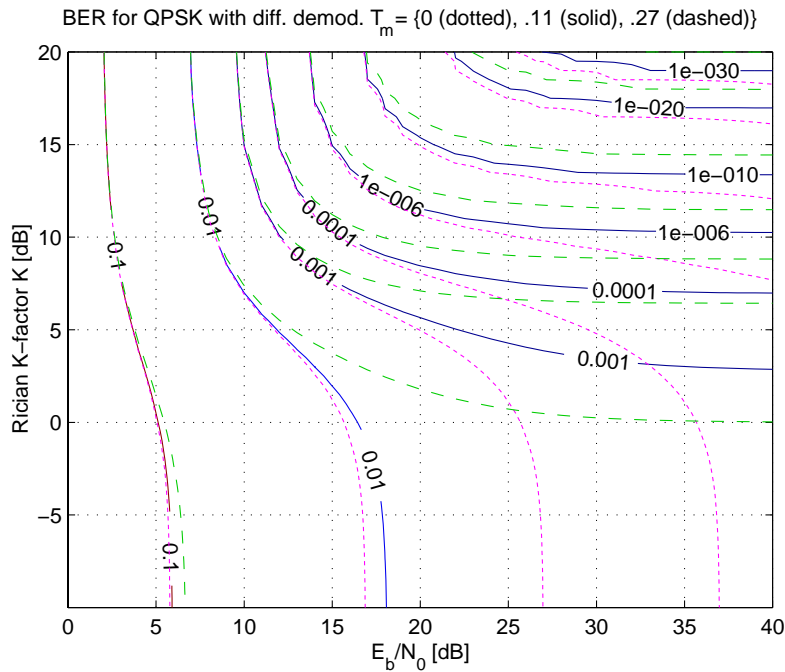


Figure 4-16: Performance of QPSK with differential detection in frequency-direction. The maximum excess delay of the channel is related to the FFT-time, expressed by T_m .

shown as a function of E_b/N_0 and K , where τ_{rms} is a parameter. Since the maximum excess delay of the channel – which should not exceed the guard interval – is a function of τ_{rms} and K , all these parameters are interrelated. The following definitions are introduced to get a set of general results. The FFT duration and GI-duration are connected by a fixed factor, which is usually in the range of 4 ... 10. The maximum excess delay of the channel can be written $\tau_{max} = 10\tau_{rms}K_1$, according to the definition of Section 2.3.3.3 (see eq. (2-24)). This leads to the normalized excess delay, defined as $T_m = \tau_{max}/T_{FFT} = 10\tau_{rms}K_1F$. In Figure 4-16, the performance of differential QPSK is shown for $T_m = \{0, 0.11, 0.27\}$. The curves for $T_m = 0$ allow a comparison with Figure 4-13. Especially for severely fading channels (low K -factors), the performance degradation is significant for the delay spreads considered.

4.4 Conclusions and Recommendations

The derivation of the OFDM system model has confirmed that data symbols can be transmitted independently over multipath fading radio channels. It has to be assumed, however, that the channel's maximum excess delay is shorter than the guard interval, and that the system has been synchronized sufficiently. Small synchronization errors lead to systematic phase rotations of the data constellation points – a property which can be exploited for estimating synchronization offsets. If the timing- or frequency-synchronization error becomes too large, the orthogonality of the sub-carriers is partly lost and the signal-to-noise ratio of the system is degraded. That is, inter-carrier-inter-

ference (ICI) and inter-symbol-interference arise. ICI can also result from very fast channel variations (Doppler spreads) or from carrier phase jitters.

The system models presented can be utilized in analytical studies of various aspects of the OFDM technique, as, for instance, in the performance evaluation. The basic model introduced assumes perfect synchronization, while an extended model considers the phase rotations due to small synchronization-offsets.

The performance analysis of an uncoded OFDM scheme is based on the classic formulas given by Proakis ([1]: Appendix B). Expressions are derived for the evaluation of different modulation schemes and for coherent and differential detection. The frequency-domain channel model (see Chapter 2) for Ricean fading channels has been applied. It allows to show performance results as a function of the channel parameters $\{P_0, K, \tau_{rms}\}$ – the normalized received power, the Ricean K-factor, and the RMS delay spread.

Assuming perfect channel estimation, or – if differential schemes are applied – complete channel correlation, the performance is determined by P_0 and K . These parameters specify the average signal power and the depth of the fades. Better performance is thus achieved over channels having a higher K-factor, because the fades are shallower.

Performing differential detection in the frequency-domain, a degradation of the results is seen, due to the small differences of the channel transfer function at adjacent sub-carriers (whose data symbols are compared). Since, for small frequency-lags, there is a very strict relationship between this correlation function and the RMS delay spread, τ_{rms} , of the channel (in particular for Rayleigh fading channels – see Appendix A), it is concluded that the performance degradation is well characterized by τ_{rms} . (To be exact, the performance is defined by the product $\tau_{rms}F$, where F is the sub-carrier spacing.) Imperfect timing-synchronization also has an impact, because systematic phase offsets are introduced between adjacent sub-carriers.

For the low-mobility OFDM based WLAN system under investigation, the correlation of subsequent symbols in time-direction is much higher than the correlation of symbols on adjacent sub-carriers. Therefore, it is recommended to apply differential detection in time-direction, not in frequency direction. In this case, systematic phase offsets are induced by imperfect carrier frequency-synchronization.

By extending the OFDM system model, it becomes possible to analyze imperfections of OFDM systems. Frequency synchronization-offsets, for example, give rise to inter-carrier-interference, which can be accounted for by an additional noise term [11]. In a similar fashion, the impact of Doppler spreads, phase noise, or channel estimation errors can be incorporated. The evaluation of such imperfections is a topic for future work. Using the original equations of [1], it is also possible to investigate diversity techniques (see e.g. [15]–[17]).

4.5 References

- [1] J. G. Proakis, *Digital Communications*, 3rd edition. New York: McGraw Hill, 1995.
- [2] R. Prasad, *Universal Personal Communications*. Boston: Artech house, 1998, ch. 10.
- [3] R. van Nee and R. Prasad, *OFDM for Wireless Multimedia Communications*. Boston: Artech House, 2000.
- [4] O. Edfors, M. Sandell, J. J. van de Beek, D. Landström, F. Sjöberg, “An Introduction to Orthogonal Frequency-Division Multiplexing,” *Research Report TULEA 1996:16*, Division of Signal Processing, Luleå University of Technology, <http://www.sm.luth.se/csee/sp/publications.html>.
- [5] O. Edfors, *Low-complexity algorithms in digital receivers*, Ph.D. Thesis, Luleå University of Technology, Sept. 1996.
- [6] M. Sandell, *Design and Analysis of Estimators for Multicarrier Modulation and Ultrasonic Imaging*, Ph.D. Thesis, Luleå University of Technology, Sept. 1996.
- [7] M. Speth, S. A. Fechtel, G. Fock, and H. Meyr, “Optimum Receiver Design for Wireless Broad-Band Systems Using OFDM—Part I,” *IEEE Trans. Commun.*, vol. 47, no. 11, pp. 1668–1677, Nov. 1999.
- [8] S. B. Weinstein and P. M. Ebert, “Data Transmission by Frequency-Division Multiplexing Using the Discrete Fourier Transform,” *IEEE Trans. Commun. Techn.*, vol. COM-19, no. 5, pp. 628–634, Oct. 1971.
- [9] A. Peled and A. Ruiz, “Frequency Domain Data Transmission Using Reduced Computational Complexity Algorithms,” *in Proc. IEEE Int. Conf. Acoust., Speech, Signal Processing*, Denver, CO, 1980, pp. 964–967.
- [10] P. Pollet, M. van Bladel, and M. Moenclaey, “BER Sensitivity of OFDM Systems to Carrier Frequency Offset and Wiener Phase Noise,” *IEEE Trans. on Commun.*, vol. 43, no. 2/3/4, pp. 191–193, Feb./March/April 1995.
- [11] P. H. Moose, “A technique for orthogonal frequency division multiplexing frequency offset correction,” *IEEE Trans. Commun.*, vol. 42, no. 10, pp. 2908–2914, Oct. 1994.
- [12] P. A. Bello, “Characterization of randomly time-variant linear channels,” *IEEE Trans. on Commun. Systems*, vol. CS-11, pp. 360–393, Dec. 1963.
- [13] R. Steele, *Mobile Radio Communications*. New York: John Wiley & Sons, 1992.
- [14] W. C. Jakes Jr., *Microwave Mobile Communications*. New York: John Wiley & Sons, 1974.

- [15] J. Lu, T. T. Tjhung, F. Adachi, and C. L. Huang, “BER performance of OFDM-MDPSK systems in frequency-selective Ricean fading with diversity reception,” *IEEE Trans. Veh. Technol.*, vol. 49, no. 4, pp. 1216–1225, July 2000.
- [16] X. Dong, T. T. Tjhung, and F. Adachi, “Error Probability Analysis for 16 STAR-QAM in Frequency-Selective Ricean Fading with Diversity Reception,” *IEEE Trans. on Veh. Techol.*, vol. 47, no. 3, pp. 924–935, Aug. 1998.
- [17] T. T. Tjhung, F. Adachi, K. H. Tan, X. D. Dong, and S. S. Ng, “BER Performance of 16 STAR-QAM in Ricean Fading with Diversity Reception,” in Proc. *PIMRC’94*, The Hague 1994, pp. 80–84.

Chapter 5 – OFDM System Proposal and Emulation System

5.1 Introduction

Main parts of this Ph.D. research have been performed under the framework of a cooperative research project between Korea Telecom and Delft University of Technology, as mentioned in the introduction. One of the goals of this project was the development of an OFDM based wideband communications system operating at up to 155 Mbit/s in 60 GHz radio channels. Wireless asynchronous transfer mode (ATM) transmission was considered in indoor and low-range (and low mobility) outdoor environments.

The first part of this chapter (Section 5.2) gives an overview of the proposed OFDM system. Most of the parameters given and choices made are motivated in the text; others have been selected rather intuitively. One purpose of the system proposal was to specify an OFDM system that could be used as a “benchmark system” in analytical studies and simulation studies of several aspects of the OFDM technique. These studies are described in the remaining chapters of this thesis. They mostly concern implementation issues of OFDM, like synchronization and channel estimation, and their performance evaluation. Some of the conclusions have been incorporated in the system proposal given here. That is, although some parameters may have been selected “ad-hoc”, their suitability was investigated and confirmed afterwards.

The proposed system consists of a central base station (BS) and several mobile terminals (MT). The base station acts as an interface between the physical transmission media of the wired ATM backbone network and the broadband radio air-interface. Therefore, it must be optimized for operating robustly and efficiently in these two very dissimilar communications media –, the highly reliable optical fiber network and the ran-

domly fading radio channel.

The target bit-rate of 155 Mbit/s is reached under ideal conditions, and when the up-link and down-link data rates are added up. Channel bandwidths in the order of 100 MHz are required; in multi-cell systems, several of these channels must be available for adjacent base stations. Such large bandwidths may be available in the 60 GHz frequency-band.

The air-interface is the main research topic of this Ph.D. thesis, hence the system proposal is focused on the physical layer. Orthogonal frequency division multiplexing (OFDM) is considered to be the key enabling technology for such high data rates in multipath fading, mobile channels. One ATM cell was assumed to be the smallest information entity to be transmitted at a time. A multiple access scheme having both time- and frequency division multiple access components (TDMA and FDMA), maps the ATM cells on the OFDM symbols, after interleaving and error correction coding. Periodic training symbols are transmitted on the down-link for synchronization and channel estimation. These training symbols are followed by signaling symbols, which are used by the medium access control (MAC) protocol to negotiate transmission capacity.

On the up-link, pre-equalization and time-division duplexing (TDD) are proposed for minimizing the signal processing required and for enabling asymmetric data rates. Reciprocity of the channel is assumed. Pre-equalization allows the efficient transmission of information entities as short as a single ATM cell on the up-link, without adding vast amounts of overhead for synchronization and channel estimation. It also reduces the signal processing needed at the base station for serving multiple mobile terminals. Slow time-variability of the radio channel is a necessity, however.

Another primary goal of the cooperative research project was the demonstration of the proposed air-interface on a hardware platform to be developed. Unfortunately, the technical specifications of the investigated systems are so demanding that an implementation is almost impossible for a small research team, as real-time DSP of two data streams is required at sampling frequencies of ~100 MHz. A drastically downscaled hardware platform is therefore used, which is presented in Section 5.3.

5.2 OFDM Based System Proposal

A highly efficient multiple access scheme is one of the main requirements of the proposed, OFDM-based, multimedia communications system. In order to minimize delays in low-rate applications and in automatic repeat request (ARQ)-schemes, which are needed to meet defined quality-of-service (QoS) requirements, the system should be able to transmit small data entities (single ATM cells) without the need for excessive signaling and synchronization overhead. This design target becomes critical because of the high data rate of up to 155 Mbit/s.

Another important aspect was to consider an option for simultaneously accessing the system with low-complexity terminals that can only cope with one quarter of the system bandwidth. Such transceivers have simplified RF front-ends and baseband processing units, which both lead to reduced power consumption. Moreover, the limited bandwidth implies a 6-dB advantage in their link-budgets.

Adaptability to current channel conditions is provided by two mechanisms. Two transmission modes (modes I and II) with different delay spread robustness can be used according to the typical channel properties of the environment. Their main difference is the length of the guard interval and the number of FFT-points and sub-carriers. A set of coding and modulation techniques allows for a trade-off between the range and the bit-rate. I.e., Using more efficient coding techniques and more robust modulation schemes, the range can be extended at the cost of a decreased data rate.

The key specifications and design paradigms considered are:

- up to 155 Mbit/s ATM data rate
- operation in the 60 GHz (mm-wave) frequency-band
- indoor pico-cells and short range outdoor environments (< 100 m diameter)
- limited mobility (max. 2–5 m/s)
- fulfill defined QoS and delay requirements
- provide high spectral efficiency
- low implementation complexity (to cope with the high data rates)
- low power consumption
- high robustness against delay spread and interference
- provide adaptability to changing channel conditions (e.g. fall-back modes)

This section introduces the OFDM system proposal, which takes the above listed requirements into consideration. It is organized as follows. In Section 5.2.1, the main transmission modes are explained, and the selected time-division duplex (TDD) frame structure and OFDM symbol configuration are introduced. The multiple access scheme having time and frequency division multiple access (TDMA, FDMA) components is described in Section 5.2.2. Section 5.2.3 presents the hardware architecture of base stations and mobile terminals in the form of block diagrams. Interleaving and coding schemes are outlined in Section 5.2.4, followed by link budget considerations in Section 5.2.5. In Section 5.4, the system proposal is summarized and preliminary conclusions are drawn.

5.2.1 Air Interface Physical Layer

The OFDM modulation technique is considered a strong candidate for the air-interface of high-speed wireless LANs and similar systems. The main advantages of OFDM in this context are its high spectral efficiency and robustness against multipath delay

spread. The latter is obtained through the introduction of a guard interval. The well-known, and extensively studied disadvantages of this modulation technique include [1]:

- Sensitivity against frequency offsets and phase jitters
- Non-constant power envelope (requiring linear power amplifiers to avoid distortion)

These issues have to be solved sufficiently, otherwise the orthogonality among data symbols is partly lost (ICI and ISI arise). To overcome, or at least ease these impairments, some of the design considerations of the proposed OFDM scheme were:

- Transmit sufficient overhead (training-symbols) on the down-link to allow the MTs to synchronize to the BS with low computational complexity and to allow for accurate and efficient channel estimation.
- Use as little carriers as possible, which is of advantage for the frequency synchronization algorithm, for the peak-to-average power ratio (PAPR) problem, and for the robustness against carrier phase jitter and Doppler spreads.

5.2.1.1 Modes of Operation

For different environments, antenna configurations and link qualities, several modes of operation are proposed. There are two incompatible “*main modes*” (mode I and mode II) that will be permanently assigned to a base station, depending on the properties of the environment. Mode II has a higher robustness against long delay spreads, which may be required in very large rooms (*cf.* Section 2.5.2). This higher robustness is obtained by increasing the guard interval duration, the symbol length, and the number of FFT points and sub-carriers. Mode I allows for maximum excess delays of about 200 ns (~ 25 ns RMS delay spread, τ_{rms}), mode II permits about 500 ns ($\tau_{rms} \cong 65$ ns). Exceeding those maximum values leads to a gradual performance degradation that may be tolerable if the signal-to-noise ratio is sufficient.

Mode I has advantages due to the smaller number of FFT points, allowing for relaxed hardware requirements. For instance, the robustness to phase noise and Doppler shifts is enhanced, the PAPR problem is reduced, and the efficiency is slightly higher, due to a more efficient frame format. These advantages may enable the design of cheaper access points for small environments, where mode I is typically appropriate and sufficient.

Another design goal was to provide the possibility to simultaneously access the network with full and reduced (one quarter) bandwidth mobile terminals, as mentioned above. These two options are denoted as the full-rate (-fr) and the quarter-rate (-qr) “*bandwidth modes*”. Using four sub-symbols per OFDM symbol, the coded ATM cells are mapped on the transmission medium in a flexible TDMA/FDMA scheme (see Section 5.2.2). Table 5-1 lists the characteristic parameters of modes I and II,

Table 5-1: Characteristic parameters of the transmission modes I and II for full and quarter bandwidth terminals

parameter	<i>mode: I</i>		<i>II</i>	
	<i>full</i>	<i>quarter</i>	<i>full</i>	<i>quarter</i>
Number of FFT points	128	32	256	64
Nr. of data + pilot sub-carriers	76 + 12	19 + 3	152 + 24	38 + 6
FFT time [μ s]	1.000		2.000	
in [samples]	128	32	256	64
Guard + windowing interval [μ s]	0.187 + 0.094		0.47 + 0.094	
in [samples]	24 + 12	6 + 3	60 + 12	15 + 3
Bandwidth (-20 dB) [MHz]	\sim 100	\sim 28	\sim 100	\sim 28
Sampling frequency [MHz]	128	32	128	32

operating at full and quarter bandwidth.

Quarter rate terminals cannot use the full transmission rate, however, they have advantages regarding the complexity of the base-band processing unit and the RF front-ends, regarding the link budget (see Section 5.2.5), and regarding the power consumption. The quarter-rate mode can also serve as a fallback mode for the full-rate users, when shortcomings are experienced in their link-budgets. (This applies particularly for the up-link). But the reduced bandwidth also implies some disadvantages. Less bandwidth means less frequency-diversity, thus – considering forward error correction coding – the performance is expected to be worse. The bit- and frame-error-rate analysis of a coded and interleaved OFDM system confirms this expectation (see Section 8.2). Frequency hopping across the four quarter-rate sub-bands would reduce this performance gap. Another possible remedy is the application of diversity schemes, as proposed in Section 8.3.

The transmission speed is determined by the modulation technique and coding scheme used. OFDM allows for high flexibility in using different modulation and coding techniques simultaneously, depending on the users' channel qualities. The main options considered are QPSK and 16-QAM modulation with coding rates of approximately $\frac{1}{2}$ and $\frac{3}{4}$. However, many other combinations can be applied as well. These “*modulation modes*” are referred to as sub-modes -H, -L, and -LL. Their description and the actual transmission rates achieved are presented in Section 5.2.1.4, Table 5-3.

5.2.1.2 Frame Format and Modulation Schemes

A time division duplexing (TDD) frame format has been proposed, which has a fixed total frame length and a flexible boundary between the down-link and the up-link in order to support asymmetric data rates. To simplify the switching of the transceivers between transmission and reception and to be able to compensate for propagation de-

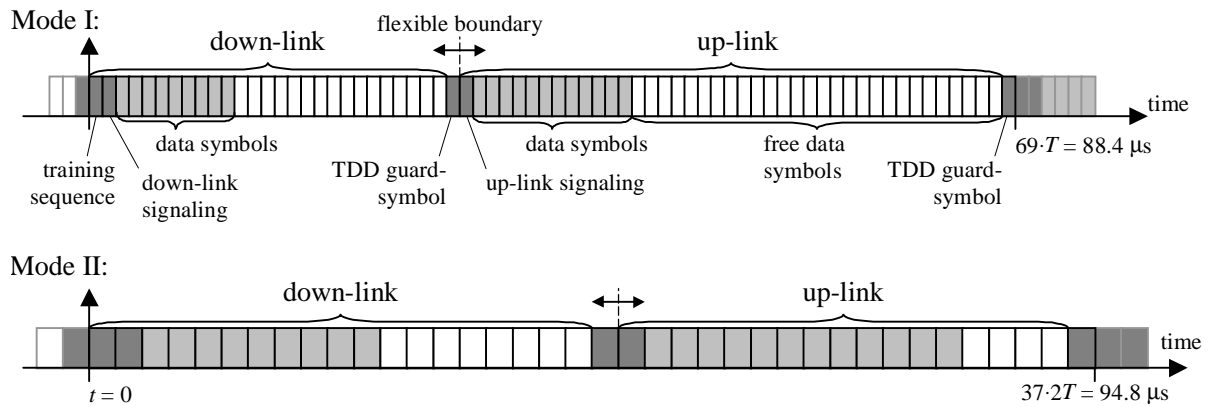


Figure 5-1: Frame structure of the time division duplex scheme in modes I and II. Each rectangle indicates one OFDM symbol.

lays, null-symbols are inserted. An illustration is given in Figure 5-1; the frame related parameters for the two transmission modes are listed in Table 5-2.

Using a TDD scheme, most synchronization can be done by the mobile terminals on the down-link. For this purpose, the base station transmits a training symbol at the beginning of each frame, being a unique OFDM symbol. This symbol is used for (frame) timing and frequency synchronization, as well as for the derivation of a channel estimate for the down-link channel. The required signal-processing algorithms are described and evaluated in Chapter 6.

There is *no* training symbol on the up-link, assuming reciprocity of the channel. In order to facilitate coherent detection on the up-link, pre-equalization techniques are suggested. I.e., the up-link data constellation points are multiplied by the inverse of the

Table 5-2: Frame related parameters of the OFDM system proposal

<i>parameter</i>	<i>mode I</i>	<i>mode II</i>	<i>mode II'</i>
OFDM symbol duration T [μs]	1.28		2.56
OFDM symbols per frame	69	37	35
frame duration [μs]	88.4	94.8	89.7
frame rate [kFrames/s]	11.31	10.54	11.15
TDD guard symbols per Frame (overhead)	2 (2.8 %)	2 (5.4 %)	2·0.5 (2.8 %)
synchronization symbols per Frame	1 (1.4 %)	1 (2.7 %)	1 (2.8 %)
signaling symbols per Frame	2 (2.8 %)	2 (5.4 %)	1 (2.8 %)
signaling channels per Frame; up + down-link (4 per OFDM symbol)	4 + 4	4 + 4	4 up-link <i>or</i> 4 down-link
modulation for signaling		BPSK	
coding rate for signaling		$\sim 1/2$	
data bits per signaling channel per Frame	9.5		19
signaling rate per signaling ch. [kbit/s]	107.5	200.4	105.9

channel transfer function that has been estimated on the down-link. Passing the pre-equalized OFDM signal through the multipath channel, the overall transfer function becomes flat or phase-linear. Channel estimation and synchronization on the up-link thereby reduce to an estimation of the magnitude of the received constellation values, and the estimation of timing-offsets and carrier phase-offsets. Chapter 7 explains those techniques.

In mode II, the number of OFDM data symbols per frame was halved in order to maintain the rate of synchronization symbols. (Below, a discussion on the frame length and channel time-variability is given.) For the sake of simplicity, the overhead symbols (TDD guard, synchronization and signaling) were adopted from mode I, resulting in an increased overhead and a doubled data rate on the signaling channel¹⁵. Doubling the period of the synchronization symbol is reasonable because the requirements on the frequency synchronization are also doubled.

Mode II' introduced in the table above is a slightly more efficient proposal compared to mode II. The efficiency is increased by alternately transmitting signaling channels on the up- and down-link, and by halving the TDD guard intervals. According to mode I, the transceivers have to be able to switch between up and down-link within the duration of one mode I OFDM symbol. Thus extending the TDD guard symbols is a waste of efficiency. It has to be evaluated, however, if the propagation delays and filter group delays can be fit within this guard period. The up-link transmission must start slightly in advance to ensure that the up-link symbols' FFT-periods arrive at the ideal time-instants.

Channel variability and mobility

In these paragraphs, the speed and character of the time-variability of the channel are briefly analyzed. Assuming the maximum speed in an indoor environment to be $v_m \cong 2$ m/s, the maximum Doppler frequency is $f_m = v_m/\lambda = 400$ Hz at 60 GHz. Defining the coherence time $(\Delta t)_c$ as the time-separation for which the spaced-time correlation function of the channel $\phi_H(\Delta t) = 0.9$, we obtain for the above f_m and Jakes' fading model [2] $(\Delta t)_c = 0.25$ ms (see eq. (4-31) in Section 4.3.1 for $K = 0$). For the above defined OFDM system, 0.25 ms are equal to ~ 200 (mode II: ~ 100) OFDM Symbols or approximately 3 frames, during which the channel is almost constant.

Alternatively, the suitability of the proposed frame duration can be evaluated based on the sampling theorem. In order to use the training sequence transmitted in the beginning of each frame for estimating the channel, the Nyquist criterion has to be fulfilled. To track the variations of a channel with maximum Doppler frequency f_m , the channel's transfer function has to be sampled at time-instants separated by at most

¹⁵ A doubled data rate on the signaling channels in mode II can be useful, because mode II may operate in bigger environments with higher numbers of potential users. Thus, a higher signaling data rate might increase the total throughput.

$\Delta t_{pilot} < 1/(2f_m)$. This yields $\Delta t_{pilot} < 1.25$ ms for $f_m = 400$ Hz. Thus the frame duration of ~ 90 μ s guarantees sufficient oversampling of the channel estimates. We anticipate that the proposed OFDM system is suitable for such slowly time-variant radio channels, but not for (much) faster mobility. Performance results for the air-interface over time-variant channels are given in Section 6.5 of this thesis.

5.2.1.3 OFDM Symbol Configuration

Sub-bands and OFDM sub-symbols

Figure 5-2 shows the OFDM symbol configurations in modes I and II. Several zero-carriers are introduced. The zeros at $f_{c,0} + \{-24, 0, +24\}$ MHz are used to separate the four quarter rate sub-bands, where $f_{c,0}$ is the center frequency of the full-rate OFDM channel.

The zero at $f_{c,0}$ is also required to avoid problems with carrier feed-through and AD/DA converter offsets, as explained in Section 4.2.2.3. For the same reason, zero-carriers are used at the center frequencies of the quarter rate channels, which are located at $f_{c,0} + \{-36, -12, 12, 36\}$ MHz.

In mode II, the number of (data and pilot) sub-carriers is doubled. Three zero sub-carriers are separating the OFDM sub-bands in order to keep the sub-band center frequencies at fixed positions. These extended guard-bands may be of benefit to avoid inter-sub-band-interference, because the requirements on carrier stability are higher in mode II. Alternatively, two of the zero sub-carriers may be used as additional pilots.

Discussion of pilot assignment and purpose of pilots

The pilots present in the system cannot be used for channel estimation, because their frequency spacing is too large. In stead, they are used for synchronization purposes and for coherent demodulation as follows. On the down-link and up-link, the pilots are needed for the estimation of carrier phase-offsets due to residual carrier frequency-errors, which lead to a common phase rotation of all sub-carrier constellation values (see Section 4.2.4.2). On the up-link, they are also used for the tracking of up-link time-delays, which cause a progressive phase rotation of the sub-carriers (see Section 4.2.4.1).

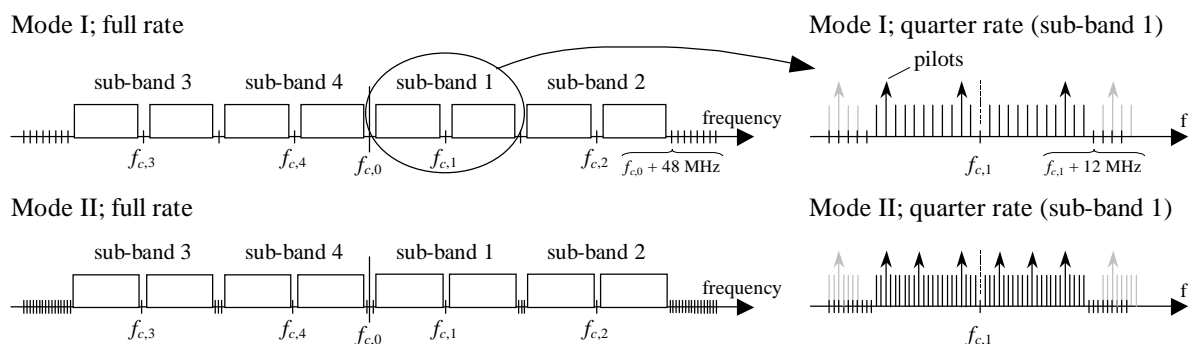


Figure 5-2: OFDM symbol configurations in the different operation modes

Those delays must be known very accurately, when coherent demodulation is applied.

On the one hand, pilots should be distributed evenly across the signal bandwidth in order to exploit frequency diversity when some of them are in deep fades. On the other hand, a constant spacing between adjacent pilots can be problematic in a multipath channel with two main paths. For a two-path channel with relative delay time τ_δ , the channel transfer function has minima separated by $1/\tau_\delta$. Thus, if the pilot spacing $\Delta f_{pilot} = 1/\tau_\delta$, all pilots might be in a deep fade at the same time. A short calculation is given to show that the latter problem can probably be neglected in the system under investigation.

Distributing the number of pilots proposed for the system evenly across the signal bandwidth leads to a constant spacing of 8 and 4 MHz among adjacent pilots, in modes I and II, respectively. Such a Δf_{pilot} corresponds to a τ_δ of 125 and 250 ns, respectively, or equivalently, to path-length differences of 37.5 and 75 m. Due to the very limited sizes of the radio cells in the proposed system and due to the low transmission powers, it is rather unlikely that rays with such large path-length difference can significantly interfere with each other. Therefore, a constant pilot spacing can be used, which also simplifies the algorithm for extracting the up-link timing-offset (see Section 7.5.2).

A pilot assignment with a non-uniform spacing is presented in Section 5.2.4.

Spectral shape

The spectral shape of the proposed OFDM operation modes is shown in Figure 5-3, assuming a perfect power amplifier. That means, out-of-band radiation because of non-linear distortion of the signal in non-linear amplifiers is not included. Note that the

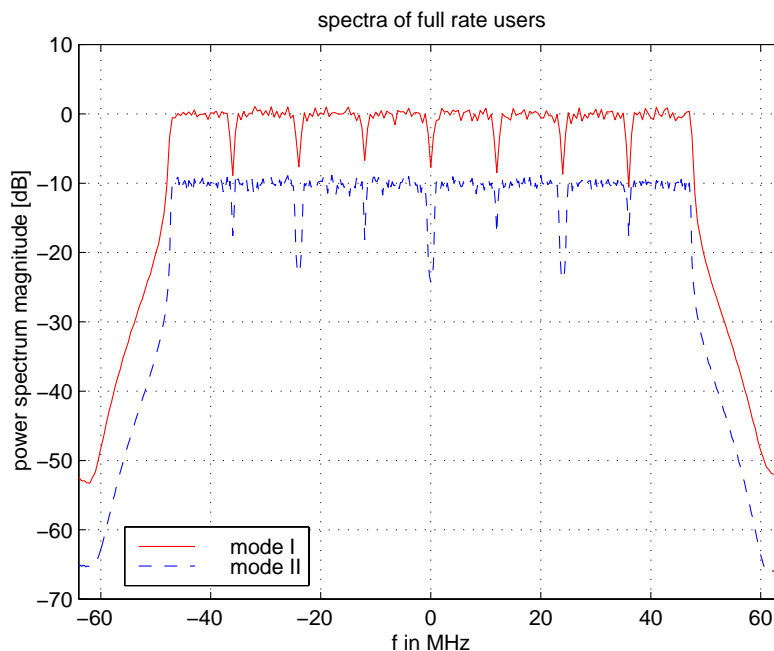


Figure 5-3: Spectra of the OFDM signals in different operation modes. Null-carriers are used to separate the four sub-bands and to avoid data transmission at the DC-carrier(s).

spectra of mode II are shifted by -10 dB in that figure. It is seen that the spectral shape is very similar for modes I and II. The steep decay at the band edges is due to the time-domain windowing applied (see Figure 4-2, Section 4.2.2.2). The purpose of this type of windowing is the reduction of out-of-band radiation in order to allow a close spacing of adjacent frequency-bands (channels) used by the system in different radio cells. In the current system proposal, the length of the window is quite significant, being $\sim 10\%$ and $\sim 5\%$ of T_{FFT} for mode I and II, respectively. While such a long windowing interval can be seen as an extension of the guard interval, it also means a loss of effective transmission power, additional to the loss due to the guard interval. Considering a real system, filters are required for channel-selection, aliasing suppression (ADC), and signal reconstruction (DAC). The specifications of those filters can be slightly relaxed, due to the windowing.

5.2.1.4 Data Transmission Rates

Table 5-3 lists the data transmission rates that can be achieved in the different operation modes with various modulation and coding schemes and for full and quarter bandwidth terminals. It is a topic for further research, whether the proposed modulation and coding techniques are the ideal combinations.

The gross data rates listed in Table 5-3 are the numbers of data bits per OFDM symbol divided by the duration of an OFDM symbol. Thus, the overheads introduced for signaling (signaling channels and signaling overheads appended to ATM cells), synchro-

Table 5-3: Transmission rates using different modulation and coding techniques (LL: Very low speed; L: Low speed; H: High speed). Values in brackets are for mode II'.

<i>mode</i>	<i>band-width mode</i>	<i>modu-lation</i>	<i>coding rate</i>	<i>OFDM sym-bols per ATM cell</i>	<i>data bits / OFDM symbol</i>	<i>gross data rate in Mbit/s</i>	<i>ATM bit-rate in Mbit/s</i>
I-LL	full	QPSK	$\frac{1}{2}$	6	76	59.3	51.2
	quarter			24	19	14.8	12.8
I-L	full	QPSK	$\frac{3}{4}$	4	114	89.0	76.7
	quarter			16	28.5	22.2	19.2
I-H	full	16-QAM	$\frac{3}{4}$	2	228	178.0	153.5
	quarter			8	57	44.5	38.4
II-LL	full	QPSK	$\frac{1}{2}$	3	152	59.3	47.7 (50.4)
	quarter			12	38	14.8	11.9 (12.6)
II-L	full	QPSK	$\frac{3}{4}$	2	228	89.0	71.6 (75.6)
	quarter			8	57	22.2	17.9 (18.9)
II-H	full	16-QAM	$\frac{3}{4}$	1	456	178.0	143.1 (151.3)
	quarter			4	114	44.5	35.8 (37.8)

Table 5-4: Summary of all overheads required for wireless access and ATM. The ‘total’ values are relative to the gross data rate, i.e., the data rate including coding.

<i>description</i>	<i>mode I</i>	<i>mode II</i>	<i>mode II'</i>
TDD guard symbols	2.8 %	5.4 %	2.8 %
synchronization training sequence	1.4 %	2.7 %	2.8 %
signaling in signaling channels	2.8 %	5.4 %	2.8 %
total overhead per frame	7.2 %	13.5 %	8.6 %
signaling appended to ATM cells (4/57 bytes)	7 %	7 %	7 %
total overhead for wireless access	13.7 %	19.6 %	15.0 %
overhead of ATM headers (5/53 bytes)	9.4 %	9.4 %	9.4 %
total overhead relative to gross data rate	21.9 %	27.2 %	23 %

nization, and time division duplexing have not been subtracted. Pilots are excluded. The sub-modes -H, -L and -LL use different modulation and FEC-techniques, namely, QPSK and 16-QAM modulation with rate $\frac{1}{2}$ - and rate $\frac{3}{4}$ -coding, as seen from the table.

Depending on the modulation and coding scheme, a varying number of OFDM symbols is required for the transmission of one ATM cell (see also Section 5.2.2). Each ATM cell consisting of 48 data bytes and 5 header bytes is augmented by 4 bytes for the signaling required by the MAC-protocol. I.e., a data entity comprises 456 information bits, which make 912 and 684 coded bits, respectively, with rate $\frac{1}{2}$ - and rate $\frac{3}{4}$ -coding. The amount of signaling information was estimated based on the work presented in [3].

The ATM bit-rates listed in the last column still include the overhead of the ATM headers, but none of the overheads introduced for the wireless access. Defining the gross data rate as 100 %, the overheads are summarized in Table 5-4.

5.2.2 Up- and Down-link Multiple Access Scheme

This section gives an overview of the above-introduced frame structure and OFDM symbol configurations, which make up the multiple access scheme. TDMA and FDMA components are combined, as indicated in Figure 5-4. TDD is proposed as a duplexing scheme. A fixed frame structure of 69 (in mode I; mode II: 37) OFDM symbols results, with a flexible boundary between the up- and the down-link. The FDMA component (sub-bands) is suggested in order to simultaneously allow mobile terminals that are using only one quarter of the full system bandwidth – the quarter-rate users. The BS operates in mode I or II, depending on the present environment (see Section 5.2.1.1).

In the beginning of each frame, a training symbol (TS) (a unique OFDM symbol) is broadcast on the down-link, which is used for time- and frequency synchronization

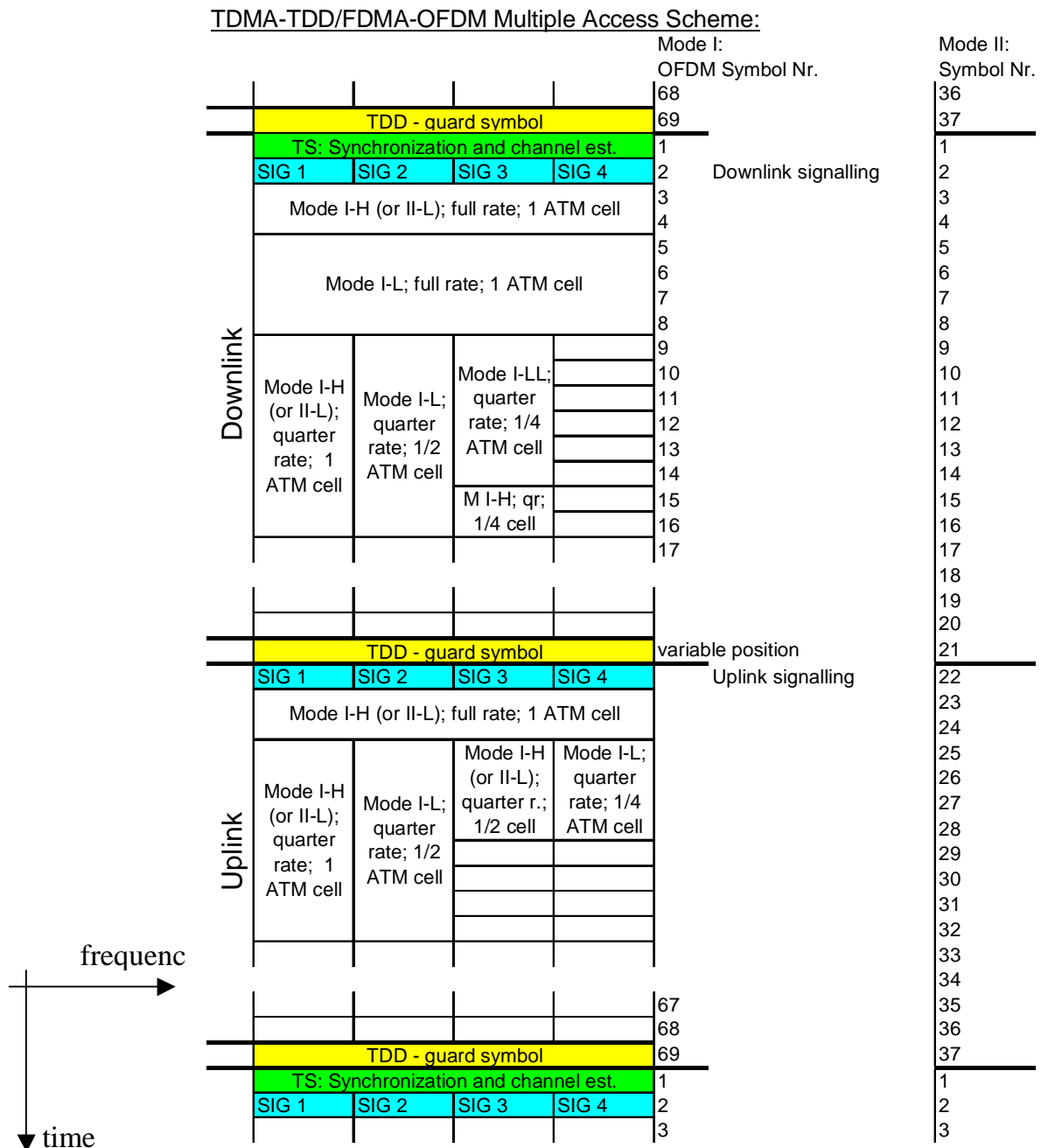


Figure 5-4: The proposed TDMA-TDD/FDMA-OFDM multiple access scheme. Each row represents one OFDM symbol, which is divided into four sub-bands. Note: Frequency hopping is not shown.

and for channel estimation (see Chapter 6). The TS is followed by four parallel signaling channels, each in a separate OFDM sub-band. To ensure highest possible reliability, BPSK modulation and rate 1/2-coding is used for all signaling (see Table 5-2).

The consecutive symbols carry the user data on the down-link. The sub-modes -H, -L and -LL use different modulation and FEC-techniques, namely, QPSK and 16-QAM modulation, with rate 1/2- and rate 3/4-coding. Depending on the modulation and coding schemes, a varying number of OFDM symbols is required for the transmission of one

ATM cell (see Table 5-3). To efficiently map ATM cells on this fixed frame structure, it is considered to allow the transmission of half or quarter ATM cells per frame as well.

On the up-link, another four dedicated signaling channels are available. No training symbols are used there to maximize the spectral efficiency. In stead, the application of pre-equalization is suggested in order to facilitate coherent detection, which requires a reciprocal channel. This principle is discussed in detail in Chapter 7.

Super-frame structures should be defined to efficiently implement the mapping of ATM cells on the given frame-structure using the multiple access schemes described, using a centralized, scheduled MAC protocol.

5.2.3 Architecture of the Transceivers

5.2.3.1 Base Station (Access Point)

The architecture of the base-band system and RF front-end of the base station is rather simple. However, the MAC and control sub-layers have rather high complexity, since the data streams of multiple MTs have to be multiplexed in the BS, requiring ARQ, power control, signaling, and other functions. And they have to operate at very high speed. Using pilots and/or blind techniques, transmission delays and carrier phase offsets have to be estimated for each user (see Section 7.5.2).

A block diagram of the base-band and RF parts is given in Figure 5-5. Note that none of the required filter stages are shown for the sake of simplicity.

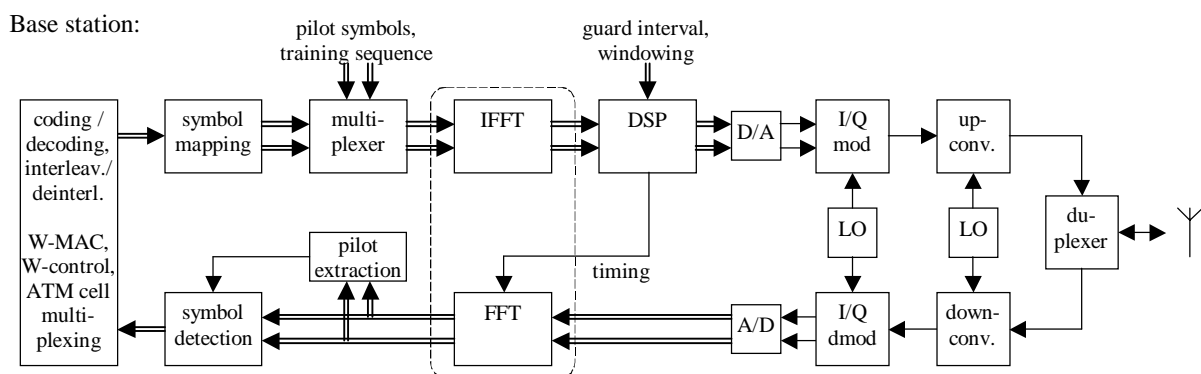


Figure 5-5: Architecture of the base-band system and RF front-end of the base stations.

5.2.3.2 Mobile Terminal

The base-band system of the mobile terminals has a somewhat higher complexity, because synchronization, channel estimation, and pre-equalization algorithms have to be implemented. The block diagram is depicted in Figure 5-6.

Note the hardware feedback signal for frequency-synchronization. Interesting simplifications of the synchronization tasks required (timing, frequency, sampling frequency)

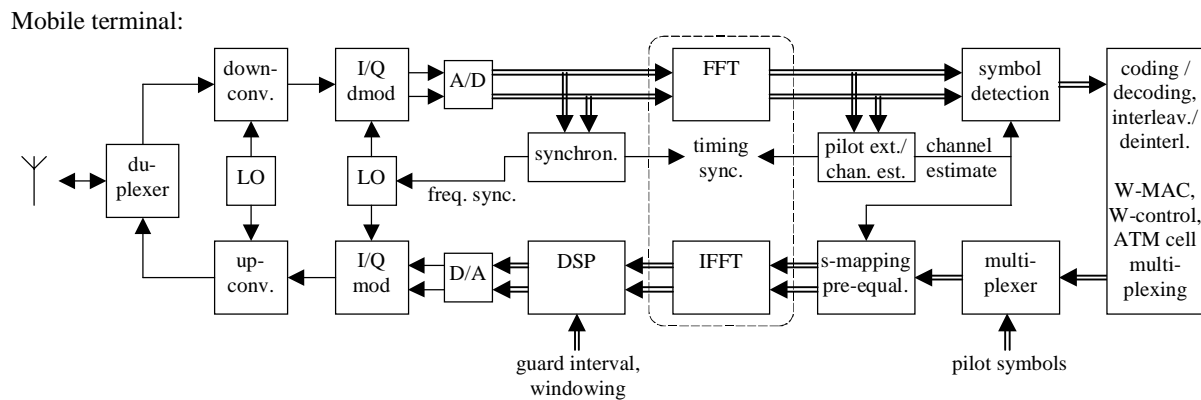


Figure 5-6: Architecture of the base-band system and RF front-end of the mobile terminals

can be achieved by locking all local oscillators (LO) and the sampling clocks on one adjustable frequency source. Thereby, synchronizing for one of the frequency-offsets in hardware (using the feedback signal), all other frequency-offsets are cancelled simultaneously, which simplifies the implementation of the proposed OFDM system. Note that this principle also requires the oscillators of the base station to be locked on one another to provide fixed ratios among their frequencies.

5.2.4 Forward Error Correction Coding

5.2.4.1 Forward Error Correction Coding

Standard convolutional coding schemes with soft decision Viterbi decoding can be applied. Possible parameters for the encoder and decoder are a coding rate of $\frac{1}{2}$ and a constraint length of 7. The rate $\frac{3}{4}$ coding used in modes -L and -H (see Table 5-3) can be derived from the rate $\frac{1}{2}$ code by puncturing.

Note that the same codes are used in the IEEE 802.11 and in the HIPERLAN/2 wireless LAN standards [1], [4]. This was the only reason for selecting these codes for our proposal. No research towards optimization of the coding scheme was performed. Error rate results for the coding and interleaving schemes are presented in Chapter 8.

5.2.4.2 Interleaving Schemes

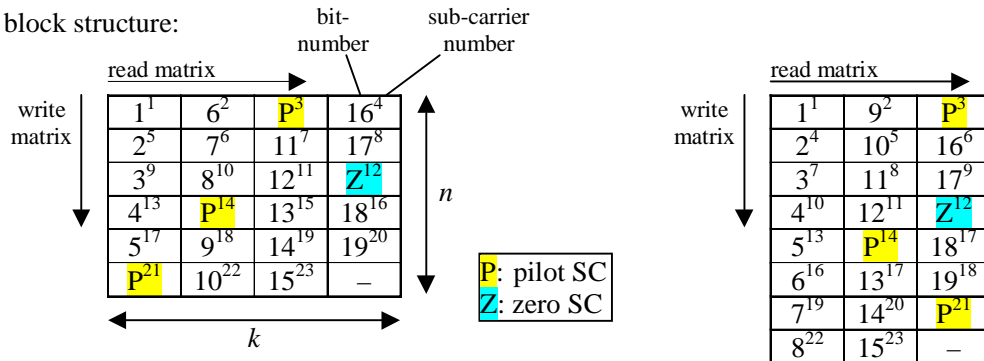
Bit-level interleaving is used to break-up burst errors into, ideally independent, well-distributed errors, which can be corrected more efficiently by conventional coding schemes. Because of the frequency-selective fading channel experienced by the OFDM system, errors usually result from the sub-carriers being attenuated by the channel. This often results in burst errors – the application of an interleaver is thus necessary.

Block interleavers are proposed for the investigated transmission system. The convolutionally encoded data bits to be transmitted are written column-wise into a rectangular array of k columns and n rows, where k denotes the degree (or depth) of the inter-

Interleaver 1 (degree $k = 4$):

interleaver 2 (degree $k = 3$):

block structure:



spreading of coded bits over sub-carriers (numbers indicate bit-numbers of coded bits):

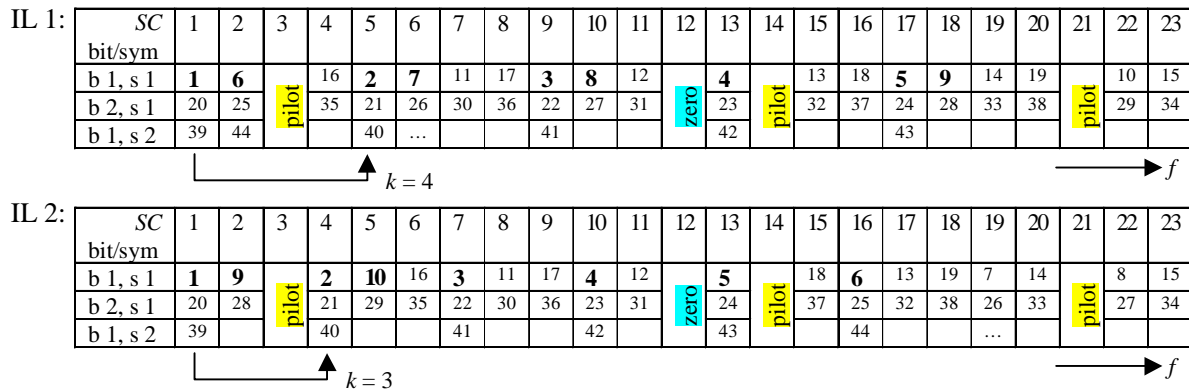
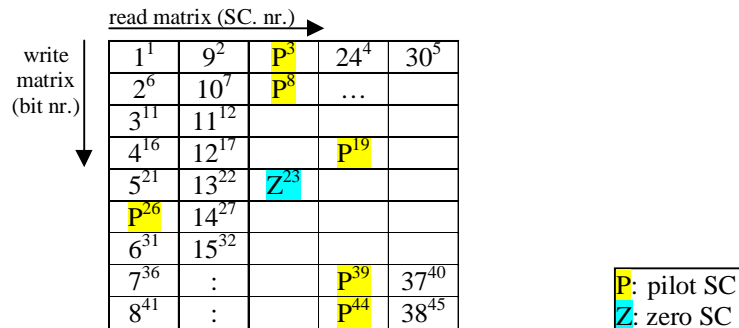


Figure 5-7: Interleaving schemes for transmission mode I-LL, quarter rate.

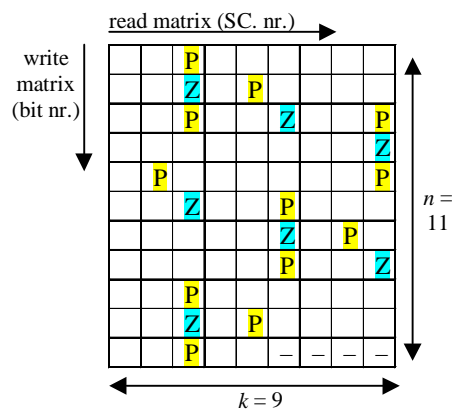
leaver. The bits to be modulated on the OFDM sub-carriers are read from this array row-wise. Two consecutive bits of the coded sequence are therefore separated by k sub-carriers in an OFDM symbol. Note that only one bit of the QPSK or 16-QAM constellations is defined at a time, because the whole symbol undergoes the same fading, implying that all its bits have the same error probability. Thus defining a whole data symbol (sub-carrier) at once would counteract the goal of breaking up error bursts.

Not only the two or four bits transmitted (in one QPSK or 16-QAM symbol) over one sub-carrier undergo the same fading, but, because we consider slow time variability of the channel, sub-carriers of consecutive OFDM symbols are also affected in the same way. Therefore, the interleaving must be done in the frequency-domain, i.e., across the sub-carriers of the OFDM symbols. The block-size of the interleaver is determined by the number of sub-carriers of the OFDM scheme. Error correction coding is done over a whole ATM cell, which is carried by a number of OFDM symbols as indicated in Table 5-3. This requires that the bits are periodically written into the interleaving matrix and read from it in order to be modulated on different bits of the (QPSK or 16-QAM) data constellations and on consecutive OFDM symbols. For instance, in transmission mode I-LL quarter rate, 24 OFDM symbols are required to transmit the 912

interleaver for mode II, quarter rate:



interleaver for mode I, full rate:



interleaver for mode II, full rate:

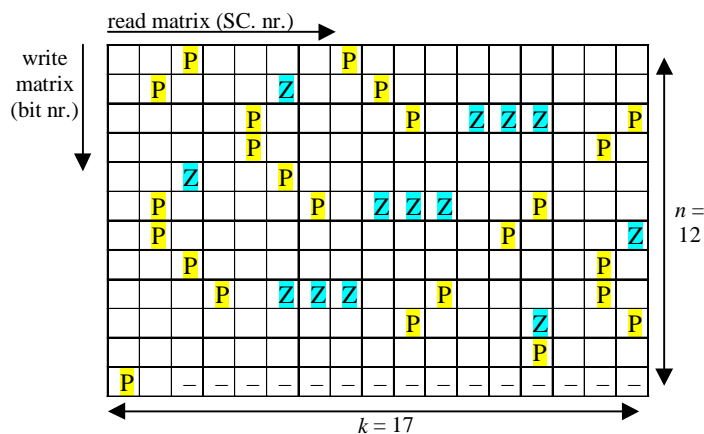


Figure 5-8: Interleaving schemes for transmission modes I; full rate, and II; full and quarter rate.

bits of one whole, rate-1/2 coded ATM cell.

Time-interleaving is not considered in order to minimize throughput delays and memory buffers. However, when frequency hopping is implemented in the quarter rate mode, time-interleaving over all OFDM symbols on which an ATM cell is mapped should be added in order to distribute the coded bits more evenly over the frequency-band.

For the quarter rate option of transmission mode I (using QPSK and rate-1/2 coding), two possible interleaving schemes are depicted in Figure 5-7. One of degree 4 (interleaver (IL) 1), the other one of degree 3 (IL 2). Next to the rectangular block-interleaving matrix, the translation of coded bits to sub-carriers and OFDM symbols is illustrated. Pilot and zero sub-carriers are included in the interleaving scheme, so that, using IL 2, subsequent coded bits are modulated alternately on odd and even sub-carriers. (To obtain this, the degree of the interleaver must be odd.) This property is desirable with the transmitter diversity schemes presented in Section 8.3.

For the other transmission modes, possible interleaver structures and pilot/zero carrier assignments are depicted in Figure 5-8. For mode II quarter rate (-qr), mode I full rate

(-fr), and mode II-fr, interleavers of depth 5, 9, and 17, respectively, are suggested. Obviously, adjacent coded bits are spread more in the full rate modes, thus we expect better performance from these schemes. Theoretical and simulation results are given in Section 8.2. To improve the performance of the quarter rate modes, it is suggested to implement frequency hopping across the four quarter-rate sub-bands or antenna diversity techniques. Some proposals for computationally efficient diversity schemes are described in Section 8.3.

5.2.5 Link Budget

A link budget for the 60 GHz frequency band is given in Table 5-5, assuming that 50 mW transmit power are available. Full and quarter rate terminals are considered in the table. Figures in *Italics* identify parameter values used in calculations, when parameter ranges are specified.

It is evident from the table that this link budget is rather critical. No fading margins are considered for the shadowing, for instance, and a path loss exponent of two was assumed. Several investigations have shown that shadowing is a very critical problem in 60 GHz communications. The leaves of a tree, for example, or the user himself may completely block a 60 GHz link [5]. The conclusion is that a line of sight (LOS) is needed in most cases.

Note that a LOS reduces or eliminates shadowing. And it results in fading distributions with higher Ricean K-factors, which means that the fades are shallow compared with Rayleigh fading channels. Both effects do allow for operation lower average SNR. A loss of the LOS most likely results in dropouts, however.

Multiple transmit/receive antennas within a room could counteract this problem, just like multiple light sources are placed within a room to achieve a more uniform light distribution and to reduce shadows (see e.g. [6]). Radio-over-fiber links were suggested to connect the RF front-ends to the base station over considerable distances.

A slightly different (and somewhat more promising) situation is indicated by the channel measurements conducted by Smulders [7]. With and without LOS, Smulders reports values of normalized received power (transmission loss including the antenna gains) between -85 and -70 dB for rooms of different sizes, and for distances up to about 30 m. The path loss exponents observed are below one, due to the antenna design used (*cf.* Section 2.5). This would allow for a good coverage within the relatively large rooms investigated.

It is concluded that the system is feasible, however, only for limited ranges (maximum 30–100 m).

Table 5-5: Link budget at 60 GHz for full and quarter rate users

<i>parameter</i>	<i>quarter rate</i>	<i>full rate</i>	<i>comments</i>
bandwidth	~28 MHz	~100 MHz	spectrum down by -20 dB
carrier frequency	60 GHz		
FFT points	32 (64)	128 (256)	in TX mode I (II)
used sub-carriers	19 (38)	88 (176)	
Power budget:			
transmit power P_{tx}	17 dBm		i.e. 50 mW
TX power back-off	6 – 10 dB		Because of signal dynamics
HPA power	23 – 27 dBm		TX power plus back-off
antenna gains $g_{tx,rx}$	3 – 6 dB		omnidirectional antennas
free space prop. loss a_p at distance d	88, 98, 108 dB at 10, 30, 100 m		calculated as $20\log(4\pi d/\lambda)$ at 60 GHz ($\lambda = 5$ mm)
other losses a_{tx}	~2 dB		connectors, cables, etc.
received power P_{rx}	-67, -77, -87 dBm at 10, 30, 100 m		$P_{tx} + g_{tx} + g_{rx} - a_{tx} - a_p$
Noise budget:			
noise bandwidth B_N	22.5 MHz	90 MHz	88 (176) sub-carriers of 1 (0.5) MHz
noise figure F	5 dB		assumed value
equiv. noise temp. T	627 K		$T = (F - 1)T_0$
noise density N_0	-170 dBm/Hz		$N_0 = T \cdot k$
noise power P_N	-97 dBm	-91 dBm	$P_N = N_0 B_N$
SNR	30, 20, 10 dB	24, 14, 4 dB	P_{rx}/P_N (at 10, 30, 100 m)
Requirement:			
frame error rate	max. 10^{-2}		with $R_c = 1/2$, $v = 5$ coding, QPSK modulation; in Rayleigh fading channels (see Chapter 8)
required E_b/N_0	min. 12 dB		
required E_c/N_0	min. 9 dB		
guard interval a_{GI}	1 dB		
implementation loss a_{imp}	3 – 5 dB		phase noise, non-linearity, channel estim., etc. (estimated)
required SNR	approx. 15 dB		$E_c/N_0 - a_{GI} - a_{imp}$

5.3 The Emulation System

A main topic of this Ph.D. thesis is the development of digital signal processing (DSP) algorithms for OFDM-based wide-band air-interfaces. The final goal of this research and development effort is the demonstration of the proposed air-interface techniques on a realistic hardware platform.

OFDM air-interface emulator:

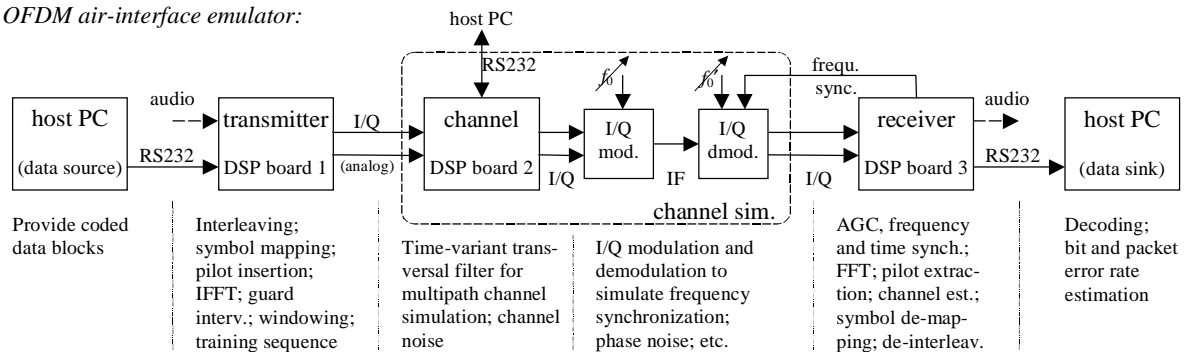


Figure 5-9: Architecture of the emulation system.

Unfortunately, the technical specifications of the investigated systems are so demanding that an implementation is almost impossible for a small research team, as real-time DSP of two data streams (the in-phase and quadrature (I/Q) components of the complex base-band signal) is required at sampling frequencies of ~ 100 MHz.

A drastically downscaled hardware platform is therefore presented (Figure 5-9) that enables the assessment of real-time DSP for such applications at low cost. Moreover, (software) implementation difficulties are largely avoided due to the reduced speed. The transmitter and receiver are each implemented on separate audio frequency (sam-

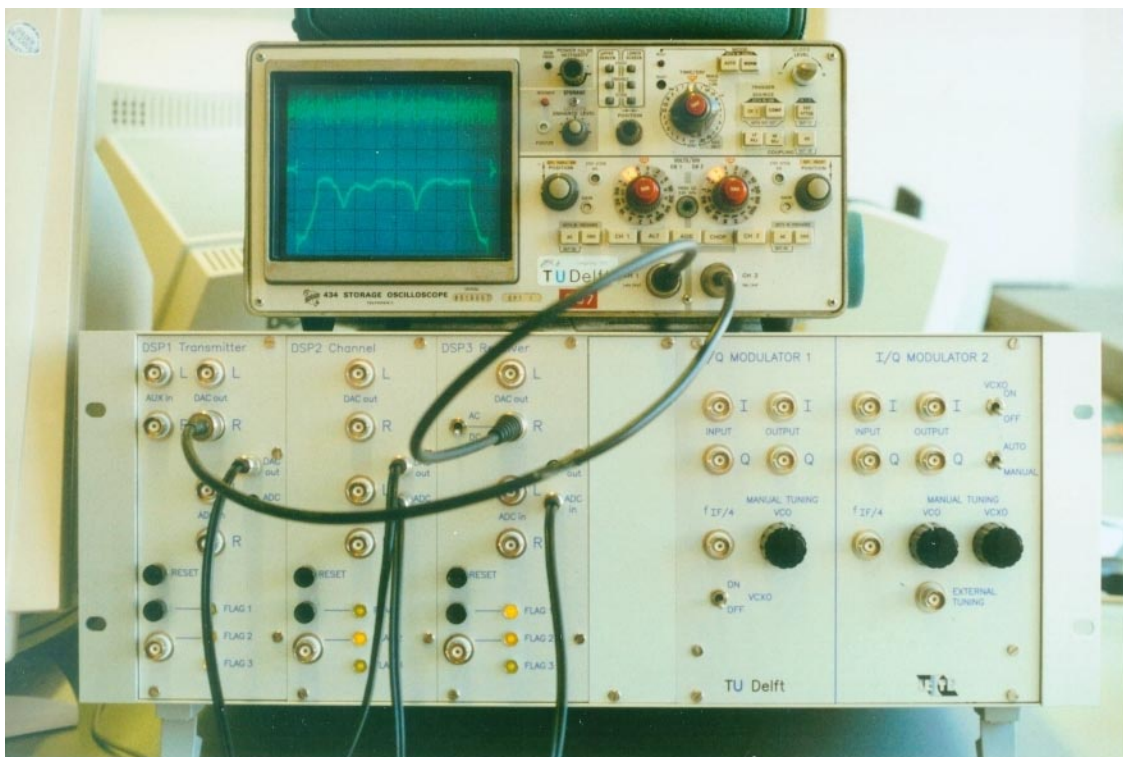


Figure 5-10: Photo of the emulation system. The oscilloscope shows the time-domain OFDM signal and its spectrum with a simulated channel. Note that the spectrum is calculated in real-time by the receiver-DSP (DSP board 3). The Korea-Telecom (KT)-version is depicted.

pling at 48 kHz) DSP boards. A third DSP board is used for simulating the multipath-fading channel, which would behave very differently at the largely reduced bandwidth. Finally, I/Q-modulation and -demodulation are emulated in analog hardware, for the realistic evaluation of frequency synchronization algorithms, a main issue in OFDM. A hardware feedback signal enables the tuning of the demodulator's local oscillator, to achieve frequency-synchronization. DSP software development was partly performed in the framework of student projects [8]–[11].

In this section, the hardware set-up of the emulation system is presented, which has been integrated in a 19" rack, as depicted in Figure 5-10. (Note that two copies of the emulation system have been built. One copy (the "KT-version") has been delivered to Korea Telecom, while the second one (the "TUD-version") is at Delft University of Technology.)

The main components of the emulator and their key specifications are described in Section 5.3.1. Some relevant measurement results on the hardware characteristics of the system are presented in Section 5.3.2. The linearity of amplifiers and other components in the signal path, the phase noise of mixer-oscillators, and filter characteristics are of major importance for OFDM systems. Finally, the signal processing for the time-variant channel simulator is outlined in Section 5.3.3.

5.3.1 Description of the Emulation System

5.3.1.1 Hardware Architecture

The basic architecture of the emulation system for the evaluation of simplex air-interfaces is shown in Figure 5-9. This figure also indicates the functionality implemented on the different hardware sub-systems.

The DSP platforms used are SHARC EZ-KIT Lite evaluation kits with the Analog Devices ADSP-21061 floating-point processor [12], which is a 32-bit DSP with 1 Mbit of internal RAM, running at 40 MHz. The boards are connected to a Windows based PC, which is used for software development and for program control at the time of execution. Development tools and an extensive documentation library are provided with the DSP boards. The tools include C-language and assembler compilers and applications for downloading and uploading programs and data from the DSP.

The ADSP evaluation boards contain 16-bit stereo analogue input and output ports with a maximum sampling frequency of 48 kHz. Further specifications of the DSP boards are given in Table 5-6.

Two MAXIM MAX2450 Evaluation kits are used for I/Q-modulation and -demodulation. Each of these boards contains an I/Q-modulator, an I/Q-demodulator, and a voltage controlled oscillator (VCO). The intermediate frequency (IF) is approx. 70 MHz. Crystal oscillators (XO) have been integrated for stabilizing the drifting VCOs of the MAXIM boards, and for reducing phase noise. The XOs are based on 16.934 MHz

Table 5-6: Main specifications of the DSP boards

<i>Parameter</i>	<i>Value</i>
CPU clock rate	40 MHz
Maximum sampling frequency f_s	48 kHz
DAC/ADC channels	2 + 2 (stereo, used for I/Q)
Full-scale input voltage	2.8 V _{pp}
Full-scale output voltage	2 V _{pp}
Pass-band of ADCs and DACs	0.4 f_s
Pass-band ripple	± 0.1 dB
Stop-band	0.6 f_s
Stop-band rejection	74 dB
DC offset (max.)	± 55 LSB

crystals driven by standard 74HCU04 CMOS inverters. (We note that 18 MHz crystals were used in the TUD-version of the emulation system.) The VCOs on the MAXIM boards, operating at twice the IF-frequency, are injection locked on the eighth harmonic of the XOs.

The XO of modulator 2 can be voltage controlled (VCXO) in order to allow the evaluation of frequency-synchronization algorithms. A control voltage is generated by DSP 3 – the “receiver” (see Figure 5-9) – via the mechanism outlined in the following paragraph. A block diagram of the I/Q-modulator and -demodulator boards is shown in

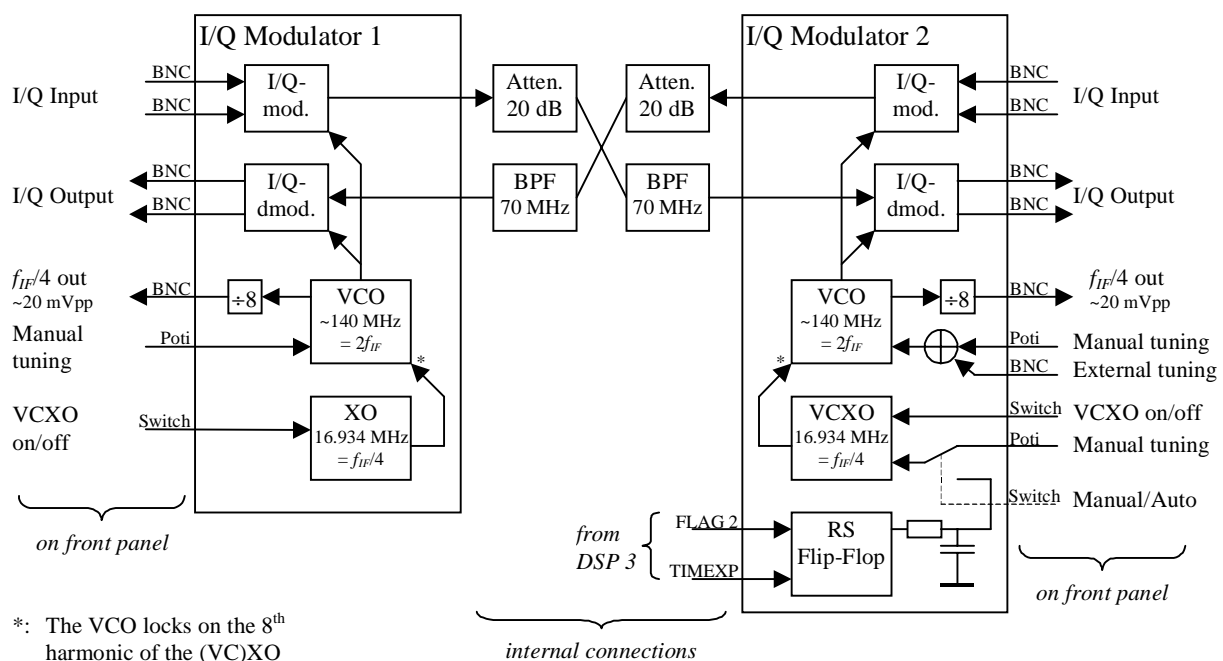


Figure 5-11: Block diagram of the internal and external wiring of the I/Q-modulator and -demodulator boards. (KT-version)

Table 5-7: Key specifications of the I/Q-modulators and -demodulators

<i>Parameter</i>	<i>Value</i>	
	<i>KT-version</i>	<i>TUD-version</i>
intermediate frequency f_{IF}	~65–80 MHz	
intermediate frequency with (VC)XOs	67.74 MHz	72 MHz
(VC)XO frequency f_{XO}	16.934 MHz	18 MHz
VCXO tuning range	$f_{XO} \pm 282$ Hz	$f_{XO} \pm 198$ Hz
VCXO tuning sensitivity (at f_{XO})	~0.7 Hz/LSB = ~230 Hz/V	~0.48 Hz/LSB = ~160 Hz/V
max. input voltage swing	1.35 V _{pp}	
max. output voltage swing	1.35 V _{pp}	
base-band attenuation input → output	~3.5 dB	
modulator input bandwidth (max.)	15 MHz (~20 kHz used)	
demodulator output bandwidth (max.)	9 MHz (~20 kHz used)	

Figure 5-11. Specifications are given in Table 5-7.

Generation of the Feedback Signal for Frequency Synchronization

DSP 3 can control the VCXO of the I/Q-demodulator by generating a pulse duration modulated (PDM) signal. For this purpose, the DSP's output pins 'FLAG 2' and 'TIMEXP' are connected to an RS-flip-flop. Periodically, e.g. at the beginning of the interrupt service routine used for acquiring the analog input samples, a short pulse is generated on FLAG 2 for setting this flip-flop. At the same time, the DSP's timer is initialized with a variable value corresponding to the desired tuning voltage (a value between 0 and 833 at 48 kHz sampling frequency). The timer now counts down from that value at the CPU clock rate, causing a short pulse on 'TIMEXP' when zero is reached. This pulse is used for re-setting the flip-flop. The outlined procedure generates a rectangular signal with a frequency equal to the sampling frequency, and with a duty cycle between 0 and 100 %. A low-pass filter converts this signal to the VCXO control voltage in the range of 2.5–5 V. Note that the CPU is not occupied by this task, except for setting FLAG 2 and writing the tuning value to a register.

5.3.1.2 Pros and Cons of the Emulation System

Advantages of the proposed emulation system compared to pure computer simulation are primarily due to the independence of the transmitter's and receiver's hardware. This introduces arbitrary (fractional) sampling instant offsets and carrier (and sampling) frequency offsets, just like in a real system. It is rather cumbersome to include such effects in e.g. a MATLAB simulation. Moreover, the assessment of real-time algorithms is possible, however, at the price of more complex software development. A pro and con for the emulator is that generally all system components must be present

in order to allow operation, which makes it more difficult to evaluate system parts independently but allows for overall assessment. Certain blocks are easily removed, as for instance the I/Q-(de)modulation hardware, or the channel simulator.

Compared with a real-time (demonstration) system, software development is drastically simplified because of the low sampling frequency used. So far no serious timing problems were encountered in the real-time software written for the emulator. Drawbacks are that the specifications of the analog-to-digital converters (ADC) and digital-to-analog converters (DAC) (bit resolution, filter characteristics, etc.) are superior to ADCs and DACs available for real wide-band systems (with sampling frequencies above 100 MHz). The same applies for filter stages and amplifiers present in the analog front-ends. Therefore, the impact of these system components is not emulated realistically. Some of those effects can be modeled on the DSPs, however, if their influence is of interest. It is impossible as well to demonstrate the investigated transmission scheme over real wide-band radio channels.

Finally, the system can be useful in the education of electrical engineers, e.g. for demonstrating modulation techniques. It can be also used in M.Sc. graduation projects, but the time to get familiar with the system and the skills required for handling real-time DSP must not be underestimated by the supervisor.

5.3.1.3 Demonstration of the Time-Division Duplex Scheme

The time-division duplex (TDD) scheme can be emulated by applying the alternating down- and up-link signals to the same channel simulator, as depicted in Figure 5-12. The two transmitted signals are added up before feeding them into the channel, just like they are added up on the (linear) radio channel in the real system. Note that during the transmission time of one of the transceivers, the other one is receiving and not generating (transmitting) a signal on its own. Therefore, the adder shown in the figure rather acts as a multiplexer. The AUX 1 (auxiliary) input of the codec of DSP board 1 is used to add the mobile's transmitted signal. This input has a programmable attenuation/gain block for matching signal levels.

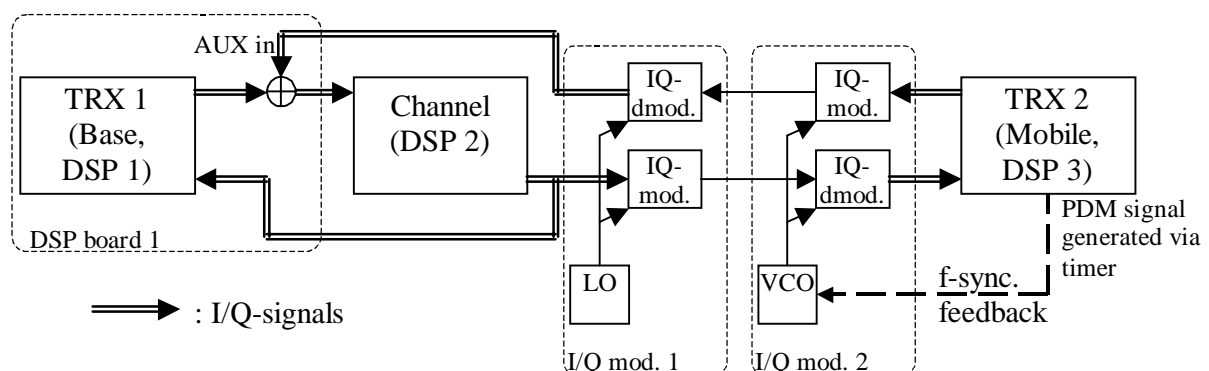


Figure 5-12: Architecture of the emulation system for evaluating the TDD techniques.

5.3.2 Hardware Characteristics

The main hardware issues in OFDM transmission systems are the linearity of amplifiers, mixers, and filters, the characteristics of ADCs, DACs, and the phase noise of oscillators used for up- and down-conversion of signals and for I/Q-modulation and -demodulation. Some of these topics are briefly addressed in this section.

5.3.2.1 Linearity and Intermodulation

For testing the possible impact of the emulator's hardware, the following set-up is suggested (see Figure 5-13). DSP-board 1 is used to generate a two-tone complex exponential signal. This signal is I/Q-modulated and -demodulated, using the I/Q-modulator and -demodulator of only one of the MAXIM boards, which are both connected to the same local oscillator (LO). There is thus no frequency offset introduced. Spectrum analysis of the demodulated I/Q-signals is performed using DSP board 3. (256 points FFT; 32 times averaging of the power spectrum estimates; no windowing.) FFT-windowing is not required here, because the generated tones are exactly put on frequency-instants of the analyzing FFT.

One of the observed spectra is depicted in Figure 5-14. Symmetrically to the two generated tones at 8.25 and 9.75 kHz, a mirror image is seen at about -32 dBc. By correcting for gain mismatch at the receiver it is possible to decrease these side-bands to about -55 dBc. The gain mismatch is mainly introduced by the I/Q-(de)modulator. This is confirmed by directly connecting the two DSP boards, where the mirror image lies at -47 dBc without mismatch correction. DC offsets are the source of the line seen at 0 Hz, -27 dBc. The other tones are intermodulation products from the mixers. Being at an excellent -55 dBc and more below the test tones, we conclude that the hardware is well suited for the implementation of an OFDM system, regarding linearity.

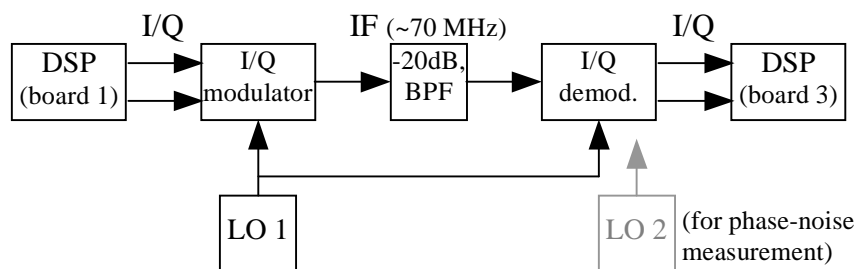


Figure 5-13: Test set-up for evaluating the non-linearity, harmonic distortions, and phase noise of the I/Q-modulator/demodulator board.

5.3.2.2 Phase Noise

Another critical parameter for OFDM modems is the phase noise performance of all mixer oscillators. Phase noise means that a spectral line, like an OFDM sub-carrier, undergoes some broadening (see Figure 5-15), resulting in inter-carrier-interference

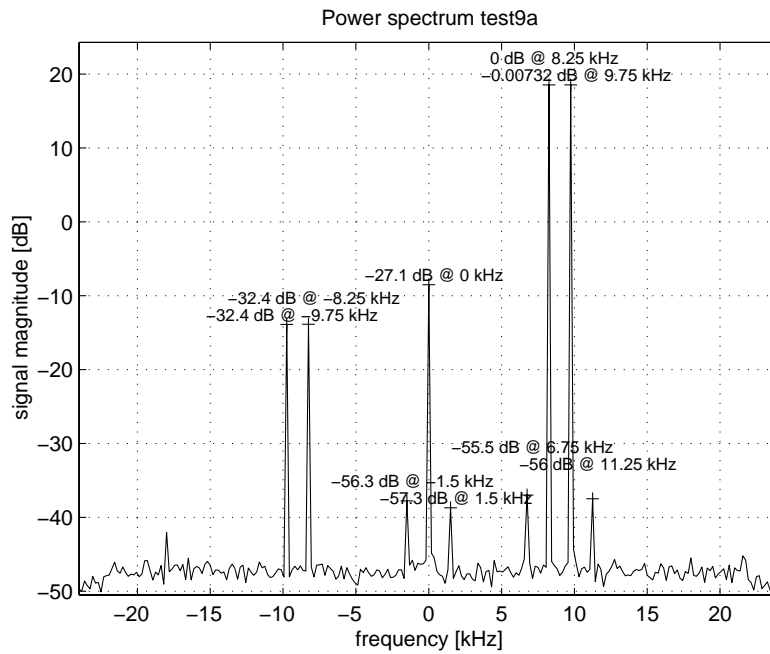


Figure 5-14: Observed spectrum at receiving DSP board. A two-tone signal was generated, IQ-modulated, and -demodulated.

(ICI).

As in the previous sub-section, this problem was assessed by spectral analysis on the demodulated I/Q-signals, using DSP board 3, where, this time, Blackman windowing was applied. The one-tone test signal was generated by DSP board 1, to be I/Q-modulated and -demodulated using different modulator boards with independent mixer os-

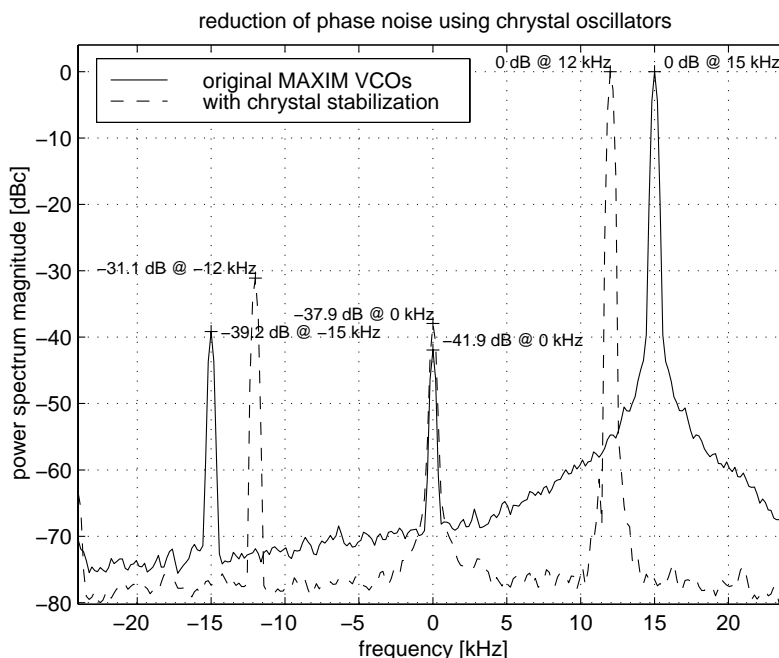


Figure 5-15: Broadening of a spectral line due to phase noise.

cillators. Two measurements are shown. The first one is for the original VCOs included on the MAXIM boards, where a 15 kHz test-signal was used. The noise floor rising towards this tone is caused by the phase noise. The two smaller tones, being again caused by DC-offsets and I/Q-mismatch, are not of interest for this test. A 50 Hz frequency modulation (interference from the mains) with a frequency deviation of ± 30 Hz was identified as one main component of the phase noise. Comparing these ± 30 Hz to the sub-carrier spacing of 375 Hz, it was decided to stabilize the VCOs using crystal oscillators, as mentioned above.

The second measurement, showing a test-tone at 12 kHz, includes these crystal oscillators. The noise floor observed in this case is due to the quantization noise of the ADCs and DACs, and due to other noise sources in the signal path, but not due to the phase-jitter of the local oscillators. Another major advantage of the crystal oscillators is their low frequency drift, which drastically simplifies the implementation of real-time synchronization algorithms.

Performance evaluations of OFDM system components and bit error rates are discussed in Chapters 6 and 7.

5.3.3 Implementation of the Channel Simulator

This section describes the implementation of the real-time, time-variant channel simulator for the emulation system.

The real-time channel simulator is based on a transversal filter (FIR-filter) whose coefficients are gradually changed in order to realize time-variability. The channel filter is written

$$r_k = \sum_{i=0}^{L-1} h_{IR,i,k} s_{(k-i)}, \quad (5-1)$$

where $\{s_k\}$ and $\{r_k\}$ are the input and output samples, respectively, and $\{h_{IR,i,k}\}$ are the tap weights at delay tap i and time index k . The number of taps is written L .

The FIR filter has complex-valued tap-weights and complex in- and outputs, since the emulation system operates with complex baseband (lowpass equivalent) signals. This requires four real multiplications and four additions/subtractions per FIR-tap. The whole filter is calculated on each (complex) input sample leading to a rather high computational load for the processor.

An $L = 30$ -tap FIR-filter is used in the channel simulator, requiring approximately 19 % of the processor's capacity at 48 kHz sampling frequency. Another 26 % of its processing power are required for generating a complex Gaussian noise sample (additive channel noise), scaling and adding it to the (filtered and scaled) signal, and for serving the interrupt service routine (ISR), in which all these tasks are performed. The coefficients of the FIR-filter are generated and updated in the main-loop of the DSP program, employing the remaining computational power.

5.3.3.1 Calculation of the Complex Tap-Weights

Power Delay Profile

The complex tap-weights of the FIR-filter are generated according to complex Gaussian random processes. They have means of zero, except at delay time zero, where a constant is added in order to enable the simulation of Ricean fading channels. The variances $\{\sigma_i^2 = \text{var}(h_{IR,i,k})\}$ of the Gaussian random variables (RV) is defined by an exponentially decaying, average power delay profile (PDP). They relate to the delay power spectrum (DPS) – which is the mathematical description of the frequency domain (FD) channel model proposed in Chapter 2 – as shown in the following derivation.

The parameters $\{\rho, \gamma, \Pi\}$ define the DPS for the case of an exponentially decaying channel response, written as

$$\phi_h(\tau) = \begin{cases} 0 & \tau < 0 \\ \rho^2 \delta(\tau) & \tau = 0, \\ \Pi e^{-\gamma\tau} & \tau > 0 \end{cases} \quad (5-2)$$

where τ is the excess delay-time variable. The relations of these parameters to the channel parameters (the normalized received power, RMS delay spread, and Ricean K-factor) can be found in Section 2.3.3.

Integration of the DPS over the delay bins corresponding to the sampling interval yields a good approximation for the desired variances $\{\sigma_i^2\}$ needed to implement the FD-model by means of a transversal filter. They are obtained as

$$\sigma_i^2 = \int_{\tau=(i-1/2)T_s}^{(i+1/2)T_s} \phi_h(\tau) d\tau = \Pi \int_{\tau=(i-1/2)T_s}^{(i+1/2)T_s} e^{-\gamma\tau} d\tau = \frac{\Pi}{\gamma} \begin{cases} [1 - e^{-\gamma T_s/2}] & i = 0 \\ [e^{-(i-1/2)\gamma T_s} - e^{-(i+1/2)\gamma T_s}] & i > 0 \end{cases} \quad (5-3)$$

where T_s is the spacing of the delay taps that is equal to the sampling period.

Time-Variant Channel Simulation

To simulate the time-variability, the complex FIR-coefficients need to be updated continuously. It was mentioned in the previous section that each coefficient of the FIR-filter can be considered as a sample of a complex Gaussian process with variance $\{\sigma_i^2\}$. Appropriate time-variability is yielded when the power spectrum of these complex Gaussian processes are shaped (colored) according to the Doppler spectrum of the radio channel to be simulated.

A very popular model of a Doppler spectrum is the U-shaped spectrum resulting from a uniform angular distribution of incident waves at a receiver moving with constant velocity. It is often called Jakes' fading spectrum [2]. A well known and efficient method of generating such colored Gaussian processes is based on Rice's sum of sinusoids [13]. The stochastic process is thereby approximated by a finite sum of appropri-

ately designed sinusoids with constant frequencies. A block diagram of such a model is found in [14]. Adapted to our application it is written

$$\begin{aligned} h_{IR,i,k} &= \sigma_i c_i \sum_{l=1}^{M_i} \left[\cos(2\pi f_{i,l,1} k T_s + \theta_{i,l,1}) + j \cos(2\pi f_{i,l,2} k T_s + \theta_{i,l,2}) \right] \quad i > 0 \\ h_{IR,0,k} &= \sigma_0 c_0 \sum_{l=1}^{M_0} \left[\cos(2\pi f_{0,l,1} k T_s + \theta_{0,l,1}) + j \cos(2\pi f_{0,l,2} k T_s + \theta_{0,l,2}) \right] + \rho e^{j(2\pi f_\rho + \theta_\rho)} \end{aligned}, \quad (5-4)$$

where c_i are normalizing constants in order to obtain variance of one from the sums of sinusoids, and M_i are the number of sinusoids added up at each delay tap. The sinusoids' parameters are their frequencies $\{f_{i,l,n}\}$ and their initial phases $\{\theta_{i,l,n}\}$, with i being the tap index, l being the index of the sinusoid, and $n = \{1,2\}$ standing for the real or imaginary component. f_ρ and θ_ρ are the frequency and initial phase of the LOS path, respectively.

Methods of finding parameters for the sinusoids are discussed in [14] and in the references therein. Also Jakes [2] describes a fading simulator based on this approach.

In our implementation, the taps are updated (one at a time) as quickly as the DSP can calculate the new sums-of-sinusoids for the current time-instant. $M_i = 10$ pairs of sinusoids are added up per delay tap. Updating one tap lasts for about 80 μ s; the whole IR (with 30 FIR-taps) is re-calculated within approx. 2.4 ms (rate of ~ 420 Hz), i.e. approximately 120 sample periods at 48 kHz. This is sufficiently frequent since the fading is rather slow compared to this time period. The maximum Doppler frequency of a typical indoor channel is 400 Hz (2 m/s movement) at 60 GHz, which scales down to only 0.15 Hz in the emulation system. Even a movement at 100 kph (28 m/s) can be easily realized, which corresponds to a maximum (downscaled) Doppler frequency of approx. 2 Hz.

Calculation of the Sinusoids' Parameters

A pure Monte Carlo approach was followed to determine the frequencies and initial phases of the summed sinusoids. No negative frequencies are considered for $\{f_{i,l,n}\}$, because the real- and imaginary sums-of-sinusoids are independently generated (see eq. (5-4)). Uniform random variables $\{\alpha_{i,l,n}\} \in [-\pi/2, \pi/2]$ describe the angles of arrival of the l -th path of the i -th delay tap. Applying these variables to $f_{i,l,n} = f_m \cos(\alpha_{i,l,n})$ yields appropriately distributed frequencies, where f_m is the maximum Doppler frequency. ($f_m = f_c v_m / c$, where f_c is the carrier frequency, v_m is the mobile's velocity, and c is the speed of light).

The initial phases of the sinusoids are selected from a uniform distribution between $-\pi$ and π .

5.4 Summary and Conclusions

In the first part of this chapter, a novel OFDM based air-interface and multiple access scheme are proposed for a wireless ATM communications system. Transmission rates up to 155 Mbit/s can be supported in slowly time-variant (indoor) channels at 60 GHz. The maximum cell radius is in the order of 30 m, under optimum conditions 100 m. A line-of-sight (LOS) to the base station is needed to obtain the maximum range, while more robust coding and modulation techniques have to be used, reducing the transmission rate.

A relatively low number of active carriers (88 in mode I) and a short FFT block-length (128) are selected in order to keep the complexity of the system low and to limit the carrier synchronization and peak-to-average power problems. Training symbols are periodically broadcast by the BS to allow the MTs to synchronize efficiently and accurately and to calculate a channel estimate. A flexible time division duplexing scheme is proposed to switch between the up- and the down-link, allowing for asymmetric data rates. Pre-equalization is utilized on the up-link to minimize the required overhead for training symbols. This enables the efficient transmission of short data packets (single ATM cells).

Several transmission modes, which apply different modulation and coding schemes, are suggested for different channel conditions, leading to various data rates. This adaptability also allows fall-back modes when shortcomings occur in the link budget. Currently, combinations of QPSK and 16-QAM modulation schemes and rate- $\frac{1}{2}$ and $\frac{3}{4}$ coding rates are considered. It remains to be evaluated, however, if the proposed combinations are the optimum ones. This is a topic for further research.

Another feature of the proposed system is the simultaneous support of two different terminal bandwidths (full bandwidth equal ~ 100 MHz and quarter bandwidth) by the BS through the use of a combined TDMA/FDMA-OFDM multiple access scheme. These so-called “quarter-rate” terminals have largely simplified hardware specifications.

The algorithm development of the main functions of the proposed air-interface is detailed in consecutive chapters of this thesis. The performance analysis of many aspects is given there. Purpose of these investigations is the evaluation of the suitability of the proposed techniques for the intended application, i.e., for wireless indoor LANs and for short-range, low-mobility outdoor systems.

The main design targets for the proposed OFDM air-interface were efficiency, simplicity, and flexibility in order to realize the extreme data rates considered. The main drawback of the proposed design is its limited range and the low data rate at long range. Methods for enhancing the performance and extending the range include:

- Diversity techniques
- Adaptive antennas for beam forming and/or multi-user detection

- Turbo coding
- Space-time coding

Note that some of these techniques have to be embedded in a system proposal (for instance coding schemes), while others can be implemented on top of an existing proposal/standard (e.g., beam forming and diversity techniques), although adaptations may be desirable.

The purpose of advanced techniques like multi-user detection is to enhance the system capacity by increasing the possible number of users and by mitigating interference effects from adjacent cells.

The strictly hierarchical structure of the proposed system, with base stations and synchronized terminals, may be a significant disadvantage in the implementation of concepts like ad-hoc networking. On the other hand, exactly this feature could make the system ideal for applications where multiple deterministic high-rate data streams have to be managed. A wireless TV-studio is a good example for such a scenario.

The second part of this chapter presents the hardware platform designed for the demonstration of the OFDM air-interface and its signal-processing algorithms. A largely downscaled DSP-based system, the so-called “emulator”, was built, where the OFDM transmitter and receiver are realized on separate DSP-boards. A third board is used for channel simulation. Analog hardware implements I/Q-modulation and -demodulation, leading to carrier frequency-offsets and enabling thereby the demonstration of real-time synchronization algorithms. System components are connected by analog (I/Q) baseband signals.

Main advantages of the emulator are its low hardware cost and the largely simplified software development compared with the real-system, due to the reduced speed. Sampling-instant and sampling- and carrier-frequency offsets are present between the transmitter and the receiver, which are hard to implement in a pure computer simulation. Moreover, the interaction of several system components is realistically modeled. Note that this may also be a disadvantage as it makes isolating the influence of a single effect more difficult.

The hardware behavior is similar to a real wide-band system, although the specifications of certain hardware components are superior in the emulation system, because of the reduced bandwidth of ~ 40 kHz (compared to ~ 100 MHz in the proposed OFDM system). It was concluded from brief studies of inter-modulation distortion, linearity, and phase noise, that the realized system is suitable for the demonstration of OFDM systems. This is confirmed by performance results given in Section 6.5.

5.5 References

- [1] R. van Nee and R. Prasad, *OFDM for Wireless Multimedia Communications*: Artech House, 2000.
- [2] W. C. Jakes Jr., *Microwave Mobile Communications*. New York: Wiley-Interscience, 1974.
- [3] D. Petras, A. Krämling, and A. Hettich, "Design Principles for a MAC Protocol of an ATM Air Interface," in Proc. *ACTS Mobile Communications Summit*, Granada, Spain, Nov. 1996, pp. 639–644.
- [4] R. van Nee, G. Awater, M. Morikura, H. Takanashi, M. Webster, and K. W. Halford, "New High-Rate Wireless LAN Standards," *IEEE Commun. Mag.*, pp. 82–88, Dec. 1999.
- [5] M. Flament, *On 60 GHz Wireless Communication Systems*. PhD Thesis, Chalmers Univ. of Techn., Göteborg, Sweden, 2000.
- [6] S. Okamura, M. Okada, and S. Komaki, "Impact of Ubiquitous Antennas to the Interference Cancellation of COFDM Systems," in Proc. *6th international OFDM-Workshop (InOWo) 2001*, Hamburg, Germany, Sept. 2001, pp. 2-1–2-4.
- [7] P. F. M. Smulders, *Broadband Wireless LANs: A Feasibility Study*. PhD Thesis, Eindhoven University of Technology, Eindhoven, The Netherlands, 1995.
- [8] P. Teneva, "Pseudo Real-time Simulation of an OFDM System for Wireless Broadband Communications: OFDM Transmitter," *Research Report*, IRCTR, Delft Univ. of Tech., Jan. 1999.
- [9] K. Büke, "DSP Manual," *Research Report*, IRCTR S-025-99, Delft Univ. of Techn., July 1999.
- [10] K. Büke, "Assessment of OFDM Based Air-interface Techniques Using an Emulation Platform: Investigation and Implementation of OFDM Synchronization Algorithms," *M.Sc. Thesis*, IRCTR S-001-00, Delft Univ. of Tech., Jan. 2000.
- [11] I. Gultekin, "DSP Software Implementation for a Broadband Air-interface Emulation Platform: Onderzoek naar de seriële interface tussen de PC en de DSP board en het maken van een GUI voor de DSP applicaties," *Graduation Thesis*, Haagse Hogeschool, June 2000 (in Dutch).
- [12] *ADSP-21061 EZ-KIT LiteTM Reference Manual*. Norwood, MA: Analog Devices Inc., 1997, <http://www.analog.com/support/dsp/documentation/Ezklrm.pdf>.
- [13] S. O. Rice, "Mathematical Analysis of Random Noise," *Bell Syst. Tech. J.*, vol. 23, pp. 282–332, July 1944; vol. 24, pp. 46–156, Jan. 1945.

- [14] M. Pätzold, U. Killat, F. Laue, and Y. Li, “On the statistical properties of deterministic simulation models for mobile fading channels,” *IEEE Trans. Veh. Technol.*, vol. 47, no. 1, pp. 254–269, Feb. 1998.

Chapter 6 – DSP Algorithm Development for the Down-Link

6.1 Introduction

The purpose of this chapter is to describe the key algorithms for down-link data transmission, which are required for the OFDM-based communications system proposed in Section 5.2.

Two main tasks have to be performed: synchronization and channel estimation. Synchronization steps include, respectively, timing and frequency synchronization. That is the correct start-time of the OFDM symbols has to be found in order to perform demodulation using the FFT, and the transmitter's and receiver's local-oscillator-frequencies have to be matched so that the sub-carriers' data symbols are obtained at the FFT's output. Estimation algorithms are proposed and evaluated for these synchronization tasks. Channel estimation is performed to determine the transfer function of the frequency-selective radio channel, which is required to equalize and detect the data symbols. Most of the techniques described are based on a special training symbol, which is periodically transmitted on the down-link (see Section 5.2).

In Section 6.2, we give an overview of the synchronization steps required, and we evaluate their performance for the proposed OFDM system. We also introduce signal-processing steps that must be utilized for coherently detecting the transmitted data. The general conclusion is that the investigated methods enable sufficiently accurate synchronization, with only one OFDM symbol used as a training symbol per frame. The overhead of this symbol is therefore well invested.

An additional synchronization step is applied for enhancing the initial timing-synchronization. With the training symbol proposed, the computational effort for this estimation step becomes extremely low, while its accuracy is very high. Novel work on this

estimation technique is presented in Appendix C of this thesis, where the estimation bias and the standard deviation are analyzed. The bias is derived for Ricean multipath channels (including Rayleigh and AWGN). It is given in terms of channel parameters, namely, the RMS delay spread and the Ricean K -factor. Moreover, the standard deviation is studied for AWGN and Rayleigh channels. The results allow for some optimization of the estimation technique.

For the final validation of the synchronization algorithms, OFDM modems have been implemented on a digital signal processor (DSP) based experimental platform, the so-called “emulation system” (see Section 5.3). The interaction of all synchronization tasks and the impact of remaining offsets on the bit-error-rate were demonstrated. It was observed from these results that a very popular class of algorithms for frequency-synchronization in OFDM systems suffers severely from DC-offsets and from carrier feed-through – hardware impairments that are hard to suppress. The work of Section 6.3 provides new insights into these issues. The influence of these factors is evaluated, leading to a novel, enhanced estimation method capable of eliminating most of the degradations.

Using the known training symbol, which has been utilized for synchronization purposes as well, channel estimation is a straightforward task. The channel transfer function is determined in the beginning of each frame by removing the known data from the received signal constellations. The obtained channel estimate is then employed to detect the data of the whole down-link frame. Therefore, a slowly time-variant channel has to be assumed, i.e., the channel should be quasi-static during the transmission of one frame.

In Section 6.4, we investigate if a short linear filter with fixed coefficients can reduce the mean-square-error of the channel estimate. The filter is to be applied in the frequency-domain in order to “smoothen” the estimated channel transfer function. Wiener filters designed for a given set of channel parameters are evaluated over a number of different environments. It is seen that a fixed filter designed for the “worst-case channel” can enhance the estimate on a quite wide range of channels. The gain achieved is reduced, however, in cases where the filter design does not match to the channel. Novel contributions in this section are the description of the channel estimation technique, which efficiently exploits the training symbol, and the selection of a fixed filter for a representative set of actual channels.

In Section 6.5, experimental performance results are presented, which were measured with the emulation system described in Section 5.3. The influence of the channel’s time-variability is seen from these results. Acceptable performance is achieved at velocities up to about 2 m/s are possible, which is appropriate for indoor environments. A simple linear extrapolation using the last two channel estimates is briefly assessed (using simulation results). It proves to enhance the maximum velocity allowed up to

about 8 m/s.

The sections are summarized separately with conclusions and recommendations.

6.2 Overview of Synchronization Steps

The synchronization scheme developed and analyzed is based on the work by Schmidl and Cox [1], with a number of modifications and extensions (see e.g. [2], [3]). According to the system proposal, the mobile terminals synchronize to a known training symbol (TS), which is continuously broadcast by the base station. One single training symbol is sufficient to perform full synchronization (and to calculate the channel estimate). Multiple training symbols can be used in low-SNR situations, in order to enhance the robustness.

Synchronization is acquired in the following steps:

- Frame and rough timing synchronization (from time-domain signal)
- Fractional frequency synchronization (from time-domain signal)
- Correction for the fractional frequency offset (mathematically)
- Application of the FFT to demodulate the TS
- Integer frequency-synchronization (based on the TS data)
- Remaining timing-offset synchronization (based on the phase rotation of the TS's data constellations)
- Estimation of and correction for sampling frequency-offsets (based on the above timing-offset estimates)
- Estimation of and correction for carrier phase offsets (based on pilot sub-carriers)

This section starts with a brief classification of synchronization algorithms and gives a number of references, which describe typical examples (Section 6.2.1). The description of the design of a training symbol is given in Section 6.2.2. We then outline in Sections 6.2.3–6.2.9 the synchronization steps and show performance results for the OFDM system under investigation (see Section 5.2). Although the proposed methods are studied in the framework of that system proposal, we'd like to emphasize that most of the principles can be applied much more generally.

6.2.1 Classification of Synchronization Techniques

Synchronization principles for OFDM can be characterized in several respects. Certain algorithms are suitable for initially acquiring coarse synchronization, while others can only track small errors in a system that has been roughly synchronized before. These classes are referred as *acquisition* and *tracking* algorithms, respectively.

Acquisition algorithms often work directly on the received, time-domain OFDM sig-

nal, exploiting its specific properties. For instance, the correlation between duplicated parts of this signal (the guard interval (GI) or a special training symbol) can be used for initial timing- and frequency-synchronization [1], [4], [5]. (The estimation steps of Sections 6.2.3 and 6.2.4 are in this class of algorithms.) Tracking algorithms typically exploit the systematic phase rotations of the data constellations, which are induced by synchronization offsets (*cf.* Section 4.2.4) [6]–[11]. This implies that these algorithms work on the output of the FFT, which requires that coarse synchronization has been acquired before, because otherwise the signal constellation points cannot be recovered. (Examples for such techniques are described in Sections 6.2.7 and 6.2.9.1.) *Pre-* and *post-FFT algorithms* can be distinguished.

Although most acquisition algorithms can be used in the tracking phase as well, their performance may be inferior compared with specific tracking algorithms. A combination of the above mentioned classes is therefore favorable for solving the synchronization problem in OFDM.

6.2.2 Design of the Training Symbol

The design of the training-symbol originates from the paper by Schmidl and Cox [1] on frequency and time-synchronization for OFDM. The first of the two training symbols (TS) used in [1] is a unique OFDM symbol because every second sub-carrier (SC) is zero. This implies that the symbol has identical halves in the time-domain, due to properties of the Fourier transform (see Figure 6-1a).

In the original scheme [1], the *odd-numbered sub-carriers are zero*, while the even sub-carriers contain a known, binary pseudo noise (PN)-sequence. Analyzing the system proposal of Section 5.2, it is seen that many of the *even-numbered sub-carriers must be zero*, because they are used to separate sub-bands and to avoid problems with DC-offsets and carrier feed-through. In order to apply the synchronization scheme to this OFDM system, we therefore use the odd-numbered sub-carriers for the PN-se-

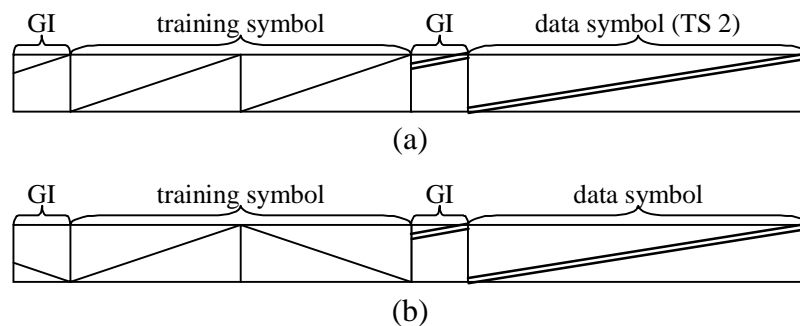


Figure 6-1: Illustration of the training symbol in the time-domain. (a): Training symbol of Schmidl's original method, where the PN-sequence is carried by the *even* sub-carriers. The symbol has identical halves in the time-domain. (b): Modified training symbol. The PN sequence is modulated on the *odd* sub-carriers, leading to a time-domain symbol with identical halves but opposite signs.

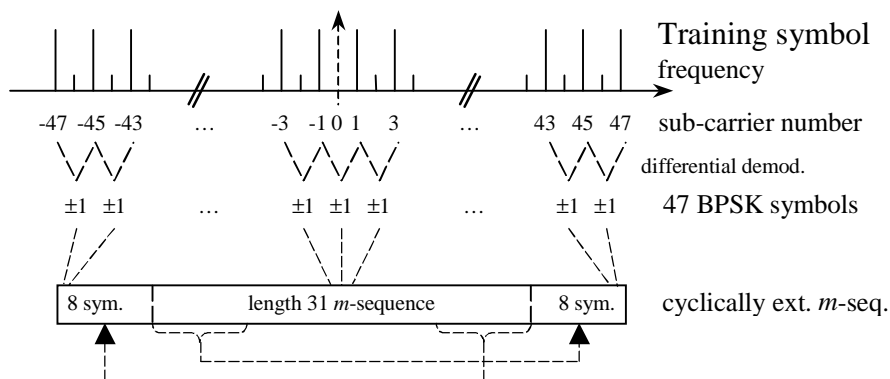


Figure 6-2: Frequency-domain diagram of the training symbol in transmission mode I-fr.

quence (see Figure 6-2). This is a novel modification of the well-known technique. Still the corresponding time-domain sequence has identical halves, but the samples of its second half have opposite signs, which is easily taken into consideration in the estimation steps. The training symbols of the original and of the modified schemes are illustrated in Figure 6-1 in time-domain.

The TS has thus 48 active sub-carriers (SC) in transmission mode I-fr. (And, respectively, {12, 96, 24} active sub-carriers in modes {I-qr, II-fr, II-qr}. The transmission modes are described in Section 5.2.) Note that all the sub-bands' edges are occupied by “pilot”-carriers, which is beneficial to channel estimation since all sub-carriers can be estimated by interpolation, and no extrapolation is needed.

Across the sub-carriers, an m -sequence is modulated using differential BPSK; i.e., the data (m -sequence) is contained in the phase difference among each pair of sub-carriers, being {+1, -1}. 47 bits are thus carried by the TS in case of TX-mode I-fr on 48 SCs. Those 47 binary symbols are a length 31 m -sequence ($m = 5$; shift-register stages 1 and 4 connected to the modulo 2 adder [12]), which is cyclically extended by 8 bits towards both ends (see Figure 6-2).

In [1], two OFDM symbols comprise the training sequence. Known data is modulated there differentially between the two OFDM symbols, for the purpose of integer frequency-synchronization. The modification used here therefore reduces the overhead introduced by one OFDM symbol per frame [2], [3].

6.2.3 Frame Timing Synchronization

In order to detect the training symbol – and thereby the frame-start –, the first step of the synchronization scheme calculates a sliding correlation sum over the length and time-lag of the periodic part (identical halves) of the training symbol in time-domain [1]. The mathematical formulation of this so-called “correlation algorithm” is given in the following equations. A metric

$$M(d) = |P(d)|^2 / (R(d))^2 \quad (6-1)$$

is used, where

$$\begin{aligned}
 P(d) &= \sum_{i=0}^{L-1} (r_{d+i}^* r_{d+i+L}) = P(d-1) + r_{d+L-1}^* r_{d+2L-1} - r_{d-1}^* r_{d+L-1} \\
 R(d) &= \sum_{i=0}^{L-1} |r_{d+i+L}|^2 = R(d-1) + |r_{d+2L-1}|^2 - |r_{d+L-1}|^2
 \end{aligned} \tag{6-2}$$

are a correlation sum with lag L and a power metric, respectively. The variable r_i expresses the sequence of received complex-valued samples of the OFDM signal. L is the separation of equal samples in the training sequence, i.e., $L = N/2$, where N is the number of FFT-points. The expressions given in (6-2) indicate an iterative way of calculating $R(d)$ and $P(d)$, which requires just one complex multiplication and two additions/subtractions per input sample. Each of the samples r_i is the sum of a signal and a noise component, $r_i = s_i + n_i$ ¹⁶. Their variances and the SNR are defined as

$$\begin{aligned}
 E\{\text{Re}[s_i]^2\} &= E\{\text{Im}[s_i]^2\} = \sigma_s^2 \\
 E\{\text{Re}[n_i]^2\} &= E\{\text{Im}[n_i]^2\} = \sigma_n^2 \\
 SNR &= \sigma_s^2 / \sigma_n^2
 \end{aligned} \tag{6-3}$$

Detection of the TS is based on comparing $M(d)$ with a fixed threshold $th \in [0,1]$. In the absence of noise, $M(d)$ takes a value of one when calculated over the TS, because samples separated by L positions are then equal (with opposite signs); thus $|P(d)|$ and $R(d)$ become equivalent. Outside the TS, the value of $M(d)$ is close to zero, as the sample-pairs spaced by L samples are (largely) uncorrelated. Figure 6-3 depicts the metric $M(d)$ as the correlation window slides across the TS.

Observe the flat top of the function $M(d)$, due to the guard interval, because the cyclic prefix also has equal samples at the required correlation-lag (in a non-dispersive channel – to be exact). Therefore, the maximum is obtained for all positions where the sliding correlation window overlaps the training symbol including its guard interval (cf. Figure 6-1 and Figure 6-3). The optimum timing is at the end of the flat top. The maximum of $M(d)$ decreases in the presence of noise, i.e., its expected value is a function of SNR [1].

6.2.3.1 Received Signal's Power Metric $R(d)$

$R(d)$ is a measure for the received signal's strength (plus noise) during the second half of the FFT period. A small modification to the derivation of $R(d)$ is suggested here. The original method has an undesirable behavior at the end of an OFDM burst, because $R(d)$ takes very small values when there is no signal at the input. Being the denominator of the expression yielding $M(d)$, this metric may show very large values in

¹⁶ Note that according to this definition the signal samples s_i are convolved with the channel impulse response.

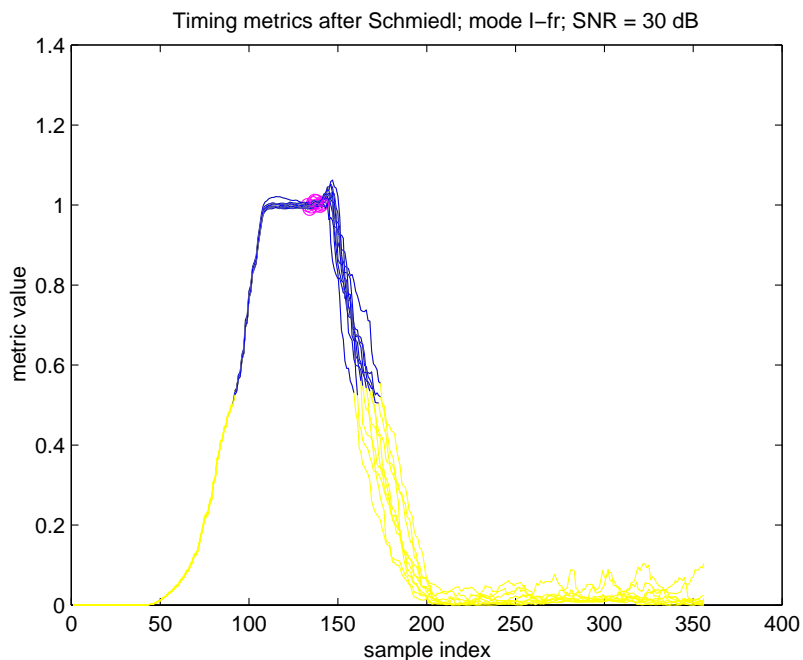


Figure 6-3: Ten simulations of the metric $M(d)$ during the training sequence. The optimum frame start corresponds to the end of the plateau.

that case, which may lead to false-detections. Extending the summation range solves this problem, i.e., $R(d)$ should be calculated over the full FFT-period and divided by two

$$R(d) = \frac{1}{2} \sum_{i=0}^{N-1} |r_{d+i}|^2 = \frac{1}{2} (R(d-1) + |r_{d+N-1}|^2 - |r_{d-1}|^2). \quad (6-4)$$

Independently, this modification was also proposed in [13].

6.2.3.2 Selecting the Threshold Value

Detecting the peak (plateau) in the metric $M(d)$ is not a trivial task. For instance, the correct threshold setting is a parameter to be optimized. Schmidl and Cox [1] have studied the distribution of $M(d)$ at the optimum position, $M(d_{opt})$, and at any position outside the TS, $M(d_{outside})$. As previously mentioned, at the optimum position, $E\{M(d_{opt})\}$ decreases with low SNR. Therefore, selecting the threshold too high will cause a missing of the peak at low SNR. Outside the TS, the expected value of the metric $M(d)$, $E\{M(d_{outside})\}$, is not a function of the SNR, but it is a function of the length of the TS in samples. The shorter the TS, the larger is this mean. Thus, selecting the threshold too low may lead to miss-detections as the threshold may occasionally be exceeded.

The variance of the metric (at the optimum position and outside the TS) increases with decreased length of the TS.

Using the stochastic description of the metric $M(d)$ as given in [1], it is possible to cal-

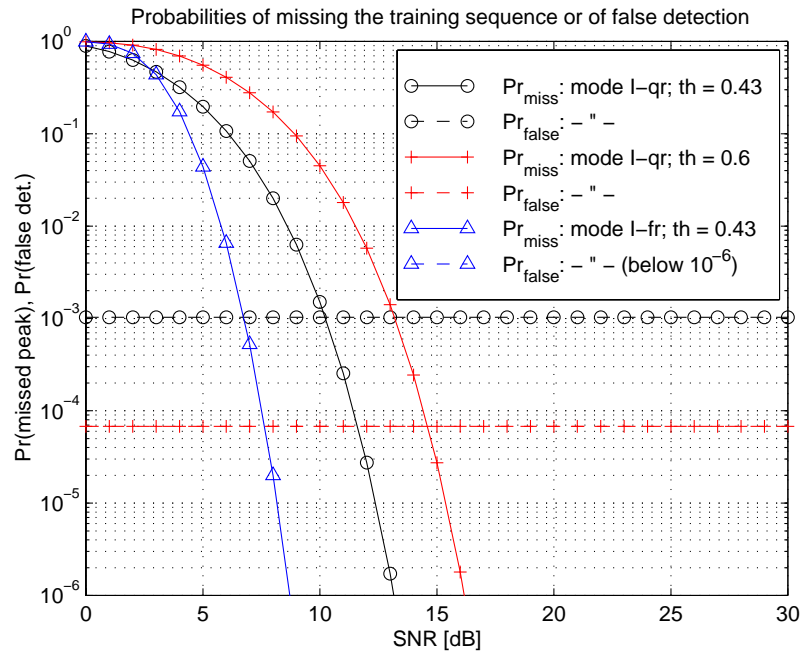


Figure 6-4: Probability of missing the training-sequence at the optimum position and probability of false detection at one particular position outside the training sequence.

culate

- (i): the probability that the metric $M(d_{opt})$ at the optimum position is smaller than a specific threshold th , thus the peak would not be detected (at that position), and
- (ii): the probability that the metric $M(d_{outside})$ is larger than the threshold, meaning that a peak would be detected where actually no peak exists.

Figure 6-4 shows the analysis of these probabilities as a function of the SNR for the full- and quarter-rate options of TX-mode I, respectively, denoted I-fr and I-qr (see Section 5.2). In case of the full-rate mode, the false detection probability is very low (below 10^{-6} , thus it is not shown in the figure). Therefore, a threshold value $th = 0.2$ can be used for mode I-fr, where the missing probability becomes even smaller compared to the results shown (for $th = 0.43$).

For the quarter rate mode, it is more difficult to find a trade-off between these two probabilities, since the missing as well as the false-detection probabilities are rather high at low SNR. A threshold value $th = 0.43$ is selected for this mode.

The probability of false detection might seem very low. However, since a miss-detection can occur at any position $d_{outside}$, the event that $M(d)$ exceeds the threshold becomes much more likely. Some attention is given to this problem in [1] and below.

6.2.3.3 Peak Detection

A procedure to detect the correct frame start should involve the following filtering step. Searching for the longest peak during the frame duration rejects most false-de-

tections, because the plateau at the optimum position always has considerable length (usually it is longer than the guard interval), while outside the TS, the metric raises for just a few samples above the threshold. (Figure 6-9 on page 181 depicts simulation results for this procedure. The probability of missing the TS is shown there as a function of the SNR.)

DC-offsets may cause additional trouble. It is easily verified that the metric $M(d)$ also takes values around one if the input signal is just a constant value. Such input may be seen in the absence of an OFDM signal (when no data or training symbols are transmitted on the down-link), if the ADCs used on the I/Q-signal components have DC offsets. Such a situation may lead to miss-detections. By monitoring the value of $R(d)$, which is a measure for the input signal's power, it is possible to identify these false detections as the signal strength is then very small.

Note as well that the periodic frame structure can be exploited to further enhance the robustness of the system. Once synchronization has been acquired, there is no need to search for the next frame's start using this technique. Tracking the residual timing-offsets is then sufficient.

The real-time implementation of the described algorithms on the emulation platform has proven their suitability (see Section 6.5).

6.2.4 Fractional Frequency-Offset Synchronization

The algorithm for frequency-synchronization is based on the fact that the phase-angle of the above-defined correlation sum at its optimum position, $P(d_{opt})$, is proportional to the carrier frequency-offset, as seen from the following derivation. We first introduce the frequency-offset to the (lowpass equivalent) signal model, written as

$$r_i = s_i e^{j(2\pi\delta f' i/N + \theta)} + n_i, \quad (6-5)$$

where $\delta f'$ is the frequency-offset normalized to the sub-carrier spacing F , and θ is the carrier phase offset. Considering that during the TS $s_i = -s_{i+L}$, we obtain from eq. (6-2) in the absence of noise

$$P(d_{opt}) = - \sum_{i=0}^{L-1} |s_{i+d_{opt}}|^2 e^{j2\pi\delta f' L/N}. \quad (6-6)$$

The estimate of the frequency-offset is obtained from the phase-angle of this expression,

$$\hat{\delta f}' = \frac{1}{\pi} \angle [-P(d_{opt})]. \quad (6-7)$$

Due to the 2π ambiguity of the phase term, only the fractional frequency-offset in the range of ± 1 sub-carriers can be determined with this method.

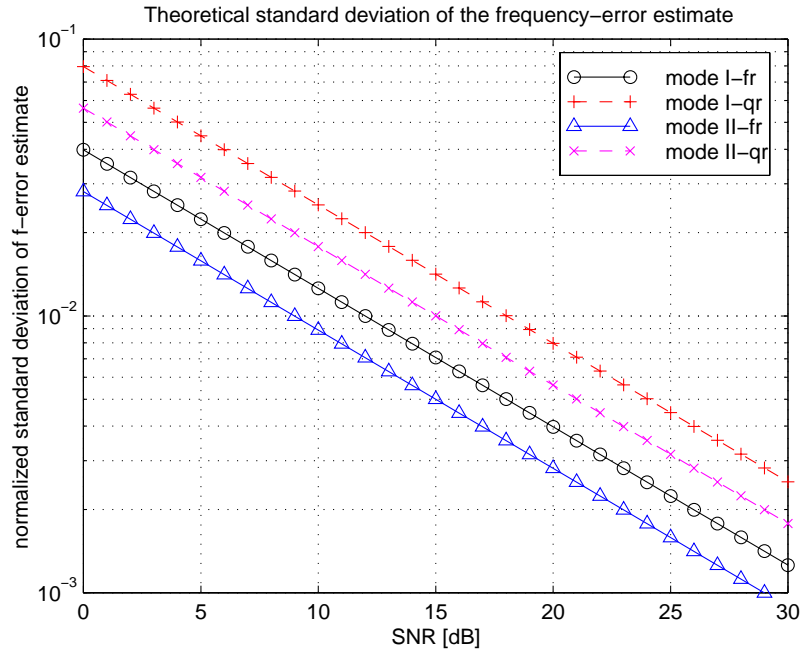


Figure 6-5: Standard deviation (normalized to the sub-carrier spacing) of the frequency estimation error vs. SNR. Theoretical results for all transmission modes.

6.2.4.1 Performance Analysis

The standard deviation of the estimate (6-7) is quantified by [4], [1]

$$\sigma_{\hat{f}'} = \frac{1}{\pi\sqrt{L \cdot \text{SNR}}}. \quad (6-8)$$

The derivation of this expression is also given in Section 6.3.2. Note that the multipath radio channel has no influence on this or on the previous equations.

Computational results are shown in Figure 6-5 for all transmission modes of the system proposal. The standard deviation is given normalized to the sub-carrier spacing $F = 1/T_{FFT}$. It is evident from the figure and from (6-8) that the estimates get better as more samples are available for the correlation processing introduced in eq. (6-2). The worst results are thus seen for mode I-qr, where the standard deviation of the frequency-offset estimates is respectively 2.5 and 8% of the SC-spacing at 10 and 0 dB SNR. These values are still acceptable, as the performance won't degrade down to about 10 dB and synchronization won't be lost down to at least 0 dB.

6.2.4.2 DC-Offset and Carrier Feed-Through

Both, DC-offsets, which may be induced for example by the ADCs of the receiver, and carrier feed-through, which is often caused by non-perfect carrier suppression in the transmitter's I/Q-modulators, degrade the performance of the frequency-offset estimation technique. A DC-offset, for instance, results in an additive constant term in $P(d_{opt})$, thus the estimate becomes biased. In Section 6.3, this problem is thoroughly

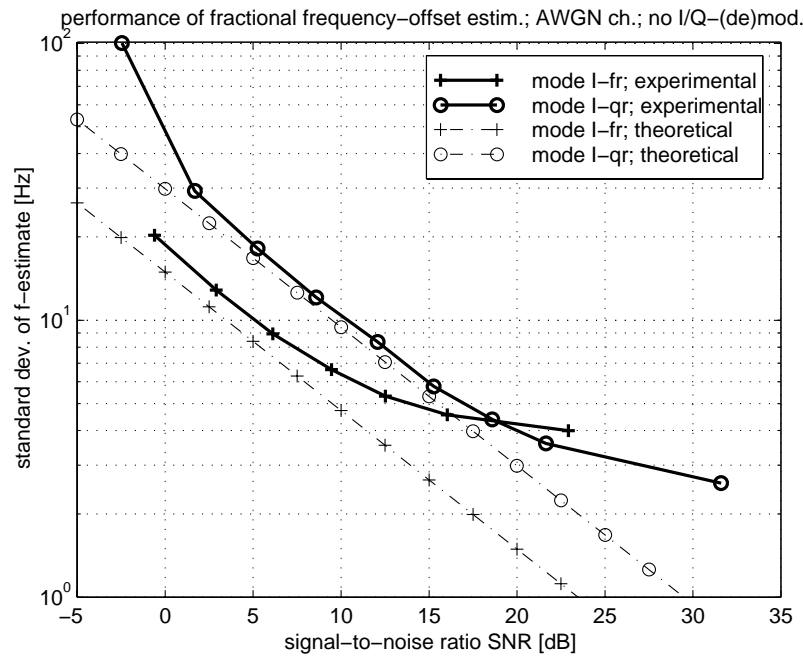


Figure 6-6: Experimental performance results of the frequency-synchronization algorithm. Compared to the analytical curve, degradation is evident due to the impact of DC-offsets. (The sub-carrier spacing $F = 375$ Hz in the emulated air-interface.)

analyzed. An extension to the algorithm is presented, which can cancel the bias in the most relevant cases.

Experimental performance results showing the degradation due to DC-offsets are depicted in Figure 6-6. These data were obtained from the DSP-based emulation platform running the proposed OFDM air-interface (in mode I-qr and I-fr)¹⁷. Analytical results are shown for comparison. The experimental results were acquired in a system set-up without (simulated) radio channel and without I/Q-modulation and -demodulation hardware. In this way, the performance of the estimation algorithm is obtained, i.e., eventual frequency-jitters of the local oscillators used for the I/Q-(de)modulation are not seen. The degradation of the experimental results compared with the theoretical curves (at high SNR) is due to DC-offsets.

6.2.5 Application of the FFT

In the previous steps, the position of the TS has been roughly located, and the frequency-offset has been estimated in the range of ± 1 sub-carrier spacing. These steps were performed using the received time-domain signal. As further synchronization pa-

¹⁷ I wish to appreciate the contributions by my students and colleagues, P. Teneva, K. Büke, I. Gultekin, A. Snijders, and V. Jović, to the soft- and hardware implementation of the emulation system, and for gathering the experimental data shown in this and in the next chapter. Detailed descriptions of their work can be found in [14]–[17].

rameters will be derived from the (known) data-constellation points of the training symbol, it is required to demodulate the TS using the FFT.

In order to thereby avoid inter-carrier-interference, frequency-synchronization must be acquired at an accuracy better than approx. 5 % of the sub-carrier spacing (see Section 4.2.4.2). As the initial (fractional) frequency-offset may be larger than that value, a frequency-offset correction will be applied to the received signal, prior to the execution of the FFT. This is achieved by multiplying the (time-domain) samples of the TS by a complex exponential sequence according to the estimated fractional frequency-offset $\hat{\delta f}'$. The correction is written as

$$\hat{r}_{d_{opt}+i} = r_{d_{opt}+i} e^{-j2\pi\hat{\delta f}'i/N}, \quad (6-9)$$

where $i = \{0, 1, \dots, N-1\}$. Computing the FFT on the sequence $\hat{r}_{d_{opt}+i}$ yields the data-symbols of the TS, $\{y_{l,TS}\}$, where $l = \{-N/2, -N/2+1, \dots, N/2-1\}$.

6.2.6 Integer Frequency-Synchronization

The integer frequency-synchronization is based on the known data carried in the TS. The even-indexed SCs are removed from this sequence (because they don't carry data; cf. Figure 6-2) and differential demodulation is applied in order to recover the known PN-sequence. Neglecting noise, the demodulated symbols are written as

$$\begin{aligned} \Delta y_{n,2} &= y_{2n-2,TS}^* y_{2n,TS} \\ &\equiv \begin{cases} \{\pm 1\} h_{2n-2,TS}^* h_{2n,TS} e^{j\Delta\Psi_2} & \text{if } y_{2n-2} \text{ and } y_{2n} \text{ are data symbols,} \\ 0 & \text{otherwise} \end{cases} \end{aligned} \quad (6-10)$$

where $n = \{-N/4+1, -N/4+2, \dots, N/4-1\}$. The phase term

$$\Delta\Psi_2 = \Psi_{2n-2,TS} - \Psi_{2n,TS} = 4\pi\delta t / T_{FFT} \quad (6-11)$$

results from the remaining timing-offset δt (see eq. (4-26) in Section 4.2.4). The channel response is assumed to be highly correlated at each neighboring pair of sub-carriers, therefore, the products of the channel coefficients are approximately real-valued factors. The unknown signs express the data symbols.

The position of the PN-sequence in the demodulated training symbols is an indication of the integer frequency-offset. For instance, in transmission mode I-fr of the proposed OFDM system, a (cyclically extended) length-31 m -sequence $m_n = \{\pm 1\}$, $n = \{-15, -14, \dots, 15\}$ is carried in the TS (see Figure 6-2). The integer frequency-offset is found by searching for the magnitude-maximum of the metric

$$M_{\text{int}}(e) = \sum_{n=-15}^{15} m_n^* \Delta y_{n+e,2}, \quad (6-12)$$

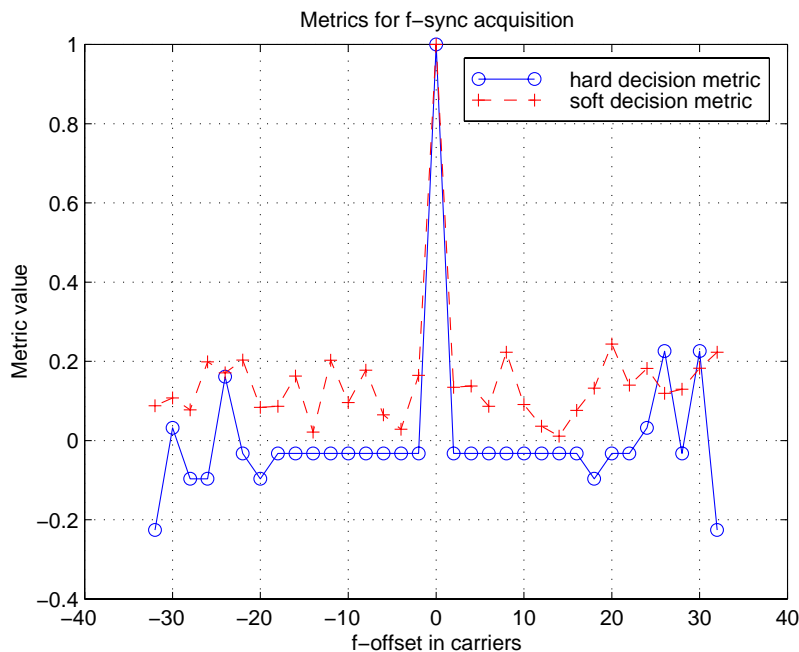


Figure 6-7: Soft- and hard decision metrics used for integer frequency-offset correction.

for $e = \{-16, -15, \dots, 16\}$. We obtain $\hat{\delta f}_i = 2 \arg \max_e (|M_{\text{int}}(e)|)$, where $\hat{\delta f}_i$ is the integer frequency-error normalized to the sub-carrier spacing F . Note that this offset must be a multiple of two sub-carriers, since fractional frequency-offset correction up to ± 1 SC has been performed before. The sum (6-12) can be seen as a coherent accumulation of all the differentially demodulated constellation points $\Delta y_{n,2}$, because the multiplication with the original m -sequence perfectly removes the signs of the data symbols at the optimum e .

Making a decision on the data symbols prior to the calculation of $M_{\text{int}}(e)$ would allow for simplified implementation on an ASIC, as (6-12) is then easily realized in binary arithmetic. With the latter option, $M_{\text{int}}(e)$ is referred to as the “hard-decision” metric, while in the former case it is called the “soft-decision” metric. Figure 6-7 illustrates these metrics as a function of $2e$ (after normalization to the maximum magnitude).

6.2.6.1 Integer Frequency-Synchronization at the Quarter-Rate Receiver

Only a subset (about one quarter) of the data symbols $\Delta y_{n,2}$ are available for determining the integer frequency offset, when the quarter rate mobile terminal has to synchronize to a full-rate base-station. Similarly to the above introduced full-rate case, the position of the maximum of the metric $M_{\text{int}}(e)$ gives an indication of this offset. To maximize the acquisition range, it is recommended to cyclically extend the known m -sequence by the number of demodulated data symbols minus one.

The performance of this method will depend on the Hamming distance – the number of bits with opposite sign – between the demodulated sequence and the known PN-se-

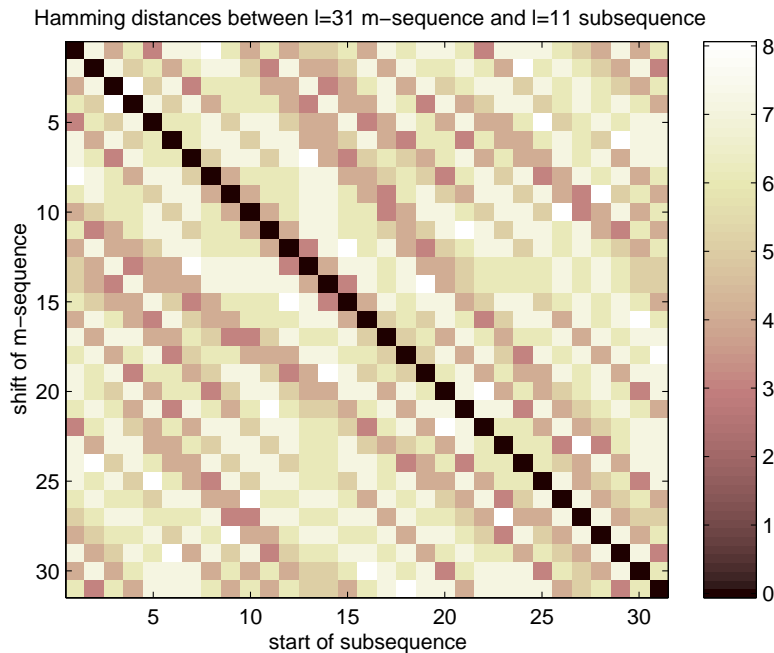


Figure 6-8: Hamming distances between any length 11 sub-sequence of the length 31 m -sequence and any length 11 sub-sequence of the cyclically extended sub-sequence.

quence. The Hamming distance of any length 11 sub-sequence of the cyclically extended $l = 31$ m -sequence to the cyclically extended $l = 31$ m -sequence is illustrated in Figure 6-8. The minimum distance is three; the maximum is eight.

6.2.6.2 Performance

Results of a performance simulation are given in Figure 6-9 for the full- and quarter-rate options of transmission mode I. Shown is the probability that the integer frequency-offset has been detected falsely as a function of the SNR, for the AWGN channel. The soft- and hard decision cases are considered. Moreover, the probability is depicted that the training symbol is missed, using the frame timing-synchronization algorithm described in Section 6.2.3.

It is evident from the results that the hard-decision algorithm fails with a probability up to 20% at low SNR. In these situations, the soft-decision algorithm is clearly better; its false detection rate is usually well below 1 %, even at 0 dB SNR. Generally, the full-rate receiver is more robust than the quarter-rate receiver. Performance results over Rayleigh fading channels are essentially equivalent.

As the integer frequency-offset is zero after its initial acquisition and correction, there is no need to re-estimate this error for each frame. The estimates can be used, however, to check if the synchronization is still correct. If a number of consecutive estimates show arbitrary values ($\neq 0$), then synchronization has probably been lost, or the signal is no longer strong enough. Not relying on a single erroneous estimate to identify such a situation enhances the robustness.

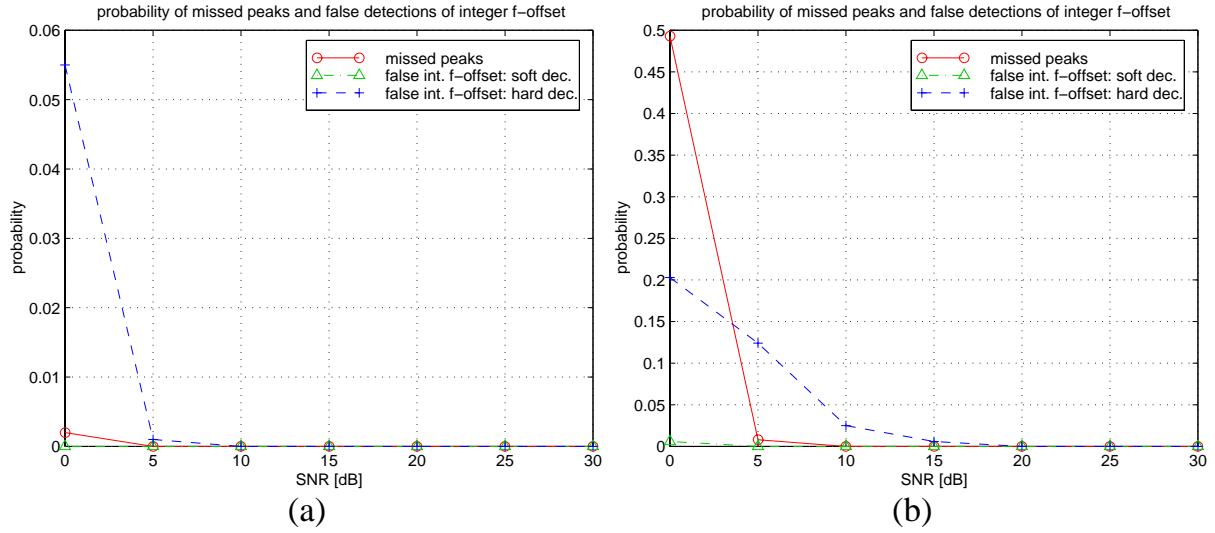


Figure 6-9: False detection probability of the integer frequency-offset. AWGN channel. (a): transmission mode I-fr; (b): mode I-qr.

Note also the relatively high probability that the peak of the frame-synchronization metric is missed with the quarter-rate receiver at very low SNR.

6.2.7 Remaining Timing-Offset Synchronization

A timing-offset causes a progressive phase rotation of the data constellation points with increasing distance to the center frequency, as elaborated in Section 4.2.4. This phase rotation is explained by the time-delay property of the Fourier transform, which says that a time-shift in the input-waveform is seen as a linearly increasing phase-shift in the frequency-domain.

Between equally spaced sub-carriers, i.e., for instance between adjacent sub-carriers, a constant differential phase-shift is therefore evident due to this progressive phase rotation. Differential demodulation in frequency-direction reveals this phase-shift, as seen in eqs. (6-10) and (6-11).

From this point it is a small step to observe that a (highly accurate) estimate of the remaining timing-offset is obtained from the phase-angle of the soft-decision metric $M_{\text{int}}(e)$ at the optimum position $e_{\text{opt}} = \hat{\delta}f_i / 2$. At e_{opt} , the known data is removed from the symbols $\Delta y_{n,2}$, therefore, the timing-offset is conveniently detected from $M_{\text{int}}(e_{\text{opt}})$, where

$$\hat{\delta}t = \frac{T_{\text{FFT}}}{4\pi} \angle M_{\text{int}}(e_{\text{opt}}) \text{ [s]} \text{ and } \hat{\delta}t' = \frac{N}{4\pi} \angle M_{\text{int}}(e_{\text{opt}}) \text{ [samples]}. \quad (6-13)$$

(T_{FFT} is the FFT-period in seconds and N is the number of FFT-points.) Note that a positive $\hat{\delta}t$ suggests late timing, i.e., the FFT window has started too late.

The progressive phase rotation has been previously suggested for timing-offset syn-

chronization, e.g., in [7]–[11]. Independently of the current work, the authors of [2] have proposed the modification of Schmidl’s training symbol [1], which yields the estimate of the timing-offset in the highly efficient way indicated above by using differential modulation in the frequency-domain. Novel work in this thesis is the performance analysis of this estimation method, which is given in Appendix C. The main results are summarized here, applied to the proposed OFDM system.

6.2.7.1 Estimation Bias on the Dispersive Channel

On multipath channels, the timing-offset is biased, since a systematic phase rotation is caused by the product of the channel coefficient on adjacent sub-carriers $h_{2(n-1),TS}^* h_{2n,TS}$ (see eq. (6-10)). This bias in terms of channel parameters is seen from the expected value

$$E\{\hat{\delta t}\} \cong \delta t - \frac{\tau_{rms}}{\sqrt{2K+1}}, \quad (6-14)$$

where τ_{rms} is the RMS delay spread of the channel, and K is the Ricean K-factor.

6.2.7.2 Estimation Variance

Analytical results for the standard deviation of the estimate have been derived in Appendix C. For AWGN channels, this performance measure is obtained from

$$\sigma_{\hat{\delta t}} = \frac{N}{4\pi} \frac{\sqrt{SNR_{SC} + N_m / 2}}{SNR_{SC} N_m} \text{ [samples]}, \quad (6-15)$$

where N_m is the number of differentially demodulated symbols summed up to obtain M_{int} (for example in eq. (6-12), $N_m = 31$), and SNR_{SC} is the SNR of the used SCs of the TS. SNR_{SC} is related to the time domain SNR (see eq. (6-3)) by

$$SNR_{SC} = SNR \frac{N}{N_{SC}}, \quad (6-16)$$

where N_{SC} is the number of active SCs in the TS.

In Appendix C, the estimates’ variance is derived for Rayleigh fading multipath channels as well (see eq. (C-23)). The obtained expression relates the spaced-frequency correlation function of the frequency-selective channel to the variance of the timing-offset estimates. The expressions for Ricean channels were not fully developed, because the Rayleigh case can be seen as a worst-case, which is sufficient to analyze in a system design. Computational results are given below.

6.2.7.3 Performance Results

Figure 6-10 shows simulation results for the fine timing-offset estimation algorithm

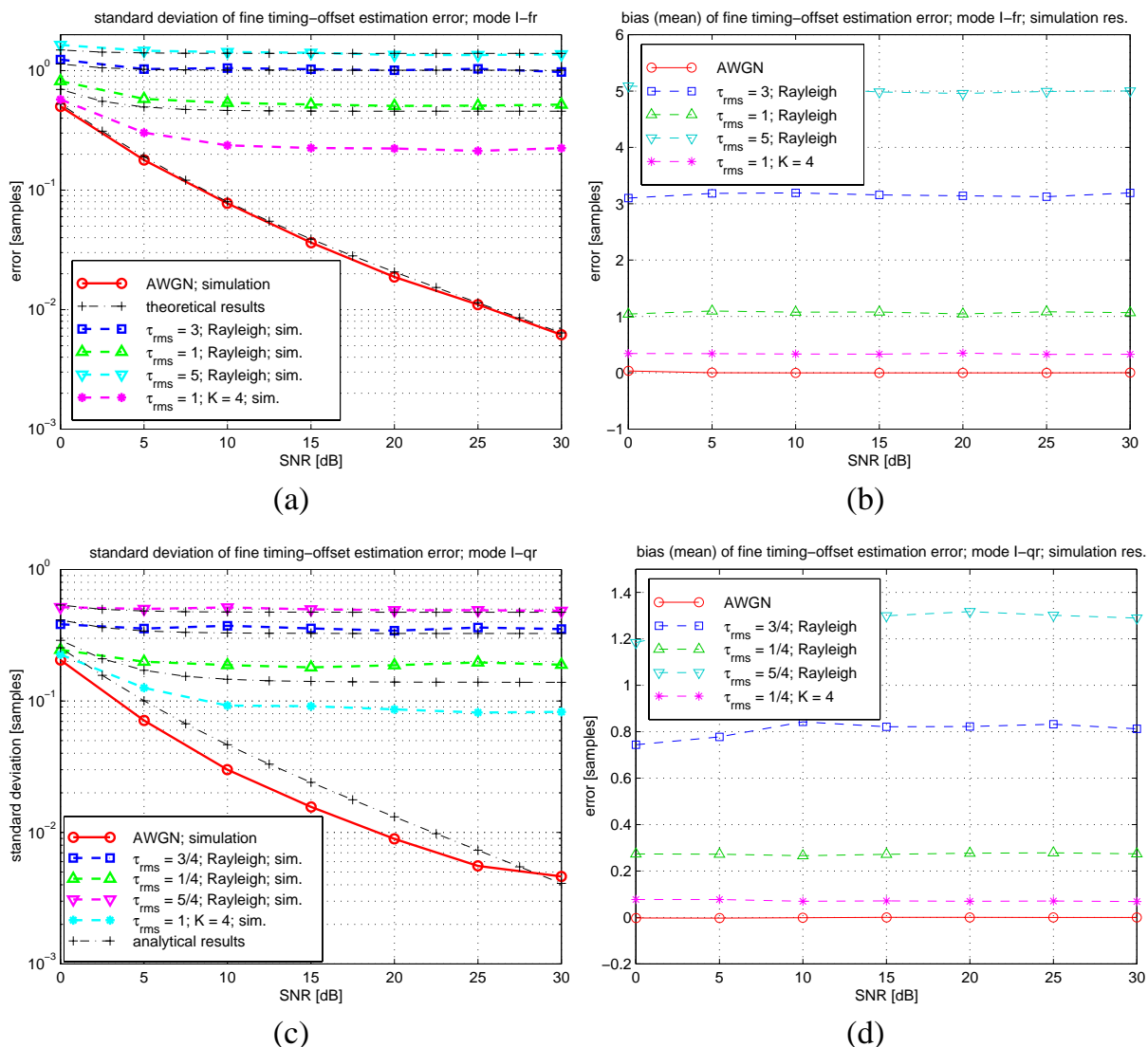


Figure 6-10: Performance of the fine timing-offset estimator. (a), (b): Mode I-fr; (c), (d): Mode I-qr; (a), (c): Standard deviations for several channels; (b), (d): Mean values (biases) obtained from computer simulations.

discussed in this section. The mean and standard deviation of the estimation error are given as a function of the SNR for modes I-fr and I-qr of the proposed OFDM system, over AWGN and different Rayleigh/Ricean channels. The simulation results of standard deviation are compared to analytical results, for the AWGN and Rayleigh cases. The simulated mean values correspond to the theoretical bias given by (6-14).

In the AWGN case, the standard deviation of these estimates is as low as 0.5 samples at an SNR of 0 dB (mode I-fr). It is much higher over the multipath channels, which is due to the variations of the spaced-frequency correlation function (correlogram) for individual channel simulations. It is seen that even fractional sample timing offsets can be estimated and tracked with the proposed algorithm. This can be used to estimate the sampling frequency offset between the transmitter and receiver (see Section 6.2.8).

Theoretical and simulation results agree well for mode I-fr. For mode I-qr, however,

the disagreement is slightly bigger for some parameter values. This is probably due to the simulation set-up implemented for the quarter rate mode, where the transmitted signal was a full-rate signal, from which the quarter rate signal was derived by frequency-shifting, low-pass filtering, and down sampling. The filter, being a rather short FIR filter (21 taps), did not perfectly cut out the desired quarter of the frequency-band: i.e., the amplitude response was not perfectly flat, and some aliasing was present at the band-edges. It is assumed that the main part of the discrepancies is caused by this signal-processing step, which was not considered in the analysis.

6.2.7.4 Correction for Timing-Offset and Compensation for the Estimation Bias

The integer part (in samples) of the estimated timing-offset is used to adjust the start sample of the FFT-interval. It is not necessary to correct explicitly for the still-remaining fractional part of this timing-offset, because the progressive phase rotation caused by it is included in the channel estimate; thus the correction is done implicitly during the equalization step performed prior to the data detection. It is noted that equalization in an OFDM system is a multiplication of the received data constellation points by the inverse of the estimated channel coefficients. For phase modulation schemes (like QPSK), a multiplication by the complex conjugate is sufficient to cancel for the phase rotations. Channel estimation is described in Section 6.4.

As the start-time of the FFT-period is estimated too late by the remaining timing-offset estimation algorithm, the maximum bias should be considered in the OFDM system design in order to prevent inter-symbol-interference. This is achieved by cyclically shifting the FFT-period (of data symbols and the training symbol) so that it actually starts a few samples before the end of the guard interval. The shift-period should correspond to the bias for the Rayleigh fading channel with maximum RMS delay spread, which is the worst-case channel in this respect. Figure 6-11 illustrates this principle.

Alternatively, this correction could be applied at the receiver, where the maximum bias is subtracted from the estimated symbol start time. This method leads to a significant progressive phase rotation, however, which must be considered in the channel estimation algorithm (see Section 6.4.2.4).

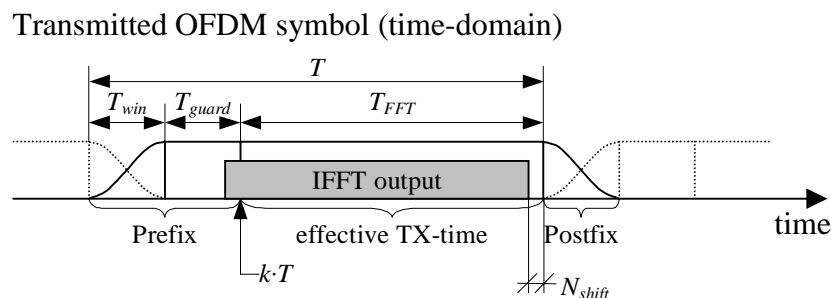


Figure 6-11: Shifting the transmitted OFDM symbol to compensate for the biased timing-offset estimates

Two more aspects have to be considered in order to perform coherent detection in OFDM systems: namely, sampling frequency offsets and carrier phase offsets. These impairments introduce phase rotations to the data constellations, which have to be corrected. In the sub-section below, we briefly discuss these issues.

6.2.8 Sampling Frequency-Offsets

The sampling clocks of ADCs and DACs are usually derived from crystal oscillators. Typically, such oscillators have a frequency inaccuracy up to $\delta f_s = 20 \dots 50$ ppm, which leads to a timing-offset of one sample after every 20,000 to 50,000 processed samples. Although these numbers seem very large, sampling frequency-errors cannot be neglected, as seen from the following analysis.

A sampling frequency-offset leads to a gradually increasing timing-offset. Using the OFDM-symbol-index k as a time-variable, the resulting timing-offset in samples is written

$$\delta t'_k = \delta t'_0 + k \delta f_s (N + N_{guard} + N_{win}), \quad (6-17)$$

where $\delta t'_0$ is the time-offset at symbol zero, and N , N_{guard} , and N_{win} are the numbers of samples in the FFT-, guard-, and windowing-intervals, respectively. To assess the impact of the sampling frequency-offset, we compare the phase rotation at the l -th sub-carrier of the k -th OFDM symbol to the phase of the same sub-carrier of the zero-th symbol. Recall that a timing-offset induces a progressive phase-rotation of the data constellation points at the receiver. The zero-th symbol could be the training symbol, where timing-offset correction and channel estimation are performed. That is, at the zero-th symbol, all phase rotations are corrected. However, k OFDM symbols later, the following phase rotation is evident, according to the system model derived in Section 4.2.4 (see eq. (4-26)) and assuming that the carrier frequency-offset is zero, $\delta f = 0$.

$$\Delta\Psi = \Psi_{l,k} - \Psi_{l,0} = 2\pi(\delta t'_k - \delta t'_0)T_s \frac{l}{T_{FFT}} = 2\pi k l \delta f_s \frac{N + N_{guard} + N_{win}}{N}, \quad (6-18)$$

where T_s is the sampling interval.

It is easily verified that a sampling frequency-offset of 50 ppm leads to a phase rotation of $\sim 52^\circ$ at the 47th sub-carrier (the outmost one) of the 48th OFDM symbol ($l = 47$, $k = 48$), for system parameters according to the mode I-fr of the system proposal of Section 5.2.

As such a phase error yields certain bit errors (with QPSK modulation), the sampling frequency-error has to be estimated and corrected. One possibility for performing this correction in hardware requires that the sampling clock and the oscillators used for I/Q-(de)modulation and up/down-conversion are all locked to the same frequency-source. Synchronizing for the carrier-frequency-offset would then automatically re-

move the sampling offset as well. Below, the signal processing is outlined, which is required to correct mathematically for the sampling frequency-offset.

6.2.8.1 Estimation of the Sampling Frequency-Offset

The sampling frequency-offset can be obtained from the timing-offset estimates of two subsequent training symbols indexed by $n - 1$ and n . This estimate is written as

$$\hat{\delta f}_{s,n} = \frac{\hat{\delta t}'_{nN_F} - \hat{\delta t}'_{(n-1)N_F}}{N_F (N + N_{guard} + N_{win})}, \quad (6-19)$$

where N_F is the number of OFDM symbols per frame, and $\hat{\delta t}'_k$ is the estimated timing-offset at OFDM symbol number k . Considering that each of the estimates $\hat{\delta t}'_k$ has a standard deviation $\sigma_{\hat{\delta t}'}$ (cf. Section 6.2.7.2), the standard deviation of $\hat{\delta f}_{s,n}$ becomes

$$\sigma_{\hat{\delta f}_s} = \sqrt{2} \sigma_{\hat{\delta t}'}, \frac{1}{N_F (N + N_{guard} + N_{win})}. \quad (6-20)$$

Evaluation with the system parameters shows that the accuracy obtained from one such estimate is not sufficiently high, particularly, if time-variant multipath channels are present¹⁸. In such cases, multiple estimates (6-19) can be averaged, yielding

$$\overline{\hat{\delta f}_s} = \frac{1}{N_{av}} \sum_{n=1}^{N_{av}} \hat{\delta f}_{s,n} = \frac{\hat{\delta t}'_{N_{av}N_F} - \hat{\delta t}'_0}{N_{av} N_F (N + N_{guard} + N_{win})}. \quad (6-21)$$

It is seen that the standard deviation is reduced by a factor of N_{av} , which quantifies the number of averaged estimates. This averaging can be conducted during the initial log-in phase, i.e., when the mobile terminal initially communicates with a base station. During this phase, communication is done via the signaling symbols, which are transmitted immediately after the training symbol ($k = 1$). These symbols are therefore much less affected by the sampling frequency-offset, making a correction unnecessary.

6.2.8.2 Correction for the Sampling Frequency-Offset

Once the sampling frequency-offset has been determined, a multiplication of the received signal constellations with a complex exponential term with inverse phase of eq. (6-18) can cancel for the phase distortions. Thereby, k can be seen as the symbol index within a down-link frame, where the training symbol is indexed by zero.

¹⁸ The simulation and analytical results presented in Section 6.2.7 assume that the time-offset is estimated over totally uncorrelated realizations of multipath radio channels. Since the channel transfer functions at subsequent training symbols are correlated, the standard deviation due to the changing channel is much smaller, when only pairs of subsequent estimates are investigated. Thus the sampling frequency-offset estimation over Rayleigh channels performs better than suggested by the results in Figure 6-10 and eq. (6-20). This is confirmed by experimental results presented in Section 6.5.

6.2.9 Carrier Phase-Offset

A carrier phase-offset leads to a common phase rotation of the signal constellation points, as seen from the system model derived in Section 4.2.4 (see eq. (4-26)). At the training symbol, this common phase rotation is also incorporated in the channel estimate. Therefore it is implicitly corrected by the (one-tap) equalization. However, if residual frequency-offsets exist, the phase-offset is not constant on consecutive OFDM symbols, but it gradually increases, just like the timing-offset increases due to a sampling frequency-offset¹⁹. The pilots can be used to estimate this common phase rotation. Coherently adding the pilots (after equalizing for the channel and removing the data) increases the SNR of the sum by the number of pilots N_P compared with the SNR of a single sub-carrier. Moreover, spreading the pilots over the whole frequency-band exploits the frequency-diversity of the radio channel. If a sub-carrier is in a deep fade, its contribution to the sum is small and has therefore little impact on the phase-estimate.

A consecutive multiplication of all data constellations by a complex exponential with inverse phase angle yields the correction of such offsets.

6.2.9.1 Estimation of Carrier Frequency-Offset

The progressing phase-offset due to a frequency error can be used for estimating the carrier frequency-offset in an alternative way. The phase offset at the k -th OFDM symbol is given by (see eq. (4-26), in Section 4.2.4)

$$\theta_k = \theta_0 + 2\pi\delta f k T = \theta_0 + 2\pi\delta f' k \frac{N + N_{guard} + N_{win}}{N}, \quad (6-22)$$

where δf is the frequency-offset in Hz, $\delta f'$ is the frequency-offset normalized to the sub-carrier spacing F , and T [s] is the total symbol duration (FFT plus guard plus windowing intervals). The frequency-offset can thus be estimated from the difference of the phase estimates of subsequent OFDM symbols,

$$\delta \hat{f} = \frac{1}{2\pi T} (\hat{\theta}_k - \hat{\theta}_{k-1}), \text{ or } \delta \hat{f}' = \frac{1}{2\pi} \frac{N}{N + N_{guard} + N_{win}} (\hat{\theta}_k - \hat{\theta}_{k-1}). \quad (6-23)$$

As the phase difference can take values between $\pm\pi$, the unambiguous range of this estimate is $N / (N + N_{guard} + N_{win}) \cdot F / 2$, which is less than half of the sub-carrier spacing. This small acquisition range and the fact that the method requires prior execution of the FFT (because the pilot constellations have to be recovered), limit the applicabil-

¹⁹ Note that a frequency-offset of ± 12 or ± 24 sub-carriers is required to demodulate one of the four sub-bands of the full-rate signal using a quarter-rate receiver (in mode I). (In mode II, the required offset is ± 24 or ± 48 sub-carriers.) Therefore, in this operation mode, a systematically progressing common phase rotation is evident.

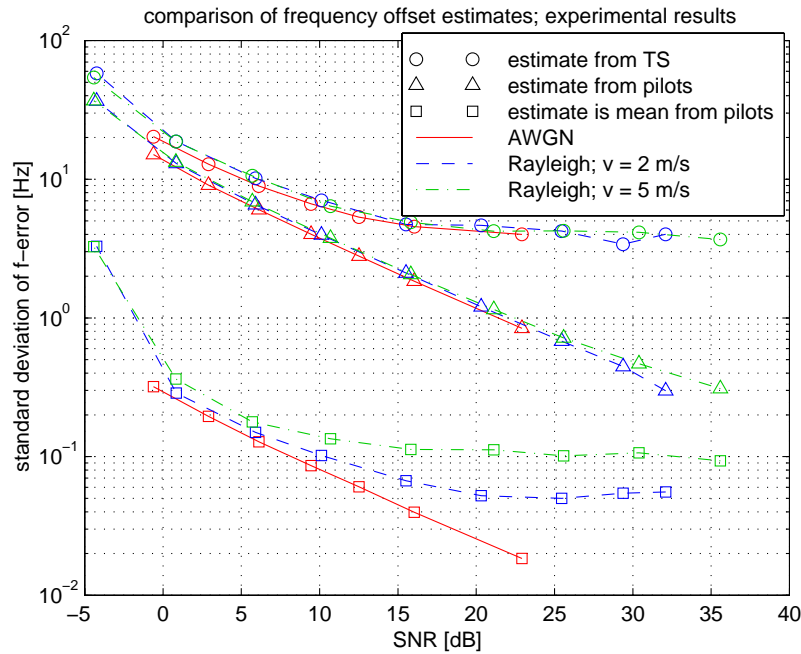


Figure 6-12: Standard deviation of frequency-offset estimates obtained with several estimation techniques. Experimental results without I/Q-(de)modulation hardware. SC-spacing $F = 375$ Hz.

ity of the method to the tracking phase. Assuming that the phase estimates are obtained from pilot tones, the variance of the frequency estimate depends primarily on the number of pilots and on the accuracy of the channel estimate. Again, the estimates of subsequent symbol-pairs can be averaged in order to enhance the accuracy, which results in a highly robust method of frequency-offset estimation.

A set of experimental results is depicted in Figure 6-12. The standard deviation of different estimators is shown as a function of the SNR. In order to obtain these results, the I/Q-(de)modulation hardware was excluded from the signal path. Two types of results are given for the method presented in this section, namely, the standard deviation of one single estimate, and the standard deviation of the averaged estimate using the data symbols of a whole down-link frame (48 symbols). Experiments were performed over an AWGN channel and over two Rayleigh channels with different mobility. For comparison, we also show the performance of the correlation-based estimation technique, which has been described in Section 6.2.4 (“estimate from TS”).

Again the impact of DC-offsets is evident in the results of the correlation-based technique, leading to an error floor. Since the average signal powers have been selected equivalently, these results are about equal for the three different channels investigated. Equivalent results are also seen for the standard deviation of single estimates derived from the pilots. DC-offsets and carrier feed-through do not deteriorate the performance of this estimation scheme. Averaging can enhance the performance by a factor up to the number of averaged estimates, which is in our case 47. Here, some impact of the

time-variant channel is observed in irreducible error floors, because the channel influences the phase of the received signal constellations as well.

Note the excellent performance for the averaged estimate. The standard deviation is (far) below 1 Hz for any SNR above 0 dB. This is below 1 % of the sub-carrier spacing of the implemented system, being $F = 375$ Hz.

6.2.10 Summary and Conclusions

In this section, the key algorithms have been described required for synchronizing an OFDM receiver for the system proposal of Section 5.2. The following synchronization steps are needed to conduct coherent demodulation of the data symbols. These steps are all based on either the special (known) training symbol, or on pilot sub-carriers.

In order to recover the data constellation points using the FFT, time- and frequency-synchronization must be achieved. Otherwise, the orthogonality between sub-carriers is (partly) lost, i.e., inter-carrier-interference and inter-symbol-interference are introduced. These synchronization steps are initially achieved by processing the time-domain input signal of the receiver. The correlation properties of the special training symbol yield estimates for the (frame) timing and carrier frequency-offset.

Secondly, (progressing) phase rotations due to sampling frequency and remaining carrier frequency-offsets have to be corrected. Pilots and the phase rotation of the known data symbols of the training symbol are used to estimate these offsets. After initial synchronization has been acquired, these estimates also enable the tracking of residual time- and frequency-offsets with very high accuracy.

One training symbol is employed in each frame of 69 symbols (in mode I), corresponding to an overhead of 1.4 %. (37 and 35 symbols comprise a frame in mode II and II', respectively, i.e. the overhead is about 2.8 %.) This overhead is well invested, as it enables the efficient estimation of all synchronization parameters, with sufficient accuracy. Performance results are shown in this section for mode I. The synchronization performance of mode II is superior, because more signal energy is available for the signal processing, due to the doubled symbol period.

It is noted that the training symbol is also employed for computationally efficient channel estimation schemes, which are presented and discussed in Sections 6.4 and 6.5.3.

6.3 Impact of DC-Offsets and Carrier Feed-Through on Fractional Frequency-Synchronization

This section further analyzes the fractional frequency-offset estimation technique, which was described in Section 6.2.4 as step two of the synchronization procedure proposed. Specifically, the impact of DC-offsets and carrier feed-through (CFT) is investigated. Such impairments are introduced by the receiver's and transmitter's hard-

ware, respectively.

The analysis presented is applicable to a whole class of frequency-synchronization algorithms, which utilize duplicated sequences in the OFDM signal, as e.g. the guard interval (cyclic prefix) or a dedicated, periodic training symbol. The phase angle of the correlation sum over the duplicated parts is an accurate measure for the carrier frequency offset (*cf.* Section 6.2.4).

The mathematical analysis of the impairments leads to an extended frequency-offset estimation algorithm that can be used to cancel the undesirable effects.

Orthogonal frequency division multiplexing (OFDM) is a broad-band transmission scheme splitting the high-rate data stream into several parallel sub-channels in order to mitigate the effects of multipath fading (see Section 4.2). “Classic” OFDM systems are assumed, which use a so-called guard interval (GI) (cyclic prefix) in order to maintain the orthogonality among sub-channels over time dispersive channels. Accurate frequency synchronization is a prerequisite for these schemes, because even small inaccuracies (down to 2 % of the frequency spacing among sub-carriers) lead to inter-carrier-interference (ICI) [4], [6], [18].

A popular algorithm for estimating the frequency-offset is based on the correlation sum over duplicated parts within the OFDM signal, as for instance the GI (see [5]) or a specific training symbol ([1], [4]). The phase angle of the correlation sum is a measure for the frequency-offset. The algorithm is computationally highly efficient because it is calculated directly from the time-domain signal, not requiring a prior (fast) Fourier transform (FFT). Its accuracy is sufficient for most practical applications.

From experimental results obtained from the implementation of two OFDM systems ([19], [20]) on the DSP-based emulation platform presented in Section 5.3, a performance degradation of the frequency synchronization schemes was observed, when compared to theoretical results from [1], [4], [5]. (See the experimental performance results given in Figure 6-6 and Figure 6-12.) DC-offsets introduced by the analog-to-digital converters (ADCs) of the receiver and carrier feed-through from the I/Q-modulators of the transmitter were identified as the main sources for this degradation.

This section presents the mathematical analysis of the influence of those hardware imperfections, which cause biased estimates and increased estimation error variances. An extended algorithm is presented that perfectly cancels the impact of the DC-offset, and for most cases, the impact of CFT as well. The computational cost of the extension is extremely low, amounting to $2M$ additional complex additions and one additional complex multiplication, where M is the length of the duplicated sequence in samples.

The analysis is presented in the following sub-sections. Section 6.3.1 presents the signal model and a number of definitions used in the analysis. The correlation algorithm is reviewed in Section 6.3.2, and its performance is analyzed in the presence of noise, DC-offset, and CFT. In Section 6.3.3, the proposed extension is described and analyzed. Performance results are given in Section 6.3.4, which have been obtained from

computer simulations, from the experimental platform (see Section 5.3), and from the analytical expressions derived. Conclusions and recommendations are summarized in Section 6.3.5.

6.3.1 Mathematical Modeling and Definitions

The sampled OFDM signal at the receiver – in complex lowpass-equivalent form – is written as

$$r_i = (s_i + V_{CFT})e^{j(2\pi\delta f i / N + \theta)} + V_{DC} + n_i, \quad (6-24)$$

where i is the sample index, N is the FFT-length, s_i is the transmitted OFDM signal convolved by the channel impulse response, $\{n_i\}$ are independent Gaussian noise samples, δf is the carrier frequency offset normalized to the sub-carrier (SC) frequency-spacing, θ is a carrier phase offset, and V_{DC} and V_{CFT} are the (complex-valued) DC- and CFT-components, respectively.

Note that, in this section, δf denotes the *normalized* frequency-offset, not the frequency-offset in Hz. This variable change has been introduced for the sake of notational convenience.

The signal and noise powers are respectively defined as $2\sigma_s^2 = E\{|s_i|^2\}$ and $2\sigma_n^2 = E\{|n_i|^2\}$, leading to the signal-to-noise ratio $SNR = \sigma_s^2 / \sigma_n^2$ (cf. eq. (6-3)). Furthermore, it is appropriate to relate the magnitude of the DC- and CFT-components to the OFDM signal power, written $\gamma_{DC} = |V_{DC}|^2 / 2\sigma_s^2$ and $\gamma_{CFT} = |V_{CFT}|^2 / 2\sigma_s^2$. The attenuation of the CFT by the fading channel is not considered in this study.

6.3.2 Analysis of the Synchronization Algorithm

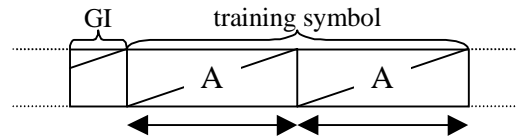
6.3.2.1 Review of the Algorithm

The correlation sum used for frequency (and coarse time) synchronization is given by

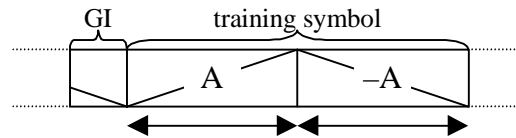
$$P_{opt} = \sum_{i=0}^{M-1} r_i^* r_{i+L}, \quad (6-25)$$

where L is the correlation lag (the distance in samples between the two identical sequences of the OFDM signal) and M is the length of the sequences. For notational convenience, we let the index of the first sample of the first sequence be $i = 0$. The magnitude of the sum (6-25) has a maximum at this position, where the correlation window matches the duplicated sequences (cf. Section 6.2.3). Therefore, looking for this maximum is a means for initial time-synchronization. The phase angle of (6-25) is a measure for the frequency-offset, because the multiplicative complex exponential sequence in (6-24) leads to a constant phase offset between each pair of samples in the correlation sum.

Original Schmidl method (PN-sequence on even sub-carriers):



Modified Schmidl method (PN-sequence on odd sub-carriers):



Guard interval-based method:

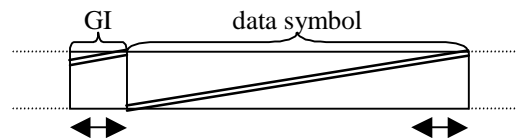


Figure 6-13: Illustration of the OFDM signal-parts used for synchronization in different methods. The arrows indicate the duplicate sequences, which are correlated by eq. (6-25).

This principle has been employed in multiple variations. In [5], the correlation sum between the GI and its equivalent at the end of the OFDM symbol is used. Therefore, $L = N$, and $M = N_{guard}$, the number of samples in the GI. Moose [4] and Schmidl [1] introduce specific training symbols (TS), which have periodic parts in the time-domain. We will focus on Schmidl's method, who suggests an OFDM symbol as TS, where only the even SCs are modulated with data, while the odd SCs are zero. The FFT properties demand that such a symbol consists of two identical halves in the time-domain, i.e., $L = M = N/2$. The third method considered here is a novel modification of Schmidl's method. Modulating the odd SCs in stead of the even ones and setting the even SCs to zero leads to a symbol with identical halves but opposite signs (*cf.* Section 6.2.2). The modified symmetry has advantages in certain OFDM symbol configurations, as, for instance, in the OFDM system proposed in Section 5.2. Moreover, the DC component of such a symbol is zero. An illustration of these schemes is given in Figure 6-13.

The following expression yields the estimate of the frequency-offset, where the negative sign is required for the modified Schmidl method.

$$\hat{\delta f} = \frac{N}{2\pi L} \angle(\pm P_{opt}) \quad (6-26)$$

In the following sub-sections, the performance of the estimation technique is separately evaluated in the presence of noise, DC-offset, and CFT.

6.3.2.2 Performance Analysis in the Presence of Noise

The analysis of the signal model (6-24) reduced to frequency (and phase) offsets and

additive noise leads to an expression for the estimate's standard deviation as a function of the SNR. The derivation outlined below can be also found in [1], [4], [5].

Without DC-offset and CFT, the correlation sum P_{opt} (eq. (6-25)) becomes

$$P_{opt} = \sum_{i=0}^{M-1} \left[s_i^* e^{-j(2\pi\delta f \frac{i}{N} + \theta)} + n_i^* \right] \left[s_{i+L} e^{j(2\pi\delta f \frac{i+L}{N} + \theta)} + n_{i+L} \right]. \quad (6-27)$$

During the correlation window, $s_i = \pm s_{i+L}$ (²⁰), which leads to

$$P_{opt} = \pm e^{j2\pi\delta f L / N} \sum_{i=0}^{M-1} |s_i|^2 + \sum_{i=0}^{M-1} \left[s_i^* e^{-j(2\pi\delta f \frac{i}{N} + \theta)} n_{i+L} + s_{i+L} e^{j(2\pi\delta f \frac{i+L}{N} + \theta)} n_i + n_i^* n_{i+L} \right]. \quad (6-28)$$

The negative sign applies for the modified Schmidl method. With the definition of the signal power, the first sum can be approximated by $2M\sigma_s^2$. Because the second sum is a zero mean complex Gaussian random variable (RV) (with approximate variance $2M2\sigma_s^22\sigma_n^2$), the expectation of P_{opt} has a phase angle proportional to the frequency-offset. (That is, the estimate of the frequency-offset is unbiased.) The component of this RV being perpendicular to this phase angle causes the estimation inaccuracies. Since for small arguments $x \ll \pi/2$, $\text{atan}(x) \cong x$, the standard deviation of the estimates becomes

$$\sigma_{\delta f} \cong \frac{N}{2\pi L} \frac{\text{std}[\text{Im}(P_{opt} e^{-j2\pi\delta f L / N})]}{E[|P_{opt}|]} \cong \frac{N}{2\pi L} \frac{2\sqrt{M}\sigma_s\sigma_n}{2M\sigma_s^2} = \frac{N}{2\pi L} \sqrt{\frac{1}{M \cdot \text{SNR}}}. \quad (6-29)$$

This result complies with the results from [1], [4], [5]. It is seen that the standard deviation decreases as the number of samples accumulated in the correlation sum increases, and as the correlation lag increases. An increase of the latter decreases the unambiguous range of the estimate, however (see (6-26)).

6.3.2.3 Impact of DC-Offsets

To keep the involved expressions simple and compact, we next concentrate on the DC-offset only – noise and CFT are assumed to be zero. This yields

$$P_{opt} \cong \pm 2M\sigma_s^2 e^{j2\pi\delta f L / N} + M|V_{DC}|^2 + 2 \left\{ \begin{array}{l} \text{Re} \\ j \text{Im} \end{array} \left(\sum_s^* V_{DC} e^{-j\pi\delta f L / N} \right) \right\} e^{j\pi\delta f L / N}, \quad (6-30)$$

where the positive sign and $\text{Re}(\bullet)$ apply for the conventional methods, and the negative sign and $j\text{Im}(\bullet)$ apply for the modified Schmidl method. $\sum_s' = \sum_{i=0}^{M-1} s_i e^{j(2\pi\delta f i / N + \theta)}$ is the

²⁰ Note that in case of the guard interval based method, inter-symbol-interference is neglected to assume $s_i = \pm s_{i+L}$. In case of the training symbol method, the channel impulse response must be shorter than the guard interval.

sum of M (almost independent) complex Gaussian RVs s_i , therefore, Σ_s' is also complex Gaussian with variance of $\sim 2M\sigma_s^2$. This assumes random data being modulated on the OFDM symbol under investigation. For a fixed TS, Σ_s' is a complex constant with a phase angle varying with θ . Since, in presence of a frequency-offset, θ is uniformly distributed in $[0, 2\pi)$, the expectation of the last term of (6-30) is zero, in both cases.

Assuming a random TS, the error's standard deviation is given by the standard deviation of the last term of (6-30) in a direction orthogonal to $e^{j2\pi\delta f L/N}$, related to the expected magnitude of P_{opt} (compare with the derivation of (6-29)).

$$\begin{aligned}\sigma_{\delta f} &\equiv \frac{N}{2\pi L} \frac{2 \text{std} \left[\begin{array}{l} \left\{ \begin{array}{l} \text{Re}(\Sigma_s^* V_{DC} e^{-j\pi\delta f L/N}) \\ \text{Im}(\Sigma_s^* V_{DC} e^{-j\pi\delta f L/N}) \end{array} \right\} \left\{ \begin{array}{l} -\sin(\pi\delta f L/N) \\ \cos(\pi\delta f L/N) \end{array} \right\} \end{array} \right]}{2M\sigma_s^2} \\ &= \frac{N}{2\pi L} \frac{2\sqrt{M}\sigma_s |V_{DC}|}{2M\sigma_s^2} \left\{ \begin{array}{l} \sin(\pi\delta f L/N) \\ \cos(\pi\delta f L/N) \end{array} \right\} = \frac{N}{2\pi L} \sqrt{\frac{2\gamma_{DC}}{M}} \left\{ \begin{array}{l} \sin(\pi\delta f L/N) \\ \cos(\pi\delta f L/N) \end{array} \right\}\end{aligned}\quad (6-31)$$

While for the standard methods (where $\sin(\bullet)$ and $\text{Re}(\bullet)$ apply) this standard deviation is zero at $\delta f = 0$, the degradation is at a maximum for the modified Schmidl method.

The second term of (6-30) introduces a bias to the estimated frequency-offset, if $\delta f \neq 0$. For small relative DC-components, the magnitude of this term in a direction orthogonal to $e^{j2\pi\delta f L/N}$ leads to the bias

$$\varepsilon_{\delta f} \equiv \frac{N}{2\pi L} \frac{E[\text{Im}(P_{opt} e^{-j2\pi\delta f L/N})]}{E[|P_{opt}|]} \equiv \frac{N}{2\pi L} \frac{M|V_{DC}|^2 \sin(-2\pi\delta f L/N)}{\pm 2M\sigma_s^2} = \mp \frac{N}{2\pi L} \gamma_{DC} \sin(2\pi\delta f \frac{L}{N}). \quad (6-32)$$

The solution with the negative sign results for Schmidl's original method and for the guard interval method. The modified Schmidl method shows a positive bias. Computational results are presented in Section 6.3.4 and compared with simulation results.

6.3.2.4 Impact of Carrier Feed-Through (CFT)

In an equivalent way, bias and error-variance are derived for the simplified case that the performance is degraded by CFT only. The correlation sum then becomes

$$P_{opt} = \left[\pm 2M\sigma_s^2 + M|V_{CFT}|^2 + 2 \left\{ \begin{array}{l} \text{Re}(\Sigma_s^* V_{CFT}) \\ j \text{Im}(\Sigma_s^* V_{CFT}) \end{array} \right\} \right] e^{j2\pi\delta f L/N}, \quad (6-33)$$

with $\Sigma_s = \sum_{i=0}^{M-1} s_i$. The negative sign and $j\text{Im}(\bullet)$ apply for the modified Schmidl method. It is readily seen from (6-33) that only for that method some degradation has to be expected. For the other schemes, CFT just introduces an additional component in the direction of $e^{j2\pi\delta f L/N}$. The following results are thus relevant for the modified

Schmidl method, only.

If the TS is modulated with random data, then Σ_s is a complex Gaussian RV with approximate variance $2M\sigma_s^2$, just like Σ'_s . This results in an error deviation of about

$$\sigma_{\hat{\delta f}} \cong \frac{N}{2\pi L} \frac{2\sqrt{M}\sigma_s |V_{CFT}|}{2M\sigma_s^2} = \frac{N}{2\pi L} \sqrt{\frac{2\gamma_{CFT}}{M}}. \quad (6-34)$$

If, however, the TS carries a constant PN sequence, then Σ_s is a complex constant and the modified Schmidl method yields a biased estimate with an error of

$$\varepsilon_{\hat{\delta f}} \cong \frac{N}{2\pi L} \frac{2\text{Im}(\Sigma_s V_{CFT}^*)}{2M\sigma_s^2}. \quad (6-35)$$

Note that this bias depends on the phase angle of the CFT-component. If this phase changes for a set of realizations (which is the case in a realistic system set-up in lack of perfect frequency-synchronization), the bias may appear to be a noise component. Computational results are given in Section 6.3.4.

6.3.2.5 Common DC-offset and CFT

In the common presence of a DC-component and CFT, an additional term is present in P_{opt} , compared with eqs. (6-30) and (6-33). This term in direction $e^{j\pi\delta f L/N}$ is similar to the term in (6-30) in this direction, but with Σ'_s replaced by $V_{CFT} M I_e = V_{CFT} \sum_{i=0}^{M-1} e^{j(2\pi\delta f i/N + \theta)}$. The additional term in P_{opt} is written as

$$P_{opt} = \dots + 2\text{Re}(V_{DC} V_{CFT}^* M I_e^* e^{-j\pi\delta f L/N}) e^{j\pi\delta f L/N}. \quad (6-36)$$

For any method, this term leads to an additional bias and to further reduced accuracy, as seen from simulation results in Section 6.3.4. The total expression for P_{opt} becomes

$$\begin{aligned} P_{opt} = & \left[\pm 2M\sigma_s^2 + M |V_{CFT}|^2 + 2 \left\{ \begin{array}{l} \text{Re} \\ j \text{Im} \end{array} (\Sigma_s^* V_{CFT}) \right\} \right] e^{j2\pi\delta f L/N} + \\ & + \left[2\text{Re}(V_{DC} V_{CFT}^* M I_e^* e^{-j\pi\delta f L/N}) + 2 \left\{ \begin{array}{l} \text{Re} \\ j \text{Im} \end{array} (\Sigma_s^* V_{DC} e^{-j\pi\delta f L/N}) \right\} \right] e^{j\pi\delta f L/N} + \\ & + M |V_{DC}|^2 \end{aligned} \quad (6-37)$$

An illustration of the estimates obtained with the modified Schmidl technique in a system corrupted by DC-offsets and CFT is given in Figure 6-14, by the solid line. These experimental results were acquired from the DSP-based emulation system described in Section 5.3. The analog I/Q-modulators and -demodulators have been utilized to introduce some constant frequency-offset. A fixed TS has been used; therefore, the “randomness” of the estimates is caused by the carrier phase offset, which changes “randomly” due to the frequency-offset. No noise has been added; no fading channel

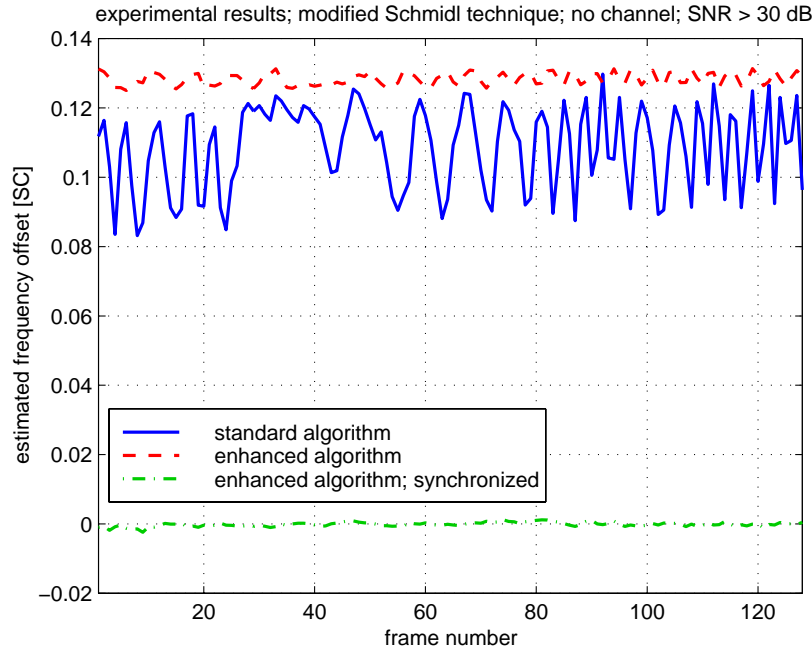


Figure 6-14: Illustration of the degradation of the frequency-offset estimation algorithm in presence of DC-offsets and carrier feed-through (CFT). A significant improvement is achieved by using the enhanced algorithm proposed in Section 6.3.3.

was included. The other two traces are described below.

6.3.3 Extension of the Algorithm

The above analysis has shown that in particular the modified Schmidl method is susceptible to DC-offsets and CFT. The other techniques suffer less from these impacts, especially for small frequency-offsets. However, in the acquisition phase, where the frequency-error is large, a significant degradation is possible. Degradation is also unavoidable, if the frequency-error correction is done mathematically (by multiplying the received signal with a complex harmonic; see eq. (6-9)) and not by hardware. This section proposes an extension to the correlation algorithm, which is capable of canceling the major impairments at low computational cost.

Subtraction of

$$P_{corr} = \frac{1}{M} \sum_{i=0}^{M-1} r_i^* \sum_{i=0}^{M-1} r_{i+L} \quad (6-38)$$

from P_{opt} gives the improvement mentioned, as seen from the analysis of

$$P_{corr} = \left(\pm \frac{1}{M} |\Sigma_s|^2 + M |V_{CFT}|^2 |I_e|^2 + 2 \left\{ \begin{array}{l} \text{Re} \\ j \text{Im} \end{array} \left(\Sigma_s^* V_{CFT} I_e \right) \right\} \right) e^{j2\pi\delta f \frac{L}{N}} + M |V_{DC}|^2 + \left[2 \left\{ \begin{array}{l} \text{Re} \\ j \text{Im} \end{array} \left(V_{DC} \Sigma_s^* e^{-j\pi\delta f \frac{L}{N}} \right) \right\} + 2 \text{Re} \left(M V_{DC} V_{CFT}^* I_e^* e^{-j\pi\delta f \frac{L}{N}} \right) \right] e^{j\pi\delta f \frac{L}{N}} \quad (6-39)$$

The negative sign and $j\text{Im}(\bullet)$ apply for the modified Schmidl method. After the subtraction, the interfering terms from (6-30) and (6-36) are perfectly cancelled. For the modified Schmidl method, a small impact remains from the CFT-component in (6-33), as seen from the $j\text{Im}(\bullet)$ term in

$$P_{opt} - P_{corr} = \left[\pm 2M\sigma_s^2 \mp \frac{1}{M} |\Sigma_s'|^2 + M|V_{CFT}|^2 (1 - |I_e|^2) + 2V_{CFT} \left\{ \begin{array}{l} \text{Re} \\ j\text{Im} \end{array} (\Sigma_s^* - \Sigma_s^* I_e) \right\} \right] e^{j2\pi\delta f L/N}. \quad (6-40)$$

It is noted that this term disappears for small δf , because Σ_s^* then becomes equal to $\Sigma_s^* I_e$. The performance is analyzed below by computer simulations. In the sole presence of noise, the standard deviation is given by (6-29), with M replaced by $(M - 1)$ in order to account for the subtractive (second) term in (6-40).

The improvement achieved by this enhanced algorithm for the modified Schmidl method is seen from the experimental results depicted in Figure 6-14. The estimates' variance is drastically reduced, particularly in the synchronized case, where the frequency-offset is zero. The estimates' bias and standard deviation are analyzed below.

6.3.4 Analytical and Simulation Results

Simulation results are presented in this section to support the above analysis. The OFDM system proposed in Section 5.2 is investigated in mode I, full-rate. It has an FFT-length of $N = 128$ points and a guard interval of $N_{guard} = 24$ samples. The modified Schmidl scheme and the GI-based scheme are evaluated. Within the TS used with the former, 48 of the odd-indexed SCs are modulated with random data (see Section 6.2.2). 88 SCs are modulated during the regular OFDM symbols, which are used with the latter technique. A Rayleigh fading channel with an exponentially decaying delay power profile at an RMS delay spread of 3 samples has been included.

6.3.4.1 Estimation Bias

In Figure 6-15, simulation results are presented for the estimation bias as a function of the relative strength of the DC-offset and/or the CFT-component, γ_{DC} and γ_{CFT} . Equal strength was assumed for the case that both impairments are present. A frequency-offset of 25 % of the SC-spacing was introduced (denoted in the figure as 0.25 SC). For comparison, analytical results are given for the bias due to DC-offset.

This DC-induced systematic error is seen to raise to significant values, when $\gamma_{DC} > -10$ dB, a value that may be reached particularly when the received signal is attenuated by the fading channel.

A CFT-component alone does not cause any systematic offset, since random data is assumed on the TS. But in combination with a DC-offset, the bias is influenced. Both schemes show similar characteristics.

The extended algorithm presented in Section 6.3.3 can fully remove the degradation in

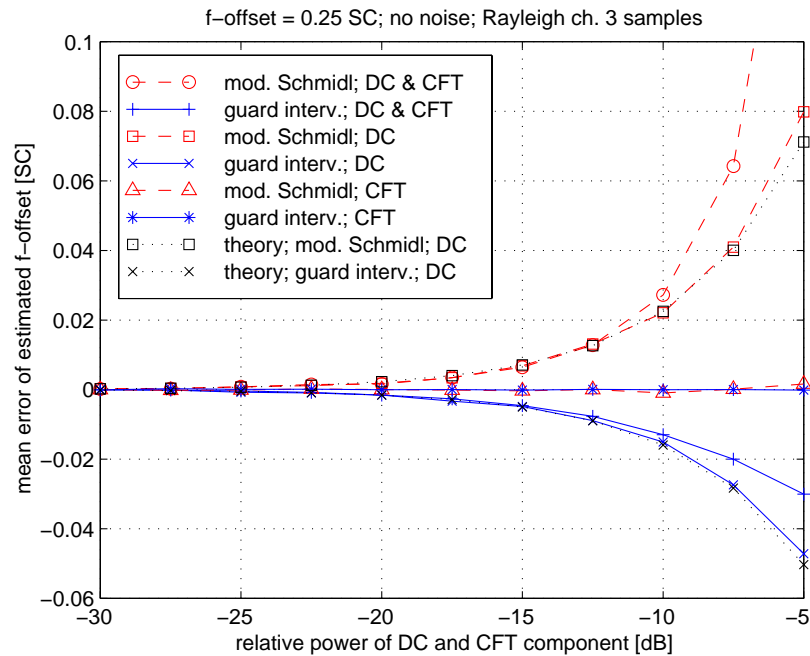


Figure 6-15: Estimation bias of frequency-synchronization in the presence of a DC-offset and/or a carrier feed through (CFT) component. Simulated offset $0.25F$.

the cases depicted.

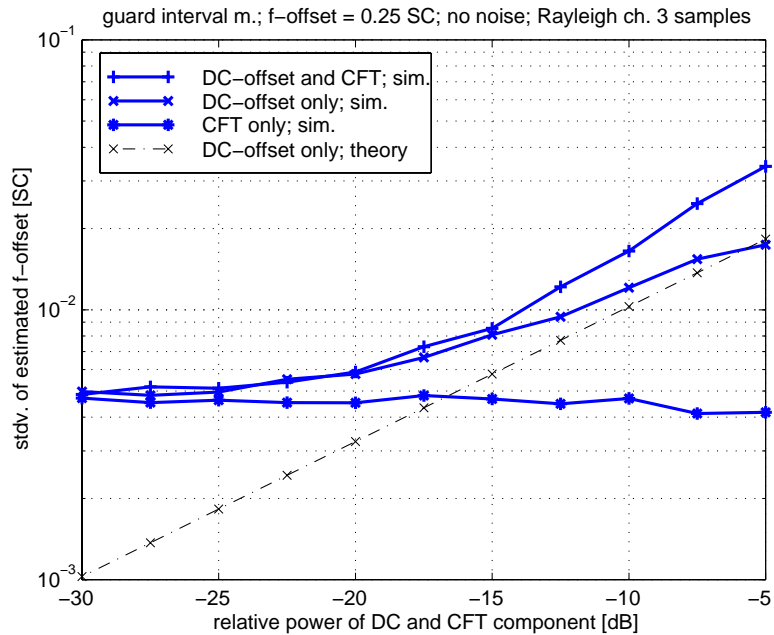
6.3.4.2 Standard Deviation of the Estimates

Different behavior of the two schemes is evident from the estimates' standard deviations shown in Figure 6-16. The performance of the guard interval (GI) based technique is indicated in Figure 6-16a. Clearly seen is an error floor at about 0.5% of the SC-spacing, which is caused by inter-symbol-interference during the guard interval due to the time-dispersive channel. This effect was not considered in the analysis, therefore, it is not seen from the analytical result, which is depicted for the case of a DC-offset. Simulation and analytical results agree at large γ_{DC} (relative power of the DC-component). Again, CFT alone does not lead to performance degradation.

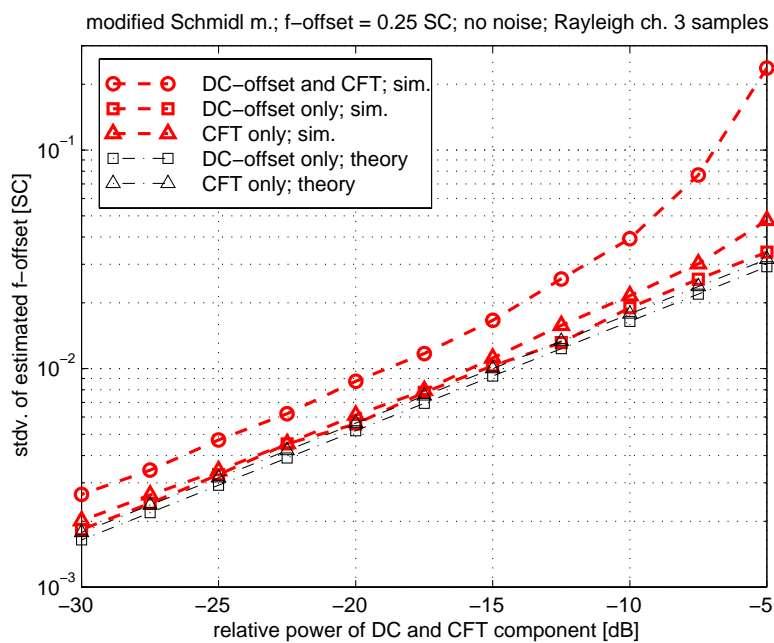
Both, DC-offsets and CFT degrade the modified Schmidl scheme (Figure 6-16b), where the analytical results are seen to appropriately describe the performance. The small discrepancy is due to the assumption that Σ_s and Σ'_s are the sums of independent, complex Gaussian random variables, which is not perfectly true in a practical OFDM scheme as the one simulated.

The degradation becomes significant when the relative power of the DC- and CFT-components is above -10 dB.

The performance as a function of the SNR is given in Figure 6-17, for a relative DC-offset and CFT power of -10 dB, and for a frequency-offset of 10 % of the SC-spacing. The figure shows the potential improvement by using the enhanced technique pro-



(a)



(b)

Figure 6-16: Performance of frequency-synchronization in the presence of a DC-offset and/or a carrier feed through (CFT) component. Simulated offset $0.25F$. (a): Estimation bias. (b): Standard deviation of the estimates.

posed in Section 6.3.3.

For the GI-based method (solid curves), the performance limit is set by the time-dispersive channel, being at about 0.5% SC. The theoretical result ('+—+') shows the performance that would be reached over an AWGN channel. There is a clear improvement for the enhanced technique. It is noted that the original algorithm's error

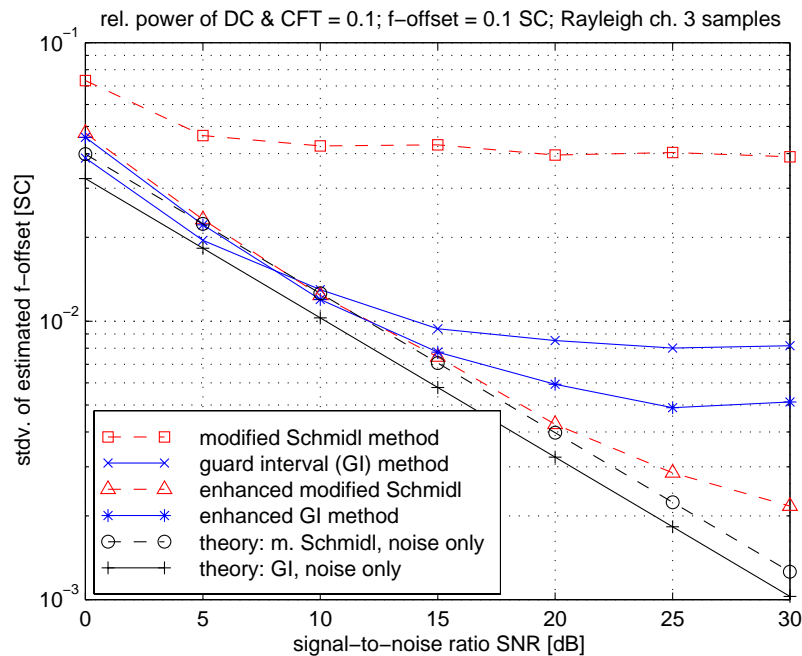


Figure 6-17: Estimation accuracy as a function of SNR, for DC-offset and CFT of 0.1. The improvement by the enhance estimation technique is seen.

floor of 0.8% SC ('×—×') increases for larger frequency-offsets δf , while the enhanced method ('*—*') is not influenced by δf .

The time-dispersive channel does not affect the Schmidl methods (dashed lines). However, for the modified variant and the standard algorithm, the DC- and CFT-components lead to an error floor (which is independent of δf) (see '□—□'). This error floor is drastically reduced by the extended algorithm proposed in Section 6.3.3 ('Δ—Δ'). The remaining error floor increases, however, as the frequency-offset δf increases. The performance at $\delta f = 0$ approaches the theoretical result for the noise-influenced case, which is indicated by '○—○'. Since the degradation disappears for $\delta f = 0$, the modified method utilizing the extended algorithm is as well suited for frequency tracking as the original method.

6.3.4.3 Experimental Results

A set of experimental results is given in Figure 6-18 for the modified Schmidl method, and for system parameters equal to the parameters used in the simulations. The estimates' standard deviation is shown as a function of the SNR over the AWGN channel. These results have been derived from the DSP-based emulation platform described in Section 5.3. I/Q-modulation and -demodulation are implemented in this system in analog hardware, in order to realistically evaluate frequency-synchronization algorithms. However, this hardware was removed for acquiring some of the results shown, which gives an indication of the impact of the mixer oscillators, and allows analyzing the performance of the estimation algorithm itself.

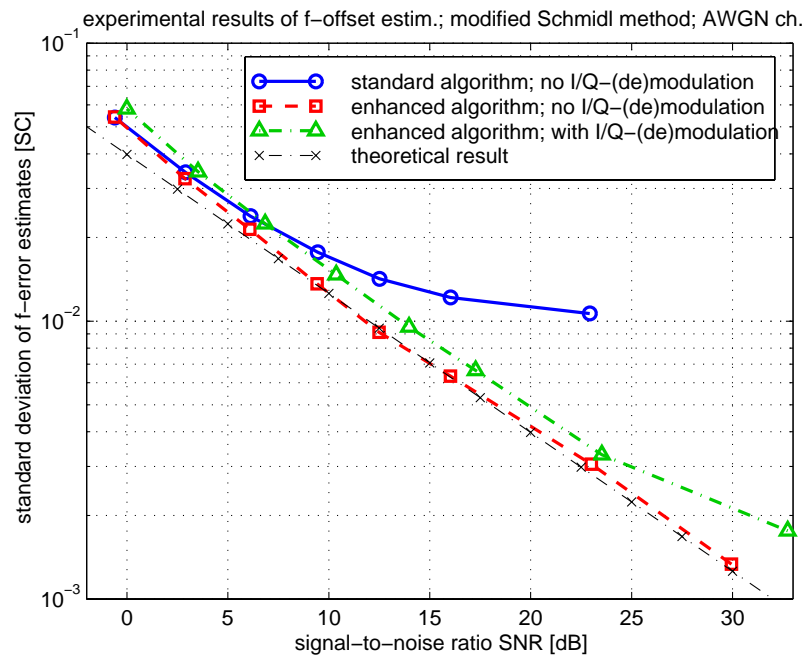


Figure 6-18: Experimental results (standard deviation of the frequency-error estimates vs. SNR) over AWGN channels.

Comparing the standard algorithm to the theoretical result, degradation is seen at high SNR. As the I/Q-(de)modulators were not present in the experimental system when this result was acquired, the curve shows the variance of the estimator influenced by DC-offsets, only. CFT did not exist, because there was no frequency-offset. Although the absolute performance results are still promising – even in the degraded case –, reduced signal strength (for instance within a fade) would lead to loss of synchronization and outages.

This degradation at high SNR is not evident in the results for the enhanced algorithm proposed in Section 6.3.3. The performance of the estimation algorithm under influence of DC-offsets is seen from the curve, where the I/Q-(de)modulators were excluded. This curve agrees almost perfectly with the theoretical one. The second result was obtained, while frequency-synchronization was performed in real-time (I/Q-(de)modulation included). Some implementation loss is observed there.

6.3.5 Conclusions and Recommendations

Correlation-based algorithms are very efficient means of frequency-synchronization for OFDM, and therefore very popular. This section addresses the issue of DC-offsets and carrier feed-through components, which degrade the performance of those techniques. From the analysis it is seen that estimation biases are introduced in the presence of those impairments, and that the estimates' standard deviation is enlarged. The analysis has also led to an extension of the algorithm, capable of correcting for the most significant interference due to DC-offset and carrier feed-through.

A novel variation of Schmidl's synchronization scheme [1] is discussed, where the odd

sub-carriers of the training symbol are modulated with the known PN-sequence in stead of the even ones. This modified training symbol was proposed for the OFDM system described in Section 5.2, where it allows decreasing the complexity and optimizing the performance of the synchronization and channel estimation schemes. Unfortunately, the modification makes the technique more susceptible to the impairments due to DC-offsets and CFT. The extended algorithm is capable of removing the estimation bias and it cancels the performance degradation in the tracking phase, i.e., when the frequency-offset is zero. Therefore, the application of the extended algorithm is strongly recommended for the modified synchronization method.

When the above-mentioned modification is not applied, then the impairments disappear naturally in the synchronized state, i.e., when the receiver's oscillators have been tuned to the transmitter's. The original algorithms are thus well suited for frequency tracking, even without the enhancement proposed. Certain system proposals assume, however, that the correction for frequency-offsets is done mathematically, by multiplying the received signal with a complex exponential sequence, prior to the execution of the FFT. This allows compensating for the frequency shift introduced by the oscillator offsets in order to restore the orthogonality of the OFDM sub-carriers. The actual frequency offset, however, is not cancelled; thus the degradation of the frequency-offset estimator is present. The enhanced algorithm can improve the performance in such systems as well.

6.4 Channel Estimation

Channel estimation is performed using the same training symbol as for synchronization. A known PN-sequence is modulated on the odd (pilot) sub-carriers (SC) of this symbol (see Figure 6-2). The number of pilot SCs in this symbol is thus 48 for transmission mode I-fr. (And, respectively, 12, 96, and 24 for modes I-qr, II-fr, and II-qr.)

Channel estimation can be done with largely different levels of complexity. The most simple scheme removes the modulation from the pilots yielding the channel estimate on the odd SCs. Linear interpolation (averaging) can be used to obtain the channel estimates on the even SCs. These estimates (the channel transfer function (TF) at the data sub-carriers) will be used to demodulate the data on all consecutive down-link symbols. Enhancements to this method include the following techniques.

Taking linear combinations of the channel attenuations at the pilots can reduce additive channel noise. This is actually a filtering operation across the SCs in order to smoothen the estimated channel TF. Different approaches for optimizing the filtering (Wiener filters; MMSE principle) and/or minimizing the computational effort (e.g.: transform domain processing) have been investigated in the literature (see e.g. [21], [22]). Section 6.4.1 presents the Wiener solution and elaborates on reducing the number of operations and memory required for its application. A disadvantage of the optimum Wiener solution is the dependency of the result on the current propagation envi-

ronment; namely the spaced-frequency correlation function of the channel and the noise level. In Section 6.4.2, the tradeoffs are investigated when one fixed set of filter coefficients is used for different actual channels. It will be seen that little is gained by such a solution in terms of bit-error-rates.

The second type of enhancements concerns the time-variability of the channel. During the reception of the data symbols of the current frame, the channel (slowly) changes. This will lead to increasing bit-error rates the “older” the channel estimate gets –, if the channel estimate is not up-dated accordingly. Channel tracking can be done in different ways. For instance, the channel coefficients can be predicted based on previous training symbols. The most basic scheme would linearly extrapolate to get the channel estimate for the current symbol, using the estimates from the last two training symbols. The substantial performance improvement enabled by this principle is seen from simulation results given in Section 6.5. More advanced techniques for predicting channel coefficients could use (adaptive or fixed) linear filters. Decision feedback principles, where data symbols are used to track the channel’s changes without introducing further training sequences, are another alternative (see e.g. [23]).

6.4.1 Wiener Filtering for Noise Reduction

An enhanced channel estimate – with reduced error – is obtained from linear combinations of the rough estimate at the pilot SCs. This process is written in matrix notation as

$$\hat{\mathbf{h}} = \mathbf{W}\mathbf{p}, \quad (6-41)$$

where $\hat{\mathbf{h}} = \mathbf{h} + \boldsymbol{\varepsilon}$ is the enhanced estimate of the channel attenuation vector (channel TF) $\mathbf{h} = [h_0, h_1, \dots, h_{M-1}]^T$, $\mathbf{p} = [p_0, p_1, \dots, p_{L-1}]^T$ is the vector of channel attenuations (plus noise) at the pilot-SCs’ positions, and \mathbf{W} is the Wiener filter, an M by L matrix. (M is the number of channel coefficients to be estimated, which is equal to the number of data sub-carriers, and L is the number of pilots, which is in our case the number of odd SCs in the TS.) The remaining error $\boldsymbol{\varepsilon}$ is minimized in the mean square error sense (MMSE-solution), applying the orthogonality principle $E\{\boldsymbol{\varepsilon}\mathbf{p}^{*T}\} = \mathbf{0}$. This leads to the well-known result for the filter \mathbf{W}

$$\mathbf{W} = \mathbf{R}_{\mathbf{h}\mathbf{p}}\mathbf{R}_{\mathbf{p}\mathbf{p}}^{-1}, \quad (6-42)$$

where $\mathbf{R}_{\mathbf{h}\mathbf{p}} = E\{\mathbf{h}\mathbf{p}^{*T}\}$ is the M by L cross-correlation matrix between the channel TF at all sub-carriers and the pilot SCs, and $\mathbf{R}_{\mathbf{p}\mathbf{p}} = E\{\mathbf{p}\mathbf{p}^{*T}\}$ is the L by L autocorrelation matrix of the pilots. Note that \mathbf{p} is corrupted by AWGN, $\mathbf{p} = \mathbf{h}_p + \mathbf{n}$, thus $\mathbf{R}_{\mathbf{p}\mathbf{p}} = E\{(\mathbf{h}_p + \mathbf{n})(\mathbf{h}_p + \mathbf{n})^{*T}\} = \mathbf{R}_{\mathbf{h}_p\mathbf{h}_p} + \sigma_N^2\mathbf{I}_L$, where \mathbf{h}_p is the length L vector of channel attenuations at the pilots, \mathbf{n} is a vector of noise samples of variance σ_N^2 , and \mathbf{I}_L is an L

by L identity matrix. (see e.g. [24], [25] for more details on Wiener filtering)

6.4.1.1 Mean square error

The average mean square error (MSE) of the channel estimates $\hat{\mathbf{h}} = \mathbf{h} + \boldsymbol{\varepsilon}$ is obtained from the main diagonal of the error term's autocorrelation matrix $\mathbf{R}_{\boldsymbol{\varepsilon}\boldsymbol{\varepsilon}}$, i.e.,

$$\sigma_{\boldsymbol{\varepsilon}}^2 = \frac{1}{M} \text{trace}\{\mathbf{R}_{\boldsymbol{\varepsilon}\boldsymbol{\varepsilon}}\}. \quad (6-43)$$

(The trace operator computes the sum over the main diagonal). Assuming that the transformation of the pilots to the channel estimate (filtering) is done with a general linear filter \mathbf{G} ($\hat{\mathbf{h}} = \mathbf{G}\mathbf{p}$), the following expression is obtained for $\mathbf{R}_{\boldsymbol{\varepsilon}\boldsymbol{\varepsilon}}$

$$\mathbf{R}_{\boldsymbol{\varepsilon}\boldsymbol{\varepsilon}} = \mathbf{G}\mathbf{R}_{\mathbf{pp}}\mathbf{G}^{*T} - \mathbf{G}\mathbf{R}_{\mathbf{hp}}^{*T} - \mathbf{R}_{\mathbf{hp}}\mathbf{G}^{*T} + \mathbf{R}_{\mathbf{hh}}, \quad (6-44)$$

where $\mathbf{R}_{\mathbf{hh}}$ is the M by M autocorrelation matrix of the channel vector \mathbf{h} .

This result simplifies to

$$\mathbf{R}_{\boldsymbol{\varepsilon}\boldsymbol{\varepsilon}} = \mathbf{R}_{\mathbf{hh}} - \mathbf{W}\mathbf{R}_{\mathbf{hp}}^{*T}, \quad (6-45)$$

if the filter \mathbf{G} is the Wiener filter $\mathbf{G} = \mathbf{W}$, due to the orthogonality principle applied.

6.4.1.2 Reduction of computations and memory

For instance, in case of TX-mode I-fr, the length of the vector \mathbf{h} is 88 according to the number of data plus pilot SCs. The length of the vector \mathbf{p} is 48. Assuming that the filter matrix \mathbf{W} has been pre-calculated, then the calculation of one channel estimate would require $48 \times 88 = 4224$ complex multiplications, and the same amount of complex filter coefficients. This section describes how to reduce the resources needed for this calculation by linearly combining the most relevant pilots, only.

The most significant noise reduction is obtained by linearly combining the channel estimates of the current and the directly neighboring SCs, since they have the largest correlation among each other. The following scheme is proposed with the design constraint that each estimated channel coefficient should be calculated from L or $L + 1$ pilots, where L is an odd number. Two FIR Wiener filters (of respective lengths L and $L + 1$) are designed for channel estimation on the odd and even SCs. They are applied when there are respectively $(L - 1)/2$ or $(L + 1)/2$ pilots available on *both* sides of the SC to be estimated (see Figure 6-19). It is easily shown that the Wiener filter for any of those odd or even SCs is the same (because the channel is assumed to be wide-sense-stationary in frequency-domain), thus two short FIR filters can be utilized for calculating most of the estimates.

Special treatment is given to the SCs on the band edges, which do not have the required number of pilots on both sides available. The L lowest (and uppermost) pilots are used to estimate the $L - 1$ lowest (and uppermost) SCs. An L by $L - 1$ Wiener filter

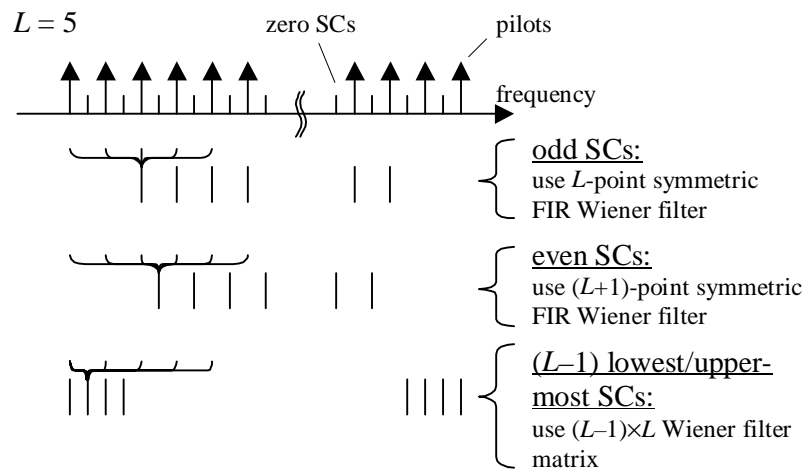


Figure 6-19: Principle of channel estimation at reduced complexity for $L = 5$.

is used for this.

This principle is visualized in Figure 6-19. The required resources reduce to approx. $(L + 0.5) \times 88$ complex multiplications and approx. $L(L + 1)$ complex memory locations for coefficients. E.g., if $L = 5$, this makes 484 multiplications and 30 memory registers, which is a very significant reduction compared to the original numbers. The performance evaluation is presented in Section 6.4.2.

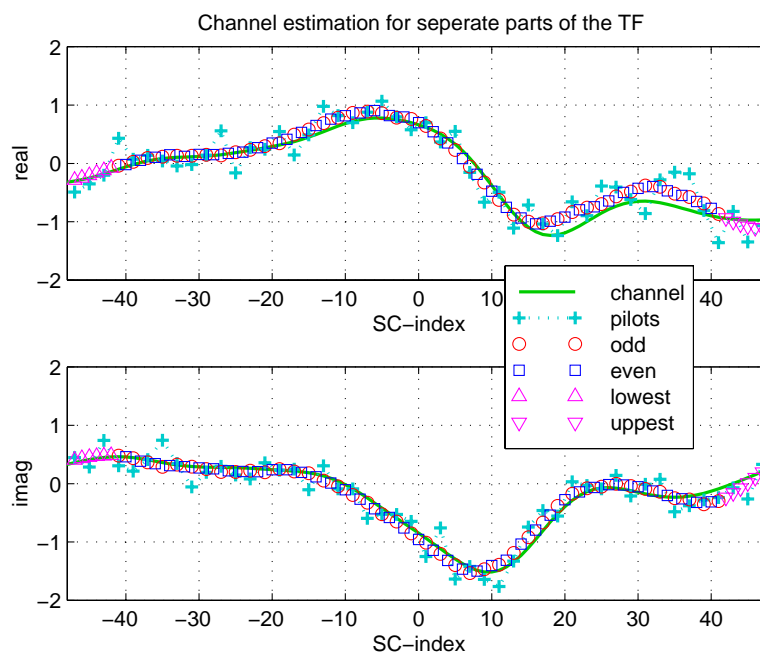


Figure 6-20: Illustration of the enhanced channel estimation scheme at reduced complexity (for $L = 7$). Indicated by 'o', '□', 'Δ', '▽' are the estimated channel coefficients. The original channel without noise is shown by the solid line; the noise-corrupted pilots are marked by '+'. 'o' and '□' are for odd and even SCs, 'Δ' and '▽' are for the lowest and uppermost SCs.

The FIR Wiener filter is designed by replacing the vector $\hat{\mathbf{h}}$ in eq. (6-41) by a single channel coefficient denoted \hat{h} . Accordingly, the matrices \mathbf{W} and \mathbf{R}_{hp} reduce to row vectors \mathbf{w} and \mathbf{r}_{hp} .

Figure 6-20 illustrates how a complete estimate of the channel transfer function is obtained, using the four filters mentioned above.

6.4.1.3 Introducing the Channel Model

The correlation matrices used in designing the Wiener filters must be calculated from the channel model. For the frequency-domain channel model introduced in Chapter 2, the spaced-frequency correlation function is given by (cf. eq. (2-22))

$$\phi_H(\Delta f) = \frac{P_0}{K+1} \left(K + \frac{1}{1 + j2\pi\Delta f\tau_{rms}K_1} \right), \quad (6-46)$$

where the channel is defined by its average power P_0 , its RMS delay spread τ_{rms} , and its Ricean K-factor K , and Δf is the frequency spacing for which the autocorrelation function is evaluated. The constant K_1 relates to the factor K as $K_1 = (K+1)/\sqrt{2K+1}$. An exponentially decaying delay spectrum is assumed, with a direct path at excess delay time $\tau = 0$.

To evaluate the effect of time-synchronization errors, possible timing-offsets are conveniently incorporated in this correlation function. A time-shift δt in the excess delay time-domain – the domain of the Fourier transform of $\phi_H(\Delta f)$ – corresponds to a progressive phase rotation in $\phi_H(\Delta f)$

$$\tilde{\phi}_H(\Delta f) = \phi_H(\Delta f) e^{j2\pi\delta t\Delta f} = \frac{P_0}{K+1} \left(K + \frac{1}{1 + j2\pi\Delta f\tau_{rms}K_1} \right) e^{j2\pi\delta t\Delta f}. \quad (6-47)$$

These continuous time correlation functions can be used to calculate the auto- and cross-correlation matrices needed in the filter design. As an example, the derivation of the vector $\mathbf{r}_{hp} = E\{h\mathbf{p}^{*T}\}$ is demonstrated, which is needed for the calculation of the MMSE filter for the odd SCs. The frequency-spacing of the OFDM sub-carriers is denoted F . Using (6-46) or (6-47) allows to evaluate

$$\begin{aligned} \mathbf{r}_{hp} &= E\{h\mathbf{p}^{*T}\} = E\{h(\mathbf{h}_p + \mathbf{n})^{*T}\} = E\{h\mathbf{h}_p^{*T}\} = \\ &E\{h_i[h_{i-L+1} \quad h_{i-L+3} \quad \cdots \quad h_{i+L-1}]^*\} = \\ &[\phi_H(-(L-1)F) \quad \phi_H(-(L-3)F) \quad \cdots \quad \phi_H((L-1)F)]^* \end{aligned} \quad (6-48)$$

The other correlation vectors and matrices are obtained in an equivalent way.

6.4.2 Computational Results

Performance results are presented in this section in terms of the mean square error

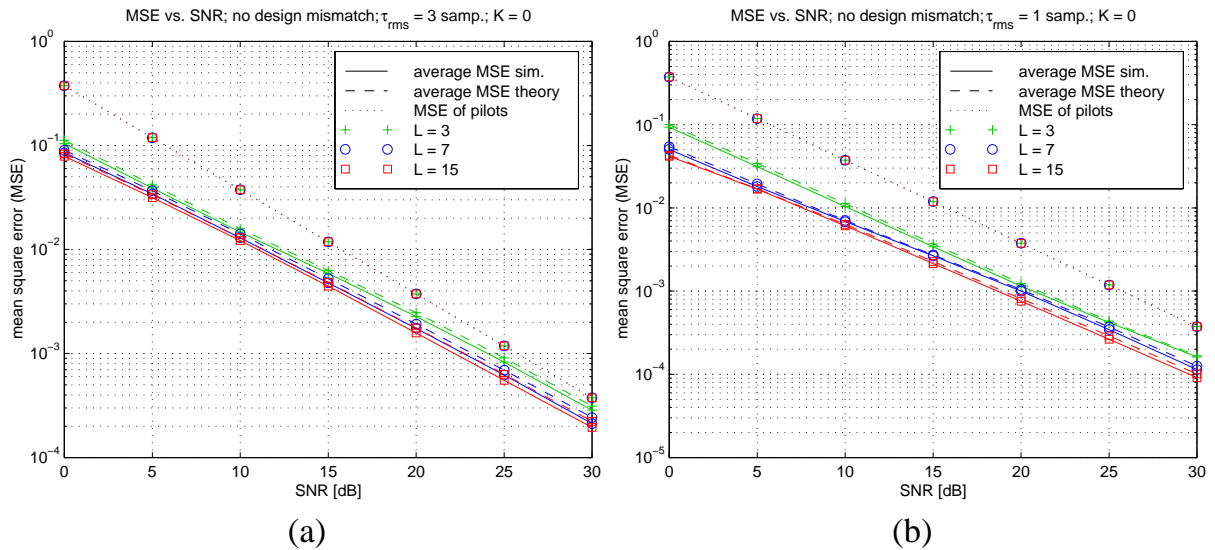


Figure 6-21: Comparison of MSE results vs. SNR for different channel estimation filter lengths. Rayleigh channels; (a): $\tau_{rms} = 3$ samples; (b): $\tau_{rms} = 1$ sample.

(MSE) and bit-error-rate (BER), as a function of the signal-to-noise ratio. Particularly, we investigate the tradeoff between a solution optimized to the current channel/noise parameters and a fixed solution, where a single set of filter parameters is used for a variety of channels. Moreover, the influence of timing-offsets is evaluated with an emphasis on the systematic timing-offset introduced by the timing-synchronization scheme.

6.4.2.1 Number of Multiplications

Firstly, we investigate the influence of the number L of (complex) multiplications per estimated channel coefficient on the mean square error performance. Figure 6-21 compares theoretical and simulation results for different L . Two Rayleigh fading channels are considered with RMS delay spreads of $\tau_{rms} = \{1, 3\}$ samples. The channel estimation filters were optimized (adapted) to these channel parameters and to the current signal-to-noise ratio (SNR). I.e., new filters were designed for each measurement point shown. As a reference, the MSE of the pilot SCs is shown prior to any post-processing. It is seen that using 15 multiplications per channel coefficients, only very small improvements in terms of MSE occur compared to using 3 or 7 multiplications. The gain is slightly more significant for the $\tau_{rms} = 1$ sample channel, since higher correlation between pilots can be exploited. We conclude that a filter length of 3 to 7 is sufficient. Furthermore, in the figure, analytical MSE results are compared to simulation results. The excellent agreement suggests that both types of results are appropriate.

6.4.2.2 Filter Design for Fixed SNR

Figure 6-22 shows MSE results for the case that the channel estimation filters were designed for a fixed SNR, while the channel is varied over a whole range of SNR-values.

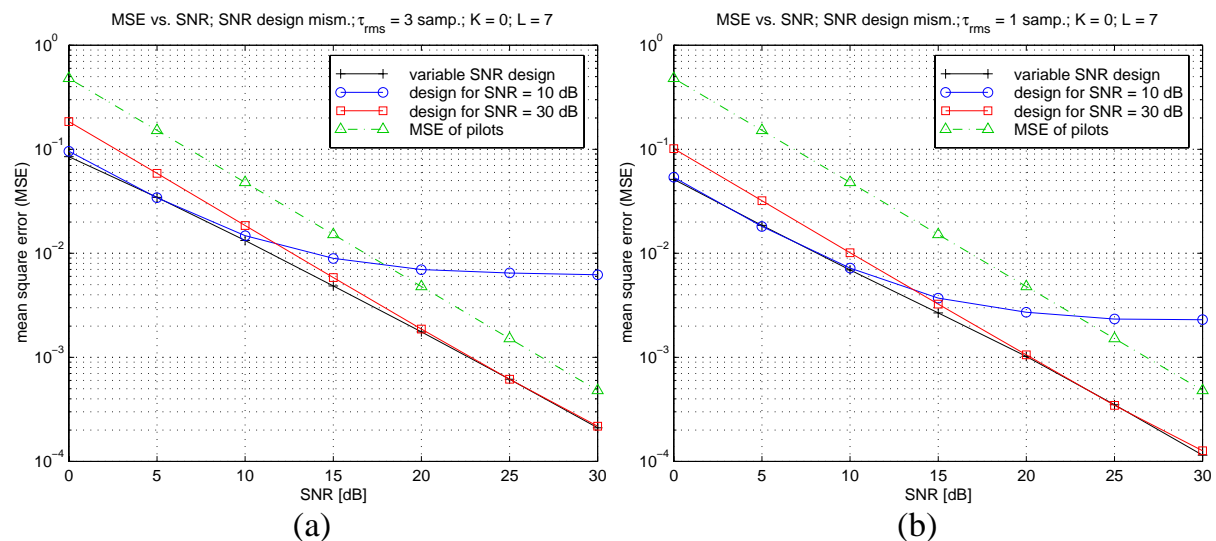


Figure 6-22: Performance of filter designs for fixed SNR in terms of MSE vs. actual SNR. Rayleigh channels; (a): $\tau_{rms} = 3$ samples; (b): $\tau_{rms} = 1$ sample.

The SNR values mentioned relate to the SNR of the pilot SCs. These are approx. 4.3 dB above the time-domain SNR shown on the abscissas of the performance plots. The design for low SNR shows an error floor at high SNR, where the filtered channel estimate is becoming worse than the rough estimate without any filtering. Designing the filter for high SNR means losing some accuracy in the low-SNR range, but the performance stays superior to the unfiltered case. Again it is seen that higher gains can be achieved over less dispersive channels (when the filters are adapted to the channel's RMS delay spread).

6.4.2.3 Filter Design for a Fixed Channel

The next step is the design of a filter for fixed channel parameters (and for fixed SNR = 30 dB). As seen from Figure 6-23, the best common design results from considering the channel with most frequency selectivity (i.e., highest τ_{rms}). No noise floors are observed, when the filters are designed for the $\tau_{rms} = 5$ samples channel (see Figure 6-23c). It is also seen, however, that less is gained over any channel when this design is used. We conclude that a fixed filter design should be done for the channel with the largest τ_{rms} allowed by the guard interval of the OFDM system, and for high SNR.

6.4.2.4 Impact of Timing-Offsets

As seen from eq. (6-47), timing-offsets do have influence on the channel correlation function as well. Therefore, an adaptive Wiener filter has to be optimized for this parameter too. In particular, the bias of the fine timing-offset estimation algorithm presented in Section 6.2.7 should be considered in the design of the channel estimator. The bias is given by eq. (6-14).

Computational results of the MSE estimator performance are shown in Figure 6-24 in

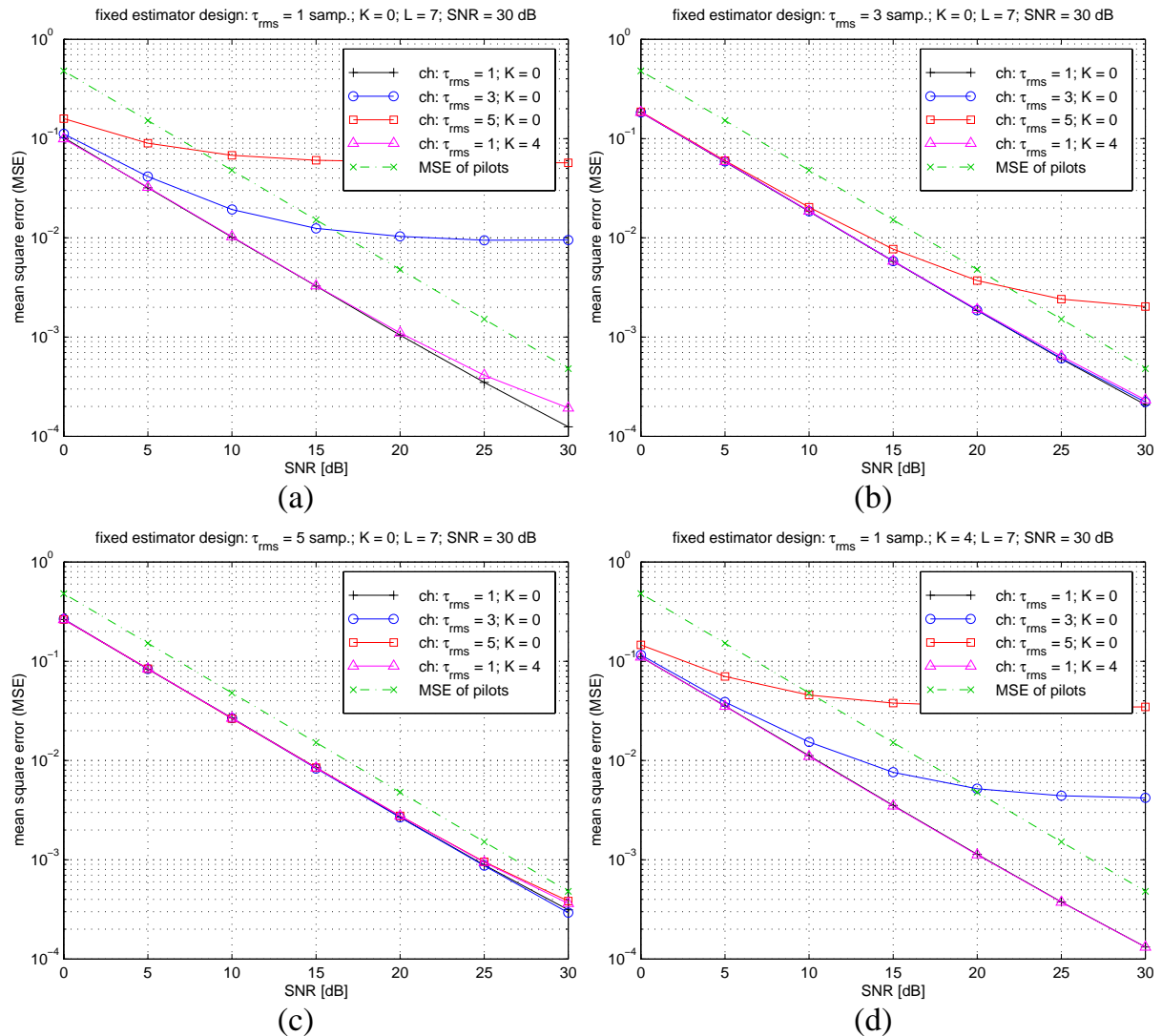


Figure 6-23: MSE performance of channel estimation vs. SNR for fixed estimation filters. The four sub-figures depict results for several channel parameters used for the filter design. (All channel estimators have been designed for SNR = 30 dB). The MSE is evaluated over a range of actual channel parameters.

order to evaluate the importance of this issue. One fixed filter (designed for a $\tau_{rms} = 3$ samples Rayleigh channel at SNR = 30 dB and with $L = 7$) is evaluated over a $\tau_{rms} = 3$ and a $\tau_{rms} = 1$ sample channel, for timing offsets of $\{-3, 0, 3\}$ samples. Quite a significant degradation is evident at high SNR, especially, when the delays are positive. Positive delays mean that the phase of the transfer function increases more rapidly vs. frequency; more rapidly than the phase increase accounted for by the correlation function. This leads to errors. Negative delays, on the other hand, (up to a certain extent) mean slower increase of the phase than the design target, which is less critical for the estimator's performance.

Since the fine timing-offset estimator described in Section 6.2.7 is biased, the channel estimation filter should be designed for such offsets. MSE results for this case are depicted in Figure 6-25, where the filter was designed for a $\tau_{rms} = 3$ samples Rayleigh

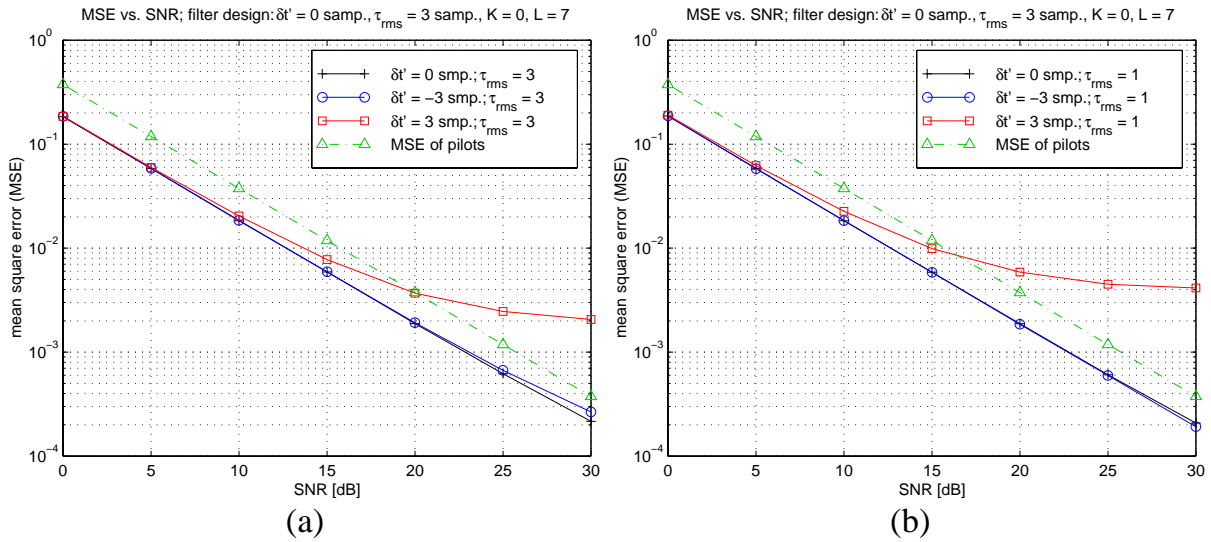


Figure 6-24: MSE results of a fixed channel estimator in presence of timing offset. Filter designed for zero offset, $\tau_{rms} = 3$ samples Rayleigh channel at SNR = 30 dB. (a): Actual channel has $\tau_{rms} = 3$ samples; (b): Actual channel has $\tau_{rms} = 1$ sample.

channel at SNR = 30 dB, and for the corresponding expected timing-offset of 3 samples (see eq. (6-14)). In Figure 6-25a, an actual channel with matching $\tau_{rms} = 3$ samples is investigated for time offsets of {3, 0, 6} samples, corresponding to the expected bias plus {0, -3, +3} samples. The results are almost equivalent to the results shown above in Figure 6-24a. In Figure 6-25b, a channel with $\tau_{rms} = 1$ samples is considered, for time offsets of {1, -2, 4} samples, which is again the expected offset plus {0, -3, +3} samples. Less degradation is seen in this case, which is because the relative positive offset is now smaller than in the case shown in Figure 6-24b.

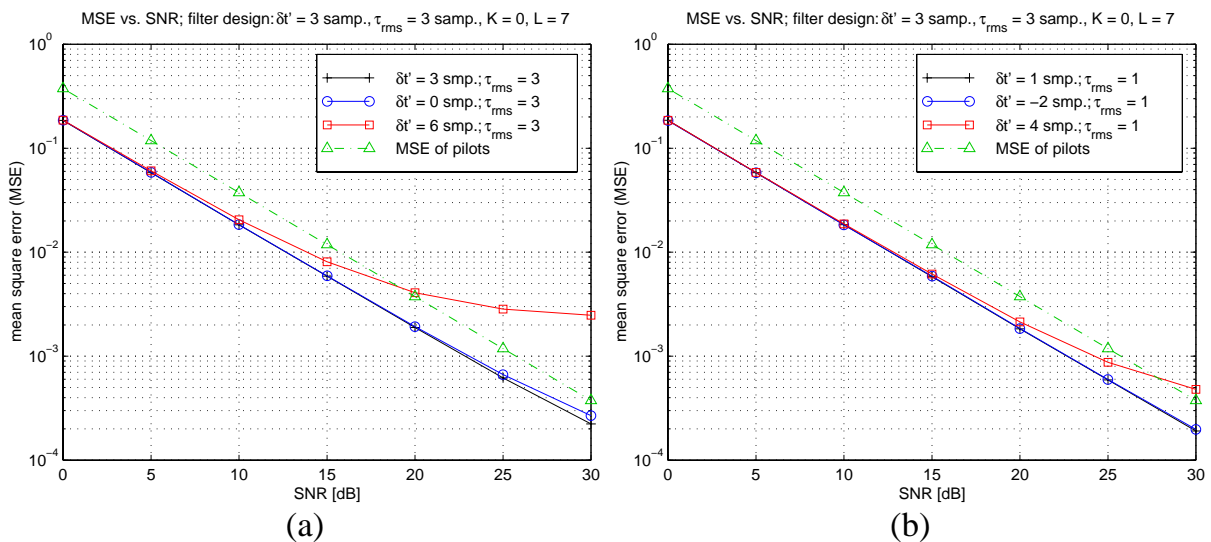


Figure 6-25: MSE results of a fixed channel estimator in presence of timing offset. Filter designed for offset of 3 samples, $\tau_{rms} = 3$ samples Rayleigh channel at SNR = 30 dB. (a): Actual channel has $\tau_{rms} = 3$ samples; (b): Actual channel has $\tau_{rms} = 1$ sample.

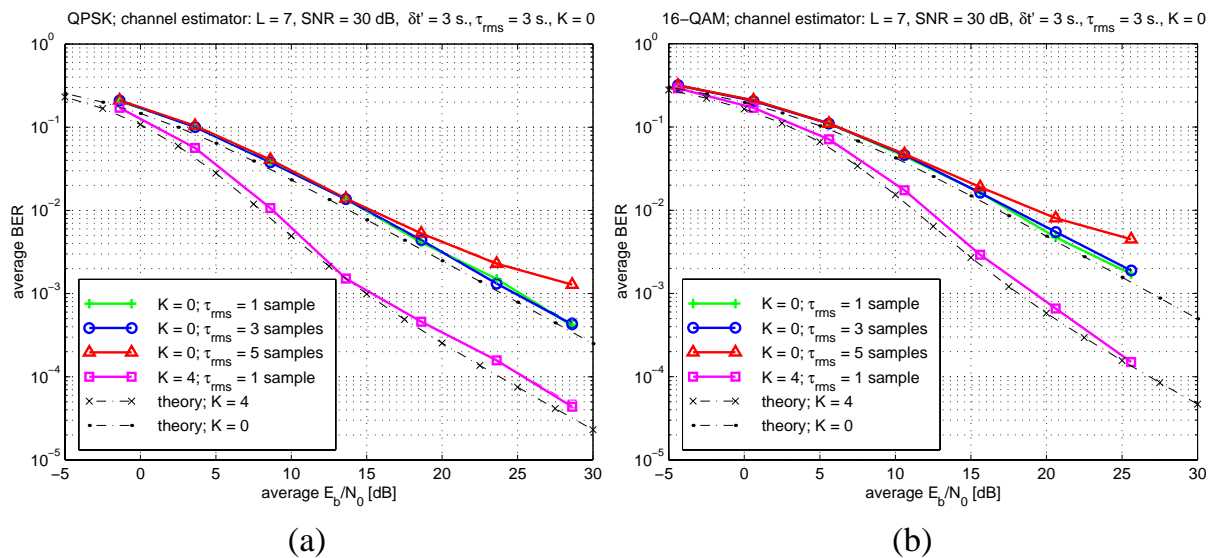


Figure 6-26: BER results vs. SNR for various radio channels. The parameters in the figures' headers specify the design parameters of the channel estimator. (a): QPSK modulation; (b): 16-QAM.

We conclude that the bias of the timing-offset estimation technique might degrade the performance of channel estimation schemes that conduct filtering across the frequency-domain. It is recommended to consider this bias in the design of the channel estimator.

6.4.2.5 Bit-Error-Rate Results

Using the same fixed estimation filter design investigated above ($L = 7$, $SNR = 30$ dB, $\tau_{rms} = 3$ samples, $K = 0$, $\delta t' = 3$ samples), bit-error rate (BER) simulations were performed for various sets of channel parameters. Results are depicted in Figure 6-26 as a function of E_b/N_0 . QPSK and 16-QAM modulation schemes were investigated. Analytical plots are included in the figures as a benchmark, for which perfect channel knowledge was assumed.

A small degradation of approx. 1 dB is evident, compared to the theoretical plots. Only for the $\tau_{rms} = 5$ samples channel, an error floor is seen to arise for high SNR (at the SNR-range depicted). The timing-offset estimation bias was considered in all simulations. Except for the 3-dB difference in E_b/N_0 , results are equivalent for QPSK and 16-QAM modulation. Note that the 3-dB difference in E_b/N_0 is equal to a 6-dB difference in time-domain SNR and in the SNR of the data symbols (sub-carriers), because respectively two and four bits are transmitted per QPSK or 16-QAM symbol.

6.4.2.6 Performance Using the Unfiltered Estimate

In this sub-section, performance results are presented for the basic estimation technique, which just removes the pilot data to obtain the estimates at the odd sub-carriers. To determine the channel coefficients of the even sub-carriers, the estimates of the two

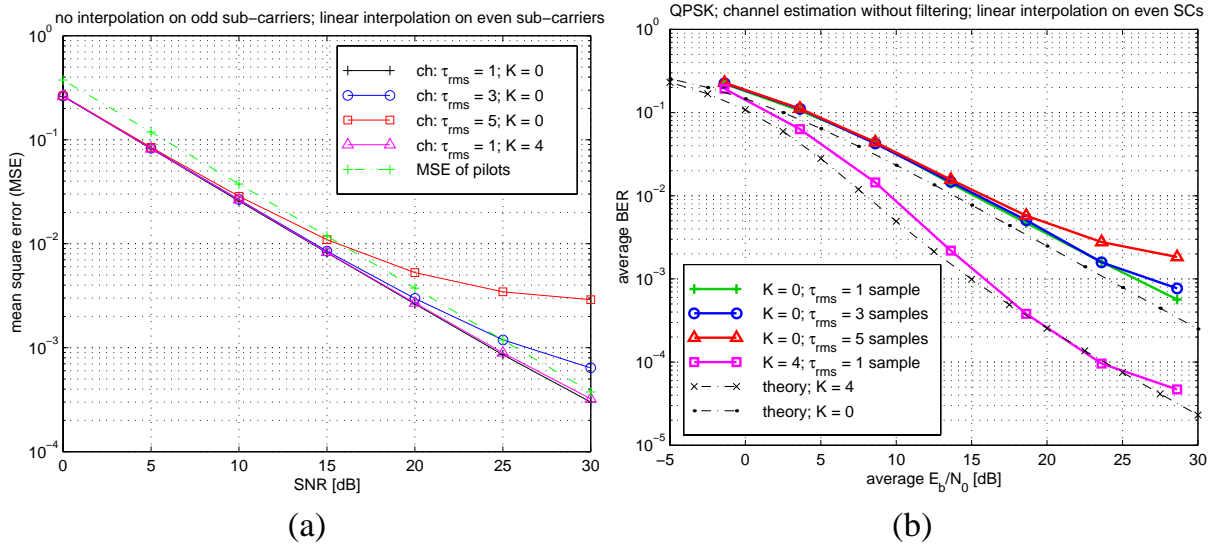


Figure 6-27: Performance of the basic channel estimation method using interpolation at the even sub-carriers and no processing on the odd ones. (a): MSE results; (b): BER results for QPSK.

adjacent carriers are averaged (linear interpolation). Figure 6-27 depicts the performance of this technique in terms of the MSE and the BER for QPSK. It is remarkable to observe that the BER results are hardly worse than the results for the complex scheme evaluated above, although error floors are observed in the MSE results for the channels with more frequency-selectivity (= longer RMS delay spread).

The discrepancy between the average MSE results of the estimate and the MSE of the pilot SCs is due to the averaging used on the even SCs. Averaging two noisy estimates halves the noise variance. Therefore, the average MSE (odd and even SCs) is by about a factor of 1.5 better than the MSE of the pilots, which is also the MSE of the odd SCs. This applies at low SNR, where noise is dominant. At high SNR, the averaging introduces an error compared to the actual channel transfer function, particularly on channels with more frequency-selectivity, i.e., on channels with higher RMS delay spread. In this range, the Wiener solution may show clear advantages, if its design parameters are well selected (see Figure 6-23).

The results of this simple technique are that promising, because the SNR at the pilot SCs is almost double the SNR of data SCs when the average transmitted power is kept constant, as the number of pilots in the TS is about half the number of data SCs. If there were a pilot on each sub-carrier, the average MSE would be a factor of three higher at low SNR. On the other hand, the error floors were not present.

6.4.3 Concluding Remarks

The channel estimation scheme presented in this section is based on periodically transmitted training symbols (TS). The mean-square-error (MSE) of the estimated channel transfer function is reduced by calculating linear combinations of the rough estimates,

which are obtained from the known TS. (Filtering is performed in the frequency-domain.) It has been shown by analysis that with only a few complex multiplications per estimated channel coefficient, the MSE performance of the estimator can be optimized. Even a fixed set of parameters can yield good performance on a wide variety of channels, if selected appropriately. Thereby, the bias of the timing-offset estimator should be considered, as timing-offsets introduce progressive phase-rotations to the data constellations. These phase rotations will be reflected in the channel estimate. It is assumed that an adaptive filter can yield optimum results on a variety of practical channels. However, the computational effort and the complexity increase with every additional processing step.

BER results show that little is gained with the proposed filtering techniques, compared to the most basic estimation method. This basic method just removes the data from the (odd-indexed) sub-carriers to get the channel coefficients. On the even sub-carriers, where no pilot data is transmitted, averaging of two adjacent estimates is performed. The second advantage – next to the surprisingly good performance – is the fact that no adaptability is needed to optimize this estimator. It is therefore recommended to utilize this basic estimation method, in practice.

Note that the time-variability of the radio channel was not considered in the above analysis. This impairment introduces an irreducible error floor to the BER results, as seen from the experimental results below. It will be shown that simple channel prediction techniques are capable of significant improvements.

6.5 Experimental Results

In this section, experimental performance results are presented and discussed, which have been acquired from the emulation system presented in Section 5.3. The main aspects of the implemented OFDM air-interface comply with the system proposal given in Section 5.2. Transmission mode I has been realized, which utilizes a 128-point FFT in the full rate option. The number of OFDM symbols transmitted on the down-link had been fixed to 48 symbols per frame. Pseudo random data was modulated on those symbols using QPSK, in order to determine the bit error rate (BER) at the receiver. 69 symbols comprise one frame, which includes the training symbol and guard symbols for time-division-duplexing. The signal processing steps of the realized OFDM receiver agree with the procedures presented in Section 6.2.

BER performance results and the standard deviation of the fine timing-offset estimation technique (see Section 6.2.7) are presented in Section 6.5.1 for the full-rate receiver. In Section 6.5.2, the BER performance of the quarter-rate receiver is discussed, which demodulates one of the four sub-bands of the transmitted full-rate signal. A general discussion of the results is given in Section 6.5.3. Particularly, we address the performance limitation due to the channel's time-variability, and we analyze a technique to predict these time-variations.

6.5.1 Performance Results for the Full-Rate Receiver

6.5.1.1 AWGN Channel

This sub-section presents performance results for the AWGN channel as a function of the signal-to-noise-ratio (SNR). Several hardware set-ups are compared in order to analyze the impact of various system components. Particularly, the I/Q-modulator and -demodulator were modified in order to study their influence and to evaluate the influence of real-time frequency-synchronization. The following configurations were investigated:

- (1) I/Q-modulator/demodulator excluded
- (2) I/Q-modulator/demodulator included with free-running VCOs
- (3) I/Q-modulator/demodulator included with crystal oscillator (XO) stabilized VCOs (note that two measurements are shown for this set-up)

Figure 6-28 compares bit error rate (BER) results for these cases. Ten measurements were conducted at each SNR-value. About one million of bits were transmitted for each measurement. The BER-curves versus the SNR show the averages of these measurement sets; the error-bars indicate the ranges between the minimum and maximum values observed. An analytical result is shown as a benchmark, where perfect channel estimation is assumed. Compared to this curve marked by 'x', approx. 2 dB of loss are evident for the implemented system. This loss is made up of the imperfect channel es-

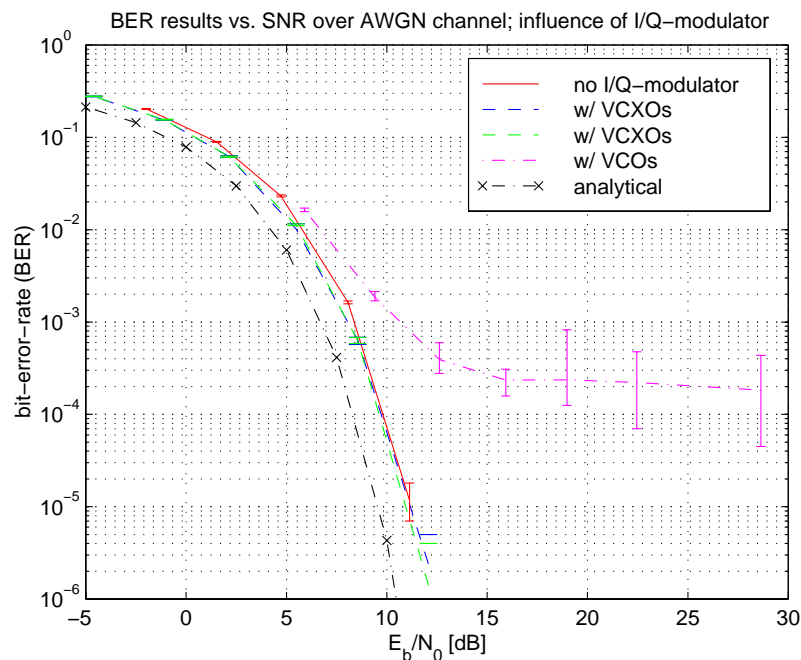


Figure 6-28: Experimental results of bit error rate (BER) as a function of the signal-to-noise ratio (SNR) for AWGN channels. The influence of the I/Q-(de)modulation block can be observed.

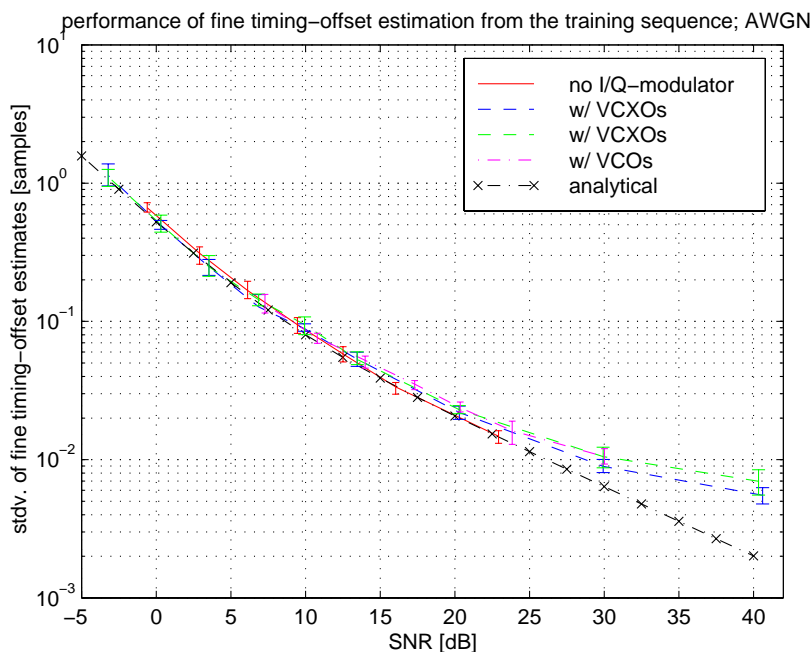


Figure 6-29: Standard deviation of the remaining timing-offset estimation algorithm vs. SNR. AWGN channel. Experimental results.

timization and of hardware-induced implementation losses (non-linearity; intermodulation; etc.). There is no difference between results from set-up (1) – no I/Q-(de)modulation, and set-up (3) – I/Q-(de)modulation using the XOs. This indicates that the real-time frequency-synchronization algorithm is sufficiently robust. An error floor at a BER of approx. $2 \cdot 10^{-4}$ results from the phase noise and frequency jitter of the free-running VCOs for set-up (3), where free-running LC-oscillators were applied.

Standard deviation results for the timing-offset estimator (see Section 6.2.7) indicate that the hardware's influence on this algorithm is negligible (see Figure 6-29). The flattening of the curves observed in the high SNR-region occurs at standard deviation values as low as 0.01 samples and is therefore not investigated further.

6.5.1.2 Performance over Time-variant Rayleigh Channels

The following figures depict performance results over time variant Rayleigh fading channels. Again, the impact of I/Q-(de)modulation using the XOs is investigated by comparison to results without I/Q-(de)modulation. Results are given for two different simulated radio channels. Their common parameter is the RMS delay spread of 3 samples, which corresponds to an impulse response length in the order of the guard interval. The channel-variance was selected according to a mobile moving at 2 and 5 m/s, considering a carrier frequency of 60 GHz

BER results are shown in Figure 6-30. Compared to the analytical curve, for which perfect channel knowledge was assumed, the experimental results show error floors due to the channel's time-variability, because the channel estimate obtained at the be-

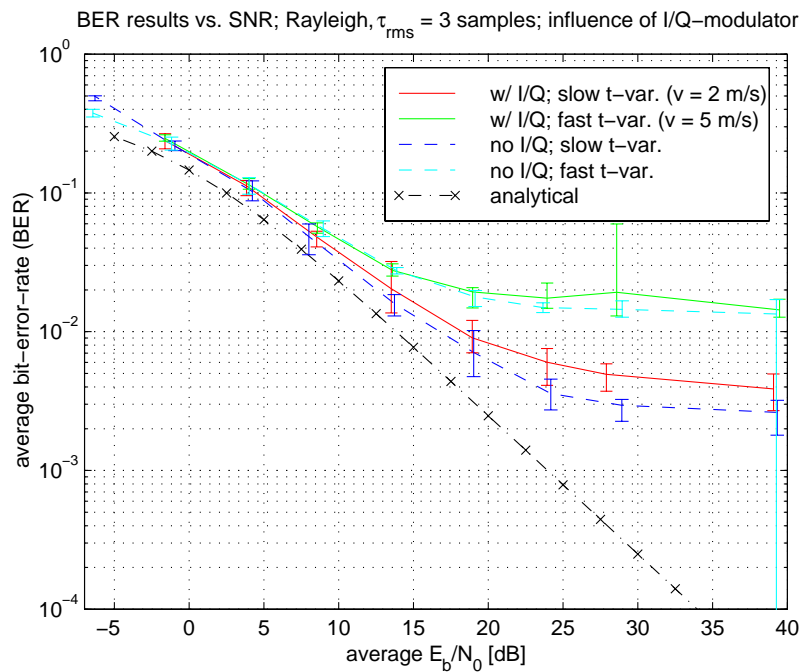


Figure 6-30: Performance results for Rayleigh channels with $\tau_{rms} = 3$ samples and different time-variability. The impact of the real-time frequency-synchronization and of the I/Q-(de)modulation hardware is evident.

gining of each frame is used to demodulate all data symbols of the current frame. Therefore, the performance is worse for the channel with higher velocity. This topic is further discussed in Section 6.5.3.

Inserting the I/Q-(de)modulators with the crystal oscillators leads to some additional degradation. The source of these implementation losses was not fully determined. Reasons for these degradations may include the slightly reduced accuracy of the frequency synchronization – particularly when the received signal is attenuated by a fade –, and inter-carrier interference due to intermodulation distortion.

Experimental results of the standard deviation of the timing-offset estimation algorithm show a behavior different to the simulation results and analytical results shown in Section 6.2.7 (see Figure 6-31 and Figure 6-10). According to these previous results, the multipath-fading channel causes a standard deviation-floor of about one sample for a channel with an RMS delay spread of three samples. The experimental results in Figure 6-31 show this error floor at below one sample. The reason for this behavior is that the experimental result is obtained from the time-difference of two subsequent timing estimates, because no absolute time-reference is available at the receiver. That is, the error floor of the standard deviation curves is caused by the change of the channel transfer function in-between two training symbols. Although this function does change, consecutive realizations are well-correlated, which leads to smaller standard deviation values compared to the theoretical results, where the stan-

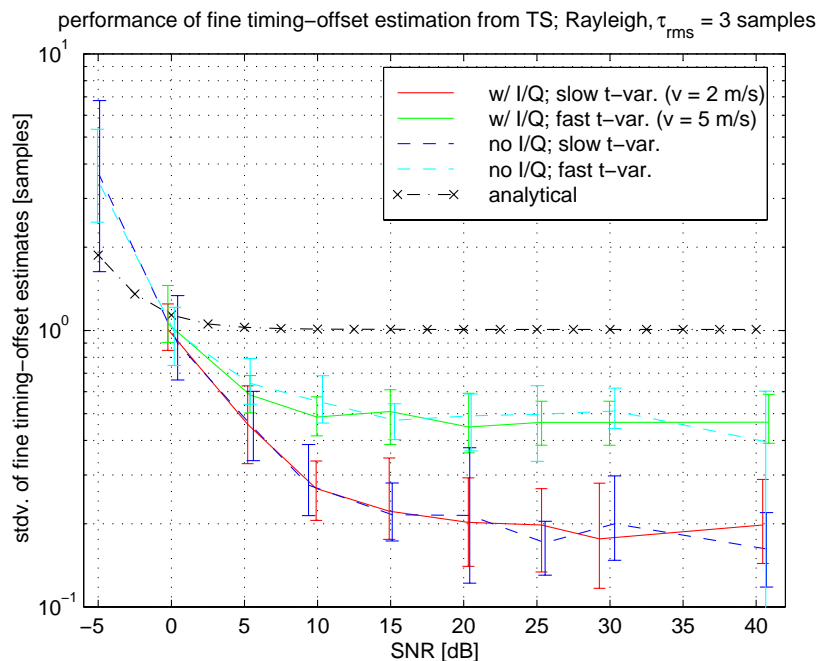


Figure 6-31: Standard deviation of fine timing-offset estimates vs. SNR over Rayleigh channels with $\tau_{rms} = 3$ samples. The influence of the frequency-synchronization is evident.

standard deviation is investigated in case of uncorrelated channel realizations. This also explains the dependency of the results on the mobile’s velocity, as the correlation decreases when the speed increases.

The I/Q-(de)modulation hardware has hardly any influence on this performance measure.

The influence of channel parameters on BER-results is further evaluated in Figure

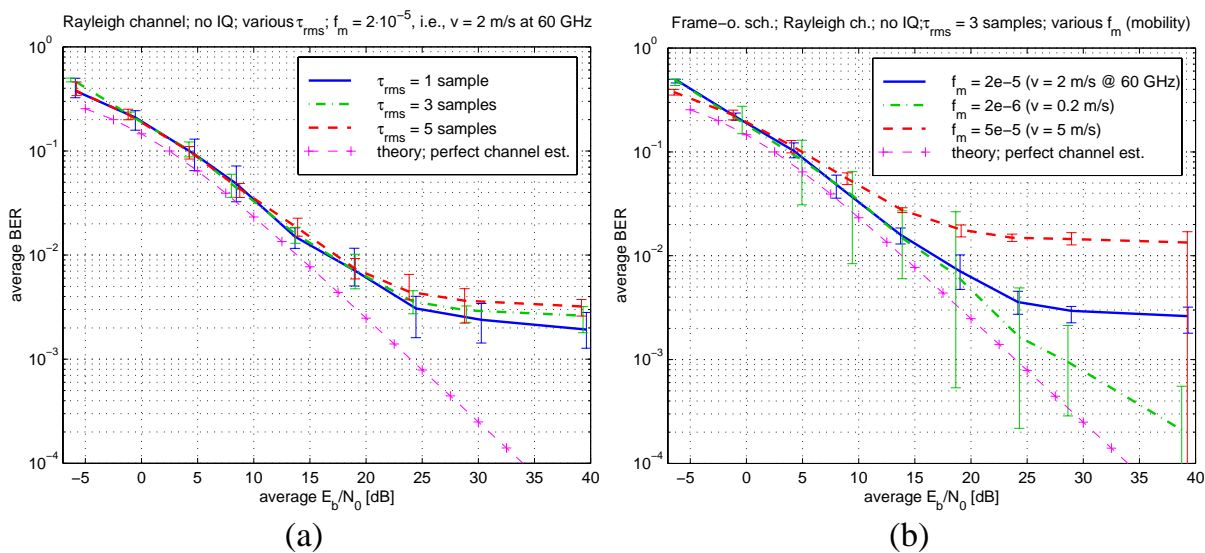


Figure 6-32: BER vs. SNR for Rayleigh fading channels. (a): Dependency of the BER on the RMS delay spread of the channel. (b): Dependency on the mobile’s velocity.

6-32, where the BER performance vs. SNR is depicted for Rayleigh channels with different mobility and different RMS delay spread τ_{rms} . No I/Q-(de)modulation was present. While the impact of τ_{rms} at a given velocity is small (see Figure 6-32a), a clear influence of the mobile's velocity is observed again (see Figure 6-32b). Note that the individual measurement results span a larger range on the slower channels, because the signal may be in a “good” or “bad” fading situation for considerable time while a measurement point is acquired (recall that ten measurements are performed per SNR-value).

6.5.2 Performance Results for the Quarter-Rate Receiver

In this section, experimental results are presented for the down-link from a full-rate (mode I) transmitter (base-station) to a quarter-rate receiver (mobile). The idea of the quarter rate option is to enable mobile-terminals that can access the system with base-band processing algorithms running at one quarter of the sampling frequency. In the system implemented on the emulator, the transmitter operates on 44.1 kHz sampling rate, while the receiver runs on 11.025 kHz (see also below). The anti-alias filters of the receiver's ADCs thereby suppress all signal components that lie outside of the desired frequency band.

6.5.2.1 Results over the AWGN Channel

The BER for the quarter rate receiver vs. SNR is depicted in Figure 6-33. Results for different hardware set-ups are compared to the analytical result for perfect channel estimation. The performance is slightly inferior to the performance of the full-rate receiver given in Figure 6-28.

The degradation with respect to the idealized analytical result has increased to approximately 2.5 – 3 dB, compared to 2 dB for the full-rate mode. Also the irreducible BER, when the free-running VCOs are used, has increased slightly from $2e-4$ to about $4e-4$. These additional losses are most likely due to the smaller accuracy of common phase rotation estimates obtained from the pilots (*cf.* Section 6.2.9), since the full rate mode has 12 pilots to exploit, while the quarter rate mode has only three (see Section 5.2).

To enable the demodulation of any of the four sub-bands, the transmitter can shift the generated signal in frequency by means of multiplication with a complex exponential sequence. In this way, the results were obtained without I/Q-(de)modulators, and with the crystal oscillators stabilized VCOs. Unfortunately, the tuning range of the crystal oscillators is not sufficient to perform this frequency shifting. With the free-running VCOs, however, the shifting can be performed by I/Q-modulation and -demodulation, using local oscillators with an appropriate frequency-offset.

It is quite difficult to accurately measure the SNRs in this transmission mode. The values shown in the figures of these sections are obtained from estimates of the signal plus noise power and of the noise power. Both powers are measured from the time-

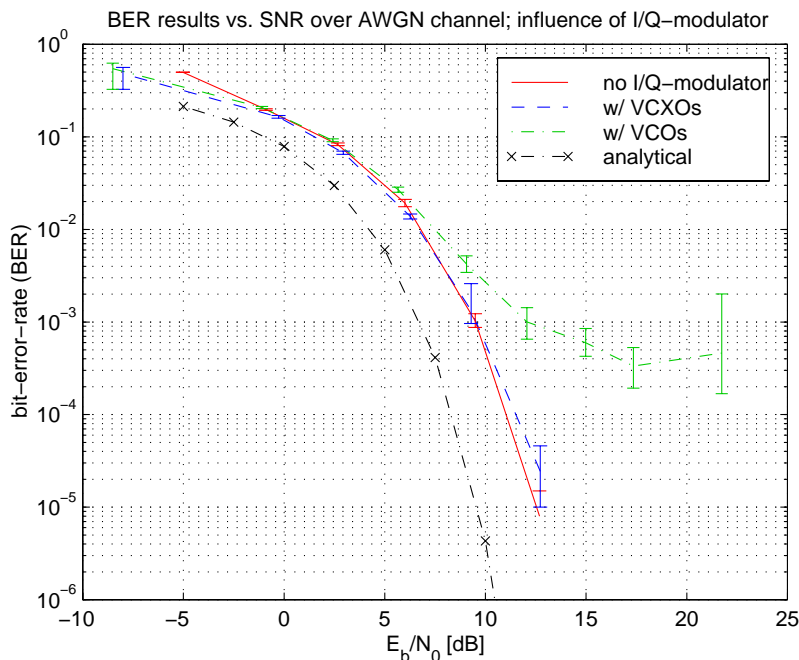


Figure 6-33: BER for the quarter rate receiver vs. SNR. Results for different hardware set-ups are compared to the analytical result for perfect channel estimation.

domain received signal, which is limited in bandwidth by the ADCs' anti-aliasing filters. However, these filters also pass parts of the adjacent sub-bands, therefore it is difficult to estimate which ratio of the signal power belongs to the demodulated sub-band. The 22/29-th part of the incoming signal was assumed to belong to the desired signal, where 22 is the number of data sub-carriers, and 29 is the number of FFT-points minus three zero-carriers.

6.5.2.2 Results over Fading Channels

The potential limitation for the QR-receiver over fading channels is the possible lack of sufficient frequency diversity, in particular, when the channel's RMS delay spread is low. In such cases, the whole OFDM signal may be affected similarly by fades, resulting in significant loss of received signal strength. Apart from extensive error bursts introduced in such situations, the challenge is to stay synchronized. The results shown indicate that our receiver is sufficiently robust for such situations.

Figure 6-34a shows BER-results for a fixed value of RMS delay spread (RDS) τ_{rms} and for several velocities $v = \{0.2, 2, 5\}$ m/s (at 60 GHz). Figure 6-34b depicts the BER for a fixed velocity of 2 m/s and various RDS $\tau_{rms} = \{0.23, 0.7, 1.1\}$. (These values relate to the receiver's sampling rate of 11.025 kHz. At the channel simulator, which is running at 48 kHz sampling rate, $\{1, 3, 5\}$ samples were selected.)

Again a significant dependency on the channel's time-variability is observed, for the same reasons as given above. The average results are not significantly worse than the results for the FR-receiver (compare Figure 6-30), however, the deviation of single

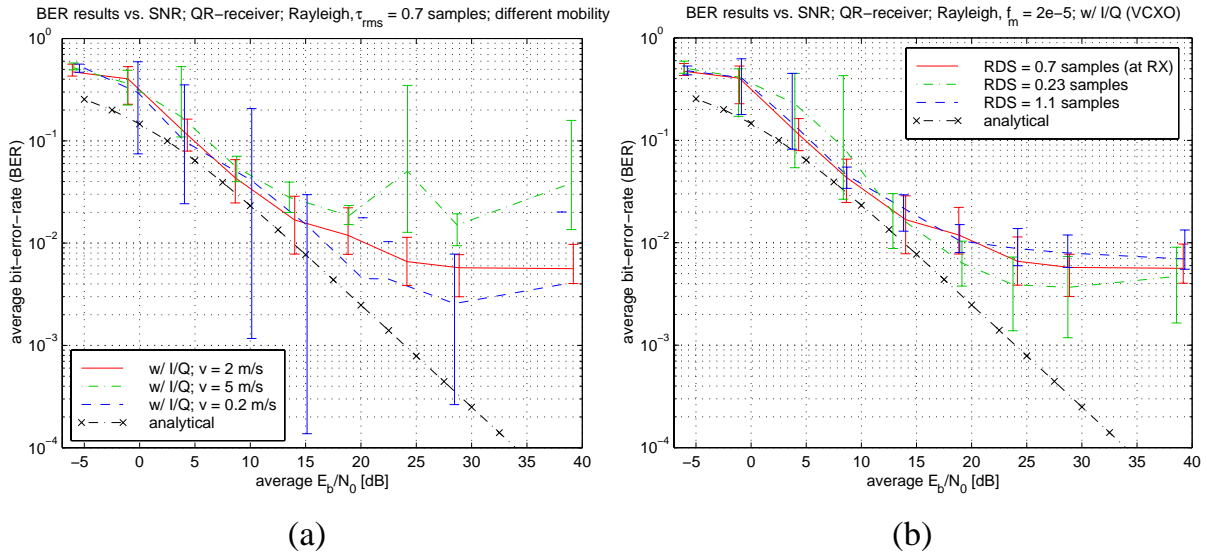


Figure 6-34: BER results vs. SNR for the QR-receiver over Rayleigh fading channels. I/Q-(de)modulators are present, using the VCXOs. (a): Varied mobility. (b): Varied RMS delay spread.

measurement points from the means is increased, especially, for the slowly varying channels and for low RMS delay spread. The reason is the decreased frequency-diversity for the QR-system, which leads to a rather flat fading channel over the reduced bandwidth.

6.5.3 Discussion of the Channel's Time-Variability

For both modes it is seen that the time-variability of the channel leads to irreducible error floors, because the channel estimate obtained at the beginning of a frame is used to demodulate all data symbols of the current frame. The accuracy of this estimate thus decreases for data symbols that are transmitted later within the frame, i.e., with more distance to the training symbol. Assuming that a BER of about 1 % can be still corrected by the coding scheme, it is concluded that the mobility of the system is limited to a maximum speed of about 2 m/s, which is just sufficient for indoor applications (*cf.* Figure 6-30, Figure 6-32, and Figure 6-34). It is desirable to increase the robustness of the system in this respect, in order to reduce the probability of outages and to enhance the applicability of the system.

Computationally simple techniques for tracking/predicting the channel's changes were investigated in the graduation work by David Murargi [26].

The most basic method considered performs linear extrapolation to predict the channel coefficient of the current data symbol, using the channel estimates from the last two training symbols. Denoting the second last and the last estimates at carrier i as $\{\hat{h}_{i,TS_{-1}}, \hat{h}_{i,TS_0}\}$, respectively, the predicted channel coefficient is calculated from

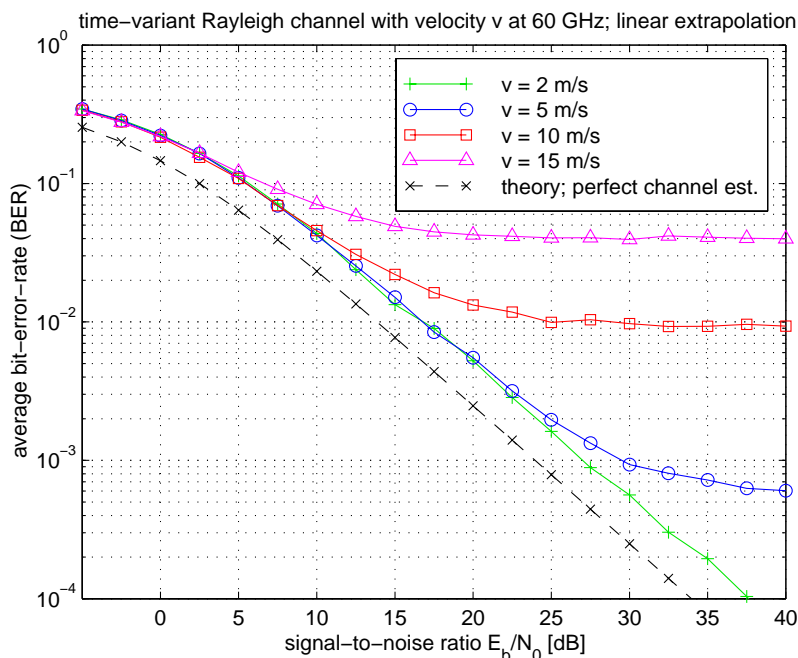


Figure 6-35: Simulated average BER for time-variant Rayleigh fading channels with different mobility. The channel coefficients used for coherent detection of the QPSK symbols were predicted by linear extrapolation using the last two channel estimates derived from training symbols.

$$\hat{h}_{i,k} = \hat{h}_{i,TS_0} + \frac{k}{N_F} (\hat{h}_{i,TS_0} - \hat{h}_{i,TS_{-1}}), \quad (6-49)$$

where $k = \{1, 2, 3, \dots\}$ is the index on the data symbol within a frame (the distance in OFDM symbols of the current data symbol to the training symbol), and N_F is the frame length (the number of OFDM symbols in-between two training symbols). Pre-calculating the (constant) coefficients, it is seen that only two multiplications and one addition are required per predicted channel coefficient. Despite the simplicity of the method, the performance improvement is significant, as seen from the simulation results presented below.

The relevant parameters in the computer simulation were selected according to the OFDM system implemented on the emulation system (and thus according to the OFDM system proposal of Section 5.2), in order to be able to compare the simulation results to the above-presented experimental results. Only one sub-carrier was simulated, having the system model of Section 4.2.3 in mind, which shows that the OFDM sub-carriers can be considered independent under certain conditions. A time-variant Rayleigh channel with a Jakes Doppler spectrum [27] has been implemented (*cf.* Section 5.3.3).

The performance results presented in Figure 6-35 suggest that the maximum velocities allowed have increased by a factor of about four. The significant improvement obtained justifies the small additional complexity.

Even bigger improvements are possible with optimized prediction techniques. For instance, Wiener filters can be used to calculate the predicted channel coefficients from a linear combination of the last L channel estimates. Simulation results from [26] show that thereby a further enhancement of the maximum speed is possible, by a factor of about two. The big disadvantage of this technique is that the Wiener filter is only appropriate for one particular velocity. Adaptive filters are required to obtain optimum results. Otherwise, sub-optimum performance is achieved, comparable to the estimation problem discussed in Section 6.4. Moreover, the computational complexity of these techniques is significantly higher.

6.5.3.1 Inter-Carrier-Interference due to Doppler Spread

The inter-carrier-interference (ICI) (interference among sub-carriers of the OFDM scheme) induced by the Doppler spread of the radio channel is another issue related to the channel's time-variability. The analysis below shows that this problem is negligible for the system proposal under investigation.

In [6], [28] two approximations are given for the carrier-to-interference ratio (CIR) due to Doppler spread, assuming the “classical” Jakes Doppler spectrum. The equations presented are equivalent, except for a small constant factor. We therefore restrict the analysis to the more conservative one, which is presented in [6]. It is written as

$$CIR = \frac{6}{\pi^2} \frac{F^2}{f_m^2}, \quad (6-50)$$

where F is the frequency-spacing among sub-carriers and f_m is the maximum Doppler frequency, $f_m = v_m \cdot f_c / c$ (v_m is the mobile's velocity, f_c is the carrier frequency, and c is the speed-of-light). This yields respectively $CIR = \{46, 40 \text{ dB}\}$ for transmission modes I and II where $F = \{1, 0.5 \text{ MHz}\}$, at $v_m = 20 \text{ m/s}$. Even for this velocity, being about an order of magnitude higher than the design target, no considerable degradation is expected due to ICI, due to the relatively large sub-carrier spacing.

6.5.4 Conclusions and Recommendations

Its implementation on an experimental platform (the so-called “emulation system” presented in Section 5.3) strongly supports the claim that the proposed OFDM system is suitable for the application considered, i.e., for indoor wireless LANs. Particularly the synchronization scheme developed has proven robust and reliable over the channels that are expected in such environments. Good performance was observed even for the “worst-case scenario”, a time-variant, frequency-selective Rayleigh channel with a delay profile about 20 % longer than the guard interval. More critical is the performance of the quarter rate-receiver. Its small bandwidth (only 22 sub-carriers are used in mode I-qr) leads to situations where the whole signal is attenuated by a fade, because the frequency-diversity of the wide-band signal cannot be sufficiently exploited. It is recommended to implement frequency hopping to reduce this issue.

The small implementation losses also indicate the suitability of the emulation system's hardware for the demonstration of OFDM systems. It has to be assumed, however, that the emulator's hardware with its downscaled bandwidth of about 40 kHz is far superior to the hardware of a real system at 60 GHz, which has a bandwidth of about 100 MHz.

One of the main impairments seen from the BER-results is due to the time-variability of the radio channel. In the implemented scheme, the channel estimate derived at the beginning of a frame from the known training symbol is used to demodulate the data of 48 consecutive OFDM symbols. As the channel changes continuously, the inaccuracy of this estimate increases, which leads to an irreducible error floor. The maximum velocity allowed by such an estimation scheme is in the order of 2 m/s, according to the experimental results. This is just sufficient for an indoor system. But it may be insufficient, if there are fast moving objects in the room, like machinery or automated vehicles in a production facility. Simulation results have indicated that a basic channel prediction scheme can increase the allowed mobility up to about 8 m/s, at a small increase in complexity.

6.6 References

- [1] T. M. Schmidl and D. C. Cox, "Robust frequency and timing synchronization for OFDM," *IEEE Trans. Commun.*, vol. 45, no. 12, pp. 1613–1621, Dec. 1997.
- [2] Y. H. Kim, Y. K. Hahm, H. J. Jung, and I. Song, "An efficient frequency offset estimator for timing and frequency synchronization in OFDM systems," in *Proc. IEEE 1999 Pacific Rim Conf. on Commun., Computers and Signal Proc.*, pp. 580–583.
- [3] D. Matic, N. Petrochilos, A.J.R.M. Coenen, F. Schoute, R. Prasad, "Acquisition of synchronisation parameters for OFDM using a single training symbol," in *Proc. Second International Workshop on Multi-Carrier Spread-Spectrum and Related Topics*, Oberpfaffenhofen (Germany), Sept. 1999.
- [4] P. H. Moose, "A technique for orthogonal frequency division multiplexing frequency offset correction," *IEEE Trans. Commun.*, vol. 42, no. 10, pp. 2908–2914, Oct. 1994.
- [5] J.-J. van de Beek, M. Sandell and P. O. Börjesson, "ML estimation of time and frequency offset in OFDM systems", *IEEE Trans. Signal Processing*, vol. 45, no. 7, pp. 1800–1805, July 1997.
- [6] M. Speth, S. A. Fechtel, G. Fock, and H. Meyr, "Optimum Receiver Design for Wireless Broad-Band Systems Using OFDM—Part I," *IEEE Trans. Commun.*, vol. 47, no. 11, pp. 1668–1677, November 1999.

- [7] B. McNair, L. J. Cimini, Jr., N. Sollenberger, “A Robust Timing and Frequency Offset Estimation Scheme for Orthogonal Frequency Division Multiplexing (OFDM) Systems,” in *Proc. IEEE 49th Vehicular Techn. Conf. (VTC’99-spring)*, Houston, USA, May 1999, pp. 690–694.
- [8] N. Petrochilos, A. Trindade, D. Matic, and R. Prasad, “Blind Channel Synchronization and Equalisation Algorithm for OFDM Wireless Communications,” in *Proc. WPMC 2001*, Aalborg, Denmark, Sept. 2001.
- [9] D. Lee and K. Cheun, “A new Symbol Timing Recovery Algorithm for OFDM Systems,” *IEEE Trans. Consumer Elec.*, vol. 43, no. 3, pp. 767–775, Aug. 1997.
- [10] D. K. Kim, S. H. Do, H. B. Cho, H. J. Choi, and K. B. Kim, “A New Joint Algorithm of Symbol Timing Recovery and Sampling Clock Adjustment for OFDM Systems,” *IEEE Trans. Consumer Elec.*, vol. 44, no. 3, pp. 1142–1149, Aug. 1998.
- [11] D. Matic, N. Petrochilos, A. Trindade, F. Schoute, P. Comon, and R. Prasad, “OFDM Synchronization Based on the Phase-Rotation of Sub-Carriers,” in *Proc. IEEE 51st Vehicular Techn. Conf. (VTC 2000-spring)*, Tokyo, Japan, May 2000, pp. 1260–1264.
- [12] J. G. Proakis, *Digital Communications*, 3rd Edition. New York: McGraw Hill, 1995.
- [13] H. Minn and V. K. Bhargava, “A simple and efficient timing offset estimation for OFDM systems,” in *Proc. IEEE 51st Vehicular Techn. Conf. (VTC 2000-spring)*, Tokyo, Japan, May 2000, pp. 51–55.
- [14] P. Teneva, “Pseudo Real-time Simulation of an OFDM System for Wireless Broadband Communications: OFDM Transmitter,” *Research Report*, IRCTR, Delft University of Technology, Jan. 1999.
- [15] K. Büke, “Assessment of OFDM Based Air-interface Techniques Using an Emulation Platform: Investigation and Implementation of OFDM Synchronization Algorithms,” *M.Sc. Thesis*, IRCTR S-001-00, Delft University of Technology, Jan. 2000.
- [16] I. Gultekin, “DSP Software Implementation for a Broadband Air-interface Emulation Platform: Onderzoek naar de seriële interace tussen de PC an de DSP board en het maken van een GUI voor de DSP applicaties,” *Graduation Thesis*, Haagse Hogeschool, June 2000 (in Dutch).
- [17] A. Snijders, “Emulator: De testopstelling voor OFDM,” *Graduation Thesis*, IRCTR S-030-00, Technische Hogeschool Rijswijk, Nov. 2000 (in Dutch).
- [18] P. Pollet, M. van Bladel, and M. Moeneclaey, “BER sensitivity of OFDM systems to carrier frequency offset and Wiener phase noise,” *IEEE Trans. Commun.*, vol. 43, no. 2/3/4, pp. 191–193, Feb./March/April 1995.

- [19] K. Witrisal, K. Büke, Y.-H. Kim, R. Prasad, and L. P. Ligthart, "Air-interface Emulation for Wireless Broadband Communications Applied to OFDM," in *Proc. IEEE Symposium on Personal Indoor and Mobile Radio Communications (PIMRC'2000)*, London, Sept. 2000, pp. 1251–1255.
- [20] K. Witrisal, Y.-H. Kim, R. Prasad, and L. P. Ligthart, "Experimental Study and Comparison of OFDM Transmission Techniques," in *Proc. 5th international OFDM-Workshop*, Hamburg (Germany), Sept. 2000, pp. 5-1–5-5.
- [21] O. Edfors, *Low-complexity algorithms in digital receivers*. Ph.D. Thesis, Luleå University of Technology, Sept. 1996.
- [22] M. Sandell, *Design and Analysis of Estimators for Multicarrier Modulation and Ultrasonic Imaging*. Ph.D. Thesis, Luleå University of Technology, Sept. 1996.
- [23] P. K. Frenger, N. Arne, and B. Svensson, "Decision-directed coherent detection in multicarrier systems on Rayleigh fading channels," *IEEE Trans. Veh. Technol.*, vol. 48, no. 2, pp. 490–498, March 1999.
- [24] L. L. Scharf, *Statistical Signal Processing: Detection, Estimation, and Time Series Analysis*, Addison-Wesley, 1991.
- [25] C.W. Therrien, *Discrete Random Signals and Signal Processing*. Englewood Cliffs: Prentice Hall, 1992.
- [26] D. Murargi, "Channel Estimation Enhancement in OFDM Systems for Wireless Multimedia Communications," *Graduation Thesis*, Delft Univ. of Technol., Rep. Nr. IRCTR: S-023-01, July 2001.
- [27] W. C. Jakes Jr., *Microwave Mobile Communications*. New York: Wiley-Interscience, 1974.
- [28] Y. Zhao and S. Haggman, "Sensitivity to Doppler Shift and Carrier Frequency Errors in OFDM Systems – The Consequences and Solutions," in *Proc. IEEE 46th Vehicular Techn. Conf. (VTC 1996)*, Atlanta, GA, USA, April/May 1996, pp. 1564–1568.

Chapter 7 – DSP Algorithm Development for the Up-Link

7.1 Introduction

In this chapter, the potential of a pre-equalization scheme for the up-link of a time division duplex (TDD) OFDM system (see Section 5.2) is investigated. The application of this principle is suggested to enhance the spectral efficiency by omitting the usage of training sequences on the up-link. This is desired in order to enable the efficient transmission of very short data packets, like single ATM cells, without adding the overhead of a training symbols to each packet. Moreover, at the base station, the complexity of synchronization is kept low, which is of advantage considering that the base station has to serve multiple mobile users at extremely high data rates.

The main purpose of applying pre-equalization is to enable coherent detection without channel estimation. With pre-equalization, the frequency-selective channel is turned flat or phase linear, depending on the pre-equalization technique implemented and on the modulation scheme. Basic strategies are described to thereby keep the transmission power constant. In one of the schemes described, for instance, this is achieved by attenuating strong sub-carriers while weak ones are boosted. Sub-carriers that are very severely attenuated by fades are set to zero in order to limit the overall attenuation. Synchronization steps for retrieving the data at the base-station are explained and evaluated. Those include the estimation of the timing-offset, the carrier phase offset, and the received magnitude.

In Section 7.2, the concept of pre-equalization is introduced and discussed, and the mathematical models of OFDM are reviewed. Section 7.3 studies the power-limiting techniques, followed by a number of performance results in Section 7.4. The synchronization steps required for the coherent detection of the up-link data streams are out-

lined and coarsely evaluated in Section 7.5. Section 7.6 shows experimental performance results derived with the emulation platform of Section 5.3. Conclusions are drawn in Section 7.7.

7.2 Pre-Equalization in OFDM

7.2.1 OFDM System Model

Assuming an OFDM system using a guard interval (GI), a dispersive radio channel with a maximum excess delay being shorter than this GI, and perfect synchronization, the OFDM system can be modeled as a set of parallel Gaussian channels (see Section 4.2.3). On the input of this system model, which is written as

$$y_{i,k} = x_{i,k} h_{i,k} + n_{i,k}, \quad (7-1)$$

are the symbol constellation points $\{x_{i,k}\}$ that are applied to the IFFT block of the transmitter; at its output are the constellation points $\{y_{i,k}\}$ after the receiver's FFT. i is the index on the subcarrier (SC), being proportional to the SC's distance to the center frequency, and k is the OFDM symbol index, a time-variable. The attenuation factors $\{h_{i,k}\}$ and the AWGN samples $\{n_{i,k}\}$ denote the channel's influence on the transmitted symbol constellation points. Since these factors are complex-valued, each constellation point typically suffers attenuation according to the magnitude of $\{h_{i,k}\}$, and phase rotation according to its phase.

Note that the attenuation factors seen as a function of frequency and time are equivalent to the transfer function of the channel $h_{i,k} = H(iF, kT)$. (F is the frequency-spacing of adjacent SCs; T is the total OFDM symbol period.) In a real environment, this is usually a time-variant function. Within the transmission of a few subsequent OFDM symbols however, the channel can be considered time-invariant. Therefore, the time-index k will be neglected in the mathematical expressions describing the pre-equalization scheme.

7.2.2 Impact of Synchronization Errors

Small synchronization errors, i.e., timing errors δt in the order of a few samples ($<$ length of the GI), frequency offsets δf of a few percent of F , and carrier phase offsets θ introduce additional phase rotations (and inter-carrier-interference) (see Section 4.2.4). Incorporating these offsets, the system model becomes

$$y_{i,k} = x_{i,k} h_{i,k} \text{sinc}(\delta f T_{FFT}) e^{j\Psi_{i,k}} + n'_{i,k}, \quad (7-2)$$

with

$$\Psi_{i,k} = \theta + 2\pi\delta f \left(kT + \frac{T_{FFT}}{2} + \delta t \right) + 2\pi\delta t \left(\frac{i}{T_{FFT}} \right). \quad (7-3)$$

T_{FFT} is the effective FFT period, the part of the (received) OFDM symbol applied to the FFT for demodulation, and $n'_{i,k}$ is the noise term incorporating inter-carrier-interference in case of a frequency-offset.

7.2.3 Channel Reciprocity and Pre-Equalization

The assumption of reciprocity in the context of an OFDM system means that a SC transmitted on the up-link at a certain frequency suffers the same attenuation and phase rotation as a SC transmitted on the down-link at the same frequency. In other words, the channel transfer functions on the up-link and down-link are equivalent.

The idea of pre-equalization seeks to exploit this property in the context of a time-division duplex (TDD) scheme. The receiver performs channel estimation and synchronization on the down-link, obtaining an estimate of the channel attenuation factors $\{\hat{h}_i\}$. (Note that the time-index k is being omitted from here on.) Multiplying the constellation points of the up-link data symbols with the inverse of these factors $\{1/\hat{h}_i\}$ prior to applying them to the transmitter's IFFT will cancel the signal distortion by the up-link channel, thereby simplifying the detection of the data at the base-station.

In such a system, down-link and up-link data packets will be transmitted at the same frequency band in an alternating pattern (see Section 5.2). It is obvious that the channel should not change after its estimation on the down-link until the estimate is used on the up-link for pre-equalization. Small variation leads to error floors in uncoded BER-results, as seen from the experimental data presented in Section 7.6.

Another problem of pre-equalization is the large power required for faded SCs. Assume for instance, a SC is in a deep fade, i.e., it is attenuated by say 30 dB compared to the average SC-energy. In order to compensate for this attenuation, the SC would have to be boosted by 30 dB, requiring a large amount of transmission power and a high DAC-resolution at the mobile²¹. Section 7.3 describes approaches of limiting the additional transmit power needed.

7.2.4 Is the Channel Reciprocal?

Reciprocity is a property of the radio channel, which is commonly accepted by radio engineers. It has been used in several system proposals and theoretical studies, because it leads to a number of potential advantages [1]–[6]. In TDD-code division multiple access (CDMA) systems, for instance, pre-rake filtering has been proposed for the transmitter, which can eliminate the need for a rake receiver at the mobile (if applied for the down-link), or it can simplify multi-user detection at the base station [2]–[4].

Other advantages of TDD schemes include antenna diversity or beam-forming tech-

²¹ Another reason for why it is problematic to do perfect pre-equalization for such deeply faded SCs is that their phases typically change quickly during deep fades. Therefore, even if the transmit power can be provided, the phase may be wrong, leading to a wrong decision (*cf.* [1]).

niques, where, at the base-station, a combining scheme optimized for the up-link can be used on the down-link as well. TDD schemes can also apply closed loop power control [2], [5].

Some studies, however, report on non-reciprocal behavior of the mobile radio channel [7], [8], which would eliminate the above-mentioned advantages. In [7], electromagnetic coupling effects are suggested as the source for asymmetries. Concerning interference effects, there is no doubt that differences exist between the up- and down-links. Asymmetries may also exist in the RF front-ends between reception and transmission. These fixed differences can be compensated by means of calibration. It is possible that such asymmetries and the required calibration may be affected by electromagnetic coupling.

At the time being, we cannot draw final conclusions on the possibility of exploiting channel reciprocity in the proposed transmission scheme. The potential advantages offered by such a scheme, however, have motivated the study presented in this chapter.

7.3 Power Limiting Strategies for Pre-equalization

This section describes strategies of limiting the power amplification due to pre-equalization. We will seek constant output power after pre-equalization.

7.3.1 Phase Pre-Equalization for Phase-Modulation Schemes

For pure phase modulation schemes, like QPSK, it is sufficient to perform the pre-equalization for the phase of the constellation values, turning the channel phase-linear. This means multiplying the data constellation points $d_i \in \{e^{j2\pi m/M}\}$ ($m = 0, 1, \dots, M-1$ for M -ary modulation) with a phase factor equal to the inverse of the channel's phase rotation:

$$x_i = d_i e^{-j\angle \hat{h}_i} \quad (7-4)$$

Applying these symbols to the parallel Gaussian channels of the OFDM system model (7-1) yields at the receiver

$$y_i = d_i e^{-j\angle \hat{h}_i} h_i + n_i = d_i |h_i| e^{j[\angle h_i - \angle \hat{h}_i]} + n_i. \quad (7-5)$$

Assuming that the channel estimate's phase has been correct, the phase distortion term becomes zero. Thus the received symbols suffer from attenuation according to the magnitudes $\{|h_i|\}$ and from additive noise. Figure 7-1 depicts such distorted symbol constellations for QPSK-modulated SCs. Note that there will be systematic phase rotations in the presence of synchronization errors, which can be estimated from pilot SCs or from the limited symbol alphabet properties of the data symbols. These systematic phase distortions must be corrected.

Performance results are shown and discussed in Section 7.4.1.

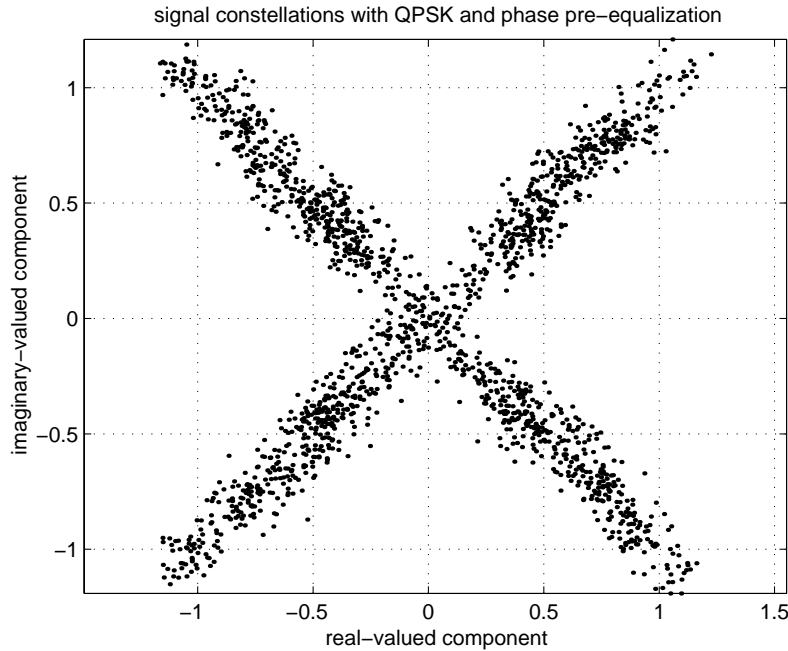


Figure 7-1: Received signal constellation points with phase pre-equalization for QPSK. Additive noise is present but no synchronization-offsets on the up-link.

7.3.2 Phase and Magnitude Pre-Equalization with Power Limiting

Higher order modulation schemes, as 16-QAM, need phase and magnitude estimates for simplifying their coherent detection. Accordingly, pre-equalization must also compensate for the different attenuation factors at the OFDM-SCs.

Ideal pre-equalization is written mathematically as

$$x_i = d_i e_i, \quad e_i = \hat{h}_i^{-1}, \quad (7-6)$$

where the $\{e_i\}$ denote the pre-equalization function being simply the inverse of the channel estimate, and the $\{d_i\}$ stand for the constellation points of the modulation scheme. As mentioned above, this technique might significantly boost the average power of the constellation points $\{x_i\}$, causing the output power to vary largely depending on the current channel. Since such effects are not desirable in digital communications systems, methods are proposed to limit or eliminate them.

7.3.2.1 Normalization

The method presented in this section normalizes the pre-equalization function, resulting in constant transmitted power. This normalization is achieved by dividing the $\{e_i\}$ by their RMS value, written

$$\tilde{e}_i = e_i \sqrt{\frac{N_{SC}}{\sum_{i \in i_{SC}} |e_i|^2}} = \hat{h}_i^{-1} \sqrt{\frac{N_{SC}}{\sum_{i \in i_{SC}} |\hat{h}_i^{-1}|^2}}, \quad (7-7)$$

where N_{SC} is the total number of used (data & pilot) SCs, and i_{SC} are their indices. This normalization will actually lead to an attenuation of the average received power. While SCs being largely attenuated by the channel are boosted by the pre-equalization technique, the power of strong sub-carriers must be reduced to keep the transmitted power constant. It is seen from eq. (7-7) that very small channel estimates $\{\hat{h}_i\}$ will have a large contribution to the RMS value of the normalization term, leading to greater attenuation on the average. We will seek to limit the maximum attenuation.

The attenuation factor due to pre-equalization is defined as the ratio of the normalized received powers with and without pre-equalization,

$$A_{pre} = \frac{P_0}{P_{0,pre}}. \quad (7-8)$$

Without pre-equalization, the normalized received power is calculated from the mean of the power transfer function (TF) at the used sub-carriers (*cf.* eq. (7-1)),

$$P_0 = \frac{P_{rx}}{P_{tx}} = \frac{1}{N_{SC}} \sum_{i \in i_{SC}} |h_i|^2, \quad (7-9)$$

where P_{rx} and P_{tx} are the received and transmitted powers. Note that $x_i = d_i$ without pre-equalization.

Substituting (7-6) with (7-7) for x_i in the OFDM system model (7-1) yields the constellation points at the receiver *with pre-equalization* as

$$y_i = d_i h_i \tilde{e}_i + n_i = d_i h_i \hat{h}_i^{-1} \sqrt{\frac{N_{SC}}{\sum_{i \in i_{SC}} |\hat{h}_i^{-1}|^2}} + n_i. \quad (7-10)$$

Assuming that the channel estimate is equal to the actual channel, $\hat{h}_i = h_i$, the normalized received power with pre-equalization becomes

$$P_{0,pre} = \frac{P_{rx,pre}}{P_{tx,pre}} = \frac{N_{SC}}{\sum_{i \in i_{SC}} |\hat{h}_i^{-1}|^2}. \quad (7-11)$$

Note that the transmitted power with pre-equalization, $P_{tx,pre}$ is equal to P_{tx} , due to the normalization. Therefore, the ratio of the two normalized received powers is the average attenuation or power loss due to pre-equalization,

$$A_{pre} = \frac{P_0}{P_{0,pre}} = \frac{\sum_{i \in i_{SC}} |\hat{h}_i^{-1}|^2 \sum_{i \in i_{SC}} |h_i|^2}{N_{SC}^2} = \frac{\sum_{i \in i_{SC}} |e_i|^2 \sum_{i \in i_{SC}} |h_i|^2}{N_{SC}^2}. \quad (7-12)$$

This factor is generally larger than one, due to the amplification effect of the $1/x$ operation on small arguments. (It is equal to one if the channel is flat). It can be calculated by the mobile terminal, using the down-link channel estimate and assuming $\hat{h}_i = h_i$.

7.3.2.2 Limiting the Attenuation

The second strategy of the proposed pre-equalization scheme is the limitation of this factor. It is accomplished by zeroing the pre-equalization function $\{e_i\}$ for the most attenuated SC, until the attenuation falls below the threshold A_{max} . The following steps are executed repeatedly:

- Calculate the attenuation factor A_{pre} using (7-12). Stop the procedure if $A_{pre} \leq A_{max}$.
- Find the index of the most attenuated sub-carrier $i_{min} = \arg \min_i \{|\hat{h}_i|\}$ and set the pre-equalization function for this sub-carrier to zero, $e_{i_{min}} = 0$.
- Continue with the first step.

I.e., no power at all is put on those SCs being most severely attenuated by the channel. The data transmitted on these SCs will be lost, which the coding scheme has to correct for. Figure 7-2 illustrates this principle. The power normalization using eq. (7-7) is done *after* limiting the attenuation factor. Performance results are shown in Section

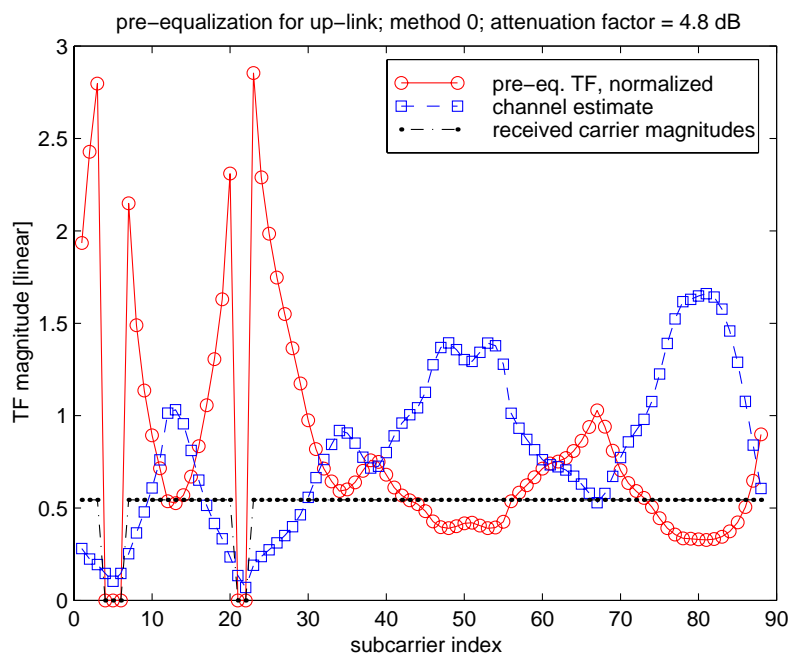


Figure 7-2: Attenuation limiting for pre-distortion by setting the most attenuated SCs to zero.

7.4.2.

Keller and Hanzo [1] have suggested a similar method of pre-equalization. However, they do not consider power-normalization. Instead, they do allow the output power to vary to a certain extent. Our approach has the advantage that the requirements on the power amplifier, which is a critical element of OFDM systems, are not enforced.

7.4 Performance Results

The performance results discussed in this section were obtained from computer simulations. (Experimental results are presented in Section 7.6.) Transmission mode I-f (see Section 5.2) was investigated for all results shown, where a 128-point FFT is employed, and 76 data sub-carriers and 12 pilot sub-carriers are used. The following elements of the transmission system have been considered or neglected.

- Channel estimation on the down-link
Has been considered. The channel estimate is required in order to calculate the pre-equalization function $\{e_i\}$. The channel estimation scheme implemented is the one described in Section 6.4. Seven-tap filters have been designed for a fixed set of channel parameters, namely: Rice-factor $K = 0$ (Rayleigh channel); RMS delay spread $\tau_{rms} = 3$ samples; and $SNR_{SC} = 30$ dB (SNR at the SCs of the TS). The bias of the down-link timing-offset estimation was considered as well, being $\delta t' = 3$ samples for these channel parameters.
- Synchronization on the down-link
Not considered. Small timing-offsets on the down-link will be included in the channel estimate and thereby corrected. Frequency-offsets larger than $\sim 2\%$ would result in performance degradations as mentioned and evaluated in Section 4.2.4.
- Time-variability of the channel
Not considered. Time-variations in between the channel estimation and the transmission of the up-link OFDM symbols will lead to non-ideal pre-equalization and further performance degradation [1]. In these simulations we will concentrate on the performance achievable in a static environment. Time-variability was present in the performance results derived from the experimental platform (see Section 7.6).
- Estimation of the constellation points' magnitude on the up-link
Is considered in some of the simulations for the 16-QAM modulation scheme. The performance loss resulting from estimating this parameter from a single data symbol is evaluated in Section 7.5.1.
- Up-link timing-offset estimation
Is considered in some of the simulations. The performance loss resulting from estimating this timing offset using the pilots of only one OFDM symbol is evaluated in Section 7.5.2.

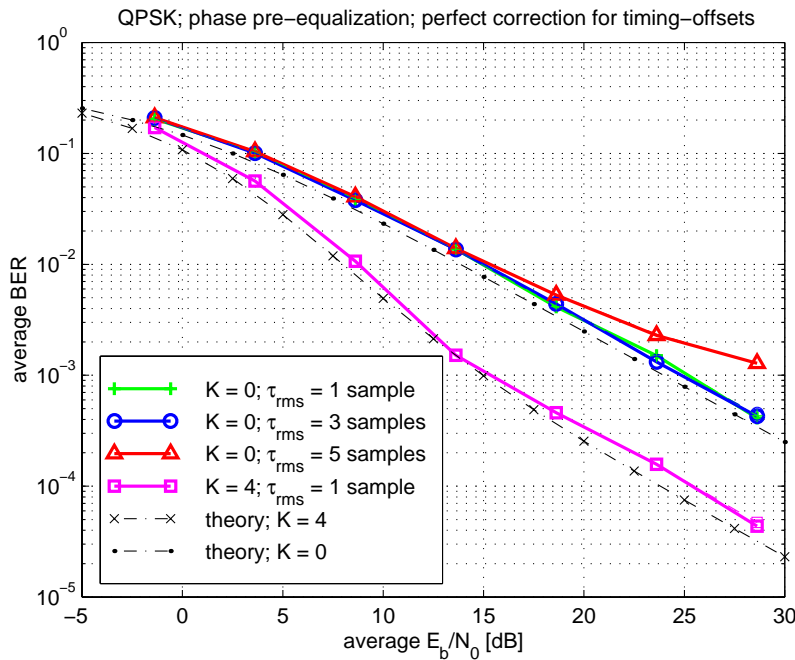


Figure 7-3: Performance of phase pre-equalization with QPSK under the assumptions of ideal up-link timing-offset correction and a time-invariant channel.

7.4.1 Application of Phase Pre-Equalization for QPSK

For pure phase modulation schemes, phase pre-equalization can be applied on the up-link, as described in Section 7.3.1.

Assuming that the up-link timing-offset can be estimated and compensated perfectly, and assuming a time-invariant channel, the performance on the up- and down-link is equivalent. Simulation results for several channels are shown in Figure 7-3. Note that up- and down-link results cannot be distinguished since they lie exactly on top of each other. As a benchmark, the theoretical performance is depicted that could be achieved with perfect channel estimation and synchronization. The small degradation of the simulation results is caused by the channel estimation scheme that has been taken into consideration (see Section 6.4).

A certain performance improvement for the up-link can be achieved by optimizing the power assignment to individual sub-carriers. In [9], the optimum assignment is studied for minimizing the average bit-error rate of an OFDM system. If applied with phase-modulation schemes, no modifications at the receiver are needed. (See also [10].)

7.4.2 Application of Pre-Equalization with Power Limiting

The pre-equalization scheme with limitation of the output power (see Section 7.3.2) is evaluated in this section. Up to a certain extent, namely as long as the power limitation criterion is not violated, also the attenuation magnitudes are pre-equalized. This is required for efficient detection of higher order modulation schemes, like 16-QAM.

Note that the power attenuation due to pre-equalization is considered in the SNR-values of all simulation results to allow a fair comparison with down-link results. If the SNR would be measured at the receiver, the BER-curves would shift to the left, suggesting much better performance vs. E_b/N_0 .

7.4.2.1 Results for QPSK Modulation

Considering the QPSK modulation scheme, it is of interest whether the average BER can be improved by applying phase and magnitude pre-equalization. Such a behavior may be anticipated, since more energy can be put on SCs that are attenuated by the channel, while less is needed on reliable SCs. The impact of the maximum attenuation factor allowed is investigated. BER results for several channels and several maximum attenuation factors are depicted in Figure 7-4.

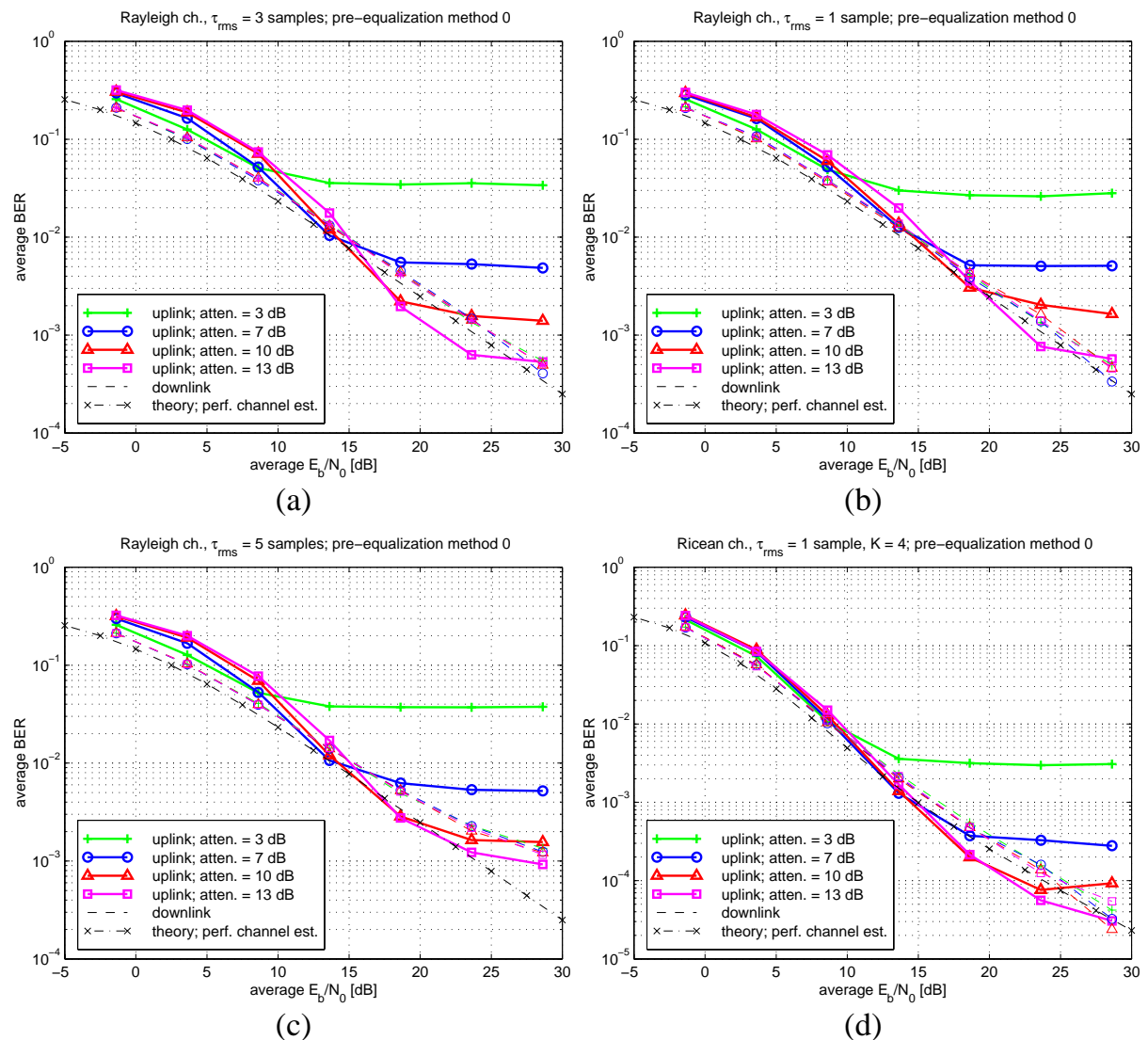


Figure 7-4: Performance results for up-link pre-equalization for QPSK. Deletion of SCs is used for power limitation. (a), (b), (c): Rayleigh channel with $\tau_{rms} = \{3, 1, 5\}$ samples, respectively. (d): Ricean channel with $K = 4$ and $\tau_{rms} = 1$ sample.

The general trend of all these plots is similar. At low SNR, the results are worse than the down-link results due to the attenuation factors considered in the E_b/N_0 values. At medium SNRs, the curves typically show a steeper slope than the down-link curves, because the channel including pre-equalization approximates an AWGN channel. The noise floors seen at the high SNR-region are due to the power limitation method setting some SCs to zeros.

Higher maximum attenuation factors result in slightly larger loss at low SNR but also in lower noise floors at high SNR. At certain points, the up-link outperforms the down-link. To find an optimum value for the maximum attenuation factor, error correction coding should be considered too. If the FEC-scheme can perfectly correct an average channel BER of 10^{-2} , there is no need to select the attenuation factor larger than 7 dB, following Figure 7-4. Note however that channel variability is not considered.

The behavior is largely independent of the channel parameters as seen from comparing the plots among each other.

7.4.2.2 Results for 16-QAM

Pure phase pre-equalization cannot be applied for higher order modulation schemes having amplitude and phase modulation components. The proposed pre-equalization with attenuation limiting and constant, normalized transmit power is evaluated in this section for 16-QAM. Figure 7-5 shows computer simulation results for various channel parameters.

Again, the influence of the maximum attenuation factor is depicted. The results and conclusions are quite consistent to the results for QPSK. Around the typical working point of the FEC-decoder (BER $\sim 10^{-2}$), the up-link performance is similar to the down-link. (Note again that the attenuation factor is considered in the average E_b/N_0 values shown.) The E_b/N_0 required is approx. 3 dB higher than for QPSK, translating to a required increase in transmission power of approx. 6 dB, because four bits are transmitted per sub-carrier in stead of two in the QPSK case. (E_b is the symbol energy per bit – see Section 4.3.3, eq. (4-44)).

7.5 Synchronization Parameter Estimation on the Up-link

Pre-equalization can transform a frequency-selective fading channel into a flat one (with some restrictions). This can simplify the detection of the data on the receiver's site. Carrier- and sampling-frequency synchronization can also be done by the mobile, based on estimates from the down-link. A few parameters still need to be estimated by the receiver (the base station) in order to perform coherent detection. Those are:

- timing offset,
- carrier phase offset, and
- (the common) magnitude of the constellation points

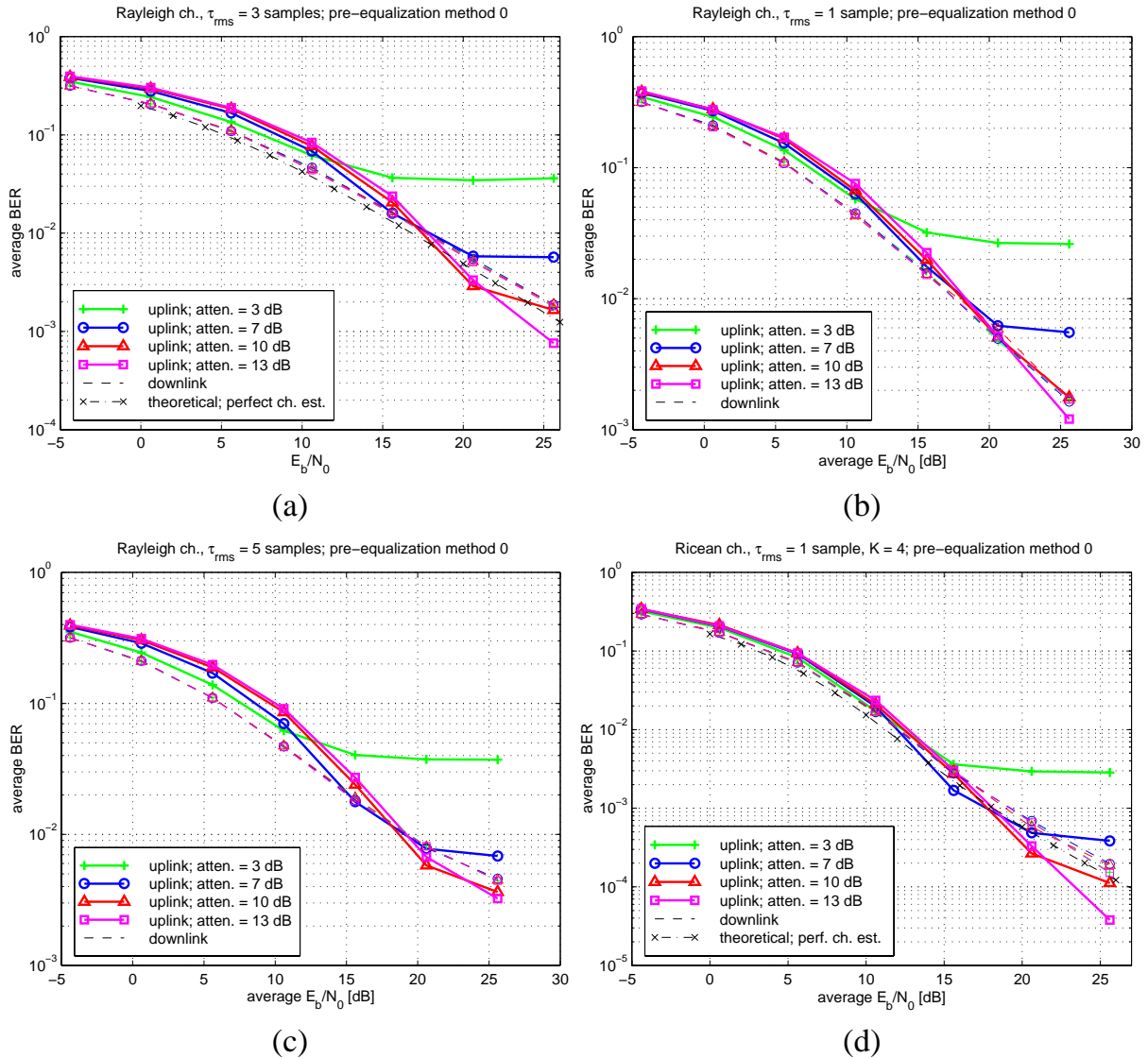


Figure 7-5: Performance results for up-link pre-equalization with 16-QAM. Deletion of SCs is used for power limitation. (a), (b), (c): Rayleigh channel with $\tau_{rms} = \{3, 1, 5\}$ samples, respectively. (d): Ricean channel with $K = 4$ and $\tau_{rms} = 1$ sample.

These parameters depend on the distance between the two transceivers and on the propagation environment. Therefore, they are different for each mobile accessing the base station and they are time-variant to various degrees. This section describes methods to estimate them.

7.5.1 Magnitude of the Constellation Values

Pre-equalization can make the channel flat, however, it can not correct for the (location-dependent) path loss. Higher order modulation schemes consist of phase and amplitude modulation components, therefore, a magnitude reference is needed for their coherent detection.

The magnitude reference can be estimated from the average power of the data and

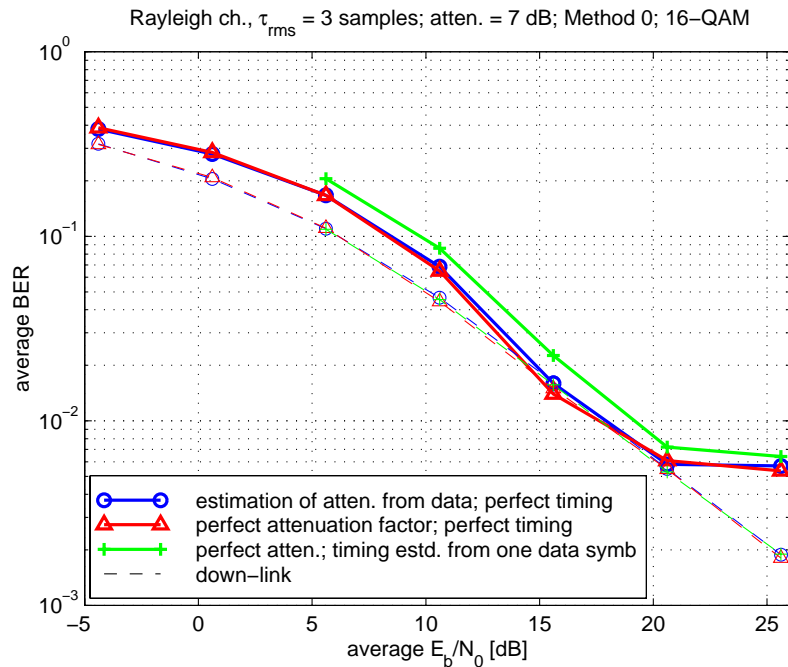


Figure 7-6: BER-result for the up-link and for 16-QAM with and without magnitude and timing-offset estimation (solid lines). The dashed lines indicate the down-link performance, being equivalent for the three cases compared.

pilot SCs. A problem arises, however, when the channel noise is large, because the power average will then include the noise power. The estimates are thus biased. The training symbol may be used to estimate the SNR (see [11]) in order to correct the power estimate.

However, even if the biased estimate obtained from the power average is used, it is found that the BER-performance results are sufficiently close to the reference results, where perfect knowledge of the received signal's magnitude is assumed. An example result for 16-QAM is depicted in Figure 7-6. Details on the computer simulation can be found in Section 7.4.

7.5.2 Estimation of the Up-link Timing-Offset

Timing errors introduce a so called 'progressive' phase rotation to the signal constellation points, i.e., a phase rotation proportional to the frequency distance of the SCs to the center frequency (see Section 7.2.2). The receiver can estimate the timing-offset and then correct for it by multiplying the constellations with a complex exponential sequence corresponding to the inverse of this systematic phase rotation. The information on the timing-offset must be fed back to the transmitter in order to optimize the arrival time of the up-link OFDM symbols of different users, and to avoid interference among users and inter-symbol-interference.

7.5.2.1 Up-link Timing Synchronization Using the Signaling Symbol

The first data symbol transmitted by any (mobile) user on the up-link must be a ‘user registration’ or ‘request for transmission capacity’ message, sent during the OFDM symbol for up-link signaling. This is a reserved OFDM symbol right in the beginning of the up-link portion of the frame format (see Section 5.2). The mobile may only transmit in this time-slot after it has achieved synchronization to the base station.

The limited symbol alphabet of the BPSK modulation ($M = 2$) used on this OFDM symbol enables extracting the timing offset without knowing the data transmitted. The principle is similar to the principle of fine timing-offset estimation proposed in Section 6.2.7. Differential demodulation between adjacent SCs is performed, yielding in the noiseless case (with (7-2) and (7-3), where the time-index k is omitted, and with (7-10))

$$\Delta y_{i,1} = y_i y_{i-1}^* = \{\pm 1\} h_i \tilde{e}_i h_{i-1}^* \tilde{e}_{i-1}^* \text{sinc}^2(\delta f T_{FFT}) e^{j(\Psi_i - \Psi_{i-1})}, \quad (7-13)$$

This expression can be simplified to

$$\Delta y_{i,1} = \{\pm 1\} A e^{j(\Psi_i - \Psi_{i-1})}, \quad (7-14)$$

assuming small frequency-offset δf and negligible channel-variability. The (real-valued) factor A accounts for the attenuation by the channel and by the pre-equalization; it has a value ≤ 1 . The angle-shift of these differentially demodulated constellation values from the real axis (i.e., from $\{\pm A\}$) is a measure for the timing offset, being

$$\Delta \Psi_1 = \Psi_i - \Psi_{i-1} = 2\pi \frac{\delta t[s]}{T_{FFT}} = 2\pi \frac{\delta t'[samples]}{N}. \quad (7-15)$$

In order to enhance the SNR of this measure, the modulation of $\{\pm 1\}$ is removed from the $\{\Delta y_{i,1}\}$ by making a decision on the unknown data, and subsequently adding up all the resulting complex numbers. The sum has the same phase rotation, however much bigger amplitude. A performance evaluation is shown in Section 7.5.2.3.

The unambiguous estimation range of this technique is theoretically $N/2$ samples, where N is the number of FFT-points. However, at such large offsets the uncertain decisions degrade the performance since the differentially demodulated constellation points $\{\Delta y_{i,1}\}$ get rotated closely towards the decision threshold.

Note that the decision feedback step can be replaced by squaring the $\{\Delta y_{i,1}\}$, which may be preferable at large time-offsets. The performance of the two methods should be compared.

7.5.2.2 Up-Link Timing-Offset Estimation Using the Pilot Sub-Carriers

The principle of timing-offset estimation using the pilots is similar to the principle of the above described method and the fine timing-offset estimation method using the training symbol (see Section 6.2.7). The advantage of taking the pilots lies in the fact

that their constellation values are known, in contrast to the previous method, where the data is first removed based on an uncertain decision. Again, the first step is the calculation of phase differences between pilot-pairs by means of complex multiplication with the complex conjugate. The purpose is the removal of common phase rotations, which may be due to carrier phase or frequency-offsets. The phase-difference between SCs spaced in frequency by l SC-intervals is written

$$\Delta\Psi_l = \Psi_i - \Psi_{i-l} = 2\pi \frac{\delta t[s]}{T_{FFT}} l = 2\pi \frac{\delta t'[samples]}{N} l, \quad (7-16)$$

yielding the time-offset δt [s] or $\delta t'$ [samples].

It is seen that the unambiguous range depends on the spacing l between two pilot SCs. It is $\delta t'_{unamb.}[samples] = \pm N/(2l)$, which is less than above, limiting the applicability of the method to tracking.

7.5.2.3 Performance of the Two Estimation Schemes

We try to compare computer simulation results to theoretical results. An analytical expression is available, quantifying the standard deviation of the timing-offset estimation error [samples] over an AWGN channel and for known pilot data (see Appendix C-3). This performance measure is related to the SNR and OFDM parameters as

$$\sigma_{\delta t'} = \frac{N}{2\pi l} \frac{\sqrt{SNR_{SC} + N_m/2}}{N_m SNR_{SC}}, \text{ with } SNR_{SC} = SNR \frac{N}{N_{SC}}, \quad (7-17)$$

where SNR is the signal power to noise power ratio of the time-domain signals, SNR_{SC} is the SNR of the data/pilot SCs after the FFT, N , N_{SC} , and N_m are respectively the number of FFT points, the number of active (data + pilot) SCs, and the number of differentially demodulated pilot-pairs being added up.

Unfortunately, the assumptions of an ideal AWGN channel and of perfectly known data (in the decision feedback case) are not fully met. The channel including pre-distortion attenuates the signal by a certain factor, which may vary according to the current channel conditions. Moreover, some of the SCs may have been set to zero in order not to exceed the maximum attenuation factor allowed, and there are also channel estimation errors on the down-link.

Computer simulation results are presented for mode I-fr of the proposed OFDM system (see Section 5.2), and compared to results derived from eq. (7-17). To obtain the analytical results for the timing estimation technique using the pilots, a constant pilot spacing of $l = 8$ is chosen, which is not equal but very close to the non-uniform pilot-separations in the proposed OFDM system (see Section 5.2.4.2).

The performance is shown in Figure 7-7 for maximum attenuation factors of 3 and 7 dB. In the 3-dB case, simulation results are mostly worse than the theory, because quite many SCs have been set to zero in order to stay below the low maximum at-

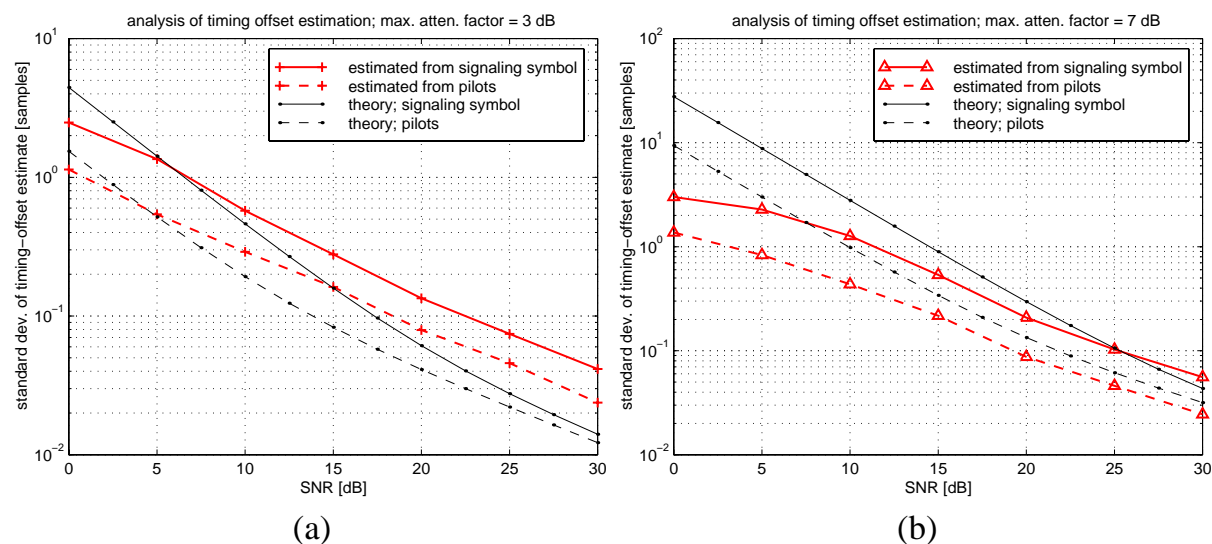


Figure 7-7: Standard deviation of timing-offset estimation error in samples. Computer simulations and theoretical results. (a): Maximum attenuation factor $A_{max} = 3$ dB. (b): $A_{max} = 7$ dB.

tenuation factor. From the results shown for the pilot-based method in the 7-dB plot, just the opposite situation is seen. The simulation results are better than the theoretical ones, because the actual attenuation factor is likely to be smaller than the maximum one considered in the theoretical plot.

Generally, the results suggest that at an SNR of about 10 dB, timing offsets can be estimated with an accuracy better than ± 1 sample. This is sufficient for the optimization of the up-link transmission time-instants. But is such accuracy also sufficient for coherent demodulation on the up-link?

Including up-link timing-offset estimation in the BER simulation leads to some performance degradation at low SNR, where the estimation errors become significant. Figure 7-8 shows results for QPSK, using pure phase pre-equalization. The pilots of only one OFDM symbol were used to estimate the timing-offset. The down-link results can be used for comparison, since they don't change (*cf.* Figure 7-3). Note that the degradation is limited to the area of high BER, which is less suitable for communications, anyway.

A result for 16-QAM modulation with phase- and magnitude pre-equalization has been shown in Figure 7-6. The impact of timing-offset estimation from the pilots of a single data symbol is depicted and compared to the ideal case without any offset. The performance is degraded by 1–2 dB.

Considering that the timing-offset does not vary rapidly, its estimate can be enhanced by averaging a few subsequent measurements. L -times averaging reduces the variance by a factor of approx. L . Note that, to apply this idea, eventual sampling frequency offsets must be taken into account.

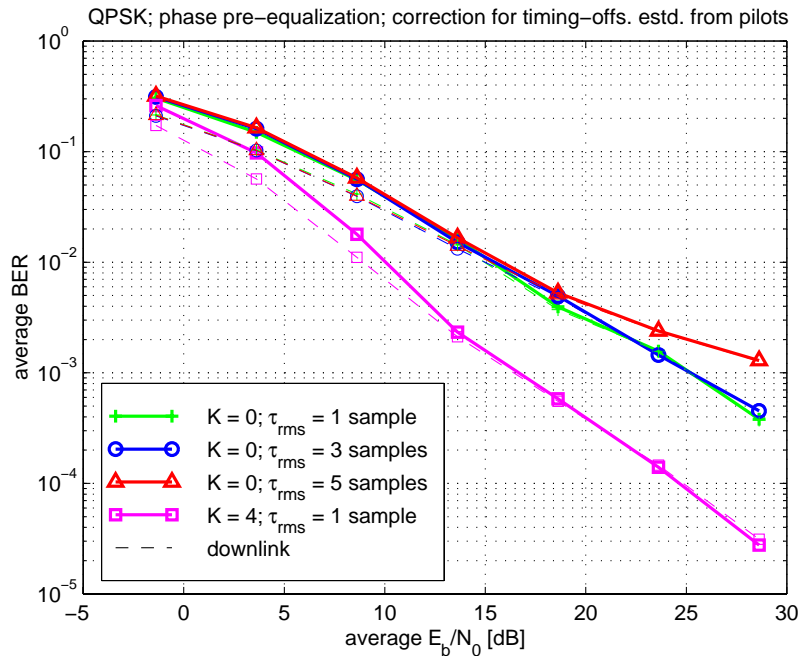


Figure 7-8: Performance of phase pre-equalization with QPSK. Time-invariant channel. Up-link timing-offset estimation from the pilots of one single OFDM symbol.

7.5.2.4 Feedback of Time-Offset

In order to optimize the performance of the up-link TDMA scheme, where each transmitted OFDM symbol may originate from a different user, the transmission times should be adjusted such that all the up-link symbols arrive at optimum time instants according to the frame format. Excess delays of the channel, which can be (slowly) time-variant as the users move around, and also group delays of filters of the transmission scheme (being time-invariant) must be taken into account.

This optimization requires feedback information from the base station to the mobile, since transmission delays cannot be estimated on a simplex link. I.e., the delay error for the up-link, which is estimated by the base-station, must be signaled back to the mobile.

As a reply to the signaling symbol from which the initial delay was estimated on the up-link, the base-station will send back an ‘acknowledgement’ message to that user, via the down-link signaling symbol. The delay information can be fed back using this symbol. To allow the detection of the delay by the signal-processing algorithm, the delay is not digitally coded and appended to the ‘acknowledgement’ message, but it is applied on the signal constellations of the down-link signal by means of an artificial progressive phase rotation. Since this signaling OFDM symbol is preceded by the training sequence used for channel estimation, this phase rotation can be estimated independently from down-link delays. This can be achieved by applying the (decision feedback) estimation method introduced in Section 7.5.2.1. The advantage of the ‘analog’ feedback is that neither additional digital data needs to be transmitted, nor (FEC)

coding/decoding and modulation/demodulation are needed, which reduces delays and simplifies the implementation.

7.6 Experimental Results

Experimental performance results are presented in this section, which have been obtained from the emulation system presented in Section 5.3 (see Figure 5-12).

7.6.1 Performance over Different Radio Channels

The degradation (error floor) due to the channel variability is evident in the experimental results depicted in Figure 7-9. The phase pre-equalization scheme for QPSK has been implemented on the emulator, with system parameters according to transmission mode I-fr of the proposed OFDM system (see Section 5.2). Up-link results are inferior to down-link results because of the larger time-distance between the training symbol and the up-link time-slots. For the AWGN channel, both results are equivalent. The impact of the speed of the channel's variability is seen from Figure 7-10. Both up- and down-link show increased irreducible error floors for higher speeds of movement. The bars indicating the range between minimum and maximum results measured (10 measurements were performed at each SNR-value) suggest that this range is larger on the up-link. In particular the channel with slowest variability shows a very large span between measurements. This is most likely caused by the inaccuracy of the synchroni-

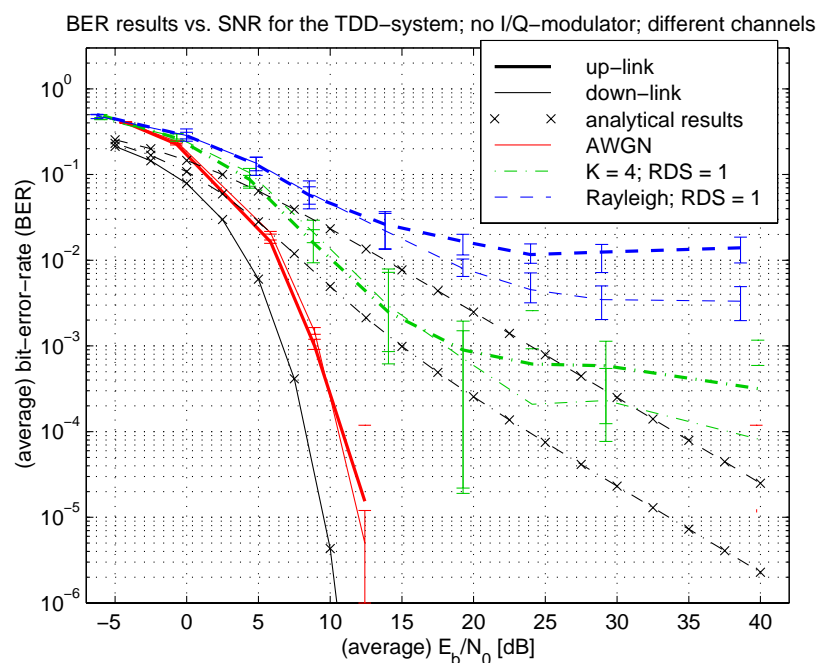


Figure 7-9: Experimental performance results for the phase pre-equalization scheme using QPSK.

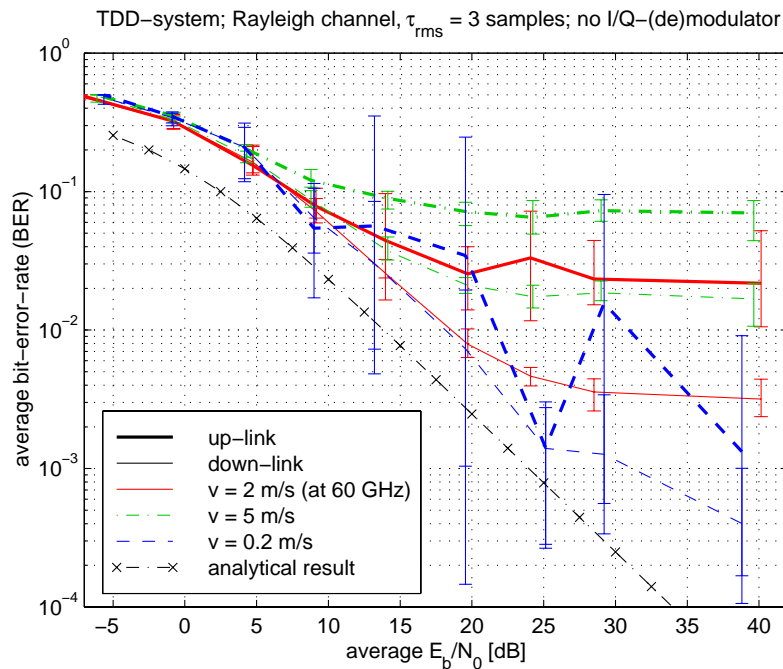


Figure 7-10: BER of the TDD system vs. SNR for Rayleigh fading channels with fixed RMS delay spread ($\tau_{rms} = 3$ samples); for varied velocities, $v_m = \{0.2, 2, 5\}$ m/s (at 60 GHz).

zation steps needed for coherent detection at the base station. The progressive phase shifts caused by timing-errors are estimated from the pilots and corrected for. The performance of these estimation and correction steps seems to deteriorate under bad (instantaneous) channel conditions. Enhancing the robustness for such situations is an issue for further research.

As the error floor for Rayleigh channels exceeds bit error rates of 10^{-2} at pedestrians speed, a simple form of channel tracking/prediction should be considered. In Section 6.5.3, linear extrapolation was briefly evaluated to tackle this problem.

The impact of the channel's excess delay is evident from Figure 7-11, where the BER is shown as a function of SNR, for Rayleigh fading channels with various RMS delay spreads ($\tau_{rms} = \{1, 3, 5\}$ samples) and for a fixed velocity $v_m = 2$ m/s (at 60 GHz).

While the performance on the down-link is relatively constant (thin lines), more significant variations are observed from the up-link results. Note that the range of measurement results increases with τ_{rms} . From this observation we conclude that the additional performance degradation is again due to the inaccuracy of timing-offset estimates on the up-link. The robustness of the applied technique to this problem should be enhanced.

7.6.2 Impact of the I/Q-Modulator and -Demodulator

Figure 7-12 illustrates the influence of the I/Q-(de)modulation hardware, which was not present in the system when the above presented measurements were done. The fig-

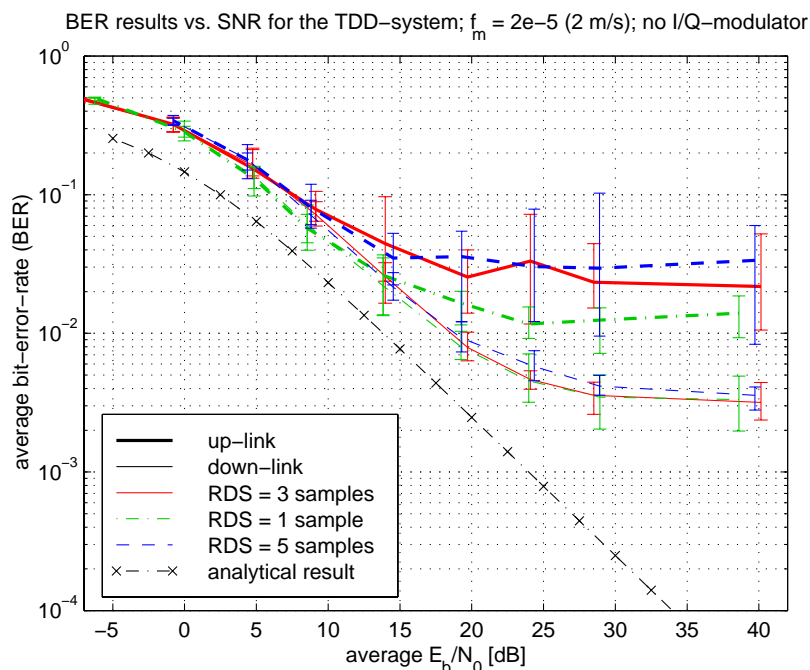


Figure 7-11: BER of the TDD system vs. SNR for Rayleigh fading channels with variable RMS delay spread ($\tau_{rms} = \{1, 3, 5\}$ samples) and for fixed velocities, $v_m = 2$ m/s (at 60 GHz).

ure depicts the BER vs. SNR for a Rayleigh fading channel with $\tau_{rms} = 3$ samples and for $v_m = 2$ m/s. The similarity of the curves suggests that the I/Q-(de)modulation hardware has no significant influence on the performance, as also concluded from the down-link results presented in Section 6.5.

7.7 Conclusions

Pre-equalization techniques are proposed for the up-link of the OFDM based wireless communications system. They are computationally quite efficient: the mobile has to calculate the pre-equalization function once per frame (which unfortunately involves the inversion of complex numbers) and multiply the data constellation points by it (prior to the IFFT used at the OFDM transmitter). The base station only has to estimate (precisely) the timing-offset for each mobile, a reference magnitude for the received signal constellation points, and the carrier phase offset. The computational effort for these operations is relatively low. No frequency-synchronization is needed on the up-link due to the time-division duplex scheme. Neither is channel estimation required, or any feedback of channel state information.

Keeping the complexity of the base station low is somewhat contrary to the commonly applied strategy of decreasing the complexity of the mobile terminals in order to enable power efficient terminals. The additional signal processing required at the mobile terminals is not very complex, however. And the additional complexity is very well

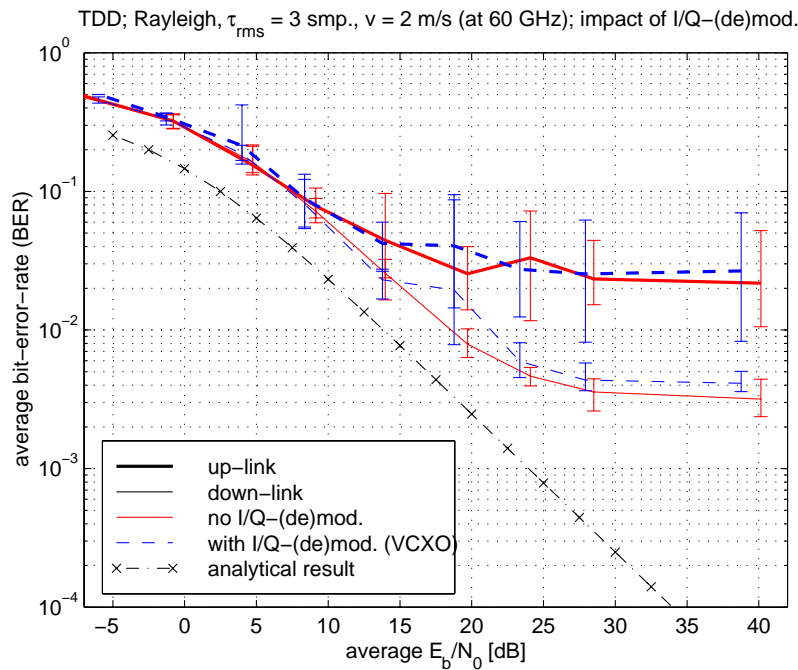


Figure 7-12: Impact of the I/Q-(de)modulation hardware on the BER vs. SNR for the TDD system. The results are for a Rayleigh fading channel with $\tau_{rms} = 3$ samples and $v_m = 2$ m/s.

invested, considering that the base station is accessed by many users at very high data rates, which requires lots of processing power for managing these multiple data streams with low delays. MAC and ARQ schemes have to be executed, for instance. Moreover, the spectrum and the transmission power for the training symbols is saved on the up-link, and very “tight” multiple access schemes are enabled, because the overhead for training symbols, guard-periods and guard frequency bands for separating multiple users is very low.

Assuming a working point of the FEC-coding scheme at an average channel BER of approx. 10^{-2} , the performance on the up-link is very similar to the down-link. A realistic channel estimation scheme has been considered in all computer simulations. Using QPSK modulation, an E_c/N_0 (energy per coded bit over noise power density) of about 15 dB is required for such performance, equivalent to a SNR (time-domain) of ~ 16 dB. The same BER is reached with 16-QAM for an E_c/N_0 of ~ 18 dB, equivalent to an SNR of ~ 22 dB. Note, however, that usually the performance of the coding scheme is largely dependent on the frequency diversity available over the channel bandwidth (see Chapter 8). This may reduce the above-mentioned SNRs. On the other hand, the time-variability of the channel was not included in the simulations leading to those results.

It is recommended for further work to perform computer simulation studies for the up-link that incorporate error correction coding and also the time-variant channel.

7.8 References

- [1] T. Keller and L. Hanzo, “Sub-band adaptive Pre-equalised OFDM Transmission,” in Proc. *IEEE VTC’99 (fall) conference*, Amsterdam (Netherlands), Sept. 1999, pp. 334–338.
- [2] G. J. R. Povey and M. Nakagawa, “A Review of Time Division Duplex – CDMA Techniques,” in Proc. *IEEE 5th Intern. Symp. on Spread Spectrum Techniques and Applications*, 1998, pp. 630–633.
- [3] R. Esmailzadeh, M. Nakagawa, and E. A. Sourour, “Time-Division Duplex CDMA Communications,” *IEEE Personal Communications*, vol. 4, no. 2, pp. 51–56, April 1997.
- [4] R. Esmailzadeh, E. A. Sourour, and M. Nakagawa, “Pre-RAKE diversity combining in time-division duplex CDMA mobile communications,” *IEEE Trans. Veh. Technol.*, vol. 48, no. 3, pp. 795–801, May 1999.
- [5] R. Esmailzadeh and M. Nakagawa, “Time-Division Duplex Method of Transmission of Direct Sequence Spread Spectrum Signals for Power Control Implementation,” *IEICE Trans. Commun.*, vol. E76-B, no. 8, Aug. 1993, pp. 1030–1038.
- [6] H. Koorapaty, A. A. Hassan, and S. Chennakeshu, “Secure Information Transmission for Mobile Radio,” *IEEE Commun. Letters*, vol. 4, no. 2, pp. 52–55, Feb. 2000.
- [7] G. J. M. Janssen, *Robust receiver techniques for interference-limited radio channels*, Ph.D. Thesis, Delft Univ. of Techn., Delft, The Netherlands, June 1998.
- [8] M. Hämmäläinen, J. Talvitie, V. Hovinen, and P. Leppänen, “Wideband Radio Channel Measurement in a Mine,” in Proc. *IEEE 5th Intern. Symp. on Spread Spectrum Techniques and Applications*, 1998, pp. 522–526.
- [9] M. Ditzel and W. A. Serdijn, “Optimum Energy Assignment for Frequency Selective Fading Channels,” in Proc. *PIMRC 2001 (12th International Symposium on Personal Indoor Mobile Radio Communications)*, San Diego, Oct. 2001, pp. D-104–D-108.
- [10] J. Jang, K. B. Lee, and Y.-H. Lee, “Frequency-Time Domain Power Adaptation for a Multicarrier System in Fading Channels,” in Proc. *PIMRC 2001 (12th International Symposium on Personal Indoor Mobile Radio Communications)*, San Diego, Oct. 2001, pp. D-100–D-103.
- [11] T. M. Schmidl and D. C. Cox, “Robust frequency and timing synchronization for OFDM,” *IEEE Trans. Commun.*, vol. 45, no. 12, pp. 1613–1621, Dec. 1997.

Chapter 8 – Performance Evaluation and Enhancement of COFDM

8.1 Introduction

A coded OFDM (COFDM) system exploits the frequency-diversity of the wide-band (frequency-selective) radio channel for ensuring good performance even though some sub-carriers (SC) may be largely attenuated by fades. The performance evaluation of a coded system is quite tedious. Analytical methods are difficult to apply – in particular for Ricean fading channels –, and computer simulations require incredible computing power. In Section 8.2, a semi-analytical approach is utilized, the so-called “Concept of Effective E_b/N_0 ” [1]. This method calculates – based on channel simulations – effective E_b/N_0 -values, which, on an AWGN channel, would lead to equivalent error probabilities. A set of channel simulations therefore yields a set of BER-estimates.

In this thesis, a novel extension to this method is proposed. We try to derive from the frequency-domain (FD) channel model (see Chapter 2) a PDF for the effective E_b/N_0 . Knowing this PDF, we can calculate average BERs and also outage probabilities. Thereby, the performance analysis technique becomes fully analytical, because the channel simulations are now replaced by the known PDF of the effective E_b/N_0 . It will become evident, however, that an uncertainty remains (an offset depending on channel and OFDM system parameters), which so far still requires computer simulations to be determined.

Longer channel delay spreads imply higher frequency-diversity, and therefore better performance for the coded OFDM system. (Provided that the delay spread does not exceed the guard interval duration.) A (relatively) flat fading channel is thus the worst situation, because the channel may attenuate all (or most) sub-carriers simultaneously, leading to long error bursts, which are difficult to correct. In order to enhance the ro-

bustness of the system – in particular in these situations –, antenna diversity techniques are discussed in Section 8.3.

A novel class of diversity techniques for OFDM is introduced, which employs cyclic delays (and weighing factors). The methods can be applied at the transmitter and at the receiver. They are computationally highly efficient, because the (simple) signal processing steps are performed on the time-domain OFDM signals. That is, the IFFT and FFT blocks are only executed once. Basic performance results show the potential improvement by the proposed techniques. Topics for further work are addressed.

Conclusions and recommendations are presented in Section 8.4.

8.2 Performance of a Coded OFDM System

Applying the concept of effective signal-to-noise ratio (E_b/N_0) proposed by Nanda and Rege [1] to an OFDM system model, estimates of frame error rates (FER) are obtained for convolutional coding and bit-level interleaving²². The effective E_b/N_0 for a fading channel is defined as the E_b/N_0 on an equivalent AWGN channel that results in the same FER. The problem of calculating a FER is thus changed to the problem of calculating the effective E_b/N_0 . In [1], two methods are proposed to translate a vector of E_b/N_0 values that describe the fading of subsequent channel bits to the effective E_b/N_0 . The procedure of performance evaluation is therefore a semi-analytical one. Channel simulations are performed and transformed to (instantaneous) error probabilities. A set of channel simulations (for given channel parameters like average SNR) thereby leads to a set of effective E_b/N_0 -values and furthermore to a set of respective FER-values. In a second step, the average FER or the outage probability (the probability that the FER is above a given threshold) can be calculated. These methods are briefly reviewed in this section; their application to OFDM is elaborated.

Using the FD-channel model of the frequency-selective radio channel (see Chapter 2), the probability density function (PDF) of the effective E_b/N_0 is studied for OFDM systems in quasi-static channels. Having appropriate PDFs for this parameter enables the calculation of average FERs and outage probabilities for given channel and system parameters, and a comparison and assessment of these. The performance analysis thereby becomes fully analytical.

Other analytical work on the performance of coded transmission over fading channels is mostly based on the calculation of pair-wise error probabilities (see Section 8.2.1.3) over Rayleigh fading channels [2]. The influence of non-perfect interleaving was in-

²² A data frame is a data packet transmitted via the air-interface. In the system proposed in Section 5.2, ATM cells constitute such data packets. Each packet is coded individually. Note that the packets (data frames) are not equal to OFDM symbols nor to the frames of the multiple access scheme (see Section 5.2).

investigated in [3], [4]. Sandell has applied this concept to OFDM for a Rayleigh fading channel with a rectangular power delay profile [5]. This approach was not further pursued in this Ph.D. research program. One reason was that, because the analysis developed in these references is based on zero-mean Gaussian processes, it appears difficult to apply it to Ricean fading channels.

The current section proceeds with a review, analysis, and evaluation of the concept of effective E_b/N_0 and its application to the OFDM based wireless ATM transmission system under investigation (Sections 8.2.1 and 8.2.2). In this context, the FER can be seen as an ATM cell-loss probability. Finding appropriate PDFs for the statistical description of the effective E_b/N_0 is elaborated in Section 8.2.3. Performance results are presented in Section 8.2.4, followed by a brief summary in Section 8.2.5.

8.2.1 Review of the Concept of Effective E_b/N_0

The idea behind the concept of effective E_b/N_0 is to find an analytical relationship between the signal-to-noise ratios of the coded bits of a data frame and the frame error probability. The discussed concept applies for frame-oriented, convolutionally coded transmission over fading channels, with bit-level interleaving. Here, the method is applied to an OFDM based system for wide-band data communications, where the parallel OFDM sub-channels are modeled by a set of parallel Gaussian channels (see Section 4.2.3). A quasi-static channel is assumed, with respect to the transmission time of a block of OFDM symbols carrying one ATM cell – the data frame under consideration. That is, each OFDM symbol of a data-frame is affected equally by the channel. Therefore, interleaving is performed in the frequency-direction only (see Section 5.2.4.2).

8.2.1.1 Calculation of the Effective E_b/N_0

Due to the frequency selective fading channel, each OFDM sub-carrier has an individual SNR, which is given as (*cf.* eq. (4-14), Section 4.2.3)

$$(E_c/N_0)_l = E\{|x_l|^2\}|h_l|^2/\sigma_N^2, \quad (8-1)$$

where $\{h_l\}$ are the channel coefficients, expressing the channel transfer function, $\{x_l\}$ are the signal constellations, and σ_N^2 is the variance of the additive channel noise per sub-carrier. The index $l = \{1, 2, \dots, L\}$ designates the sub-carriers, just like the index i used in Section 4.2.3. Note that a different indexing system has been introduced for notational convenience; the time index k has been dropped. Considering the coding rate and the number of bits per sub-carrier n_m , the SNR per data bit on the l -th sub-carrier is written

$$(E_b/N_0)_l = (E_c/N_0)_l/(R_c n_m). \quad (8-2)$$

In this equation, R_c is the rate of the convolutional code, defined as the ratio of infor-

mation bits and coded bits. Note that the loss of signal power due to the discarded guard interval is not accounted for.

Following [1], the L $(E_b/N_0)_l$ values of the data-bearing sub-carriers are written as an L -dimensional vector $\underline{E_b/N_0}$, which completely specifies the channel conditions:

$$\underline{E_b/N_0} = [(E_b/N_0)_1 \quad (E_b/N_0)_2 \quad \cdots \quad (E_b/N_0)_L] \quad (8-3)$$

The objective is to determine the relationship between the frame error probability P_{FE} and the vector $\underline{E_b/N_0}$, written as

$$P_{FE} = f(\underline{E_b/N_0}) \quad (8-4)$$

Assuming an AWGN channel, a relationship between P_{FE} and E_b/N_0 can be determined based on analysis or simulation, for a given convolutional code and frame length N_c (number of *coded* bits per data packet). It is assumed that this relationship, expressed by

$$P_{FE,AWGN} = h(E_b/N_0) \quad (8-5)$$

is known. For a given L -dimensional vector $\underline{E_b/N_0}$, the scalar $(E_b/N_0)_{eff}$, called the effective signal-to-noise ratio, is defined as the E_b/N_0 in an equivalent AWGN channel, which yields the same frame error probability. This is written as

$$P_{FE} = f(\underline{E_b/N_0}) = h((E_b/N_0)_{eff}), \quad (8-6)$$

where

$$(E_b/N_0)_{eff} = g(\underline{E_b/N_0}). \quad (8-7)$$

Note that up to this point only the formulation of the problem is changed, no approximation has been introduced. Approximations are used for estimating $(E_b/N_0)_{eff}$ from a vector $\underline{E_b/N_0}$.

8.2.1.2 Estimation of $(E_b/N_0)_{eff}$

Two estimation methods are described in [1], for both of which the evaluation of the following equations is required

$$(E_b/N_0)_{eff}^{(k)} = \left\{ (E_b/N_0)_{J(k)} + (E_b/N_0)_{J(k+1)} + \cdots + (E_b/N_0)_{J(k+D-1)} \right\} / D. \quad (8-8)$$

In this expression, the symbol $J(k+i)$ denotes the index of the E_b/N_0 value corresponding to the coded bit in position $k+i$, where $k = \{1, 2, \dots, N_c - D + 1\}$ and $i = \{0, 1, \dots, D-1\}$. N_c is the length of a data frame in (coded) bits, and D is the sequence-length over which the d_{free} error bits in a minimum distance error-event are spread. Thus (8-8) represents the average E_b/N_0 over any D subsequent coded bits.

These D E_b/N_0 values are taken from the L different E_b/N_0 values of the OFDM sub-

carriers in an order described by the interleaving scheme. The symbol $J(k + i)$ introduces the interleaving scheme. It maps the N_c coded bits of a data frame on the L data-bearing sub-carriers of a set of $m = N_c/(L \cdot n_m)$ subsequent OFDM symbols. Note that it is sufficient to calculate the first L averages (8-8), assuming the application of a periodic interleaving scheme (*cf.* [1]), because the $(L + 1)$ -st average will be equal to the first one, and so on.

Estimate 1

Estimation method one simply selects the smallest of the $(E_b / N_0)_{eff}^{(k)}$ values, based on the reasoning that the most likely error event will occur at the sequence of D bits being received with the smallest total signal energy. Thus, estimate 1 is expressed as

$$(E_b / N_0)_{eff} = \min_k \{ (E_b / N_0)_{eff}^{(k)} \}. \quad (8-9)$$

Estimate 2

Estimate two is calculated from the average of the FERs corresponding to all values $\{ (E_b / N_0)_{eff}^{(k)} \}$. This is written as

$$P_{FE} = \sum_{k=1}^{N_c - D + 1} h((E_b / N_0)_{eff}^{(k)}) / (N_c - D + 1). \quad (8-10)$$

The effective E_b/N_0 is then

$$(E_b / N_0)_{eff} = h^{-1}(P_{FE}). \quad (8-11)$$

Note that with estimate 1, a change of the *average* SNR E_b/N_0 – which corresponds to a *common* change of *all* E_b/N_0 -values in the vector $\underline{E_b/N_0}$ –, leads to an equivalent change of $(E_b/N_0)_{eff}$. Such a linear relationship is not evident in case of estimate 2. Estimate 1 therefore drastically simplifies the analysis of error probabilities as a function of average SNR. For this reason, and because of the good results obtained (see below), most of the further analysis concentrates on “estimate 1”.

8.2.1.3 Derivation and Assessment of the FER for the AWGN Channel

Upper bounds on error probabilities for convolutional codes and AWGN channels are given in most books on coding or digital communications (see e.g. [6], [7]). These bounds use information on the weight structure of the codes, i.e., the number of code sequences must be known that have a certain Hamming distance (HD) to the transmitted sequence. Since convolutional codes have, per definition, no start or ending, so called first-event error probabilities are evaluated, being the probabilities that an erroneous path merges at a certain node under consideration in stead of the correct path. The numbers of erroneous paths merging in any node B and having Hamming distances $d = d_{free} + \{0, 1, 2, \dots\}$ from the correct path are denoted $\{a_d\}$.

Table 8-1: Parameters of rate $\frac{1}{2}$ maximum free distance codes (see [7], Appendix A)

Constraint length v	Generators in octal	d_{free}	$(a_d, d = d_{free}, d_{free} + 1, \dots)$	$[c_d, d = d_{free}, d_{free} + 1, \dots]$
3	5, 7	5	(1, 2, 4, 8, 16)	[1, 4, 12, 32, 80]
5	23, 35	7	(1, 3, 5, 11, 25)	[2, 7, 18, 49, 130]
7	133, 171	10	(11, 0, 38, 0, 193)	[36, 0, 211, 0, 1404]

The probability of deciding in favor of a path with HD of d to the correct path is called the pair-wise error probability. It is upper bounded for a binary symmetric channel (BSC) with error probability p by (see [6], p. 490)

$$P_2(d) = \left(2\sqrt{p(1-p)}\right)^d \quad (8-12)$$

For coherent BPSK (or QPSK) modulation over AWGN channels and maximum-likelihood soft-decision decoding, it can be shown that

$$P_2(d) = Q\left(\sqrt{2dR_c E_b / N_0}\right) < \exp(-dR_c E_b / N_0), \quad (8-13)$$

where Q is the integral over the Gaussian PDF (see [6], p. 40). The Q -function can be upper bounded by the exponential function given in eq. (8-13). (Results calculated by the Q -function will be referred as ‘bound 1’, results from the exponential approximation as ‘bound 2’.)

Finally, an upper bound (union bound) on the first-event error probability is written as

$$P_e < \sum_{d=d_{free}}^{\infty} a_d P_2(d), \quad (8-14)$$

where d_{free} is the HD of the minimum distance error event.

The frame error probability P_{FE} is determined from its complementary event, the probability that no error event occurs during the transmission of V information bits belonging to one frame. This event is well approximated by

$$\overline{P_{FE}} = 1 - P_{FE} \geq (1 - P_e)^V, \quad (8-15)$$

being the probability that correct decisions were made at V nodes (or decoding steps). The frame error rate is found as

$$P_{FE} \leq 1 - (1 - P_e)^V \quad (8-16)$$

Similarly, a bound on the bit error probability can be obtained by including in the summation in (8-14) the number of information bit errors resulting from each error event, expressed by $c_d = a_d f(d)$ (see [6], p. 488). Thus we can write an upper bound on the bit error probability

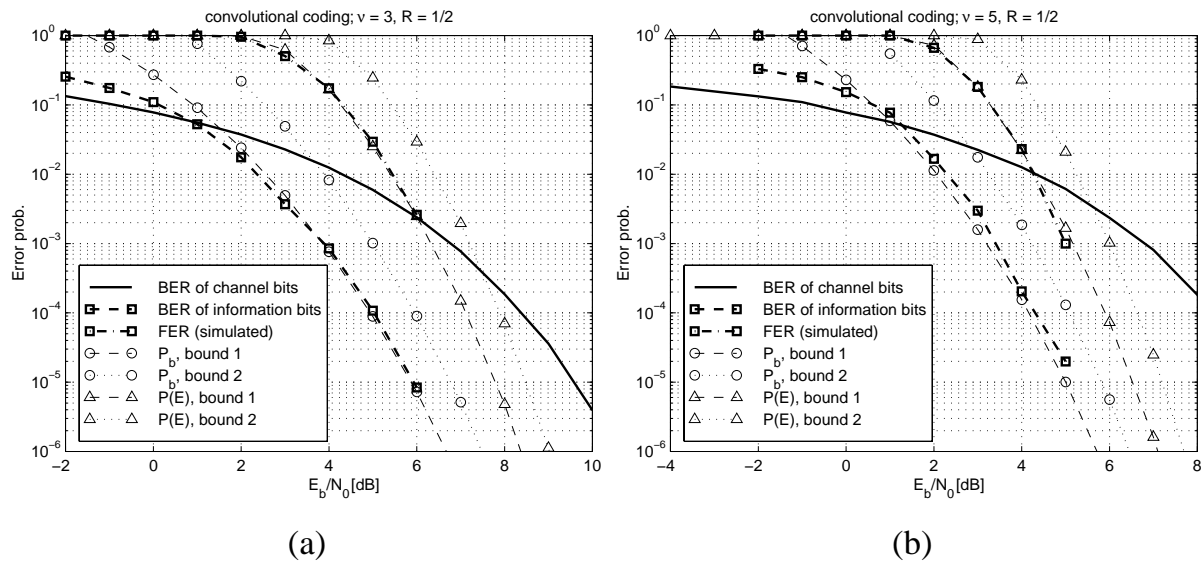


Figure 8-1: Performance of rate- $1/2$ convolutional codes over AWGN channels. (a): constraint length (= shift register stages + 1) $\nu = 3$; (b): $\nu = 5$

$$P_b < \frac{1}{k_c} \sum_{d=d_{free}}^{\infty} c_d P_2(d), \quad (8-17)$$

where k_c is the number of input bits of the encoder. $k_c = 1$ in case of a binary encoder. $\{a_d\}$ and $\{c_d\}$ are listed in Appendix A of [7] for a number of useful codes. Table 8-1 gives a few examples.

Performance Results

In this section, results are presented for the above equations and compared to computer simulations. Two different rate- $1/2$ convolutional codes with constraint lengths of $\nu = 3$ and $\nu = 5$ were evaluated (see Table 8-1).

In the simulations, 8-level soft-decision Viterbi decoding²³ was implemented with memory lengths of 20 and 25 for the $\nu = 3$ and $\nu = 5$ code, respectively. QPSK modulation was used.

It is seen from the results depicted in Figure 8-1 that the simulated and theoretical er-

²³ Prior to the 8-level quantization, the received signal constellations y_l were multiplied by $\sqrt{(E_c/N_0)_l}$. This yields almost optimum performance (for QPSK and BPSK) when constant quantization levels and metric values (optimized for $(E_c/N_0)_l = 0$ dB) are used for quantized soft-decision decoding. This conclusion was drawn based on the evaluation of optimum metrics following [8]. With the above-mentioned pre-multiplication, the optimum metrics largely remain constant over a large range of $(E_c/N_0)_l$ values. Note that, except for a constant factor related to N_0 , this multiplication is equivalent to multiplying the FFT-output by the complex conjugates of the channel estimate, \hat{h}_l^* , which is also an efficient means for compensating for the phase distortion introduced by the channel. This solution is specific for QPSK (or BPSK) modulation, however.

ror probabilities match very closely for bound 1 (using the Q-function), especially for the $\nu = 3$ code. For the $\nu = 5$ code, the simulation results are slightly worse than their upper bound, for two reasons. Firstly, P_e is calculated using only the first five summation terms in eq. (8-14). And secondly, 8-level quantization is used in the simulation, in stead of unquantized soft-decision decoding.

The mismatch observed at high error rates is due to the definition of the union bound. All possible sequence error probabilities are simply added, thus, at high channel error rates, the bound accounts for more than one error on one single node. This may even lead to error probabilities larger than one.

Bound 2 yields results that are approx. 1 dB worse.

8.2.2 Assessment of the Concept of Effective E_b/N_0

In this section, the concept of effective E_b/N_0 is evaluated by computer simulations, considering the OFDM system proposal introduced in Section 5.2.

8.2.2.1 OFDM System Configuration

The OFDM system parameters in this assessment were selected according to the quarter rate transmission mode I-LL (see Section 5.2.1). Rate-1/2 convolutional coding with QPSK modulation is used, where the data stream is transmitted over 19 data bearing sub-carriers. Thus 24 OFDM symbols are required for carrying one complete ATM cell (19 sub-carriers \times 2 bits per sub-carrier \times 24 = 912 bits = 1 coded ATM cell plus signaling overhead). The simulation and estimation of $(E_b/N_0)_{eff}$ assumes the mapping of an ATM cell to subsequent OFDM symbols and time-invariance of the channel during transmission of the whole ATM cell. Interleaving is performed in the frequency-domain (FD) only (across the 19 active sub-carriers), which is appropriate because of the assumption of time-invariance. Two possible interleaving schemes have been introduced in Section 5.2.4. A constraint length $\nu = 5$ code was used, having $d_{free} = 7$ and $D = 10$.

8.2.2.2 Computer Simulation Results

For one particular value of average $E_b/N_0 = 2$ dB, the simulation program generates a number of different frequency-selective channel realizations (approx. 250). The channel model is characterized by an exponentially decaying delay power spectrum. Figure 8-2a and d show typical TFs for different RMS delay spread, $\tau_{rms} = \{10, 55 \text{ ns}\}$, respectively. The sub-carrier spacing of the OFDM system is $F = 1$ MHz.

For each channel realization, a number of ATM cells (max. 100) is transmitted in order to obtain the FER and BER. Additionally, the theoretical performance result is calculated, using the concept of effective E_b/N_0 . The results are compared based on scatter plots (Figure 8-2b and e) and cumulative plots (Figure 8-2c and f).

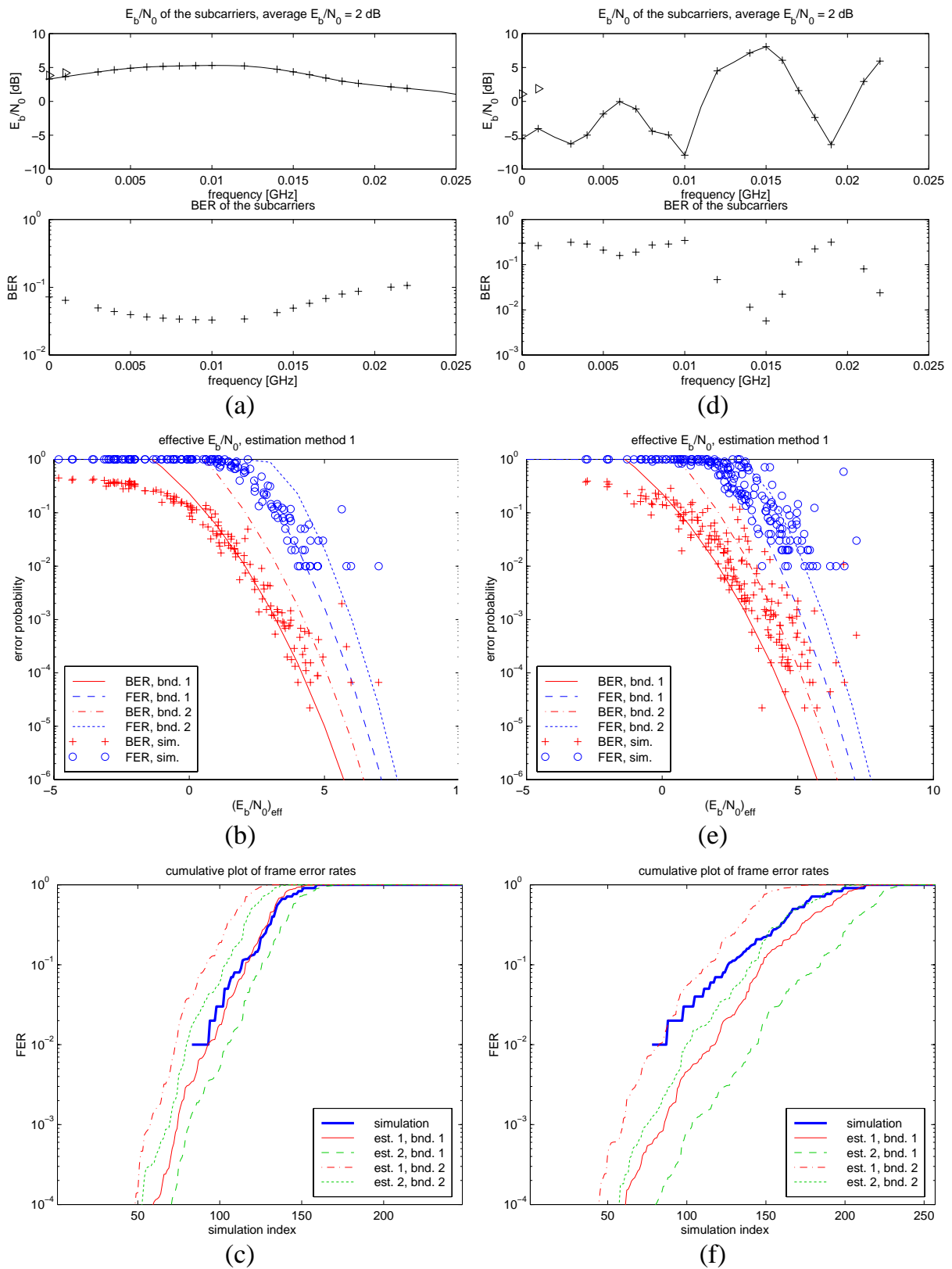


Figure 8-2: Assessment of the concept of effective E_b/N_0 applied to OFDM. (a)–(c): Channel has $\tau_{rms} = 10$ ns; (d)–(f): $\tau_{rms} = 55$ ns. (a), (d): Typical realizations of the channel transfer function with estimates 1 and 2 of $(E_b/N_0)_{eff}$ ('>') and the BER per sub-carrier; (b), (e): Scatter plots of FER and BER vs. effective E_b/N_0 ; (c), (f): Cumulative plots of simulated and predicted FER.

The matching of the cumulative plots shows the suitability of the investigated method. In particular, estimation method 1 in combination with bound 1 (evaluating Q -functions for obtaining $P_{FE} = h[(E_b/N_0)_{eff}]$) yields an excellent approximation for the investigated system environment. It should be noted, however, that the matching is better for the channel having $\tau_{rms} = 10$ ns than for the second channel. This is explained by the fact that in the first case the fading can be characterized as “gentle”, while it is much more severe in the second case (compare Figure 8-2a and d). The gently fading channel leads to more accurate estimates of $(E_b/N_0)_{eff}$, evident in the smaller variance of the performance results around the theoretical curves (see Figure 8-2b and e). It is concluded that, in case of a more severely fading channel, using ‘bound 2’ in combination with estimation method 1 may be preferable. This option generally yields an upper bound on the actual performance, while the estimation obtained with ‘bound 1’ may be too optimistic in some cases.

8.2.3 PDF of the Effective E_b/N_0

8.2.3.1 Average Error Rate and Outage Probability

Using the concept of effective E_b/N_0 , frame and bit error probabilities can be predicted for specific (simulated) fading channels. It is suggested in [1] to use this method in hybrid simulation models, i.e., simulating the fading channels and analytically evaluating their error rate performance.

A more sophisticated way of performance evaluation can be derived from this concept by finding the PDF of $(E_b/N_0)_{eff}$ denoted $p(\tilde{\gamma}_b | \bar{\gamma}_b)$, where $\tilde{\gamma}_b = (E_b/N_0)_{eff}$ and $\bar{\gamma}_b$ is the average E_b/N_0 , i.e. $\bar{\gamma}_b = E\{E_b/N_0\}$. From this PDF and (8-6), the average FER is written

$$\overline{P_{FE}}(\bar{\gamma}_b) = \int_0^{\infty} h(\tilde{\gamma}_b) p(\tilde{\gamma}_b | \bar{\gamma}_b) d\tilde{\gamma}_b. \quad (8-18)$$

The outage probability is defined as the probability that the FER is greater than some threshold value $P_{FE,th}$.

$$P_{out}(\bar{\gamma}_b) = \Pr(P_{FE} > P_{FE,th}) = \Pr(\tilde{\gamma}_b < \tilde{\gamma}_{b,th}) = \int_0^{\tilde{\gamma}_{b,th}} p(\tilde{\gamma}_b | \bar{\gamma}_b) d\tilde{\gamma}_b, \quad (8-19)$$

where $\tilde{\gamma}_{b,th}$ is the effective E_b/N_0 resulting in $P_{FE} = P_{FE,th}$, i.e., $P_{FE,th} = h(\tilde{\gamma}_{b,th})$. $\tilde{\gamma}_{b,th}$ can be derived from the results given in Section 8.2.1.3.

8.2.3.2 Derivation of the PDF of $(E_b/N_0)_{eff}$

Basically, two different methods can be used to obtain the PDF $p(\tilde{\gamma}_b | \bar{\gamma}_b)$:

- Curve fitting to simulation results
- Theoretical approaches

One theoretical approach investigates the PDF of the wide-band-average (normalized received) power of the frequency selective channel. Assuming that the interleaved bits are uniformly distributed over a certain bandwidth, the expressions (8-8) – which are used in the calculation of $(E_b/N_0)_{eff}$ – correspond to such average powers. The derivation of the PDF of the wide-band-average power, written as $p_{p_a}(x)$, is elaborated in Appendix D for Rayleigh and Rician fading channels.

8.2.3.3 Application to $(E_b/N_0)_{eff}$

Two methods have been investigated to obtain the PDF of $(E_b/N_0)_{eff}$ from the PDF of the wide-band average power. Method 1 takes $p_{p_a}(x)$ for the minimum bandwidth over which a minimum length error-sequence of D consecutive coded bits is spread due to the interleaving. Method 2 takes $p_{p_a}(x)$ for the total bandwidth occupied by the OFDM signal. It was found that method 1 yields better results for estimate 1 of $(E_b/N_0)_{eff}$, on which we concentrate in this thesis. The bandwidths taken for the derivation of the PDFs $p_{p_a}(x)$ are listed in Table 8-2.

Results are shown in Figure 8-3 for Rayleigh fading channels and in Figure 8-4 for the Rician case. Different channel parameters and the full rate (FR) and quarter rate (QR) transmission (TX) modes (see Section 5.2) are investigated. Shown in each figure are:

- simulation results for the cumulative distribution function (CDF) of $(E_b/N_0)_{eff}$,
- a log-normal CDF fitted to the simulation outcomes,
- the theoretical exact CDF (see Appendix D), and
- another log-normal CDF for analytically derived parameters.

CDFs are depicted in stead of PDFs, because the fitting in the lower tail is of great importance for the accuracy of outage-rate results. This is observed much better from CDFs.

The fitted (fitted to the simulated PDF) and theoretical (parameters derived from the channel model) log-normal PDFs can be compared well using their parameters (see Table 8-3, and Table 8-4). Observe that the standard deviations agree almost perfectly. However, the means of the theoretical PDFs are too large due to the $\min\{\bullet\}$ operation or non-linear averaging applied in estimating $(E_b/N_0)_{eff}$, which was not taken into consideration (*cf.* eqs. (8-9)–(8-11)). The mismatch of the means can be corrected for

Table 8-2: Bandwidths used to calculate the PDFs of $(E_b/N_0)_{eff}$.

	<i>estimate 1</i>	<i>estimate 2</i>
full-rate (FR) mode	62 MHz	94 MHz
quarter-rate (QR) mode	17 MHz	22 MHz

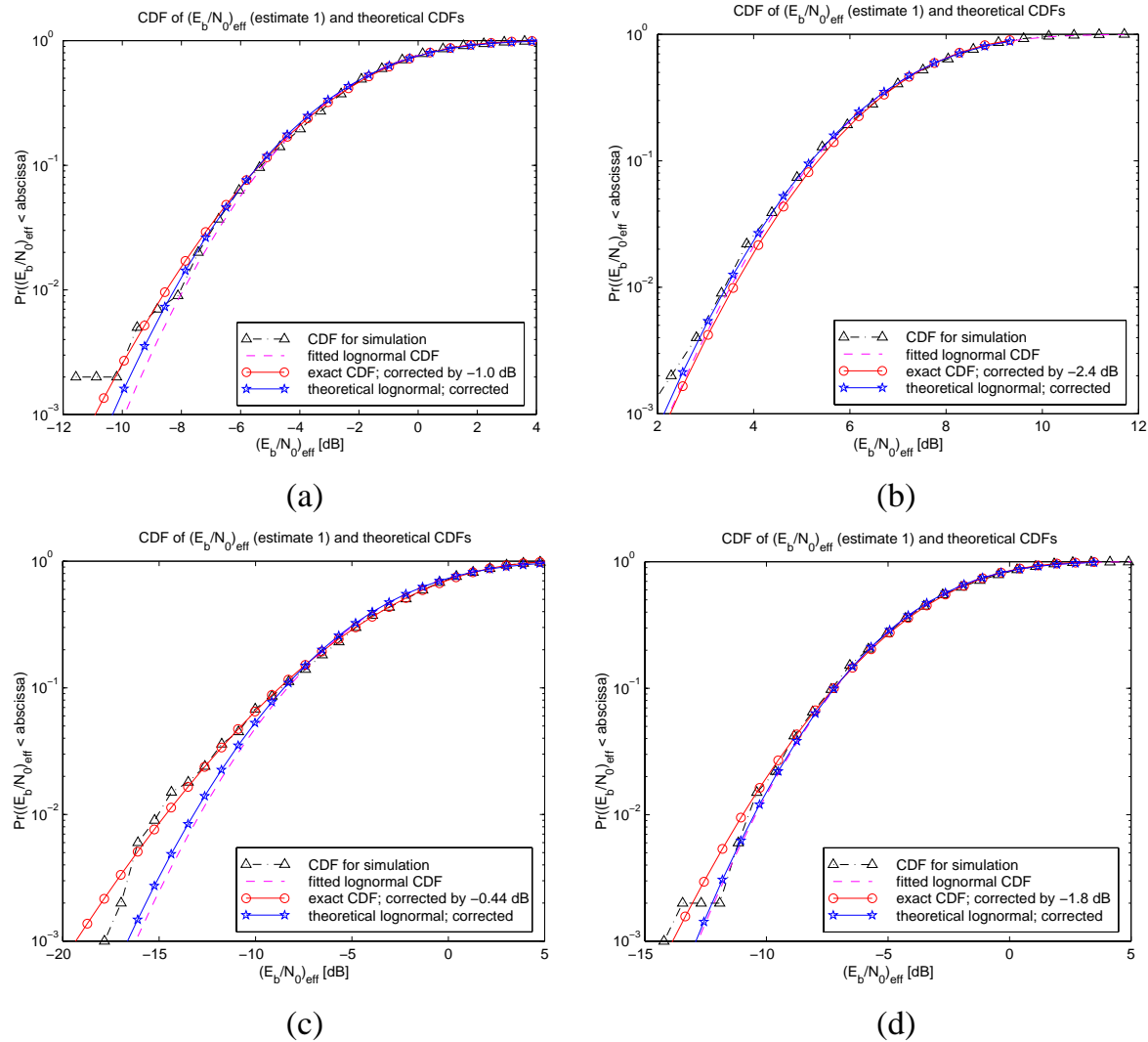


Figure 8-3: Comparison of simulated distributions of $(E_b/N_0)_{\text{eff}}$, estimate 1 with a fitted lognormal CDF, the shifted exact CDF of wide-band average power, and its approximation by the lognormal CDF. Rayleigh fading channels are shown. The parameters are listed in Table 8-3 (boldface rows). (a): $\tau_{\text{rms}} = 55$ ns, QR TX-mode; (b): $\tau_{\text{rms}} = 55$ ns, FR TX-mode (SNR = 10 dB); (c): $\tau_{\text{rms}} = 10$ ns, QR TX-mode; (d): $\tau_{\text{rms}} = 10$ ns, FR TX-mode.

Table 8-3: Parameters of the lognormal PDFs (in dB) fitted to simulation results and theoretical parameters obtained from the channel model. For Rayleigh fading channels.

Parameters			Estimate 1					Estimate 2				
TX-mode	τ_{rms} [ns]	$\overline{\text{SNR}}$ [dB]	theoretical mean	theoretical stdv.	fitted mean	fitted stdv.	corr. factor	theoretical mean	theoretical stdv.	fitted mean	fitted stdv.	corr. factor
QR	55	0	-0.77	2.72	-1.80	2.59	-1.03	-0.64	2.48	-0.91	2.37	-0.27
QR	55	10	9.23	2.72	8.20	2.59	-1.03	9.36	2.48	8.64	2.40	-0.72
FR	55	10	9.72	1.68	7.35	1.64	-2.37	9.81	1.44	8.11	1.41	-1.69
QR	10	0	-1.90	4.48	-2.34	4.34	-0.44	-1.73	4.22	-1.68	4.10	0.05
FR	10	0	-1.02	3.14	-2.82	3.11	-1.80	-0.77	2.72	-1.05	2.68	-0.28

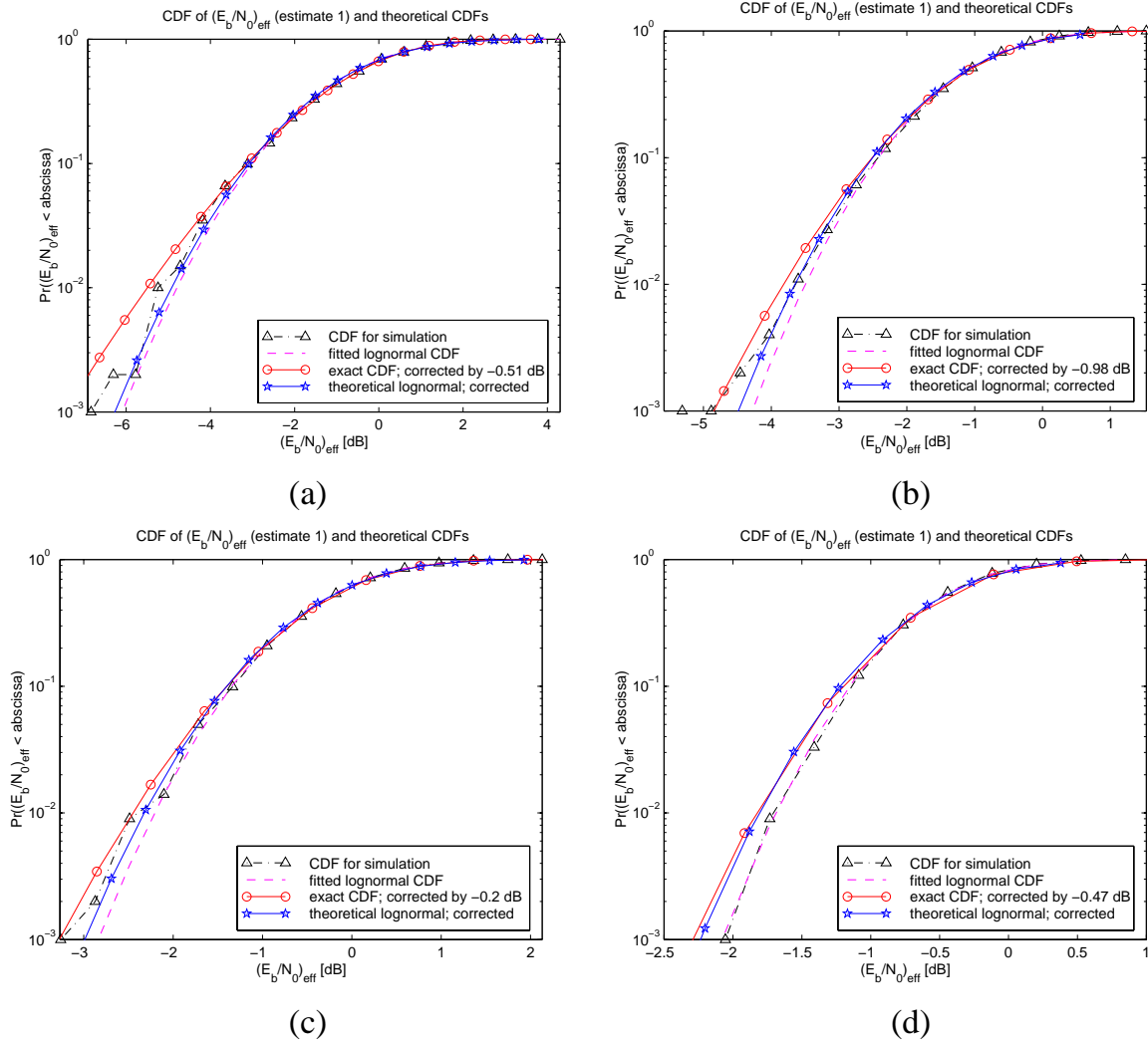


Figure 8-4: Comparison of simulated distributions of $(E_b/N_0)_{\text{eff}}$, estimate 1 with a fitted lognormal CDF, the shifted exact CDF of wide-band average power, and its approximation by the lognormal CDF. Ricean fading channels are evaluated. The parameters are listed in Table 8-4 (boldface rows). (a), (b): $\tau_{\text{rms}} = 12.5$ ns, $K = 8.3$ dB; (a): QR TX-mode; (b): FR TX-mode; (c), (d): $\tau_{\text{rms}} = 6.4$ ns, $K = 14.8$ dB; (c): QR TX-mode; (d): FR TX-mode.

Table 8-4: Parameters of the lognormal PDFs (in dB) fitted to simulation results and theoretical parameters obtained from the channel model. For Ricean fading channels. $\overline{SNR} = 0$ dB.

Parameters			Estimate 1					Estimate 2				
TX-mode	τ_{rms} [ns]	K [dB]	theoretical		fitted		corr. factor	theoretical		fitted		corr. factor
			mean	stdv.	mean	stdv.		mean	stdv.	mean	stdv.	
QR	12.5	8.3	-0.33	1.75	-0.84	1.69	-0.51	-0.29	1.61	-0.39	1.60	-0.10
FR	12.5	8.3	-0.14	1.08	-1.11	1.02	-0.98	-0.10	0.90	-0.21	0.89	-0.11
QR	22.2	0	-1.01	3.12	-1.89	3.19	-0.88	-0.86	2.86	-1.07	2.94	-0.21
FR	22.2	0	-0.40	1.91	-2.17	1.82	-1.77	-0.29	1.59	-0.58	1.49	-0.29
QR	6.4	14.8	-0.09	0.86	-0.29	0.81	-0.20	-0.08	0.80	-0.07	0.79	0.00
FR	6.4	14.8	-0.04	0.55	-0.51	0.49	-0.47	-0.03	0.46	-0.04	0.45	-0.02

by shifting the theoretical PDFs. This was done in the figure, leading to an excellent fitting of the theoretical PDFs and the simulation results. For estimate 1 of $(E_b/N_0)_{eff}$, the mismatch depends on τ_{rms} , K , the BW of the OFDM signal, and on the interleaving scheme; for estimate 2 (not investigated here), the average E_b/N_0 also influences this correction factor. Typical values for this offset, denoted as c_m , are between 0 and -2.5 dB (see Table 8-3 and Table 8-4). The exact numbers can be determined from computer simulations. The correction is formulated as

$$p'_{P_a}(x) = (1/c_m) p_{P_a}(x/c_m). \quad (8-20)$$

8.2.3.4 PDF of Estimate 1 of $(E_b/N_0)_{eff}$

Using the correction factor c_m , the PDF of the average power $p_{P_a}(x)$ is matched to the PDF of estimate 1 of $(E_b/N_0)_{eff}$ at $\bar{\gamma}_b = 1$. This leads to the PDF of estimate 1 as a function of the average power, being

$$p(\tilde{\gamma}_b | \bar{\gamma}_b) = \frac{1}{\bar{\gamma}_b c_m} p_{P_a}\left(\frac{\tilde{\gamma}_b}{\bar{\gamma}_b c_m}\right). \quad (8-21)$$

From (8-19) and (8-21), the outage probability can be directly related to the CDF of $(E_b/N_0)_{eff}$ and to the CDF of the wide-band average power.

$$P_{out}(\bar{\gamma}_b) = F_{P_a}\left(\frac{\tilde{\gamma}_{b,th}}{\bar{\gamma}_b c_m}\right) \quad (8-22)$$

The results as a function of $\bar{\gamma}_b$ would thus have the same shape as the CDFs shown in Figure 8-3 and Figure 8-4, however, mirrored at the $(E_b/N_0)_{eff} = 0$ dB-axis and shifted by $\tilde{\gamma}_{b,th}$.

Since, for estimate 2, the correction factor is a function of the average SNR, $c_m(\bar{\gamma}_b)$, the above equations are not exact for that case.

8.2.4 Performance Results and Discussion

Further evaluation of the proposed method of performance evaluation can be achieved by analyzing special (theoretical) cases of fading channels. Namely, the flat fading channel as one extreme, where all sub-carriers experience the same attenuation (and phase distortion), and independent fading of each transmitted coded symbol as the other extreme. Results for practical channels with correlated fading will be located in-between these cases.

The special cases are analyzed and evaluated in the first part of this section, for Rayleigh distributed fading. Secondly, performance results are presented for practical Rayleigh and Ricean fading channels.

8.2.4.1 Special Cases: Flat and Independent Rayleigh Fading

Considering flat fading, both estimates of the effective E_b/N_0 are equivalent and equal to the $(E_b/N_0)_l$ of any sub-carrier. Thus, the curves shown in Figure 8-1 exactly describe the frame and bit error probabilities for one particular channel realization. By averaging over the PDF of E_b/N_0 , which is defined by the fading statistics, average error rates and outage rates can be calculated. For the Rayleigh fading channels, the PDF of E_b/N_0 is a chi-square distribution with two degrees of freedom, i.e., an exponential distribution (see [6], p. 45).

Flat fading results in the worst possible performance in Rayleigh fading environments (for a given OFDM system and error correction coding scheme), because all carriers undergo the same fading and might thus be simultaneously attenuated by a deep fade. No frequency-diversity is present in this case.

The best possible performance on Rayleigh fading channels can be expected in the second special case, assuming completely independent fading of subsequent coded bits. In this case, the frequency-diversity is maximized.

Evaluation of the second special case is done using the concept of effective (E_b/N_0) , where a chi-square distribution is used to model the PDF of $(E_b/N_0)_{eff}$. Appropriate parameters have to be found for this PDF to obtain performance results. The following considerations are made.

In the most probable error event, the decoder selects an erroneous sequence having the minimum Hamming distance of d_{free} to the correct, transmitted sequence. The PDF of the sum of d_{free} squared, independent, Rayleigh distributed random variables is described by a chi-square distribution with $2d_{free}$ degrees of freedom.

$$p(\tilde{\gamma}_b | \bar{\gamma}_b) \cong \frac{1}{\Gamma(d_{free})} \left(\frac{d_{free}}{\bar{\gamma}_b} \right)^{d_{free}} \tilde{\gamma}_b^{d_{free}-1} \exp(-d_{free} \tilde{\gamma}_b / \bar{\gamma}_b) \quad (8-23)$$

Bound 2 is used for evaluating the performance for this special case, to be on the safe side, since no correction is applied for the $\min\{\bullet\}$ operation in eq. (8-9).

Computational Results

In Figure 8-5, theoretical results of average frame error rate (FER) are compared to computer simulation results for the two special cases. The same (rate $R_c = 1/2$, constraint length $\nu = 3$ (Figure 8-5a) and $\nu = 5$ (Figure 8-5b)) codes are analyzed, which were evaluated over AWGN channels in Section 8.2.1.3 (Figure 8-1). Up to 20000 transmitted ATM cells were simulated, at each value of average SNR. Alternatively, the simulation for a specific SNR was interrupted after detecting 100 erroneously received frames. (One frame is equivalent to an ATM cell). A good matching of the results is observed from the figure.

The comparison of different coding schemes in terms of the average FER and outage probability is illustrated in Figure 8-6. Additionally, results are given for a rate $R_c = 1/2$,

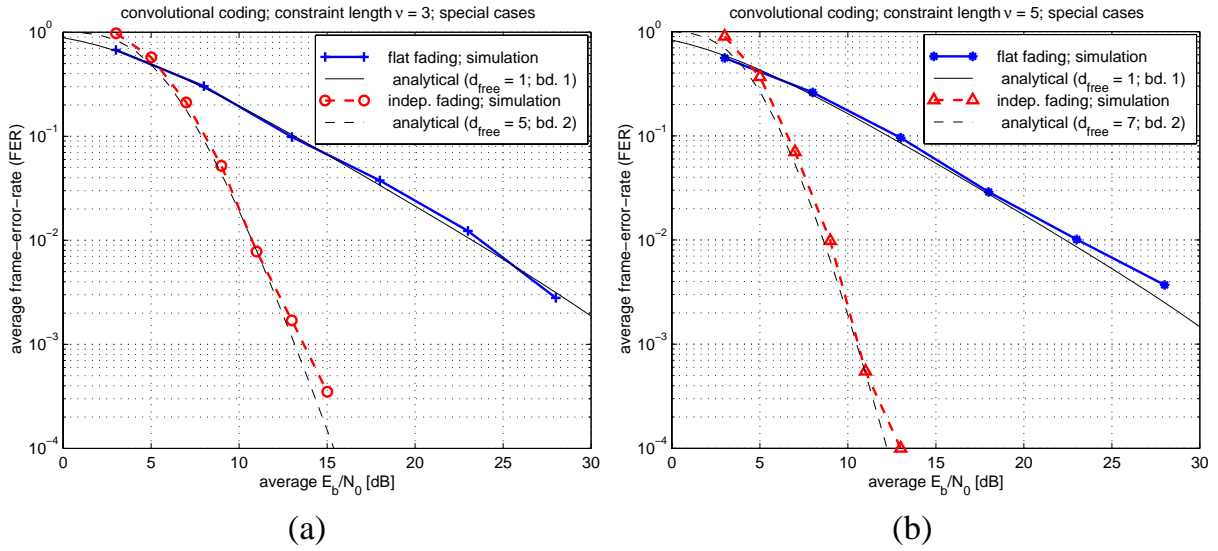


Figure 8-5: Average FER for the two special cases: Flat fading and independent Rayleigh fading. Comparison of theoretical results to computer simulations for two different convolutional coding schemes; rate $R_c = 1/2$, constraint length $\nu = \{3, 5\}$.

constraint length $\nu = 7$ code. It was not possible to assess the latter code with computer simulations because of the excessive simulation time required. (One ATM cell takes approx. 20 minutes).

The figure clearly indicates that higher performance gains are obtained with more complex coding schemes. This holds especially for the case of independently fading sub-carriers.

Outage probabilities may give a better indication of the performance in fading channels. In the scenario of a broad-band computer communications system, the outage

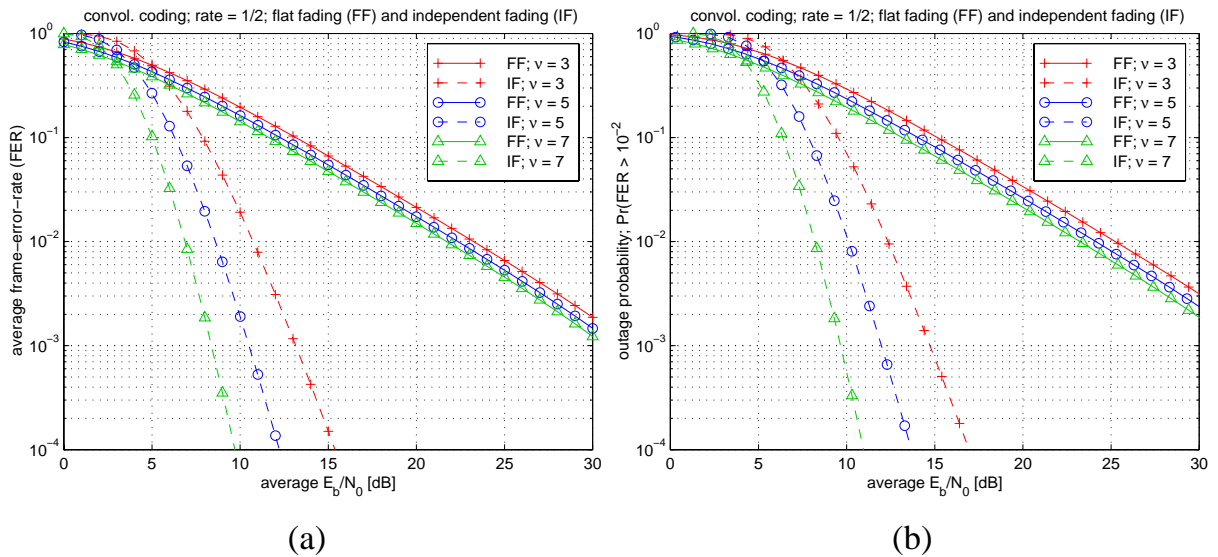


Figure 8-6: Comparison of different rate $R_c = 1/2$ coding schemes for the two special channels. (a): Average FER; (b): Outage probability

probability $P_{out} = \Pr(P_{FE} > 10^{-2})$ quantifies the probability that the FER exceeds one percent at a certain location, with a certain average E_b/N_0 . In other words, if the channel is considered time-invariant, the probability is quantified that the current channel leads to an FER exceeding a certain level. In all other cases (for the given local-area-average SNR), the system performs better. The outage rate is thus usually a stricter performance bound than the average BER or FER.

It is evident from Figure 8-6 that outage rate results (for $\text{FER} > 10^{-2}$) are almost equivalent to results of average FER, except for an SNR gap of about 1 ... 2 dB. I.e., about 1 ... 2 dB more SNR is required to reach a certain level of outage probability ($\text{FER} > 10^{-2}$) than to reach the same level of average FER. Due to the way these results were obtained (by a ‘convolution’ of the error probability curve of the AWGN channel with the PDF of the effective E_b/N_0), there is reason to assume that this similarity of the result-curves is a general property. Other cases studied below confirm this conclusion. The rather steep decay of the error probability curve for the AWGN case (see Figure 8-1) compared with the flat shapes of the $(E_b/N_0)_{eff}$ -PDFs (see Figure 8-3 and Figure 8-4) explain this property.

The uncorrelated channel shows more than 12 dB gain (at $\text{FER} = 10^{-2}$ and at $P_{out} = 10^{-2}$) compared with the fully correlated, flat fading channel.

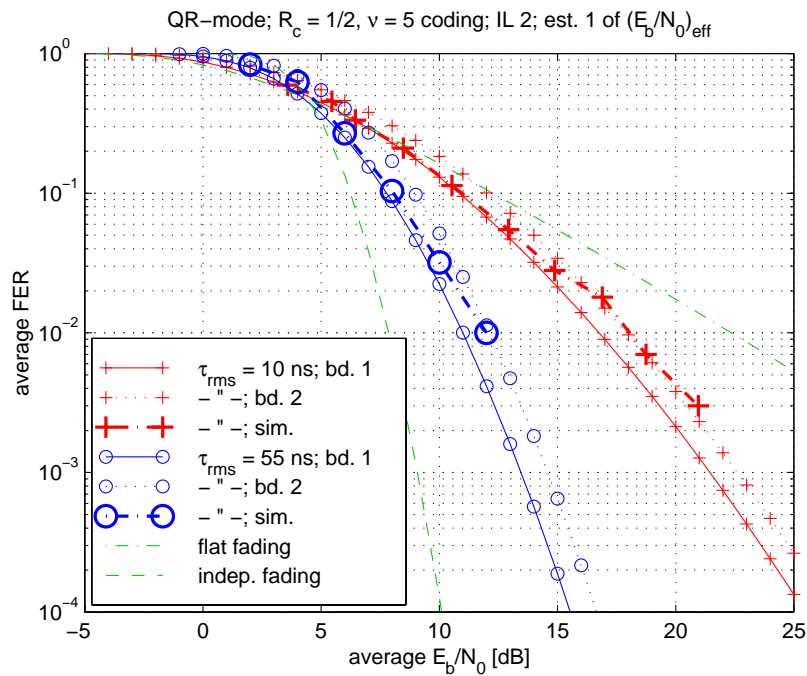
8.2.4.2 Results for Rayleigh Channels

Results of average FER as a function of $\bar{\gamma}_b$ are depicted in Figure 8-7a and b, for the QR and FR TX-modes, respectively. Two Rayleigh fading channels with $\tau_{rms} = 10$ ns and 55 ns were evaluated. For comparison, theoretical results are also given for the two special cases discussed above.

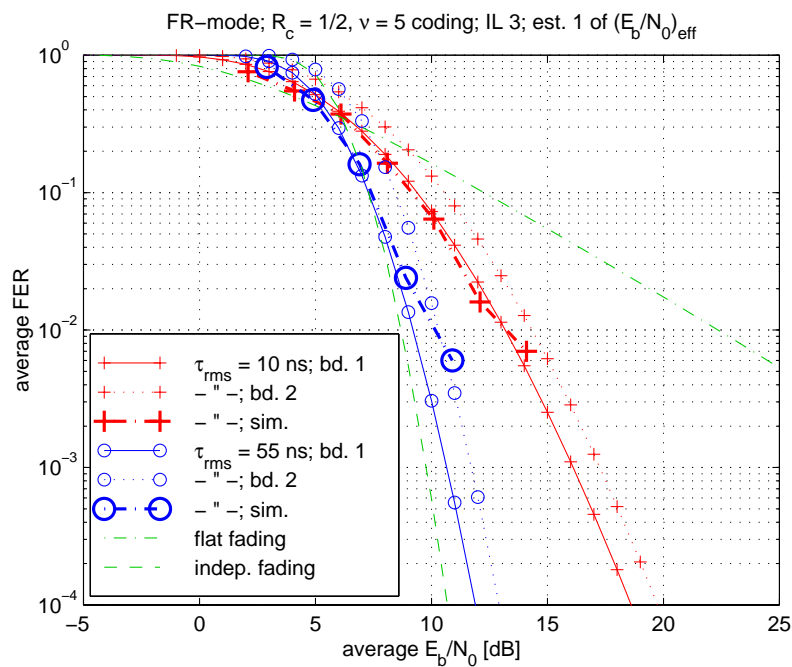
It is clearly seen that the FR mode outperforms the QR mode. This result is not surprising, because in the FR-mode, the interleaver can spread the coded bits over a much larger bandwidth, thus the correlation of the fading of consecutive coded bits is reduced. In other words, more frequency-diversity can be exploited by the coding/interleaving scheme. The less correlation, the closer the performance approaches the bound for the special case of independent fading.

More frequency-diversity also explains the superior performance on channels with higher delay spread. Remember that it was assumed in the OFDM system model that the delay spread of the channel is shorter than the guard interval, i.e., there is no ISI. To mitigate the shortcoming of the QR-scheme, frequency-hopping in combination with time-interleaving during one transmitted packet can be applied.

Simulation results match remarkably well with the theoretical curves. Note that simulations for higher $\bar{\gamma}_b$ are less representative because too few error events (sometimes < 10) were observed. Extremely long simulation times made it impracticable to increase the accuracy. Generally, the simulation results are between the two theoretical bounds (see eq. (8-13)). Bound 2 is rather conservative, while bound 1 is sometimes too opti-



(a)



(b)

Figure 8-7: Average frame error rate as a function of the average signal-to-noise ratio for two Rayleigh fading channels having $\tau_{\text{rms}} = 10$ ns, and $\tau_{\text{rms}} = 55$ ns. (a) QR TX-mode with approx. 25 MHz bandwidth; (b) FR mode with approx. 100 MHz. Note: A fitted log-normal PDF of $(E_b/N_0)_{\text{eff}}$ has been used here to depict the result for the special case of independent fading.

mistic. The average FER has been obtained with an accuracy in the order of ± 1 dB. Similar conclusions can be drawn from the outage-probability results, which are de-

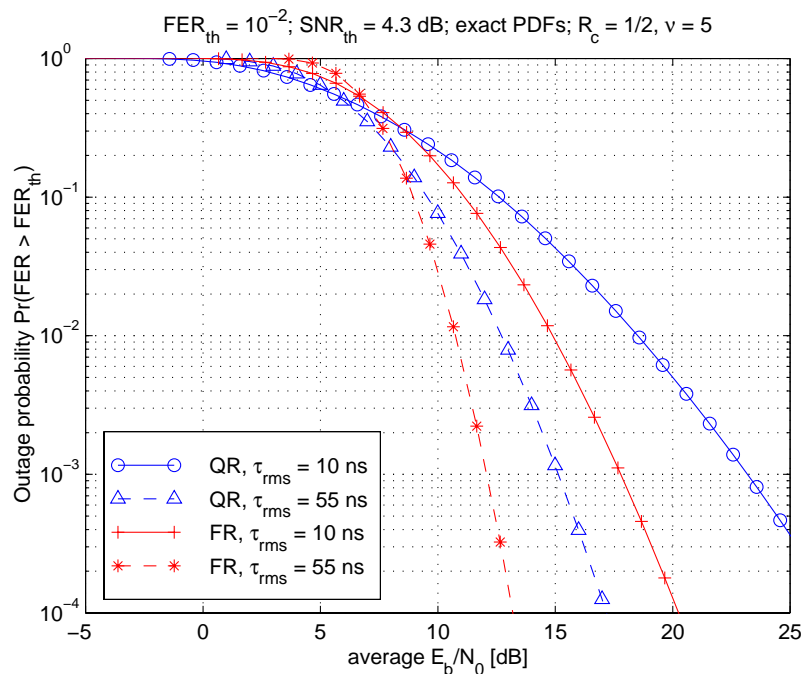


Figure 8-8: Analytical outage probabilities for different Rayleigh channels and for full- and quarter-rate terminals.

pictured in Figure 8-8 for the same system and channel parameters. No simulation results were available to assess these analytical results. Note again, the resemblance of these results with the average FER plots.

8.2.4.3 Results for Ricean fading channels

Results for two Ricean fading channels and for the two transmission modes are depicted in Figure 8-9. Generally, the performance over Ricean channels is superior compared with Rayleigh channels.

A comparison to simulation results is shown for the $\tau_{rms} = 12.5$ ns, $K = 8.3$ dB channel. The analytical error rates are by approx. 0.5 dB worse than these simulation results, in case of the FR transmission mode. This is different for the QR-mode.

Again a clear advantage of the FR mode compared to the QR mode is observed, which is due to the increased frequency-diversity implied by the larger bandwidth. However, the difference is much smaller (< 2 dB at $FER = 10^{-2}$) than over the Rayleigh fading channels (~ 5 dB for the $\tau_{rms} = 10$ ns channel at $FER = 10^{-2}$). In practice, the higher transmission power enabled by the smaller bandwidth (6 dB in the link budget) can be used to compensate for this slightly higher SNR requirement.

The performance difference of the two transmission modes is hardly observed for the second Ricean channel investigated. The high Ricean K-factor of $K = 14.8$ dB ($\tau_{rms} = 6.4$ ns) yields almost equivalent, excellent performance for both transmission modes. Results are only about 1 dB worse than results for the AWGN channel.

Outage probability results are given in Figure 8-10.

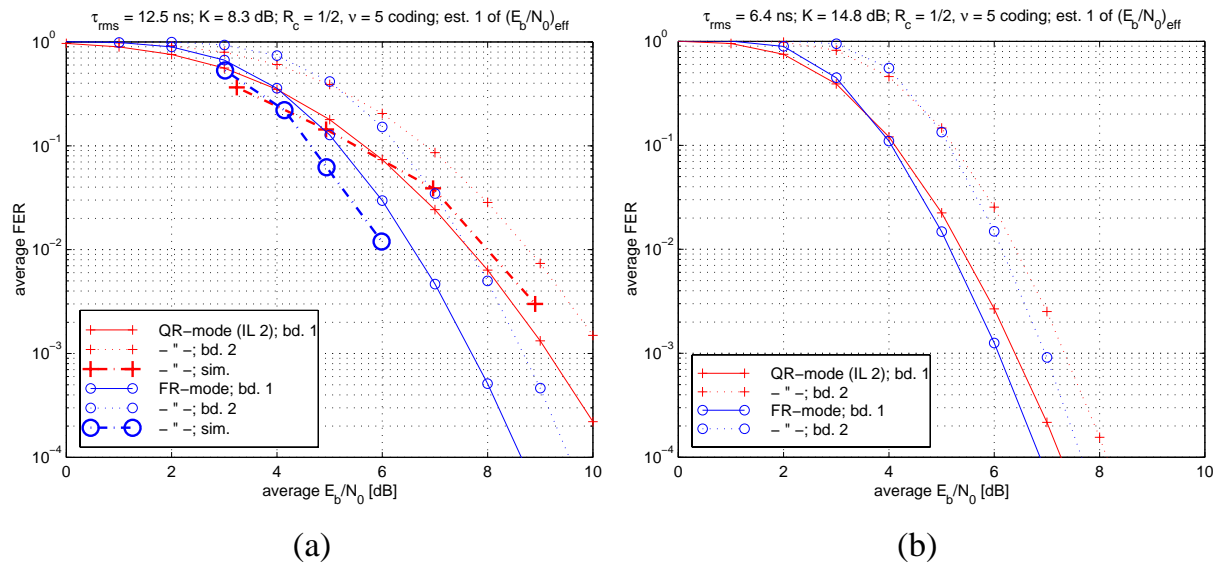


Figure 8-9: Average frame error rate as a function of the average signal-to-noise ratio for two Ricean fading channels. (a) $\tau_{rms} = 12.5$ ns, $K = 8.3$ dB; (b) $\tau_{rms} = 6.4$ ns, $K = 14.8$ dB

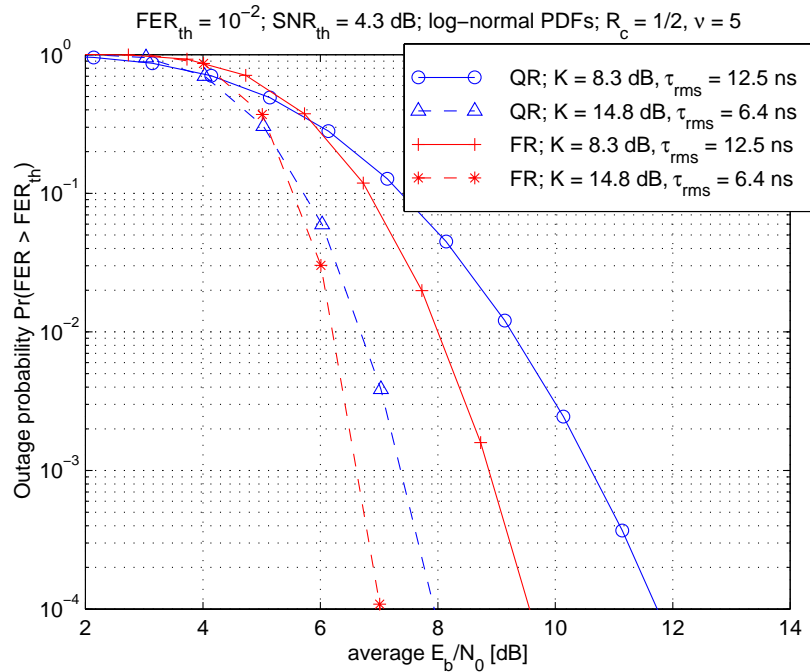


Figure 8-10: Analytical outage probability results for Ricean channels and for full- and quarter-rate terminals.

8.2.5 Summary

In this section, the estimation of frame error rates (FER) is demonstrated, for packet oriented OFDM transmission systems including convolutional coding and bit-level interleaving. The concept of effective E_b/N_0 [1] is used to achieve this goal without the need for time-intensive computer simulations. This procedure requires the following steps:

- For a given channel realization (a channel transfer function (TF)), the E_b/N_0 -values at individual coded symbols are transformed into one scalar, the so-called effective E_b/N_0 (see eq. (8-9)).
- This effective E_b/N_0 is then translated to a bit or frame error probability (see Section 8.2.1.3).

A set of channel realizations thus leads to a set of performance results, at given average E_b/N_0 and channel parameters. These results may be averaged consecutively. The original method [1] proposes the simulation of channel realizations to derive the performance results.

An extension/modification has been introduced in this section. The idea is to determine the PDF of the effective E_b/N_0 for a given set of channel parameters $\{\tau_{rms}, K, \text{average } E_b/N_0\}$ and for given OFDM system parameters, which allows for the analytical evaluation of average error probabilities and outage probabilities (Section 8.2.3.1). The derivation of this PDF requires the following steps:

- Calculate analytically the PDF of the wide-band average power (for the bandwidth over which the coded symbols are spread in the most likely error event; see Section 8.2.3.3)
- Correct for the bias between the average-power PDF, and the PDF of the effective E_b/N_0 . This bias (approx. 0 ... 2.5 dB) can be determined exactly by computer simulations.

Except for the last step, the method is thus fully analytical. Based on the following rules-of-thumb, the correction factor may be roughly estimated, in order to skip the simulation step.

- More frequency-diversity usually implies higher correction factors. I.e., larger bandwidth and larger τ_{rms} require a larger correction factor.
- If the interleaving leads to almost independently fading coded bits, then 2.5 dB correction are appropriate.
- A channel that introduces only about one significant fade to the whole signal requires a correction of about 0.5 dB.

It should be possible to empirically find a relation between – for instance – the coherence bandwidth or frequency-domain level crossing rate of the channel and the correction factor, considering the system bandwidth. The investigation and formulation of such a relation is subject for further work.

Conclusions on performance results are summarized in Section 8.4.

8.3 Performance Enhancement using Antenna Diversity

Coded OFDM systems exploit the frequency-diversity of wide-band radio channels to enable robust data communication over frequency-selective fading channels. The coded data stream is therefore well spread over the bandwidth of the signal spectrum, using an interleaving scheme in the frequency-direction. The channel's frequency-selectivity, and thus the potential frequency-diversity, depends on the delay spread of the channel. The longer the delay spread, the more fades are present per unit of bandwidth, which is of advantage for the coded and interleaved transmission scheme, because errors occur more independently. (See the performance results in Section 8.2.4).

The proposed antenna diversity schemes aim to improve the performance in the opposite situation. If the channel delay spread is very short, then the whole OFDM signal is faded equally (i.e., the channel is flat), which may induce long error bursts that are hard to correct. There is not sufficient frequency-selectivity in this case to be exploited by the coding and interleaving schemes. Using a set of transmit or receive antennas, the presented diversity schemes can randomize the channel response and thereby increase the frequency diversity. Note that the discussed methods can be used at the transmitter and/or at the receiver.

The first strategy to achieve such gains employs cyclic delays applied to the effective parts of the OFDM symbols (Section 8.3.1). Another method transmits the even and odd sub-carriers via separate antennas (Section 8.3.2). A common property of these novel diversity techniques is their high computational efficiency. In the first scheme, the signal processing is done on the time-domain OFDM signal, thus the Fourier transform does not need to be duplicated. In the second scheme, the FFT is divided in two halves.

To employ a conventional diversity technique, all blocks of an OFDM receiver including the FFTs must be present M -times (M is the number of diversity branches). Such a scheme for the receiver is shown in Figure 8-11. There, for each sub-carrier the

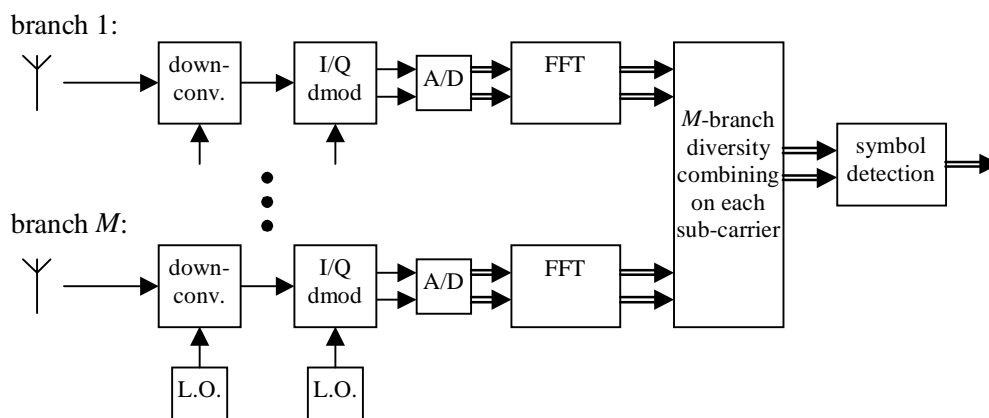


Figure 8-11: Block diagram of an OFDM receiver allowing conventional diversity techniques on each sub-carrier.

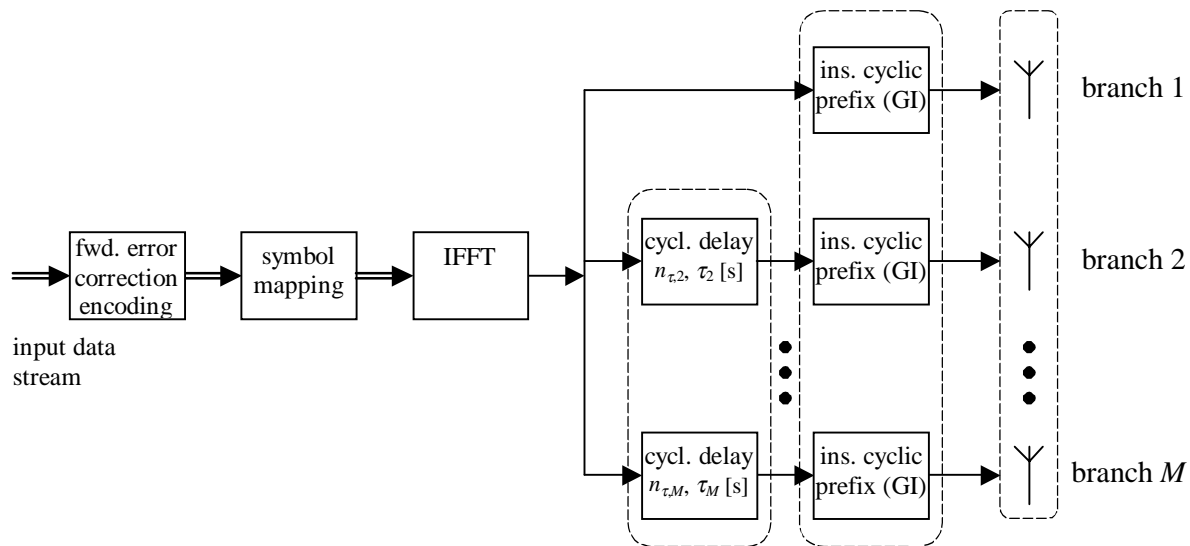


Figure 8-12: Diversity technique using cyclic delays for the transmitter.

output values of the M FFT blocks are combined using the well-known methods for space diversity, as, for instance, selection diversity, maximal ratio combining, equal gain combining, etc..

8.3.1 Antenna Diversity for OFDM Using Cyclic Delays

The core idea of this novel scheme concerns the introduction of cyclic delays to the effective parts (FFT-parts) of the OFDM signals transmitted/received via several antennas.

For the transmitter, the novel diversity technique is depicted in Figure 8-12. Up to the IFFT, which is used to modulate data constellations on the OFDM sub-carriers and whose output is the time-domain OFDM signal, a conventional OFDM system is present. In order to generate signals for a number of transmit antennas, cyclic delays (of $n_{\tau,i}$ samples or τ_i seconds, $i = \{1, 2, \dots, M\}$; $\tau_1 = 0$) are introduced to the (effective) FFT-parts of the OFDM symbols. A cyclic delay means that the $n_{\tau,i}$ samples shifted beyond the effective part are transmitted in the beginning of that part of the symbol (see Figure 8-13). In the conventional manner, the cyclic prefix (guard interval) is

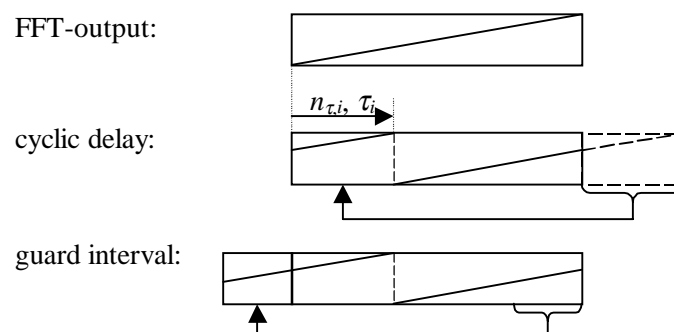


Figure 8-13: Applying a cyclic delay to the effective part of the OFDM symbol.

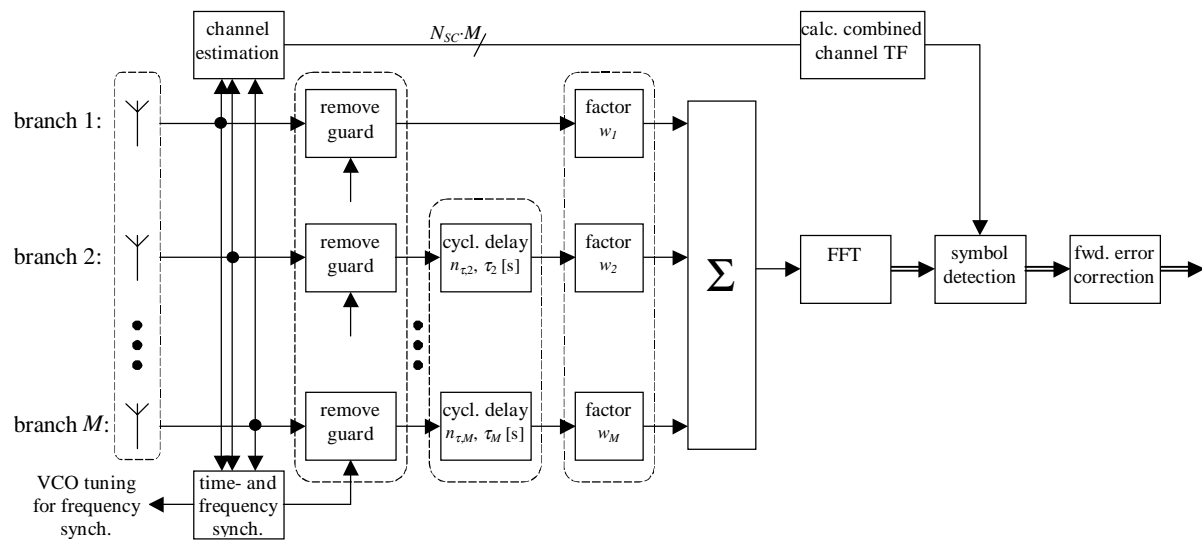


Figure 8-14: Diversity technique using cyclic delays and weighting factors for the receiver.

transmitted prior to the effective part.

The method presented is similar to the delay diversity scheme described in [9]. The cyclic delays allow for much longer delays, however, which are otherwise limited to fractions of the guard interval period to avoid inter-symbol-interference. This fact is paramount for applying the proposed technique at the transmitter, where no information is available on the length of the current channel's impulse response.

Similarly, cyclic delays can be applied to the OFDM signals received via multiple antennas, in order to perform diversity combining at the OFDM receiver prior to the FFT (see Figure 8-14). Utilized at the receiver, the delay times can be adapted (optimized) based on individual channel estimates for each diversity branch. Moreover, weighing factors $\{w_i\}$ can be applied to allow for more flexibility. (A pre-FFT diversity scheme based on such weighing factors, but without delays, is analyzed in [10].) The optimization of the parameters is subject for further research. Since the channel transfer functions are (usually) not available at the transmitter, such an optimization is not possible there. Therefore, the application of weighing factors at the transmitter is less promising, although it is generally possible.

The operation of the diversity schemes, and some design considerations for the delay times (for a non-adaptive scheme) are discussed below.

8.3.1.1 Illustration of the Method

As seen from the idealized system model derived in Section 4.2.3, the OFDM subcarriers are attenuated and phase distorted according to the channel transfer function (TF). The diversity scheme randomizes the TF of the composite channel as follows. The TFs $H_i(f)$ (time-variability is neglected) of a Rayleigh fading channel are correlated, zero-mean, complex Gaussian random processes. The superposition of the channel TFs of individual antennas is therefore also a Rayleigh channel, as the sum of zero-

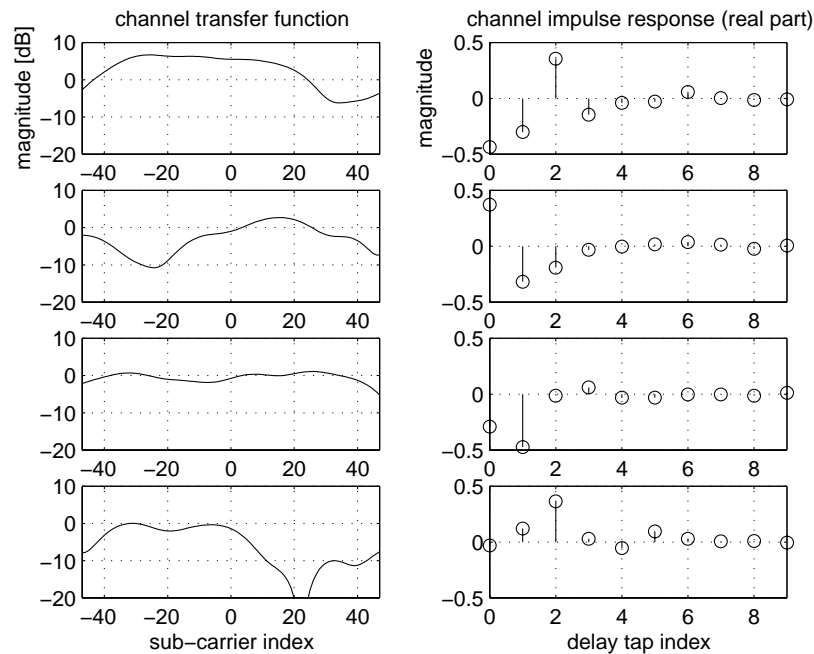


Figure 8-15: Four (independent) channel realizations. The left-hand side depicts the channels' magnitude transfer functions; the right-hand side illustrates the real-parts of the impulse responses.

mean Gaussian processes is yet another zero-mean Gaussian process. The correlation properties are altered, however, by the cyclic delays introduced. The following equation gives the TF for the composite channel. It is seen that the cyclic delays introduce progressive phase rotations to the TFs.

$$H_{\Sigma}(f) = \frac{1}{\sqrt{M}} \sum_{i=1}^M H_i(f) e^{-j2\pi\tau_i f} . \quad (8-24)$$

The normalization by $1/\sqrt{M}$ is introduced to keep the transmission power constant, when the method is used at the transmitter. At the receiver, this factor can account for the channel noise that adds up incoherently. The noise for the combined channel can then be considered equal to the noise of a single channel. Note that the weighing factors are not incorporated in this brief analysis.

The correlation properties of the composite channel are investigated in the following sub-section. Here, we firstly illustrate the principle of the diversity technique, and we discuss the necessity that signals of *multiple* antennas are combined and that delays are introduced.

Figure 8-15 depicts the transfer functions and impulse responses of four independent frequency-selective channels. Having short impulse responses, their frequency-selectivity is limited. It is seen that the channels have similar fading characteristics, particularly, their impulse responses have similar length. Superimposing these channels without delays, the sum of channels is just another channel with a similar IR and fre-

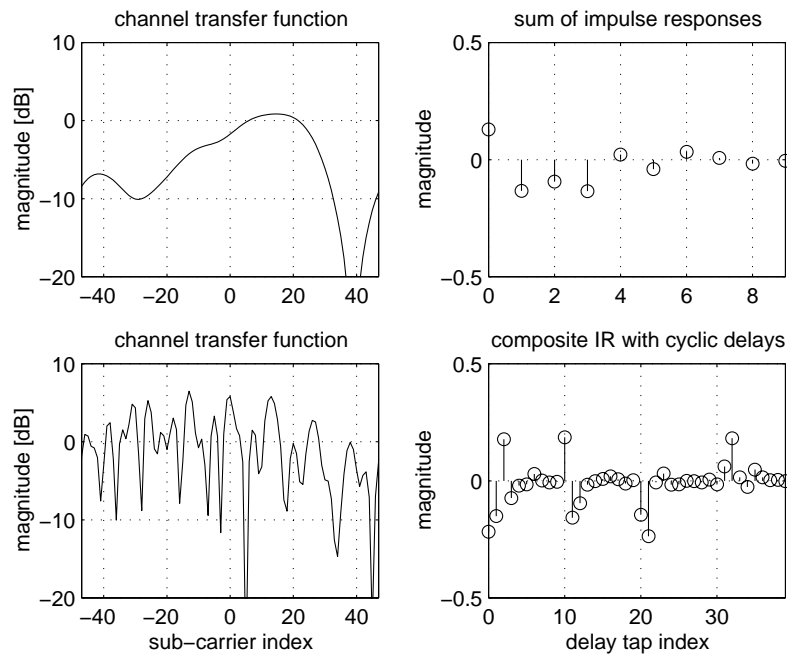


Figure 8-16: Transfer functions (left-hand side) and impulse responses (right-hand side) of the composite channels. The figures in the first row show the channel of the superposed channel *without* the introduction of cyclic delays. The characteristics of this channel are equivalent to the characteristics of the component channels. In the second row, cyclic delays were applied, leading to a clear randomization of the channel transfer function.

quency-selectivity, as seen from the top-row of figures in Figure 8-16. Nothing is lost or gained in this case.

Introducing the cyclic delays, the composite channel consists of all those IRs, shifted by the respective delay times. This leads to a much-extended overall IR, corresponding to a more random channel TF, as seen from the second row of graphs in Figure 8-16. Thereby, inter-symbol-interference is avoided due to the cyclic way of applying the delays.

It is not possible to obtain a similar randomization by combining (with delays) multiple copies of the received signal of a single antenna. This would be equivalent to the application of a transversal filter to the received signal. If the filter can be adapted, it is well possible to equalize the transfer function and to get a flat channel response. Unfortunately, the noise level is thereby modified accordingly; therefore nothing is gained. Combining (cyclically) delayed copies of the signal without weighing factors, for instance, means a multiplication of the channel TF by a filter TF that has zeros at certain positions. Clearly, such filtering cannot enhance the performance of an OFDM system.

8.3.1.2 Analysis and Selection of the Delay Times

Let us briefly analyze the correlation properties of the combined channel. It is assumed

that the (independent) component channels have similar stochastic properties, expressed by a common spaced-frequency correlation function $\phi_H(\Delta f) = E\{H_i^*(f)H_i(f + \Delta f)\}$. The sum (8-24) is a sum of zero-mean complex Gaussian random processes, which gives another zero-mean complex Gaussian process, as mentioned above. Accounting for the phase rotations, the spaced-frequency correlation of the composite channel is written as

$$\phi_{H_\Sigma}(\Delta f) = \phi_H(\Delta f) \frac{1}{M} \sum_{i=1}^M e^{-j2\pi\tau_i\Delta f}. \quad (8-25)$$

The correlation is reduced, because the magnitude of the sum term is less or equal to one [9]. Appropriately selecting τ_i , it is possible to force a zero in this correlation function for the frequency separation corresponding to the separation of subsequent coded bits. Unfortunately, for double the separation, the normalized sum in (8-25) becomes one again (if two branch diversity is used). The bit at triple that distance is then in a zero again. Additional diversity branches enable the nulling of more subsequent bits.

A large reduction of the correlation function is obtained, for instance, when zeros are forced to be on directly adjacent sub-carriers, i.e., on sub-carriers separated by $\Delta f = \{F, 2F, \dots, (M-1)F\}$, where F is the sub-carrier spacing. This makes the correlation function at frequency-separations of integer multiples of F

$$\phi_{H_\Sigma}(kF) = \begin{cases} \phi_H(kF) & \text{if } k = lM \\ 0 & \text{otherwise} \end{cases}, \quad (8-26)$$

where $\{k, l\}$ are integer variables. Such a result is obtained for delays

$$\tau_i = \frac{i-1}{MF} \text{ or } n_{\tau_i} = (i-1) \frac{N}{M}, \quad (8-27)$$

where N is the number of FFT-points. Note that, when using this parameter set, it is important that the interleaving depth is selected differently to M , otherwise the correlation of the fading on subsequent coded bits is not reduced at all.

8.3.2 Even/odd Sub-carrier Transmitter Diversity

This section describes another computationally highly efficient method to achieve antenna diversity gain using multiple transmitter antennas.

Figure 8-17 shows the block diagram for the case of two transmitter antennas. As in a conventional OFDM transmitter, the input data stream is forward error correction encoded and mapped on constellation points of any (typically low-order) modulation scheme. The de-multiplexer separates the constellation points to be transmitted as odd and even sub-carriers. Two $N/2$ -point IFFTs are executed on these constellations. To produce the N samples of a (full bandwidth) OFDM signal, the (complex-valued) output samples of the FFTs are essentially duplicated. The resulting signals now occupy

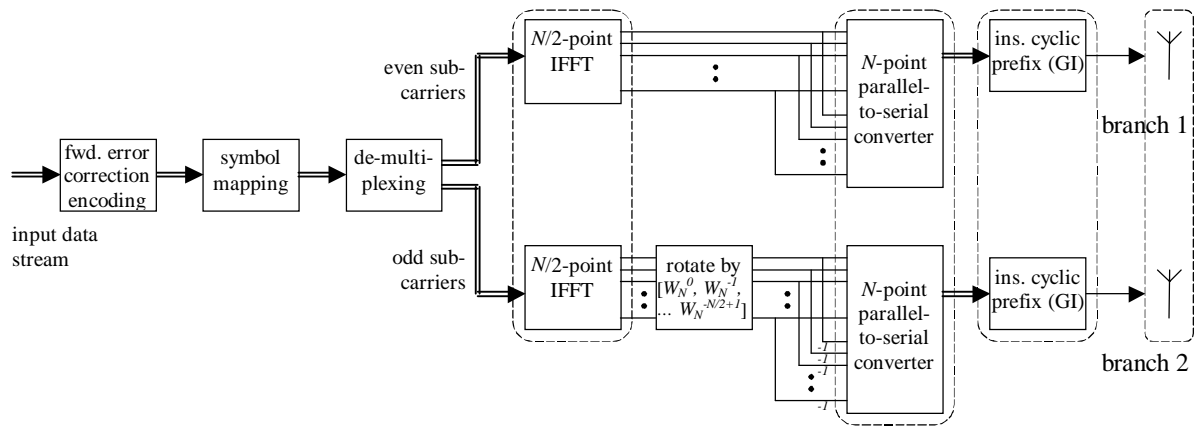


Figure 8-17: Block diagram of the even/odd sub-carrier transmitter diversity scheme.

exactly every second sub-carrier. The signal of branch one is directly applied to the first RF transmitter, after adding the cyclic prefix. This signal occupies the even sub-carriers; the odd sub-carriers are zero.

To fill in the odd sub-carriers, a multiplication of the second signal with the complex exponential sequence $[W_N^0, W_N^{-1}, \dots, W_N^{-N/2+1}]$ is required, where $W_N = \exp(j2\pi/N)$. This shifts the second signal in the frequency domain by one sub-carrier. The signal thus occupies the odd sub-carriers after conversion to RF.

A more efficient way of calculating the $N/2$ complex multiplications is shown in Figure 8-17. The $N/2$ -output samples of the IFFT of branch two are multiplied by $[W_N^0, W_N^{-1}, \dots, W_N^{-N/2+1}]$. This yields the first $N/2$ (complex-valued) time-samples for transmission. The second $N/2$ time-samples are obtained by flipping the signs of the first $N/2$ samples, since $W_N^{-i} = -W_N^{-(N/2+i)}$. Thereby, $N/2$ complex multiplications are saved. Note the equivalence of the proposed technique to the last step of a decimation-in-time FFT algorithm [11].

The two signals are modulated on equal frequency RF carriers for transmission via two antennas. On the (linear) channel, the signals are superimposed and then received with a conventional OFDM receiver. To enhance the channel estimation, it will be of benefit for the OFDM receiver to know about the implementation of this diversity technique. Then the receiver can estimate separately the two channels being present on the even and odd sub-carriers.

The scheme can be extended to higher numbers of diversity branches M . Efficient implementation as presented in Figure 8-17 is possible if M is an integer power of two.

Note that the correlation function for this technique is equivalent to the correlation function given by eq. (8-26) (assuming independent component channels). The performance is thus expected to be equal to the performance of the delay diversity technique, with delays according to eq. (8-27). The simulation results given below confirm the anticipated behavior.

8.3.3 Performance

Simulation results of frame-error-rates (FER) are given in Figure 8-18a, for the diversity scheme using cyclic delays and for Rayleigh fading channels. The same simulation parameters have been selected as in Section 8.2.4.2. Since the greatest gain is expected for the quarter-rate transmission mode (due to its small bandwidth) and for the $\tau_{rms} = 10$ ns channel (due to the low frequency-selectivity), this case is considered here. The OFDM system model assumes perfect synchronization and channel estimation.

We investigate the transmitter diversity scheme, where the transmitted power per diversity branch was divided by the number of branches, M , in order to maintain a constant total transmit power (see eq. (8-24)). Equivalent results would be obtained for the receiver diversity schemes without optimizing the delays $\{\tau_i\}$ and weighing factors $\{w_i\}$.

Delays of $\{0,4\}$ and $\{0,2,4,6\}$ samples were introduced for the two and four-branch diversity schemes, respectively. Such delays yield zeros in the correlation function at adjacent coded bits, when applying a depth four interleaver (Interleaver 1, IL 1, from Section 5.2.4.2). For comparison, the FER is also shown without diversity and for the special case that all sub-carriers are faded independently.

It is seen that, at a FER of 1 %, a gain of almost 10 dB is possible for the special case (independent fading) over the single antenna result. About 5 and 7 dB are obtained with two- and 4-branch diversity, respectively.

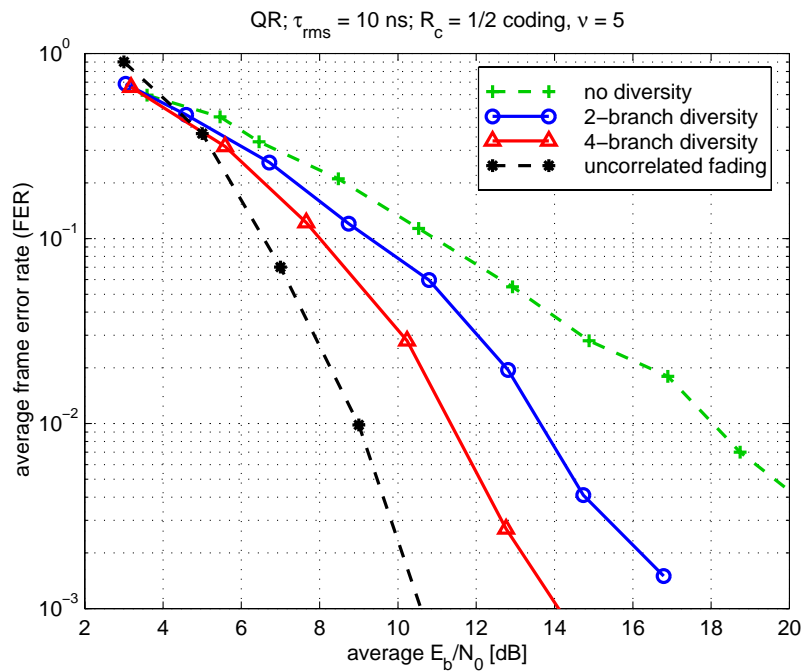
Simulation results for the even/odd sub-carrier scheme (two branch) and – for comparison – for a two-branch selection diversity technique are depicted in Figure 8-18b. The performance of the former is similar to the delay diversity scheme for two branches (see Figure 8-18a), as expected.

Selection diversity, which is utilized at the receiver (see Figure 8-11), adaptively chooses on each sub-carrier the signal constellation from the strongest branch. Due to this adaptivity, about 3 dB gain is obtained, compared to the transmitter diversity scheme. The slopes of the FER-curves are about equal, however.

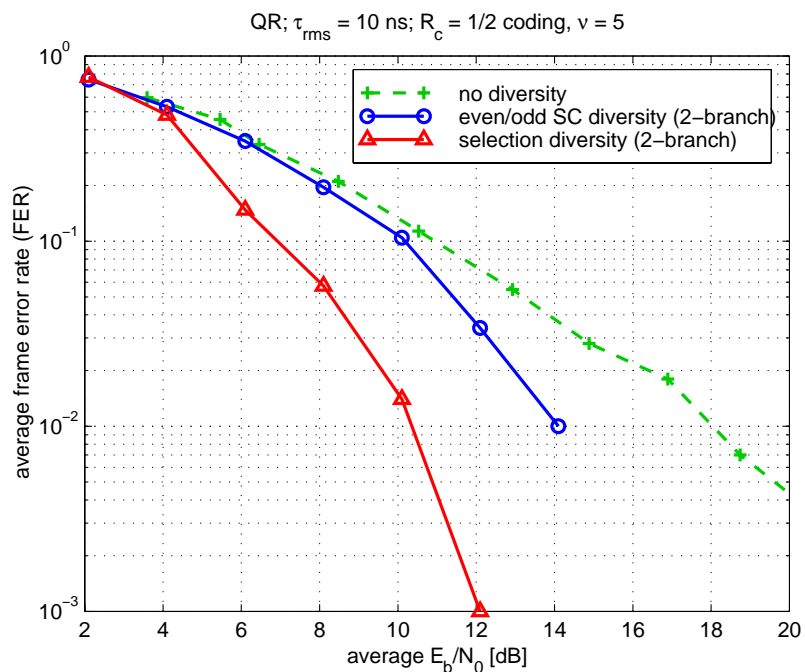
8.3.3.1 Performance Evaluation using the Concept of Effective (E_b/N_0)

The PDF of the effective (E_b/N_0) has been studied by modeling the distribution of the wide-band average received power of the frequency-selective channel over the bandwidth over which the minimum distance error event is spread by the interleaver (Section 8.2.3). In this section, we briefly discuss the impact of antenna diversity on this PDF.

The composite channel for the non-adaptive diversity schemes is the superposition of M independent wide-band channels. Therefore, we assume that for M -branch antenna diversity, the wide-band average power is described by the sum of M independent ran-



(a)



(b)

Figure 8-18: Frame error rate results for a rate- $1/2$ convolutional code with a constraint length of five. QR transmission mode; $\tau_{rms} = 10$ ns Rayleigh channel. (a): Delay diversity with nulling of the correlation function at adjacent coded bits. (b): Even/odd sub-carrier diversity scheme and two-branch selection diversity.

dom variables (RV) that describe the wide-band average power of the component channels. The analysis of the Eigenvalues for the combined channel correlation function (8-26) confirms this assumption. Remember that the Eigenvalues specify the vari-

Table 8-5: Parameters of log-normal PDFs (mean and standard deviation in dB) fitted to the distributions of the effective (E_b/N_0) (estimate 1) for several channels and delay-diversity settings. IL: Interleaving scheme: IL 1 has depth 4; IL 2 has depth 3; a depth 9 interleaver is used for the FR-mode (see Section 5.2.4.2). DIV 1: Delays are chosen such to force zeros in the correlation function at adjacent sub-carriers. DIV2: Zeros are forced at adjacent coded bits according to the interleaver. DIV 1 is used unless otherwise specified.

<i>Nb.</i>	<i>M</i>	τ_{rms} [ns]	<i>TX-mode</i>	<i>mean</i>	<i>stdv.</i>	<i>comment</i>
1	1			-2.3	4.3	one branch; for reference
2	2			-2.0	3.0	IL 1; DIV 2
3	2	10	QR	-1.8	2.9	IL 2; DIV 1
4	4			-1.8	2.2	IL 1; DIV 2
5	4			-1.7	2.2	IL 2; DIV 1
6	1			-1.8	2.6	one branch; for reference
7	2	55	QR	-1.9	2.0	IL 2
8	4			-1.7	1.6	IL 2; stdv. approaches limit
9	-	-	QR	-2.0	1.3	independent fading; for reference
10	1			-2.8	3.1	one branch; for reference
11	2	10	FR	-2.5	2.2	
12	4			-2.9	1.8	stdv. approaches limit
13	1			-2.7	1.6	one branch; for reference
14	2	55	FR	-2.9	1.4	stdv. approaches limit
15	4			-3.2	1.2	stdv. approaches limit
16	-	-	FR	-3.3	1.0	independent fading; for reference

ances of independent Gaussian RVs that are added up to model the distribution of the wide-band average received power (see Appendix D, eq. (D-4)). Investigating the influence of antenna diversity, it is seen that the original Eigenvalues are replaced by groups of M equal Eigenvalues of $1/M$ the original value. (Considering the power-normalization by $1/\sqrt{M}$). This leads, compared to the non-diversity case, to a PDF having an equal mean and a variance divided by M (see eqs. (D-8)).

Unfortunately, the exact PDF as defined by eq. (D-7) cannot be used in this case for modeling the PDF of the composite channel's average power, because this equation requires all Eigenvalues to be different. We do not give here the exact PDF for this case. In stead, we investigate the influence of M -branch diversity-combining on the parameters of the approximated PDFs. In particular, we focus on the mean and standard deviation of the log-normal PDF. Computer simulations of channel realizations have been used to fit this PDF to the distribution of effective (E_b/N_0).

Some general behavior is evident from these parameters, which are listed in Table 8-5.

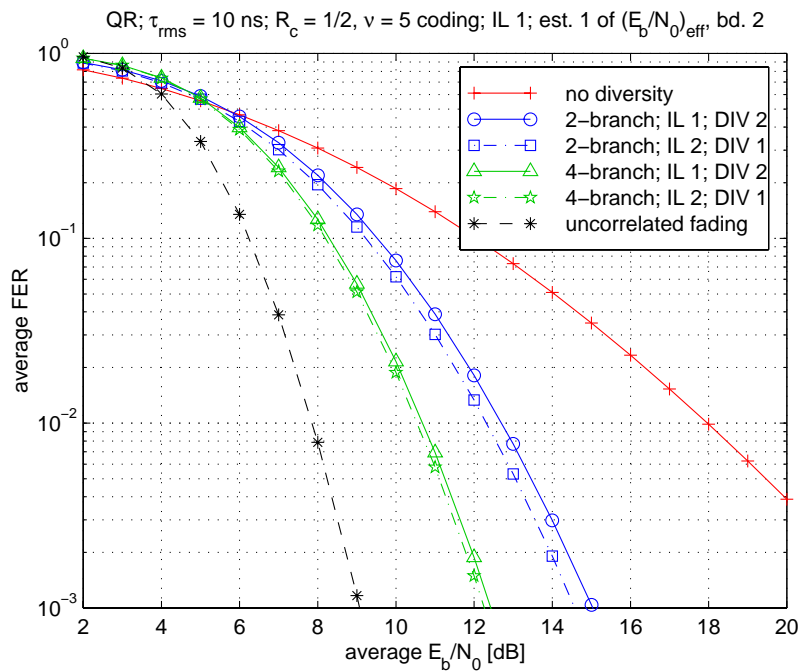


Figure 8-19: Theoretical performance results in terms of average FER, obtained by the concept of effective E_b/N_0 .

For instance, the standard deviation for M -branch diversity is well predicted by dividing its dB-value without diversity ($M = 1$) by \sqrt{M} . This empirical rule only works however, until the standard deviation for the special case that all sub-carriers fade independently is approached (see lines 9, 16 in the table). This limit can not be exceeded (lines 8, 12, 14, 15). The mean values (in dB) remain almost constant.

Figure 8-19 depicts performance results for the quarter-rate receiver over the $\tau_{rms} = 10$ ns channel. The results were derived by using the concept of effective (E_b/N_0) with the log-normal PDFs for the parameters listed in Table 8-5, lines 1–5, and 9. These curves are to be compared to Figure 8-18a, where good agreement is evident. Moreover, two delay settings and interleaving schemes are compared, which are seen to result in largely equivalent performance.

8.3.4 Discussion of the Diversity Schemes

A considerable performance improvement is the main advantage of the techniques investigated, as seen from the performance results. Basically, the transmitter diversity schemes can be employed without modifying the receiver. However, care must be taken with synchronization and channel estimation techniques and to some extent with the interleavers. That is, the parameters of all system components should be carefully chosen to minimize interference effects among them. The following points have to be considered.

Channel estimation schemes sometimes exploit the correlation between the channel coefficients of adjacent sub-carriers in order to reduce the noise floor of the channel

estimates. Eliminating this correlation by the suggested diversity techniques, it is clear that such principles would perform sub-optimally or fail. For instance, in the channel estimation scheme proposed for the OFDM system under investigation, the even-indexed sub-carriers are determined by interpolating between the two adjacent (odd-indexed) sub-carriers, which are estimated from pilots in the training symbol (see Section 6.4). This interpolation must fail, if correlation among adjacent sub-carriers lacks. Timing synchronization offsets introduce a progressive phase rotation, as shown in Section 4.2.4. This progressive phase rotation can be accurately determined from a known training symbol, yielding an accurate estimate of the residual timing offset (see Section 6.2.7). Again, high correlation among the sub-carriers has to be assumed in order to achieve good performance in presence of a frequency-selective channel. This correlation is largely destroyed, however, by the diversity technique. A possible remedy for this issue is to calculate the timing-offset estimate over the still-correlated sub-carriers. (The ones spaced by M sub-carriers, if the $\{\tau_i\}$ are selected according to the criterion given in eq. (8-27).)

In Schmidl's method [12] (see Section 6.2.3), (frame) timing-synchronization is done by looking for a unique training symbol, which carries information only on the even-indexed sub-carriers. The odd sub-carriers are zero. Such symbols do not occur in a conventional OFDM signal, unless they are explicitly inserted. Using the even/odd sub-carrier diversity technique, however, signals with very similar properties may be evident at the receiver, whenever one of the signals is strong while the other one is deeply attenuated. If known data is modulated on the training symbol, the frame start can be confirmed by demodulation. Note that this problem may also occur for the two-branch delay diversity technique, if the $\{\tau_i\}$ are selected according to eq. (8-27), due to the equivalent correlation properties.

The above issues only apply if the diversity schemes are utilized at the transmitter. At the receiver, synchronization and channel estimation can be done prior to the diversity combining, as shown in Figure 8-14.

The amplitude distribution of the combined channel is another point to be considered. If the component channels are Rayleigh distributed then the sum of the channels will be Rayleigh distributed as well, and performance gain is obtained due to the enhanced frequency-diversity. The depth of the fades won't be influenced.

On channels with shallower fades – for instance Ricean channels with considerably high K -factors –, the performance is generally improved due to the lower probability of “deep fades”. Applying the proposed diversity schemes in this case, the combined channel (see eq. (8-24)) would have deeper fades due to the randomization. A possible performance gain by the non-adaptive techniques is therefore questionable.

8.4 Conclusions and Recommendations

In Section 8.2, the concept of effective E_b/N_0 [1] was successfully applied to OFDM based wireless ATM transmission systems. It enables performance evaluation in terms of bit and frame error rates for coded and interleaved data transmission over fading channels.

A novel extension to this concept is proposed. By determining the PDF of the effective E_b/N_0 , the calculation of *outage probabilities* and *average error probabilities* is enabled. Based on an analytical approach investigating the PDF of the wide-band-average received power of the frequency-selective Rayleigh and Ricean fading channels, appropriate models have been found for these distribution functions. The log-normal PDF can serve as an approximation, as seen from simulation results. The parameters of the PDF of the effective E_b/N_0 are derived analytically from the channel model except for a correction factor in the range of 0 ... 2.5 dB. This factor must be determined by channel simulations, or it can be roughly estimated based on the observation of the typical channel behavior. A description of this correction factor as a function of system and channel parameters is subject for further research. This would yield a fully analytical method of performance evaluation.

The methods developed enable the fast and accurate comparison of coding and interleaving techniques. The distribution of the wide-band-average power is also useful for the analysis of other OFDM system components. For instance, the outage probability of synchronization algorithms can be evaluated, as their performance depends on the signal power received over the total bandwidth of the OFDM signal.

The performance results show clear improvements with increased frequency-selectivity of the channel (longer delay spreads), and with increased system bandwidth. (When the fading distribution remains unchanged, e.g. Rayleigh.) These factors raise the frequency-diversity that can be exploited by the coding scheme. Accordingly, worst performance corresponds to the case where all OFDM sub-carriers fade equally (flat fading), and best performance is obtained for independently fading sub-carriers. These special cases have been evaluated. About 12 dB of gain are evident between them, at an average frame-error-rate of one percent. Results for practical channels lie in-between these borders.

Comparing the analytical results of outage probability ($FER > 10^{-2}$) to the results of average FER remarkable resemblance is evident. At the selected threshold FER and coding scheme, an SNR gap of about 1 ... 2 dB is the only difference between equivalent levels of outage probability and average FER. The way these performance measures are related to the PDF of the effective E_b/N_0 leads to the conclusion that this is a quite general property.

Novel antenna diversity schemes have been proposed to improve the frequency-diversity in the undesirable case that all sub-carriers fade (about) equally (flat-fading). Con-

siderable diversity gain can be obtained by appropriately combining the signals of multiple receiver antennas, or by transmitting appropriate signals via multiple transmit antennas.

The first scheme discussed is a delay diversity technique employing cyclic delays to avoid inter-symbol-interference. Applied at the transmitter (where no channel information is available), the frequency-diversity of the channel is increased. Applied at the receiver, channel estimates for individual diversity branches can be employed to optimize the diversity combining. This optimization is a subject for further investigations.

The second scheme transmits sub-sets of the sub-carriers via different antennas, which also improves the frequency-diversity. Both schemes require uncorrelated fading channels, i.e., the antennas must be sufficiently separated in space, by at least about one wavelength.

A common feature of the proposed techniques is their extremely low computational complexity, compared with conventional diversity schemes that would require a multiplication of main parts of the OFDM receiver including the FFTs. The novel schemes work with the time-domain OFDM signals in one case, and in the other case, partial FFTs are executed for each diversity branch.

Generally, the *transmitter* diversity techniques can be used with a conventional OFDM receiver. Care must be taken, however, with synchronization and channel estimation algorithms.

The results analyzed show about 5 and 7 dB gain for two and four diversity branches, compared to the single antenna results, for the schemes that apply no optimization. Such large gains are only feasible in almost flat channels, however. The gains are reduced in channels that already have more frequency-diversity.

8.5 References

- [1] S. Nanda and K. M. Rege, "Frame error rates for convolutional codes on fading channels and the concept of effective E_b/N_0 ," *IEEE Trans. Veh. Technol.*, vol. 47, no. 4, pp. 1245–1250, Nov. 1998.
- [2] R. van Nobelen and D. P. Taylor, "Analysis of the Pairwise Error Probability of Noninterleaved Codes on the Rayleigh-Fading Channel," *IEEE Trans. Commun.*, vol. 44, no. 4, pp. 456–463, Apr. 1996.
- [3] J. K. Cavers and P. Ho, "Analysis of the Error Performance of Trellis-Coded Modulations in Rayleigh-Fading Channels," *IEEE Trans. Commun.*, vol. 40, no. 1, pp. 74–83, Jan. 1992.
- [4] P. Ho and D. Fung, "Error Performance of Multiple-Symbol Differential Detection of PSK Signals Transmitted over Correlated Rayleigh Fading Channels," *IEEE Trans. Commun.*, vol. 40, no. 10, pp. 1566–1569, Oct. 1992.

-
- [5] M. Sandell, *Design and Analysis of Estimators for Multicarrier Modulation and Ultrasonic Imaging*. Ph.D. Thesis, Luleå University of Technology, Sept. 1996.
 - [6] J. G. Proakis, *Digital Communications*, 3rd edition. New York: McGraw Hill, 1995.
 - [7] C. Lee, *Convolutional Coding: Fundamentals and Applications*. Boston: Artech House, 1997.
 - [8] G. C. Clark, J. B. Cain, *Error-Correction Coding for Digital Communications*. New York: Plenum Press, 1981.
 - [9] Y. Li, J. C. Chuang, and N. R. Sollenberger, “Transmitter Diversity for OFDM Systems and Its Impact on High-Rate Data Wireless Networks,” *IEEE J. Select. Areas Commun.*, vol. 17, no. 7, pp. 1233–1243, July 1999.
 - [10] M. Okada and S. Komaki, “Pre-DFT Combining Diversity Assisted COFDM,” *IEEE Trans. Veh. Technol.*, vol. 50, no. 2, pp. 487–496, March 2001.
 - [11] A. V. Oppenheim and R. W. Schaffer, *Discrete-Time Signal Processing*, 2nd Edition, Upper Saddle River, NJ: Prentice Hall, 1999.
 - [12] T. M. Schmidl and D. C. Cox, “Robust frequency and timing synchronization for OFDM,” *IEEE Trans. Commun.*, vol. 45, no. 12, pp. 1613–1621, Dec. 1997.

Chapter 9 – Conclusions and Recommendations

In this chapter, the main conclusions (C1–C63) of this dissertation are summarized, and recommendations for further research (R1–R13) are given.

9.1 Part I: Channel Characterization

9.1.1 Modeling of the Frequency-Selective Radio Channel

A second order, wide-sense stationary stochastic model is presented to characterize the frequency-selective transfer function of wide-band radio channels.

The model describes the small-scale behavior of the channel within a “local area”. It is defined by a fixed set of model parameters, which can be related to physical channel parameters. Different parameter-sets may apply at different local areas. A parameter set relates to a constant *power* delay profile, which assumes that the ray-magnitudes do not change abruptly for small displacements of the transmitter or receiver.

For a limited observation bandwidth, however, the channel parameters do change also within a local area, because the channel impulse response is not fully resolvable. That is, multiple impinging rays interfere at the resolvable delay time-bins, whose duration relates to the inverse of the observation bandwidth.

C1	A fixed set of channel parameters can characterize the small-scale fading within a local area, corresponding to a fixed set of parameters in the quasi wide sense stationary uncorrelated scattering (QWSSUS) -type of channel model used.
----	--

C2 Due to a limited observation bandwidth, channel parameters appear to vary within a local area.

An exponentially decaying delay power spectrum, the mathematical description of the time-dispersive and frequency-selective radio channel, agrees well with the expected physical behavior of a mm-wave indoor radio channel, where the transmitter and the receiver are typically located within the same room.

- C3 The actual channel impulse response has little impact on stochastic channel properties, like the level crossing rate of the channel transfer function, for a given set of channel parameters (average power, Ricean K -factor, and RMS delay spread).
- C4 Therefore, it is concluded that the proposed channel model can be applied in other frequency-bands and environments as well.

9.1.2 Channel Measurement Technique using the FD-Level Crossing Rate

- C5 The RMS delay spread (RDS) of a multipath radio channel is proportional to the frequency-domain level crossing rate (LCR_f) of the frequency-selective channel transfer function.

For Rayleigh fading channels, the general proof of this relation is given. For Ricean channels, the proof is based the channel model studied in Chapter 2.

- R1 The derivation of the general proof of the relation given in C5 for Ricean fading channels is a subject for further research.

The relation of C5 can be used to estimate the RDS from measurements of the *power* transfer-function of the channel versus frequency, which is sufficient to determine the LCR_f . The Ricean K -factor and the average received power can be estimated from such power measurements as well, leading to complete sets of parameters for the channel model proposed in Chapter 2. That is, a novel channel measurement procedure has been developed, using simplified non-coherent measurement equipment, because only the *power* transfer function of the channel needs to be scanned.

- C6 Complete sets of channel parameters can be estimated from non-coherent measurements of the channel's (power) transfer function.

- C7 The relationship and the actual proportionality factor used for estimating the RDS are insensitive to changes in the channel model or channel impulse response.

- C8 For Rayleigh fading channels, the relationship is completely independent of the channel impulse response.

Measurement noise tends to increase the LCR_f , leading to overestimation of the RDS. This issue has to be taken into account when applying the proposed technique for channel measurements.

- R2 A basic analysis of the problem is given and some possible solutions are indi-

cated, but there is room for further work.

C9 To limit the influence of noise on the novel measurement technique, the sampling interval in the frequency-domain has to be selected as large as possible.

R3 Another topic for further research is an elaborate comparison of the proposed novel measurement technique to conventional techniques and to other ways of data processing.

The level crossing rate in the frequency domain (LCR_f) depends in very distinct ways on the channel parameters average power, Ricean K -factor, and RMS delay spread. This leads to the conclusion that those parameters comprise a most significant set of parameters for characterizing the frequency-selective radio channel.

C10 The RMS delay spread and the Ricean K -factor are equally important for characterizing the frequency-selective radio channel.

9.2 Part II: OFDM System Proposal and Evaluation

9.2.1 OFDM System Modeling

The derivation of the OFDM system model has confirmed that using the OFDM modulation technique, data symbols can be transmitted independently over multipath radio channels.

C11 There is no interference among subsequent OFDM symbols (inter-symbol-interference – ISI) or among adjacent sub-carriers (inter-carrier-interference – ICI), if the following conditions are fulfilled: (Otherwise interference is introduced leading to some performance degradation.)

- The channel impulse response must be shorter than the guard interval.
- Time-synchronization must be sufficiently accurate: all multipath components must remain within the guard interval.
- No carrier frequency-offset, carrier phase-noise, Doppler spread, and sampling frequency-offset.
- All system components must be linear.

Using this system model and the channel model of Chapter 2, the bit-error-rate (BER) of an uncoded OFDM system has been evaluated for coherent and differential detection and for various modulation schemes.

C12 The performance generally depends on the Ricean K -factor of the channel and on the average received signal power. Increasing any of these parameters reduces the average BER.

The fading channel induces error floors, particularly if differential detection is applied.

C13 For the delay spread and time-variability encountered in a wide-band indoor communications system, differential detection in the time-direction is much superior to differential detection in the frequency-direction, because the channel's time-variability between subsequent OFDM symbols is lower than the variation among adjacent sub-carriers.

The equations introduced are a basis for evaluating other degrading effects as listed above. However, more research is required for the implementation and comparison of all these factors.

9.2.2 OFDM Air-Interface and Multiple Access Scheme Proposal

A novel OFDM based air-interface and multiple access scheme is proposed for a wireless communications system. Transmission rates up to 155 Mbit/s can be supported in slowly time-variant channels at 60 GHz.

C14 Time-division duplexing enables asymmetric data rates.

C15 The application of various coding and modulation schemes provides adaptability to varying channel conditions.

A so-called “quarter-rate” mode simultaneously supports simplified terminals operating at a quarter of the full system bandwidth.

C16 It is recommended to implement frequency hopping in the quarter-rate mode to avoid performance degradation due to the decreased frequency-selectivity caused by the reduced bandwidth.

C17 The quarter-rate mode can be used by terminals with largely reduced hardware requirements, and as a fall-back mode when the link-budget becomes critical.

Training-symbols are periodically transmitted on the down-link for robust synchronization and channel estimation; pre-equalization is employed on the up-link.

C18 This makes a highly efficient multiple access scheme, where little overhead is needed to separate multiple users in time or frequency. Small data entities like single ATM cells can thus be supported.

C19 A periodically transmitted training symbol embedded in a fixed frame structure allows for robust synchronization (on the down-link), introducing very little overhead (1.4–2.8 %).
--

C20 Pre-equalization used on the up-link leads to a highly efficient multiple access scheme and to simplified data detection algorithms at the base station with low additional complexity at the mobile.

C21 The multiple access scheme described is optimized for a centralized scheduled multiple access control (MAC) protocol, which makes the system attractive for applications where multiple constant-rate wide-band data streams are present. Examples are wireless video or audio recording studios.

The strictly hierarchical structure using base stations and mobile terminals may be a disadvantage, as it will pose big difficulties when the proposed air-interface is utilized for ad-hoc networks.

R4 The co-channel interference among cells with equal carrier frequencies is a topic for further research, in this context.

A major drawback of the system is its limited range.

R5 Future work may focus on diversity techniques, adaptive antennas, or turbo coding in order to enhance the range.

9.2.3 Issues in utilizing the 60 GHz Frequency-Band

C22 Shadowing is a critical problem in a mobile system operating in the 60 GHz band, because the radio link may drop when the line-of-sight (LOS) path gets obstructed by the user. Even the leaves of a tree may block the LOS (in outdoor environments), causing link failure.

C23 Multiple base-station antennas at well-separated locations within a room may reduce this problem.

R6 Additional research has to address the challenges of hardware technologies required for the 60 GHz RF-front-ends. Amplifier linearity and oscillator phase noise are important issues in OFDM, where strict specifications have to be fulfilled with low-power and low-cost devices.

9.2.4 Synchronization and Channel Estimation on the Down-Link

The key synchronization steps for the proposed OFDM system are described and evaluated in Chapter 6. A training symbol (TS) periodically transmitted on the down-link enables robust synchronization at low computational complexity. The overhead introduced is small.

C24 Multiple, subsequently performed synchronization stages enable the estimation of all relevant synchronization-offsets and their correction, using the training sequence and the pilot sub-carriers.

By processing the time-domain TS, coarse timing and frequency synchronization is acquired. The TS is then transformed to the frequency-domain, where its known data is used for refining the estimates of the synchronization offsets.

- C25 The performance of the synchronization steps is sufficient for the system proposal considered, at average signal-to-noise ratios (SNR) down to about 0 dB. I.e., the system can stay synchronized even if the SNR required for reliable data communication is not available any more.
- C26 Further enhancement is possible by appropriately combining offset estimates obtained from multiple subsequent training symbols.

Synchronization may be lost in severe shadowing situations.

- R7 Emphasis should be put on the development of algorithms that allow the transmission system to quickly recover from outages in such cases.
- C27 Large simplifications in the required processing steps are achieved by locking all local oscillators and the sampling clock to a common (tunable) frequency source. Doing so, all frequency-offsets are cancelled simultaneously by synchronizing for just one of them.

The analysis of a fine timing-offset estimation scheme is presented, which is original work. The estimates' standard deviation is given for AWGN channels as a function of the SNR and as a function of parameters of the TS, allowing for some optimization of the TS. Unfortunately, a multipath radio channel deteriorates the estimation accuracy. A bias is introduced, which can be expressed in terms of the channel parameters, employing the channel model of Chapter 2.

C28 In dispersive channels, time-synchronization schemes show a positive bias, which is for Rayleigh channels roughly equal to the RMS delay spread of the channel.

C29 In order to compensate for this bias, the FFT-period of the OFDM signal should be cyclically shifted to start a few samples before the end of the guard interval.

C30 It has been discovered that DC-offsets and carrier feed-through may have a significant impact on the performance of a popular class of frequency-synchronization algorithms, which evaluate correlation sums over periodic parts in the (time-domain) OFDM signal.

C31 A simple extension to these algorithms can eliminate the induced performance degradation in the most relevant cases.

The training symbol can be used to obtain a channel estimate, as known data is carried on it.

C32 Efficient channel estimation can be performed using this training symbol, due to the relatively slow time-variability of the channel.

C33 (Wiener) filtering in the frequency-domain can reduce the mean-square-error of the estimated channel transfer functions.

However, the achieved BER performance improvement is small. Moreover, adaptability becomes an issue because a Wiener filter has to be optimized for the current channel conditions.

C34 It has been realized that timing offsets must be considered in the design of the Wiener filter, i.e., the bias of the timing-offset estimation scheme has to be taken into account.

C35 In practice, non-adaptive filters can be used giving sub-optimum results.

C36 At small additional loss, filtering can be fully omitted.

C37 Due to the small gain achieved with enhanced channel estimation techniques at drastically increased complexity, their application is not recommended.

9.2.5 Pre-Equalization for the Up-Link

Data transmission on the up-link is based on pre-equalization, where the frequency-selectivity of the radio channel is (partly) compensated at the transmitter's side using the channel estimate from the down-link.

C38 Pre-equalization eliminates the need for training symbols (on the up-link), turning the communications system more efficient, particularly if short data packets are transmitted.

C39 Coherent detection becomes possible at reduced complexity, because channel estimation is not required.

C40 Accurate timing-offset estimation and synchronization are needed on the up-link. Furthermore, the carrier phase offset and the magnitude of the received symbols have to be estimated. (The latter is only required if higher order quadrature amplitude modulation (QAM) schemes are applied.)

The radio channel is assumed quasi-static and reciprocal.

R8 The assumption of channel reciprocity in a practical hardware set-up (the equivalence of the channel transfer functions on the up- and down-links) should be confirmed by an experimental study.

C41 Pure phase pre-equalization can be utilized for phase modulation techniques, where just the phase distortion is compensated.

R9 Optimum power assignment can be added to minimize the average BER. This is a topic for further research.

C42 Full (phase and magnitude) pre-equalization is required for higher order QAM schemes.

C43 The main objective of the technique described in this thesis is to maintain a constant transmit power. Therefore, deeply attenuated sub-carriers are not used for data, as they would require too much of the transmit power. Error correction coding can recover this data at the receiver.

C44 The average <i>uncoded</i> BER performance on the up-link is similar to the BER of the down-link, assuming a static channel.
--

R10 In further research, error correction coding and the channel's time-variability should be included in the performance analysis.

R11 Pre-equalization can be combined efficiently with adaptive modulation. This is another topic for further research.

9.2.6 Emulation System and OFDM Implementation

The emulation system developed is a downscaled hardware platform that can be used for the demonstration of wide-band air-interface techniques like OFDM.

C45 Synchronization aspects can be implemented and studied in real-time, as the system introduces realistic carrier and sampling frequency-offsets between the transmitter and the receiver. Other hardware impairments are present as well, like DC-offsets and carrier feed-through.

C46 The system specifications are suitable for the implementation of OFDM air-interfaces regarding the linearity and carrier phase noise.

C47 Software implementation difficulties are largely avoided due to the drastically reduced processing speed.

The key algorithms of the investigated OFDM air-interface have been implemented on the emulation system.

C48 The implementation of synchronization algorithms has shown that time- and frequency-synchronization are achieved at sufficient accuracy, resulting in excellent performance results.

C49 This demonstrates that the orthogonality of data symbols can be maintained sufficiently well, in a practical, implemented OFDM transmission system.

C50 The sampling frequency-offset between the transmitter and the receiver (of 20–50 ppm) has to be considered in the signal processing algorithms of the OFDM receiver. Its estimation is rather time-consuming.

C51 Thus it is recommended to omit this critical step and implicitly correct for the

sampling frequency-offset by locking the sampling clock on the easily synchronized mixer oscillator, as described above.

C52 The reduced bandwidth of the quarter rate terminals implies reduced frequency-diversity, thus the robustness and the performance are degraded, compared with full-rate receivers.

C53 The impact of DC-offsets and carrier feed-through on the correlation-based frequency-synchronization algorithm, and the effectiveness of the enhanced, insensitive algorithm, have been validated experimentally with the emulation system.

The performance limitation due to the time-variant channel has been studied.

C54 Error floors are sufficiently low to be corrected by forward error correction coding, under the low-mobility conditions assumed. However, the margins are small, thus simple channel prediction (linear extrapolation) should be implemented, allowing for significant enhancements at low additional complexity.

9.2.7 Performance Evaluation and Enhancement of COFDM

The concept of “effective E_b/N_0 ” can be applied for the performance evaluation of convolutionally coded and interleaved OFDM schemes in frequency-selective channels. In this method, the simulated channel transfer function is converted to a scalar value, the effective E_b/N_0 , which is then related to the (bit or frame) error probability.

C55 The PDF of the scalar “effective E_b/N_0 ” enables the analysis of average error probabilities and outage probabilities. This PDF is a function of channel and OFDM system parameters, including the average SNR, the signal bandwidth, and the interleaving scheme of the OFDM system.

Analytical approaches have been developed for the derivation of this PDF, however, a multiplicative factor remains uncertain, which should be determined by means of computer simulations.

R12 Deriving an analytical expression for this parameter is a topic for further research, which would turn the performance evaluation scheme to a fully analytical one.

C56 From the way average error probabilities and outage probabilities are derived from the PDF of the effective E_b/N_0 , it has been concluded that both performance curves as a function of the SNR are very similar. A constant gap between these curves depends on the error rate for which the outage probability is calculated.

C57 The performance of an OFDM system improves when the delay spread of the channel increases, because more frequency-diversity can then be exploited. (Under the condition that the maximum excess delay remains shorter than the guard

interval.)

C58 Systems with larger bandwidth also show some performance advantage, for the same reason.

Novel, computationally efficient antenna diversity schemes are proposed. Their main idea is the introduction of cyclic delays to the effective parts of OFDM symbols transmitted/received via separate antennas.

C59 The novel antenna diversity schemes increase the frequency-diversity in situations where the channel is relatively flat, or where the system bandwidth is small. Significant performance gain is thereby obtained.

C60 The principle can be applied at the transmitter, at the receiver, or at both.

C61 The IFFT/FFT blocks are not duplicated; thus the complexity increase is low.

C62 Applied at the receiver, the delay times can be optimized based on estimates of the channel transfer functions for each antenna.

C63 Complex-valued weight factors can be introduced.

R13 The development of optimum combining strategies and their performance comparison to conventional diversity techniques (which require multiple FFTs at the receiver) are topics for further research.

Appendix A – Correlation Coefficient for the Discrete Impulse Response

In order to relate the RMS delay spread τ_{rms} of a multipath channel described by its discrete impulse response (IR) to the frequency-domain level crossing rate (LCR_f), the correlation coefficient ρ_c has to be calculated from the IR. This is the goal of this appendix. The derivation starts with a review of the definitions of the channel's IR, transfer function (TF), and RMS delay spread (*cf.* (2-1), Section 2.2.2). We show in this appendix that, in the limit $F \rightarrow 0$, the correlation coefficient can be approximated by

$$\rho_c \cong 1 - (2\pi\tau_{rms}F)^2. \quad (\text{A-1})$$

It is remarkable that the channel IR has no influence on this equation, suggesting that – for the Rayleigh fading channel – the proportionality factor relating the LCR_f to τ_{rms} is independent of the channel model or channel IR. This is a very important observation for the application of the relation to channel measurements.

This result can be generalized to any band-limited, Rayleigh distributed, WSS stochastic process. It is proven that there exists a fixed function of r' , relating the level crossing rate to the second centralized moment of the normalized power spectrum (or periodogram) of the (zero-mean) complex Gaussian process underlying the Rayleigh process. This appendix focuses on the application of the relation to channel measurements, without losing generality.

A-1 Definitions

The static, time-dispersive (= frequency-selective) radio channel is described by its complex, lowpass equivalent IR

$$h(\tau) = \sum_{i=0}^{L-1} \beta_i e^{-j\theta_i} \delta(\tau - \tau_i), \quad (\text{A-2})$$

where $\{\beta_i\}$, $\{\theta_i\}$, and $\{\tau_i\}$ are the path gains, phases, and delay times, respectively, and L is the number of paths. The time-invariant TF is obtained from the IR via the Fourier transform.

$$H(f) = \sum_{i=0}^{L-1} \beta_i e^{-j[2\pi f\tau_i + \theta_i]} \quad (\text{A-3})$$

The similarity of this equation to Rice's sum of sinusoids suggests that $H(f)$ could be the underlying complex Gaussian process of any Rayleigh process $R(f) = |H(f)|$ (compare [1], (3.7-2) – (3.7-4)).

The RMS delay spread τ_{rms} is defined from the IR as

$$\tau_{rms} = \sqrt{\overline{\tau^2} - \bar{\tau}^2}, \quad (\text{A-4})$$

where $\bar{\tau}^k = \left(\sum_{i=0}^{L-1} \tau^k \beta_i^2 \right) / \left(\sum_{i=0}^{L-1} \beta_i^2 \right)$, $k = \{1, 2\}$. τ_{rms} is seen to be the second centralized moment of the normalized power delay profile. For simplified notation we introduce $p_i = \beta_i^2 / \left(\sum_{i=0}^{L-1} \beta_i^2 \right)$, yielding $\bar{\tau}^k = \sum_{i=0}^{L-1} \tau^k p_i$.

A-2 Calculation of the Correlation Coefficient

The correlation coefficient $\rho_c = |\psi_1|^2 / \psi_0^2$ is derived from the autocorrelation function of the underlying complex Gaussian process, $\psi_m = \frac{1}{2} E\{Z_n Z_{n+m}^*\}$. In the case of the frequency selective radio channel, this function is called the spaced-frequency correlation function, being

$$\psi_m = \frac{1}{2} E\{H(f), H^*(f + mF)\} = \frac{1}{2} \sum_{i=0}^{L-1} p_i e^{j2\pi\tau_i mF}, \quad (\text{A-5})$$

where F is the sampling *interval* in the frequency-domain.

To calculate ψ_m for one particular channel realization, the expectation operator should be considered as the average over the frequency f . But this equation also holds for a set of channels with common stochastic properties, or for any Rayleigh process, where the right-hand side of the equation is the Fourier transform of the process' (normalized) power spectrum (compare [1], eq. (3.7-11)). The squared magnitude of ψ_m is

$$\begin{aligned}
|\psi_m|^2 &= \psi_m \psi_m^* = \frac{1}{4} \left(\sum_{i=0}^{L-1} p_i e^{j2\pi\tau_i m F} \right) \left(\sum_{k=0}^{L-1} p_k e^{-j2\pi\tau_k m F} \right) \\
&= \frac{1}{4} \left[\sum_{i=0}^{L-1} p_i^2 + \sum_{i=0}^{L-1} \sum_{k=i+1}^{L-1} p_i p_k \left(e^{j2\pi(\tau_i - \tau_k) m F} + e^{-j2\pi(\tau_i - \tau_k) m F} \right) \right]. \quad (\text{A-6}) \\
&= \frac{1}{4} \left[\sum_{i=0}^{L-1} p_i^2 + 2 \sum_{i=0}^{L-1} \sum_{k=i+1}^{L-1} p_i p_k \cos 2\pi(\tau_i - \tau_k) m F \right]
\end{aligned}$$

For $F \rightarrow 0$ (for $|\psi_1|^2$) and $F = 0$ (for ψ_0^2), the cos-term can be replaced by $\cos x = 1 - x^2/2$ and $\cos 0 = 1$, respectively. This yields

$$\begin{aligned}
|\psi_1|^2 &\cong \frac{1}{4} \left[\sum_{i=0}^{L-1} p_i^2 + 2 \sum_{i=0}^{L-1} \sum_{k=i+1}^{L-1} p_i p_k \left(1 - 2\pi^2 (\tau_i - \tau_k)^2 f_s^2 \right) \right] \\
&= \frac{1}{4} \left[4\psi_0^2 - 4\pi^2 f_s^2 \sum_{i=0}^{L-1} \sum_{k=i+1}^{L-1} p_i p_k (\tau_i - \tau_k)^2 \right]. \quad (\text{A-7})
\end{aligned}$$

Noting that, due to the normalization of the $\{p_i\}$, $\psi_0^2 = \frac{1}{4}$, we obtain $\rho_c \cong 1 - 4\pi^2 F^2 \sum_{i=0}^{L-1} \sum_{k=i+1}^{L-1} p_i p_k (\tau_i - \tau_k)^2$. It remains to be shown that the double sum in this expression is equal to τ_{rms}^2 in order to get (A-1).

$$\begin{aligned}
\tau_{rms}^2 &= \sum_{i=0}^{L-1} \tau_i^2 p_i - \left(\sum_{i=0}^{L-1} \tau_i p_i \right) \left(\sum_{k=0}^{L-1} \tau_k p_k \right) \\
&= \sum_{i=0}^{L-1} \tau_i^2 p_i - \sum_{i=0}^{L-1} \tau_i^2 p_i^2 - 2 \sum_{i=0}^{L-1} \sum_{k=i+1}^{L-1} \tau_i \tau_k p_i p_k \quad (\text{A-8})
\end{aligned}$$

The double sum in ρ_c can be expanded to

$$\begin{aligned}
\sum_{i=0}^{L-1} \sum_{k=i+1}^{L-1} p_i p_k (\tau_i - \tau_k)^2 &= \sum_{i=0}^{L-1} \sum_{k=i+1}^{L-1} (\tau_i^2 + \tau_k^2) p_i p_k - 2 \sum_{i=0}^{L-1} \sum_{k=i+1}^{L-1} \tau_i \tau_k p_i p_k \\
&= \sum_{i=0}^{L-1} \sum_{k=0, k \neq i}^{L-1} \tau_i^2 p_i p_k - 2 \sum_{i=0}^{L-1} \sum_{k=i+1}^{L-1} \tau_i \tau_k p_i p_k, \quad (\text{A-9}) \\
&= \sum_{i=0}^{L-1} \tau_i^2 p_i (1 - p_i) - 2 \sum_{i=0}^{L-1} \sum_{k=i+1}^{L-1} \tau_i \tau_k p_i p_k
\end{aligned}$$

where the last step follows from $\sum_{k=0}^{L-1} p_k = 1$. The equivalence is readily seen from these expressions.

A-3 References

- [1] S. O. Rice, "Mathematical Analysis of Random Noise," *Bell Syst. Tech. J.*, vol. 23, pp. 282–332, July 1944; vol. 24, pp. 46–156, Jan. 1945

Appendix B – FD-Level Crossing Rate in the Presence of Noise

Goal of this appendix is to quantify the impact of noise on the frequency-domain (FD) level crossing rate (LCR_f). Moreover, it is desirable to separate the channel's and the noise's contributions to the LCR_f .

B-1 Derivation of the FD-Level Crossing Rate

The level crossing rate is related to second order statistical properties of the complex Gaussian random process underlying the mathematical channel model. In the case of the FD-channel model, this random process is the channel transfer function without the line-of-sight component ρ , written as $H'(f) = \rho H(f) + j_i H(f)$. The required parameters can be calculated from the auto-covariance of the channel's TF, $\phi_{H'}(\Delta f)$ (eq. (3-34), without ρ^2):

$$\begin{aligned} \tilde{\phi}_{H'}(\Delta f) &= \phi_{H'}(\Delta f) + P_N \text{sinc}(\Delta f / F); \\ \phi_{H'}(\Delta f) &= \Pi \left[\tau_1 \text{sinc}(\tau_1 \Delta f) e^{-j\pi\tau_1 \Delta f} + \frac{e^{-j2\pi\tau_1 \Delta f}}{\gamma + j2\pi\Delta f} \right], \end{aligned} \quad (\text{B-1})$$

where $\{\Pi, \tau_1, \gamma, \rho\}$ are parameters of the FD-channel model (see Section 2.3.2), P_N is the variance of the additive noise process (see Section 3.4.1), and F is the FD sampling interval. For notational convenience we introduce $u = \tau_1 \gamma$, specifying the 'shape' of the delay power spectrum of the channel, and $u_1 = u + 1$, $u_2 = u^2 / 2 + u + 1$, and $u_3 = u^3 / 3 + u^2 + 2u + 2$. Furthermore, the normalized noise power $N' = P_N / (2\psi_0) = P_N \gamma / (\Pi u_1)$ is used.

In order to obtain the LCR_f , we have to evaluate the first derivative of $\phi_{,H',H'}(\Delta f)$ at

$\Delta f = 0$, written $\dot{\phi}_0$, and the second derivative of $\phi_{r,H}(\Delta f)$, written $\ddot{\psi}_0$, where $\phi_H(\Delta f) = 2[\phi_{r,H}(\Delta f) + j\phi_{r,H_i,H}(\Delta f)]$ ([1]–[3]; see Section 3.2.1). Due to the noise's symmetric spectrum, $\dot{\phi}_0$ is not influenced by the additive noise ($\dot{\phi}_0 = -\pi\Pi u_2/\gamma^2$), and $\ddot{\psi}_0$ becomes

$$\ddot{\psi}_0 = \ddot{\psi}_0 - \frac{\pi^2}{6} \frac{N}{F^2} = -2\pi^2 \frac{\Pi u_3}{\gamma^3} - \frac{\pi^2}{6} \frac{N'\Pi u_1}{F^2\gamma}. \quad (\text{B-2})$$

It is evident from this equation that the sampling interval F has an important influence on this expression. Increasing F by a certain factor has the same effect as decreasing the noise power N' by the squared factor (while $N' \ll 1$, to be exact).

Using an expression from [3], the LCR_f is written

$$\tilde{N}_R(r) = \frac{r\sqrt{2\tilde{\beta}}}{\pi^{3/2}\tilde{\psi}_0} e^{-\frac{r^2+\rho^2}{2\tilde{\psi}_0} \pi/2} \int_0^{\pi/2} \cosh\left(\frac{r\rho}{\tilde{\psi}_0} \cos\theta\right) \left\{ e^{-(\tilde{\alpha}\rho \sin\theta)^2} + \sqrt{\pi}\tilde{\alpha}\rho \sin(\theta) \text{erf}(\tilde{\alpha}\rho \sin\theta) \right\} d\theta, \quad (\text{B-3})$$

where $\tilde{\alpha} = -\frac{\dot{\phi}_0}{\tilde{\psi}_0\sqrt{2\tilde{\beta}}}$, $\tilde{\beta} = -\ddot{\psi}_0 - \frac{\dot{\phi}_0^2}{\tilde{\psi}_0}$, and $\tilde{\psi}_0 = \frac{1}{2}\tilde{\phi}_{H'}(0) = \frac{1}{2}\Pi u_1/\gamma(1+N')$. This equation

can be evaluated straightforwardly. However, in order to separate the influence of noise on the LCR_f , two approximations are introduced.

B-2 Approximation 1

For simplifying the expressions involved, it is appropriate to assume that $N' \ll 1$, i.e. $(1+N') \cong 1$, yielding $\tilde{K} \cong K$, $\tilde{P}_0 \cong P_0$, $\tilde{r}' \cong r'$, and $\tilde{\psi}_0 \cong \psi_0$. Analytical results (see [4]) have shown that this approximation causes errors below 1 % at practical values of r' , and for $N' \leq 0.01$. As in Section 3.2.1, we define the variables $\{a', b, c, d\}$ from the elementary terms of (B-3). With the above approximations and the definitions from Sections 2.3.3 and 3.4.1, these are

$$a' = \frac{r\sqrt{2\tilde{\beta}}}{\pi^{3/2}\psi_0} = \frac{4}{\sqrt{\pi}} r' \sqrt{K+1} \sqrt{\left(\frac{u_3}{u_1} - \frac{u_2^2}{u_1^2}\right) \frac{1}{\gamma^2} + \frac{N'}{12F^2}} \quad (\text{B-4a})$$

$$b = \frac{r^2 + \rho^2}{2\psi_0} = r'^2 (K+1) + K \quad (\text{B-4b})$$

$$c = \frac{r\rho}{\psi_0} = 2r' \sqrt{K(K+1)} \quad (\text{B-4c})$$

$$d = \tilde{\alpha}\rho = -\sqrt{K}u_2 / \sqrt{u_1u_3 - u_2^2 + \frac{N'\gamma^2}{12F^2}u_1^2}. \quad (\text{B-4d})$$

The terms with the factor N'/F^2 in $\{a', d\}$ account for the noise's influence. These are

also the expressions that depend on τ_{rms} , since τ_{rms} is proportional to $1/\gamma$ (cf. Section 2.3.3)

$$\tau_{rms} = \frac{1}{\gamma} \sqrt{\frac{1}{K+1} \frac{u_3}{u_1} - \frac{1}{(K+1)^2} \frac{u_2^2}{u_1^2}}. \quad (\text{B-5})$$

Analytical evaluations of eq. (B-3) have shown rather small impact of the noise-term on the integral. For $0 \leq \Xi = N'/(F\tau_{rms})^2 \leq \infty$, the integral changes by about 50 % for $K = 10$ and $u = \infty$, and even less for lower K-factors and lower values of u .

Because of the small influence of the rest of the equation, we shall concentrate on the term a' to investigate the relation of the LCR_f and τ_{rms} for the noise-afflicted case. Using (B-5), a' becomes

$$a' = \frac{4}{\sqrt{\pi}} r' (K+1)^{3/2} \sqrt{\frac{u_1 u_3 - u_2^2}{(K+1)u_1 u_3 - u_2^2} \tau_{rms}^2 + \frac{N'}{12F^2} \frac{1}{(K+1)^2}}, \quad (\text{B-6})$$

leading to an expression of the following form for the LCR_f

$$\tilde{N}_R^{(a1)}(r') = \sqrt{A \tau_{rms}^2 + \frac{N'}{F^2} B} \cdot g(r', K, u, \Xi). \quad (\text{B-7})$$

As mentioned above, the factor $g(r', K, u, \Xi)$, which includes the integral expression, is mainly determined by the parameters $\{r', K, u\}$; it hardly changes when Ξ is varied between 0 and ∞ .

B-3 Approximation 2

Studying the asymptotic behavior of (B-3) in the limits $\tau_{rms}^2 \gg \frac{B N'}{A F^2}$ and $\tau_{rms}^2 \ll \frac{B N'}{A F^2}$

leads to the second simplification. In these limits, the sum-of-root expression of (B-7) can be replaced by the root of only one of the two terms. The first case means that the noise is negligible and yields the known proportionality between LCR_f and τ_{rms} (see (3-5))

$$\begin{aligned} \tilde{N}_R^{(a1)}(r' | N' = 0 \text{ or } \tau_{rms} \rightarrow \infty) = \\ \tau_{rms} \sqrt{A} \cdot g(r', K, u, \Xi = 0) = \tau_{rms} f(K, u, r'). \end{aligned} \quad (\text{B-8})$$

The second case is interpreted as the noise becoming dominant for the LCR_f , thus no relation between the LCR_f and τ_{rms} is evident in the following equation. As a result, the estimation of τ_{rms} must fail for such a measurement.

$$\begin{aligned} \tilde{N}_R^{(a1)}(r' | N' \rightarrow \infty \text{ or } \tau_{rms} = 0) = \\ \frac{\sqrt{N'B}}{F} g(r', K, u, \Xi = \infty) = \frac{\sqrt{N'}}{F} h(r', K) \end{aligned} \quad (\text{B-9})$$

It can be shown that $\tau_{rms} = 0$ (or $\Xi \rightarrow \infty$) yields $d = 0$, which eliminates from $g(r', K, u, \Xi = \infty)$ the dependency on u ⁽²⁴⁾. Thus the LCR_f is solely determined by the noise parameters and the K-factor.

Bringing $g(r', K, u, \Xi)$ for these two special cases under the square root, i.e.

$$\begin{aligned} \tilde{N}_R^{(a2)}(r') &= \sqrt{A \tau_{rms}^2 g^2(r', K, u, \Xi = 0) + B \frac{N'}{F^2} g^2(r', K, u, \Xi = \infty)} = \\ &= \sqrt{\tau_{rms}^2 f^2(r', K, u) + \frac{N'}{F^2} h^2(r', K)} \end{aligned} \quad (\text{B-10})$$

results in an expression having the same asymptotic behavior (for $\tau_{rms} = 0$ and $\tau_{rms} \rightarrow \infty$) as (B-7). Comparing the two approximations numerically shows that, for any τ_{rms} and for most values of r' and u , the maximum relative error between them is (well) below 1 %. Only if $r' \ll 1$ or $r' < 0.5$ and $u > 1$, it increases up to ~4 %.

This yields the compact relation given by (B-10) and by (3-35), between the LCR_f , τ_{rms} and $\sqrt{N'}/F$.

B-4 References

- [1] S. O. Rice, “Mathematical Analysis of Random Noise,” *Bell Syst. Tech. J.*, vol. 23, pp. 282–332, July 1944; vol. 24, pp. 46–156, Jan. 1945.
- [2] S. O. Rice, “Statistical Properties of a Sine Wave Plus Random Noise,” *Bell Syst. Tech. J.*, vol. 27, pp. 109–157, 1948.
- [3] M. Pätzold, U. Killat, F. Laue and Y. Li, “On the Statistical Properties of Deterministic Simulation Models for Mobile Fading Channels,” *IEEE Trans. Veh. Technol.*, Vol. 47, No. 1, pp. 254–269, Feb. 1998.
- [4] K. Witrisal and A. Bohdanowicz, “Influence of Noise on a Novel RMS Delay Spread Estimation Method,” in Proc. *PIMRC 2000 (Symposium on Personal Indoor Mobile Radio Communications)*, London, Sept. 2000, pp. 560–566.

²⁴ To prove this statement, note that $\tau_1 = 0$ and $\gamma = \infty$, for $\tau_{rms} = 0$.

Appendix C – Analysis of Fine Timing-Offset Estimation

In this appendix, the performance of the fine-timing offset estimation technique outlined in Section 6.2.7 is analyzed. After a brief review of the method and introduction of the system model (Section C-1), we derive the estimation bias for Ricean (and Rayleigh) channels (Section C-2). Only in case of non-dispersive (AWGN) channels, the estimate is unbiased.

The standard deviation of the estimates is analyzed in Section C-3 for the AWGN channel, and in Section C-4 for Rayleigh channels. The Ricean case is not elaborated. However, the necessary modifications to the analysis are indicated.

C-1 Review of Estimation Technique and System Model

The OFDM system model in presence of a small timing synchronization error is given in Section 4.2.4.1. It is written as

$$y_{i,k} = x_{i,k} h_{i,k} e^{-j2\pi i \delta t / T_{FFT}} + n_{i,k} = x_{i,k} h_{i,k} e^{-j2\pi i \delta t' / N} + n_{i,k}, \quad (\text{C-1})$$

where δt and $\delta t'$ are the timing offsets in seconds and in samples, respectively. $\{x_{i,k}\}$ and $\{y_{i,k}\}$ are the transmitted and the received symbol constellations, $\{n_{i,k}\}$ are independent Gaussian noise samples, and $\{h_{i,k}\}$ are the channel coefficients, where i and k are the sub-carrier and symbol indices, respectively. The index i can take values in the range $i = \{-N/2, -N/2+1, \dots, N/2-1\}$. T_{FFT} is the FFT-period [s] and N is the number of FFT-points.

This system model assumes that no inter-symbol-interference is caused by the timing-offset. That is, the channel impulse response including the timing-offset must be shorter than the guard interval.

It is evident that a timing-offset gives rise to a progressive phase rotation of the signal

constellations. The phase rotation is zero at the center frequency and it linearly increases towards the edges of the frequency band. The method of estimating the remaining timing-offset (after coarse frame-synchronization) is based on detecting this progressive phase rotation.

Known data is differentially modulated on the training symbol (TS) in frequency-direction, as defined in Section 6.2.1. The first step towards the estimation of δt is the differential demodulation of the TS-data, written as

$$\Delta y_{n,l} = y_{l(n-1),TS}^* y_{ln,TS} = \Delta x_{n,l} h_{l(n-1),TS}^* h_{ln,TS} e^{j2\pi l \delta t / T_{FFT}} + x_{l(n-1),TS}^* h_{l(n-1),TS}^* e^{-j2\pi l(n-1)\delta t / T_{FFT}} n_{ln,TS} + x_{ln,TS} h_{ln,TS} e^{-j2\pi l n \delta t / T_{FFT}} n_{l(n-1),TS}^* + n_{ln,TS} n_{l(n-1),TS}^* . \quad (C-2)$$

In this equation, l is the frequency-separation between differentially modulated sub-carrier pairs. The data symbols carried on them are denoted $\Delta x_{n,l} = x_{l(n-1),TS}^* x_{ln,TS}$. The index $n = \{1, 2, \dots, N_m\}$ is another index on the sub-carriers carrying data²⁵, where N_m is the number of sub-carrier pairs. For the TS described in Section 6.2.1, $l = 2$, and $\{\Delta x_{n,l}\} = \{\pm 1\}$ (cf. Section 6.2.7). TS indicates OFDM symbols, which are used as training symbols.

It is seen that the phase of the data symbols is corrupted by noise, by the channel coefficients, and by the systematic phase-rotation due to the timing-offset. Note that the channel coefficients of adjacent sub-carriers are correlated, thus $h_{l(n-1),TS}^* h_{ln,TS} \cong |h_{ln,TS}|^2 \cong |h_{l(n-1),TS}|^2$ plus some (complex valued) noise.

The metric $M_{int}(e)$, which is used for integer frequency-offset correction, provides an efficient way of accurately estimating the timing-offset δt . Assuming that the integer frequency-offset has been corrected, the metric at its peak position is written

$$M_{int}(e_{opt}) = \sum_{n=1}^{N_m} m_n \Delta y_{n,l} . \quad (C-3)$$

As multiplying the symbols $\Delta y_{n,l}$ by the (conjugated) data sequence $m_n = \Delta x_{n,l}^*$ removes the phase modulation, this metric is an accumulation of the energy of all differentially demodulated symbols. Its phase corresponds to the phase offset induced by the timing-offset. Therefore, the estimate of the timing offset is derived from

$$\hat{\delta t} = \frac{T_{FFT}}{2\pi l} \angle M_{int}(e_{opt}) \text{ [s]} . \quad (C-4)$$

The channel also induces a systematic phase rotation leading to an estimation bias, as

²⁵ Note that with the notation used in (C-2), the sub-carriers are indexed from 0 to lN_m , not from $-N/2$ to $N/2-1$. This modified indexing largely simplifies the notation. It also (implicitly) introduces a systematic common phase rotation, which, however, does not have any effect on the problem under investigation.

analyzed in the following sub-section. The noise terms are zero-mean, i.e., they do not cause any systematic error.

C-2 Estimation Bias over Dispersive Channels

Unfortunately, the estimate of the timing offset (C-4) is corrupted by the channel TF, expressed by the product $h_{l(n-1),TS}^* h_{ln,TS}$ in eq. (C-2), which also causes a systematic phase offset. The expectation of that term is seen to be the spaced-frequency correlation function of the channel. For a wide sense stationary channel (in frequency-domain) it is written

$$E\{h_{l(n-1),k}^* h_{ln,k}\} = \phi_H(lF). \quad (\text{C-5})$$

Assuming a Ricean channel model with an exponentially decaying delay power spectrum and a line-of-sight (LOS) component at (excess) delay time $\tau = 0$, it is possible to relate this correlation function to channel parameters, namely, the RMS delay spread (τ_{rms}) and the Ricean K -factor (K). Using results from Chapter 2 (see eq. (2-22)), we obtain

$$\phi_H(lF) = \frac{P_0}{K+1} \left(K + \frac{1}{1 + j2\pi lF\tau_{rms}K_1} \right), \quad (\text{C-6})$$

where $K_1 = (K+1)/\sqrt{2K+1}$, and P_0 is the normalized received power $P_0 = E\{|h_{i,k}|^2\}$. The phase angle of this term is

$$\angle\{\phi_H(lF)\} = \text{atan} \frac{-2\pi lF\tau_{rms}K_1}{K[1+(2\pi lF\tau_{rms}K_1)^2]+1} \cong -\frac{2\pi l\tau_{rms}}{T_{FFT}\sqrt{2K+1}}. \quad (\text{C-7})$$

The approximation is based on the following relations.

The denominator in the atan-term can be simplified to $(K+1)$, because $(2\pi lF\tau_{rms}K_1)^2 \ll 1$ at small l . This relation is satisfied for OFDM systems whose design is based on a guard interval length $T_{GI} \leq T_{FFT}/4$. Remember that the guard interval itself is selected in order to cope with the dispersive channel, thus the maximum excess delay of the channel $\tau_{max} \leq T_{GI}$. For the exponentially decaying delay power spectrum, this maximum excess delay is given as (approx.) $\tau_{max} = 10\tau_{rms}K_1$ (see Section 2.3.3.3), hence, $10\tau_{rms}K_1 \leq T_{FFT}/4$, which yields with $F = 1/T_{FFT}$ that $F\tau_{rms}K_1 \leq 1/40$.

Secondly, $\text{atan}(x) \cong x$ is used, which is valid for $|x| \ll \pi/2$. In order to fulfill this condition, $2\pi l\tau_{rms}/T_{FFT} \ll \pi/2$ must be given, i.e., $\tau_{rms} \ll T_{FFT}/4l$. This is again proven via the above relations. Taking into consideration that $K_1 \geq 1$ leads to $\tau_{rms} \leq T_{FFT}/40$. That is, the approximation can be used for small l .

Due to this systematic phase offset, the timing-offset is biased by

$$E\{\hat{\delta t}\} \cong \delta t - \frac{\tau_{rms}}{\sqrt{2K+1}}, \quad (C-8)$$

in presence of a multipath channel with parameters τ_{rms} and K .

Note that correction for this bias minimizes the progressive phase-rotation induced by the channel. This is desirable, for instance, if differential detection in frequency-direction is applied (see Section 4.3). We also use this result in the investigation of the channel estimation scheme in Section 6.4.

As the start-time of the FFT-period is estimated too late by this algorithm, the maximum bias should be considered in the OFDM system design in order to prevent inter-symbol-interference. This is achieved by cyclically shifting the FFT-period (of the data symbols and the training symbol) so that it actually starts a few samples before the end of the guard interval (see Figure 6-11 in Section 6.2.7).

C-3 Estimation Variance on the AWGN Channel

Goal of this section is the derivation of the variance (and standard deviation) of the estimated timing offset for the case of the AWGN channel, where the channel transfer function is expressed as $h_{i,k} = 1$. The noise variance on the sub-carriers is written $E\{|n_{i,k}|^2\} = 2\sigma^2$. Furthermore, it is assumed that the magnitude of the data symbols is unity, i.e., $|x_{i,k}| = 1$. These definitions lead to the SNR per (modulated) sub-carrier being $SNR_{SC} = 1/(2\sigma^2)$.

The following considerations relate this SNR to the time-domain SNR, which is given in eq. (6-3). The total signal power $2\sigma_s^2$ is shared among N_{SC} active (modulated) sub-carriers, while the total noise power $2\sigma_n^2$ is distributed over the N FFT-points. Therefore,

$$SNR = \frac{2\sigma_s^2}{2\sigma_n^2} = \frac{N_{SC} \cdot 1}{N \cdot 2\sigma^2} = \frac{N_{SC}}{N} SNR_{SC}. \quad (C-9)$$

For deriving the standard deviation of the estimate $\hat{\delta t}$, we assume – without loss of generality – that the timing-offset is zero. Noise is therefore the only cause of a deviation of the metric $M_{int}(e_{opt})$ from the real axis. This leads to the following approximate expression for the desired standard deviation, where $\text{atan}(x) \cong x$ for $|x| \ll \pi/2$ was used.

$$\sigma_{\delta t} = \frac{T_{FFT}}{2\pi l} \sqrt{\text{var}\{\text{atan}[M_{int}(e_{opt})]\}} \cong \frac{T_{FFT}}{2\pi l} \frac{\sqrt{\text{var}\{\text{Im}[M_{int}(e_{opt})]\}}}{E[M_{int}(e_{opt})]} \quad (C-10)$$

The main problem is thus to calculate the variance of the imaginary part of $M_{int}(e_{opt})$.

Applying the above-introduced definitions, the metric $M_{\text{int}}(e_{\text{opt}})$ is written

$$M_{\text{int}}(e_{\text{opt}}) = \sum_{n=1}^{N_m} (x_{l(n-1),TS}^* + n_{l(n-1),TS}^*) (x_{ln,TS} + n_{ln,TS}) x_{l(n-1),TS} x_{ln,TS}^* = \sum_{n=1}^{N_m} (1 + x_{l(n-1),TS} n_{l(n-1),TS}^*) (1 + x_{ln,TS}^* n_{ln,TS}) \quad (\text{C-11})$$

For simplified notation, we introduce $n_n = n_{ln,TS} x_{ln,TS}^*$. Remember that $|x_{ln,TS}| = 1$, therefore, the variance of n_n is $2\sigma^2$, equal to the variance of $n_{ln,TS}$.

The next step is to isolate the imaginary part of $M_{\text{int}}(e_{\text{opt}})$, which follows from

$$M_{\text{int}}(e_{\text{opt}}) = \sum_{n=1}^{N_m} (1 + \text{Re}[n_{n-1}] - j \text{Im}[n_{n-1}]) (1 + \text{Re}[n_n] + j \text{Im}[n_n]). \quad (\text{C-12})$$

Note that both, the real and imaginary parts of $\{n_n\}$ are independent, zero-mean Gaussian random variables with variance σ^2 . Therefore, the expectation of the above expression is $E\{M_{\text{int}}(e_{\text{opt}})\} = N_m$.

Separating the imaginary part yields

$$\text{Im}[M_{\text{int}}(e_{\text{opt}})] = -\text{Im}[n_0] + \text{Im}[n_{N_m}] + \sum_{n=1}^{N_m} (\text{Re}[n_{n-1}] \text{Im}[n_n] - \text{Re}[n_n] \text{Im}[n_{n-1}]). \quad (\text{C-13})$$

The variance of this random variable is²⁶

$$\text{var}\{\text{Im}[M_{\text{int}}(e_{\text{opt}})]\} = 2\sigma^2 + 2N_m\sigma^4. \quad (\text{C-14})$$

We finally obtain with (C-10)

$$\sigma_{\delta i} \cong \frac{T_{\text{FFT}}}{2\pi l} \frac{\sqrt{2\sigma^2 + 2N_m\sigma^4}}{N_m} = \frac{T_{\text{FFT}}}{2\pi l} \frac{\sqrt{\text{SNR}_{\text{SC}} + N_m/2}}{N_m \text{SNR}_{\text{SC}}}. \quad (\text{C-15})$$

Replacing T_{FFT} by N (number of FFT-points) yields the standard deviation in samples.

A number of observations are made from (C-15). At high SNR ($\text{SNR}_{\text{SC}} \gg N_m/2$), the standard deviation decreases with $1/\sqrt{\text{SNR}_{\text{SC}}}$. At low SNR, it decreases with $1/\text{SNR}_{\text{SC}}$. The number of demodulated sub-carrier pairs N_m (at high SNR) and their separation l decrease the standard deviation proportionally. Note, however, that the SNR_{SC} decreases (at fixed SNR) if the number of modulated sub-carriers N_{SC} is increased (see eq. (C-9)). In total the standard deviation (at high SNR) can be reduced by a factor of

²⁶ The complete analysis has shown that the variance of the real part is not equal to the variance of the imaginary part. The former is given as $\text{var}\{\text{Re}[M_{\text{int}}(\text{opt})]\} = (2N_m - 1)2\sigma^2 + 2N_m\sigma^4$. In the expression for the imaginary part, many of the $\text{Im}[n_n]$ -terms are cancelled due to the negative sign in (C-12).

approximately \sqrt{q} , when l is increased by the factor q , while N_m (and N_{SC}) is decreased by $1/q$, keeping the SNR constant. That is, the estimation performance is better when a training symbol with less but farther spaced, sub-carriers is used. On the other hand, the unambiguous estimation range is thereby reduced.

Computational results are presented in Section 6.2.7 (Figure 6-10) for the proposed OFDM transmission scheme in modes I-qr and I-fr. It is seen from this figure that, for the given design of the training symbol and detection technique, the performance over the AWGN channel allows for an excellent standard deviation below 0.1 samples at an SNR of 10 dB.

The performance degrades, however, over multipath channels. This behavior has been anticipated, as it is generally hard to define an exact arrival time of a signal that has been transmitted over a time-dispersive channel. The error variance over Rayleigh fading channels is analyzed in the sub-section below.

C-4 Estimation Variance on Rayleigh Fading Channels

To simplify the analysis of the error variance due to the multipath channel, noise is neglected. The metric then becomes

$$M_{\text{int}}(e_{\text{opt}}) = \sum_{n=1}^{N_m} h_{l(n-1),TS}^* h_{l n,TS} e^{j2\pi l \delta t / T_{\text{FFT}}} . \quad (\text{C-16})$$

The expectation of this term demonstrates that the estimate, which is obtained from the phase of $M_{\text{int}}(e_{\text{opt}})$, is biased, since a systematic phase offset is introduced by the channel. This offset corresponds to the phase of the channel's spaced-frequency correlation function at lag lF , $\phi_H(lF)$ (see Section C-2). The phase is not equal to zero for an asymmetric channel delay profile, as for instance for an exponentially decaying delay spectrum (see Section 2.3.3.2). The expectation of $M_{\text{int}}(e_{\text{opt}})$ is

$$E\{M_{\text{int}}(e_{\text{opt}})\} = N_m E\{h_{l(n-1),TS}^* h_{l n,TS}\} e^{j2\pi l \delta t / T_{\text{FFT}}} = N_m \phi_H(lF) e^{j2\pi l \delta t / T_{\text{FFT}}} . \quad (\text{C-17})$$

For the analysis, we assume that the systematic phase rotation due to time-offset δt exactly cancels the phase rotation due to the channel. This is achieved by letting the time-offset be $\delta t = -T_{\text{FFT}} / (2\pi l) \angle \phi_H(lF)$. The estimation variance induced by the channel is now evident from deviations of the metric from the real axis. Thus, eq. (C-10) can be applied again to calculate the estimation variance.

For simplified notation, we introduce $h_n = h_{l n,TS} e^{-jn \angle \phi_H(lF)}$, which leads to

$$M_{\text{int}}(e_{\text{opt}}) = \sum_{n=1}^{N_m} h_{n-1}^* h_n , \quad (\text{C-18})$$

incorporating the above-mentioned time-offset. We furthermore separate the channel coefficients h_n into their real and imaginary parts, written $h_n = a_n + jb_n$. The correlation

functions

$$R_h[k] = E\{h_{n-k}^* h_n\} = \phi_H(lkF) e^{-jk\angle\phi_H(lF)} = E\{(a_{n-k} - jb_{n-k})(a_n + jb_n)\} = 2R_{aa}[k] + 2jR_{ab}[k] \quad (\text{C-19})$$

will be required in the analysis below.

Note the similarity of the problem analyzed to the problem of calculating the variance of a correlation function estimated from N_m samples of a discrete random process. These computations are for instance found in [1]. In our case, however, the variance of the imaginary part is of interest, which is very different to the variance of the complex correlation function that is given in [1].

The variance of the imaginary part of the metric is obtained from

$$E\{\text{Im}^2[M_{\text{int}}(e_{\text{opt}})]\} = E\left\{\text{Im}\left[\sum_{n=1}^{N_m} h_{n-1}^* h_n\right] \text{Im}\left[\sum_{m=1}^{N_m} h_{m-1}^* h_m\right]\right\} = E\left\{\sum_{n=1}^{N_m} (a_{n-1}b_n - a_n b_{n-1}) \sum_{m=1}^{N_m} (a_{m-1}b_m - a_m b_{m-1})\right\} = \sum_{n=1}^{N_m} \sum_{m=1}^{N_m} E\{a_{n-1}b_n a_{m-1}b_m + a_n b_{n-1} a_m b_{m-1} - a_{n-1}b_n a_m b_{m-1} - a_n b_{n-1} a_{m-1}b_m\} \quad (\text{C-20})$$

Discussing Rayleigh fading channels, the variables a_n and b_n are real-valued, zero-mean Gaussian random variables. We can therefore apply [2]

$$E\{wxyz\} = E\{wx\}E\{yz\} + E\{wy\}E\{xz\} + E\{wz\}E\{xy\}, \quad (\text{C-21})$$

which leads to

$$E\{\text{Im}^2[M_{\text{int}}(e_{\text{opt}})]\} = 2 \sum_{k=-(N_m-1)}^{N_m-1} (N_m - |k|) \times \{2R_{ab}^2[1] - R_{ab}[k+1]R_{ab}[k-1] - R_{aa}[k+1]R_{aa}[k-1] + R_{aa}^2[k] + R_{ab}^2[k]\} \quad (\text{C-22})$$

where $k = m - n$. Finally, the variance of the imaginary part of the metric is written as

$$\text{var}\{\text{Im}[M_{\text{int}}(e_{\text{opt}})]\} = E\{\text{Im}^2[M_{\text{int}}(e_{\text{opt}})]\} - E^2\{\text{Im}[M_{\text{int}}(e_{\text{opt}})]\} = \frac{1}{2} \sum_{k=-(N_m-1)}^{N_m-1} (N_m - |k|) \{[R_h[k]]^2 - \text{Re}(R_h[k+1]R_h^*[k-1])\} \quad (\text{C-23})$$

This expression leads to the standard deviation with eqs. (C-10), (C-17), (C-19), and (C-6). Noise can be re-introduced by adding the error variances due to the channel and due to the noise. Independence of the noise processes has to be assumed thereby.

Computational results are depicted and discussed in Section 6.2.7, Figure 6-10.

C-5 References

- [1] C.W. Therrien, *Discrete Random Signals and Signal Processing*. Englewood Cliffs: Prentice Hall, 1992.
- [2] A. Papoulis, *Probability, Random Variables, and Stochastic Processes*, 3rd edition. New York: McGraw-Hill, 1991.

Appendix D – PDF of Wide-band Average Received Power

D-1 PDF of Average Received Power for Rayleigh Fading Channels

This section describes the derivation of the PDF of wide-band average received power of a frequency-selective Rayleigh fading channel. Starting with a discrete-frequency, complex lowpass equivalent TF, the normalized received power averaged over a given bandwidth is written

$$P_a = \frac{1}{N} \sum_{i=0}^{N-1} |H(iF)|^2, \quad (\text{D-1})$$

where F is the spacing between FD-samples, and N is the number of samples averaged. Thus the bandwidth considered is approximately $BW = NF$. In matrix notation, we get

$$P_a = \mathbf{x}^{*T} \mathbf{x}, \quad \mathbf{x} = 1/\sqrt{N} [H(0), H(F), \dots, H((N-1)F)]^T \quad (\text{D-2})$$

The elements of \mathbf{x} are identically distributed, zero-mean, complex Gaussian random variables (RV). They are correlated as specified by the spaced-frequency correlation function of the channel $\phi_H(\Delta f)$ (see Section 2.4.3 and (D-19)). It is assumed that the channel is wide-sense stationary (WSS) in the frequency domain, corresponding to the property of uncorrelated scattering in time domain. The complex-valued auto-correlation matrix for \mathbf{x} is defined as

$$\mathbf{R}_{\mathbf{xx}} = E\{\mathbf{xx}^{*T}\} = \begin{bmatrix} \phi_H(0) & \phi_H(F) & \cdots & \phi_H((N-1)F) \\ \phi_H(-F) & \phi_H(0) & \cdots & \phi_H((N-2)F) \\ \vdots & \vdots & \ddots & \vdots \\ \phi_H(-(N-1)F) & \phi_H(-(N-2)F) & \cdots & \phi_H(0) \end{bmatrix}. \quad (\text{D-3})$$

The eigenvalue decomposition can be applied to diagonalize the correlation matrix. This yields a vector $\mathbf{x}' = \mathbf{E}^{*T} \mathbf{x}$ of independent, zero-mean, complex Gaussian RVs (because the elements of \mathbf{x} are zero-mean Gaussian; see [1], pp. 50 ff.), where \mathbf{E} is a matrix whose columns are the eigenvectors. The eigenvalues λ_i are the variances of the elements of $\mathbf{x}' = [x'_0 \ x'_1 \ \dots \ x'_{N-1}]$. They are real-valued because the correlation matrix is hermitian symmetric (see e.g. [1], p. 50). With this decomposition, our original problem (D-2) becomes

$$P_a = \mathbf{x}'^{*T} \mathbf{E}^{*T} \mathbf{E} \mathbf{x}' = \mathbf{x}'^{*T} \mathbf{x}' = \sum_{i=0}^{N-1} |x'_i|^2, \quad (\text{D-4})$$

because $\mathbf{E}^{*T} \mathbf{E} = \mathbf{I}$. For simplification, terms with (variance) $\lambda_i \ll \max_k(\lambda_k)$ may be omitted because their contribution to the sum is insignificant.

The squared-magnitude of a complex Gaussian RV $p_i = |x'_i|^2$ with variance $2\sigma_i^2 = \lambda_i$ has an exponential PDF with characteristic equation ([2], pp. 41 ff.)

$$\Phi_{p_i}(\omega) = \frac{1}{1 - j2\omega\sigma_i^2} = \frac{1}{1 - j\omega\lambda_i}. \quad (\text{D-5})$$

The PDF of a sum of random variables is obtained from the product of their characteristic equations ([2], p. 36), i.e.

$$\Phi_{P_a}(\omega) = \prod_{i=0}^{N-1} \Phi_{p_i}(\omega) = \prod_{i=0}^{N-1} \frac{1}{1 - j\omega\lambda_i}. \quad (\text{D-6})$$

Applying the inverse Fourier transform yields the PDF²⁷

$$p_{P_a}(x) = \frac{1}{2\pi} \int_{-\infty}^{\infty} \Phi_{P_a}(\omega) e^{-j\omega x} d\omega = \sum_{i=0}^{N-1} \frac{A_i}{\lambda_i} \exp(-x/\lambda_i), \quad (\text{D-7})$$

where $A_i = 1 / \prod_{k=0, k \neq i}^{N-1} (1 - \lambda_k / \lambda_i)$.

The characteristic function is used to find the first and second moments of the PDF. These are

$$\begin{aligned} E\{P_a\} &= -j \left. \frac{d\Phi_{P_a}(\omega)}{d\omega} \right|_{\omega=0} = \sum_{i=0}^{N-1} \lambda_i \\ E\{P_a^2\} &= (-j)^2 \left. \frac{d^2\Phi_{P_a}(\omega)}{d\omega^2} \right|_{\omega=0} = \sum_{i=0}^{N-1} \lambda_i^2 + \left(\sum_{i=0}^{N-1} \lambda_i \right)^2 \\ \sigma_{P_a}^2 &= E\{P_a^2\} - (E\{P_a\})^2 = \sum_{i=0}^{N-1} \lambda_i^2 \end{aligned} \quad (\text{D-8})$$

²⁷ This result requires that all eigenvalues are different of another. It was obtained by replacing the product of fractions in eq. (D-6) by a sum of fractions.

D-1.1 Approximations

Some commonly used standard PDFs were compared to the exact PDF (D-7) for decreasing the number of parameters from N (i.e. number of eigenvalues) down to two or three. Another advantage of such approximations is that their parameters usually give a much better indication of the shape of the distribution function than a vector of eigenvalues (e.g. the mean and standard deviation of a log-normal PDF in dB). The fitting of the following PDFs was tested:

- The generalized chi-square distribution (having a non-integer degree of freedom)
- The log-normal distribution
- The Gaussian distribution

The Gaussian PDF (central limit theorem) is an appropriate approximation only in case of averaging over extremely large bandwidths. One problem is that the Gaussian PDF is not restricted to positive values, which must be the case for power values.

The Weibull distribution was tried as well, but it has a “thicker” tail than the generalized chi-square distribution, whose tail is already thicker than the exact distribution’s.

D-1.1.1 Generalized Chi-square Distribution (Squared Nakagami)

Because the PDF of a sum of n_f *independent*, identically distributed, squared Gaussian RVs is described by a chi-square distribution of n_f degrees of freedom, it is reasonable to try to describe the sum of *dependent* squared Gaussian RVs by a chi-square PDF with a generalized (non-integer) n_f -parameter. The chi-square PDF is written as

$$p_Y(y) = \frac{1}{\sigma^{n_f} 2^{n_f/2} \Gamma(n_f/2)} y^{n_f/2-1} \exp(-y/2\sigma^2), \quad y \geq 0. \quad (\text{D-9})$$

The parameter σ in this equation is the standard deviation of the underlying Gaussian RVs.

It can be shown that this PDF is equivalent the PDF of a *squared* Nakagami random variable: (It is noted that the Nakagami distribution is an amplitude PDF, thus squaring makes sense to obtain a power PDF.) The Nakagami distribution is written [2]

$$p_R(r) = \frac{2}{\Gamma(m)} \left(\frac{m}{\Omega} \right)^m r^{2m-1} e^{-mr^2/\Omega}, \quad (\text{D-10})$$

where Ω and m are defined as

$$\begin{aligned} \Omega &= E\{R^2\} \\ m &= \Omega^2 / E\{(R^2 - \Omega)^2\} \end{aligned} \quad (\text{D-11})$$

The ratio of moments m is called the fading figure. The PDF of the squared amplitude $Y = R^2$ is thus

$$p_Y(y) = \frac{1}{\Gamma(m)} \left(\frac{m}{\Omega} \right)^m y^{m-1} e^{-my/\Omega}. \quad (\text{D-12})$$

It can be seen that this distribution is equivalent to a chi-square distribution with $2m$ degrees of freedom (i.e. $m = n_f/2$), substituting for $\Omega/m = 2\sigma^2$.

The general method used for fitting two analytical PDFs compares their first ν moments, where ν is the number of free parameters to be determined. In case of the generalized chi-square PDF, the number of parameters is two, n_f and σ . The first and second moments are:

$$\begin{aligned} E\{Y\} &= n_f \sigma^2 (= \Omega) \\ E\{Y^2\} &= 2n_f \sigma^2 + n_f^2 \sigma^4 \\ \sigma_Y^2 &= E\{(Y - E\{Y\})^2\} = 2n_f \sigma^2 (= \Omega^2 / m) \end{aligned} \quad (\text{D-13})$$

It is seen that these two moments correspond to the definition of Ω and m of the Nakagami distribution (see expressions in brackets and (D-11)). The fitting is accomplished by comparing these expressions to equations (D-8).

D-1.1.2 Log-normal PDF

Parameters for the log-normal PDF can be obtained in two different ways. Method number one matches the first two moments of the exact PDF (see eqs. (D-8)) to the first two moments of the log-normal PDF (moments on linear scale). The log-normal PDF is written as²⁸

$$f_z(z) = \frac{1}{\sigma_{\ln} z \sqrt{2\pi}} \exp\left(-(\ln z - m_{\ln})^2 / 2\sigma_{\ln}^2\right), \quad (\text{D-14})$$

its first and second moments are

$$\begin{aligned} E\{Z\} &= \exp(m_{\ln} + \sigma_{\ln}^2/2) \\ E\{Z^2\} &= \exp(2m_{\ln} + 2\sigma_{\ln}^2) \end{aligned} \quad (\text{D-15})$$

Comparing these expressions to eqs. (D-8) finally yields

$$\begin{aligned} m_{\ln} &= \ln \left[\frac{\left(\sum_{i=0}^{N-1} \lambda_i\right)^2}{\sqrt{\sum_{i=0}^{N-1} \lambda_i^2 + \left(\sum_{i=0}^{N-1} \lambda_i\right)^2}} \right] \\ \sigma_{\ln}^2 &= \ln \left[\frac{\left(\sum_{i=0}^{N-1} \lambda_i^2\right)}{\left(\sum_{i=0}^{N-1} \lambda_i\right)^2} + 1 \right] \end{aligned} \quad (\text{D-16})$$

Since power values are often written in [dB], it is convenient to convert the parameters m_{\ln} and σ_{\ln} to dB-values. This is accomplished by using

$$\begin{aligned} m_{\ln} [\text{dB}] &= m_{\ln} 10 / \ln(10) \\ \sigma_{\ln} [\text{dB}] &= \sigma_{\ln} 10 / \ln(10) \end{aligned} \quad (\text{D-17})$$

²⁸ Computing the logarithm of realizations of a log-normal random process results in a Gaussian (normal) process. The parameters m_{\ln} and σ_{\ln} are the mean and standard deviation of this Gaussian random process.

It will be seen from the computational results that the log-normal PDF for these parameters does not match well at the lower tail of the PDF. Reason for this is the non-symmetry (skewness) of the log-normal PDF when it is investigated over a linear scale. It leads to a matching of the moments but does not take special care about values in the lower tail of the PDF.

An alternative approach transforms the exact PDF to a logarithmic scale in order to fit the resulting distribution to a Gaussian PDF. The parameters for this Gaussian PDF are obtained from integrating over the exact PDF (D-7) yielding

$$\begin{aligned} m_{\ln} &= E\{\ln(P_a)\} = -\gamma + \sum_{i=0}^{N-1} A_i \ln(\lambda_i) \\ \sigma_{\ln}^2 + m_{\ln}^2 &= E\{\ln^2(P_a)\} = 2 + \sum_{i=0}^{N-1} A_i [\ln^2(\lambda_i) - 2\gamma \ln(\lambda_i)] \end{aligned} \quad (\text{D-18})$$

The Euler constant $\gamma = 0.5772157$.

D-1.2 Analytical and Simulation Results

Since it was observed that the actual properties of the (small-scale) fading channel model do not severely influence the fading characteristics in the frequency domain²⁹, an exponentially decaying model for the DPS is used in all computer simulations and analytical computations.

For such a channel, with parameters $\{\tau_{rms}, K, P_0\}$, the correlation function required for calculating the eigenvalues is given as (see Section 2.4.3, eq. (2-22))

$$\phi_H(\Delta f) = E\{H^*(f)H(f + \Delta f)\} = \frac{P_0}{K+1} \left(K + \frac{1}{1 + j2\pi\Delta f\tau_{rms}K_1} \right), \quad (\text{D-19})$$

where $K_1 = (K+1)/\sqrt{2K+1}$, and Δf is the frequency-separation.

It is seen that the correlation function is uniquely defined by the $\tau_{rms} \cdot \Delta f$ product for a particular set of parameters $\{K, P_0\}$. The PDF of wide-band average power will thus depend on the product of τ_{rms} and the observed bandwidth (BW), and on the Ricean K-factor. P_0 just shifts the PDF along the power-axis. For Rayleigh fading channels, $K = 0$, hence we investigate here the PDF for different $\tau_{rms} \cdot BW$ products.

D-1.2.1 Computational Results

In Figure D-1, results are presented in form of CDFs with a “normal probability scale” on the ordinate and with a logarithmic (dB) scale on the abscissa. Log-normal PDFs thus appear as straight lines. Our analysis particularly concentrates on the lower tail of the distribution functions, which is most important in communications applications where one is usually interested in the probability that the average power is below a

²⁹ The characteristics defined by the level crossing rate, coherence bandwidth, and similar properties derived from second order stochastic parameters (see Section 3.2 and Appendix A), provided that the channel parameters $\{\tau_{rms}, K, P_0\}$ are not changed.

Table D-1: Errors and levels of the different approximations at probability values (CDF level) of 10^{-2} and 10^{-3} . All values in [dB].

CDF prob.	$\tau_{rms} \cdot BW$	exact PDF level	generalized chi-square		log-normal (log fit)		log-normal (linear fit)		Gaussian	
			level	error	level	error	level	error	level	error
10^{-2}	0.027	-19.1	-19.8	-0.7	-15.2	3.9	-9.9	9.2	–	–
	0.11	-15.7	-18.9	-3.2	-13.7	2.1	-9.7	6.0	–	–
	0.43	-10.1	-13.2	-3.1	-9.4	0.7	-8.0	2.1	–	–
	1.7	-5.6	-6.5	-1.0	-5.5	0.04	-5.1	0.5	–	–
	7.0	-2.8	-3.1	-0.2	-3.2	-0.3	-2.7	0.1	-4.0	-1.2
10^{-3}	0.027	-25.9	-28.7	-2.8	-19.3	6.6	-12.7	13.3	–	–
	0.11	-21.2	-27.5	-6.3	-17.4	3.8	-12.4	8.8	–	–
	0.43	-13.4	-19.1	-5.6	-12.1	1.3	-10.3	3.1	–	–
	1.7	-7.4	-9.2	-1.8	-7.2	0.2	-6.6	0.8	–	–
	7.0	-3.8	-4.2	-0.4	-4.2	-0.4	-3.6	0.2	-7.0	-3.2

certain threshold value. Shown are the computer simulation results (for 1000 channel realizations), the exact CDF obtained from eq. (D-7), the generalized chi-square approximation, two log-normal approximations, and the Gaussian PDF. All results are derived for an NRP of $P_0 = 0$ dB.

Firstly it is observed that the exact PDF does not fail to model the simulated distribution curve. The tail of the chi-square PDF is generally too thick, whereas the tails of the log-normal approximations are too thin.

It is seen that different approximations are more or less suitable for different $\tau_{rms} \cdot BW$ products. For very small bandwidths ($\tau_{rms} \cdot BW < 0.05$), the chi-square PDF for $n_f = 2$ degrees of freedom is an excellent choice, which is a trivial result since the average power will turn to a squared Rayleigh PDF in this case.

For larger bandwidths ($0.05 < \tau_{rms} \cdot BW < 4$), the log-normal PDF with parameters obtained using eq. (D-18) (designated ‘logfit’) yields the best results. This range of $\tau_{rms} \cdot BW$ is most likely encountered in practical systems like indoor wireless LANs.

For even higher bandwidths ($\tau_{rms} \cdot BW > 4$), the log-normal distribution with parameters obtained using eq. (D-16) gives better approximations at probability levels in the range of $[10^{-3} \dots 1]$. At lower probability values, the second log-normal PDF is still superior. The Gaussian PDF becomes satisfactory only for very large $\tau_{rms} \cdot BW$ products $\gg 10$.

Table D-1 lists the dB-values of the different PDFs at probability values of 10^{-2} and 10^{-3} , and the errors of the approximations. The error is defined as the distance in dB between the approximation and the exact curve at the specified probabilities.

From these results it is concluded that small approximation errors < 1 dB at 10^{-3} are only possible if $\tau_{rms} \cdot BW > 1$. Except for the exact PDF, there is no simple standard distribution function that models the wide band average power well in any case of $\tau_{rms} \cdot BW$. The lognormal (logfit) PDF gives good results over a large (and practical) range of parameters. Moreover, the parameters of the lognormal PDF are convenient to

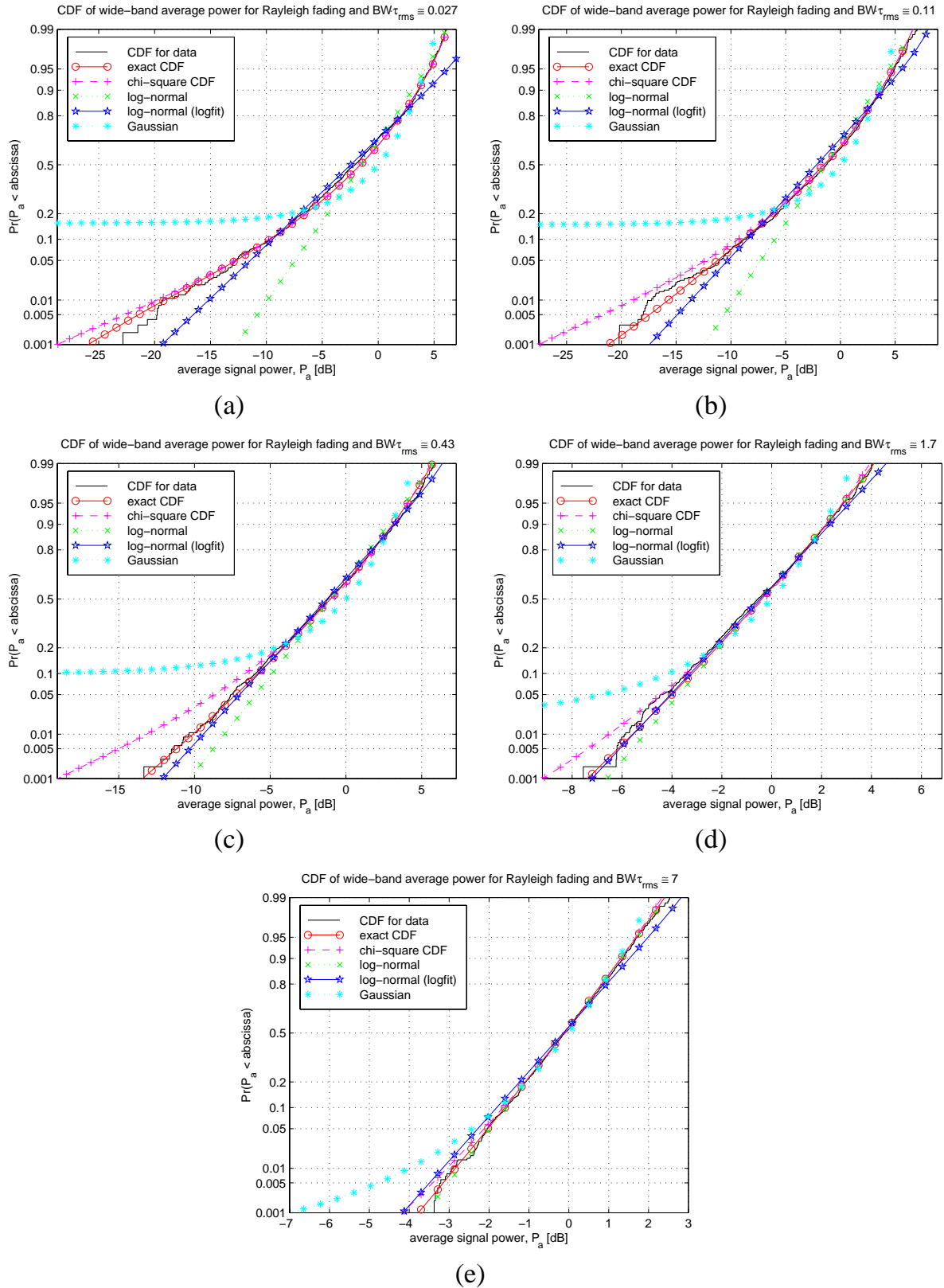


Figure D-1: CDFs of the wide-band average power for Rayleigh fading channels and different $\tau_{rms} \cdot BW$ (RMS delay spread times bandwidth) products

compare different results. If very accurate results are required, the exact PDF should be used if $\tau_{rms} \cdot BW < 1$. In this case, the number of eigenvalues remains small, which allows for a reasonably simple evaluation of the expressions involved (see eq. (D-7)).

D-2 PDF of Average Power for Ricean Fading Channels

The derivation of the PDF of wide-band average power for Ricean Channels follows the same principle as applied for the Rayleigh channel. The problem is defined equivalently, i.e., $\tilde{P}_a = \mathbf{x}^{*T} \mathbf{x}$ (compare eqs. (D-1), (D-2)). However, the elements of \mathbf{x} are now *non-zero mean*, identically distributed, correlated, complex Gaussian random variables. Again, an eigenvalue decomposition is applied to transform the random vector \mathbf{x} with correlated elements to a random vector $\tilde{\mathbf{x}} = \tilde{\mathbf{E}}^{*T} \mathbf{x}$ with uncorrelated and thus statistically independent elements³⁰. This is desirable for the derivation of the PDF from the sum of random variables. The matrix of eigenvectors $\tilde{\mathbf{E}}$ must be derived from the covariance matrix $\mathbf{C}_{\mathbf{xx}} = E\{(\mathbf{x} - \mathbf{m})(\mathbf{x} - \mathbf{m})^{*T}\}$ so that the elements of the resulting vector $\tilde{\mathbf{x}}$ are uncorrelated (\mathbf{m} is the vector of mean values of the elements of \mathbf{x}). The mean values of $\tilde{\mathbf{x}}$ are given as $\tilde{\mathbf{m}} = \tilde{\mathbf{E}}^{*T} \mathbf{m}$; its elements' variances are defined by the eigenvalues λ_i of $\tilde{\mathbf{E}}$. Again our original problem becomes (compare to eq. (D-4))

$$\tilde{P}_a = \tilde{\mathbf{x}}^{*T} \tilde{\mathbf{E}}^{*T} \tilde{\mathbf{E}} \tilde{\mathbf{x}} = \tilde{\mathbf{x}}^{*T} \tilde{\mathbf{x}} = \sum_{i=0}^{N-1} |\tilde{x}_i|^2. \quad (\text{D-20})$$

In case of Ricean channels, the summation terms are squared, *non-zero mean*, complex Gaussian RVs $\tilde{p}_i = |\tilde{x}_i|^2$. The characteristic function of such a RV is found as the characteristic equation of a non-central chi-square PDF of 2 degrees of freedom

$$\Phi_{\tilde{p}_i}(\omega) = \frac{1}{1 - j2\omega\sigma_i^2} \exp\left(\frac{j\omega|\tilde{m}_i|^2}{1 - j2\omega\sigma_i^2}\right) = \frac{1}{1 - j\omega\lambda_i} \exp\left(\frac{j\omega|\tilde{m}_i|^2}{1 - j\omega\lambda_i}\right), \quad (\text{D-21})$$

where σ_i^2 is the variance of the underlying Gaussian RV and \tilde{m}_i is the complex-valued mean of the i -th component of \mathbf{x} . The PDF of the sum of RVs (the average power) is obtained from the product of their characteristic equations,

$$\Phi_{\tilde{p}_a}(\omega) = \prod_{i=0}^{N-1} \Phi_{\tilde{p}_i}(\omega) = \prod_{i=0}^{N-1} \left[\frac{1}{1 - j\omega\lambda_i} \exp\left(\frac{j\omega|\tilde{m}_i|^2}{1 - j\omega\lambda_i}\right) \right]. \quad (\text{D-22})$$

To the knowledge of the author it is not possible to calculate the PDF for this characteristic equation analytically. A numerical implementation was thus realized, which applies the FFT algorithm for the required Fourier transform. A high number of FFT points is needed to obtain the PDF over a sufficiently high dynamic range (2^{15} points correspond to ~45 dB of power range).

The first three centralized moments were derived analytically by evaluating the derivatives of the characteristic equation.

³⁰ Only in case of Gaussian random variables it is given that uncorrelated random variables are also statistically independent (see [1], p. 58).

$$\begin{aligned}
m_{\tilde{P}_a} &= E\{\tilde{P}_a\} = \sum_{i=0}^{N-1} (\lambda_i + |\tilde{m}_i|^2) \\
\sigma_{\tilde{P}_a}^2 &= E\left\{\left(\tilde{P}_a - E\{\tilde{P}_a\}\right)^2\right\} = \sum_{i=0}^{N-1} (\lambda_i^2 + 2\lambda_i |\tilde{m}_i|^2) \\
\gamma_{1,\tilde{P}_a} &= E\left\{\left(\tilde{P}_a - E\{\tilde{P}_a\}\right)^3\right\} = \sum_{i=0}^{N-1} (2\lambda_i^3 + 6\lambda_i^2 |\tilde{m}_i|^2)
\end{aligned} \tag{D-23}$$

These expressions will be used for fitting standard PDFs to the complex exact equation.

D-2.1 Approximations

The fitting of the following PDFs was tested for the Ricean case:

- The generalized, non-central chi-square distribution
- The log-normal distribution
- The Gaussian distribution

D-2.1.1 Generalized, Non-central Chi-square Distribution

The reasoning for using this PDF as an approximation for the PDF of wide-band average power is equivalent to the reasoning given for the generalized (central) chi-square PDF in the Rayleigh case. Because of averaging *non-zero* mean Gaussian random variables, the *non-central* version of the chi-square distribution is selected, which describes the PDF of a sum of n_f magnitude squared Gaussian RVs with nonzero mean μ_i . It is written

$$p_Y(y) = \frac{1}{2\sigma^2} \left(\frac{y}{s^2}\right)^{(n_f-2)/4} e^{-(s^2+y)/2\sigma^2} I_{n_f/2-1}\left(\sqrt{y} \frac{s}{\sigma^2}\right) \quad y \geq 0, \tag{D-24}$$

where n_f is the degree of freedom, $s^2 = \sum_{i=0}^{n_f-1} \mu_i^2$, and $I_\alpha(x)$ is the α -th order modified Bessel function of the first kind. We consider a generalized version of this PDF, where n_f can be non-integer. The first three (centralized) moments are

$$\begin{aligned}
m_Y &= E\{Y\} = n_f \sigma^2 + s^2 \\
\sigma_Y^2 &= E\{(Y - E\{Y\})^2\} = 2n_f \sigma^4 + 4\sigma^2 s^2 \\
\gamma_{1,Y} &= E\{(Y - E\{Y\})^3\} = 8n_f \sigma^6 + 24\sigma^4 s^2
\end{aligned} \tag{D-25}$$

Two methods were assessed for obtaining the three unknown parameters of this PDF. The first one calculates s^2 from the sum of the magnitude squared means of the elements of $\tilde{\mathbf{x}}$, or equivalently, the sum of the means of the elements of \mathbf{x} (because the eigenvalue decomposition is a unitary transformation); i.e., $s^2 = \sum_{i=0}^{N-1} |\tilde{m}_i|^2 = \sum_{i=0}^{N-1} |m_i|^2$. Next, n_f and σ^2 are calculated by comparing the first two moments, yielding

$$\begin{aligned}
\sigma^2 &= \sum_{i=0}^{N-1} (\lambda_i^2 + 2\lambda_i |\tilde{m}_i|^2) / 2 \sum_{i=0}^{N-1} (\lambda_i + 2|\tilde{m}_i|^2) \\
n_f &= \sum_{i=0}^{N-1} (\lambda_i) / \sigma^2
\end{aligned} \tag{D-26}$$

Results for this method are designated “chi-square CDF, M1, 2” in the results section. The second method compares the first three moments, resulting in a quadratic equation for the parameter σ^2 .

$$\sigma_{1,2}^2 = \frac{\sigma_{\tilde{P}_a}^2}{2m_{\tilde{P}_a}} \pm \sqrt{\left(\frac{\sigma_{\tilde{P}_a}^2}{2m_{\tilde{P}_a}}\right)^2 - \frac{\gamma_{1,\tilde{P}_a}}{8m_{\tilde{P}_a}}} \quad (\text{D-27})$$

Usually, only one of the solutions is positive valued and thus taken for σ^2 . In some cases, however, a complex conjugate pair of solutions is obtained, when the expression under the root is negative. In these cases, only the real part, i.e., the term preceding the root, is taken. Having σ^2 , n_f and s^2 are obtained from

$$\begin{aligned} s^2 &= \frac{\gamma_{1,\tilde{P}_a}}{16\sigma^4} - \frac{m_{\tilde{P}_a}}{2} \\ n_f &= \frac{m_{\tilde{P}_a} - s^2}{\sigma^2} \end{aligned} \quad (\text{D-28})$$

Results are found in the next section, designated as “chi-square CDF, M1-3”.

D-2.1.2 Log-normal PDF

Exactly the same two methods as in the Rayleigh case are used. The first one compares the first two moments yielding

$$\begin{aligned} m_{\ln} &= \ln\left(\frac{E\{\tilde{P}_a\}}{\sqrt{E\{\tilde{P}_a^2\}}}\right) \\ \sigma_{\ln}^2 &= \ln\left(\frac{E\{\tilde{P}_a^2\}}{(E\{\tilde{P}_a\})^2}\right) \end{aligned} \quad (\text{D-29})$$

Again the PDF for these parameters does not fit well in the important lower tail, which can be seen from the results given in the following section (designated “log-normal, M1, 2”).

As above, method two directly calculates the parameters for the log-normal PDF from

$$\begin{aligned} m_{\ln} &= E\{\ln(\tilde{P}_a)\} = \int_0^\infty \ln(x) p_{\tilde{P}_a}(x) dx \\ \sigma_{\ln}^2 + m_{\ln}^2 &= E\{\ln^2(\tilde{P}_a)\} = \int_0^\infty \ln^2(x) p_{\tilde{P}_a}(x) dx \end{aligned} \quad (\text{D-30})$$

Numerical methods were applied to solve these equations. Results are designated as “log-normal (log-fitting)”.

D-2.2 Analytical and simulation results

As in the previous section, we compare the simulated cumulative distribution function to the exact theoretical one and various approximations (see Figure D-2 and Table D-2). It was tried to select typical and representative parameter pairs of Ricean K -factor and $BW \cdot \tau_{rms}$. The average power (normalized received power) was taken at 0 dB. The smallest $BW \cdot \tau_{rms}$ products correspond to a case very similar to flat fading, which could

be described exactly by the non-central chi-square distribution for $n_f = 2$ degrees of freedom. The bandwidth is multiplied by 4 and 16 yielding the other parameter sets investigated. Results are given for $K = \{2, 4, 10\} = \{3, 6, 10 \text{ dB}\}$.

It is seen from all plots, that the exact CDF appropriately describes the PDF of wide-band average power. Depending on the $BW \cdot \tau_{rms}$ product and the Ricean K-factor, different approximations are more or less appropriate.

From the plots for rather small bandwidths (Figure D-2a, d, g) a bad fitting of the log-normal distributions is seen, which appear as straight lines in these plots. However, increasing the bandwidth, the errors decrease at all K-factors. Generally, the errors also decrease when increasing K. As for the Rayleigh distribution, better results are obtained when the parameters for the log-normal are calculated by the second method, designated "log-fitting".

In all cases, the best approximations are obtained by the chi-square PDF, when the first three moments are used for deriving its parameters. Unfortunately, the quadratic equation that has to be solved for σ^2 yields a complex conjugate pair of solutions in some cases (however, with very small imaginary parts). Simply the real part was taken in these cases. They are marked in Table D-2 by *.

The comparison of the exact CDFs for different bandwidths and K-factors is depicted in Figure D-3.

Table D-2: Errors and levels of the different approximations at probability values (CDF level) of 10^{-2} and 10^{-3} . All values in [dB]. The * indicates cases, where the real part of the complex conjugate pair of solutions for σ^2 was taken (see text).

CDF prob.	K [dB]	$\tau_{rms} \cdot BW$	exact PDF		chi-square, M 1, 2		chi-square, M 1-3		log-normal (M 1, 2)		log-normal (log-fitting)		Gaussian	
			level	error	level	error	level	error	level	error	level	error	level	error
10^{-2}	3	0.081	-13.3	-15.2	-1.9	-14.3	-1.1	-7.5	5.8	-10.4	2.8	-	-	
		0.32	-8.1	-10.0	-1.9	-8.5	-0.4	-6.1	2.0	-7.1	1.0	-	-	
		1.3	-4.3	-4.8	-0.5	-4.6 *	-0.3	-3.8	0.5	-4.0	0.3	-7.8	-3.5	
	6	0.065	-10.2	-10.8	-0.6	-10.4	-0.2	-6.1	4.1	-7.9	2.4	-	-	
		0.26	-6.4	-7.3	-0.9	-6.5	-0.1	-4.9	1.4	-5.5	0.8	-	-	
		1.0	-3.4	-3.7	-0.3	-3.5 *	-0.1	-3.0	0.3	-3.2	0.2	-4.8	-1.4	
	10	0.045	-5.8	-5.9	-0.1	-5.9	-0.02	-4.3	1.6	-4.9	1.0	-12.5	-6.6	
		0.18	-4.1	-4.3	-0.3	-4.1	-0.03	-3.4	0.6	-3.7	0.4	-6.1	-2.1	
		0.72	-2.3	-2.4	-0.1	-2.3 *	-0.03	-2.1	0.2	-2.1	0.1	-2.7	-0.5	
10^{-3}	3	0.081	-18.2	-22.9	-4.7	-21.6	-3.4	-9.7	8.5	-13.4	4.8	-	-	
		0.32	-11.1	-15.5	-4.5	-12.2	-1.0	-7.9	3.2	-9.2	1.9	-	-	
		1.3	-5.8	-6.8	-1.1	-6.4 *	-0.6	-4.9	0.9	-5.2	0.6	-	-	
	6	0.065	-15.0	-18.1	-3.1	-16.7	-1.7	-7.9	7.1	-10.2	4.8	-	-	
		0.26	-8.8	-11.2	-2.4	-9.2	-0.3	-6.4	2.4	-7.2	1.6	-	-	
		1.0	-4.6	-5.2	-0.6	-4.8 *	-0.2	-4.0	0.6	-4.1	0.5	-9.6	-5.0	
	10	0.045	-8.7	-9.0	-0.3	-8.8	-0.07	-5.6	3.1	-6.3	2.4	-	-	
		0.18	-5.6	-6.3	-0.6	-5.7	-0.07	-4.5	1.1	-4.8	0.9	-	-	
		0.72	-3.1	-3.3	-0.2	-3.1 *	-0.04	-2.8	0.3	-2.8	0.2	-4.2	-1.1	

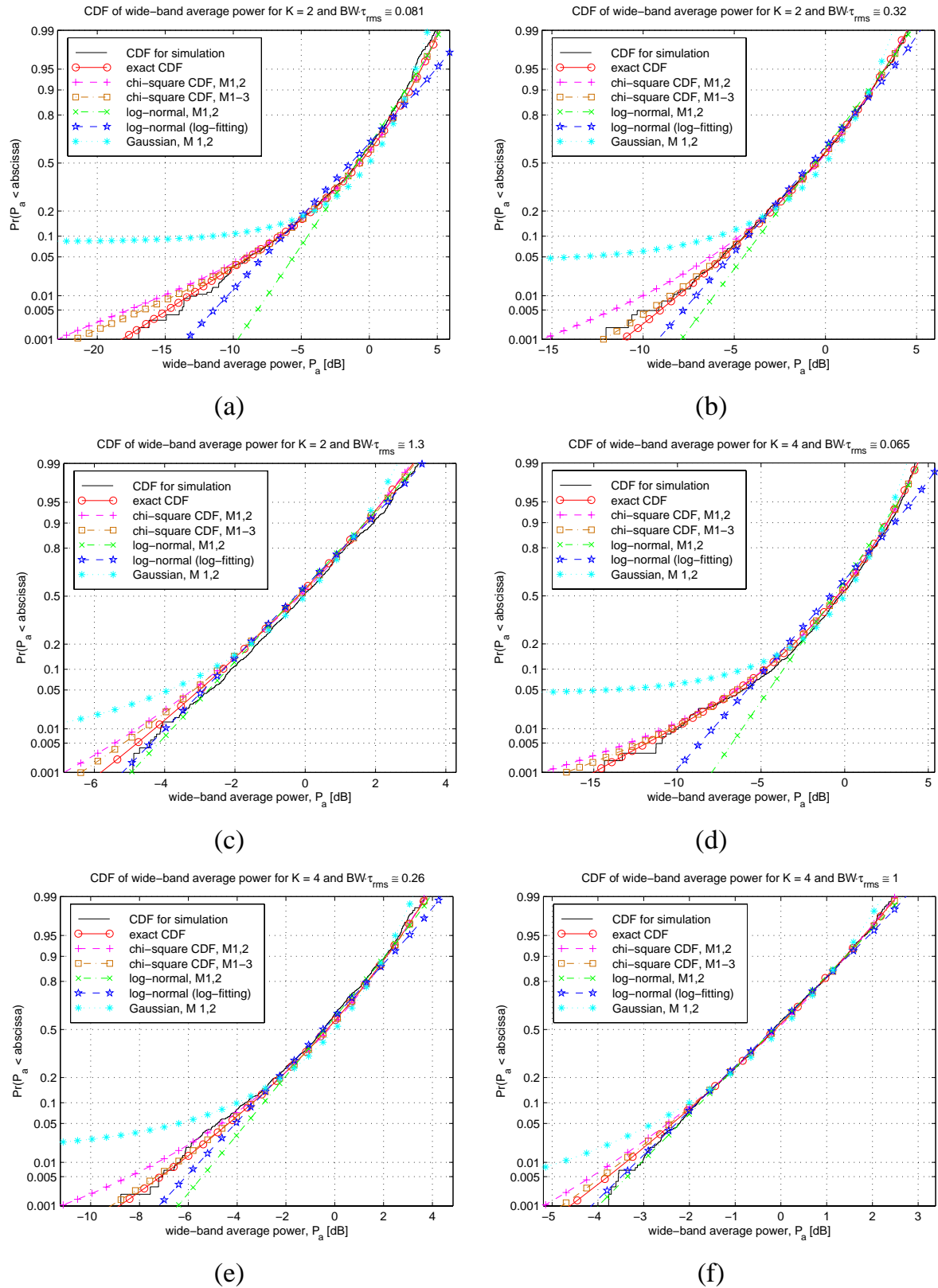


Figure D-2: CDFs of the wide-band average power for the Ricean fading case and different $BW \cdot \tau_{rms}$ products. Comparison of approximations and assessment of the exact equation.

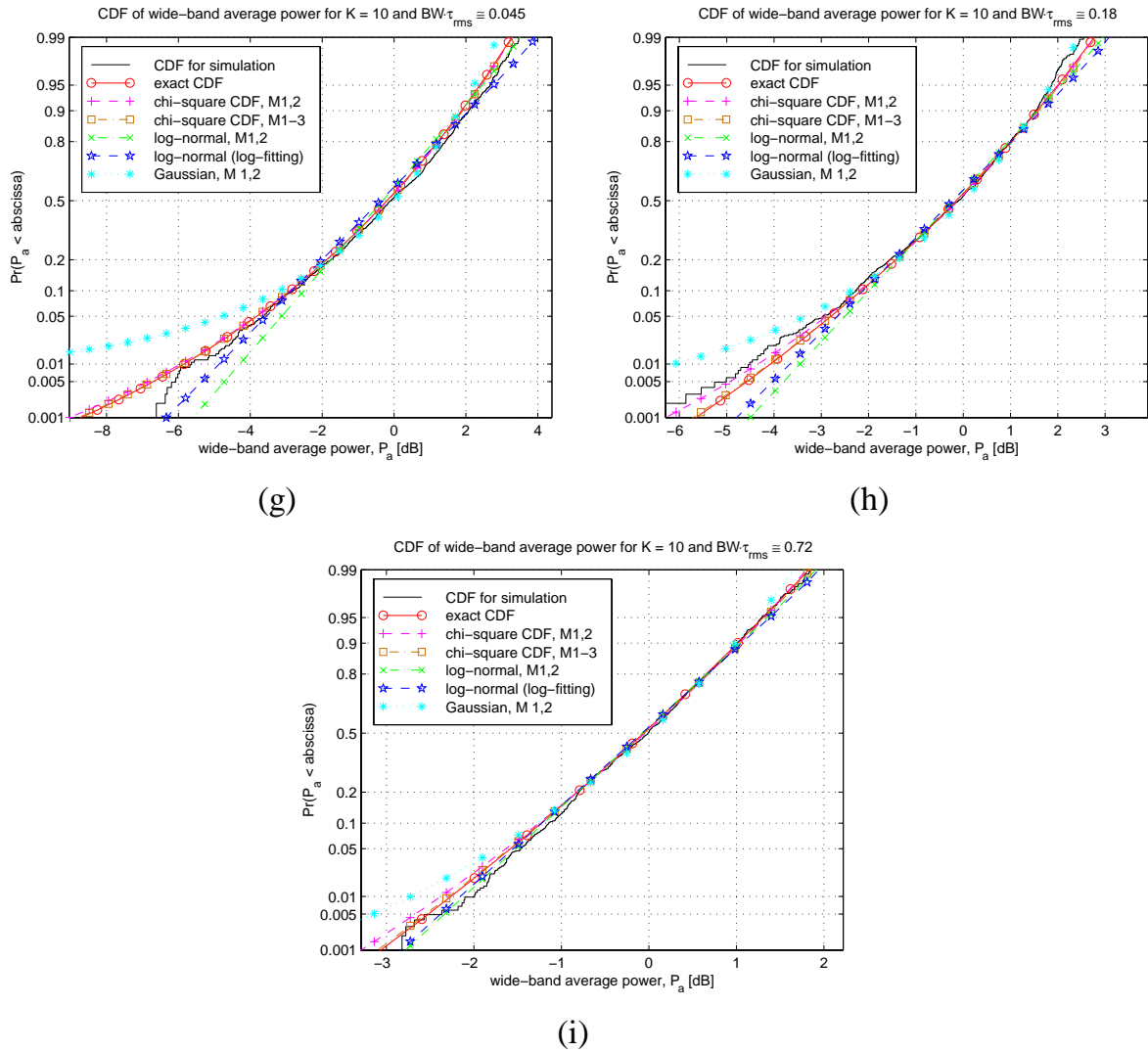


Figure D-2: (continued) CDFs of the wide-band average power for the Ricean fading case and different $BW \cdot \tau_{rms}$ products. Comparison of approximations and assessment of the exact equation.

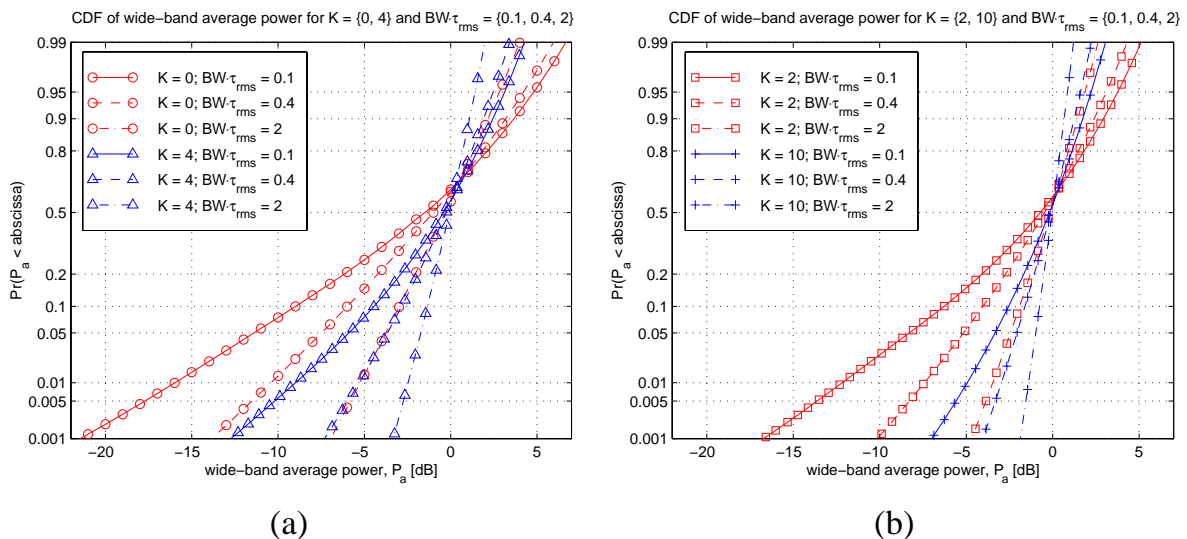


Figure D-3: Wide-band average power for various parameters K and $BW \cdot \tau_{rms}$.

D-3 References

- [1] C. W. Therrien, *Discrete Random Signals and Signal Processing*. Englewood Cliffs: Prentice Hall, 1992.
- [2] J. G. Proakis, *Digital Communications*, 3rd Edition. New York: McGraw Hill, 1995.

List of Acronyms

3G; 4G	3 rd ; 4 th generation mobile system
ABF	average bandwidth of fades
ADC	analog-to-digital converter
ARQ	automatic repeat request
ASIC	application specific integrated circuit
ATM	asynchronous transfer mode
AWGN	additive white Gaussian noise
BER	bit error rate
BPSK	binary phase shift keying
BS	base station
CDF	cumulative distribution function
CDMA	code division multiple access
CEWPC	center for wireless personal communications
CIR	carrier-to-interference ratio
COFDM	coded OFDM (orthogonal frequency division multiplexing)
COST	European co-operation in science and technical research
CW	continuous wave
DAC	digital-to-analog converter
DC	direct current
DFT	discrete Fourier transform
DPS	delay power spectrum
DSP	digital signal processor (processing)
FD	frequency-domain
FDMA	frequency division multiple access

FEC	forward error correction coding
FER	frame error rate
FIR	finite impulse response
FFT, FT	(fast) Fourier transform
FR, -fr	full rate
GI	guard interval
GIS	geographical information system
GSM	global system for mobile communications
HD	Hamming distance
HIPERLAN	high performance wireless LAN (European WLAN standard)
I/Q	in-phase/quadrature (channels of a complex baseband signal)
ICI	inter-carrier-interference
IDFT	inverse discrete Fourier transform
IF	intermediate frequency
IFFT	inverse fast Fourier transform
IMT-2000	international mobile telecommunications by 2000
IR	impulse response
IRCTR	international research center for telecommunications-transmission and radar
ISI	inter-symbol-interference
KT	Korea Telecom
LAN	local area network
LCR; LCR_f	level crossing rate; level crossing rate in the frequency domain
LO	local oscillator
LOS	line-of-sight
LSB	least significant bit
MAC	multiple access control
MBS	mobile broadband systems
MMAC	multimedia mobile access communications (Japanese WLAN standard)
MMSE	minimum mean-square-error
MSE	mean-square-error
MT	mobile terminal
NRP	normalized received power
OFDM	orthogonal frequency division multiplexing
PAPR	peak-to-average power ratio
PDF	probability density function

PDM	pulse duration modulation
PDP	power delay profile
PN	pseudo noise
PSD	power spectral density
PSK	phase shift keying
QAM	quadrature amplitude modulation
QoS	quality of service
QR	quarter rate
QPSK	quadrature phase shift keying
QWSSUS	quasi wide-sense stationary uncorrelated scattering
RACE	research into advanced communications systems in Europe
RAM	random access memory
RDS	RMS delay spread
RF	radio frequency
RMS	root mean square
RS	reset/set (flip-flop)
RV	random variable
RX	receive(r)
SC	sub-carrier
SNR	signal-to-noise ratio
TD	time-domain
TDD	time division duplex
TDMA	time division multiple access
TF	transfer function
TRX	transceiver
TU; TUD	technical university; TU-Delft
TX	transmit(ter)
UMTS	universal mobile telecommunications system
US	uncorrelated scattering
VCO	voltage controlled oscillator
VCXO	voltage controlled crystal oscillator
WLAN	wireless local area network
WSS	wide-sense stationary
WSSUS	wide-sense stationary uncorrelated scattering
XO	crystal oscillator

Publications by the Author

Journal Papers

- [1] K. Witrisal, Y.-H. Kim, and R. Prasad, "A new method to measure parameters of frequency-selective radio channels using power measurements," *IEEE Transactions on Communications*, vol. 49, no. 10, Oct. 2001, pp. 1788–1800.
- [2] K. Witrisal, "On estimating the RMS delay spread from the frequency-domain level crossing rate," *IEEE Communications Letters*, vol. 5, no. 7, July 2001, pp. 287–289.
- [3] K. Witrisal, Y.-H. Kim, and R. Prasad, "RMS delay spread estimation technique using non-coherent channel measurements," *IEE Electronics Letters*, vol. 34, no. 20, Oct. 1998, pp. 1918–1919.
- [4] K. Witrisal, Y.-H. Kim, L. P. Ligthart, and R. Prasad, "Computationally efficient antenna diversity techniques for OFDM using cyclic delays," to be published in *Korea Telecom Journal*.

Conference Papers

- [5] K. Witrisal, Y.-H. Kim, R. Prasad, L. P. Ligthart, "Pre-equalization for the Uplink of TDD OFDM Systems," in Proc. *PIMRC 2001 (12th International Symposium on Personal Indoor Mobile Radio Communications)*, San Diego, CA, Oct. 2001, pp. E-93–E-98.
- [6] K. Witrisal, Y.-H. Kim, R. Prasad, L. P. Ligthart, "Antenna diversity for OFDM using cyclic delays," in Proc. *SCVT-2001 (8th Symp. on Commun. and Vehic. Technol. in the Benelux)*, Delft (Netherlands), Oct. 2001, pp. 13–17.

- [7] K. Witrisal, "Impact of DC-offsets and Carrier Feed-through on Correlation-based Frequency Synchronization for OFDM," in Proc. *6th international OFDM-Workshop (InOWo)*, Hamburg (Germany), Sept. 2001, pp. 15-1–15-5.
- [8] K. Witrisal, G. Landman, and A. Bohdanowicz, "Practical Application of a Novel Method for Estimating the RMS Delay Spread from Power Measurements," in Proc. *EPMCC 2001 (4th European Mobile Communications Conference)*, Vienna (Austria), Feb. 2001.
- [9] K. Witrisal, K. Büke, Y.-H. Kim, R. Prasad, and L.P. Ligthart, "Air-interface Emulation for Wireless Broadband Communications Applied to OFDM," in Proc. *PIMRC 2000 (11th International Symposium on Personal Indoor Mobile Radio Communications)*, London, Sept. 2000, pp. 1251–1255.
- [10] K. Witrisal and A. Bohdanowicz, "Influence of Noise on a Novel RMS Delay Spread Estimation Method," in Proc. *PIMRC 2000 (11th International Symposium on Personal Indoor Mobile Radio Communications)*, London, Sept. 2000, pp. 560–566.
- [11] K. Witrisal, Y.-H. Kim, R. Prasad, and L.P. Ligthart, "Experimental Study and Comparison of OFDM Transmission Techniques," in Proc. *5th international OFDM-Workshop*, Hamburg (Germany), Sept. 2000, pp. 5-1–5-5.
- [12] K. Witrisal, R. Prasad, L. P. Ligthart, "OFDM Technology for Realizing Broadband Wireless Multimedia Communications," in Proc. *Korea Telecom International Symposium (KTIS '99)*, Seoul (Korea), Oct. 1999, pp. 307–312.
- [13] K. Witrisal, Y.-H. Kim, and R. Prasad, "A Novel Approach for Performance Evaluation of OFDM with Error Correction Coding and Interleaving," in Proc. *VTC'99-fall (IEEE Vehicular Technology Conference)*, Amsterdam, Sept. 1999, pp. 294–299.
- [14] J. M. M. de Nijs, K. Witrisal and R. Prasad, "Characterization and Simulation of the 18 GHz Radio Channel," presented at the *COST 259 7th Meeting of the Management Committee*, COST-259 TD(99)020, Thessaloniki (GR), Jan. 1999.
- [15] J. Purwaha, A. Mank, D. Matic, K. Witrisal and R. Prasad, "Wide-band Channel Measurements at 60 GHz in Indoor Environments," in Proc. *IEEE Benelux 6th Symposium on Vehicular Technology and Communications*, Brussels, Belgium, Oct. 1998.
- [16] R. El Hattachi, J. M. M. de Nijs, K. Witrisal and R. Prasad, "Characterization and Simulation of the 18 GHz Radio Channel," in Proc. *IEEE Benelux 6th Symposium on Vehicular Technology and Communications*, Brussels, Belgium, Oct. 1998.

- [17] K. Witralsal, Y.-H. Kim, and R. Prasad, "Frequency-Domain Simulation and Analysis of the Frequency-Selective Ricean Fading Radio Channel," in *Proc. PIMRC'98 (9th International Symposium on Personal Indoor Mobile Radio Communications)*, Boston, MA, Sept. 1998, pp. 1131–1135.
- [18] K. Witralsal, Y.-H. Kim, and R. Prasad, "Frequency-Domain Simulation and Analysis of the Frequency-Selective Radio Channel for the Performance Analysis of OFDM," in *Proc. 3. OFDM Fachgespräch*, Braunschweig (Germany), Sept. 1998.
- [19] K. Witralsal, Y.-H. Kim, H.-M. Pyo, and R. Prasad, "Wireless Broadband Communications in mm-Waves: Frequency-Domain Simulation of the Frequency Selective Radio Channel," in *Proc. 3rd ACTS Mobile Communications Summit*, Rhodes (Greece), 1998, pp. 885–887.

Reports

- [20] K. Witralsal, "Emulator Implementation – Software Update," *Project KWATT*, Supplementary Report, IRCTR S-009-01, Delft Univ. of Tech., Feb. 2001.
- [21] K. Witralsal, "Algorithm Development and System Proposal," *Project KWATT*, 6th (Final) Progress Report, IRCTR S-028-00 and IRCTR S-029-00, Delft Univ. of Tech., Nov. 2000.
- [22] K. Witralsal, "Emulation System Implementation," *Project KWATT*, 5th Progress Report, IRCTR S-015-00 and IRCTR S-016-00, Delft Univ. of Tech., May 2000.
- [23] K. Witralsal, "Demonstration and Emulation System Studies," *Project KWATT*, 4th Progress Report, IRCTR S-035-99 and IRCTR S-036-99, Delft Univ. of Tech., Nov. 1999.
- [24] K. Witralsal, "OFDM Performance Evaluation," *Project KWATT*, 3rd Progress Report, IRCTR S-015-99 and IRCTR S-016-99, Delft Univ. of Tech., May 1999.
- [25] K. Witralsal, "OFDM System Proposal," *Project KWATT*, 2nd Progress Report, IRCTR S-033-98 and IRCTR S-034-98, Delft Univ. of Tech., Nov. 1998.
- [26] K. Witralsal, "Channel Modeling at 60 GHz," *Project KWATT*, 1st Progress Report, IRCTR S-010-98 and IRCTR S-011-98, Delft Univ. of Tech., May 1998.

Relation to this Thesis

This Thesis is based, in part, on previously published work as listed above. The table below indicates the minor and major relations between these publications and the chapters of this thesis.

Relations between the publications and the chapters of this thesis. ●: major relation; ○: minor relation

<i>Publication</i>	<i>Ch. 2</i>	<i>Ch. 3</i>	<i>Ch. 4</i>	<i>Ch. 5</i>	<i>Ch. 6</i>	<i>Ch. 7</i>	<i>Ch. 8</i>
1	●	●					
2	○	●					
3	○	●					
4							●
5				○	○	●	
6							●
7					●		
8		●					
9				●	○		
10		●					
11				○	●		
12	○	○	○	●			○
13							●
14	○	●					
15	○	●					
16	○	●					
17	●	●					
18	○	○	●				
19	●			○			
20				●	●	●	
21				●	●	●	
22				●	○		
23				●	○		●
24				○			●
25			●	●			
26	●	●					

Samenvatting

Het doel van dit proefschrift: “OFDM Air-interface Design for Multimedia Communications”, vormt het onderzoek naar belangrijke aspecten voor de ontwikkeling van breedband radioverbindingen. “Orthogonal frequency division multiplexing” (OFDM) wordt beschouwd als een mogelijke oplossing voor de transmissie van data met extreem hoge snelheid over tijd-dispersieve radiokanalen. In OFDM wordt de datastroom opgedeeld in meerdere deelstromen welke met sterk verlaagde snelheid over parallelle sub-kanalen verzonden worden.

Het eerste deel van dit proefschrift behandelt de modellering van het tijd-dispersieve en frequentie-selectieve radio kanaal, op basis van Gaussische stochastische processen van de tweede orde. Een nieuwe methode wordt ontwikkeld voor de karakterisering van het radio kanaal. Hierbij wordt de “level crossing rate” van de frequentie-selectieve overdrachtsfunctie van het radiokanaal gebruikt om de “RMS delay spread” te schatten. Deze techniek maakt het mogelijk het radio kanaal te karakteriseren op basis van eenvoudige niet-coherente metingen waarin het vermogen als functie van de frequentie bepaald wordt.

De “Air-interface” en het “multiple access” schema van een op OFDM gebaseerd communicatiesysteem worden geïntroduceerd en onderzocht in deel twee van dit werk. De maximale data snelheid van 155 Mbit/s wordt bereikt in een optimaal radiokanaal bij een beperkte snelheid van de terminal (loopsnelheid). Draadloze computernetwerken zijn een typische toepassing voor dit systeem.

Algoritmen voor synchronisatie en kanaalschatting worden ontwikkeld en geëvalueerd. Hierbij wordt een bekend trainingssymbool gebruikt, welke periodiek in het begin van een vaste framestructuur verzonden wordt. De conclusie is dat robuuste en efficiënte synchronisatie en kanaalschatting – dit zijn kritische procedures in een OFDM ontvanger – mogelijk zijn, door gebruik te maken van een trainingssymbool,

waarbij slechts een kleine overhead geïntroduceerd wordt.

Een diepgaande analyse is gemaakt van een aantal onderwerpen op het gebied van synchronisatie: de schatting van de tijd-offset in dispersieve kanalen, en de invloed van “DC-offset” en “carrier feed-through” op een veel gebruikte frequentie-synchronisatie techniek. Voor het laatste probleem is een oplossing ontwikkeld.

Voor de “up-link” kan “pre-equalization” gebruikt worden in een “time-division duplexing (TDD)” frameformaat. Deze methode compenseert voor het frequentie selectieve gedrag van het radiokanaal, waarbij de detectie van data vereenvoudigd wordt. De synchronisatie wordt hierbij overwegend in de mobiele stations uitgevoerd. Dit betekent een distributie van de grote complexiteit die daarvoor nodig is. Er worden concepten geïntroduceerd, om een gelijkblijvend vermogen van het uitgezonden signaal te bereiken, en om de resterende synchronisatiestappen op te lossen.

De belangrijkste signaal verwerkingsalgoritmen van de OFDM zender-ontvangers zijn geïmplementeerd en geëvalueerd op een experimenteel systeem bestaande uit DSP borden. Het systeem werkt in real-time maar met een sterk gereduceerde datasnelheid.

Foutcorrigerende codering vormt een belangrijk onderdeel van OFDM systemen. Daarbij worden de datasymbolen goed over de “grote” bandbreedte van het OFDM signaal verdeelt om de frequentie-diversiteit te exploiteren. De foutenkans van een gecodeerd OFDM systeem is geëvalueerd. Hieruit volgt dat een grotere bandbreedte en een langere kanaal impulsresponsie (in een beperkte mate) tot betere resultaten leiden. Een nieuwe methode voor antenne-diversiteit wordt geïntroduceerd. Deze techniek kan de foutenkans met weinig toegevoegde complexiteit aanzienlijk verlagen bij een kleine bandbreedte van het radiokanaal of een korte impulsresponsie.

In het algemeen kan worden geconcludeerd dat OFDM een efficiënte en robuuste techniek is om data met hoge snelheid te verzenden. Enkele kritische implementatie-aspecten moeten daarbij opgelost worden, zoals bijvoorbeeld de lineariteit van versterkers, en de faseruis van oscillatoren.

Klaus Witrisal

Acknowledgements

I owe my gratitude to my supervisors, Prof. Leo Ligthart, Prof. Ramjee Prasad, and Dr. Gerard Janssen, who gave me all the support needed to finalize this thesis. Particularly, I wish to acknowledge the confidence of Gerard Janssen and Prof. Prasad in my abilities, when they initially encouraged me to come to Delft as a Ph.D. candidate, after working with me on my graduation project. Moreover, I am most grateful to Prof. Ligthart for taking over the task of the “promotor” after Prof. Prasad left the University, ensuring the continuity of my work. I wish to thank all my supervisors for their permanent encouragement and for their comments and discussions on my thesis and on my scientific papers.

Large parts of this work have been performed under a cooperative research project between Network Access Lab of Korea Telecom, Seoul, and the IRCTR (International Research Centre for Telecommunications-transmission and Radar) of TU Delft. This cooperation was a unique experience for me, as I had the opportunity of working with the friendly Korean people and discovering their culture. I am indebted to Korea Telecom and Delft University for providing the opportunity to carry out this research. I want to thank all the colleagues and students who have contributed to this work, particularly, Dr. Yong-Ho Kim of Korea Telecom, and Dr. Hodayoun Nikookar, Frans Bremer, Vladimir Jović, and Han Reijmers of Delft University. The implementation of the experimental platform was made possible through the support by the technical staff of the IRCTR.

I am thankful to the students who have made substantial contributions while working on their graduation projects or on internships. I also wish to recognize the support of the secretaries in organizational matters.

To my colleagues and friends at TU Delft I am grateful for numerous inspiring discussions – about the research work and about other topics – and for the pleasant environment they created. I would like to mention personally: Nicolas Petrochilos, Antonio Trindade, Dušan Matić, Adrian Bohdanowicz, Friedrich Roth, Marten Klok, Ton

Coenen, Jos Weber, and Mohinder Jankiraman, with whom I shared many thoughts, privately and professionally. I have experienced the Netherlands as a place where foreigners are appreciated and well integrated in the society.

The foundation for this Ph.D. study was laid during my undergraduate studies. I am most grateful to my parents for providing the opportunity to conduct the study of my choice and for their personal and financial support.

Last but not least, I wish to thank my beloved wife Silke for moving with me to the Netherlands four years ago. Thank you for sharing all the pleasant and difficult moments during this time. Without your mental support I had never been able to finalize this Ph.D. project.

Curriculum Vitae

Klaus Witrissal was born in Graz, Austria on September 24, 1972. He obtained his Dipl.-Ing. (Diplomingenieur; equivalent to M.Sc.) degree in Electrical Engineering (Electronics and Telecommunications) from Graz University of Technology in 1997. During his undergraduate studies, he had the opportunity of spending six months at the Telecommunications and Traffic Control Systems Group (TVS) of Delft University of Technology. This visit was enabled by the European Union's ERASMUS program for students exchange.

In Nov. 1997, Klaus joined Delft University of Technology as a research engineer in the CEWPC (Centre for Wireless Personal Communications), a sub-division of the IRCTR (International Research Centre for Telecommunications-transmission and Radar). From Nov. 1997 till Dec. 2000 he was the main researcher on a collaborative research project between the IRCTR and Korea Telecom in the field of wireless ATM transmission in the 60 GHz frequency band. In 2001, he has been working on his Ph.D. thesis, which mainly covers the topics treated in the Korea Telecom project.

Klaus was awarded with a best student paper award at the International Symposium on Personal Indoor and Mobile Radio Communications (PIMRC) in September 1998.

In April 2001, he represented Delft University of Technology at the "KIVF" Telecom Award, a prize given by the Royal Dutch Society of Engineers to a Ph.D. candidate working in the field of telecommunications.

Since Jan. 2002, Klaus is a project leader at AVL-Ditest in Graz, Austria, working on advanced diagnostics and test/measurement instruments for the automotive industry.